# Round-Robin Analysis of the Behavior of a 1:6-Scale Reinforced Concrete Containment Model Pressurized to Failure: Posttest Evaluations

Prepared by D. B. Clauss

Sandia National Laboratories

# Round-Robin Analysis of the Behavior of a 1:6-Scale Reinforced Concrete Containment Model Pressurized to Failure: Posttest Evaluations

Prepared by
D. S. Clauss

Sandia National Laboratories
Albuquerque, NM 87185

Previous reports in series:

NUREG/CR-4913, SAND87-0891, D. B. Clauss, "Round-Robin Pretest Analysis of a 1:6-Scale Reinforced Concrete Containment Model Subject to Static Internal Pressurization," Sandia National Laboratories, Albuquerque, NM, May 1987.

# ABSTRACT

In July 1987, a 1:6-scale model of a reinforced concrete containment building was pressurized incrementally to failure at a remote site at Sandia National Laboratories. The response of the model was recorded with more than 1000 channels of data (primarily strain and displacement measurements) at 37 discrete pressure levels. The primary objective of this test was to generate data that could be used to validate methods for predicting the performance of containment buildings subject to loads beyond their design basis.

Extensive analyses were conducted before the test to predict the behavior of the model. Ten organizations in Europe and the U.S. conducted independent analyses of the model and contributed to a report on the pretest predictions (NUREG/CR-4913). Predictions included structural response at certain predetermined locations in the model as well as capacity and failure mode.

This report discusses comparisons between the pretest predictions and the experimental results. Posttest evaluations that were conducted to provide additional insight into the model behavior are also described. The significance of the analysis and testing of the 1:6-scale model to performance evaluations of actual containments subject to beyond design basis loads is also discussed.

# TABLE OF CONTENTS

**LIST OF FIGURES**

## LIST OF FIGURES (Continued)

## LIST OF TABLES

# PREFACE

This report represents the culmination of an effort that began in October 1986. A large, diverse number of organizations from all over the world were involved. Our common objective was to predict and understand the behavior of a 1:6-scale model of a nuclear power plant containment building constructed of reinforced concrete that was pressurized to failure. The broader goal was to develop validated analytical methods that could then be used to accurately predict the performance of reinforced concrete containment buildings, in particular, capacity and failure mode. In the process, we learned much about the accuracy and sources of uncertainty in current analysis techniques.

Ten organizations in Europe and the U.S. conducted independent analyses of the model and contributed to a report on the pretest predictions (NUREG/CR-4913):

- Sandia National Laboratories (SNL), USA
- Argonne National Laboratory (ANL), USA
- Electric Power Research Institute (EPRI), USA
- Commissariat a L'Energie Atomique (CEA), France
- HM Nuclear Installations Inspectorate (NII), U.K.
- Comitato Nazionale per la ricerca e per lo sviluppo dell'Energia
    Nucleare e delle Energie Alternative (ENEA), Italy
- Atomic Energy Authority, Safety and Reliability Directorate (AEA), U.K.
- Gesellschaft für Reaktorsicherheit (GRS), FRG
- Brookhaven National Laboratory (BNL), USA
- Central Electricity Generating Board (CEGB), U.K.

In addition to these ten, Taiwan Electric Power Company (TEPCO) and Japan Atomic Energy Research Institute (JAERI) also conducted analyses of the reinforced concrete containment model. However, Sandia did not receive the results of these analyses before the test and therefore TEPCO and JAERI results are not included in the round-robin reports. Also, Brookhaven National Laboratory and the Central Electricity Generating Board did not participate in posttest evaluations, the latter due to manpower restraints associated with the time demands of the Sizewell and Hinkley Point power plants.

The current report is a companion to the pretest report, which provides much of the foundation and background material to what is contained herein.

# 1.0 EXECUTIVE SUMMARY

In the unlikely event of a severe accident, the pressure and temperature inside a containment building may significantly exceed the loads for which it was designed. Because containment buildings in light water reactor nuclear power plants are the last engineered barrier to the release of radioactive material, it is important to understand the functional limits of a containment for use in emergency preparedness, accident mitigation, and safety assessment. Testing and analyses of scale models of steel and reinforced concrete containments pressurized to failure have been conducted at Sandia National Laboratories as part of the Containment Integrity Programs, which are sponsored by the U.S. Nuclear Regulatory Commission (NRC). The ultimate objective of these programs is to develop test validated methods for evaluating the performance of light water reactor containment buildings subject to loads beyond the design basis.

The most recent test was conducted on a 1:6-scale model of a reinforced concrete containment building in July 1987. This model failed due to a large tear in the liner at 145 psig (1.0 MPa) or 3.15 times its design pressure of 46 psig (0.317 MPa). Extensive analyses were conducted of this model both before and after the test by a number of organizations in the U.S. and abroad. The pretest analyses and predictions for the capacity and failure mode of the 1:6-scale model were published in May 1987 (before the test) in NUREG/CR-4913. This final report on the round-robin analysis describes comparisons of the pretest predictions with the experimental results and posttest evaluations that have led to improvements in the analytical models and insights into the failure mechanisms.

The organizations that participated in this round-robin analysis represent a diverse group of regulators, national laboratories, and industry. Those that contributed to both the pretest predictions and posttest evaluations are listed below:

- Sandia National Laboratories (SNL), USA
- Argonne National Laboratory (ANL), USA
- Electric Power Research Institute (EPRI), USA
- Commissariat a L'Energie Atomique (CEA), France
- HM Nuclear Installations Inspectorate (NII), U.K.
- Comitato Nazionale per la ricerca e per lo sviluppo dell'Energia Nucleare e delle Energie Alternative (ENEA), Italy
- Atomic Energy Authority, Safety and Reliability Directorate (AEA), U.K.
- Gesellschaft für Reaktorsicherheit (GRS), FRG

In addition to those listed above, the Central Electricity Generating Board (CEGB), U.K., and Brookhaven National Laboratory (BNL), USA, also participated in the pretest analysis report. However, CEGB and BNL did not contribute to the posttest evaluations. Analyses were also conducted by Japan Atomic Energy Research Institute and Taiwan Electric Power Company (both organizations have information exchange agreements with NRC), but because they did not begin their involvement until much later than the others, they were not formal participants in the round-robin effort.

SNL and NRC invited organizations to collaborate on the 1:6-scale model analysis beginning in early 1986. The analytical effort was coordinated by SNL. For the pretest analyses, each organization was supplied with the same basic information, which included the construction drawings, specifications, and material properties.

Descriptions of pretest predictions, which included standard plots and response milestones in addition to estimates for capacity and failure mode, were provided to Sandia in February and March 1987 for publication in the pretest analysis report. The experimental data was sent to all the organizations participating in the pretest analyses within two weeks after completion of the high pressure test. In November 1987, a meeting was held in Albuquerque that was attended by representatives of all organizations involved in the pretest analyses; the test site and model were toured and the test results and preliminary reviews of the analysis were discussed in detail. Significant exchange of ideas and results also took place at two conferences held after the test: the 9th International Conference on Structural Mechanics in Reactor Technology, held in Lausaunne, Switzerland from August 17-21, 1987, and the Fourth Workshop on Containment Integrity, held in Washington, D.C. from June 14-17, 1988.

A number of benefits have been obtained from the round-robin analysis. First, the large number of analytical approaches and interpretations led to a comprehensive instrumentation plan and improved the conduct of the test. Second, a large number of state-of-the-art finite element codes were applied to the analysis of the model -- including ABAQUS, ADINA, CASTEM, NEPTUNE, NFAP, PAFEC, and TEMP-STRESS -- and validated for global response. Third, sources of uncertainty and error in the analysis have been identified and improvements have been made in modelling. Fourth, there is an emerging consensus on modelling techniques and evaluation criterion for liner tearing. The insights obtained from the posttest evaluations have been greater than any one group could have accomplished alone; this is largely a result of the diversity in perspective and approaches taken by the round-robin analysts. Finally, the round-robin analysis has enhanced the exchange of ideas and information on containment performance and related topics, and it is sincerely hoped that the contacts and associations that have been formed through this analysis effort will continue.

The report is organized in six sections. Sections 1 through 3 provide a summary and relevant introductory and background material. Sections 4 and 5 represent the 'meat' of the report. Section 4 provides a comparison of pretest predictions and experimental results. Section 5 consists of subsections that are authored by the organizations that contributed to posttest evaluations of the 1:6-scale model, as listed above. The Civil Engineering Department at the University of Illinois conducted a posttest investigation of the shear behavior at the cylinder-basemat junction under contract to Sandia; a progress report on their work is also included in Section 5. Concluding comments are made in Section 6. A brief summary of each of these three sections is provided below.

## Pretest Predictions vs. Experimental Results

Pretest ('best-estimate') predictions for the capacity of the model varied from 130 to 190 psig (0.896 to 1.31 MPa). Analysts were also asked to provide the maximum pressure at which they had high confidence there was a low probability of failure; with just one exception, these numbers were less than the pressure at which the model failed (145 psig, 1.0 MPa). That estimates for capacity that were intended to be conservative were below the actual failure pressure is reassuring.

The main source of error in the analyses was in the interpretation of failure, not in the response calculations. The global response of the cylinder and dome, in particular the hoop behavior of the cylinder, was predicted with reasonable accuracy

by virtually all participants. Thus, a number of finite element codes appear to be suitable for reinforced concrete containment analysis. The variations in calculated global response measures are mostly associated with differences in concrete constitutive models; interestingly, a no-tension model for concrete appears to provide the best results for the cylinder and dome behavior.

More important than the choice of a finite element code or constitutive model were the assumptions adopted by the analyst. Most pretest analyses were based on axisymmetric models; the assumption of axial symmetry is probably the single most important reason that failure was not correctly interpreted by most analysts. Although most recognized the possibility of liner tearing, the subjective judgement was that local strain concentrations would not be great enough, given the high ductility of the liner, to tear the liner before some other failure mode occurred. Clearly, the lesson is that local models, with boundary conditions based on the global response, are necessary to accurately predict failure. Only EPRI followed this approach in their pretest predictions; they were able to accurately predict the range for the capacity and the mode of failure (liner tearing), but not the location of failure. Unfortunately, EPRI's approach entailed a good deal of subjective judgement, because their calculated strains were well below the ductility of the material. Certainly the test bears out EPRI's judgement, but posttest evaluations at Sandia, CEA, and GRS have led to considerable refinement of this approach, especially into the magnitude of liner strain concentrations and the design features that cause them.

The analysts that overpredicted the capacity of the model overlooked the liner tearing mode, in part because they relied on axisymmetric models. For example, a number of groups predicted hoop rebar failure in the range of 180 to 190 psig (1.24 to 1.31 MPa), which may have indeed been the case had not liner tearing occurred first. Thus, these analyses are not so much in error as they are incomplete, due to their failure to make a detailed analysis of liner tearing. Underpredictions were the result of very conservative criteria for shear failure or rebar failure (such as general yielding). In the case of rebar failure, a yield criterion for failure is clearly inappropriate. With the possible exception of large diameter bars that are bent around major penetrations, there is no evidence to suggest that the ultimate strength of the splice or rebar, whichever is lower, will not be developed prior to failure. In the case of shear failure, there is simply no generally recognized method for determining the shear capacity of a reinforced concrete section under simultaneous application of tensile loads and bending moments. Design codes are recognized to be conservative, but the degree of conservatism is not quantitatively known. The nominal shear stress at the base of the cylinder wall (where it intersects the basemat) has been estimated at 450 psi (3.10 MPa), or $5.7\sqrt{f_c}$ at the maximum test pressure of 145 psig (1.0 MPa). This is significantly higher than design codes would allow. An evaluation criterion for shear failure remains as a difficult and important challenge.

Posttest Evaluations

There were four principal areas of investigation during the posttest evaluations, with the indicated results:

i) **Liner tearing** - A number of groups conducted analyses to understand the major tear that occurred adjacent to the rectangular insert plate for the mechanical/electrical feedthrough penetration cluster, including SNL, EPRI, CEA, NII, ENEA, AEA, and GRS. The various analyses represent a diverse array of approaches with significant differences in the model

details. Yet, despite the broad differences in the analytical approaches, there are many similarities in the conclusions.

Analysis suggest that the insert plates used around penetrations by themselves cause local strain concentrations two to four times the free-field strain. However, it is the majority view that this mechanism for strain concentration is not by itself sufficient to explain the formation of tears in the liner.

The additional feature that accounts for still higher local strains near the penetrations is the liner anchorage system, specifically, the studs. The studs resist slip between the concrete and the liner. Significant slip occurs at insert plates because of their high stiffness relative to the nominal thickness liner and, as a result, the studs impose significant loads on the liner at such locations. With studs modeled, SNL, CEA, and GRS calculated liner strain concentrations of ten or more times the free-field strain near the maximum test pressure. GRS considered several different models for liner tearing, including one in which the stud embedment in the concrete was explicitly modeled. CEA performed an interesting sensitivity study; by removing the first row of studs on the nominal thickness liner next to the insert plate, they found that the maximum local strain was reduced by about half. SNL conducted additional calculations to understand the stud shear behavior that provided two interesting conclusions:

1.  When the liner is not subject to membrane yield loads prior to the application of high stud shear forces, the failure mode is expected to be stud shear failure instead of liner tearing. This suggests that simple stud shear tests do not adequately represent the behavior of the liner-anchorage system in the containment under internal pressure, and that conclusions drawn from such tests with respect to the liner-anchorage system failure mode (i.e., stud failure vs. liner tearing) may be invalid.[1]  Liner membrane yield loads, which in an actual containment precede the development of high stud shear loads, must be represented.

2.  Strains calculated with a plane stress model where the stud shear forces are modeled as point loads can be reasonably interpreted as average strains through the liner thickness if the characteristic dimension of the elements adjacent to the stud load is approximately equal to the stud radius.

Although they do not explicitly account for its effect in their analysis, EPRI feels that 'shear dislocation motion' (a discontinuity in out-of-plane (radial) displacement that occurs near major cracks adjacent to penetrations) is an important mechanism in the formation of liner tears. Sandia does not feel that this is a significant mechanism in areas with geometry similar to the mechanical/electrical feedthrough penetration

---

1. The tests typically conducted on studs and anchors are relevant to liner buckling under thermal loads. The primary design function of the anchorage system is to prevent thermally induced buckling.

cluster in the 1:6-scale model. This is a difference that needs to be resolved by additional testing.

To interpret the calculated liner strains, SNL, EPRI, ENEA, and GRS all adopted the same criterion for evaluating the liner ductility under biaxial loads, which is based on the Davis triaxiality factor. ANATECH is credited with the initial use of this criterion in application to containment liners. The progress towards an agreement on a strain criterion for liner tearing is an encouraging development.

ii) **Basemat uplift** - There was considerable variation in the pretest predictions for basemat uplift, none of which accurately reflected the measured pressure-history response of the model over the entire range of pressure. Basemat uplift is significant in that it affects the shear and moment forces in the cylinder wall at the juncture with the basemat, which may change the potential for failure at this location. The effects of the fill slab, soil stiffness, and concrete tensile behavior on basemat uplift were studied. It was found that the basemat uplift is relatively insensitive to changes in soil stiffness, but in order to accurately reflect the measured behavior, finite element models need to account for two factors that were generally not considered in pretest analyses:

- The fill slab, which stiffened the basemat response (thereby reducing uplift). Several groups modeled the fill slab explicitly with improved results. GRS performed an interesting analysis that indicates the stiffening effect of the fill slab is primarily due to the shear forces that develop to resist sliding between the fill slab and the liner. These shear forces produce a moment on the basemat in opposition to the moment from the vertical load imposed by the cylinder.

- A reduction in actual tensile strength of the basemat concrete to about half of the laboratory measured value. ANATECH proposed this approach based on in-situ data on concrete dams.

The analyses also indicated that basemat uplift had little effect on the stresses or strains in the cylinder and dome at all locations other than the base of the cylinder.

In application to actual containments, basemat uplift (actually basemat response in general) would be much more difficult to predict due to the effect of internal structures, reactor cavities, sump pump pits, and other numerous discontinuities that were not represented in the 1:6-scale model. The effect of these features is uncertain.

iii) **Shear failure** - Given the number of predictions of shear failure before the test, it is somewhat disappointing that there was not more work here. The University of Illinois used strain measurements to estimate the nominal shear stress at the cylinder base. At 145 psig, the nominal shear stress was approximately 450 psig, which is $5.7\sqrt{f_c}$. This is high relative to many of the design code rules. Unfortunately, there is still no generally recognized criterion for evaluating shear capacity of reinforced concrete sections subject to simultaneous application of tensile loads and bending moment.

iv) **Precracking** - The experimental results provide ample evidence that the cylinder and dome were essentially precracked in both the horizontal and vertical planes prior to the high pressure test (but not the basemat, at least not to the same extent). Shrinkage cracking, low pressure cycling, and the small diameter of the bars used in the model (which may not have bond properties comparable to the large bars used in full-size containments) were all cited as potential caused for cracking in the concrete. ANL conducted an interesting analysis of the effects of diurnal temperature fluctuations, which indicated that the cylinder and dome concrete could be heavily damaged by a temperature change of 40°F (17°C) from day to night (not an unusual occurrence in the Albuquerque area).

## Concluding Remarks

Before applying the lessons learned from the 1:6-scale model to actual containments, a number of issues still need to be resolved. Although there has been progress in developing analytical models for evaluating liner tearing, the following questions remain:

- Under what conditions will stud shear failure occur rather than liner tearing? How is the failure mode of the liner-anchorage system affected by scaling; by the ratio of liner thickness to stud diameter; and by membrane loading of the liner (before the development of high stud shear forces)?

- To what extent is the magnitude of liner strain concentrations affected by friction and bond between the concrete and liner; by dislocation motion at a crack; and by stud spacing?

- How is the magnitude of liner strain concentrations affected by the size and shape of insert plates? Does the shape of the insert plates affect crack propagation in the liner?

Sandia is developing a plan for 'separate-effects' tests with the objective of addressing these questions for reinforced concrete containments as well as prestressed concrete containments, which typically use line anchors to attach the liner to the concrete.

Furthermore, investigation and validation of methods for evaluating other potential failure modes is still needed. Shear failure is particularly difficult to evaluate; there is no generally recognized, reliable method of determining shear capacity of a reinforced concrete section under simultaneous application of tensile load and bending moment. Repressurization of the 1:6-scale model (after repairs are made to the liner) is one means for obtaining much needed data on the shear behavior of the cylinder-basemat intersection. Failure of large rebars where they are bent around penetrations has occurred in test specimens at relatively low plastic strains (compared to the bars ultimate strain) in an EPRI program. The effects of cold working on the available ductility of these bars should be studied further.

The fact that liner tearing was obtained in the 1:6-scale model does not by itself preclude different failure modes in actual reinforced concrete containments. For instance, the failure mode and capacity can be extremely sensitive to specific design details. If the stud spacing had been different, CEA's analysis suggest that liner tearing would have have been delayed, thereby increasing the likelihood of a

different failure mode. The rate of pressurization and effects of temperature must also be considered. At high rates of pressurization, there is a possibility that sequential failure modes could occur, i.e., for very high rates of pressurization, liner tearing may not arrest the pressure build-up within the containment and another failure mode could occur at slightly higher pressure. This is the basic reason for the emphasis on the development and validation of analysis methods. A reliable evaluation of containment performance must be based on careful, detailed analysis of the specific containment geometry and loading of interest. Analysis and testing of the 1:6-scale model have verified many (but not all) of the computational tools and analysis procedures needed to accomplish such an evaluation for reinforced concrete containments.

## 2.0 INTRODUCTION

### 2.1 Background

Containment buildings in nuclear power plants are designed as the last engineered barrier preventing the release of radioactive material to the environment. As such, the performance of LWR containments is an extremely important parameter in an evaluation of the safety of a nuclear power plant. In the unlikely event of a severe accident, the temperature and pressure inside a containment may significantly exceed the loads for which it was designed. Under these conditions, it is important to understand the nonlinear behavior of the structure and its functional limits. This information is vital to reliable emergency preparedness, accident mitigation, and risk assessment.

The U.S. Nuclear Regulatory Commission (NRC) has established a set of programs with the ultimate objective of developing test validated methods that can be used to accurately predict the performance of LWR containment buildings subject to loads beyond the design basis. The emphasis is on methodology because containment performance must be evaluated on a case-by-case basis as there has been little standardization in containment designs in the U.S. Experiments are designed to generate data that can be used to evaluate analytical methods and to make improvements and modifications to the methods as necessary. The programs are known collectively as the Containment Integrity Programs [1]; they are managed by the Containment Technology Division at Sandia National Laboratories (Sandia).

Performance of the containment system for loads beyond the design basis is based on a functional definition of failure. Since the containment function is to prevent release of radioactive material and thereby protect the public from harmful exposures, performance can be considered to be compromised when a significant leak occurs, where significant is that level at which leakage poses a detectable risk to the public, generally taken to be about 10% volume/day. For emergency preparedness and accident mitigation, it is important to have a high confidence estimate of the maximum pressure at which the containment will *not* fail. In the event of a failure, containment performance parameters that affect the amount and type of radioactive material released into the environment include:

- the capacity and timing of failure for a given accident scenario,

- the size of failure, or leak area, and

- the location of failure.

A reliable methodology for predicting containment performance must consider these issues for all potential failure mechanisms, including failure to isolate, leakage past the sealing surfaces of penetrations, and tearing or other material failures of the containment shell. The failure mechanisms being considered in the Containment Integrity Programs are listed in Table 2.1. The focus of this report is on the behavior of reinforced concrete containment shells.

Because many containment failure modes are associated with extremely complex phenomena, including highly nonlinear structural response, experimental validation of analytical methods is essential. The overpressurization test of a 1:6-scale model of a reinforced concrete containment in July 1987 is one of a number of NRC-sponsored

tests to provide benchmark data for validating analytical methods to predict containment performance. Other completed tests include four 1:32-scale steel models, a 1:8-scale steel model including an operable equipment hatch [3-5], 3 full-size electrical penetration assemblies [6], seal and gasket materials [7,8], and a full-size personnel airlock [9]. Two operable equipment hatches, one pressure-seating and the other pressure-unseating, were also tested in the 1:6-scale model [10]. These tests have provided a large, high quality experimental database.

## Table 2.1
## Potential Failure Modes of LWR Containments
## Considered in Sandia's Containment Integrity Programs

I. General Shell Failures

  A. Structural failure

    1. Steel containments:
      Shell tearing

    2. Reinforced concrete:
      Liner tearing
      Transverse shear failure
      Rebar failure

    3. Prestressed concrete:
      Liner tearing
      Shear failure
      Rebar failure
      Tendon failure

II. Penetration Failures

  A. Sealing failure

    1. Operable penetrations:
      Unseating of covers
      Sleeve ovalization
      Collapse of inflatable seals

    2. Fixed penetrations:
      Electrical Penetration Assemblies
      Isolation Valves

  B. Structural failures

    1. Bellows expansion joints

    2. Buckling:
      Torispherical heads
      Pressure-seating hatches

In general, analyses of the test specimens are conducted both before and after an experiment. The pretest analyses are used to identify potential failure modes, propose failure criteria, and obtain a 'blind' prediction of the test outcome, which is the most credible way to assess analytical capabilities. The pretest analyses also are used to select the type, range, and appropriate location of instruments and to provide guidance in the conduct of the test. Posttest analyses are used to improve the analysis method, in particular by providing additional insight into the failure mechanics.

This same philosophy was adopted in developing methodology for predicting the performance of reinforced concrete containments. An overpressurization test on a 1:6-scale model of a reinforced concrete containment was planned and executed in conjunction with both pretest and posttest analyses of the model behavior. Because of the growing recognition of the important role of containments, there was widespread interest in the test and analyses.

## 2.2 Round-Robin Coordination

A significant effort was made to identify organizations that would collaborate with Sandia to make pretest predictions for the response of the 1:6-scale model. This round-robin analysis was organized and coordinated by Sandia National Laboratories to gain insight into state-of-the-art analysis capabilities and uncertainties. Analyses were conducted by ten different organizations from the U.S. and Europe.[2] The participating organizations represent a diverse group of regulators, national laboratories, and industry:

- Sandia National Laboratories (SNL), USA

- Argonne National Laboratory (ANL), USA

- Electric Power Research Institute (EPRI), USA

- Commissariat a L'Energie Atomique (CEA), France

- HM Nuclear Installations Inspectorate (NII), U.K.

- Energia Nucleare e delle Energie Alternative (ENEA), Italy

- U.K. Atomic Energy Authority, Safety and Reliability Directorate (AEA), U.K.

- Gesellschaft für Reaktorsicherheit (GRS), FRG

- Brookhaven National Laboratory (BNL), USA

- Central Electricity Generating Board (CEGB), U.K.

Each organization was supplied with a standard information package, which included construction drawings and actual material properties for most of the materials used in the model. Each organization worked independently using their own analytical methods and funds.[3]

Several benefits were obtained from the round-robin analysis. First, because of the large number of analytical approaches and interpretations, a greater number of potential limit states were recognized. As a result, the instrumentation plan for the model is more thorough and SNL's ability to anticipate and respond to events during the high pressure test was enhanced. Second, a measure of the uncertainty in pretest predictions was obtained by comparisons of different analyses as well as comparisons between analytical and experimental results. Third, a large number of state-of-the-art finite element codes were applied to the problem and the results can be validated against the experimental results. Finally, the round-robin exercise led to greater recognition of the importance of containment performance and reliable prediction

---

2. In addition to these ten, Taiwan Electric Power Company and Japan Atomic Energy Research Institute have reached agreements with NRC that call for information exchange on the containment integrity programs. However, they did not submit results to Sandia before testing and are, therefore, not included in the ensuing discussion.

3. To be more precise, only Sandia and Brookhaven used NRC funds to conduct these calculations; the remaining organizations utilized other funding sources.

techniques; it has also facilitated the exchange of information on these and other related topics.

Each member of the group submitted pretest predictions for the performance of the model, which have been documented in Reference 11. These predictions included plots of the strain and displacement pressure history response at specified locations, which allow for direct comparison with other analytical results as well as experimental results, and estimates of capacity, failure mode, and failure location. This information provides the basis for much of the discussion in the current report.

All ten organizations conducted axisymmetric finite element analyses to predict the free-field response of the structure; in some cases, the axisymmetric calculations were augmented by membrane analysis, local analysis, and/or three-dimensional analysis. A number of different computer codes were used, including versions of **ABAQUS** (EPRI, SNL, AEA), **ADINA** (ENEA, GRS, CEGB), **CASTEM** (CEA), **NEPTUNE** (ANL), **NFAP** (BNL), and **TEMP-STRESS** (ANL). The main differences between the analytical models were in the following areas:

- failure criteria

- material behavior of concrete

- soil stiffness

- basemat representation, including consideration of the effect of the fill slab

- element formulation (continuum vs. shell elements)

- rebar modelling (lamina vs. cable or truss elements)

The experimental data was made available to the round-robin analysts almost immediately after the test so that they could assess their pretest predictions and conduct posttest analyses, as needed to improve their analytical models. These posttest evaluations and the lessons learned from the 1:6-scale model test are the primary focus of this report.

## 2.3 Organization of the Report

The report is organized in seven sections. The Executive Summary contains the major results and conclusions of the study. In the second section, background information on containment integrity research and on the coordination of the round-robin analysis is provided. Section 3 is a brief synopsis of the design of the 1:6-scale model and high pressure test highlights. The pretest predictions are compared with experimental results in Section 4. This includes response measurements and failure interpretation. Closing remarks are made in Section 6, and references are listed in Section 7. These sections were written by Clauss and may not reflect the opinions or beliefs of other participants in the round robin analysis.

Section 5 consists of subsections submitted by each organization participating in posttest evaluations; this section comprises the bulk of this report. Each subsection contains a description of the experimental comparisons and posttest evaluations by each organization of their own analysis. The authors are listed at the beginning of

each major subsection. A brief summary of the posttest evaluation efforts, which was prepared by Clauss, is provided at the beginning of Section 5.

Wherever possible, dual units (English and SI) have been used in this report, with preference given to the author's choice of units. In many of the tables and most, if not all of the figures, only one set of units is used. For the reader's convenience, the following conversions are provided:

| To convert | from: | to: | Multiply by |
|---|---|---|---|
| Pressure, stress | psi | MPa | 0.006895 |
| | MPa | psi | 145. |
| Force | lbf | N | 4.45 |
| | N | lbf | 0.225 |
| Length | in. | mm | 25.4 |
| | mm | in. | .0394 |
| | ft | m | 0.305 |
| | m | ft | 3.28 |
| Leak rate | scfm | sccm | $2.84 \times 10^4$ |

## 3.0 TEST SUMMARY

A brief summary of pressure testing of the model is presented in this section Details of the testing and experimental results are reported in Reference 13.

### 3.1 Model Characterization

A schematic of the model is shown in Figure 3.1. Briefly, the model consists of a 40 in. (1.02 m) thick flat basemat, a 9-3/4 in. (248 mm) thick circular cylinder with a radius of 11 ft (3.36 m) and a height of 22.25 ft (6.79 m), and a hemispherical dome that has a wall thickness of 7-3/4 in. (197 mm) and a radius of 11 ft (3.36 m). A steel liner, 1/16 in. (1.59 mm) thick along the inside of the basemat and cylinder and 1/12 in. (2.12 mm) thick along the dome, was designed to provide leak tightness. The liner is attached to the concrete with headed studs. There are eight layers of reinforcement, including four layers in the hoop direction, two layers in the vertical direction, and two layers of diagonal (seismic) reinforcement. Additional reinforcement is provided near penetrations and at the junction of the cylinder and basemat. The design pressure of the model was 46 psig (0.317 MPa). For the reader's convenience, the description of the model and material properties provided in the pretest analysis report [11] is reproduced in the Appendix. Additional details of the design, fabrication, and instrumentation of the 1:6-scale model can be found in Reference 12.

### 3.2 Low Pressure Testing

Prior to high pressure testing, a Structural Integrity Test (SIT) and an Integrated Leak Rate Test (ILRT) were performed on the model. The procedures and standards followed in these tests were the same or similar to SITs and ILRTs conducted on actual containments.

The SIT involved pressurization with dry compressed air to a maximum pressure of 53 psig (0.365 MPa), which is 1.15 times the model design pressure. The test was conducted from July 6 through July 10, 1987. Data from about 1200 transducers was recorded at 10 required steps in the pressurization as well as several intermediate steps. Cracks were mapped at six different locations about the model and there was extensive video and still camera coverage. Crack orientation and spacing were fairly uniform; cracks tended to follow the reinforcing bar pattern. (In the high pressure test, few new cracks were formed; instead, the existing cracks extended and increased in width.)

The ILRT was conducted from July 11 through July 13, 1987. The model was pressurized to 46 psig (0.317 MPa) and isolated. Based on the pressure decay with time, the leak rate was calculated to be approximately 0.14% mass day. Most of this was probably attributable to the isolation valve itself, which leaked noticeably during the ILRT. However, since the measured leakage was within allowable limits, there was no need to check the isolation valve and repeat the test.

The model was also subject to a number of low pressure cycles (5-15 psig) as part of the model acceptance and to check-out the pressurization and data acquisition systems.
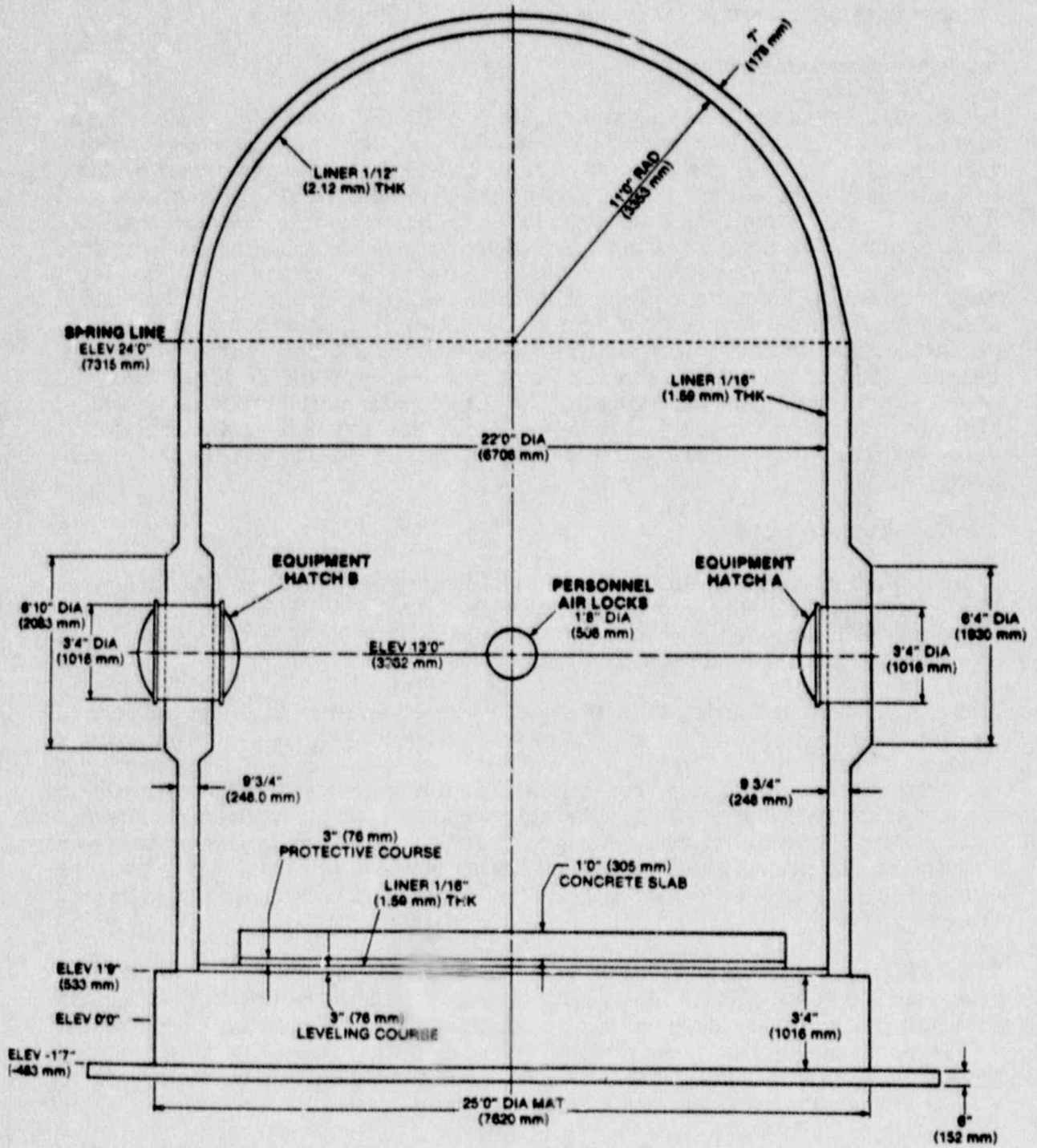
Figure 3.1 Schematic of 1:6-Scale Model

## 3.3 High Pressure Testing

The high pressure test was conducted July 28 and 29, 1987. The model was pressurized using nitrogen gas. The loading schedule is shown in Table 3.1. The pressure listed in Table 3.1 represents the controller setpoint, actual pressure in the model may have differed by about ±0.25 psig. Pressure was normally increased by the desired step size in 10-20 seconds and then held for about 20 minutes (sometimes longer) before a data scan was initiated. This delay was sufficient for the model to essentially reach an equilibrium state, although it is recognized that creep of the model would continue at a slow rate for some time after a data scan was taken. At some pressure levels, more than one data scan was made.

No significant leakage was detected from the model until the pressure was raised to 135 psig (0.93 MPa), when a leak rate of 11% mass/day (8 scfm) was recorded. At 140 psig (0.965 MPa), leakage had increased to 13% mass/day (10 scfm) and then at 143 psig (0.986 MPa) to 62% mass/day (50 scfm). The test was terminated after a little more than one hour at 145 psig (1.0 MPa) due to leakage greater than the capacity of the nitrogen gas supply, which was approximately 5000% mass/day (4000 scfm). The initial leak rate measurement recorded at 145 psig (1.0 MPa) was 234% mass/day (185 scfm), but the leak rate increased steadily with time during this last pressure hold.

During posttest inspection, the large liner tear near the rectangular insert plate surrounding mechanical/electrical feedthrough penetration cluster, as shown in Figure 3.2, was obvious. (The buckling of the liner that can be seen in Figure 3.2 occurred during unloading of the model and is not relevant to the high pressure test results.). Further inspection revealed numerous other small tears in the liner as well as a number of distressed areas (regions of significant thinning in the liner) at the locations indicated in Figure 3.3. These smaller tears also occurred adjacent to insert plates, with the exception of the two tears near Equipment Hatch B (see Reference 13 for discussion of these tears). Furthermore, every tear in the model was associated with a stud.

Analysis of the acoustic emissions recorded during the test (which help to pinpoint a location of leakage) and posttest measurements of leakage through the smaller liner tears leads to the conclusion that the leakage detected at 135 psig (0.931 MPa) was most likely past the seals on the outer cover of equipment hatch B due to unseating of the cover and not due to liner tears [13]; the evidence clearly suggests that liner tearing had not initiated anywhere in the model at this pressure. The first liner tear probably initiated between 140 and 145 psig (0.965 and 1.0 MPa), most likely at about 143 psig (0.986 MPa). There was obviously significant propagation of the tears at 145 psig (1.0 MPa). This propagation constituted a functional failure of the containment model.

Experimental results are discussed and compared with analyses in Sections 4 and 5. Except where noted, only the high pressure test results are plotted. It should also be noted that all transducers were 'zeroed' at the start of high pressure test, so residual strains and displacements from low pressure testing are not included. The data taken during the high pressure test was in general not modified to account for residual readings from low pressure testing. As shown in Section 5.9, accounting for effects of the SIT would produce a perceptible but relatively minor shift in the response pressure histories. However, this shift may be important in certain applications of the data.

Only some of the experimental data is used in this report. All of the experimental data recorded during both high and low pressure testing is available in Reference 13.

Table 3.1
Loading Schedule for High Pressure Test

| Step | Date | Time | Pressure (psig) | (MPa) |
|---|---|---|---|---|
| 1 | 28 July | 11:18 | 10 | 0.069 |
| 2 | 28 July | 11:50 | 20 | 0.138 |
| 3 | 28 July | 12:18 | 30 | 0.207 |
| 4 | 28 July | 12:41 | 40 | 0.276 |
| 5 | 28 July | 13:29 | 50 | 0.345 |
| 6 | 28 July | 14:00 | 55 | 0.379 |
| 7 | 28 July | 14:31 | 60 | 0.414 |
| 8 | 28 July | 15:08 | 65 | 0.448 |
| 9 | 28 July | 15:39 | 70 | 0.483 |
| 10 | 28 July | 16:15 | 75 | 0.517 |
| 11 | 28 July | 19:26 | 80 | 0.552 |
| 12 | 28 July | 20:35 | 85 | 0.586 |
| 13 | 28 July | 21:44 | 87 | 0.600 |
| 14 | 28 July | 23:20 | 95 | 0.655 |
| 15 | 29 July | 00:34 | 100 | 0.689 |
| 16 | 29 July | 02:03 | 102 | 0.703 |
| 17 | 29 July | 02:55 | 105 | 0.724 |
| 18 | 29 July | 03:19 | 107 | 0.738 |
| 19 | 29 July | 04:10 | 110 | 0.758 |
| 20 | 29 July | 04:37 | 112 | 0.772 |
| 21 | 29 July | 05:20 | 117 | 0.807 |
| 22 | 29 July | 06:08 | 120 | 0.827 |
| 23 | 29 July | 07:44 | 122 | 0.841 |
| 24 | 29 July | 08:49 | 125 | 0.862 |
| 25 | 29 July | 10:37 | 128 | 0.883 |
| 26 | 29 July | 11:48 | 130 | 0.896 |
| 27 | 29 July | 12:24 | 133 | 0.917 |
| 28 | 29 July | 13:38 | 135 | 0.931 |
| 29 | 29 July | 15:38 | 138 | 0.952 |
| 30 | 29 July | 16:20 | 140 | 0.965 |
| 31 | 29 July | 17:20 | 143 | 0.986 |
| 32 | 29 July | 18:06 | 145 | 1.000 |
| | 29 July | 19:23 | Termination of Test | |

Figure 3.2  Photo of Large Liner Tear Near Rectangular Insert Plate

Locations With "Measurable" Leakage

Locations With No "Measurable" Leakage

Elev. 24'-0"

SPRINGLINE

MATCHLINE

MATCHLINE

8" Main-Steam Type
Constr. Penetr.

Elev. 13'-0"

3-6

Equipment
Hatch B

Personnel
Airlock

Equipment
Hatch A

Small Electric Feed
Through Penetrations

Personnel
Airlock

4" Pressure
Nozzle

Elev. 2'-0"

Bottom of
Containment

(Not to scale)

180°

270°

0°

90°
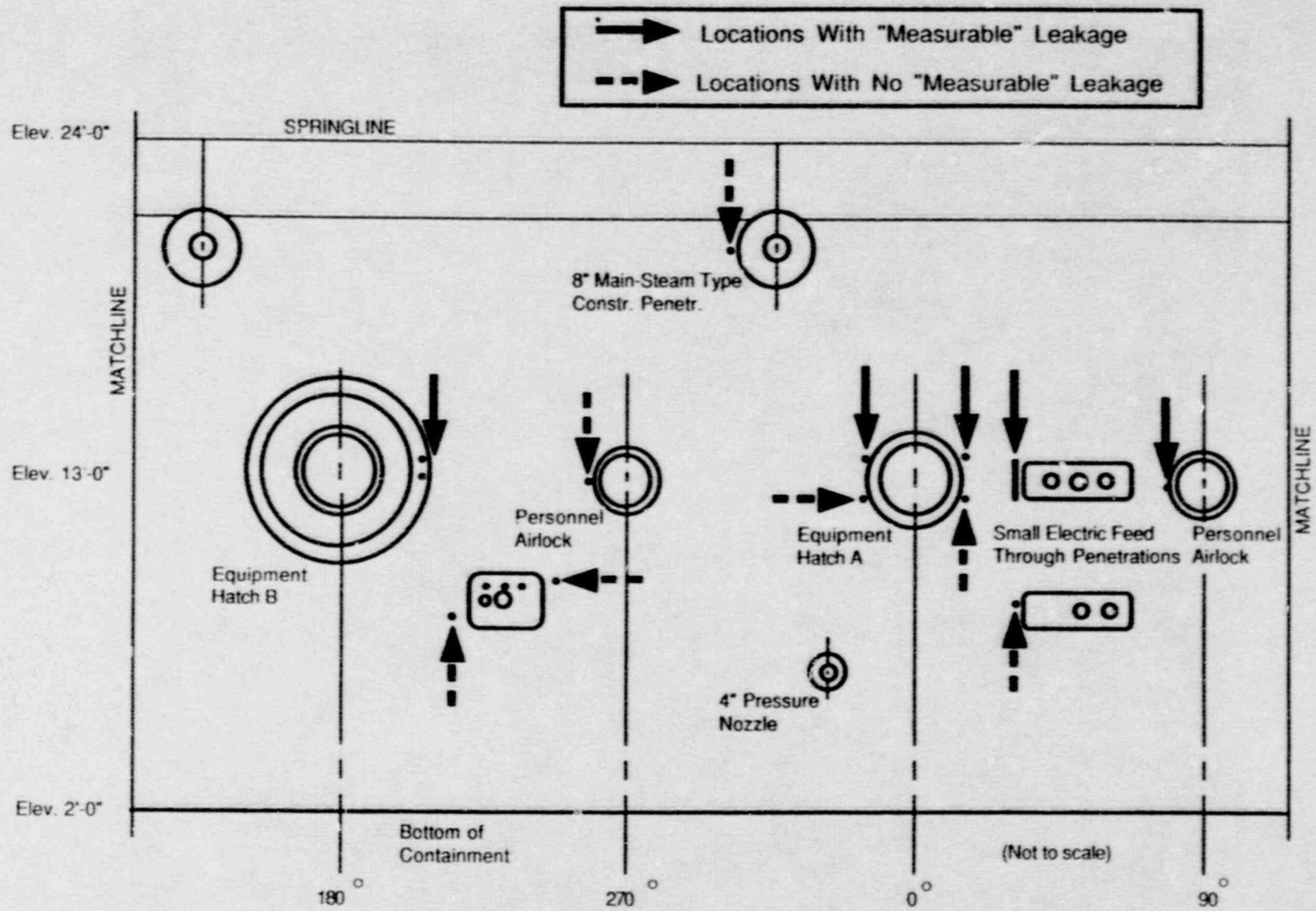
Figure 3.3 Cylinder Liner Stretchout Showing Liner Tears and Distressed Regions

## 4.0 PRETEST PREDICTIONS VS. EXPERIMENTAL RESULTS

This section focuses primarily on the comparisons of pretest prediction with experimental results based on the standard plots and other information requested for the pretest round-robin analysis report [11]. All ten organizations conducted axisymmetric finite element analyses to predict the free-field response of the structure; in some cases, the axisymmetric calculations were augmented by membrane analysis, local analysis, and/or three-dimensional analysis. A number of different computer codes were used, including versions of ABAQUS (EPRI, SNL, AEA), ADINA (ENEA, GRS, CEGB), CASTEM (CEA), NEPTUNE (ANL), NFAP (BNL), and TEMP-STRESS (ANL). The main differences between the analytical models were in the following areas: failure criteria; material behavior of concrete; soil stiffness; basemat representation, including consideration of the effect of the fill slab; element formulation (continuum vs. shell elements); and rebar modelling (lamina vs. cable or truss elements).

### 4.1 Important Milestones

Free-Field Cylinder

Significant milestones in the pressure history response of the cylinder wall (free-field) are given in Table 4.1. The initiation of general yielding of the steel liner was predicted over a fairly wide range of pressure, from 82 to 116 psig (.57 to .80 MPa). The variation is at least partly attributable to differences in the analytical models of the liner; some of the models did not treat the biaxial state of stress in the liner because the hoop and meridional stiffness are represented with separate elements. The yield pressure calculated based on a uniaxial state of stress may be 15% lower than that calculated using the von Mises yield criterion for a biaxial state of stress in which the principal stresses are both tensile. A second difficulty is introduced by the concrete. There is great uncertainty and thus wide differences in the analytical modelling on how the tensile load-carrying capability of the concrete decreases after cracking. Clearly, the calculated liner yield pressure depends on how much tensile load-carrying capability was retained for the concrete in the analytical model after cracking and on the value of strain at which the tensile load carrying capability of the concrete was assumed to reach zero. The measured results for the initiation of liner yielding at the midheight of the cylinder (free-field) also show considerable variation (see the row labeled 'Test' in Table 4.1). The variation in experimental results for liner yielding may be attributed mostly to: (1) asymmetry in the response of the structure due to penetrations, and (2) randomness in concrete cracking and bond between the liner and concrete. The differences in analytical predictions for liner yielding do not seem particularly significant in light of the variation in experimental results and in the realization that liner strains do not typically begin to increase rapidly until after general yielding of the entire wall section occurs.

In contrast to those for the liner, the calculations for initiation of general yielding in the hoop rebar produce quite similar results, with most predictions falling in a range between 120 and 130 psig (0.827 and 0.896 MPa). The variation observed in the experiment is also much less. With the exception of AEA, which reported results from a hand calculation, the results for meridional rebar yielding are also quite similar. (BNL and NII did not calculate a pressure at which meridional rebars would begin to yield because they predicted failure at a lower pressure.) Since the rebars are essentially uniaxial load carrying members, they are much simpler to model analytically. Furthermore, in the pressure ranges for which general yielding of the

rebars begins, nearly all of the analytical models assume that the concrete cannot carry any tensile load. From this standpoint, the agreement is not surprising. (It should also be noted that the value for the yield stress of the #4 rebar that was recommended for pretest analysis, 66.6 ksi (459 MPa), was estimated before testing of the material properties was completed. As given in Reference 64, the average yield stress of the #4 rebar is actually 63.6 ksi (439 MPa), which is about 5% less than the recommended value.)

Table 4.1
Pressure History Milestones (Global Response) for Initiation of Yielding
Pretest Predictions and Experimental Result

| Source | Cylinder Liner (psig) | (MPa) | Hoop Reinforcement (psig) | (MPa) | Meridional Reinforcement (psig) | (MPa) |
|---|---|---|---|---|---|---|
| SNL | 115 | 0.79 | 130 | 0.90 | 135 | 0.93 |
| ANL | 100 | 0.69 | 120 | 0.83 | 145 | 1.00 |
| EPRI | 95 | 0.66 | 120 | 0.83 | 135 | 0.93 |
| CEA | 87 | 0.60 | 130 | 0.90 | 135[a] | 0.93[a] |
| NII | 116 | 0.80 | 130 | 0.90 | NR | NR |
| ENEA | 92 | 0.63 | 120 | 0.83 | 129 | 0.89 |
| AEA | 110 | 0.76 | 138 | 0.95 | 174[b] | 1.20[b] |
| GRS | NR | NR | 120[a] | 0.83[a] | 145[a] | 1.00[a] |
| BNL | 104 | 0.72 | 124 | 0.85 | NR | NR |
| CEGB | 82 | 0.57 | 124 | 0.85 | 142 | 0.98 |
| Test[c] | 86-109 | 0.59-0.75 | 116-121 | 0.80-0.83 | 139-141 | 0.96-0.97 |

a) Reported value estimated by Clauss.
b) Result from hand calculation
c) Values reported for the test are the range of three or more representative measurements. For the liner, rosettes RO76, RO90, and RO98 were used; for the hoop rebars, bondable gages B19, B22, B24, and B25 were used; and for the meridional rebars, weldable gages WR84, WR85, WR86, WR262, WR264 were used. The von Mises stress calculated from the measured strains was compared to the yield stress of the material as given in the Appendix to determine the initiation of yielding.
NR Not reported

In the pretest round-robin analysis report, milestones for cracking in the concrete were also reported. No attempt is made to compare these predictions to experimental results. There is strong evidence to suggest that there was extensive cracking in the cylinder and dome before high pressure testing began, and as a result, comparisons for cracking are not meaningful. The possible sources of this 'precracking' are discussed in detail in Section 5 and include the following: shrinkage

cracking, cracking due to diurnal temperature variations, cracking due to low pressure cycling, and poor bond due to small diameter bars. Precracking was less apparent in the basemat. It can be argued that the initiation of cracking in the cylinder and dome is not a particularly significant event for evaluation of the ultimate performance of *lined* concrete containments.

## Local Response at Basemat-Cylinder Intersection

The behavior of the cylinder wall at its intersection with the basemat is of considerable interest because of the high shear and bending forces that arise at this location. Table 4.2 compares pretest predictions for the initiation of liner yielding, meridional rebar yielding, and basemat uplift to experimental measurements. The strains in the liner and layer 2 meridional reinforcement change vary rapidly as a function of elevation at this location (see Figures 4.31 and 4.32). Thus, the first gage to indicate yielding is used to determine the pressure reported in Table 4.2, rather than trying to indicate a range. For the meridional reinforcement at the cylinder-basemat intersection, first yield was measured at bondable gage B2, which is at an elevation about 2 in. (51 mm) below the liner knuckle. At the elevation of the top of the liner knuckle, the meridional reinforcement first yielded at a pressure of approximately 120 psig (0.83 MPa).

A number of groups (SNL, ANL, EPRI, ENEA, GRS, CEGB) also predicted crushing of the outside of the concrete cylinder wall in the range of 140 to 160 psig, except for GRS, which predicted the onset of crushing at 116 psig. Posttest inspection of the model did provide some evidence of minor crushing at this point, but it did not appear to have affected any significant thickness of the wall, only just the outer face. Sectioning of the model, which may be carried out at a later date, would be required to reach a definite conclusion on the extent of crushing.

### 4.2 Structural Response

This section is based on the standard plots reported in the pretest round-robin analysis report. The plot locations are grouped into three divisions: (1) free-field locations in the cylinder and dome, (2) local behavior at the cylinder-basemat intersection, and (3) behavior near penetrations. The latter required 3-D analysis, which was only accomplished by a few organizations prior to the test.

An attempt was made to use all measurements that could reasonably be compared with analysis. This helps to show the scatter in experimental results and thus provides a better perspective on the analytical uncertainty and error.

## Free-Field Response

The agreement among the analyses as well as between the analyses and experiment for the radial displacement and hoop reinforcement strain in free-field cylinder regions was exceptional, as shown in Figures 4.1 through 4.8. The radial displacement and hoop reinforcement strain are closely related; the hoop strain can be estimated very accurately as the ratio of the radial displacement to the cylinder radius. The analyses tend to overestimate the pressure at which general yielding of the wall occurs (the pressure at which the hoop strains and radial displacements begin to increase rapidly), but only by a relatively small amount. Hoop strain is probably the most important global response parameter for predicting failure, so the excellent correlation is reassuring.

| | Initiation of Yielding | | | | | |
| | Liner Above Knuckle | | Meridional Reinforcement | | Basemat Uplift at 145 psig (1.0 MPa) | |
| Source | (psig) | (MPa) | (psig) | (MPa) | (in.) | (mm) |
|--------|--------|-------|--------|-------|-------|------|
| SNL | NR | NR | 127 | 0.88 | 0.087 | 2.2 |
| ANL | 105 | 0.72 | 135 | 0.93 | 0.256 | 6.5 |
| EPRI | 60 | 0.41 | 130 | 0.90 | 0.882 | 22.4 |
| CEA | NR | NR | NR | NR | 0.853* | 21.7* |
| NII | 110 | 0.76 | 92 | 0.63 | 0.229 | 5.8 |
| ENEA | 92 | 0.63 | 133 | 0.92 | NC | NC |
| AEA | 110 | 0.76 | NR | NR | 0.629 | 16.0 |
| GRS | NR | NR | 130 | 0.90 | 1.118 | 28.4 |
| BNL | NR | NR | 104 | 0.72 | NA | NA |
| CEGB | 127 | 0.88 | 140 | 0.97 | 0.077 | 2.0 |
| Test[b] | 87 | 0.60 | 104 | 0.72 | .21(-.441 | 5.5-11.2 |

a) Reported value extrapolated from 142 psig (0.98 MPa) by Clauss.
b) Reported test values are based on measurements with the following gages: For the liner, weldable gage WR293; for the meridional rebar (layer 2) bondable gage B2; and for uplift, displacement gage D50 and inclinometers I4, I6, and I8.
NR Not reported
NC Model did not include basemat, so uplift was not calculated
NA Calculations only carried out to 131 psig (0.90 MPa).

The correlation for the axial response in the cylinder is not as good. Figures 4.9 through 4.12 show measured and calculated vertical displacements of the liner at various elevations relative to the cylinder base. (The data for some of the transducers has been shifted. The 'fixed' point of these transducer attached to the basemat liner at the cylinder base at locations where the liner was not in solid contact with the concrete. At these points, there was a 'snap-through' displacement of the liner as it came into contact with the concrete at the first application of pressure. The data was shifted to account for this 'snap-through' displacement.) The strain in the meridional bars (free-field) is plotted at various elevations of the cylinder in Figures 4.13 through 4.15. The difference between the various analyses is apparently due to difference in cracking models for the concrete, in particular, tension stiffening. The experimental results suggest that the most accurate representation for the concrete in the cylinder is a no-tension concrete model. The use of a no-tension concrete model for the cylinder and dome would have little effect on the hoop behavior and if anything would improve the correlation between the experimental results and calculations for hoop strains and radial displacements somewhat. Such a model also has the

advantage of simplicity. As part of the posttest evaluations, many of the analyst's also came to the conclusion that the concrete in the cylinder and dome was essentially 'precracked'. In Section 5, there are various speculations as to the causes of this precracking, including the following: shrinkage; diurnal temperature variations; low pressure cycling; and poor bond associated with small diameter bars.

The maximum principal strains in the liner are plotted as a function of pressure in Figures 4.16 through 4.18. The hoop strain is the dominant component of the maximum principal strain at each of the elevations plotted. What should be noted in these figures is the considerable variation in the experimental results, for what are all ostensibly free-field (axisymmetric) measurements. At elevation 20 ft (6.1 m), the maximum strain of the six gages plotted varied from 0.26% to 1.07% (see Figure 4.18). The strain variation may be associated with bond between the liner and concrete, concrete cracks, proximity to studs, or effects of penetrations. Whatever the exact cause, the liner response is clearly not axisymmetric even in what would normally be considered free-field regions (areas for which penetrations are not closer than about two times their diameter).

Strain in a seismic bar at elevation 20 ft (6.10 m) is plotted in Figure 4.19; the agreement among the analyses and with the experiment is satisfactory.

Results for the response of the dome are compared in Figures 4.20 through 4.28. The correlation is in general satisfactory. Since strains in the dome were typically below yield, the dome behavior is of little significance in evaluating containment performance. For this reason, an in-depth discussion of the dome response is not provided.
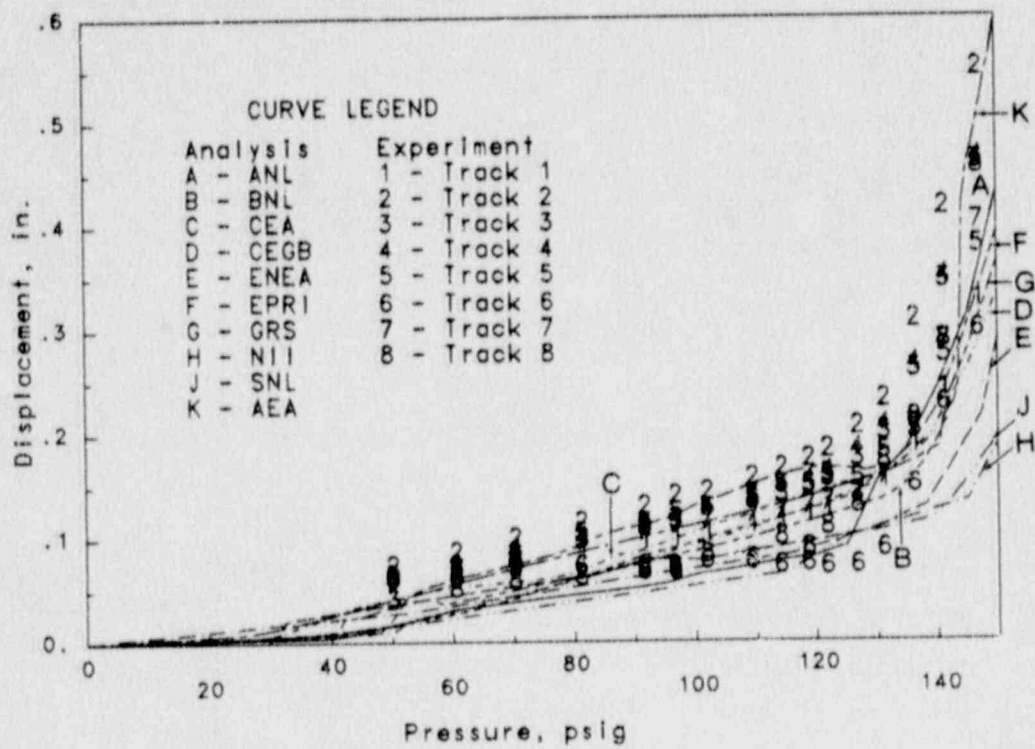


Figure 4.1 Pretest Predictions vs. Experimental Results:
Radial Displacement of Liner near El 4.1 ft (1.2 m)

4-5
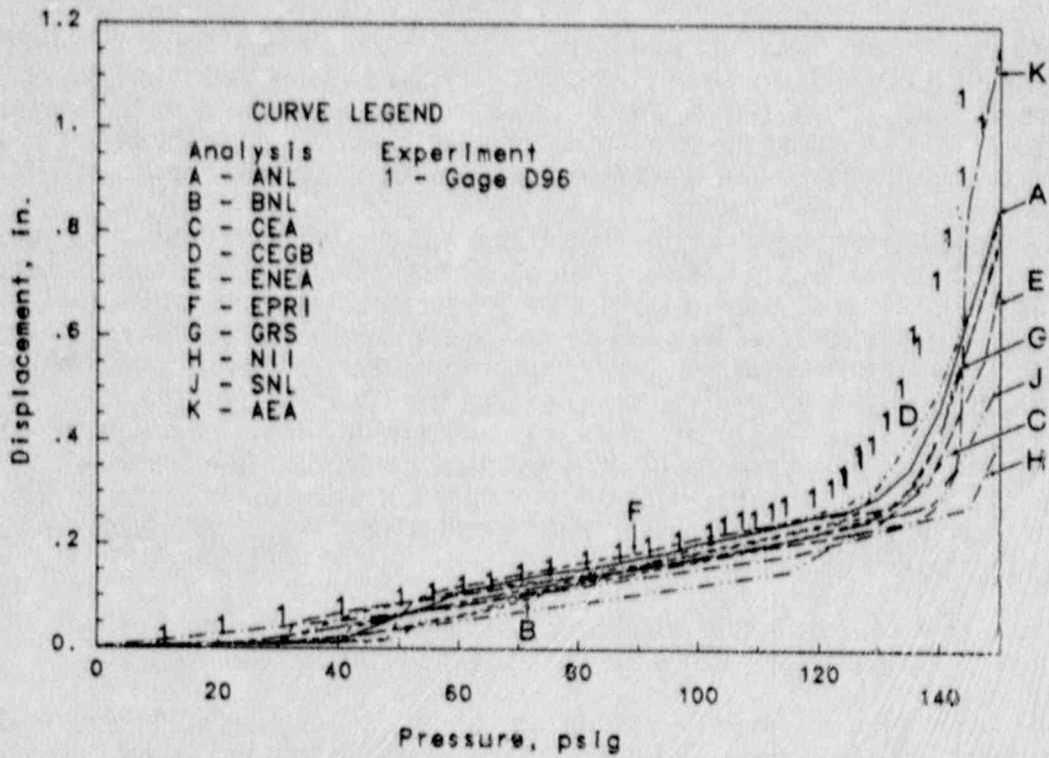
Figure 4.2 Pretest Predictions vs. Experimental Results:
Radial Displacement of Liner near El 6 ft (1.8 m)
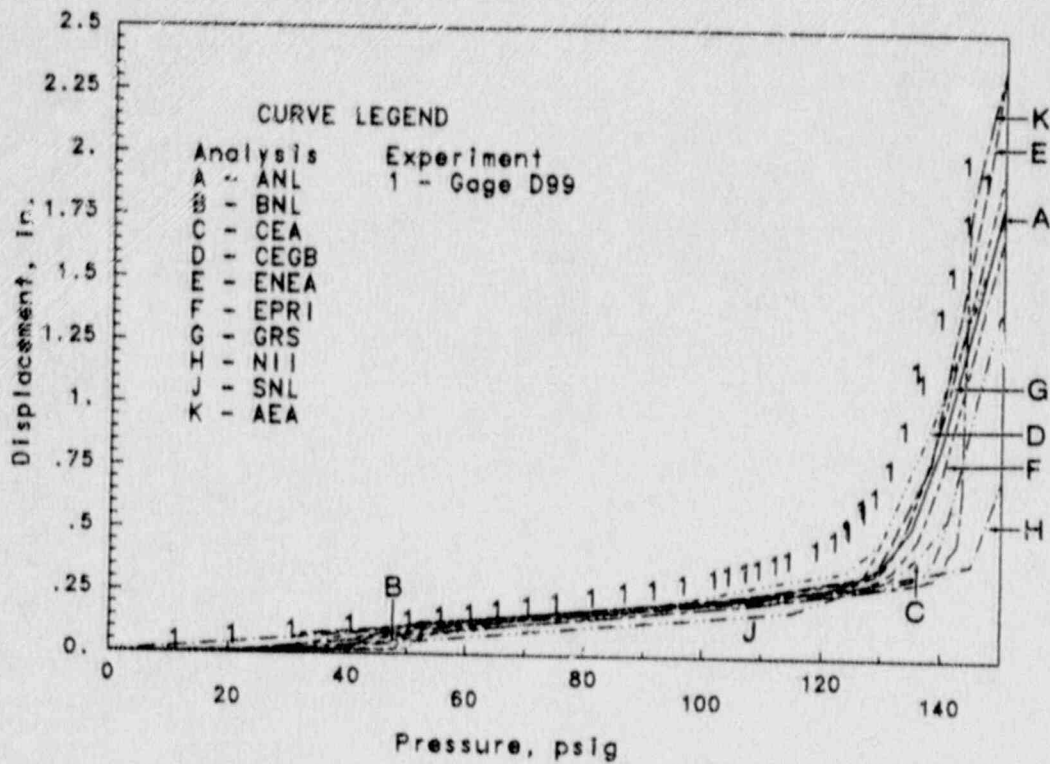


Figure 4.3 Pretest Predictions vs. Experimental Results:
Radial Displacement of Liner near El 11 ft (3.4 m)
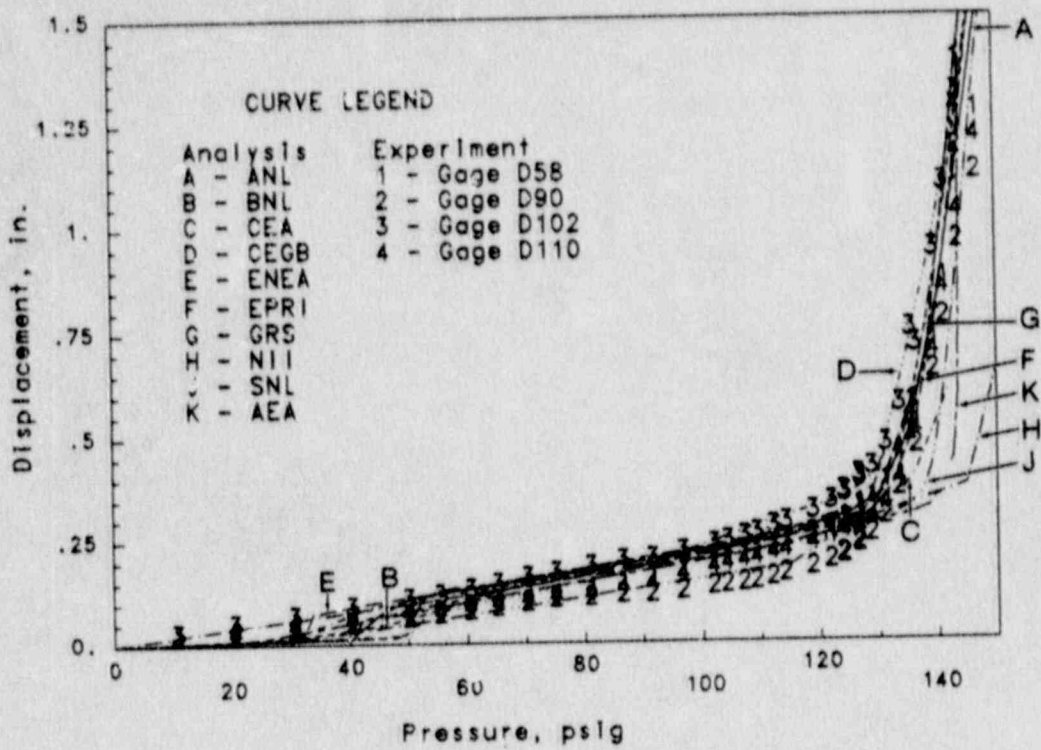
Figure 4.4  Pretest Predictions vs. Experimental Results:
Radial Displacement of Liner near El 18 ft (5.5 m)
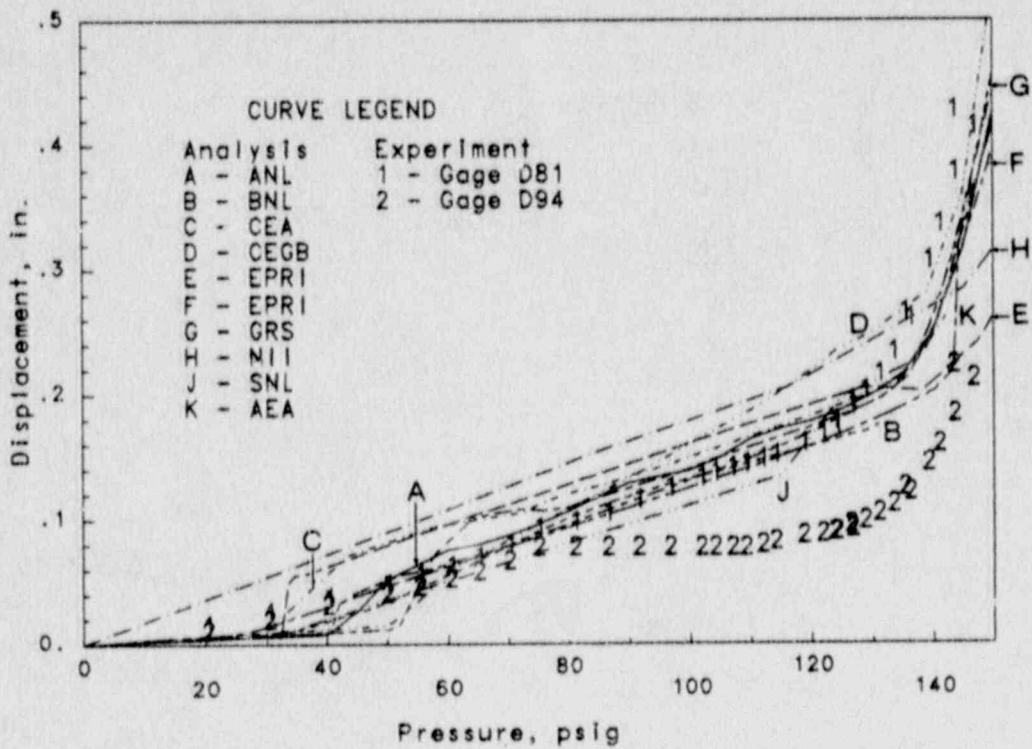


Figure 4.5  Pretest Predictions vs. Experimental Results:
Radial Displacement of Liner near El 24 ft (7.3 m)

4-7
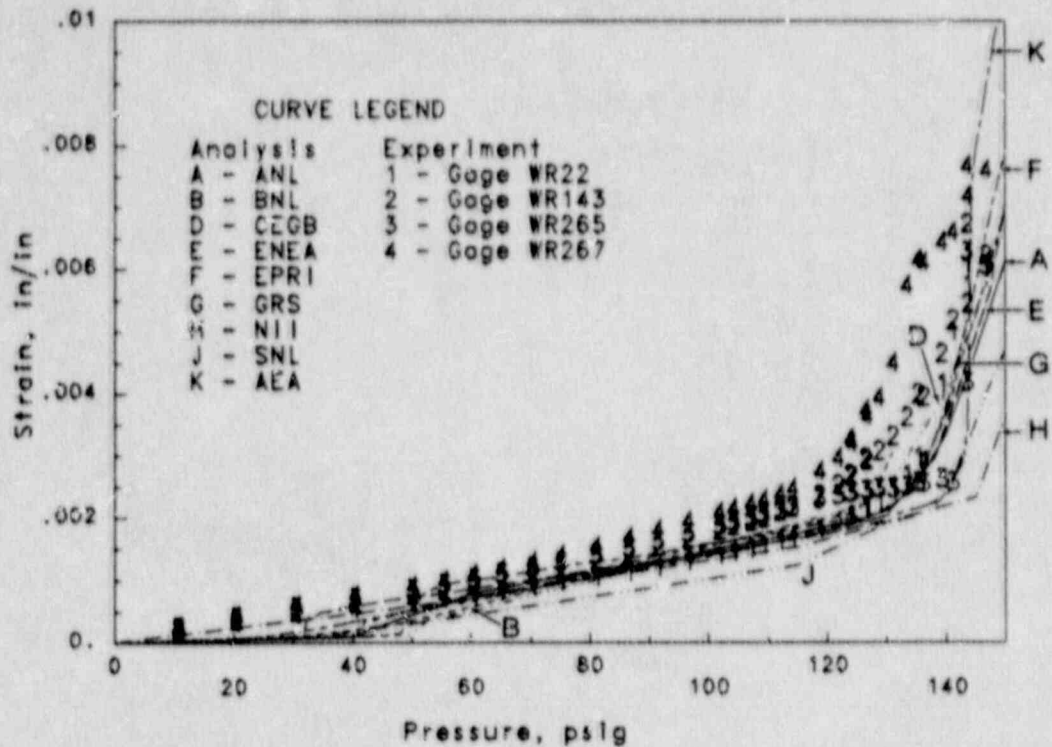
Figure 4.6  Pretest Predictions vs. Experimental Results:
Axial Strain in Layer 6 Hoop Rebar near El 6.75 ft (2.1 m)
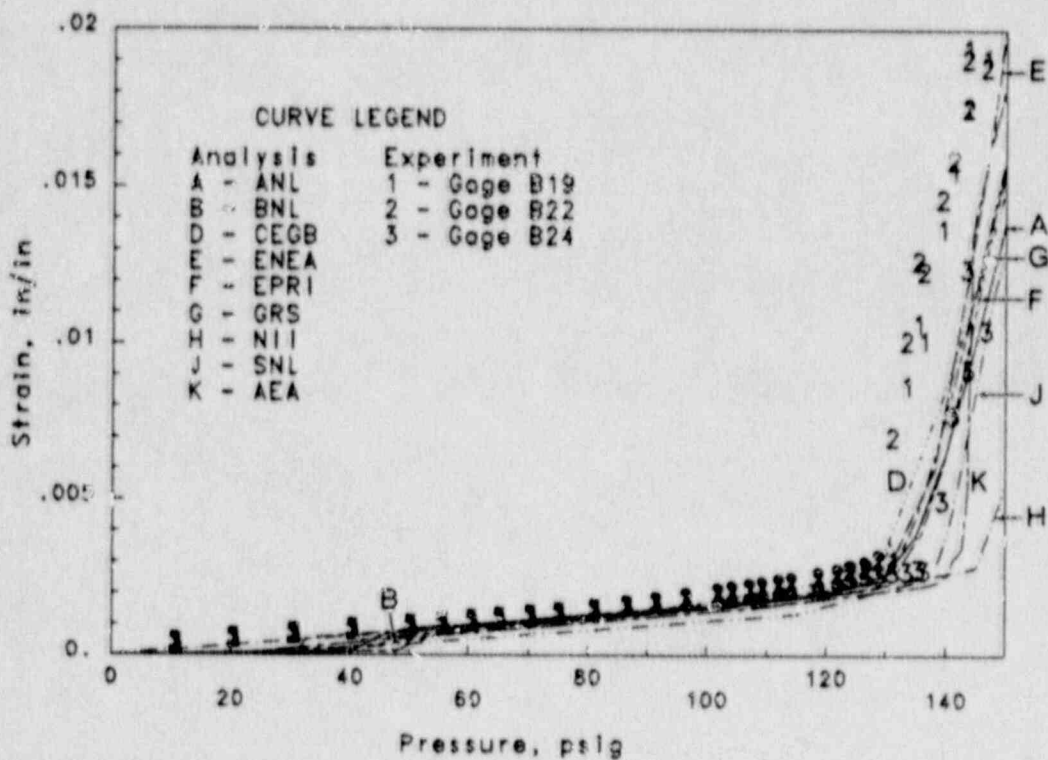


Figure 4.7  Pretest Predictions vs. Experimental Results:
Axial Strain in Layer 6 Hoop Rebar near El 13.75 ft (4.2 m)
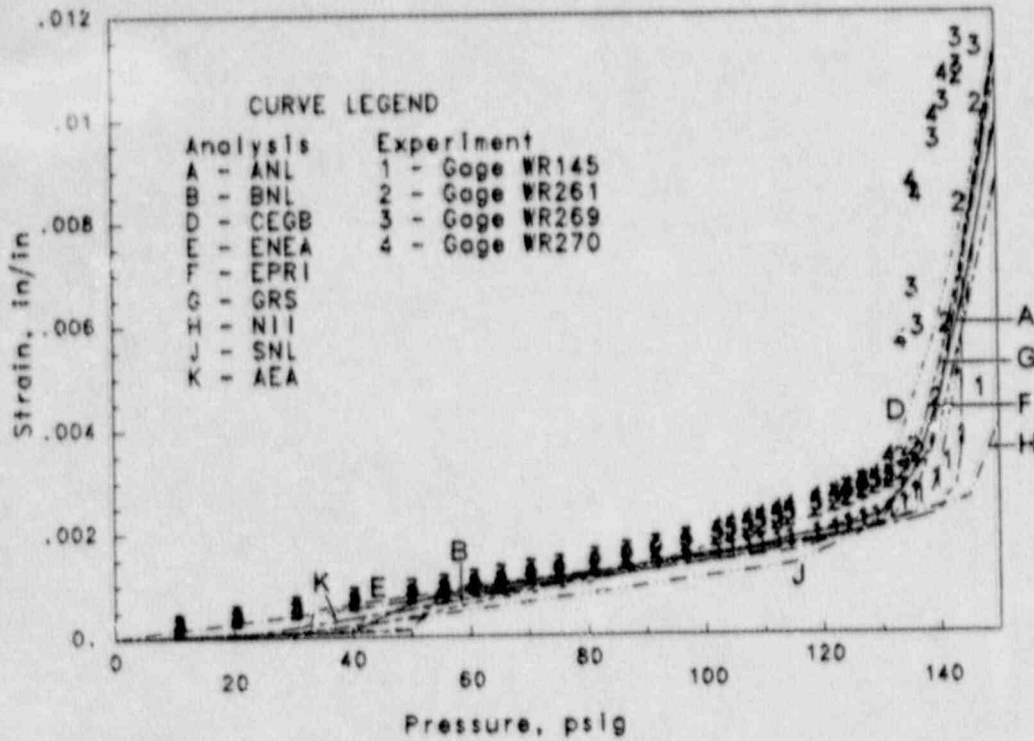
**Figure 4.8** Pretest Predictions vs. Experimental Results:
Axial Strain in Layer 6 Hoop Rebar near El 20 ft (6.1 m)
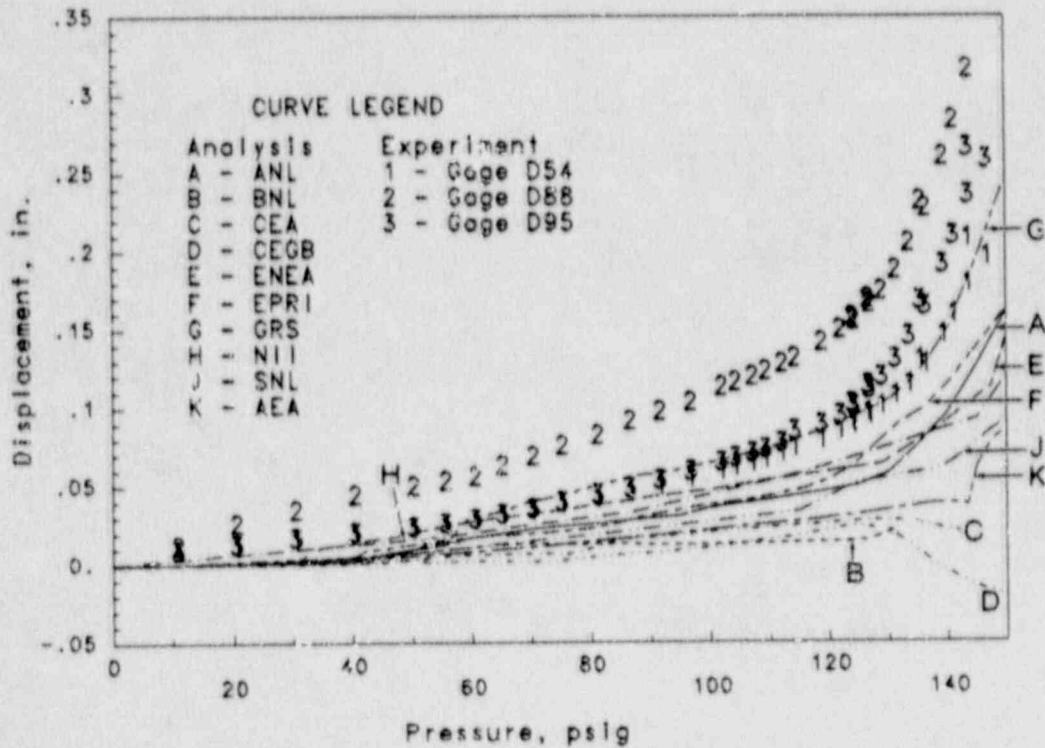


**Figure 4.9** Pretest Predictions vs. Experimental Results:
Vertical Displacement of Liner Relative to Cylinder Base near El 6 ft (1.8 m)
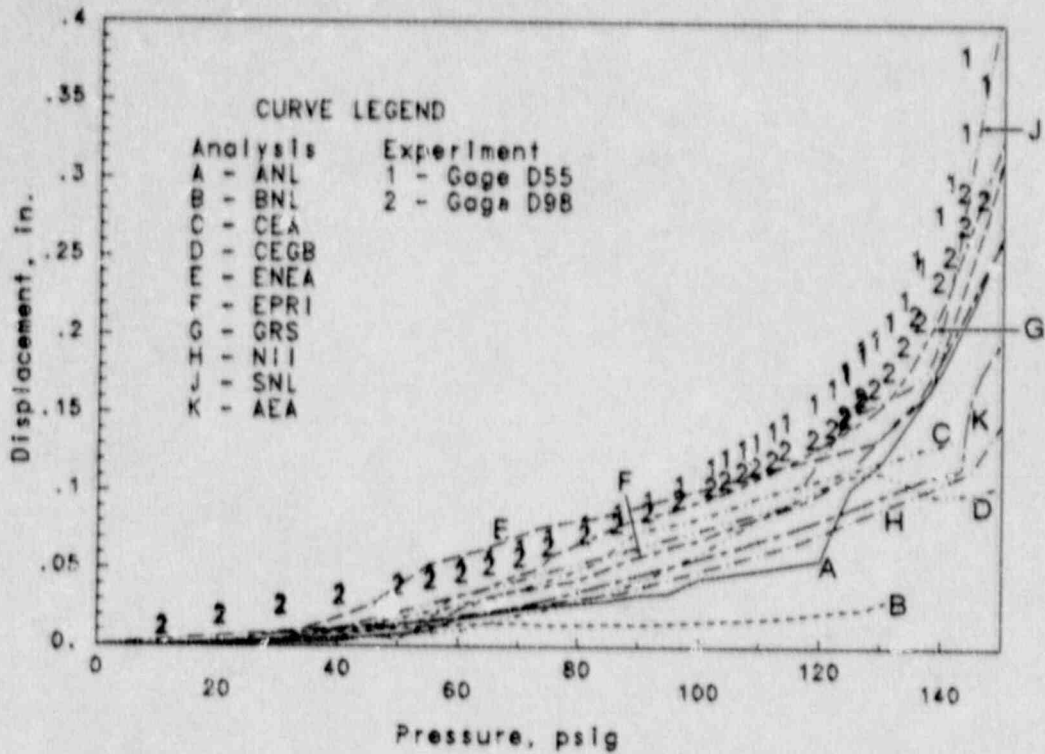
Figure 4.10 Pretest Predictions vs. Experimental Results:
Vertical Displacement of Liner Relative to Cylinder Base near El 11 ft (3.4 m)
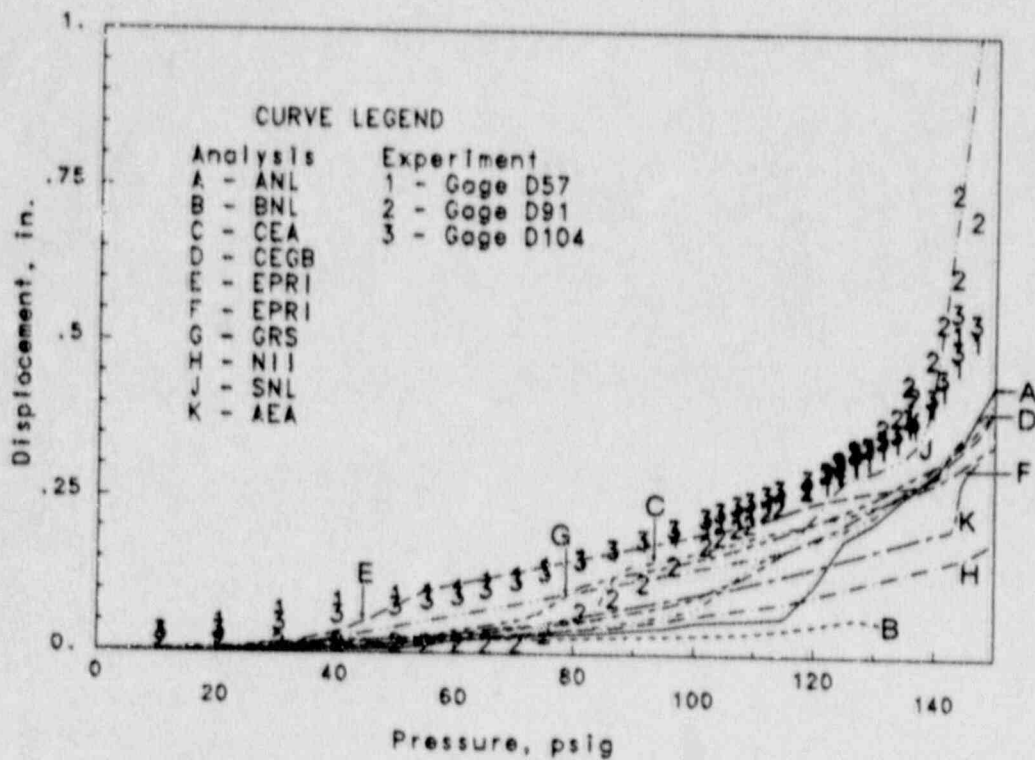


Figure 4.11 Pretest Predictions vs. Experimental Results:
Vertical Displacement of Liner Relative to Cylinder Base near El 18 ft (5.5 m)
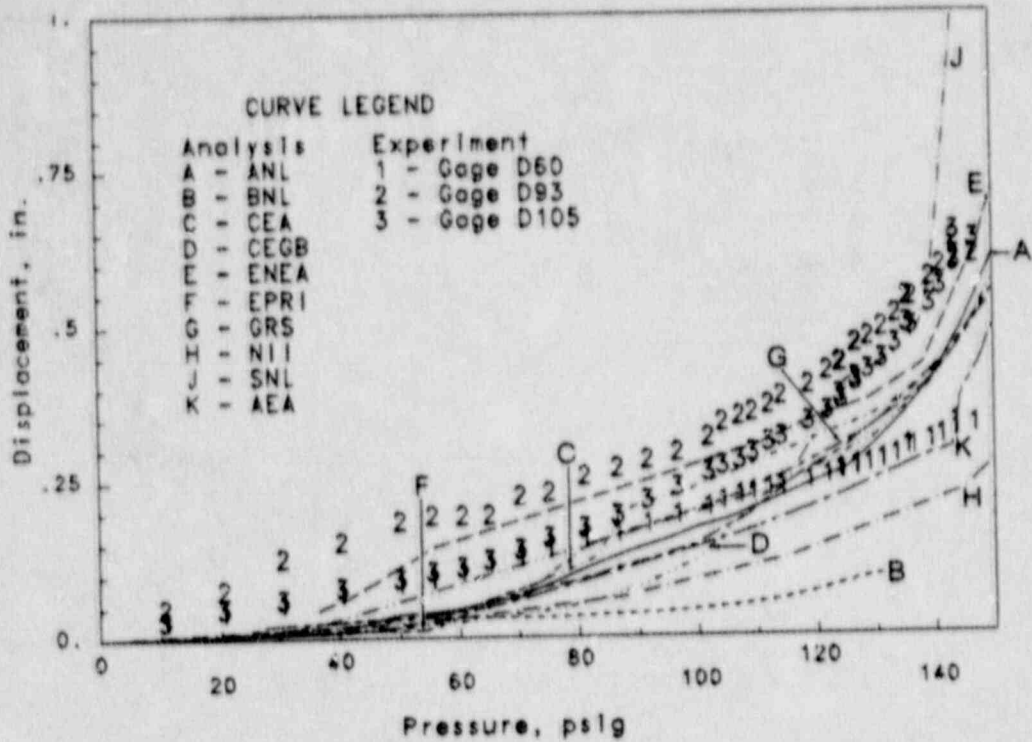
Figure 4.12 Pretest Predictions vs. Experimental Results:
Vertical Displacement of Liner Relative to Cylinder Base near El 24 ft (7.3 m)
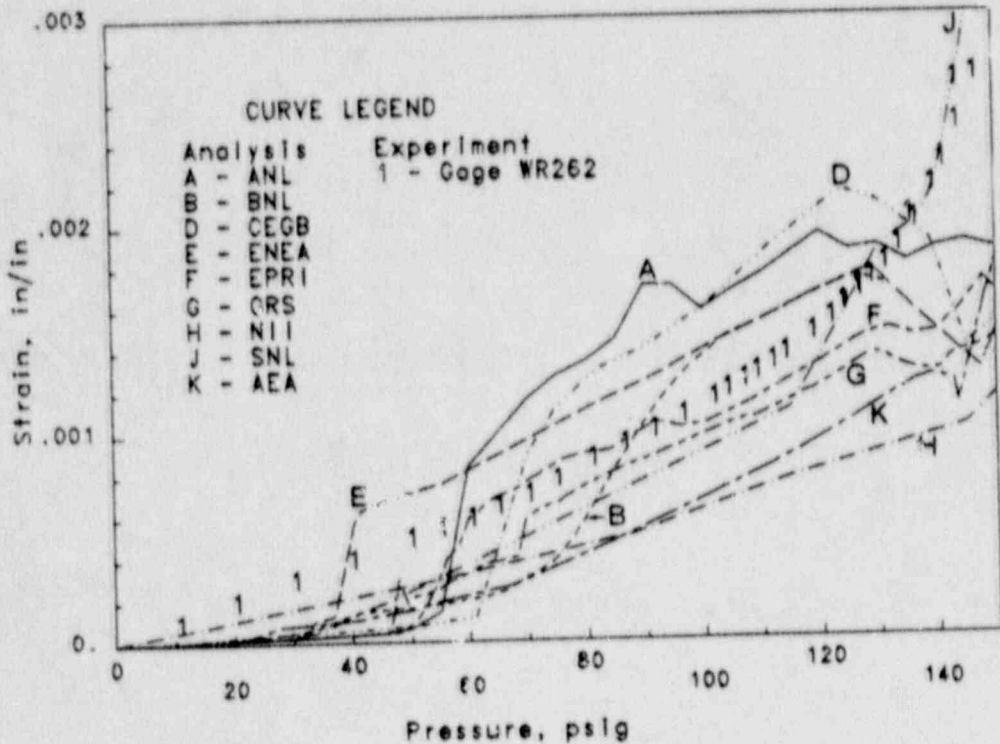


Figure 4.13 Pretest Predictions vs. Experimental Results:
Axial Strain in Layer 5 Meridional Rebar near El 6.75 ft (2.1 m)
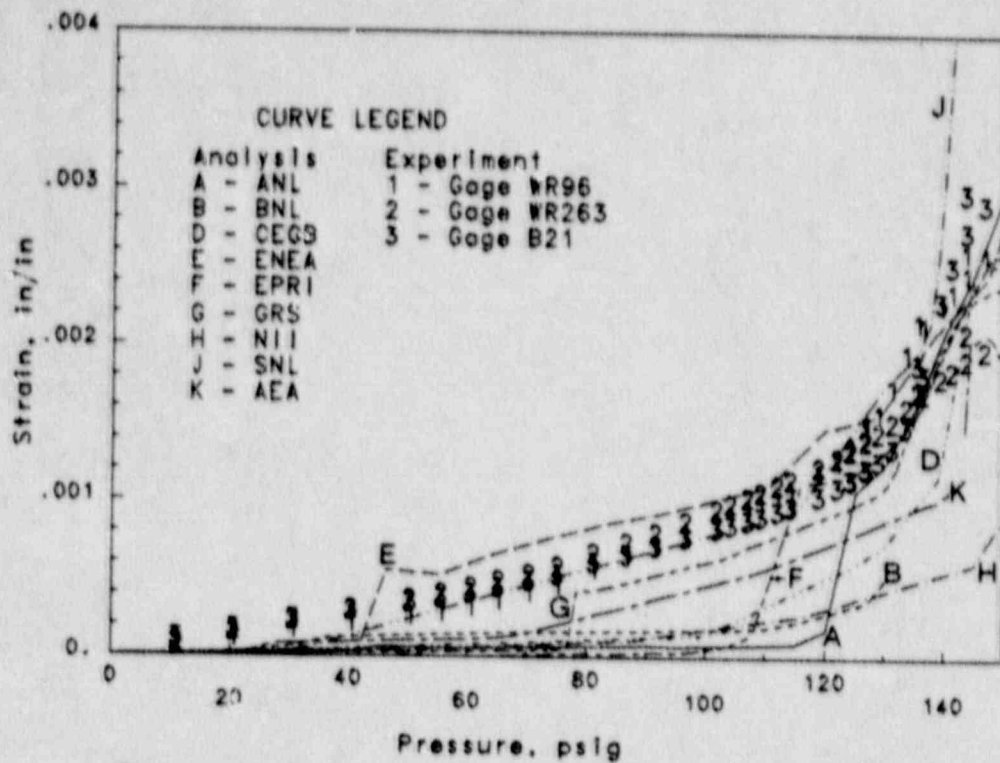
Figure 4.14 Pretest Predictions vs. Experimental Results:
Axial Strain in Layer 5 Meridional Rebar near El 13.75 ft (4.2 m)
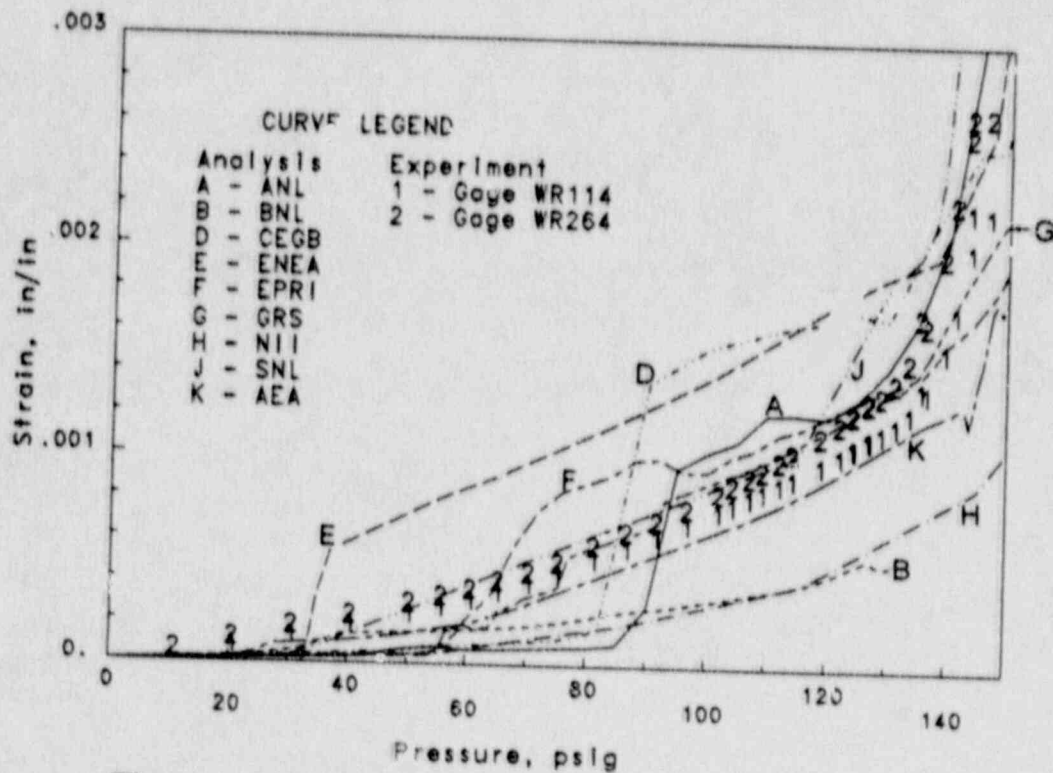


Figure 4.15 Pretest Predictions vs. Experimental Results:
Axial Strain in Layer 5 Meridional Rebar near El 20 ft (6.1 m)
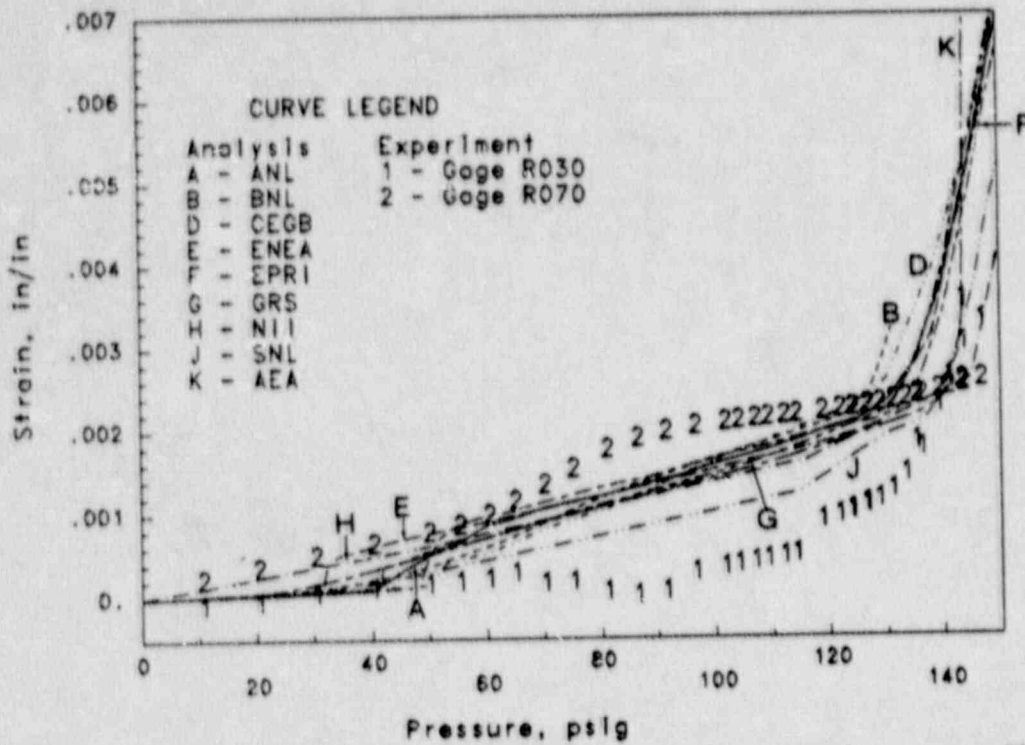
Figure 4.16  Pretest Predictions vs. Experimental Results:
Max Principal Strain on Inside Surface of Liner near El 6.75 ft (2.1 m)
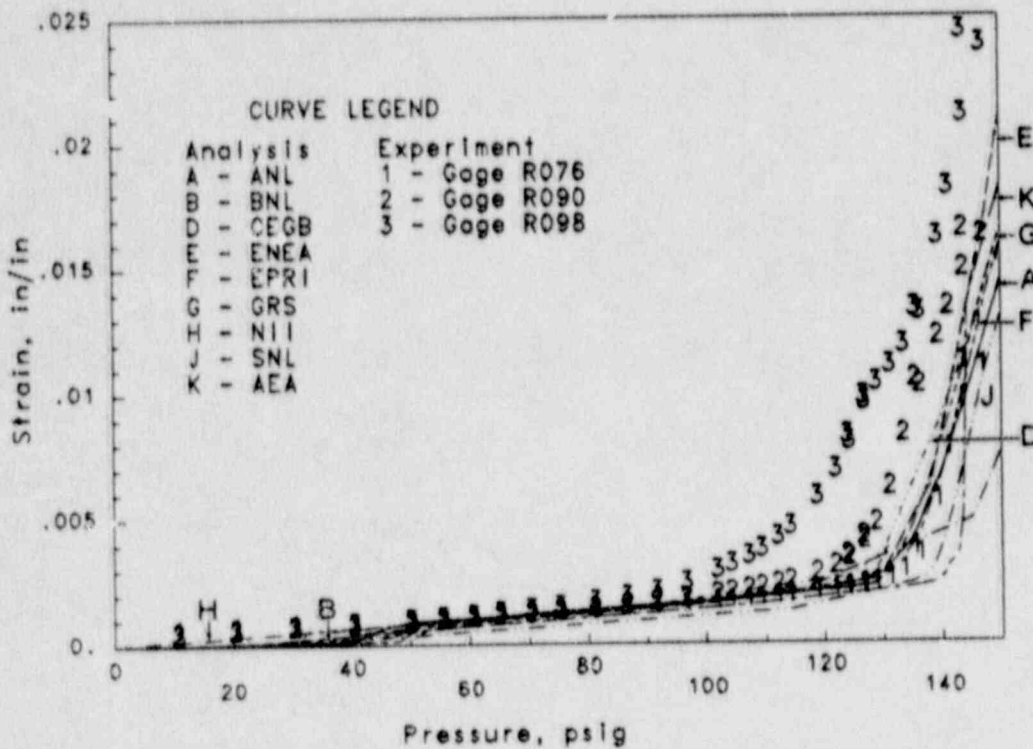


Figure 4.17  Pretest Predictions vs. Experimental Results:
Max Principal Strain on Inside Surface of Liner near El 13.75 ft (4.2 m)
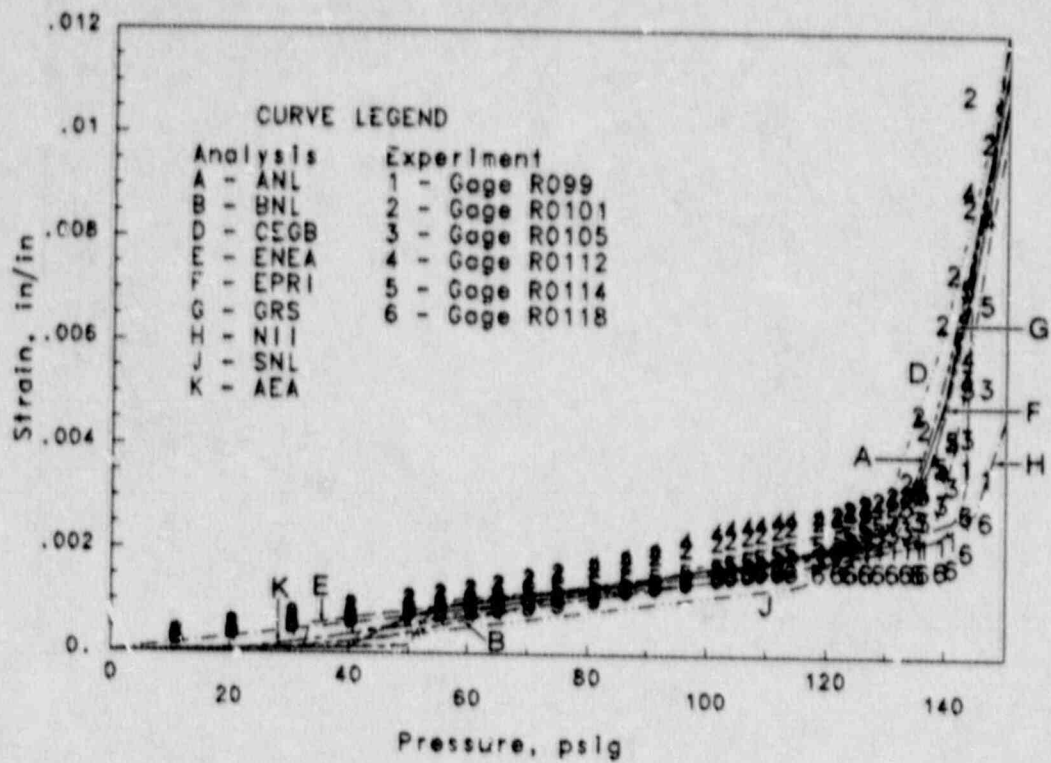
Figure 4.18 Pretest Predictions vs. Experimental Results:
Max Principal Strain on Inside Surface of Liner near El 20 ft (6.1 m)
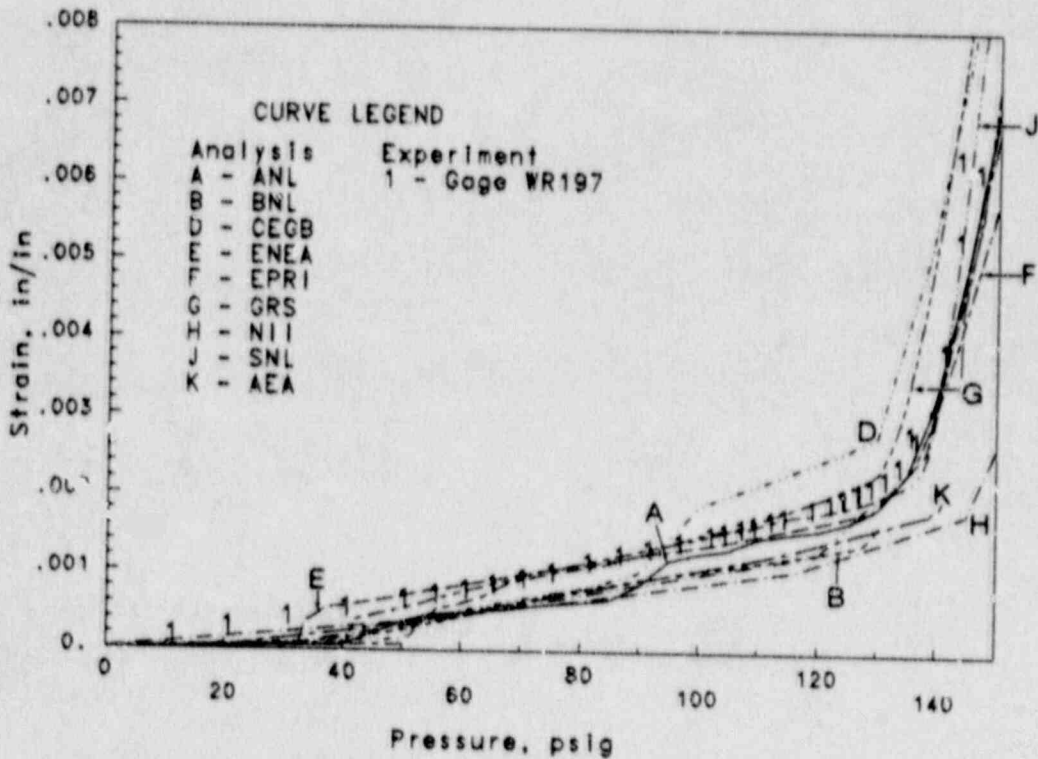


Figure 4.19 Pretest Predictions vs. Experimental Results:
Axial Strain in Layer 8 Seismic Rebar near El 20 ft (6.1 m)
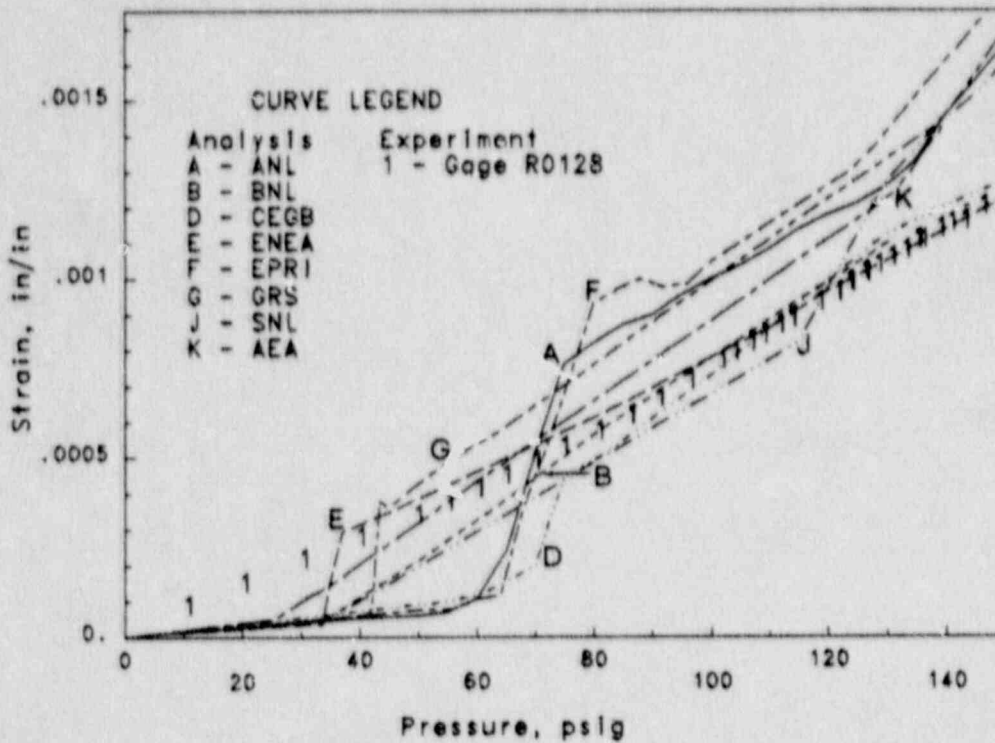
Figure 4.20 Pretest Predictions vs. Experimental Results:
Max Principal Strain on Inside Surface of Liner, φ≈37° (dome)
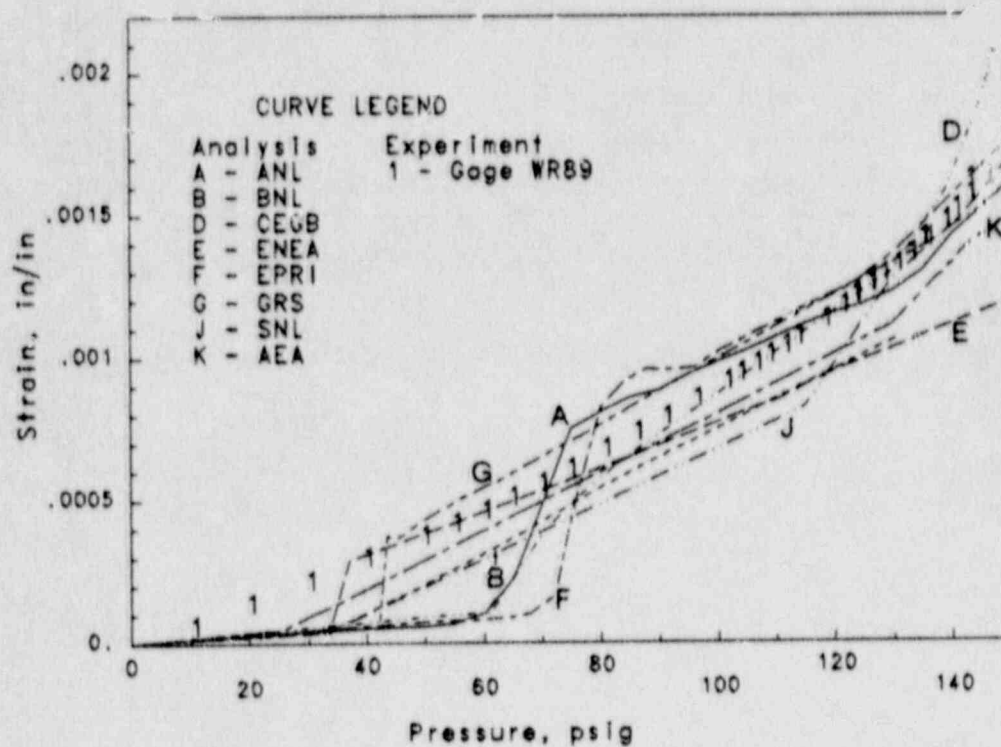


Figure 4.21 Pretest Predictions vs. Experimental Results:
Axial Strain in Layer 4 Hoop Rebar, φ≈37° (dome)
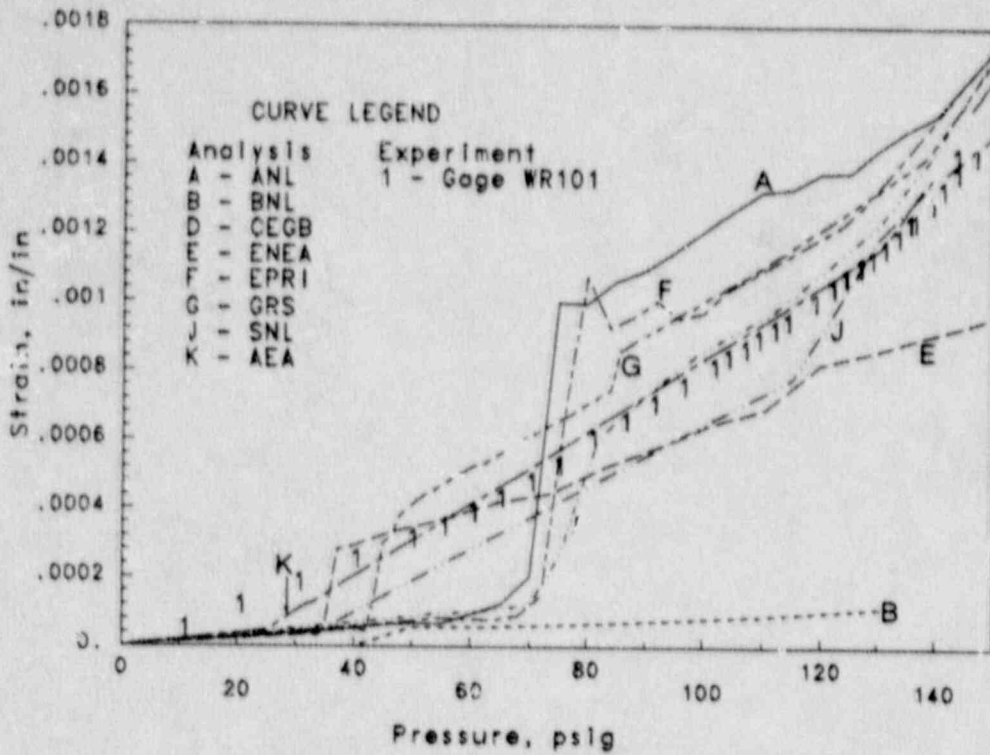
Figure 4.22 Pretest Predictions vs. Experimental Results:
Axial Strain in Layer 5 Meridional Rebar, $\phi \approx 37°$ (dome)
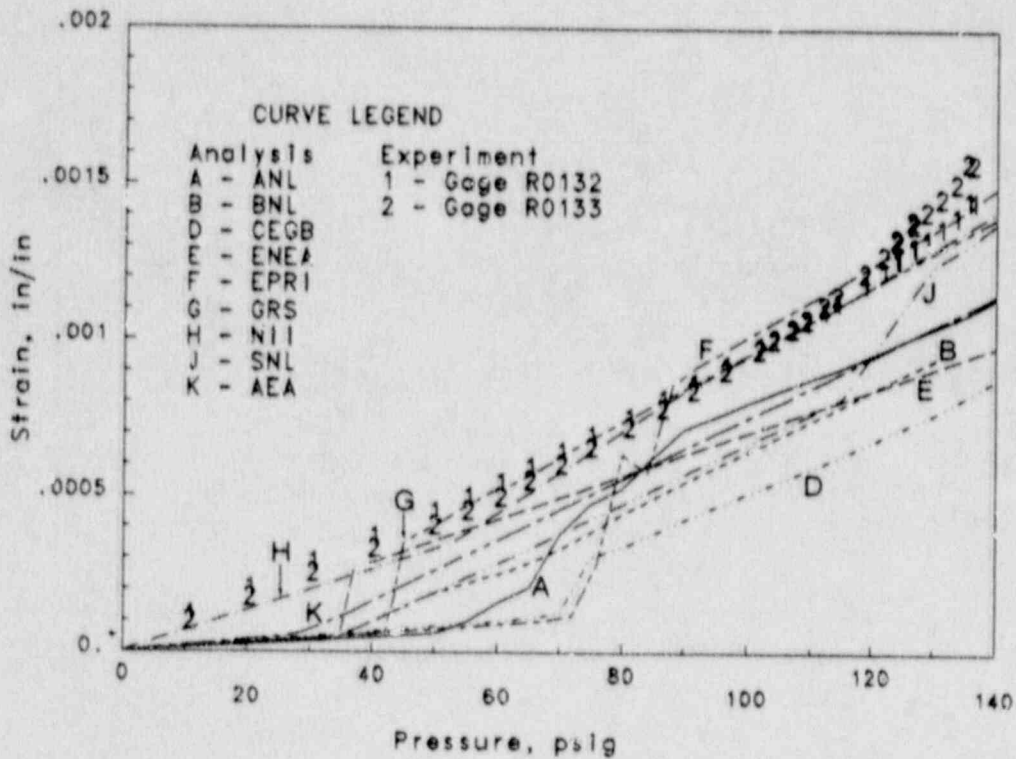


Figure 4.23 Pretest Predictions vs. Experimental Results:
Max Principal Strain on Inside Surface of Liner, $\phi \approx 72°$ (dome)
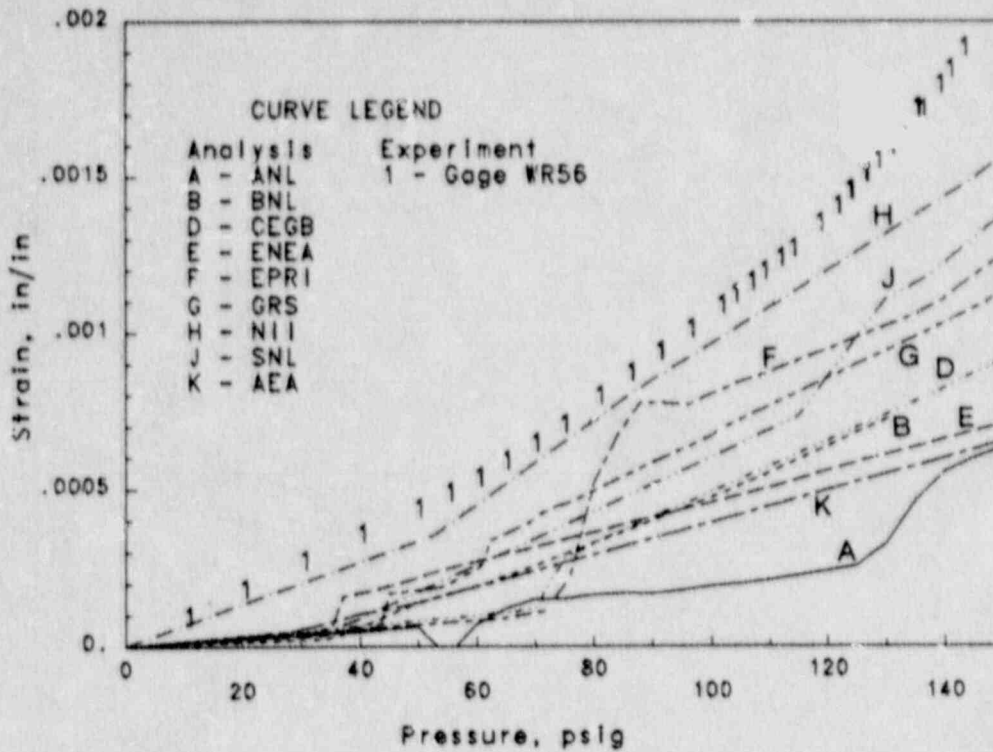
Figure 4.24  Pretest Predictions vs. Experimental Results:
Axial Strain in Layer 2 Meridional Rebar, $\phi \approx 72°$ (dome)
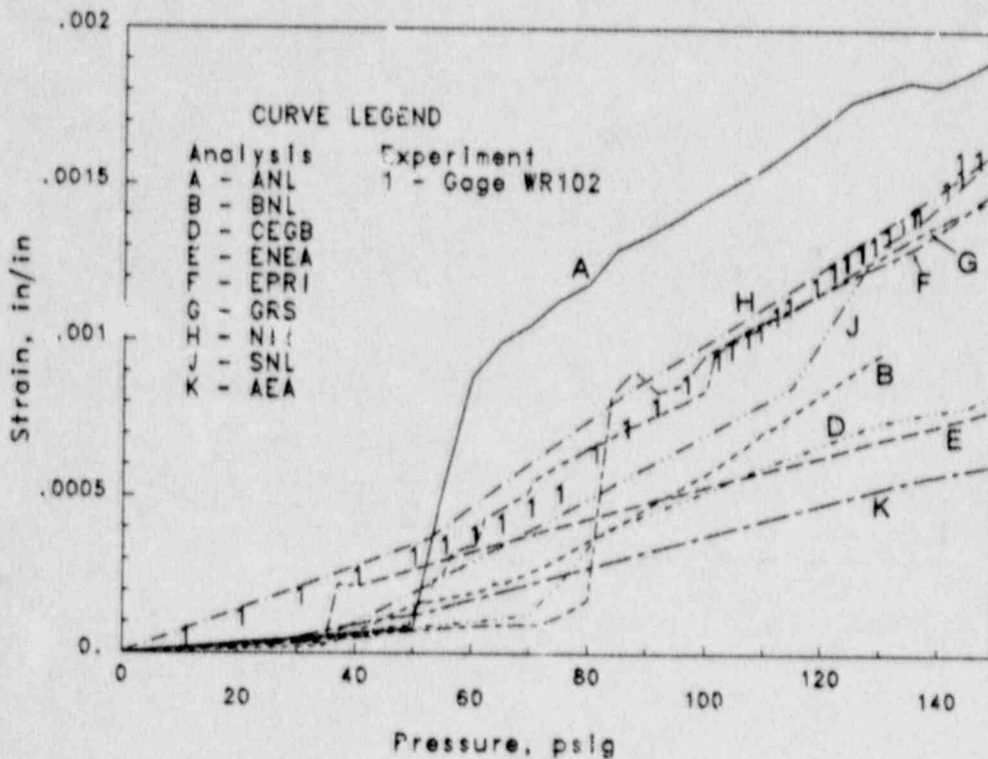


Figure 4.25  Pretest Predictions vs. Experimental Results:
Axial Strain in Layer 5 Meridional Rebar, $\phi \approx 72°$ (dome)
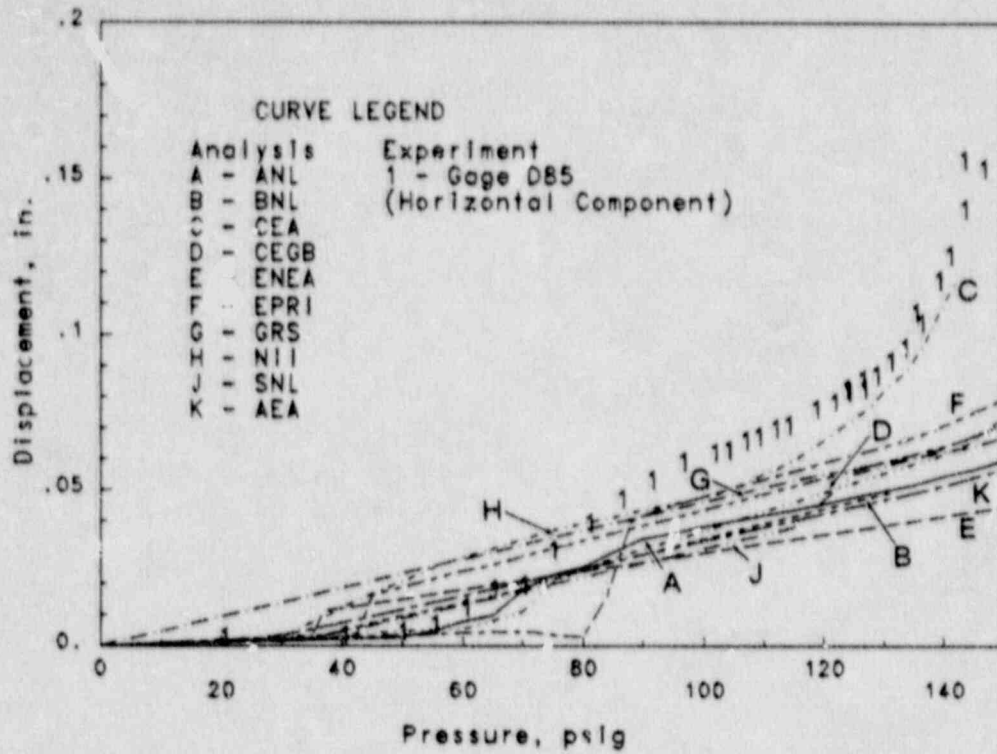
Figure 4.26 Pretest Predictions vs. Experimental Results:
Horizontal Displacement of Liner, $\phi \approx 70°$ (dome)
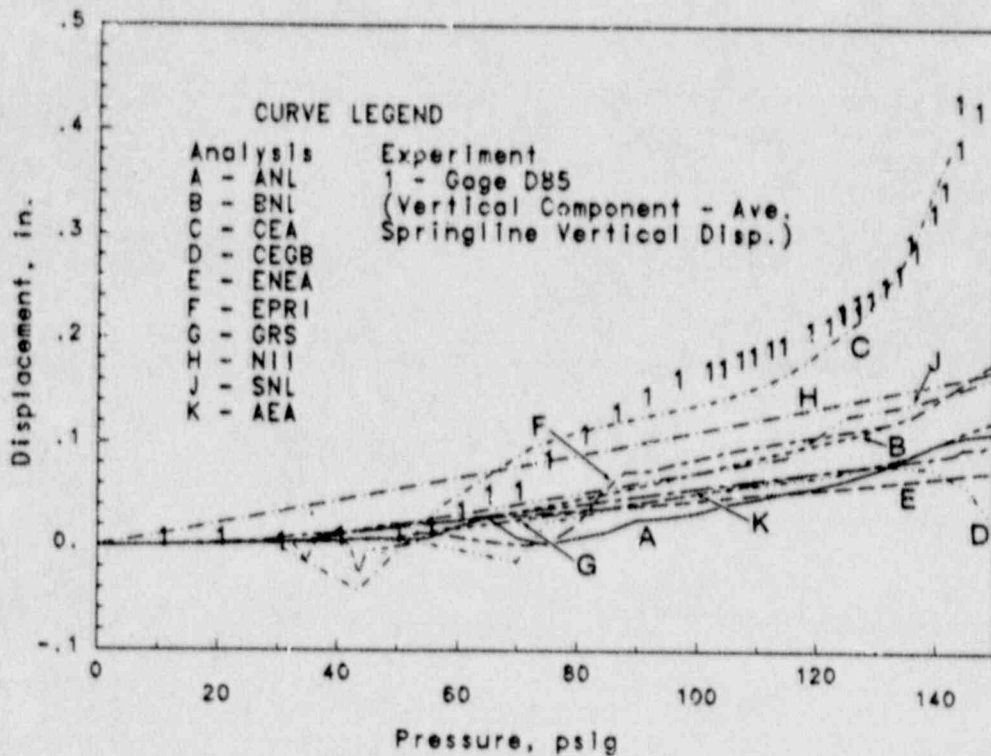


Figure 4.27 Pretest Predictions vs. Experimental Results:
Vertical Displacement of Liner Relative to Springline, $\phi \approx 70°$ (dome)
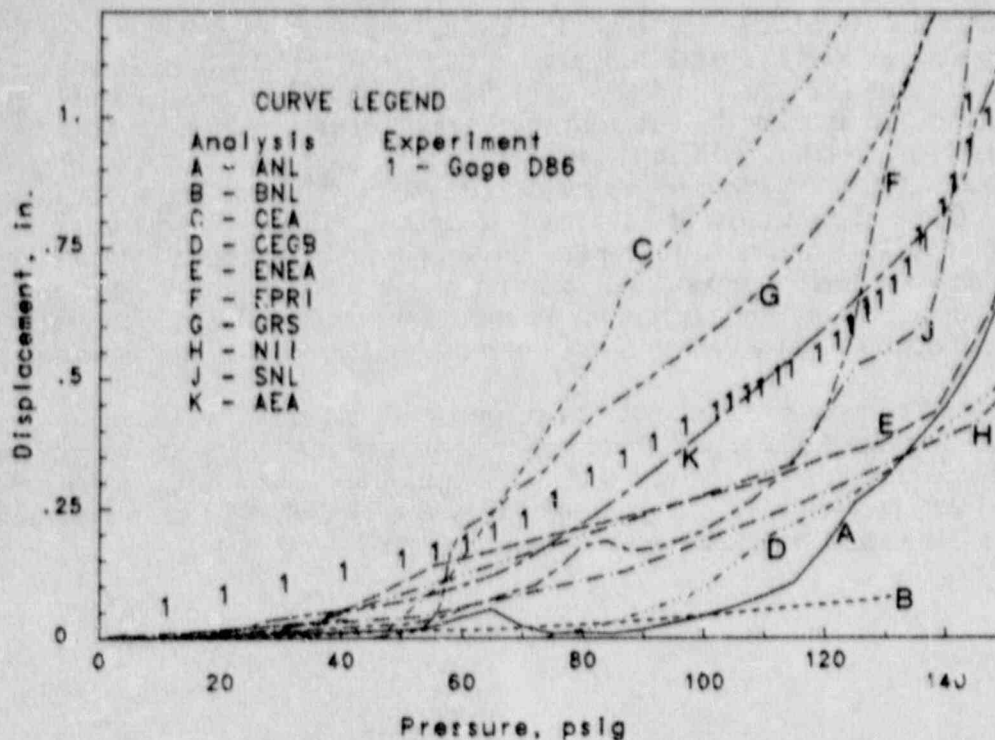
Figure 4.28 Pretest Predictions vs. Experimental Results:
Vertical Displacement of Liner at Dome Apex

## Local Response at Cylinder-Basemat Intersection and Springline

Basemat uplift is significant because it affects the shear force and bending moment at the cylinder-basemat junction. There were wide variations in the pretest predictions for basemat uplift, as indicated in Figure 4.29. The experimental data include one displacement transducer (inside the model) and three inclinometers. In the latter case, uplift was determined by multiplying the measured angle times the arm length (see Reference 12 for further details on the inclinometers). Figure 4.30 plots measured and calculated radial displacements of the cylinder wall at elevation 26 in. (0.66 m), which is just above the liner knuckle. The response at this point is also strongly coupled to the basemat response. In pretest analyses, the fill slab was either ignored or only its dead weight was considered. A number of groups performed parametric studies after the test to determine the effect of the fill slab, soil stiffness, and concrete cracking behavior on the calculation of basemat uplift. This led to significant improvement in the correlation between calculations and the experimental results. Detailed discussions can be found in Section 5.

The strains in the liner and meridional reinforcement change rapidly as a function of elevation near the cylinder-basemat intersection. The strain gage averages strain over its gage length and it can be difficult to locate gages at the point of maximum strain because this often occurs at a point of discontinuity or near a weld where application of gages is restricted. For these reasons, comparisons with analyses can be hard to interpret in regions of high strain gradient. Nevertheless, results for the liner strain above the knuckle, and the layer 2 and layer 5 meridional reinforcement are compared in Figures 4.31, 4.32, and 4.33, respectively. In Figure 4.31, gages WR281, WR287, and WR293 are at different azimuths but the same elevation,

approximately 2 ft (0.61 m). These are the closest gages on the cylinder liner to the knuckle. Gages WR282 and 283 are at the same azimuth as WR281, but approximately 2 in. (51 mm) and 4.5 in. (114 mm) above WR281, respectively. These gages indicate how quickly the strain in the liner decreases away from the knuckle. EPRI greatly overestimated the strains in the liner near the knuckle, but other analysts came reasonably close to the measured results. The bending in the cylinder is evident from comparison of Figures 4.32 and 4.33. It is interesting that the maximum bending appears to take place at an elevation of about 1.9 ft (0.58 m), which is *below* the liner knuckle. There is a 3 in. (76 mm) leveling course atop the basemat; it appears that the maximum moment is developed at the intersection of the cylinder with the basemat-leveling course interface, and not at the liner knuckle.

The measured response and calculated response at the springline is compared in Figures 4.34 through 4.36. Again, there is clear evidence of bending at this section, as can be seen from a comparison of Figures 4.35 and 4.36. The strains in the liner at the springline are also elevated (compare Figure 4.34 to 4.18), but not enough to cause any significant distress or threat to the model integrity.
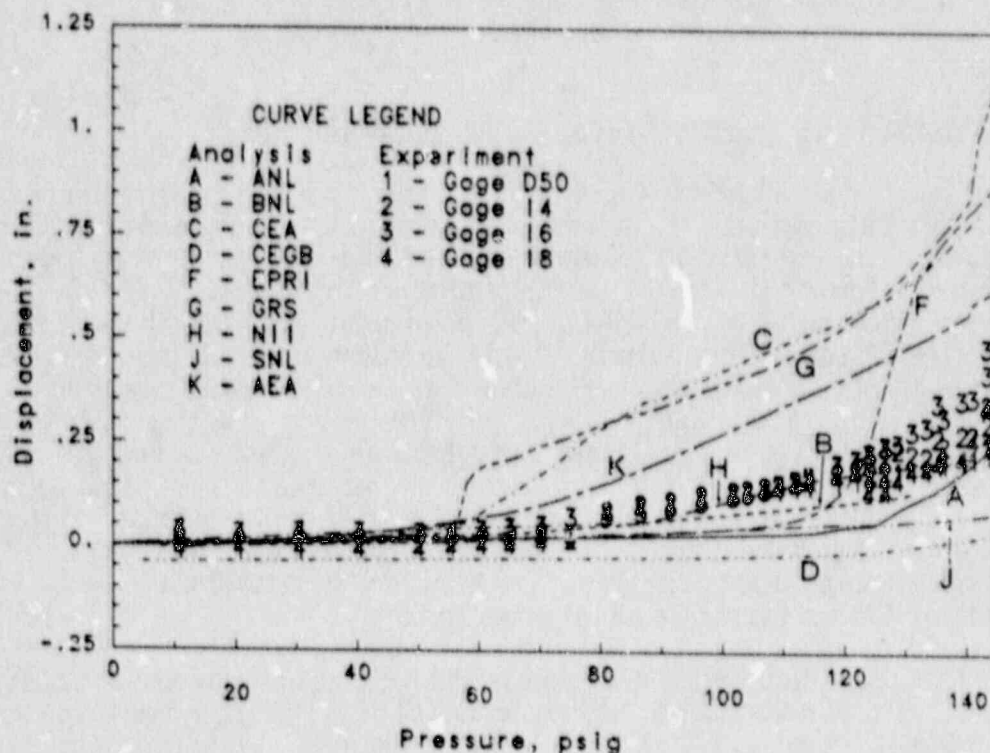


Figure 4.29 Pretest Predictions vs. Experimental Results:
Basemat Uplift Near Cylinder Wall Relative to Center of Basemat
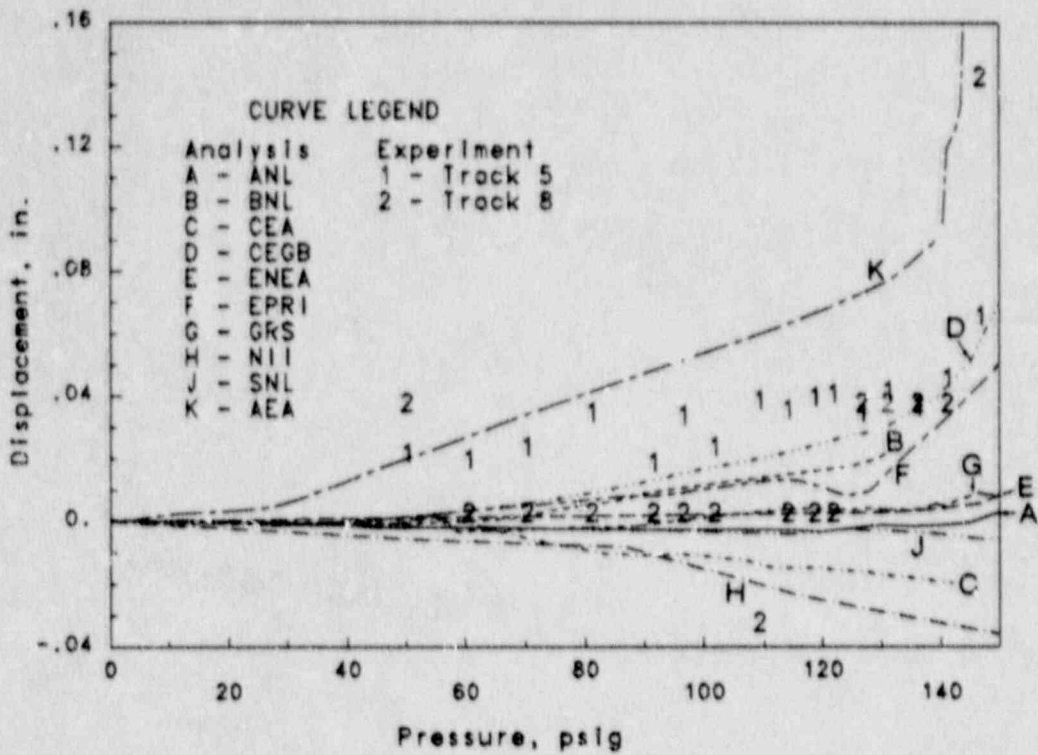
Figure 4.30 Pretest Predictions vs. Experimental Results: Radial Displacement of Liner near El 2.2 ft (0.66 m)
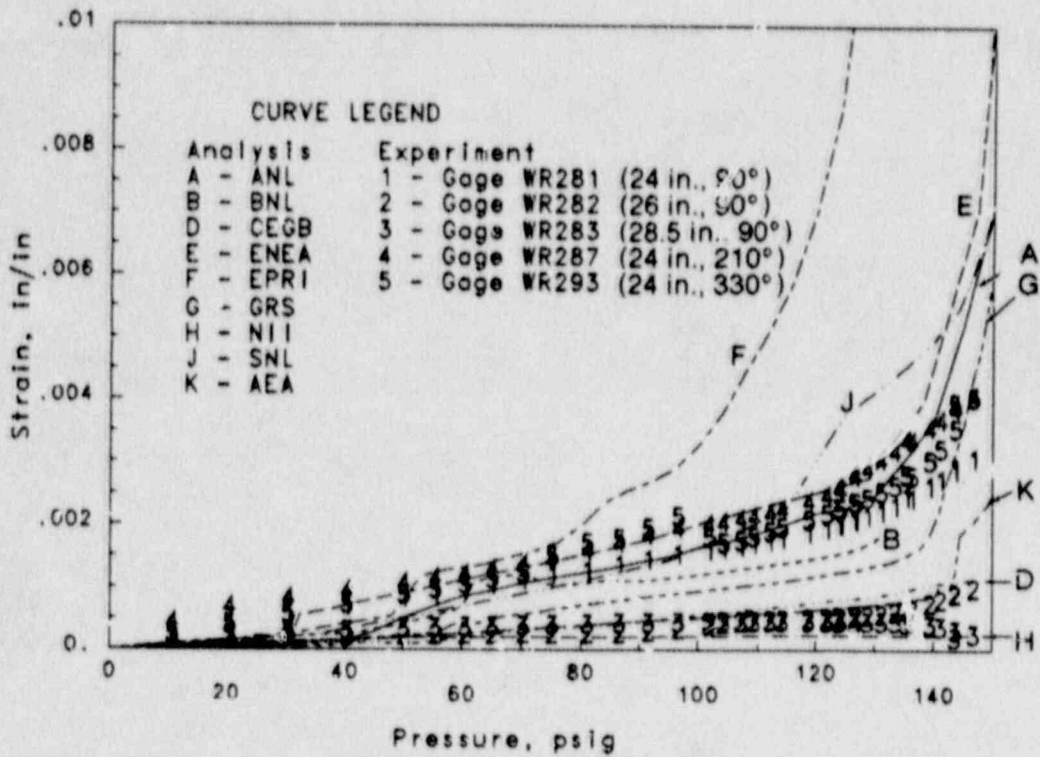


Figure 4.31 Pretest Predictions vs. Experimental Results: Max Principal Strain on Inside Surface of Liner near El 2 ft (0.61 m)
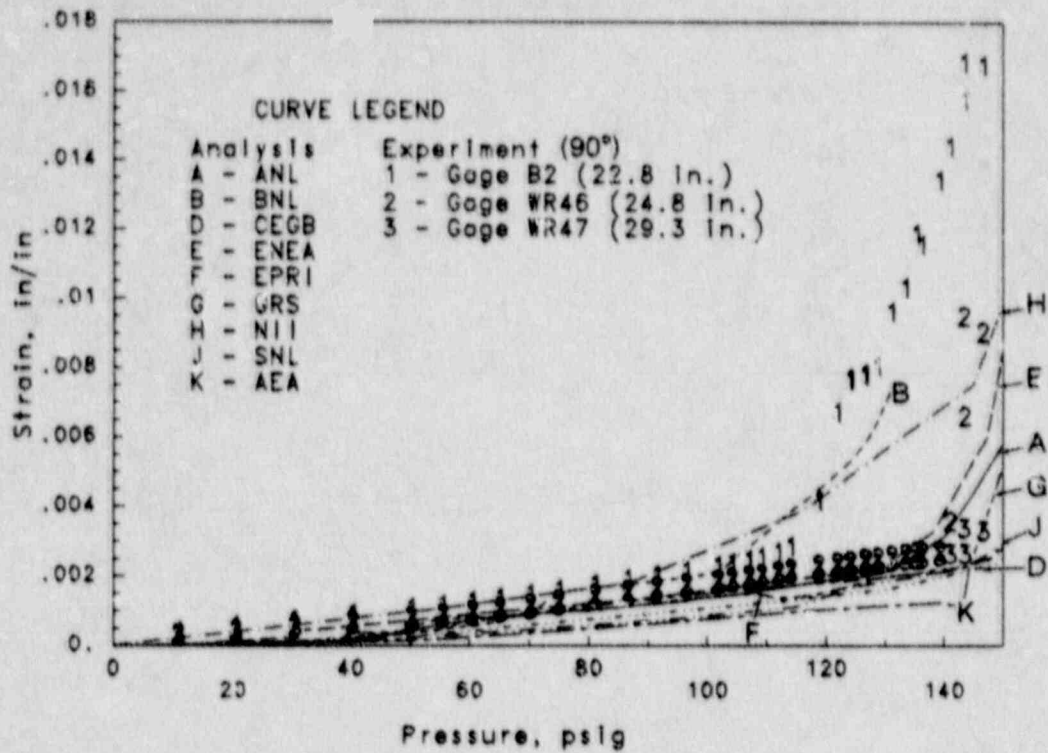
Figure 4.32 Pretest Predictions vs. Experimental Results:
Axial Strain in Layer 2 Meridional Rebar near El 2.1 ft (0.64 m)
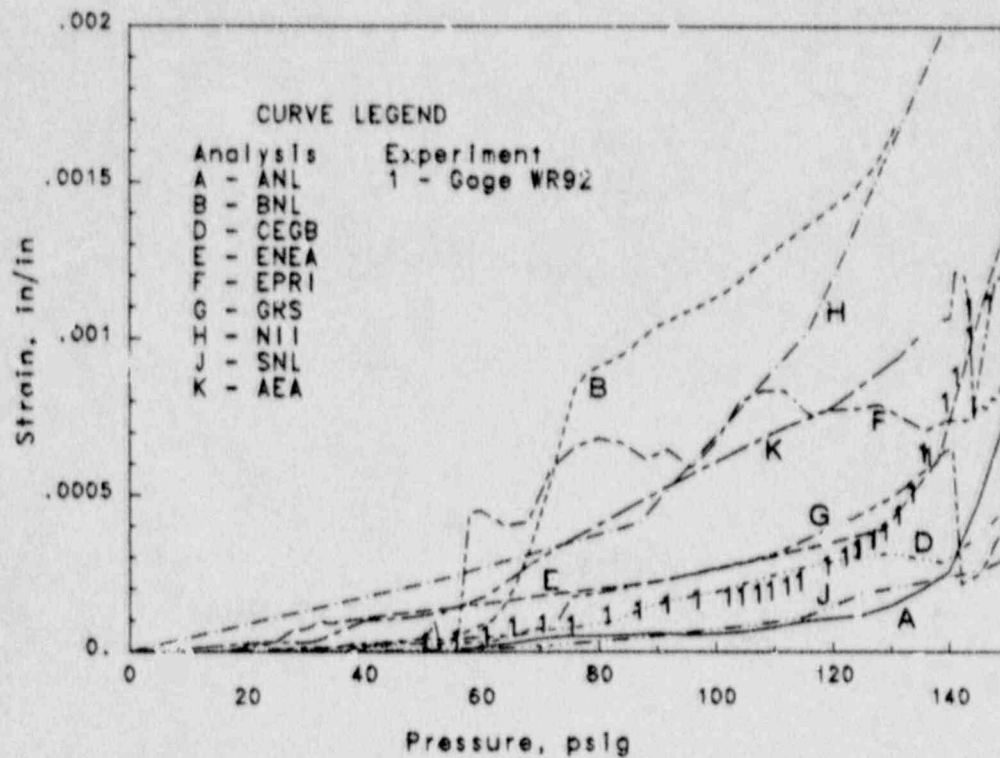


Figure 4.33 Pretest Predictions vs. Experimental Results:
Axial Strain in Layer 5 Meridional Rebar near El 2.1 ft (0.64 m)
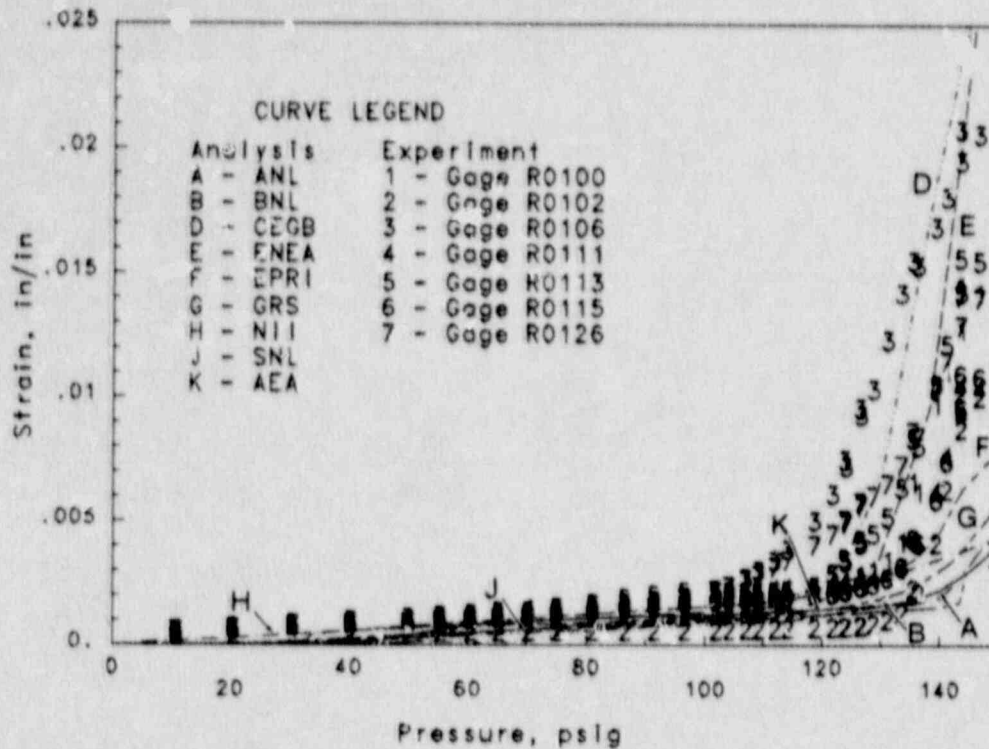
Figure 4.34  Pretest Predictions vs. Experimental Results:
Max Principal Strain on Inside Surface of Liner near El 24 ft (7.3 m)
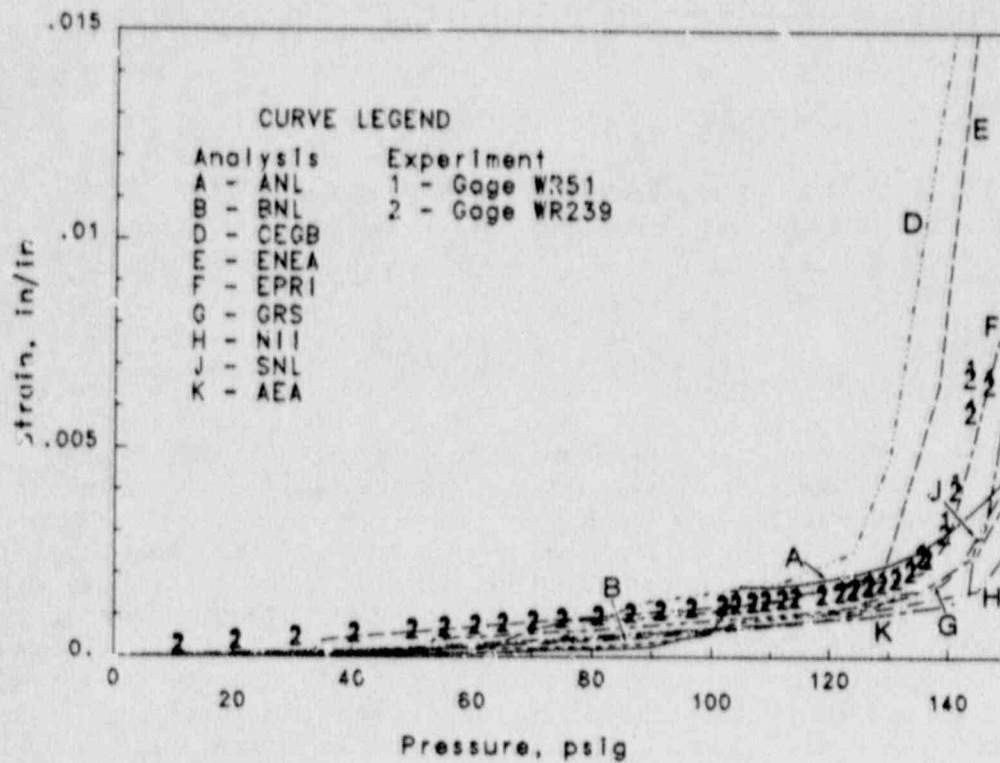


Figure 4.35  Pretest Predictions vs. Experimental Results:
Axial Strain in Layer 2 Meridional Rebar near El 24 ft (7.3 m)
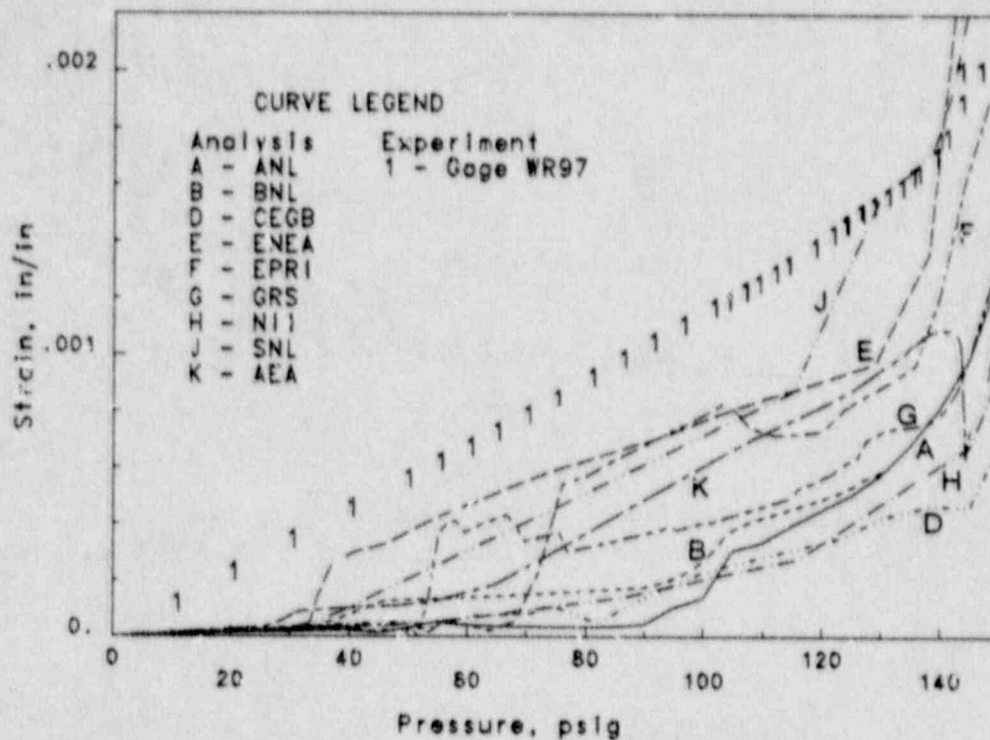
Figure 4.36 Pretest Predictions vs. Experimental Results:
Axial Strain in Layer 5 Meridional Rebar near El 24 ft (7.3 m)

## 3-D Response Near Penetrations

Only two organizations, ANL and EPRI, completed any 3-D analyses prior to the publication of the pretest round-robin report. The standard plots are included here for completeness. Figures 4.37 through 4.39 show the radial displacement of the cylinder at three different azimuths at the elevation of the constrained pipe penetration. The analysis overestimated the stiffness of the penetration at high pressure. This was also the case for EPRI's prediction for the outward radial displacement of Equipment Hatch B, which is compared to the measured result in Figure 4.40. Strain in the liner and meridional rebar near Equipment Hatch B are shown in Figures 4.41 and 4.42, respectively. ANL was able to predict ovalization of equipment hatch B with good accuracy, as indicated in Figures 4.43 and 4.44. It should be noted here that the ovalization of equipment hatch A was significantly greater than that at B; for a more complete discussion of ovalization, see Reference 14.
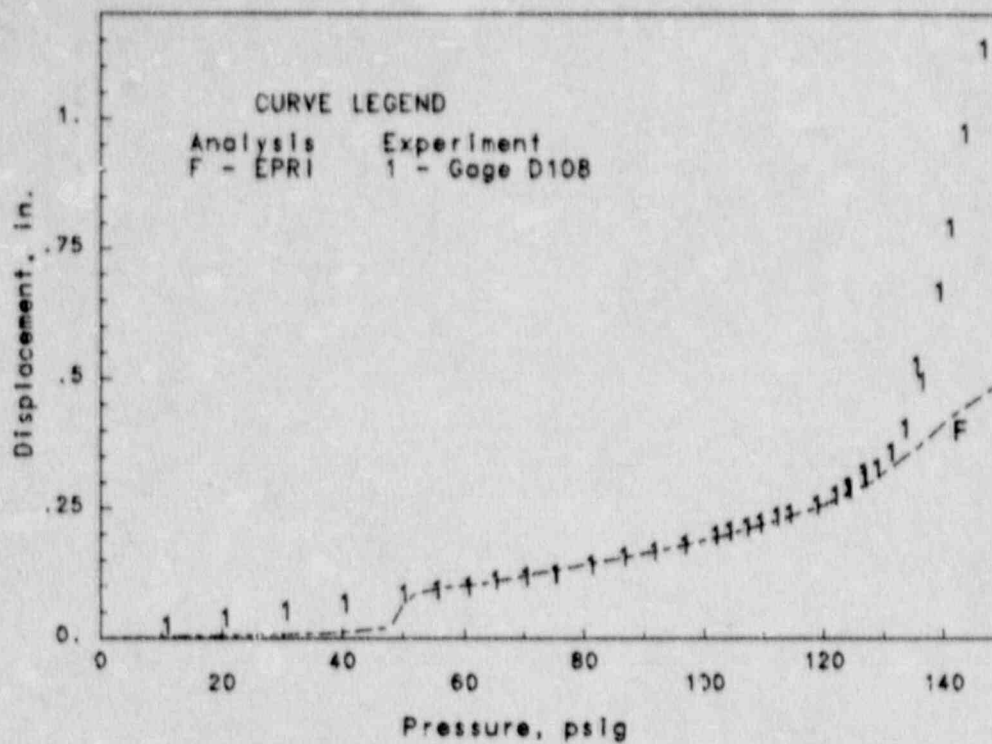
Figure 4.37  Pretest Predictions vs. Experimental Results: Constrained Pipe
Radial Displacement of Liner at El 20.1 ft (6.13 m), $\theta$ = 312°
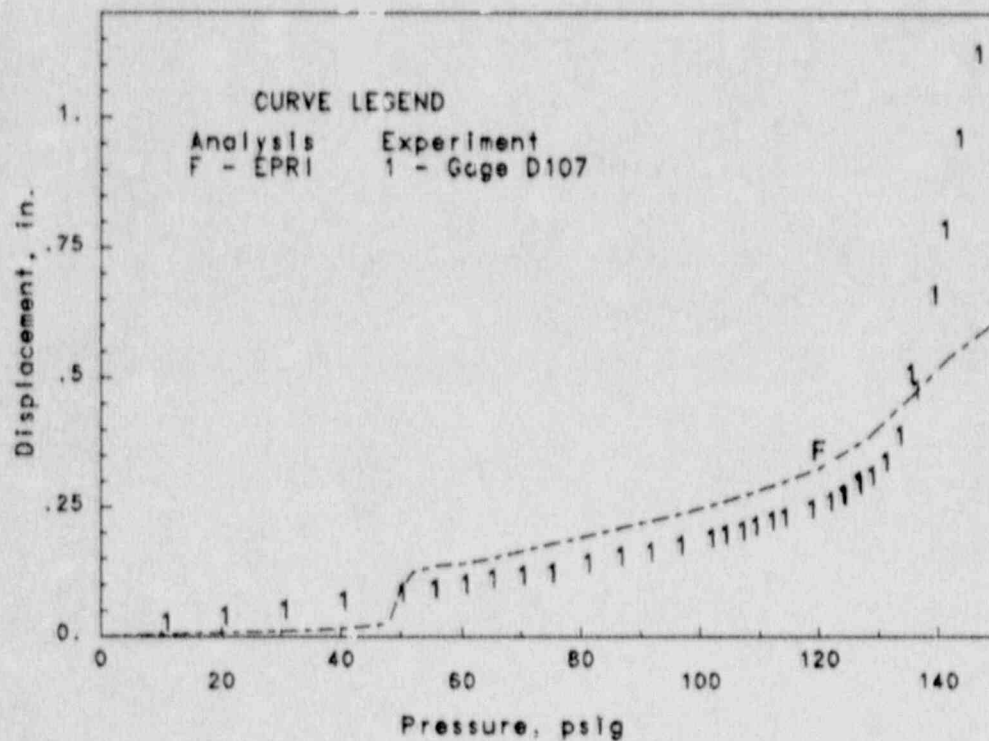


Figure 4.38  Pretest Predictions vs. Experimental Results: Constrained Pipe
Radial Displacement of Liner at El 20.1 ft (6.13 m), $\theta$ = 305°
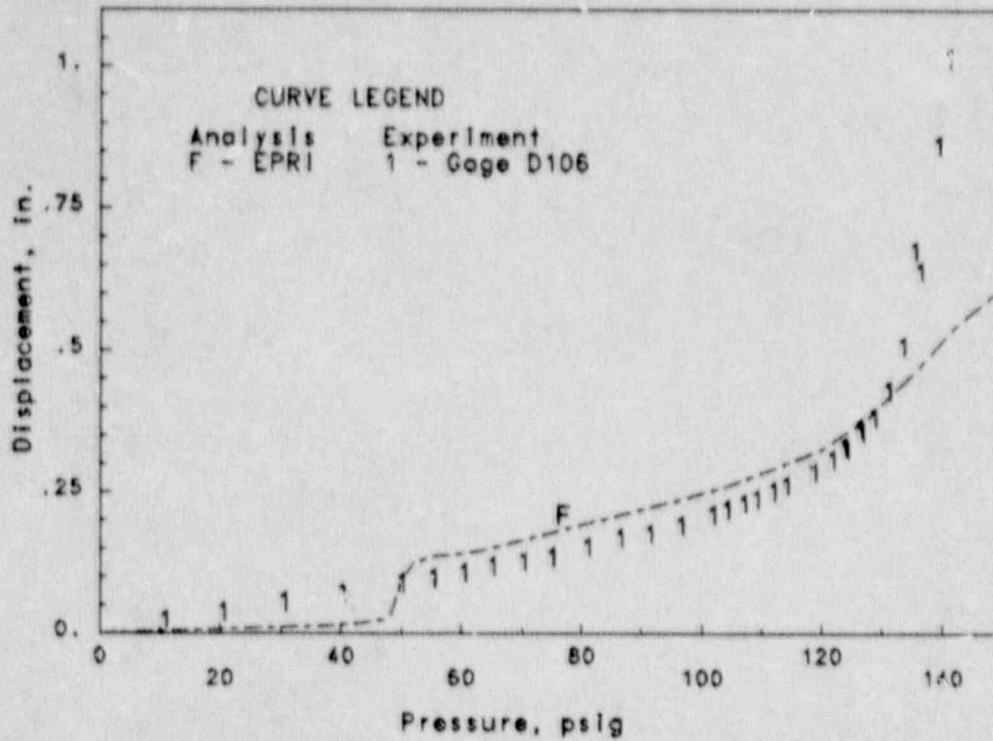
Figure 4.39 Pretest Predictions vs. Experimental Results: Constrained Pipe Radial Displacement of Liner at El 20.1 ft (6.13 m), $\theta = 290°$
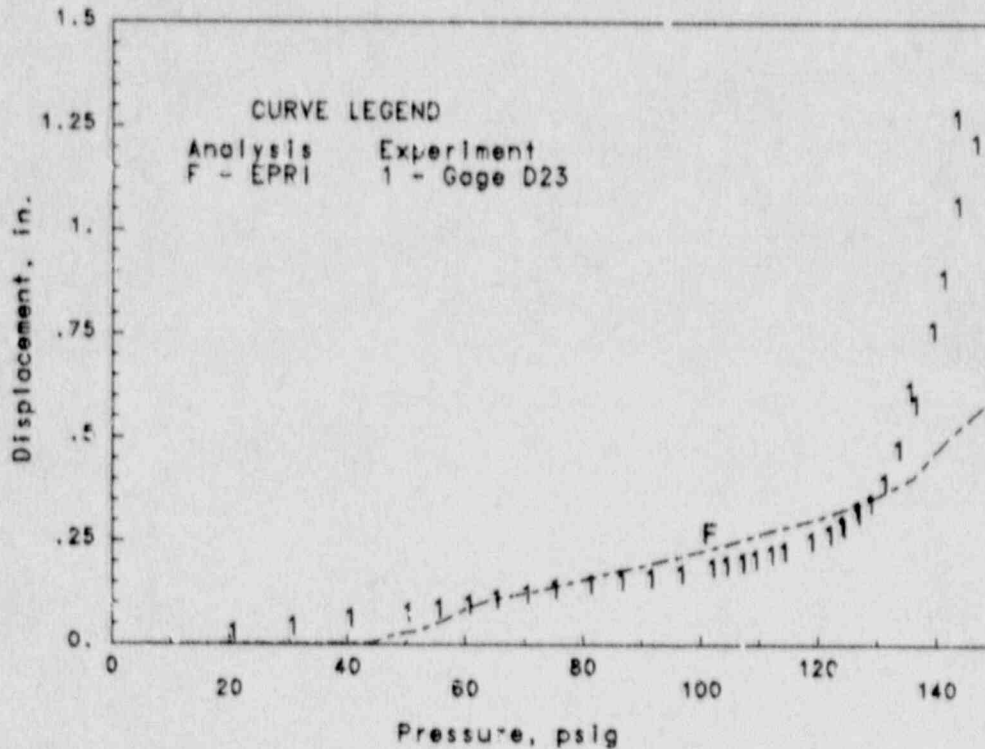


Figure 4.40 Pretest Predictions vs. Experimental Results: Equipment Hatch B Outward Radial Displacement of Sleeve at El 14.58 ft (4.45 m). $\theta = 180°$
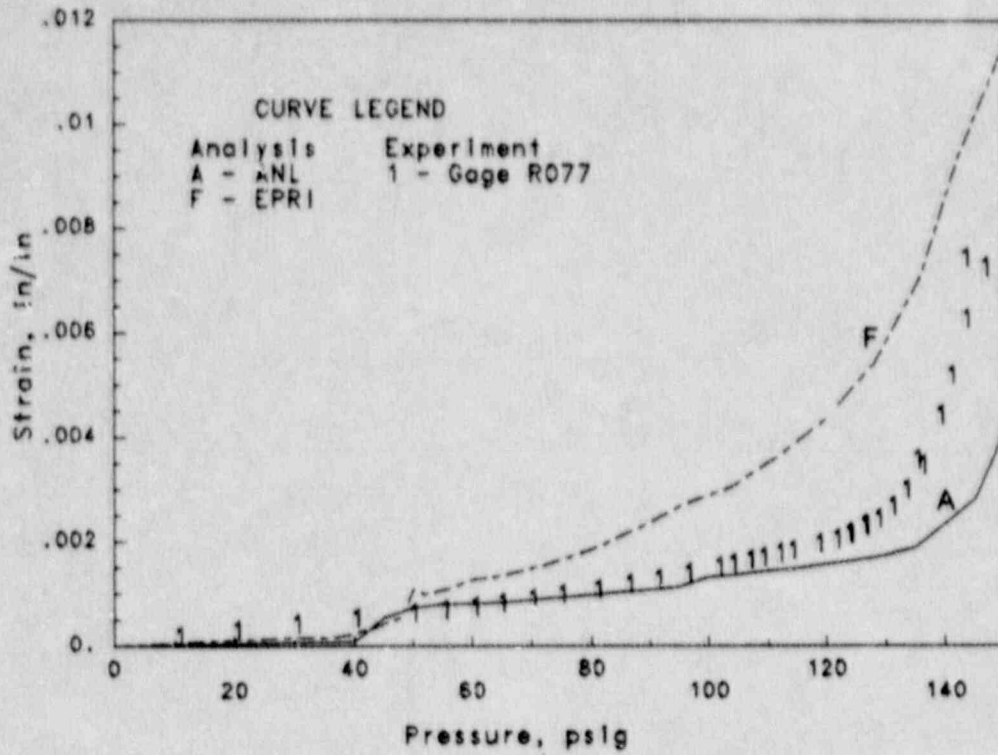
Figure 4.41 Pretest Predictions vs. Experimental Results: Equipment Hatch B
Max Principal Strain on Inside Surface of Liner at El 13 ft (3.97 m), $\theta$ = 158°
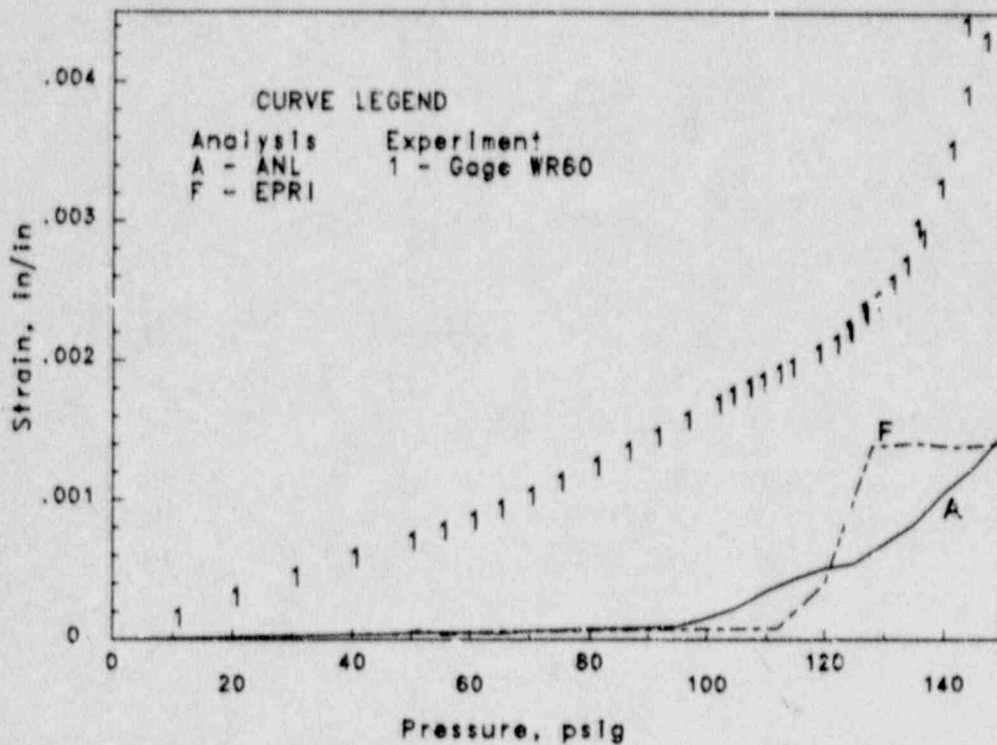


Figure 4.42 Pretest Predictions vs. Experimental Results: Equipment Hatch B
Axial Strain in Layer 2 Meridional Rebar at El 13 ft (3.97 m), $\theta$ = 158°
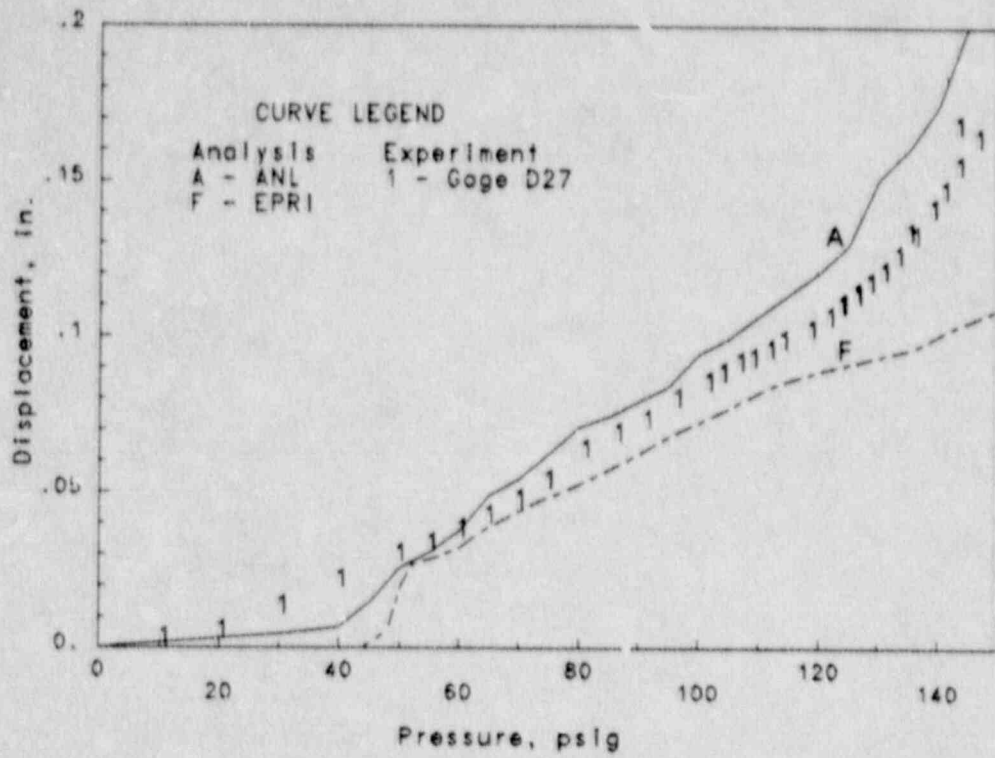
Figure 4.43  Pretest Predictions vs. Experimental Results: Equipment Hatch B
Change in Horizontal Diameter of Sleeve Near Midthickness of Cylinder Wall
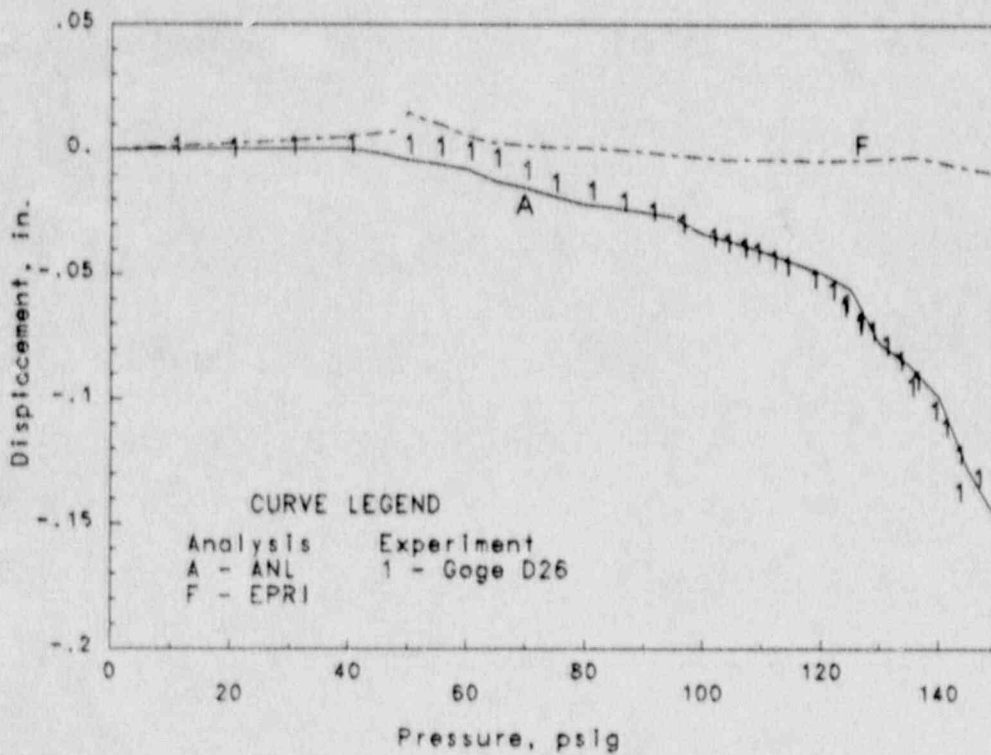


Figure 4.44  Pretest Predictions vs. Experimental Results: Equipment Hatch B
Change in Vertical Diameter of Sleeve Near Midthickness of Cylinder Wall

## 4.3 Failure Predictions

The results shown in Sections 4.1 and 4.2 suggest that it is possible to predict several measures of the global response of the containment shell with reasonable accuracy, especially for loads near the functional limit of the structure. However, interpretation of these response measures is a much more difficult task.

Before the test, there were three widely recognized failure modes for the containment model test: (1) liner tearing, (2) rebar failure, and (3) shear/flexural failure. Although liner tearing was realized in the scale model, in application to actual containment buildings, it is important to understand and to develop the analytical capability to predict all potential failure modes. A completely different failure mode may occur for seemingly small differences in design details or for different loadings.

The "best-estimate" capacity of the model and the limit state mechanism predicted by each organization before the test are compared in Table 4.3. The predicted capacity varied from 128 to 190 psig (0.800 to 1.310 MPa), which is approximately 2.8 to 4.1 times the design pressure. The main reason for the variations was the difficulty in correctly interpreting all potential failure modes. Although many of the organizations in the round-robin recognized the potential for liner tearing before the test (see pg. 6 of the pretest round-robin analysis report [11]), they did not undertake the complicated analyses required to evaluate this failure mode. In part, this may have been due to a reluctance to commit resources to investigate a failure mode that was considered to be unproven, but there was also some feeling that the high ductility of the liner relative to the rebar would preclude liner tearing from occurring before some other failure mode. Given the outcome of the test, there has, of course, been considerable attention focussed on the liner tearing mode and much has been learned about the mechanics of strain concentrations in the liner.

The attention on the liner tearing mode, in particular the large tear adjacent to the rectangular insert plate, during the posttest evaluations has led to some important developments. There is general consensus that the Davis triaxiality factor can be used to make a reasonable estimate of the effective ductility limit for the liner material. There is also general agreement that local models, with boundary conditions based on global response measures, could be used to determine the strain concentrations in the liner. The features and details that must be included in these models are not yet resolved. Nearly everyone agrees that the insert plate by itself results in a strain concentration on the order of two to three times the free-field strain. Several other analysts found that the anchorage system increases the strain concentration near the rectangular insert plate to 10 or more times the free-field strain; however, EPRI believes that shear dislocation motion is a more important mechanism than the anchorage system in causing failure. Furthermore, there are additional questions regarding the extension of these results to full-scale containments. Although there has been considerable progress, there is a need for additional testing to resolve the issues described above. This is discussed in more detail in Section 5.

In the cases of rebar failure and shear failure, even though there is general recognition of the potential failure mode, there is a lack of agreement on evaluation criterion. For instance, several groups calculated the pressure at which the hoop rebar would fail; BNL and CEA defined this as the point at which gross yielding or rapidly increasing displacements began; SNL, ANL, and GRS correlated failure with

the ultimate strength of a rebar splice. Clearly, there are significant differences in the failure criteria that were applied. The 1:6-scale model test would indicate that rebars can achieve strains well beyond gross yield. However, there is legitimate concern that large bars that are bent around penetration openings could fail before the ultimate strength of the rebar splices is obtained. This topic merits further consideration.

Criteria for evaluating shear failure also need to be developed. Design codes represent conservative approaches to capacity and use nominal shear stress on a section for comparison. In the pretest calculations, some organizations based failure predictions on the state of damage in the concrete, others used design code formulas. For shear failure, this appears to be an overly conservative approach; the reinforcement can carry considerable shear by aggregate interlock and dowel action. A more realistic approach based on actual test data is needed.

The development of a consensus approach to evaluating critical limit states by interpreting calculated response measures (displacement, strain, force, moment, stress) is an important challenge that must be met.

A final note on failure interpretation: each organization was also asked to indicate the maximum pressure at which they had high confidence the containment model would not fail (in contrast, Table 4.3 represents "best-estimate" values for failure). Of the seven organizations that responded to this inquiry, the reported values were 92, 100, 105, 127, 135, 138, and 160 psig (0.63, 0.69, 0.72, 0.88, 0.93, 0.95, and 1.10 MPa). Six of the seven high confidence numbers were, in fact, less than the actual failure pressure.

## Table 4.3
### Failure Predictions for the 1:6-Scale Model

| Source | Failure Pressure | Limit Mechanism |
|--------|------------------|-----------------|
| SNL | 168 psig 1.16 MPa | Flexural failure at the cylinder-basemat junction brought on by crushing of concrete. |
| ANL | 180-190 psig (1.24-1.31 MPa) | Either (1) failure of a hoop rebar splice near midheight, (2) failure of a weld in the liner near the basemat, or (3) failure of the liner just above the knuckle. |
| EPRI | 140-150 psig (0.97-1.03 MPa) | Liner tearing at the connection of the liner to the knuckle triggered by basemat bending. |
| CEA | 138 psig (0.95 MPa) | Plasticity of rebars corresponding to rapidly increasing displacements of the structure. |
| NII* | 130 psig (0.90 MPa) | Transverse shear failure of cylinder just above the shear reinforcement, with some smaller chance for local tearing of the liner around studs. |
| ENEA | 161-184 psig (1.11-1.27 MPa) | Failure at the cylinder base caused by combined effect of bending, tension, and shear. |
| AEA | 164 psig (1.13 MPa) | Rebar at the center of the basemat exceeds its ultimate strength. |
| GRS | 167-174 psig (1.15-1.20 MPa) | Failure at the cylinder-basemat junction. |
|  | 174-189 psig (1.20-130 MPa) | Failure of hoop reinforcement or liner tearing. |
| BNL | 128 psig (0.88 MPa) | Flexural/shear failure at the wall-basemat junction or gross yielding of hoop rebars. |
| CEGB | 160 psig (1.10 MPa) | Flexural failure at wall-basemat junction. |
| TEST | 140-145 psig (0.97-1.0 MPa) | Liner tearing adjacent to insert plates at the cylinder midheight, most notably a 22" (56 cm) long tear adjacent to the large rectangular insert plate |

* Lowest bound of estimates, see Reference 11, pg. 251.

## 5.0 POSTTEST EVALUATIONS

This section consists of contributed sections from eight of the ten organizations that participated in the round-robin pretest analysis report:

- Sandia National Laboratories (USA)

- Argonne National Laboratory (USA)

- Electric Power Research Institute (USA)

- Commissariat a L'Energie Atomique (France)

- HM Nuclear Installations Inspectorate (U.K.)

- Comitato Nazionale per la ricerca e per lo sviluppo dell'Energia Nucleare e delle Energie Alternative (Italy)

- U.K. Atomic Energy Authority, Safety and Reliability Directorate (U.K.)

- Gesellschaft für Reaktorsicherheit (FRG)

The CEGB was unable to commit additional time and effort to the round-robin activity due to their heavy involvement in the Sizewell and Hinkley Point nuclear power stations. Brookhaven National Laboratory also did not participate in posttest evaluations.

At Sandia's request, the Civil Engineering Department at the University of Illinois Urbana-Champaign (UIUC) prepared an account of their investigation into the shear capacity of the cylinder wall at its juncture with the basemat, which appears in Section 5.9. This work was performed under contract to Sandia.

No specific work assignments were made for posttest evaluations; within available manpower restrictions, each organization had the opportunity to address the issues that they felt were most significant. As a result, there was some duplication of effort in the posttest evaluations, which nevertheless provides support and validation for some of the posttest conclusions. A brief summary of the results of the posttest evaluations follows.

There were four principal areas of investigation, with the indicated results:

i) **Liner tearing** - A number of groups conducted analyses to understand the major tear that occurred adjacent to the rectangular insert plate for the mechanical/electrical feedthrough penetration cluster, including SNL, EPRI, CEA, NII, ENEA, AEA, and GRS. The various analyses represent a diverse array of approaches with significant differences in the model details. Yet, despite the broad differences in the analytical approaches, there are many similarities in the conclusions.

Analysis suggest that the insert plates used around penetrations by themselves cause local strain concentrations two to four times the free-field strain. However, it is the majority view that this mechanism for strain

concentration is not by itself sufficient to explain the formation of tears in the liner.

The additional feature that accounts for still higher local strains near the penetrations is the liner anchorage system, specifically, the studs. The studs resist slip between the concrete and the liner. Significant slip occurs at insert plates because of their high stiffness relative to the nominal thickness liner and, as a result, the studs impose significant loads on the liner at such locations. With studs modeled, SNL, CEA, and GRS calculated liner strain concentrations of ten or more times the free-field strain near the maximum test pressure. GRS considered several different models for liner tearing, including one in which the stud embedment in the concrete was explicitly modeled. CEA performed an interesting sensitivity study; by removing the first row of studs on the nominal thickness liner next to the insert plate, they found that the maximum local strain was reduced by about half. SNL conducted additional calculations to understand the stud shear behavior that provided two interesting conclusions:

1. When the liner is not subject to membrane yield loads prior to the application of high stud shear forces, the failure mode is expected to be stud shear failure instead of liner tearing. This suggests that simple stud shear tests do not adequately represent the behavior of the liner-anchorage system in the containment under internal pressure, and that conclusions drawn from such tests with respect to the liner-anchorage system failure mode (i.e, stud failure vs. liner tearing) may be invalid.[4] Liner membrane yield loads, which in an actual containment precede the development of high stud shear loads, must be represented.

2. Strains calculated with a plane stress model where the stud shear forces are modeled as point loads can be reasonably interpreted as average strains through the liner thickness if the characteristic dimension of the elements adjacent to the stud load is approximately equal to the stud radius.

Although they do not explicitly account for its effect in their analysis, EPRI feels that 'shear dislocation motion' (a discontinuity in out-of-plane (radial) displacement that occurs near major cracks adjacent to penetrations) is an important mechanism in the formation of liner tears. Sandia does not feel that this is a significant mechanism in areas with geometry similar to the mechanical/electrical feedthrough penetration cluster in the 1:6-scale model. This is a difference that needs to be resolved by additional testing.

To interpret the calculated liner strains, SNL, EPRI, ENEA, and GRS all adopted the same criterion for evaluating the liner ductility under biaxial loads, which is based on the Davis triaxiality factor. ANATECH is

---

4. The tests typically conducted on studs and anchors are relevant to liner buckling under thermal loads. The primary design function of the anchorage system is to prevent thermally induced buckling.

credited with the initial use of this criterion in application to containment liners. The progress towards an agreement on a strain criterion for liner tearing is an encouraging development.

ii) **Basemat uplift** - There was considerable variation in the pretest predictions for basemat uplift, none of which accurately reflected the measured pressure-history response of the model over the entire range of pressure. Basemat uplift is significant in that it affects the shear and moment forces in the cylinder wall at the juncture with the basemat, which may change the potential for failure at this location. The effects of the fill slab, soil stiffness, and concrete tensile behavior on basemat uplift were studied. It was found that the basemat uplift is relatively insensitive to changes in soil stiffness, but in order to accurately reflect the measured behavior, finite element models need to account for two factors that were generally not considered in pretest analyses:

- The fill slab, which stiffened the basemat response (thereby reducing uplift). Several groups modeled the fill slab explicitly with improved results. GRS performed an interesting analysis that indicates the stiffening effect of the fill slab is primarily due to the shear forces that develop to resist sliding between the fill slab and the liner. These shear forces produce a moment on the basemat in opposition to the moment from the vertical load imposed by the cylinder.

- A reduction in actual tensile strength of the basemat concrete to about half of the laboratory measured value. ANATECH proposed this approach based on in-situ data on concrete dams.

The analyses also indicated that basemat uplift had little effect on the stresses or strains in the cylinder and dome at all locations other than the base of the cylinder.

In application to actual containments, basemat uplift (actually basemat response in general) would be much more difficult to predict due to the effect of internal structures, reactor cavities, sump pump pits, and other numerous discontinuities that were not represented in the 1:6-scale model. The effect of these features is uncertain.

iii) **Shear failure** - Given the number of predictions of shear failure before the test, it is somewhat disappointing that there was not more work here. The University of Illinois used strain measurements to estimate the nominal shear stress at the cylinder base. At 145 psig, the nominal shear stress was approximately 450 psig, which is $5.7\sqrt{f_c}$. This is high relative to many of the design code rules. Unfortunately, there is still no generally recognized criterion for evaluating shear capacity of reinforced concrete sections subject to simultaneous application of tensile loads and bending moment.

iv) **Precracking** - The experimental results provide ample evidence that the cylinder and dome were essentially precracked in both the horizontal and vertical planes prior to the high pressure test (but not the basemat, at least not to the same extent). Shrinkage cracking, low pressure cycling, and the small diameter of the bars used in the model (which may not have bond properties comparable to the large bars used in full-size containments)

were all cited as potential causes for cracking in the concrete. ANL conducted an interesting analysis of the effects of diurnal temperature fluctuations, which indicated that the cylinder and dome concrete could be heavily damaged by a temperature change of 40°F (17°C) from day to night (not an unusual occurrence in the Albuquerque area).

The posttest evaluations conducted by each organization are summarized below:

SNL  Comparison with experimental results; Investigation of liner tearing with insert plate and studs; Detailed study of stud behavior..

ANL  Comparison with experimental results; Analysis of precracking in structure.

EPRI  Comparison with experimental results; study of basemat uplift; Analysis of shear and bending in cylinder wall at intersection with basemat; Investigation of liner tearing.

CEA  Comparison with experimental results; Investigation of liner strains with insert plate and studs.

NII  Comparison with experimental results; Parametric studies to study the effect of soil stiffness, concrete shear modulus, and concrete tensile strength; investigation of liner strain concentration due to insert plate.

ENEA  Comparison with experimental results; Analysis of basemat uplift and liner strain concentration due to insert plate.

AEA  Analysis of liner tear and basemat uplift.

GRS  Parameter study of basemat uplift; Analysis to estimate likely experimental scatter in rebar strains; Investigation of liner tearing including stud effects; Experimental studies of (1) bond behavior and pull-out of rebars, and (2) biaxial failure strains for liner material.

UIUC  Data conditioning; Determination of shear force in wall at intersection with basemat from experimental measurements.

## 5.1 Sandia National Laboratories

This section was authored by J. Randy Weatherby of the Applied Mechanics Division I at Sandia National Laboratories.

### 5.1.1 Introduction

The 1:6-scale model experiment has provided detailed information concerning the structural response of a reinforced concrete containment building loaded by internal pressure. This information will prove extremely valuable when containment buildings at existing nuc'... power plants are analyzed to evaluate their ability to survive loads that could ... ... during a severe accident. In fact, the main goal of the combined effort of analy... ...sting has been to establish a set of techniques that can be used for evaluating containment performance in future safety studies. The results of several studies conducted after the conclusion of the 1:6-scale model test are documented in this report. These studies fall into three major categories:

1. Comparison of strains and displacements measured in the experiment to the corresponding results from axisymmetric finite element analyses,

2. Finite element analyses of the liner near the penetration where the largest tear developed,

3. Detailed studies of the strain field in the liner near a stud anchor that is loaded in shear.

#### 5.1.1.1 Comparisons of Structural Response

In the pretest analyses conducted at Sandia [67], the containment model was treated as an axisymmetric structure. Two additional axisymmetric analyses were completed after the pretest round-robin report was released. These two analyses were identical except for the way in which the concrete was modeled. In one case, a smeared cracking model was used to track the growth of cracks in the concrete. In the second analysis, the tensile strength of the concrete was assumed to be zero. The results from these two analyses have been compared to strains and displa. ements measured at several locations throughout the containment structure. These comparisons show that, even at internal pressures less than the design pressure of the containment, the structural response was predominantly controlled by the reinforcing steel, and that the concrete contributed only marginally to the stiffness of the structure in regions where the stresses were tensile. In general the no-tension assumption for the concrete produced results that were in clos... agreement with the experimental measurements than those obtained with the sm...red cracking model.

#### 5.1.1.2 Liner Tearing

Two of the main objectives in the posttest analysis effort were (1) to determine the primary mechanisms that caused tears to form in the liner plate, and (2) to establish an analytical approach that captures these mechanisms and, at the same, remains tractable from a numerical standpoint. Ultimately, it is hoped that the work described in this report will lead to a method of analysis that can be used to pr... ... both the initiation and subsequent propagation of tears in the liner plate.

To expand our understanding of liner tearing, the region surrounding a piping penetration was analyzed with two plane stress finite element models. The region that was analyzed was the site where the largest tear developed during the overpressurization experiment. In the first model, the liner was allowed to slip freely with respect to the concrete wall of the containment. In the second analysis, the liner was linked to the concrete at discrete points through a flexible anchorage system and was allowed to freely slip at locations between the anchor points. The analytical results offer convincing evidence that, during the experiment, the largest tear initiated at an internal pressure near 145 psig (1.0 MPa) as the result of forces that developed in stud anchors located along the vertical edge of the thick plate that surrounded the piping penetrations. These forces developed as the stud anchors resisted slip between the concrete and the liner plate.

### 5.1.1.3 Strain Field Near a Stud Anchor

In analyzing the region near the piping penetration, the studs were represented by spring elements. This approach introduced point-loads into the plane stress model of the liner (i.e., all force from the stud anchor was introduced at a single nodal point). Since the state of strain near the studs controls the point of tear initiation, it was necessary to determine if the strains in the liner elements immediately connected to the point-loads were meaningful. To accomplish this goal, a three-dimensional finite element model was constructed to study the strain field that develops in the liner near a stud that is loaded in shear. The strains from the three-dimensional analysis were compared to the strains that developed next to studs in two-dimensional models where the stud forces were applied as point-loads. The results of this detailed study indicate that the plane stress continuum elements located next to the point loads should be sized so that the sides of the elements are approximately equal in length to the radius of the stud. When this requirement is met, the equivalent plastic strain in the plane stress elements provide reasonable estimates of the average value of equivalent plastic strain in the liner along the edge of the stud.

Results obtained with the three-dimensional stud-shear analyses also explain why the liner tore near studs in the 1:6-scale model test when the liner did not tear in previous tests of the liner and anchorage system where the stud anchors were loaded in shear. The results of the three-dimensional analysis show that this difference is primarily attributable to the presence of membrane tension in the liner beyond what was supplied by a single stud acting alone. In the 1:6-scale model, the liner had to carry a membrane load plus the load from the stud anchors; whereas, in the shear tests, the liner was only required to carry the load introduced by the stud.

### 5.1.2 Structural Response

### 5.1.2.1 Sequence of Analytical Models

A series of four finite element analyses were made of the 1:6-scale containment using the axisymmetric shell model shown in Figure 5.1.1. In each analysis, a different set of material parameters was used to define the stress-strain response of the concrete. The concrete model available in Version 4-5-171 of ABAQUS was used in all four cases.

In the two shell analyses described in the pretest round-robin report [67], the concrete was treated as an elastic-perfectly plastic material with a yield surface defined to reflect the difference between the tensile strength and the compressive

strength of the concrete. This was accomplished by defining the uniaxial stress-strain relationship in the concrete constitutive model so that cracking was suppressed. In the first analysis in Reference 67, the tensile "yield" strength of the concrete was set equal to the ultimate tensile strength of the concrete (500 psi; 3.45 MPa) as estimated from split-tension and direct tension experiments [12]. In the second analysis reported in Reference 67, the tensile "yield" strength of the concrete was set to a small value (10 psi; 0.07 MPa) to simulate a no-tension material. The results from these two analyses were pieced together to produce the curves in the standard plots that appear in Section 4 of this report.

Soon after completion of the round-robin report and before the overpressurization test, the containment was re-analyzed using a third set of assumptions for the mechanical response of the concrete in tension. Instead of assuming perfect plasticity, the concrete was allowed to crack and subsequently soften using the smeared cracking approach available in the ABAQUS concrete model. This analysis, which will be referred to as the *Smeared Cracking Analysis* is documented in Reference 65. Unfortunately, the softening associated with cracking gave rise to numerical problems in the nonlinear solution algorithm, preventing the reduction of force residuals to acceptable levels. (It was for this reason that cracking was suppressed in the two analyses described in Reference 67.) To force the analysis to proceed while the concrete was cracking, the DIRECT=NOSTOP option in ABAQUS was activated, and the analysis continued to the next load step after three equilibrium iterations even when the residual forces failed to satisfy the convergence criterion. Frequently the solution that was accepted at the end of the three equilibrium iterations contained out-of-balance forces that were of the same order of magnitude as typical external nodal forces arising from the internal pressure.

After the 1:6-scale containment was tested, the structure was analyzed a fourth time. In this analysis, the concrete was treated as a material with no tensile strength. This was accomplished by using the NO TENSION material option in conjunction with the concrete model in ABAQUS Version 4-5-171. The displacements and strains calculated with this analytical model were typically greater than those obtained using the elastic-perfectly plastic concrete model with a tensile strength of 10 psi (0.07 MPa)

In the discussion that follows, the results from the Smeared Cracking Analysis and the No-Tension Analysis will be compared against measurements taken during the Structural Integrity Test (SIT) and the High Pressure Test (HPT). These comparisons show that the reinforcing steel and liner control the deformation of the containment structure, and that the concrete contributes very little to the overall stiffness of the dome and cylinder at internal pressures beyond the design pressure of the containment. Furthermore, the comparison of analytical and experimental results strongly suggest that the smeared cracking model does a very poor job of modeling the mechanical behavior of the concrete. This is most evident in the comparison of results for vertical strains and vertical displacements in the cylinder wall.

### 5.1.2.2 Comparison of Experimental and Analytical Results

Before comparing the experimental data to the analytical results, a few comments about the experimental measurements are in order. First, the 1:6-scale model was pressurized on three separate occasions. During the first pressurization, the internal pressure was raised to 15 psig (1.0 MPa) to determine if the model was leak tight.

The second pressurization was the Structural Integrity Test (SIT). During the SIT, the internal pressure was increased to 52 psig (0.36 MPa), which is 15% above the design pressure. Finally, during the High Pressure Test (HPT), the model was pressurized until the liner failed at 145 psig (1.0 MPa). Measurements collected during the SIT and HPT are presented in subsequent figures. Both the displacement transducers and the strain gages were zeroed before beginning the SIT and again before the start of the HPT so that, in each test, the residual strains and displacements from prior loadings were not included.

Data was collected continuously for several hours after complete depressurization from the SIT. These measurements showed that a significant fraction of the peak strains and displacements reached in the SIT remained as residual strains after the internal pressure was returned to zero; however, these measurements also showed that these residual strains and displacements tended to decrease as a function of time. No attempt was made to correct the HPT data to account for residual strains remaining from the SIT because a period of roughly one week passed between the end of the SIT and the beginning of the HPT, and it was felt that the residual deformations at the start of the test could not be estimated accurately due to their continued relaxation. The last values of strains and displacements recorded after the SIT are listed in notes contained in Figures 5.1.2 through 5.1.10.

In addition to the relaxation of residual strains and displacements at the end of the SIT, the experimental measurements also show other evidence of time-dependent structural response. Here, the term "time-dependent response" is used to describe the phenomenon where the deformation of the structure continues to change while the applied load is held constant. Time-dependent structural response can be seen in the SIT data plots shown in Figures 5.1.2 through 5.1.10. In these plots, the time-dependent response causes the sudden jumps that appear when the deformation is plotted as a function of pressure. The jumps occur at points along the curves where measurements were taken at two different times while the internal pressure was held constant.

Other evidence of time-dependent structural response was seen during depressurization of the containment building. The strains and displacements measured during the SIT did not reach their maximum values at the maximum test pressure but, instead, continued to rise during the initial stages of depressurization[5]. This same phenomenon was also seen when the model was depressurized at the conclusion of the HPT (look closely at the last two data points in the experimental curves for the HPT plotted in Figures 5.1.2 through 5.1.10). Because the stresses in the reinforcing steel remained well below the yield strength during the SIT, the time-dependent response observed at low pressures was most likely caused by the continued extension of cracks in the concrete and slippage between the rebar and the concrete. Both of these mechanisms continued to be active even when the internal pressure was decreased slightly. The most likely causes of the time-dependent response observed at the end of the HPT are creep of the reinforcing steel and creep of the liner.

The experimental and analytical results for strains in the Layer 6 hoop reinforcement are compared in Figure 5.1.2 at an elevation of 19 ft (5.79 m) and in Figure 5.1.3 at

---

5. The data plots in Figures 5.1.2 through 5.1.10 do not show the measured response during the depressurization phase of the SIT

an elevation of 10 ft (3.05 m). The experimental data in these plots seem to indicate that, during the SIT, significant crack growth began to take place in the cylinder wall at an internal pressure somewhere between 15 and 20 psig (0.10 and 0.14 MPa). In contrast, the hoop stresses calculated in the Smeared Cracking Analysis did not exceed the tensile strength of the concrete until the pressure reached 35 psig (0.24 MPa). Based an a concrete tensile strength of 500 psi (3.45 MPa), a simple $pr/t$ calculation also yields a value of approximately 35 psig (0.24 MPa) for the internal pressure necessary to cause cracking in the cylinder wall. The initial hoop stiffness measured in the SIT was less than that predicted by the Smeared Cracking Analysis. This suggests that cracks were present in the concrete prior to the SIT. Indeed, cracks were actually visible on the surface of the containment model before the SIT was conducted.

The hoop strains computed in the Smeared Cracking Analysis remained considerably smaller than the hoop strains computed in the No-Tension Analysis even after the tensile strength of the concrete was exceeded in the cylinder region. This is because in the Smeared Cracking Analysis the tensile stress normal to the crack plane was not immediately reduced to zero after the concrete cracked; but, instead the tensile stress normal to the crack plane was decreased linearly with increasing tensile strain, reaching zero when the tensile strain normal to the crack plane was equal to the yield strain of the reinforcement ($\approx$0.2%). In the cylinder region, the difference between the hoop strains from the two analyses was insignificant above an internal pressure of 80 psig (0.55 MPa).

In Figure 5.1.4, radial displacement measurements from several gages located around the inner circumference of the cylinder at the midheight are compared to the results from the two finite element analyses. Similar plots in Figure 5.1.5 compare analytical and experimental results for the radial displacement of the springline. During the SIT, most of the radial displacement measurements at the cylinder midheight and springline indicate that the structure initially moved radially inward. This behavior is not predicted by either of the two finite element analyses and is also not consistent with hoop strain measurements made in the cylinder region. Most likely the inward motion is not a real phenomenon and is, instead, associated with the way that the displacement transducers operate at very small displacements. At the cylinder midheight, the measured values of radial displacement tend to bracket the analytical values from the Smeared Cracking Analysis and the No-Tension Analysis. At the springline, however, the radial displacements measured during the SIT and HPT tend to follow the analytical results obtained in the Smeared Cracking Analysis more closely than those computed in the No-Tension Analysis.

The strains in the vertical reinforcing bars in the cylinder region provide the best evidence of the deficiencies in the smeared cracking constitutive model. Figure 5.1.6 compares strains measured in vertical reinforcing bars near the containment midheight to the strains computed in this layer of reinforcement in the two finite element analyses. The experimental data suggests that, above an internal pressure of 50 psig (0.34 MPa), the concrete contributes very little to the overall stiffness of the structure in the vertical direction. In contrast, when the structure was analyzed using the smeared cracking model for the concrete, the vertical stress in the concrete did not exceed the tensile strength until the pressure inside the containment reached 110 psig (0.76 MPa). As a result, there is a very large discrepancy between the strains measured in the vertical bars and the strains calculated in the Smeared Cracking Analysis. On the other hand, the No-Tension Analysis matches the strains in the vertical reinforcing bars with reasonable accuracy. The same trend is observed in the

comparisons of the overall elongation of the cylinder shown in Figure 5.1.7. Here again, the measured change in the vertical length of the cylinder follows the results from the No-Tension Analysis much more closely than it follows the results obtained with the Smeared Cracking Analysis.

In Figure 5.1.8, comparisons are made between the analytical and experimental results for strains in the inside (Layer 2) vertical reinforcing bars in the cylinder wall just above the basemat. Because of bending, the strains in the inside vertical bars in this region are larger than the strains in the vertical bars located higher in the cylinder wall. Over most of the pressure range, the no-tension model comes closer to matching the experimental data than the cracking model.

Comparisons of results for rebar strains in the dome are shown in Figures 5.1.9 and 5.1.10. Both figures contain plots of the strain in the inside vertical bars (Layer 2 reinforcement). Figure 5.1.9 compares analytical and experimental results near the springline, while in Figure 5.1.10 results are compared at a location halfway up the dome. Near the springline, the strains calculated in the No-Tension Analysis were much closer to the experimentally measured values than those computed in the Smeared Cracking Analysis. The plot of the strains measured at the gage located halfway up the dome falls between the results from the No-Tension Analysis and the Smeared Cracking Analysis.

### 5.1.2.3 Problems in Modeling Concrete Cracking

Comparisons of the analytical results and the experimental results indicate that the tensile behavior of the concrete was very poorly modeled in the Smeared Cracking Analysis. In fact, at most locations in the model, a better agreement between analysis and experiment was obtained by ignoring the tensile strength of the concrete altogether. Fortunately, the liner and reinforcing steel largely control the deformation of the cylinder and dome at higher internal pressures so that even the results obtained with the Smeared Cracking Analysis were frequently close to the experimental results.

Several factors probably contributed to the poor performance of the smeared cracking model used for the concrete. One factor that was not accounted for in the concrete model was the fact that the rebar in the actual structure act as crack initiators. Because of this, the concrete cracked at a lower value of "average" stress than what was required to crack the direct tension test specimens and split-cylinder specimens that were used to establish a value for the tensile strength. A second factor that was unaccounted for in the concrete cracking model was the presence of preexisting cracks in the containment structure. Such cracks were observed in the containment structure before the 1:6 scale model was pressurized in the SIT. These cracks probably developed as the result of shrinkage in the concrete during curing, and as the result of temperature gradients that developed during daytime heating and and nighttime cooling.

The no-tension model for the concrete performed quite adequately for evaluating the response of the containment model at most locations. The no-tension model behaved better numerically than the smeared cracking model. Unfortunately, the tension model is limited in that it must be used with shell elements (if cont
elements were used, the wall of the containment would be unable to carry radial
shear forces), and it is definitely not suitable for use in evaluating the ability of the wall
section to resist shear loads that act normal to the wall (radial shear). Although

radial shear loads are a major concern near the basemat/cylinder wall juncture, it is doubtful whether any of the concrete models presently available can be used to evaluate the load-carrying capability of a section subjected to this type of loading. Given the large uncertainty that exists in the "effective" tensile strength of the concrete and also the large uncertainty in the initial state of the concrete (cracked vs. uncracked), an axisymmetric shell analysis with a no-tension material model for the concrete should provide the same level of accuracy in predicting the structural response of a heavily-reinforced containment building as a more complex axisymmetric finite element analysis where continuum elements are used in conjunction with and a smeared cracking model for the concrete.

### 5.1.3 Analysis of the Liner Near a Piping Penetration

finite element analyses were conducted to determine which mechanisms were the cause of the large breach in the liner shown in Figure 5.1.11. These strongly suggest that the tear formed as the result of large strain that evolved in the 1/16 in. (1.59 mm) liner plate along the edge of plate that surrounded the cluster of piping penetrations. The change in thickness in this region caused the liner to slip relative to the concrete wall. The concentration that ultimately caused the initiation of the tear was produced by the forces that developed in the stud anchors as they resisted slippage the liner and concrete.

Description of the Penetration Region

The cluster of penetrations next to the large tear was centered at the midheight of the cylindrical section of the containment building. A detail of this region is shown in Figure 5.1.12. The liner plate in this region had a nominal thickness of 1/16 in. (1.59 mm) while the thickened plate immediately surrounding the penetration had a nominal thickness of 3/16 in. (4.76 mm).

Both the liner and the thickened plate were anchored to the wall by headed studs that were welded to the outer surface of the plates. Figure 5.1.13 shows the dimensions of a typical stud anchor in this region. As the concrete wall was cast, the heads and shanks of the studs became embedded in the concrete. In an actual containment building, the function of the anchorage system is to prevent buckling of the liner for cases in which the liner is exposed to elevated temperatures.

The studs around the penetration were arranged in a square grid pattern as shown in Figure 5.1.14. On the liner near the thickened plate and on the thickened plate itself, the studs were placed with a 2 x 2 in. (51 x 51 mm) spacing. Away from the penetration region, the stud spacing was 6 x 6 in. (152 x 152 mm). The 2 x 2 in. (51 x 51 mm) spacing represents an accurate scaling from a typical full-sized containment, while the 6 x 6 in. (152 x 152 mm) spacing was used further away from the penetrations as a compromise in the 1:6-scale model to reduce the cost of construction. The first column of studs next to the vertical edge of the thickened plate was located approximately 0.5 in. (12.7 mm) from the edge of the thickened plate.

### 5.1.3.2 Anchorage Tests

Shear tests were conducted to determine the shear strength and shear force-deflection characteristics of the stud anchorage system [12]. The specimens used in

these experiments were fabricated by welding studs onto strips of a 1/16 in. (1.59 mm) thick plate that was identical in thickness and material type to the liner used in the cylindrical part of the 1:6-scale model. Specimens with one stud, two studs, and four studs were fabricated in the configurations shown in Figure 5.1.15. After the studs were welded to the liner plate, a concrete block was cast flush with faces of the specimens so that the studs were embedded in the concrete block (see Figure 5.1.16). In each test, load was applied through a pin located near the upper end of each specimen, and the deflection at the head of each stud was measured as a function of applied load. The force-displacement curves measured in each of these tests are shown in Figure 5.1.17. In this figure, the force that is plotted is equal to the total load applied to the specimen divided by the number of studs on the specimen. Two of the single-stud specimens apparently had weaker welds than the other specimens. If the data for these two specimens are ignored, the force per stud at maximum load in the remaining tests is approximately 1450 lb (6.45 kN). All specimens failed either in the weld or in the shank of the stud.

### 5.1.3.3 Finite Element Models

Figures 5.1.18 and 5.1.19 show the two finite element models that were used to analyze the region of the liner surrounding the cluster of piping penetrations. In the first analysis, the anchorage system was entirely neglected, while in the second analysis the stud anchors were modeled with spring elements. The effects of friction and bond between the liner and concrete are neglected in both models. The reinforced concrete wall was not modeled explicitly in these two analyses. Instead, the motion of the reinforced concrete wall was assumed to be unaffected by the presence of the penetrations and identical to that of an infinitely long hollow cylinder loaded by internal pressure. This infinite concrete cylinder was assumed to be lined with 1/16 in. (1.59 mm) thick steel plate and reinforced with the same amount of vertical, hoop, and diagonal steel as was used in the midsection of the 1:6-scale model. The tensile strength of the concrete was neglected in the infinite cylinder analysis. Details of the infinite cylinder analysis are provided in References 65 and 67. Figure 5.1.20 shows a comparison between the strains computed from the infinite cylinder analysis and the strains measured during the 1:6-scale model experiment in a vertical reinforcing bar and a horizontal reinforcing bar, both of which were located behind the thickened liner plate. The excellent agreement between the measured and computed strains justifies the assumption that the motion of the reinforced concrete wall is not appreciably affected by the presence of the penetrations.

In both finite element analyses the curvature of the cylinder wall was neglected, and the region was modeled as a flat panel. Examination of the strain-displacement equations shows that the use of a flat panel model is consistent with the assumption that the radial displacement of the cylinder wall is unaffected by the presence of the penetration and, therefore, uniform over the region.

### 5.1.3.3.1 Model without anchorage

The model shown in Figure 5.1.18 is a quarter-symmetry finite element model that was used to determine the strain field that would develop near the cluster of piping penetrations in the absence of liner anchorage. In all discussion which follows, this analysis will be referred to as the "Anchorage-Free Analysis." The boundary conditions for the model were chosen based on the assumption that displacements on the top edge, left edge, and pipe boundaries match the displacements of the idealized

infinite cylinder mentioned earlier. Referring to Figure 5.1.18, the boundary conditions used in the analysis are as follows:

- Right Edge: $u_x = 0$ (symmetry condition)

- Left Edge: $u_x = x \cdot \bar{\epsilon}_h(p)$

- Bottom Edge: $u_y = 0$ (symmetry condition)

- Top Edge: $u_y = y \cdot \bar{\epsilon}_v(p)$

- Nozzle Boundaries: $u_x = x \cdot \bar{\epsilon}_h(p)$, $u_y = y \cdot \bar{\epsilon}_v(p)$

where,

$p$ = pressure inside the containment,
$x,y$ = horizontal and vertical coordinates relative to the lower right-hand corner of the model,
$u_x,u_y$ = horizontal and vertical displacements relative to the lower right-hand corner of the model, and
$\bar{\epsilon}_h, \bar{\epsilon}_v$ = hoop and vertical strains from infinite cylinder analysis.

The displacement boundary conditions were applied in the finite element analysis through the use of a "user" subroutine linked to the ABAQUS code. This routine, which was executed at the beginning of each load increment in the analysis, determined the displacements at each location on the boundary based on the strains supplied from the infinite cylinder analysis.

### 5.1.3.3.2 Model with anchorage

The plane stress finite element model shown in Figure 5.1.19 was used to evaluate how the liner anchorage system affects the strain field in the liner. This analysis will be referred to as the "Point-Anchor Analysis" because the anchorage between the concrete and the liner was enforced at discrete points spaced throughout the region surrounding the penetration. The problem was analyzed with the nonlinear geometry option in effect to account for large strains and large deformations (note: The ABAQUS code does not account for changes in the thickness of plane stress elements. As a result, this analysis probably overestimates the stiffness of elements that are in biaxial tension). The liner plate was modeled using 4-node bilinear quadrilateral elements (CPS4) that were integrated with 2x2 Gaussian quadrature. Each stud was modeled using a discrete spring element (SPRINGA). This particular spring element has the property that the line of action for the force in the spring element remains parallel to the line segment joining the two nodes that form the ends of the element. In the analysis, the two nodes for each spring element initially occupied the same location as shown in Figure 5.1.19. One end of each spring was attached to the liner while the displacement of the opposite end of each spring was specified to follow the motion of the reinforced concrete wall. A force-deflection relationship for the springs was defined based on the results of the stud anchor shear tests that were described earlier. The idealized force-deflection curve is shown in Figure 5.1.21.

The boundary conditions for the Point-Anchor Analysis were very similar to those specified in the Anchorage-Free Analysis; however, the size of the finite element

model was reduced in the Point-Anchor Analysis. This was accomplished by eliminating the portion of the mesh between the vertical centerlines of the first two piping penetrations and assuming that no circumferential slip develops between the liner and concrete along the vertical centerline of the left-most piping penetration. This approximation was made on the basis of the results obtained from the Anchorage-Free Analysis, which showed that the circumferential slip along this vertical centerline was small. Specifically, the boundary conditions used for the mesh in Figure 5.1.19 were:

- Right Edge: $u_x = 0$ (symmetry condition)

- Left Edge: $u_x = x \cdot \bar{\epsilon}_h(p)$

- Bottom Edge: $u_y = 0$ (symmetry condition)

- Top Edge: $u_y = y \cdot \bar{\epsilon}_v(p)$

- Nozzle Boundary: $u_x = x \cdot \bar{\epsilon}_h(p)$, $u_y = y \cdot \bar{\epsilon}_v(p)$

- Concrete Side of Stud Springs: $u_x = x \cdot \bar{\epsilon}_h(p)$, $u_y = y \cdot \bar{\epsilon}_v(p)$

### 5.1.3.4 Liner Material Properties

#### 5.1.3.4.1 Uniaxial stress-strain data

A number of uniaxial tensile tests were conducted to determine the material properties of the thin liner plate (1/16 in.; 1.59 mm) and the thick liner plate (3/16 in.; 4.76 mm). The thin plate was made of A414 Grade D steel while the thicker plate around the penetrations was made of A516 Grade 60 steel. Both materials have a yield strength of approximately 50 ksi (345 MPa). Both the A414 steel and the A516 steel show considerable strain hardening after yielding. The A414 steel reaches a true stress of 82 ksi (565 MPa) at maximum load while the A516 steel exhibits slightly more hardening and reaches a true stress of approximately 92 ksi (634 MPa) at maximum load. Figures 5.1.22 and 5.1.23 show the engineering stress-strain curves of the A414 and A516 steels, respectively. A total of four uniaxial tensile tests were conducted on the thin liner plate: two in the rolling direction, and two in the transverse direction. The elongations at fracture were 21.3% and 30.0% in the rolling direction and 39.1% and 27.8% in the transverse direction for the A414 steel.

Figure 5.1.24 shows the equivalent stress-plastic strain curves used for the A414 steel and the A516 steel in the Point-Anchorage Analysis. The hardening of both materials was assumed to be zero beyond the plastic strain at maximum load in uniaxial tension. Up to the point of maximum load, these curves were based on "true" stress and "true" strain as defined by the relationships

$$\sigma_T = (1 + \epsilon_E)\sigma_E \qquad (5.1.1)$$

$$\epsilon_T = \log(1 + \epsilon_E) \qquad (5.1.2)$$

where $\sigma_T$ is the "true" stress, $\sigma_E$ is the engineering stress, $\epsilon_T$ is the "true" strain, and $\epsilon_E$ is the engineering strain.

The equivalent stress-plastic strain curves used in the analysis without liner anchorage were essential the same as those shown in Figure 5.1.24 except that the initial yield plateau was included in the curve for the thin liner plate. This initial yield plateau was eliminated in the Point-Anchorage Analysis to circumvent numerical problems associated with stiffening of the material.

### 5.1.3.4.2 Failure criterion

Several empirical criteria have been proposed for estimating the point of fracture in metals subjected to multiaxial loading conditions [46,68]. The empirically-based criterion proposed in Reference 46 suggests that the Von Mises strain at failure, $\varepsilon_f$, can be determined from the relation:

$$\varepsilon_f = \varepsilon \cdot 2^{[1-TF_D]} \tag{5.1.3}$$

where $\varepsilon$ is the tensile elongation and $TF_D$ is the Davis Triaxiality Factor defined by

$$TF_D = \frac{\sqrt{2}(\sigma_1 + \sigma_2 + \sigma_3)}{[(\sigma_1-\sigma_2)^2 + (\sigma_2-\sigma_3)^2 + (\sigma_3-\sigma_1)^2]^{0.5}} \tag{5.1.4}$$

In Equation 5.1.4, $\sigma_1$, $\sigma_2$, and $\sigma_3$ are the principal stresses, and tensile stresses are considered positive. Equation 5.1.3 holds for $TF_D > 0$. For $TF_D < 0$, the fracture strain is assumed to be equal to twice the elongation in uniaxial tension.

At the present time, there is no data which can be used to establish the accuracy of Equation 5.1.3 for estimating the fracture strain of the liner material under a multiaxial state of stress. In this work, the tearing criterion is merely used as a point of reference to compare against strains computed in the finite element analyses.

### 5.1.3.5 Analytical Results

### 5.1.3.5.1 Analysis without anchorage

In the Anchorage-Free Analysis (Figure 5.1.18), kinematic boundary conditions were applied to the edges of the model incrementally, based on the strain history calculated in the infinite cylinder analysis. Since the hoop and vertical strains in the infinite cylinder analysis are parameterized by the pressure inside the containment through the functions plotted in Figure 5.1.20, it is convenient to identify points in the loading history in terms of the internal pressure, $p$. It should be kept in mind, however, that only displacements were specified in the finite element analysis and that a pressure boundary condition was not applied directly.

The ABAQUS code uses an "absolute" error tolerance to determine convergence in nonlinear problems. All residual forces must be less than the specified error tolerance before the code moves to the next load increment. In this analysis, an error tolerance of 10 lb (45 N) was used for pressures below 130 psig (0.90 MPa), and an error tolerance of 50 lb (220 N) was used for internal pressures above 130 psig (0.90 MPa).

Since there was no anchorage or frictional loading on the liner in this model, the liner was free to slip relative to the concrete. The components of slip in the circumferential direction, $\Delta u_x$, and in the vertical direction, $\Delta u_y$, were computed from

the displacements obtained in the finite element analysis through the following relationships:

$$\Delta u_x = u_x - x \cdot \tau_h(p) \qquad (5.1.5)$$

$$\Delta u_y = u_y - y \cdot \tau_v(p) \qquad (5.1.6)$$

where $u_x$ and $u_y$ are the displacements in the circumferential and vertical directions, respectively. The components of slip in the vertical and circumferential directions at 145 psig (1.0 MPa) are shown in Figures 5.1.25 and 5.1.26. In this analysis, the slip was largest along the vertical edge of the thickened plate. At this location, the slip was primarily in the hoop direction.

The largest liner tear observed in the 1:6-scale model experiment propagated at an internal pressure of 145 psig (1.0 MPa). The equivalent plastic strain in the free-field, away from the penetration, was 1.5% at 145 psig (1.0 MPa) according to the results from the infinite cylinder analysis. At this pressure, the maximum value of equivalent plastic strain computed at any location in the penetration region was 2.8%. Figure 5.1.27 shows that this maximum was reached in the 1/16 in. (1.59 mm) liner plate near the corner of the 3/16 in. (4.76 mm) plate.

An equivalent plastic strain of 2.8% is far less than what is needed to initiate a tear in the liner. The Davis Triaxiality Factor (see Equation 5.1.4) must be less than or equal to two for a state of plane stress. The elongation of the 1/16 in. (1.59 mm) thick liner plate in uniaxial tension is approximately 30%, making the equivalent plastic strain necessary to cause liner tearing at least 15% based on the failure criterion in Equation 5.1.3. The fact that the maximum equivalent plastic strain computed in the Anchorage-Free Analysis was much less than 15% indicates that critical details were excluded from the analytical model.

### 5.1.3.5.2 Analysis with anchorage

When the penetration analysis without liner anchorage failed to produce strains sufficient to initiate a liner tear, the model in Figure 5.1.19 was constructed to study the effect of the liner anchorage system on the strain field in the penetration region. In this analysis, kinematic boundary conditions were applied to the edges of the model and to one node on each of the spring elements. The displacements specified for the nodes on the boundaries and springs were increased incrementally based on the strain history calculated in the infinite cylinder analysis. The ABAQUS convergence parameter was set to 10 lb (45 N). This value is 0.7% of the limit load measured for the studs. The convergence criterion was satisfied in each step of the analysis. The dimensions of the elements between the first column of studs on the 1/16 in. (1.59 mm) liner plate and the edge of the 3/16 in. (4.76 mm) plate were 0.1 in. (2.54 mm) in the horizontal direction and 0.25 in. (.35 mm) in the vertical direction, or 1.35 and 3.4 times the stud shank radius, respectively. The dimensions of the elements attached to the stud have a significant influence on the strains computed next to the stud anchors. This point is discussed in more detail in Section 5.1.4.

As the containment wall deformed, forces developed in the studs as they attempted to force the thickened plate to follow the motion of the wall. The vector plot in Figure 5.1.28 shows the relative magnitudes and directions of the forces that studs in the vicinity of the piping penetration exerted on the liner. Not all of the stud forces

increased monotonically with pressure as shown in Figures 5.1.30 and 5.1.31 (the studs are labeled in Figure 5.1.29). In general, the forces in the first column of studs adjacent to the thickened plate increased until a local maximum was reached in the stud force at approximately 70 psig (0.48 MPa) internal pressure. This corresponds to the pressure when the liner began to yield locally around the studs in the first column. The forces in studs S3, S6, and S7 began to increase again at 90 psig (0.62 MPa). This increase continued until the stud forces reached a maximum value of approximately 1425 lb (6.34 kN) at 145 psig (1.0 MPa) internal pressure. The peak value of the stud forces reached in studs S3, S6, and S7 was 25 lb (0.1 kN) less than the shear strength of the stud. Above 145 psig (1.0 MPa) the stud forces began to rapidly decrease, and the shear strength of the stud was never reached. This second interval of decreasing stud forces began when the equivalent plastic strain in the elements connected to studs S3, S6, and S7 reached 15%. This is the strain level where the liner material ceased to work-harden.

Although the shear strength of the studs was never reached in the studs that were attached to the 1/16 in. (1.59 mm) liner plate, the same was not true for the studs connected to the 3/16 in. (4.76 mm) liner plate. Figure 5.1.30 shows that the shear force in stud S2 increased monotonically with increasing internal pressure until it reached the ultimate shear strength of 1450 lb (6.45 kN) at an internal pressure of 132 psig (0.91 MPa). This suggests that some of the studs on the thicker plate may have fractured during the 1:6-scale model experiment.

A contour plot of the equivalent plastic strain in the liner is shown in Figure 5.1.32 for an internal pressure of 145 psig (1.0 MPa). The strains between the 3/16 in. (4.76 mm) liner plate and the first column of studs on the 1/16 in. (1.59 mm) liner plate were much larger than those existing elsewhere in the liner. The largest plastic strains were reached in the elements that were directly connected to the stud anchors. The sequence of plots in Figure 5.1.34 shows the maximum principal strain as a function of distance from the insert plate in the first row of quadrilateral elements next to the lower boundary of the mesh (see Figure 5.1.33). The abrupt changes in the maximum principal strain clearly mark the locations of the studs. These plots demonstrate how, as the internal pressure increased, the strain became increasingly localized in Element A, the element connected to the first stud next to the 3/16 in. (4.76 mm) plate. Figure 5.1.35 shows the strain concentration factor for Element A. Here, the strain concentration factor is defined as the maximum principal strain in Element A divided by the maximum principal strain in the free-field (the infinite cylinder solution). Before yielding, the maximum principal strain in Element A was twice as large as that in the free-field. As the liner began to yield locally near the stud, the strain concentration factor rose to approximately 11 and remained relatively constant for internal pressures between 100 psig (0.69 MPa) and 130 psig (0.90 MPa). Above 130 psig (0.90 MPa), the strain concentration factor began to rise at an increasing rate as strains began to localize in Element A. At 145 psig (1.0 MPa), the strain concentration factor was approximately 23.

To compare the state of strain in the liner to the failure criterion in Equation 5.1.3, the fracture strain $\epsilon_f$ was computed at each location in the model. A value of 30% was used for the elongation at failure in uniaxial tension. The predicted fracture strain was then compared to the equivalent plastic strain, $\bar{\epsilon}_p$. Figure 5.1.26 contains contour plots of the ratio of $\bar{\epsilon}_p$ to $\epsilon_f$ at three different internal pressures. Failure is predicted to occur when this ratio becomes greater than or equal to one. As expected, the failure ratio was largest in those elements connected to the first column of studs next to the insert plate. The failure ratio first reached a value of one at an

internal pressure of 143 psig (0.986 MPa). (This fact is not reflected by the contour plots in Figure 5.1.26 because the strain was so localized that the averaging process used in the plotting routine reduced the peak values of the failure ratio.) As the internal pressure increased, the zone of material in which the failure criterion was satisfied increased in size. In the neighborhood of the studs, Equation 5.1.3 predicted that the equivalent plastic strain necessary to cause fracture was approximately 60% of the elongation at failure in uniaxial tension.

### 5.1.3.5.3 Liner thickness measurements

After the test, an acoustic measuring device was used to measure the thickness of the 1/16 in. (1.59 mm) liner plate at several locations next to the 3/16 in. (4.76 mm) plate. These measurements were made in an attempt to estimate the plastic strain in the thickness direction of the liner. If, as expected, the strain in the vertical direction is small relative to the strain in the hoop direction, then the thickness strains obtained from the measurements should be approximately equal in magnitude and opposite in sign to the maximum principal strain and the equivalent plastic strain. The main objective was to determine the conditions that existed prior to the growth of the tear. For this reason, measurements were taken along the edge of the insert plate opposite from the end where the large tear was located. The liner strains along this edge of the insert plate should be very similar to those that existed in the tear region shortly before the large liner tear propagated.

Small areas of the liner near each stud were visibly thinner than the rest of the liner in the region. Unfortunately, the areas exhibiting the greatest thinning were so small that the liner thickness could not be measured at these locations using the acoustic transducer. The smallest liner thickness measurement made with the acoustic measuring device was 0.063 in. (1.60 mm). This corresponds to a strain of approximately -7% in the thickness direction. Because of uncertainties in the thickness measurements (±.001 in.) and variations in the initial thickness of the liner (±.001 in.), the actual strain in the thickness direction could have been anywhere between -4% and -10%. While this is a relatively large uncertainty, the measurements tend to confirm that the regions of high strain where the liner tear could have initiated were highly localized around the studs.

### 5.1.4 Detailed Analysis of the Strain Field Near a Stud

In the "Point-Anchor Analysis" described in the previous chapter, the studs were represented by spring elements. These spring elements introduced point-loads into the plane stress model of the liner. In a continuum problem (as opposed to a beam or plate problem), a point load results in a stress singularity (i.e., the stresses become infinite at the point of load application). For the penetration analysis, this implies that the strains in liner elements that are connected to studs will be a strong function of the element dimensions. In fact, if the penetration problem were analyzed using successively smaller liner elements, the criterion for liner tearing would be satisfied next to the studs at successively lower pressures. Since the strains near the studs are used to estimate the pressure at which liner tears initiate, it is necessary to determine if and when the strains in the elements next to the point-loads are meaningful. To investigate this point, the strain field in the liner plate adjacent to a stud was studied using two-dimensional and three-dimensional finite element models. The results of this detailed study indicate that a point-load model can be used to obtain reasonable estimates of the stud force required to initiate a liner tear next to a stud *provided that the elements connected to the stud have sides whose length is equal to the stud radius.*

Finite element analyses were also used to explain why the liner tore in the 1:6-scale model test while the liner did not tear in separate tests [12] of the liner and anchorage system in which the stud anchors were loaded in shear. In the stud-shear experiments, all of the specimens failed either by fracturing of the stud or by fracturing of the weld between the stud and liner plate. The liner plate did not exhibit appreciable thinning in the vicinity of the stud in the stud-shear tests, while the liner plate did exhibit thinning adjacent to studs located near the thickened plates that surrounded the equipment hatches and piping penetrations in the 1:6-scale model. The results of the present investigation show that this difference is primarily attributable to the presence of membrane tension in the liner beyond what is supplied by a single stud acting alone.

### 5.1.4.1 The Model Problem

The model problem that was analyzed is shown in Figure 5.1.37. In this problem, a square strip of liner plate is modeled. The upper edge of the strip is fixed against vertical motion. Initially, a traction of magnitude $\sigma_0$ is applied along the lower edge of the specimen. This stress is held constant while the center of the strip is pulled downward under displacement control to simulate the loading resulting from the shearing of a rigid stud. The initial stress, $\sigma_0$, is applied to simulate the fact that the liner in the 1:6-scale model was in a general state of tension before large stud forces developed. These loading conditions are not intended to exactly duplicate the loading seen at a specific location in the containment, rather the model problem was constructed to address the following questions:

1. How are the liner strains near the stud affected when the stud loading is accompanied by a general state of membrane tension in the liner?

2. How do specific modeling assumptions (two-dimensional versus three-dimensional analyses, point-load representations versus distributed-load representations for the stud) affect estimates of when liner tears initiate?

### 5.1.4.2 The Effect of General Membrane Tension on Liner Strains Near the Stud

The model problem was analyzed using the three dimensional finite element model shown in Figure 5.1.38. This mesh is composed of eight-node brick elements (C3D8H). Two different loading conditions were analyzed. In the first analysis (Analysis 1a), the initial stress $\sigma_0$ was set equal to zero. In the second analysis (Analysis 1b), the initial stress $\sigma_0$ was set equal to the yield strength of the liner plate to more closely simulate the conditions that developed in the 1:6-scale model. Both Analysis 1a and Analysis 1b accounted for finite strains and large geometry changes as well as material nonlinearities.

The effective stress-equivalent plastic strain curve used for the liner material is shown in Figure 5.1.39. This piecewise linear curve was constructed from true stress-true strain curves measured in uniaxial tensile tests [64]. In these experiments, the true stress and true strain were determined by interrupting each tensile test several times during the experiment and measuring the instantaneous cross-sectional area of the specimen. The true axial strain $\epsilon$ was then computed from the relationship:

$$\epsilon = \ln(A_0/A) \qquad (5.1.7)$$

where $A_0$ is the original cross-sectional area of the specimen, and A is the instantaneous cross-sectional area. The average value of the true strain just before final fracture was greater than 70% while the elongation at fracture over a 2 in. (51 mm) gauge length was approximately 30%.

Figure 5.1.40 contains a sequence of plots from Analysis 1a showing side views of the deformed shape of the liner at four different levels of stud force. Figure 5.1.41 contains similar plots from Analysis 1b. Figure 5.1.40 shows that in Analysis 1b, where an initial membrane tension was applied, the liner plate next to the stud began to thin rapidly when the stud force reached approximately 1100 lb (4.9 kN). In contrast, the liner plate did not begin to thin appreciably in Analysis 1a until the stud force had reached a value of more than 1500 lb (6.7 kN). This is consistent with the results of the stud shear experiments conducted at Sandia. In these tests the studs or stud welds failed when the force on each stud reached levels between 1400 and 1600 lb (6.2 and 7.1 kN). No visible evidence of thinning was observed in the liner plate at the conclusion of the test.

The variation in the equivalent plastic strain near the stud is shown in Figures 5.1.42 and 5.1.43 for Analysis 1a and Analysis 1b, respectively. In both cases, the gradient of the plastic strain is significant in the thickness direction. The strains in the elements that are immediately above the head of the stud are believed to be artificially high due to the manner in which the displacement boundary conditions were applied. As expected based on the deformed shapes, the plastic strains in the vicinity of the stud are much higher when the initial membrane tension is present (Analysis 1b). This is point is further illustrated by the plots in Figure 5.1.44, which show the plastic strain history at a point located at the midthickness of the liner just above the stud at the 12 o'clock position. Figures 5.1.45 and 5.1.46 show how the plastic strain at the midthickness of the liner varies as a function of position moving outward, in the vertical direction, from the center of the stud. In Analysis 1a, the elements near the fixed end of the specimen were well below the yield point (the von Mises stress in these elements was approximately 15 ksi (103 MPa) compared to a yield strength of 50 ksi (345 MPa)) when the stud force reached 1530 lb (6.81 kN) while, in Analysis 1b, the plastic strains near the fixed end of the specimen were between 6% and 7% when the stud force reached 1230 lb (5.47 kN).

### 5.1.4.3 Results from Two-Dimensional Analyses

The model problem was analyzed using the four plane stress finite element models shown in Figures 5.1.47 and 5.1.48. These models are composed of four-node quadrilateral elements (CPS4). The two-dimensional analyses corresponding to the models in Figures 5.1.47 and 5.1.48 will be referred to as Analyses 2-5. The constitutive model in the two-dimensional analyses was the same as the one used in the three-dimensional analyses. Geometric nonlinearities in the plane of the liner plate were accounted for by using the nonlinear geometry option; however, the plane stress elements do not account for changes in the plate thickness.

The objective of Analysis 2 was to determine how the plane stress assumption affects the equivalent plastic strain near the stud anchor as compared to the results obtained from a three-dimensional analysis. In Analysis 2, the finite element mesh was identical to the finite element mesh used in the plane of the liner plate in the three-dimensional model described previously. The boundary conditions and loading history applied in Analysis 2 were identical to those applied in Analysis 1b; namely, an initial traction equal to the yield strength of the liner material was applied to the

lower edge of the mesh, and then the nodes in the circular region above the stud were moved downward.

In Analyses 3-5 the stud force was introduced at a single node. The only difference between each of the three analyses is the size of the elements. In Analysis 3, the elements connected to the stud were square, and the length, h, of each side was equal to twice the radius of the stud shank, R. In the last two analyses, the square-shaped elements next to the stud were sized so that $h = R$ in Analysis 4, and $h = R/2$ in Analysis 5. This series of analyses was conducted to prove that the equivalent plastic strain in the element next to the stud anchor is a strong function of element size when the stud is modeled as a point load. Furthermore, these analyses were used to test the hypothesis that when the elements next to the point load are sized so that $h = R$, then the equivalent plastic strain calculated in those elements is a good approximation to the equivalent plastic strain next to the stud anchor as computed in a three-dimensional analysis.

The equivalent plastic strain is an important parameter that enters into the tearing criterion introduced in the previous chapter (see Equations 5.1.3 and 5.1.4). In Figure 5.1.49 the stud force is plotted as a function of the equivalent plastic strain just above the stud for the three point-load analyses and for the three-dimensional analysis, Analysis 1b. Note that Analysis 4 exhibits the best correlation with the results from the three-dimensional analysis. In Analysis 4, the element sides adjacent to the point-load were equal in length to the radius of the stud shank. The relationships between the stud force and the equivalent plastic strain ahead of the stud in Analysis 1b, Analysis 2, and Analysis 4 are compared in Figure 5.1.50.

The most important point of comparison between the various analyses is the stud force at the onset of tear initiation. Figure 5.1.51 shows a plot of the "failure ratio" at four locations through the thickness of the liner plate near the edge of the stud (Analysis 1b results). Here, the failure ratio is defined as the ratio of $\bar{\epsilon}_p$ to the failure strain $\epsilon_f$ defined in Equation 5.1.3. The failure criterion suggests that the material at Point A will fail when the stud force reaches 1120 lb (4.99 kN). Points B and C reach the failure point at slightly higher values of stud force. In reality, as a material element fails it will shed it's load to the surrounding material, thus increasing stresses in the adjacent material. In the analyses reported here, the material was assumed to continue to harden even after the failure point was reached. Judging from the rate at which the failure ratio increases at Points B, C and D, it is likely that a tear would penetrate through the thickness of the liner plate at approximately 1120 lb (4.99 kN).

Figure 5.5.52 compares the failure ratio calculated at the edge of the stud in Analysis 2 and Analysis 4 to the failure ratio at the center of the liner in Analysis 1b. The failure ration for Analysis 1b was computed at Point B shown in Figure 5.5.51. From Figure 5.1.52, Analysis 1b predicts that tearing will initiate at a stud force of 1130 lb (5.03 kN), Analysis 2 predicts that liner tearing will initiate at a stud force of 1250 lb (5.56 kN), and Analysis 4 predicts that liner tearing will initiate at a stud force of 1030 lb (4.58 kN).

## 5.1.5 Closure

The agreement between the experimental results and both sets (No-Tension Analysis and and Smeared Cracking Analysis) of axisymmetric finite element results was reasonably good, especially at higher pressures where the reinforcing steel dominated the response. In general, the stiffness of the 1:6-scale model decreased much more

rapidly than predicted by the Smeared Cracking Analysis. The poor performance of the smeared cracking material model can be partially attributed to the presence of cracks that existed in the concrete before the Structural Integrity Test was conducted. In addition, the smeared cracking model did not reflect the fact that the rebar acted as crack initiators, thus reducing the "apparent" tensile strength of the concrete.

Based on the results of this exercise, it appears that an axisymmetric shell analysis coupled with a no-tension material model for the concrete can be used to characterize the global response of a reinforced concrete containment building with reasonable accuracy. Although a shell analysis does not model the mechanisms that can lead to a radial shear failure at the basemat-cylinder wall juncture, it is also unlikely that the concrete cracking models presently available can be relied on to capture this type of phenomenon in a continuum-based finite element analysis. In short, we feel that for analyzing heavily reinforced containment structures, an axisymmetric continuum analysis using present-day smeared cracking models offers no advantage over a simpler shell analysis in which the tensile strength of the concrete is altogether ignored.

A two-dimensional plane stress analysis of the region surrounding a piping penetration suggests that the large liner tear that propagated in this region initiated as the result of concentrated shear loads that developed in the stud anchors as they attempted to resist slippage between the liner and concrete. This slippage was induced by the transition from the thinner liner plate used in most of the cylinder region to the thicker liner plate that encircled the piping penetration. Results of the penetration analysis imply that the liner tear initiated at an internal pressure slightly below 145 psig (1.0 MPa). This is very close to the internal pressure at which a sudden and very large increase in leakage was observed in the 1:6-scale model experiment.

The results from the two-dimensional penetration analysis and the more detailed studies of the strain field near a stud anchor suggest that that the primary mechanisms that cause liner tearing near penetrations in reinforced concrete containments are not three-dimensional in nature, but can be captured with a simpler two-dimensional analysis. If this proves to be the case in general, it will be possible to avoid the numerical problems associated with analyzing these regions using more complicated three-dimensional models. Such simplifications are necessary in order to make the analysis of penetrations tractable in future safety studies of containments at existing nuclear power plants.

AXIS OF SYMMETRY

DOME

CYLINDER

BASEMAT

Typical element length
≈ 7 in. throughout the
structure

Cylinder and basemat con-
nected using a multi-point
constraint on the slope and
displacement components at
these locations
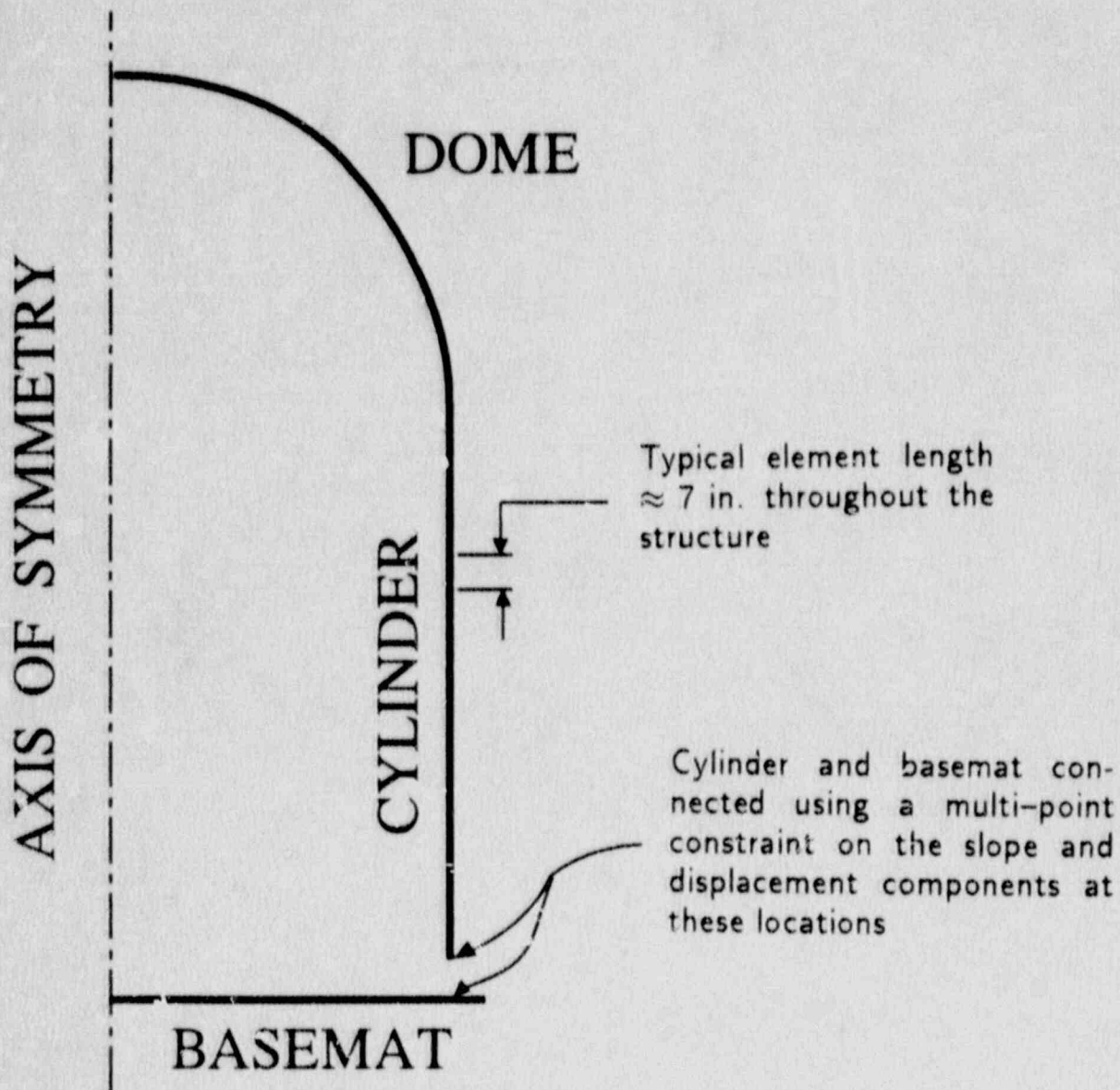
Figure 5.1.1  Shell Model Used in Axisymmetric Shell Analyses
of the 1:6-Scale Containment Building.

**Left plot:**

DASHED LINES DENOTE MEASUREMENTS
FROM LOW PRESSURE TEST (SIT)

RESIDUAL STRAIN:
.013% TO .026%

NO TENSION
MODEL

CRACKING
MODEL

B
D
A
C

STRAIN (%) — .1, .09, .08, .07, .06, .05, .04, .03, .02, .01, 0.

PRESSURE (PSIG) — 0, 10, 20, 30, 40, 50, 60

**Right plot:**

DASHED LINES DENOTE MEASUREMENTS
FROM HIGH PRESSURE TEST

CRACKING
MODEL

NO TENSION
MODEL

A
B
D
C

STRAIN (%) — 1.4, 1.2, 1., .8, .6, .4, .2, 0.

PRESSURE (PSIG) — 0, 20, 40, 60, 80, 100, 120, 140, 160

**Bottom diagram:**

SPRINGLINE

A    B    C    D

BASEMAT

180°    270°    0°    90°

CHANNEL

A – 1047
B – 1048
C – 1046
D – 1029

Figure 5.1.2 Experimental and Analytical Results for Strain in the Layer 6 Hoop Reinforcement at Elevation 19 ft (5.79 m)
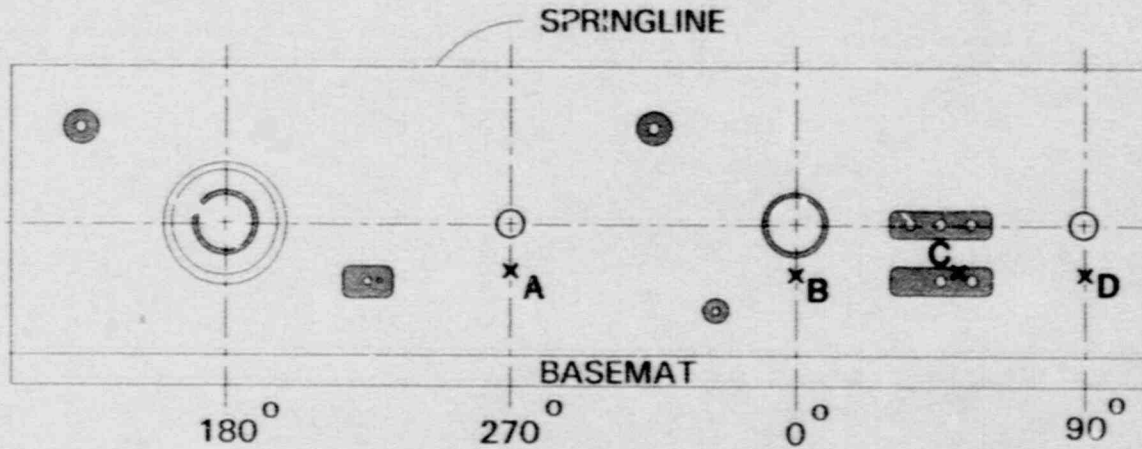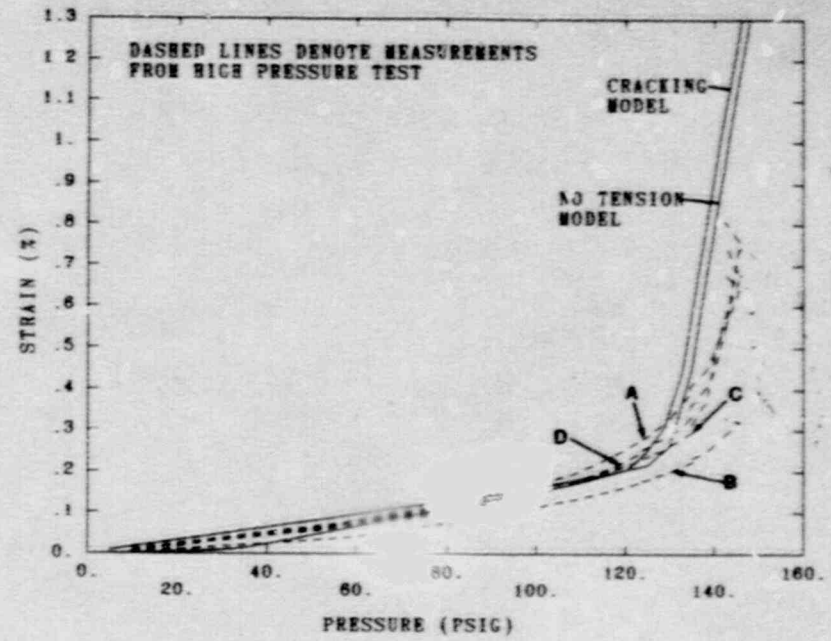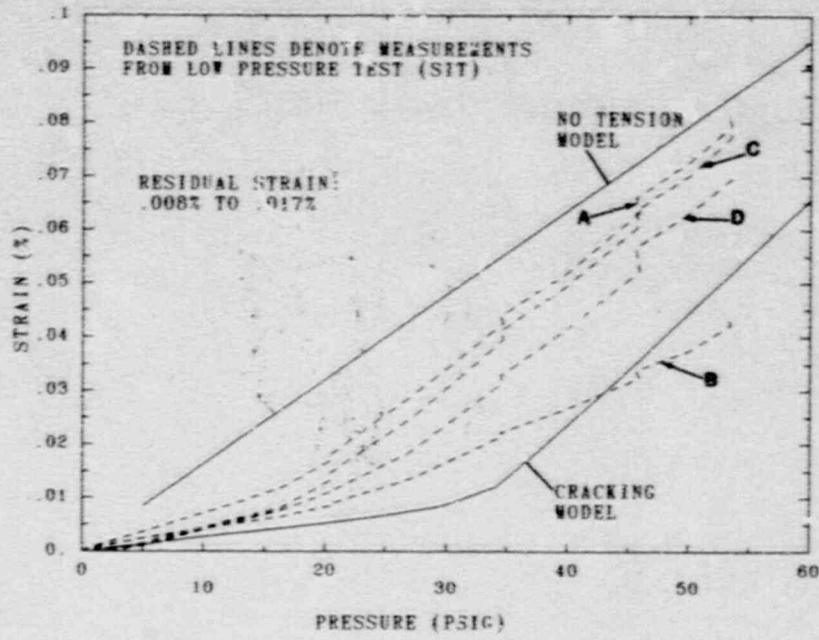
Figure 5.1.3  Experimental and Analytical Results for Strain in the Layer 6 Hoop Reinforcement at Elevation 10 ft (3.05 m)

Left graph:

DASHED LINES DENOTE MEASUREMENTS
FROM LOW PRESSURE TEST (SIT)

RESIDUAL DISPLACEMENTS:
0.022 IN. TO 0.035 IN.

NO TENSION
MODEL

CRACKING
MODEL

DISPLACEMENT (INCHES)

PRESSURE (PSIG)

Right graph:

DASHED LINES DENOTE MEASUREMENTS
FROM HIGH PRESSURE TEST

CRACKING
MODEL

NO TENSION
MODEL

DISPLACEMENT (INCHES)

PRESSURE (PSIG)

SPRINGLINE

BASEMAT

180° 270° 0° 90°

CHANNEL

A – 142
B – 219
C – 228
D – 175

Figure 5.1.4 Experimental and Analytical Results for the Radial Displacement at the Midheight of the Cylinder
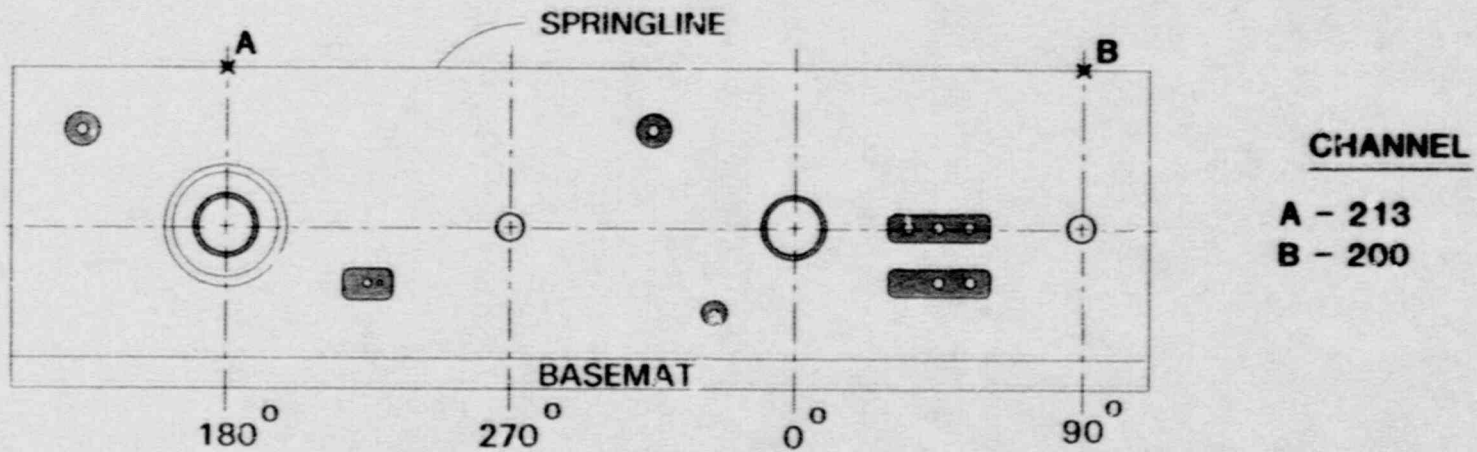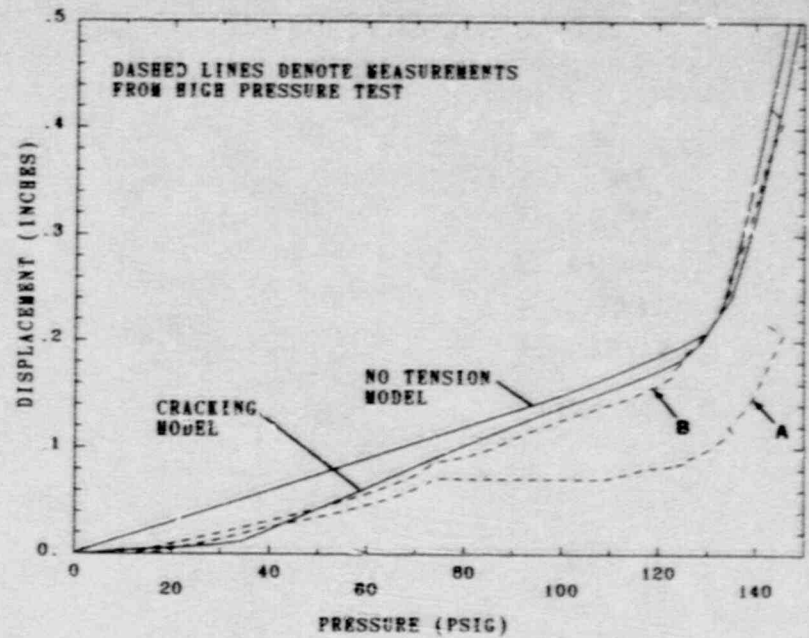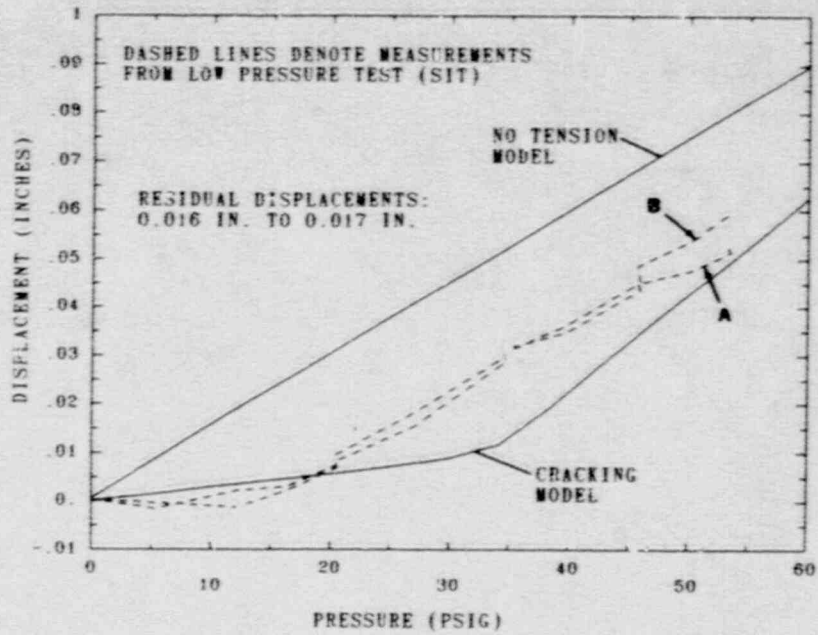
Figure 5.1.5 Experimental and Analytical Results for the Radial Displacement at the Springline
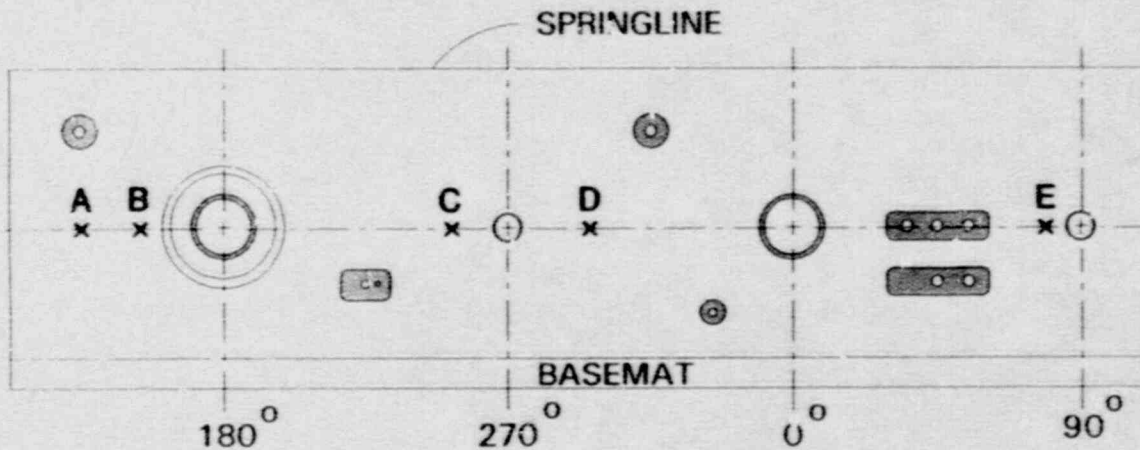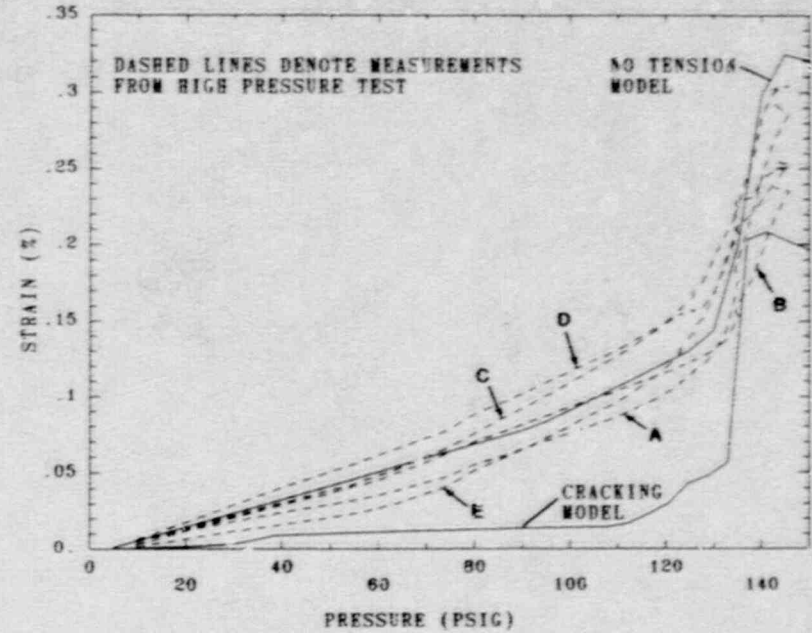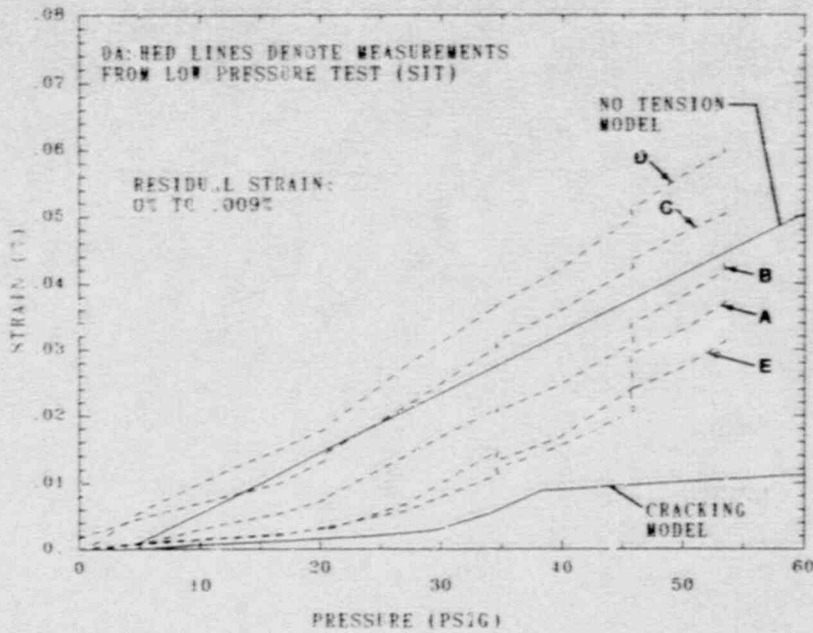
Figure 5.1.6 Experimental and Analytical Results for Strain in the Vertical Reinforcement Near the Midheight of the Cylinder

# 1

## IMAGE EVALUATION
## TEST TARGET (MT-3)
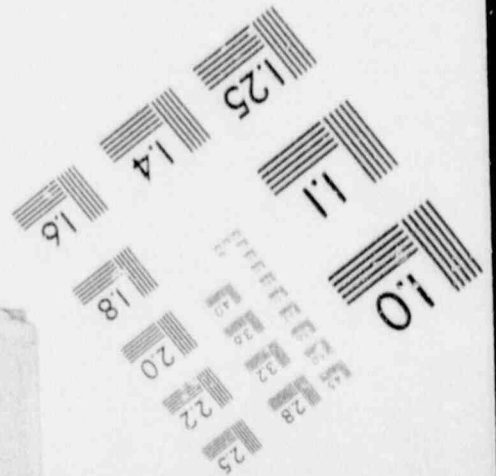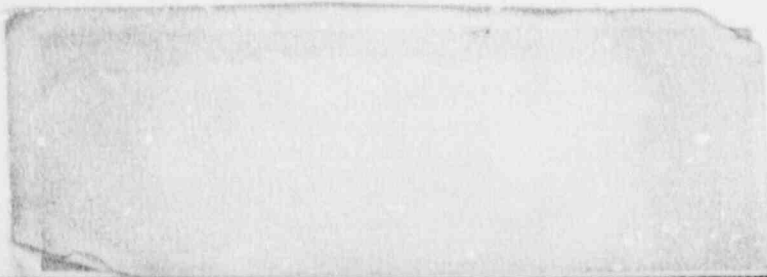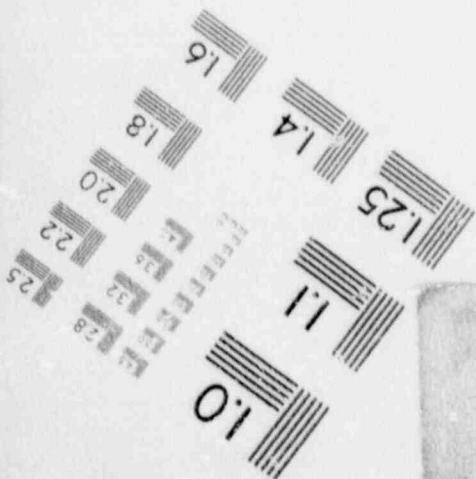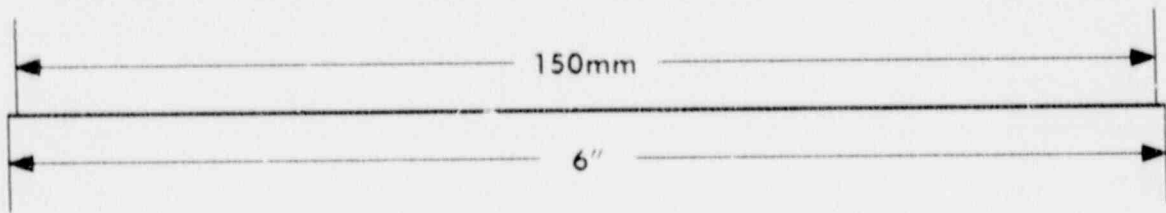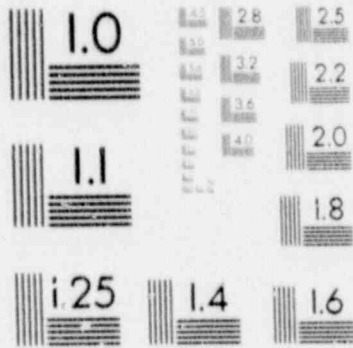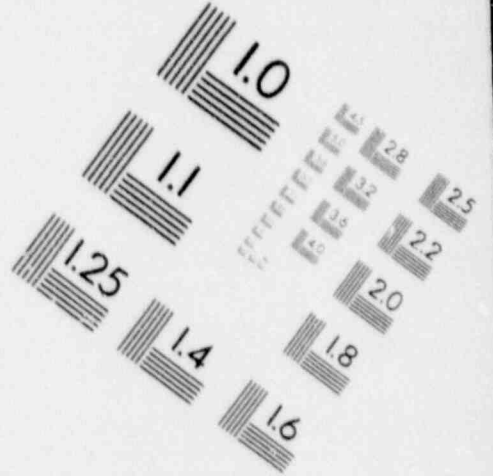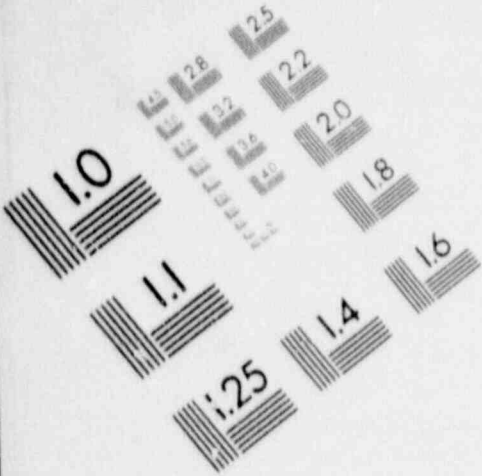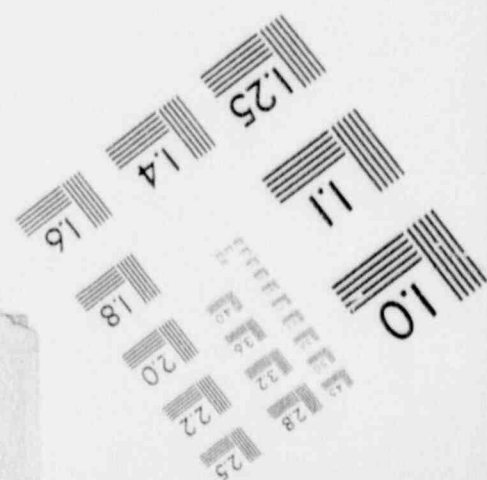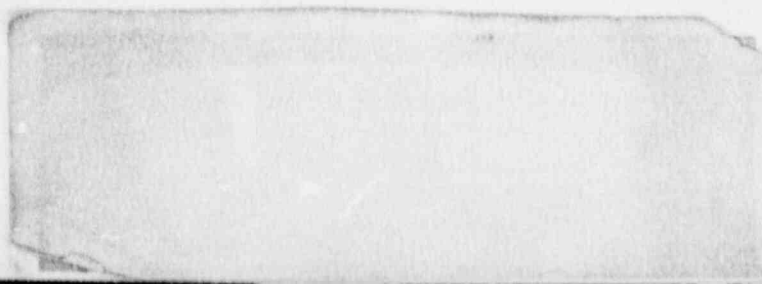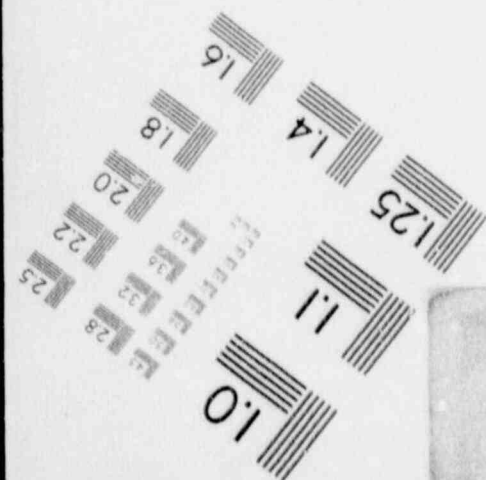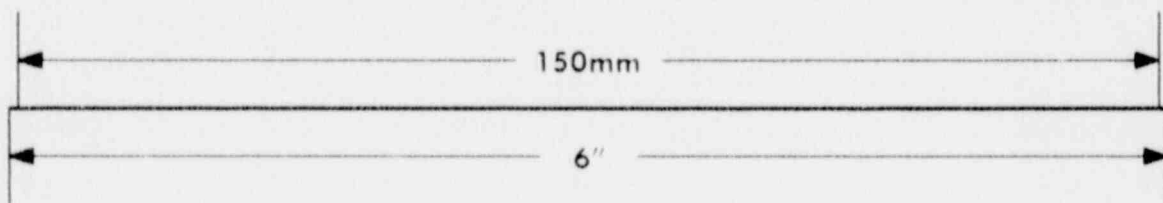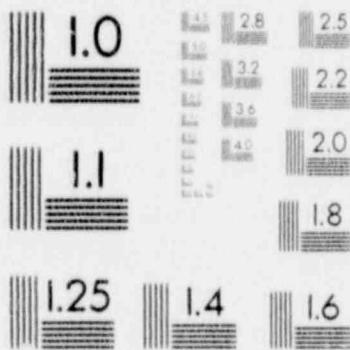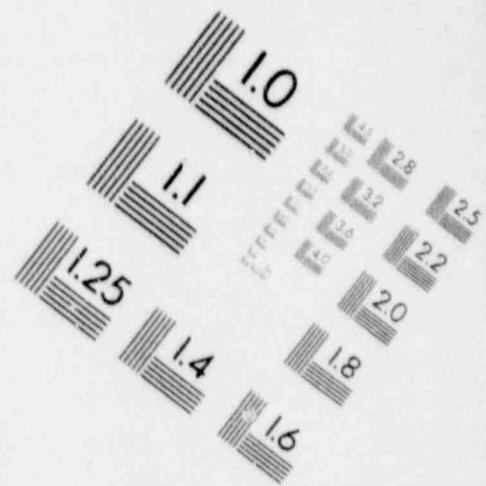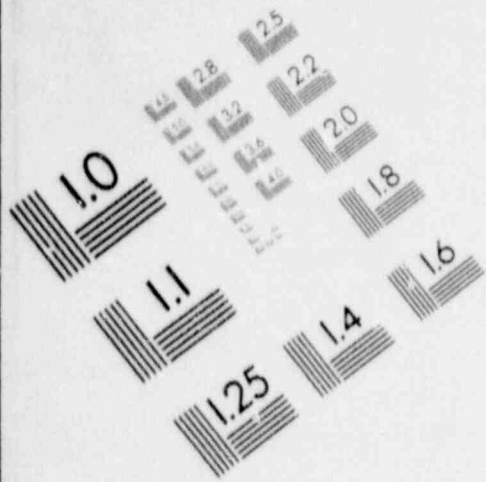
1.0
1.1
1.25    1.4    1.6

|← 150mm →|

|← 6" →|

# 1

## IMAGE EVALUATION
## TEST TARGET (MT-3)

1.0

1.1

1.25   1.4   1.6

150mm

6"

# 1

## IMAGE EVALUATION
## TEST TARGET (MT-3)

150mm

6"

# 1

**IMAGE EVALUATION
TEST TARGET (MT-3)**

150mm

6"
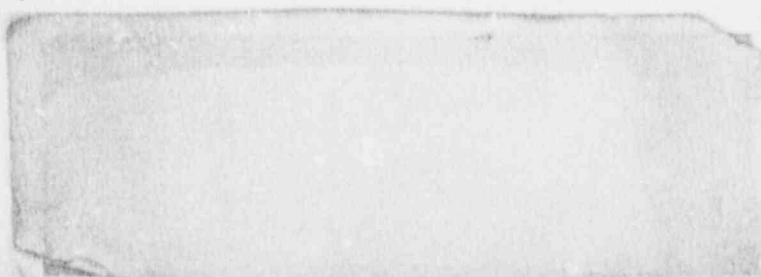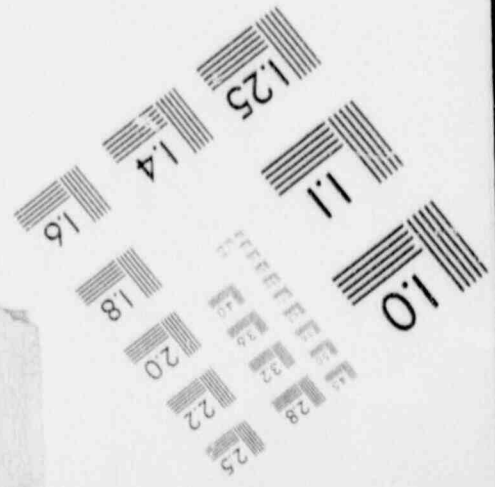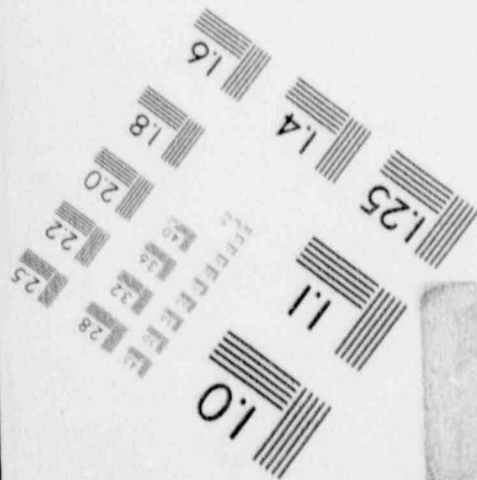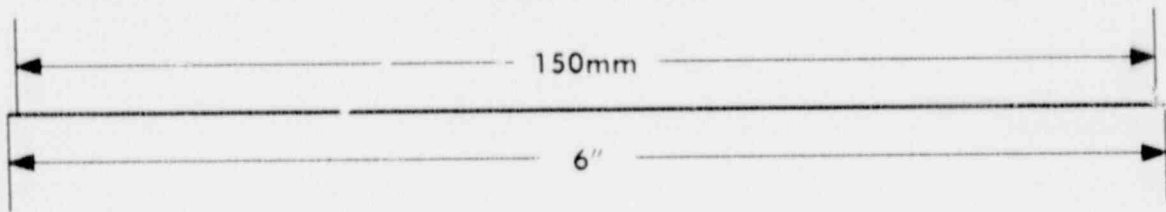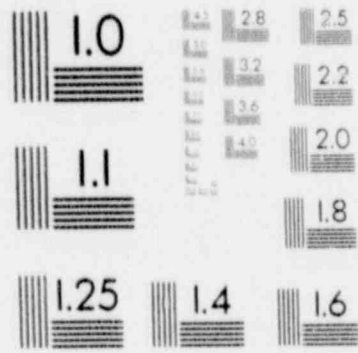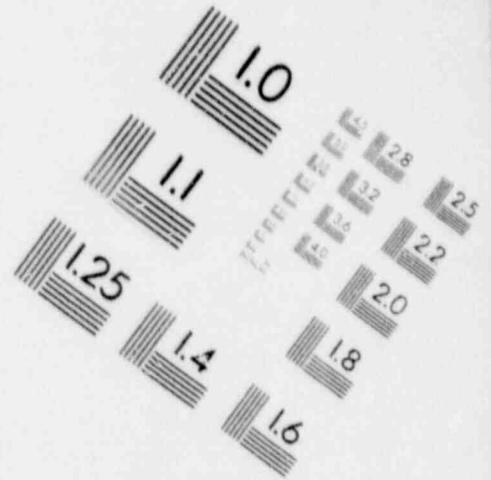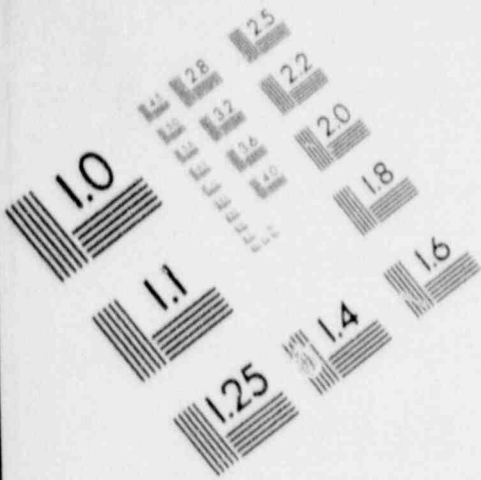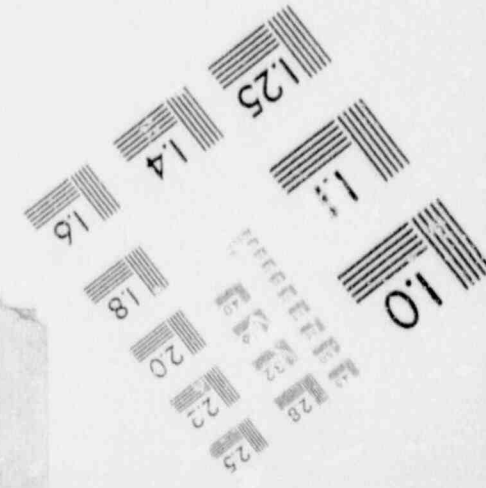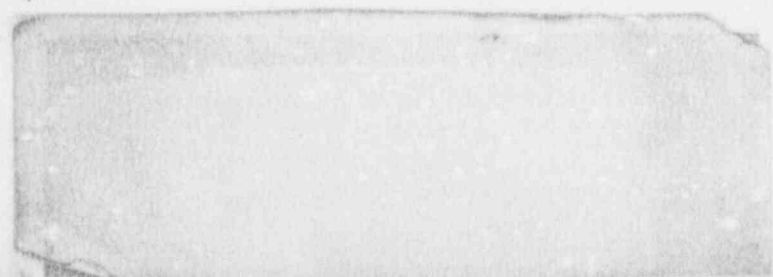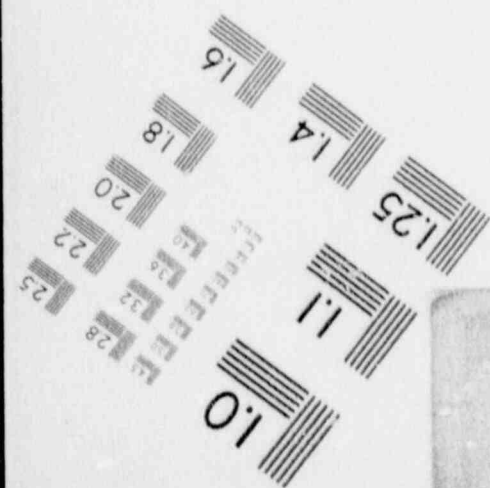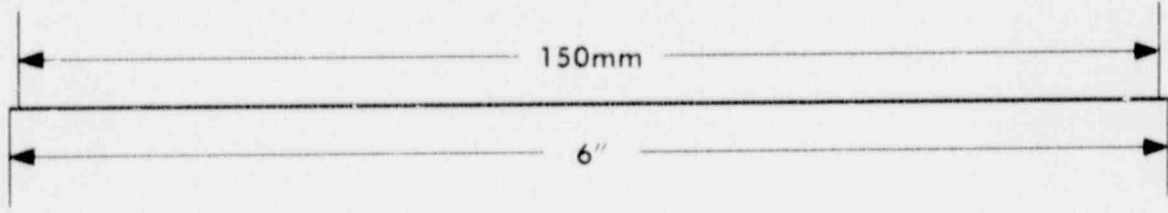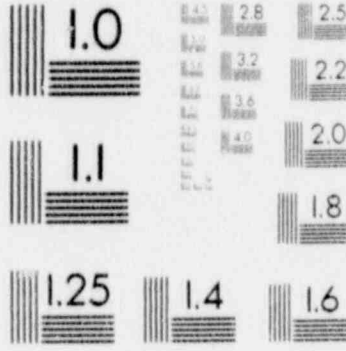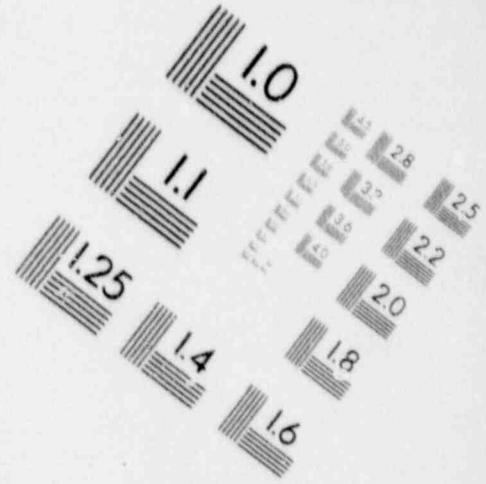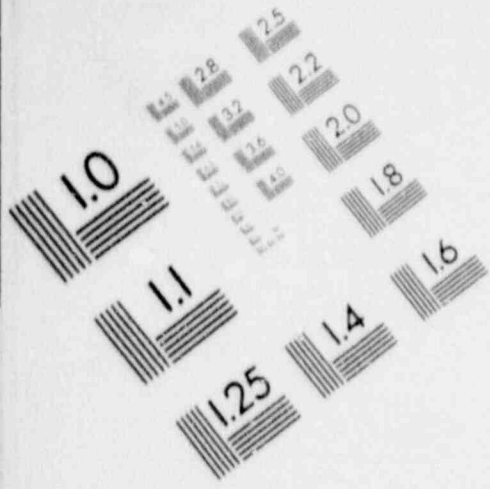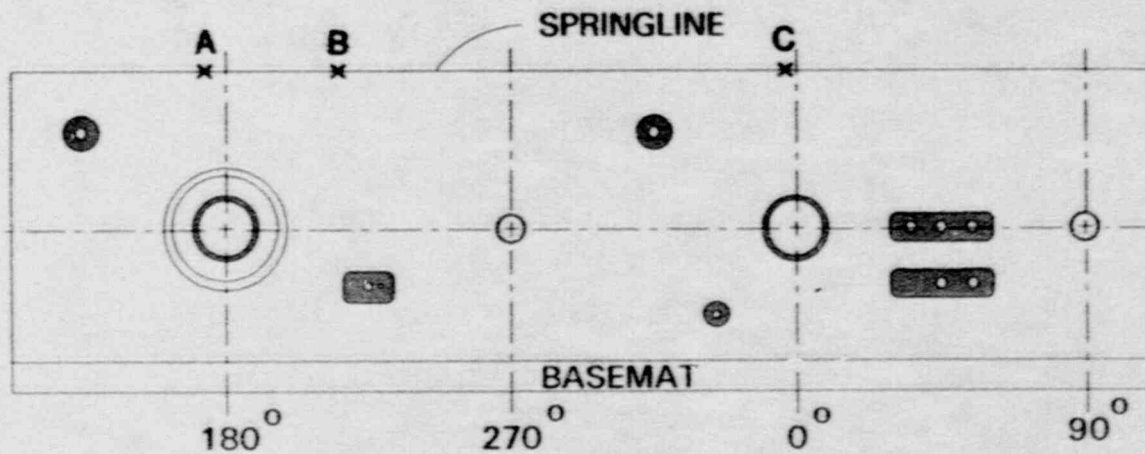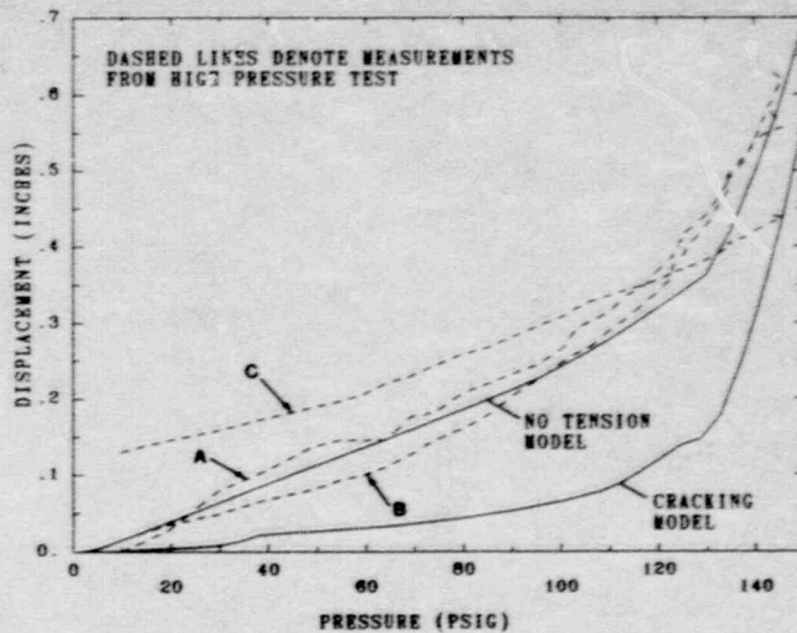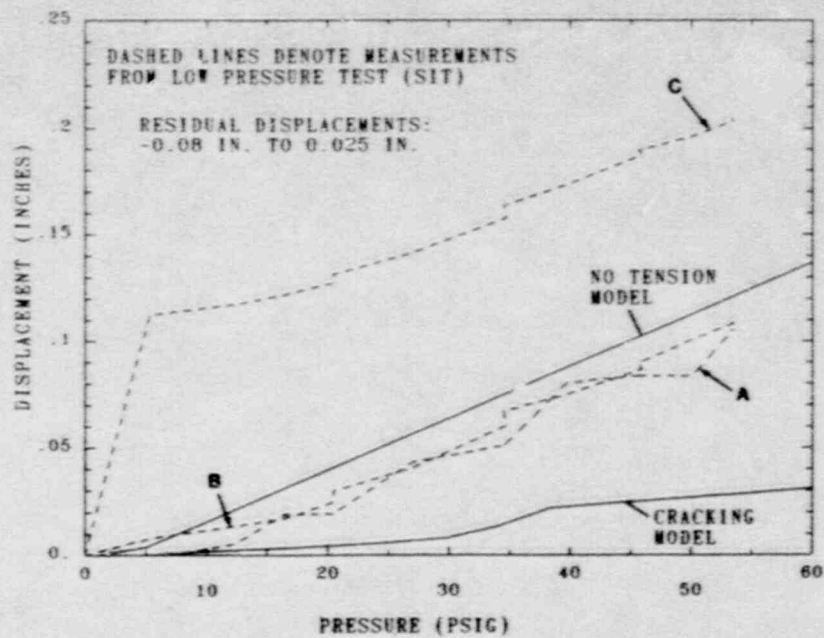
Figure 5.1.7  Experimental and Analytical Results for Vertical Elongation of the Cylinder
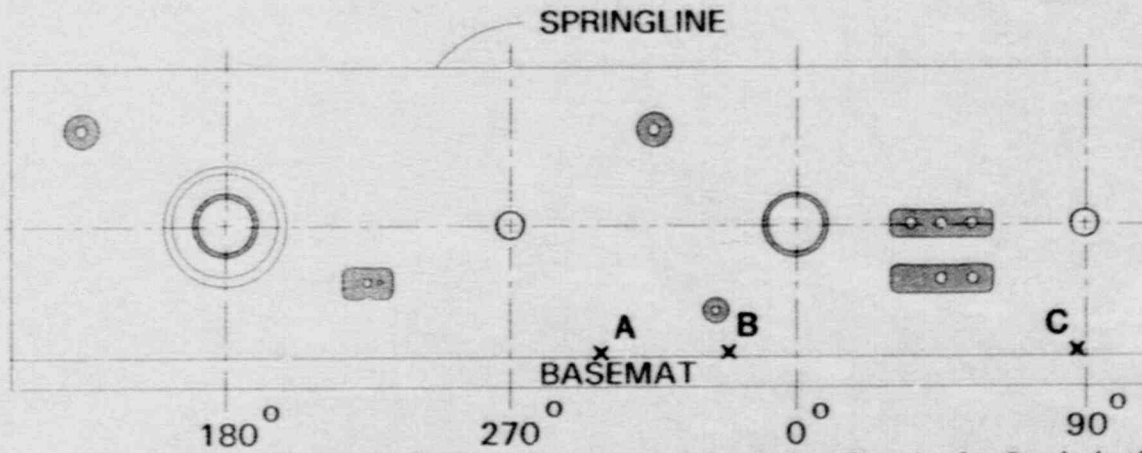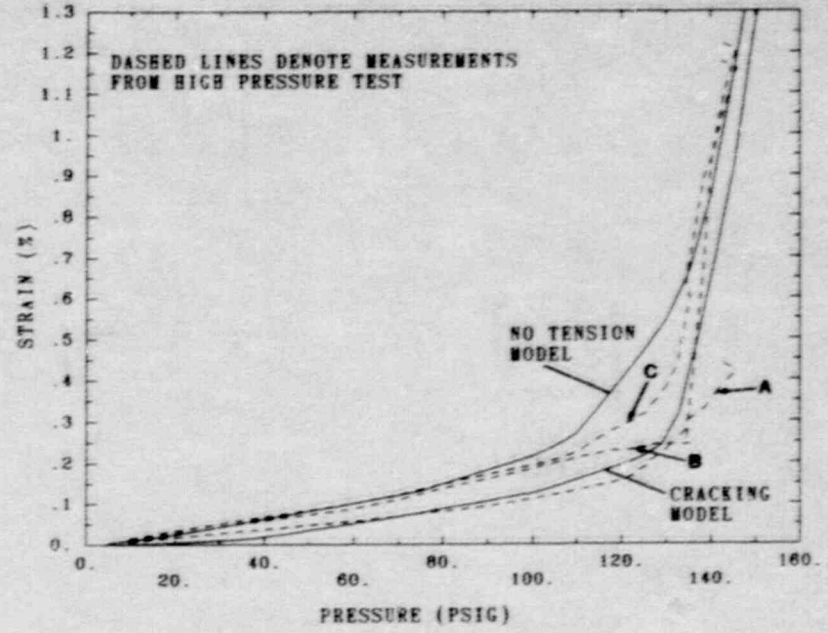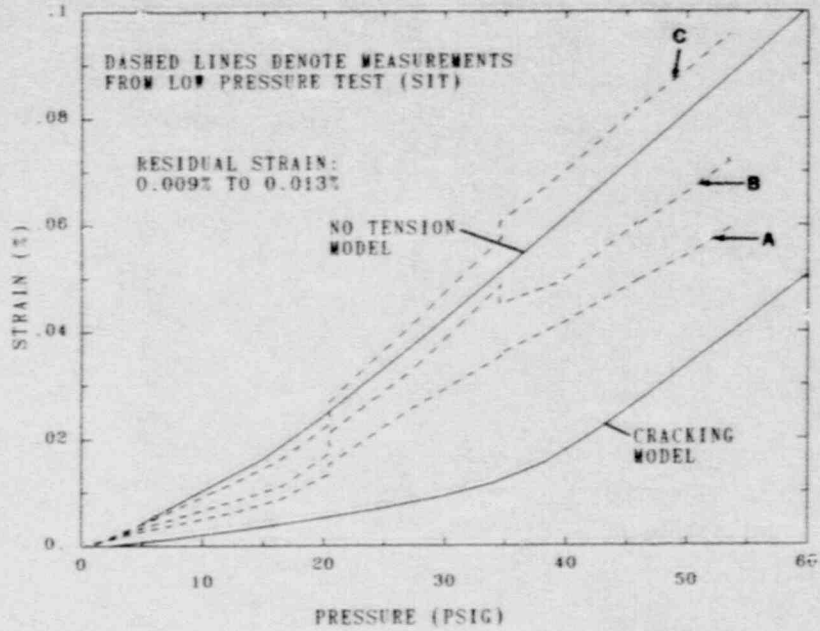
Figure 5.1.8 Experimental and Analytical Results for Strain in the Layer 2 (Inner) Vertical Reinforcement in the Cylinder Wall Near the Basemat

DASHED LINES DENOTE MEASUREMENTS
FROM LOW PRESSURE TEST (SIT)

RESIDUAL STRAINS:
0.008% TO 0.013%

NO TENSION
MODEL

CRACKING
MODEL

STRAIN (%)

PRESSURE (PSIG)

DASHED LINES DENOTE MEASUREMENTS
FROM HIGH PRESSURE TEST

NO TENSION
MODEL

CRACKING
MODEL

STRAIN (%)

PRESSURE (PSIG)

SPRINGLINE

×A          ×B          ×C
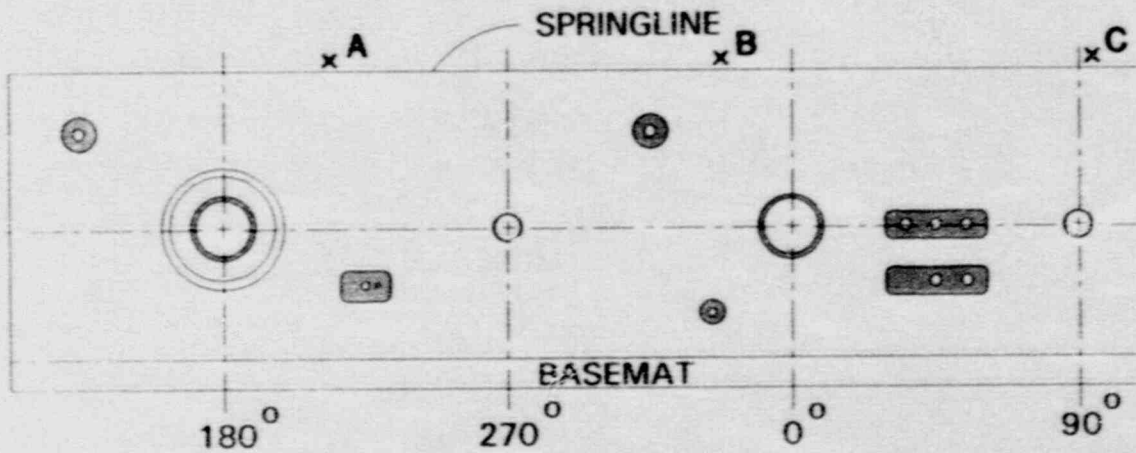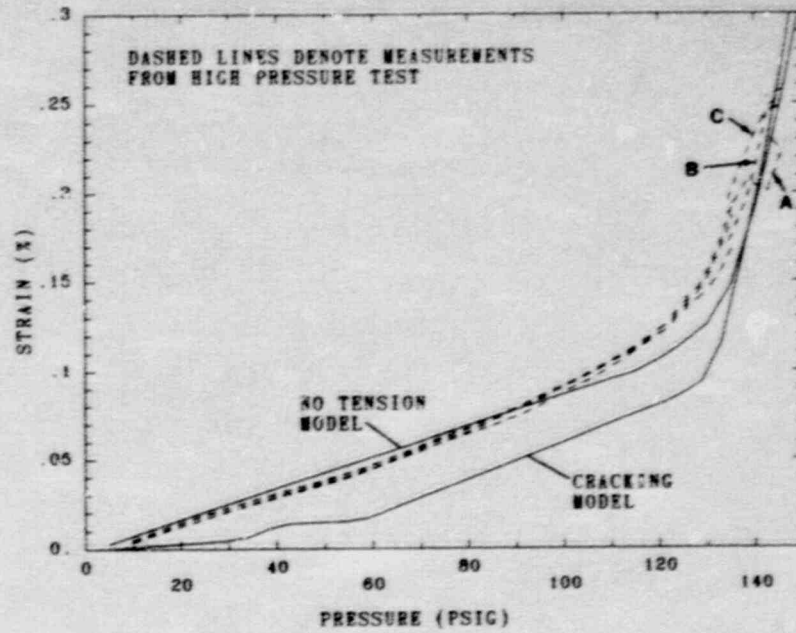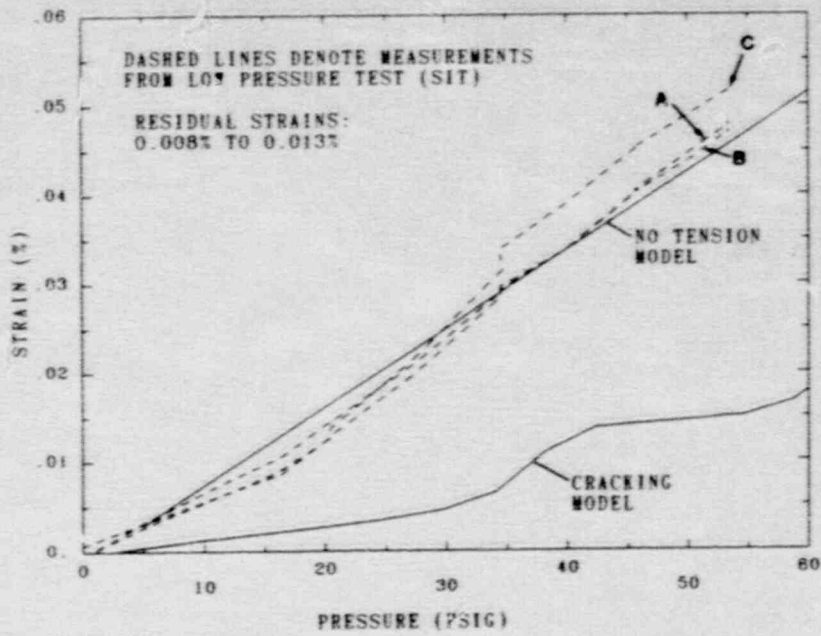
**CHANNEL**

A – 523
B – 546
C – 501

BASEMAT

180°        270°        0°        90°

Figure 5.1.9  Experimental and Analytical Results for Strain in the Layer 2
(Inner) Vertical Reinforcement in the Dome Near the Springline
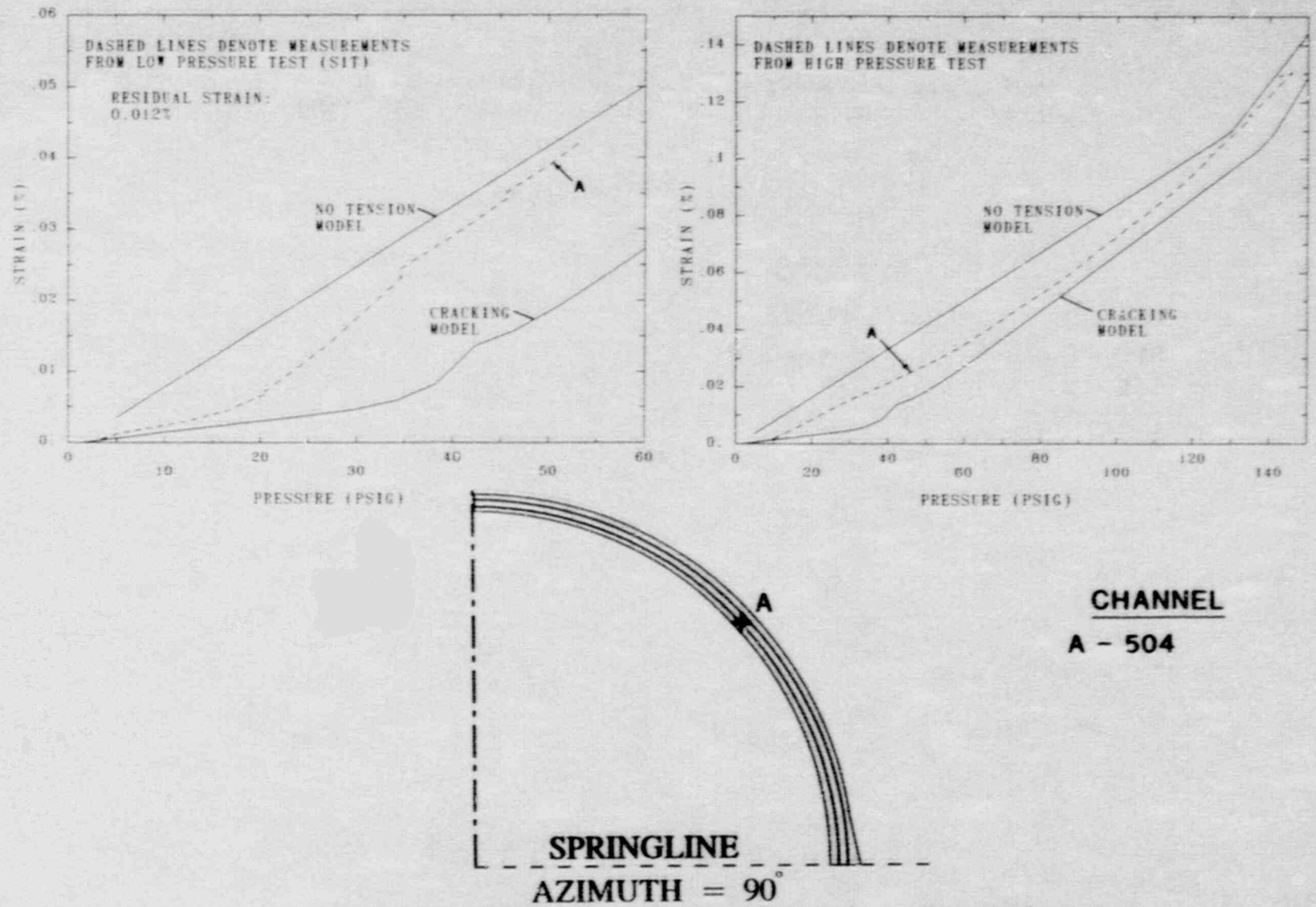
Figure 5.1.10 Experimental and Analytical Results for Strain in the Layer 2
(Inner) Vertical Reinforcement Halfway Up the Dome

Figure 5.1.11  Liner Tear Near a Cluster of Piping Penetrations
in the 1:6-Scale Model

5-33
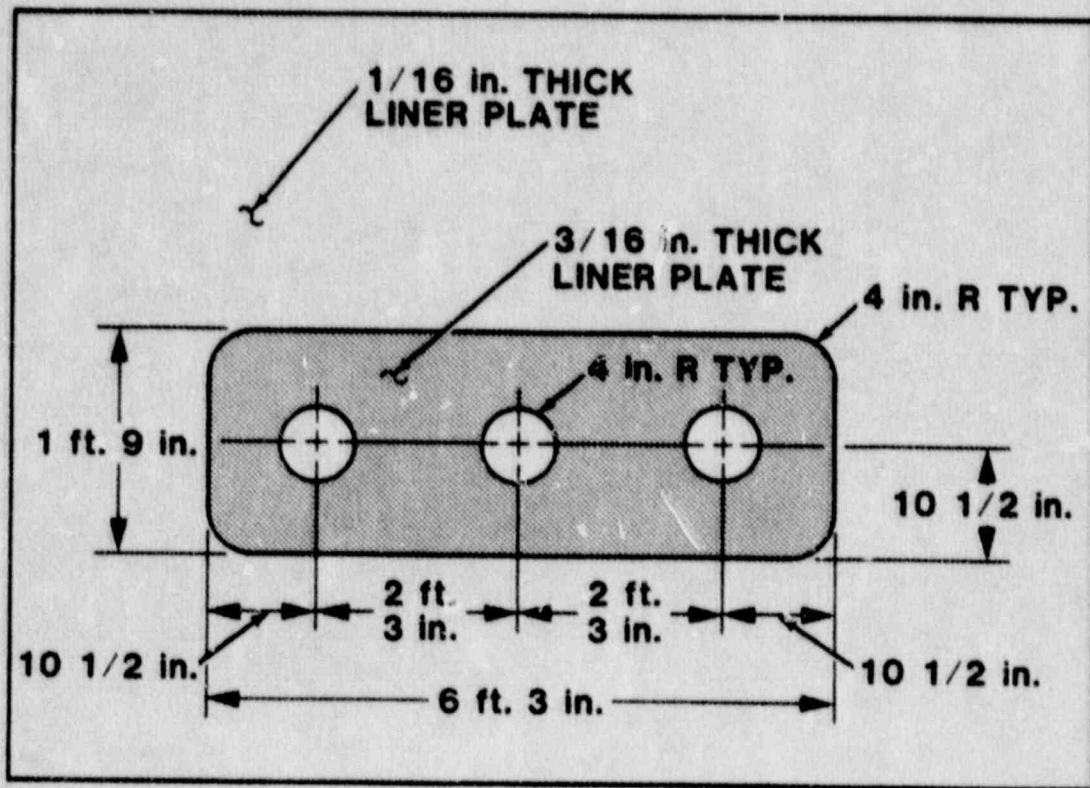
Figure 5.1.12 Details of the Region Surrounding the Piping Penetrations
at the Site of the Largest Liner Tear
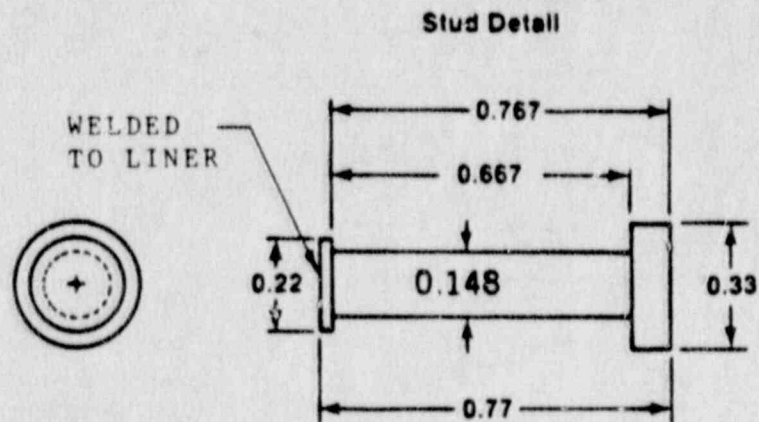


Figure 5.1.13 Dimensions of a Typical Stud Anchor
Used Near the Midheight of the Cylinder
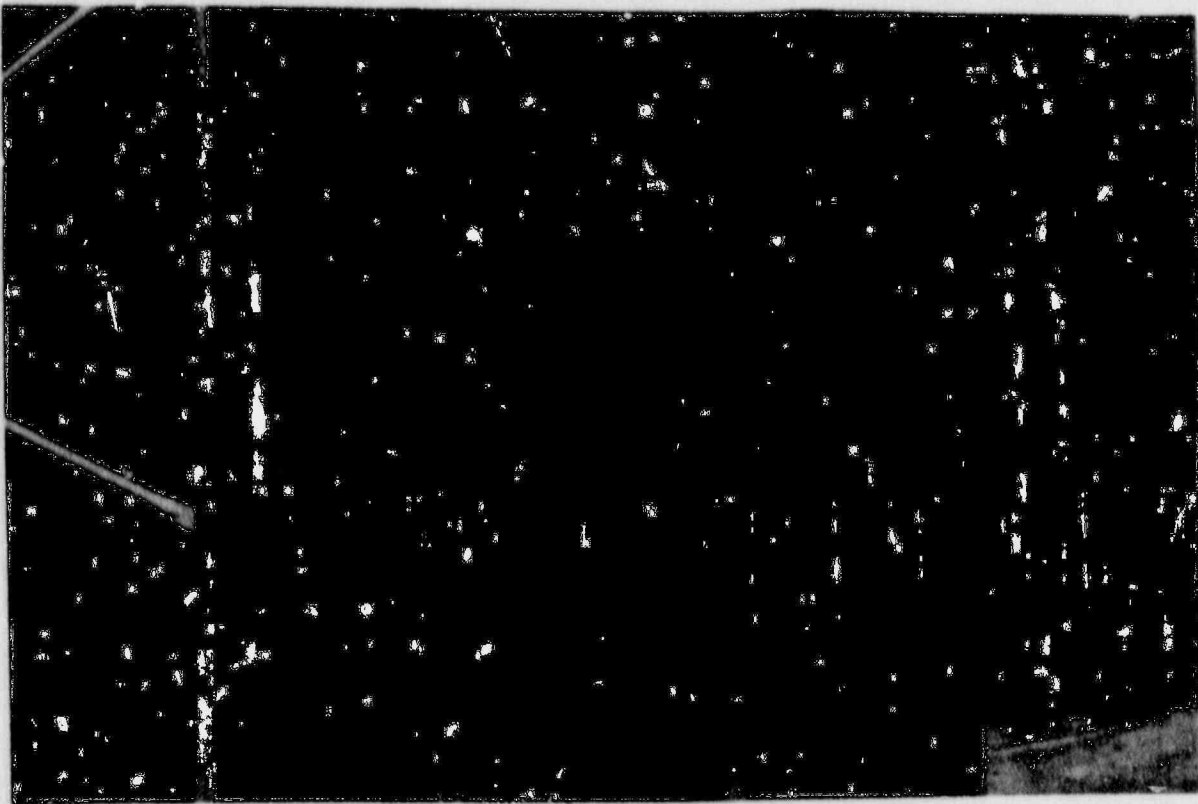
Figure 5.1.14 Arrangement of Studs in the Region Surrounding the Penetrations
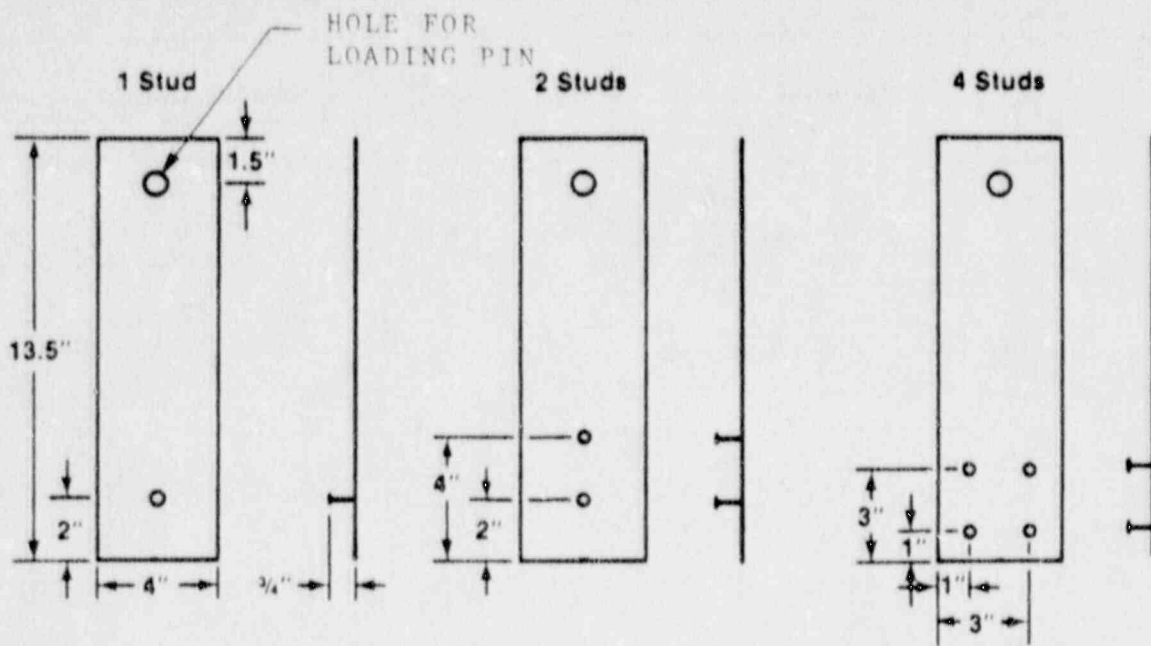


NOTE:
All Dimensions are Typical
for all Plates Except Where
Labeled. Plate Thickness is 0.065"

Figure 5.1.15 Specimens Fabricated for Stud-Shear Experiments
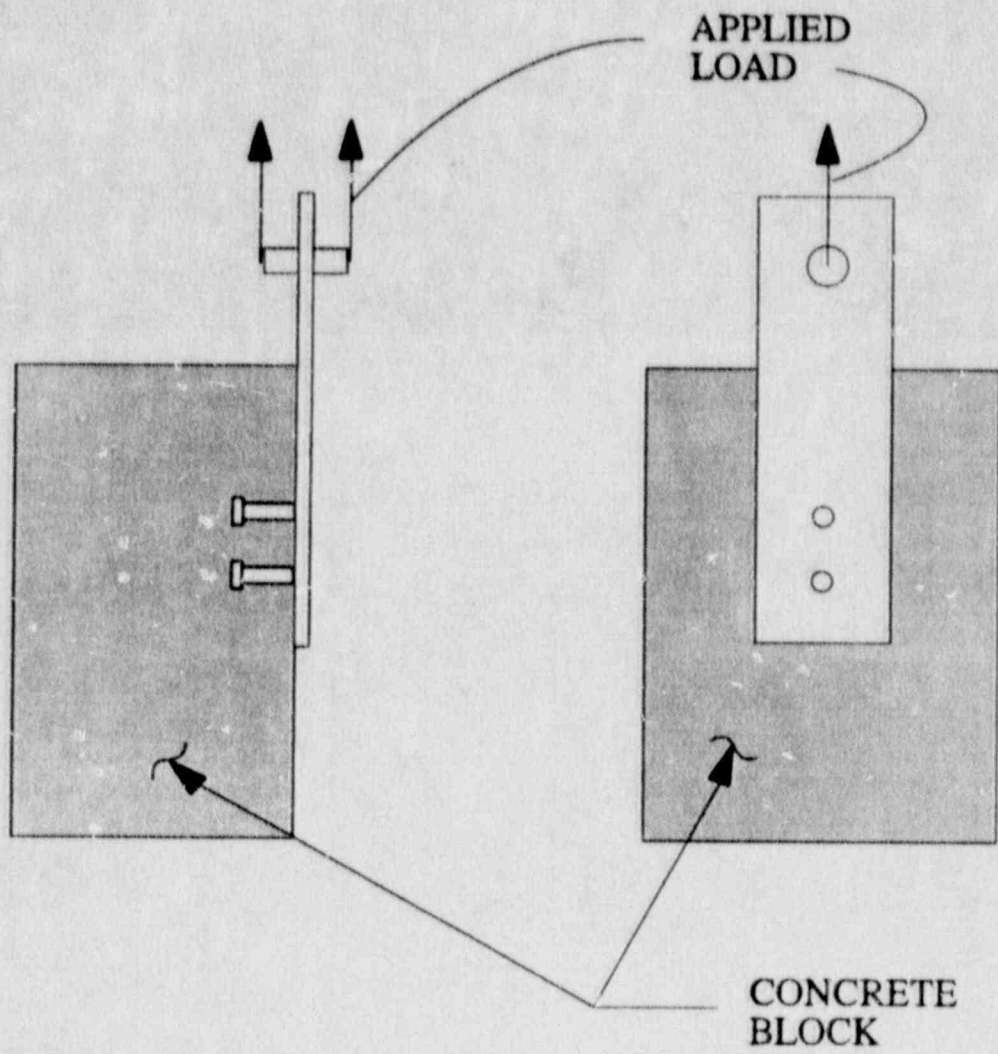
Figure 5.1.16 Schematic of a Typical Stud-Shear Experiment
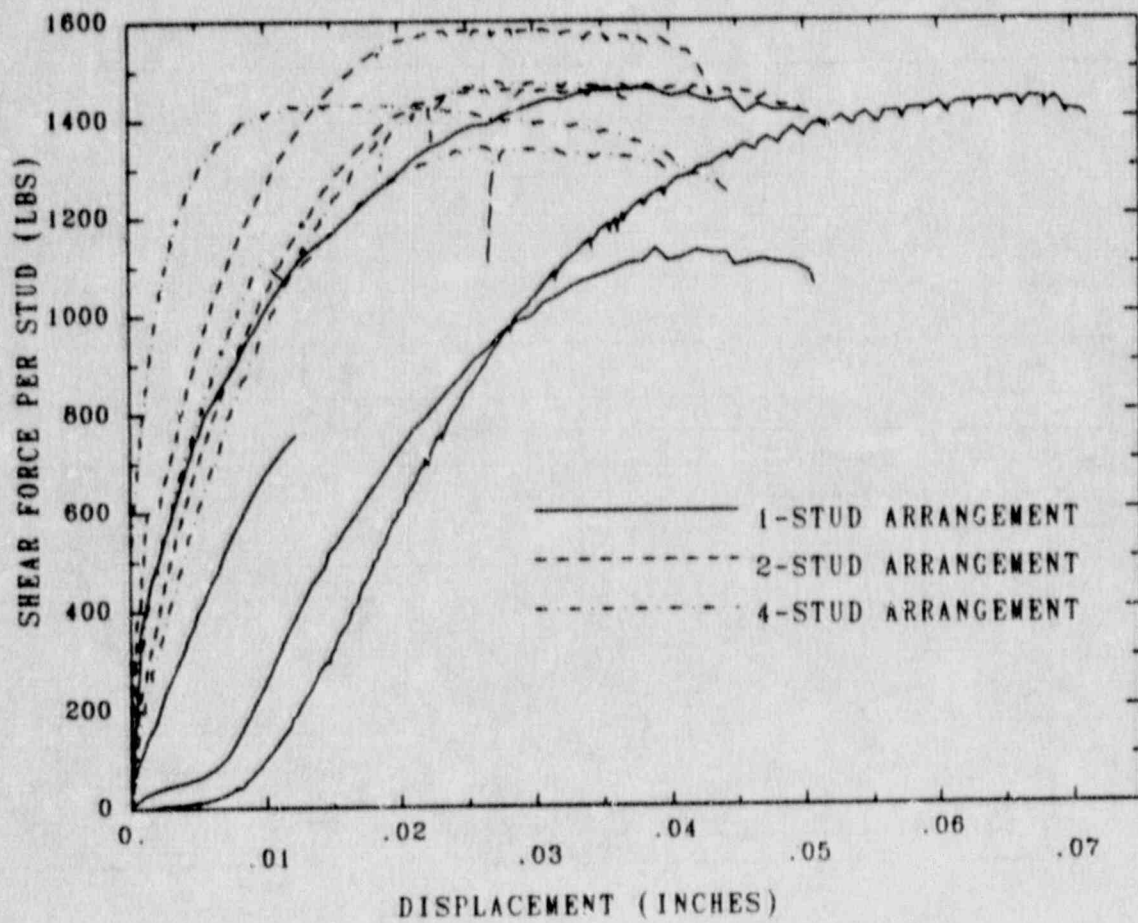
Figure 5.1.17 Force-Displacement Curves Measured in the Stud-Shear Experiments
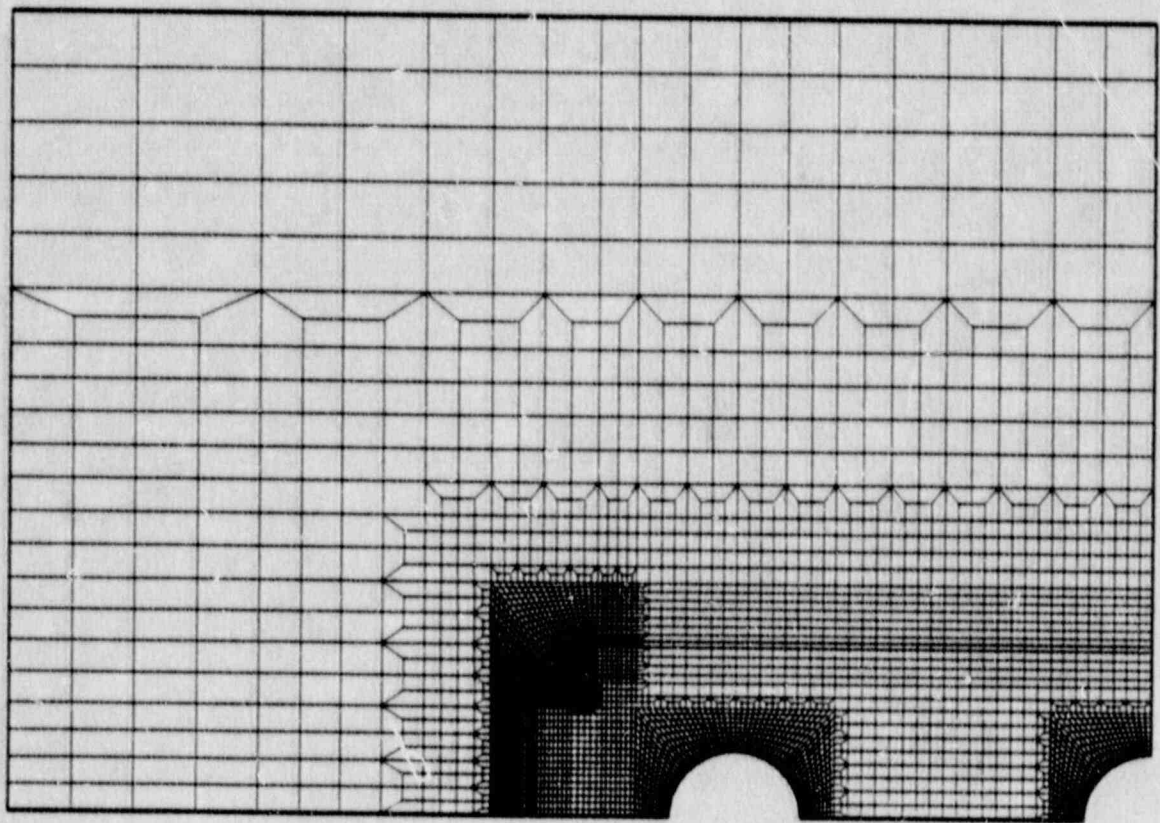
Figure 5.1.18  Plane Stress Finite Element Model
of the Penetration Region (No Liner Anchorage)
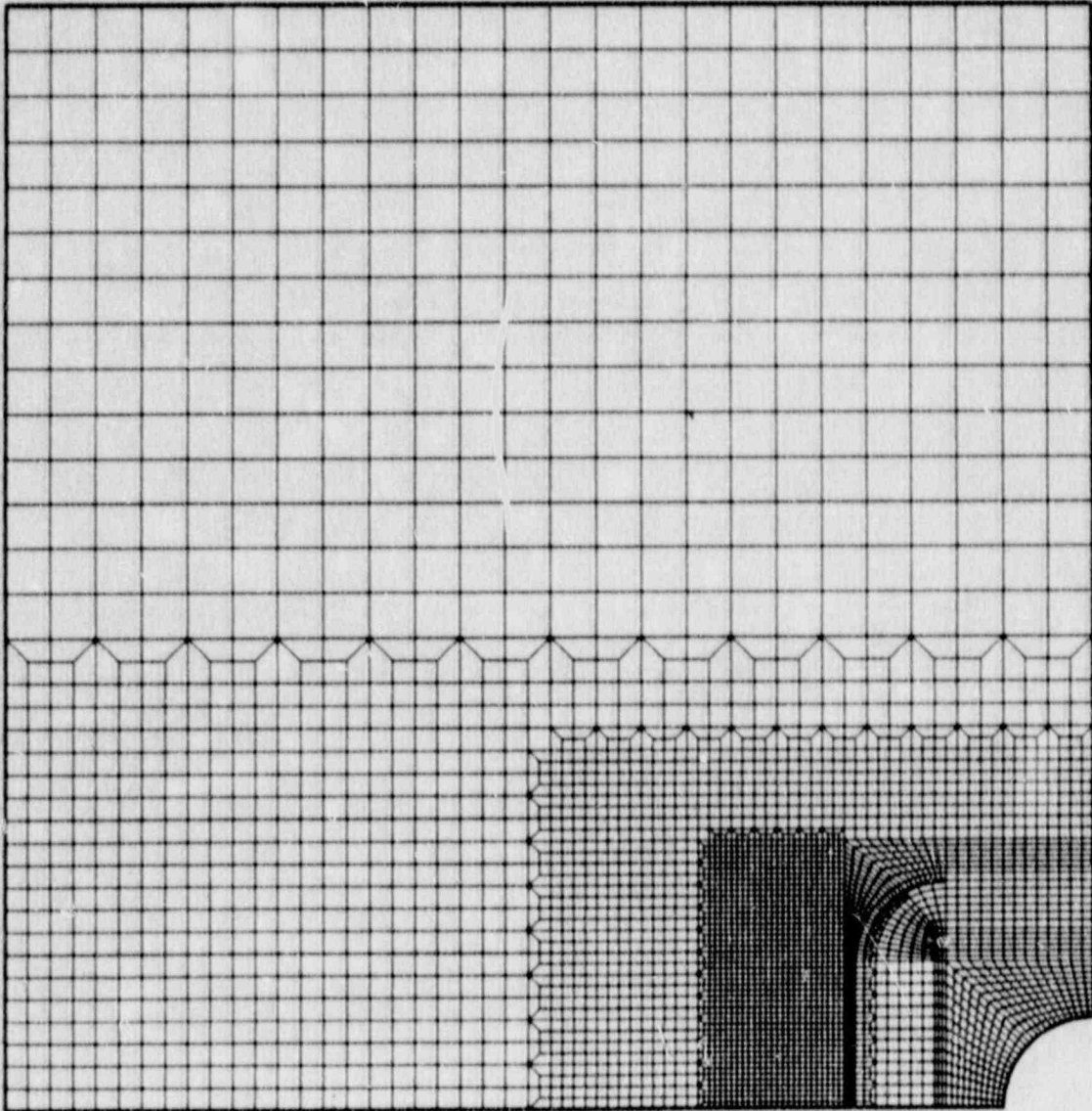
Figure 5.1.19  Plane Stress Finite Element Model
of the Penetration Region With Liner Anchorage
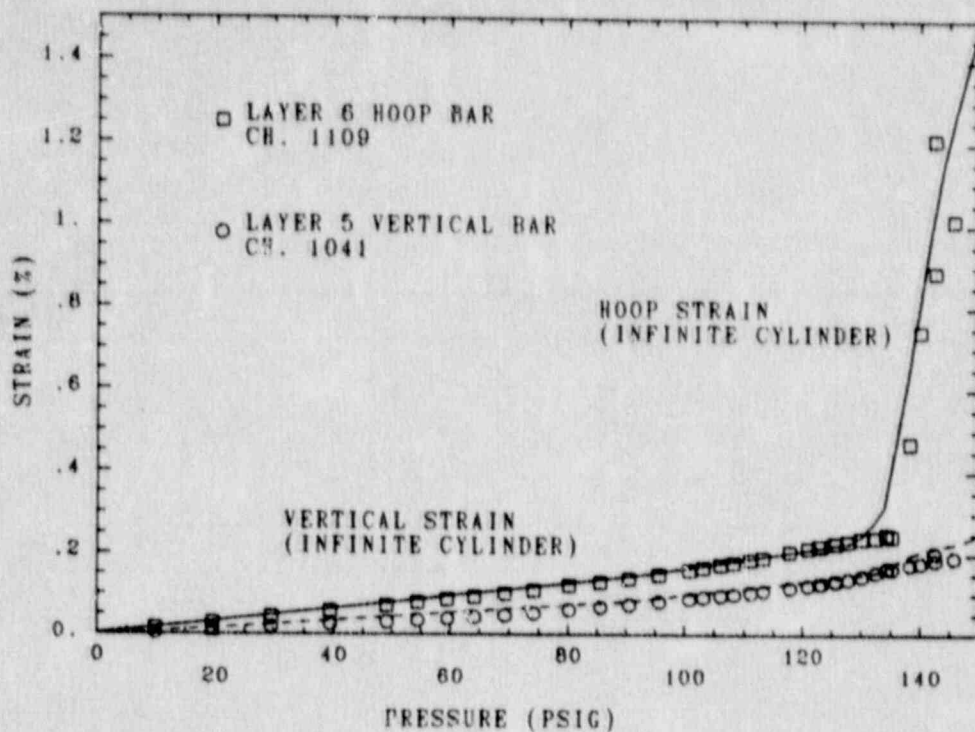
Figure 5.1.20 Comparison of Strains Computed in the Infinite Cylinder
Analysis to Strain Measurements From a Vertical Rebar and a Hoop Rebar
Located Behind the Thickened Plate Surrounding the Penetrations
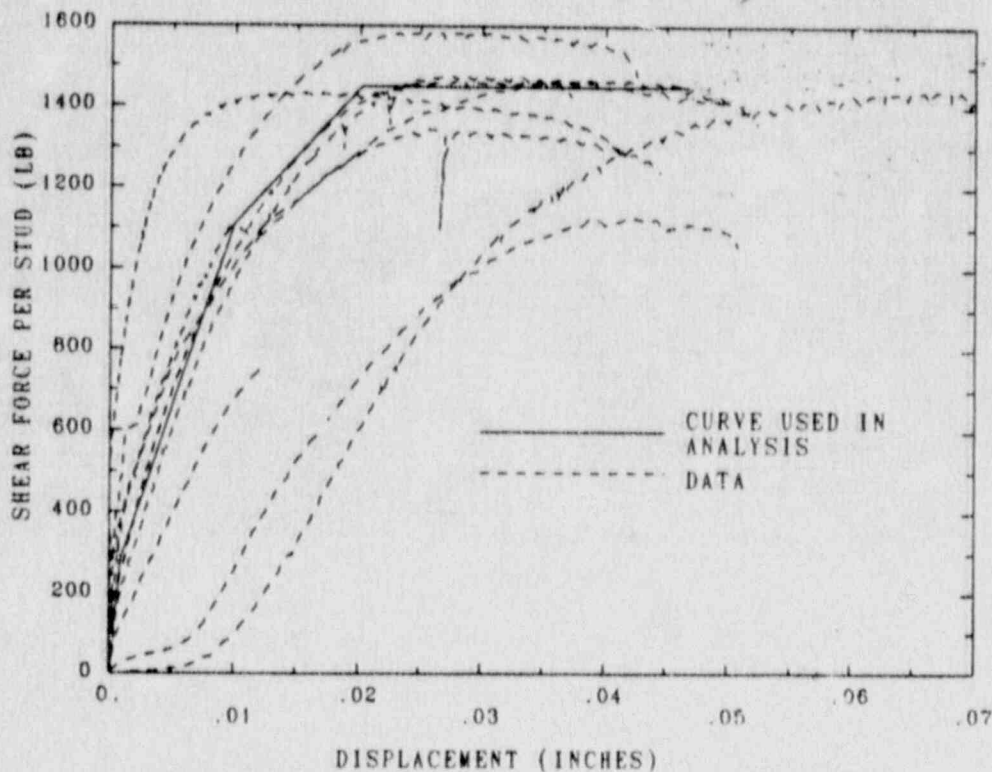


Figure 5.1.21 Idealized Shear Force-Shear Displacement Curve
Used for the Studs in the Penetration Analysis
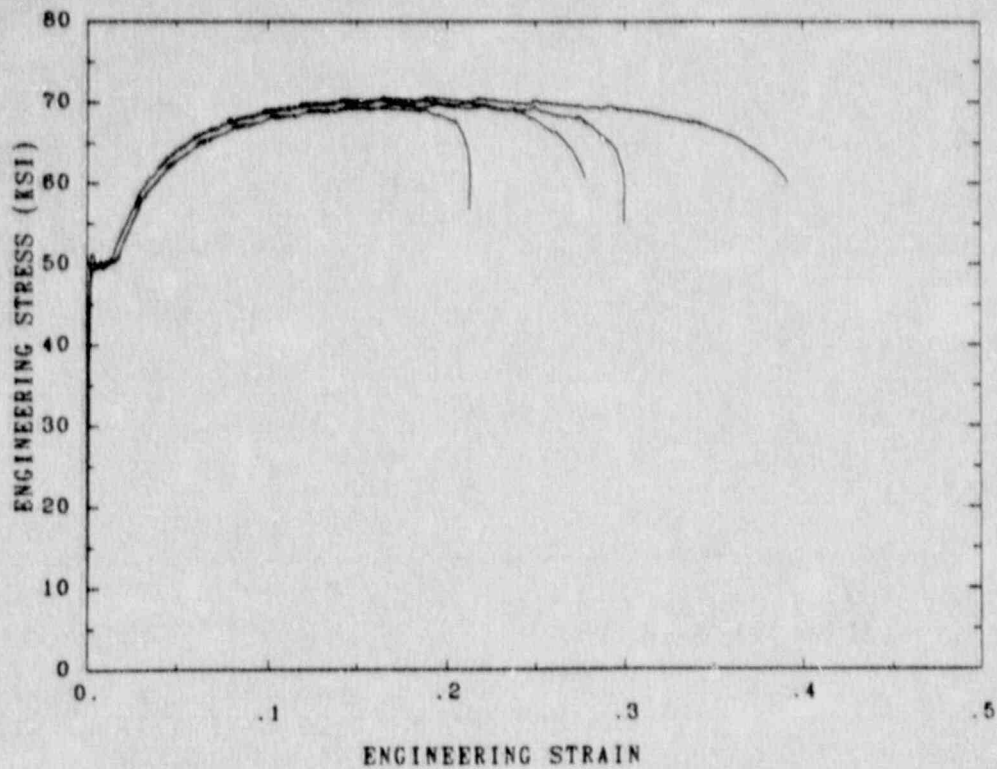
Figure 5.1.22  Engineering Stress-Strain Curves
for the A414 Grade D Steel (1/16 in. (1.59 mm) Plate)
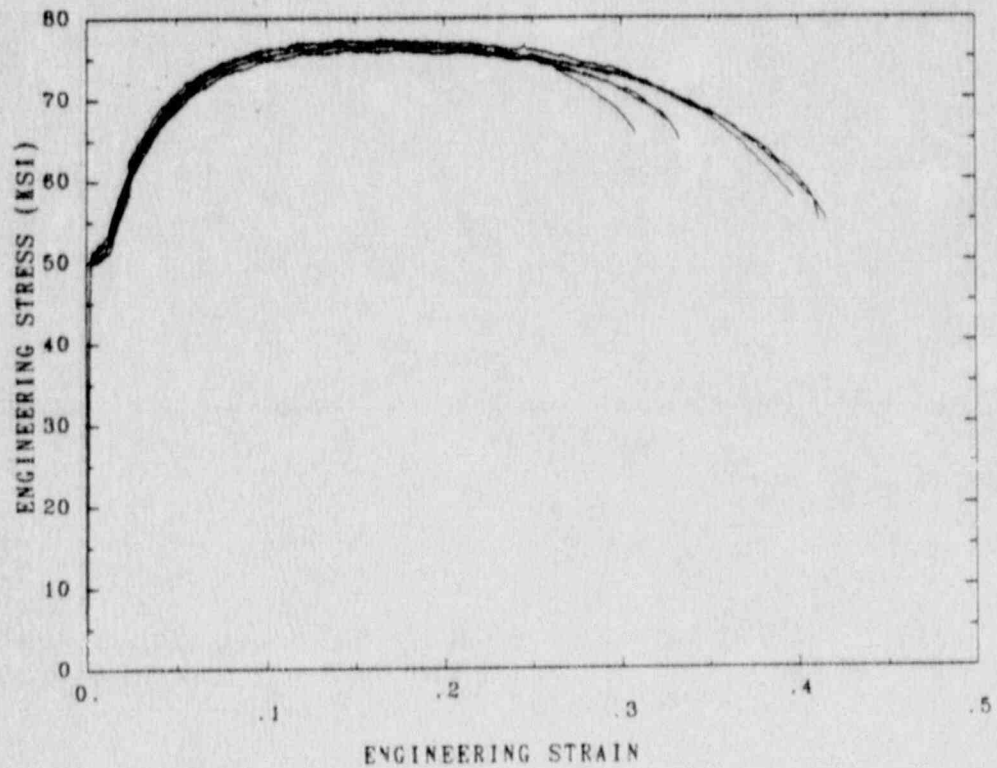


Figure 5.1.23  Engineering Stress-Strain Curve
for the A516 Grade 60 Steel (3/16 in. (4.76 mm) Plate)
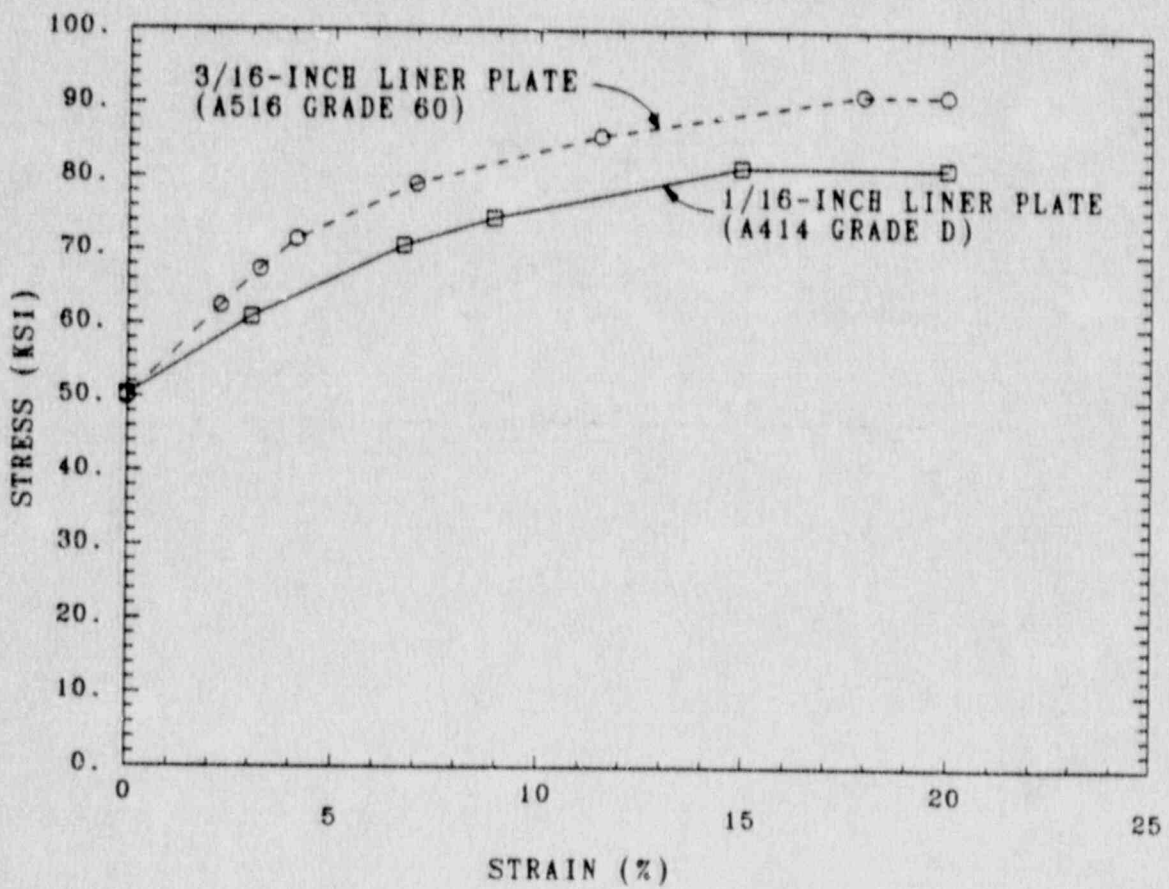
Figure 5.1.24  Idealized Curves Defining the Equivalent Stress-
Equivalent Plastic Strain Relationships for the A414 and A516 Steels
in the Point-Anchorage Analysis
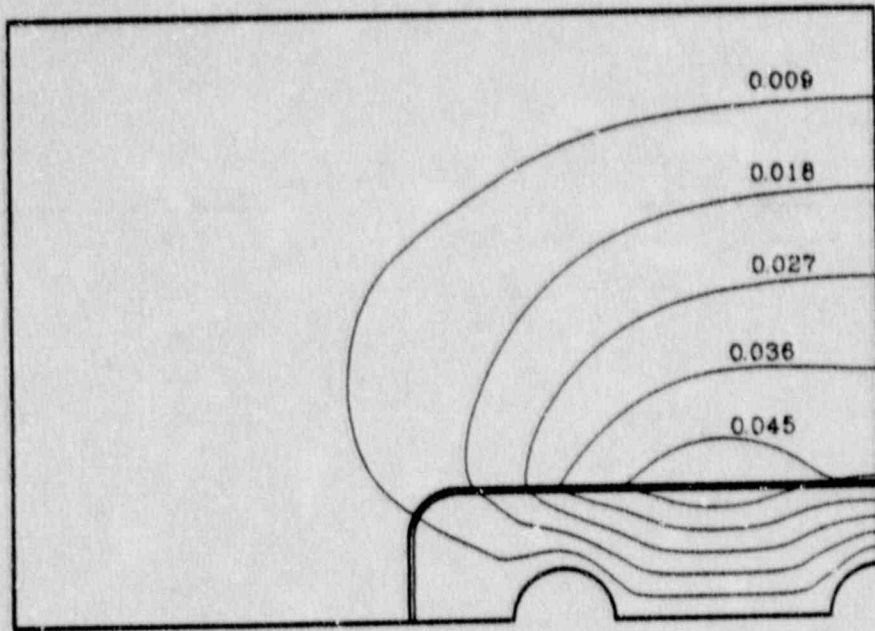
Figure 5.1.25  Vertical Component of Slippage Between the Liner and Concrete
at 145 psig (1.0 MPa) (Results from Anchorage-Free Analysis)
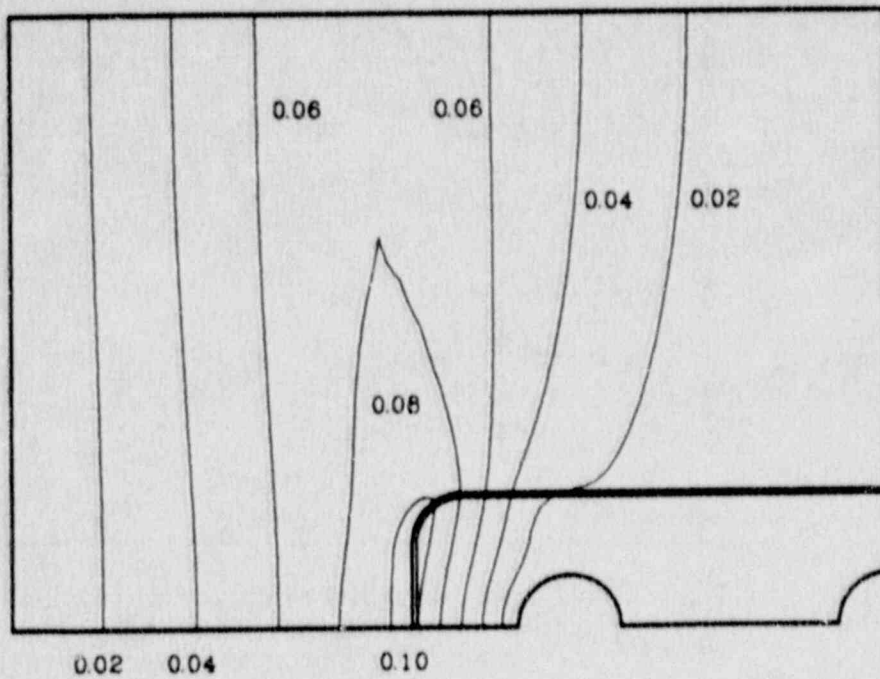


Figure 5.1.26  Circumferential Component of Slippage Between the Liner
and Concrete at 145 psig (1.0 MPa) (Results from Anchorage-Free Analysis)
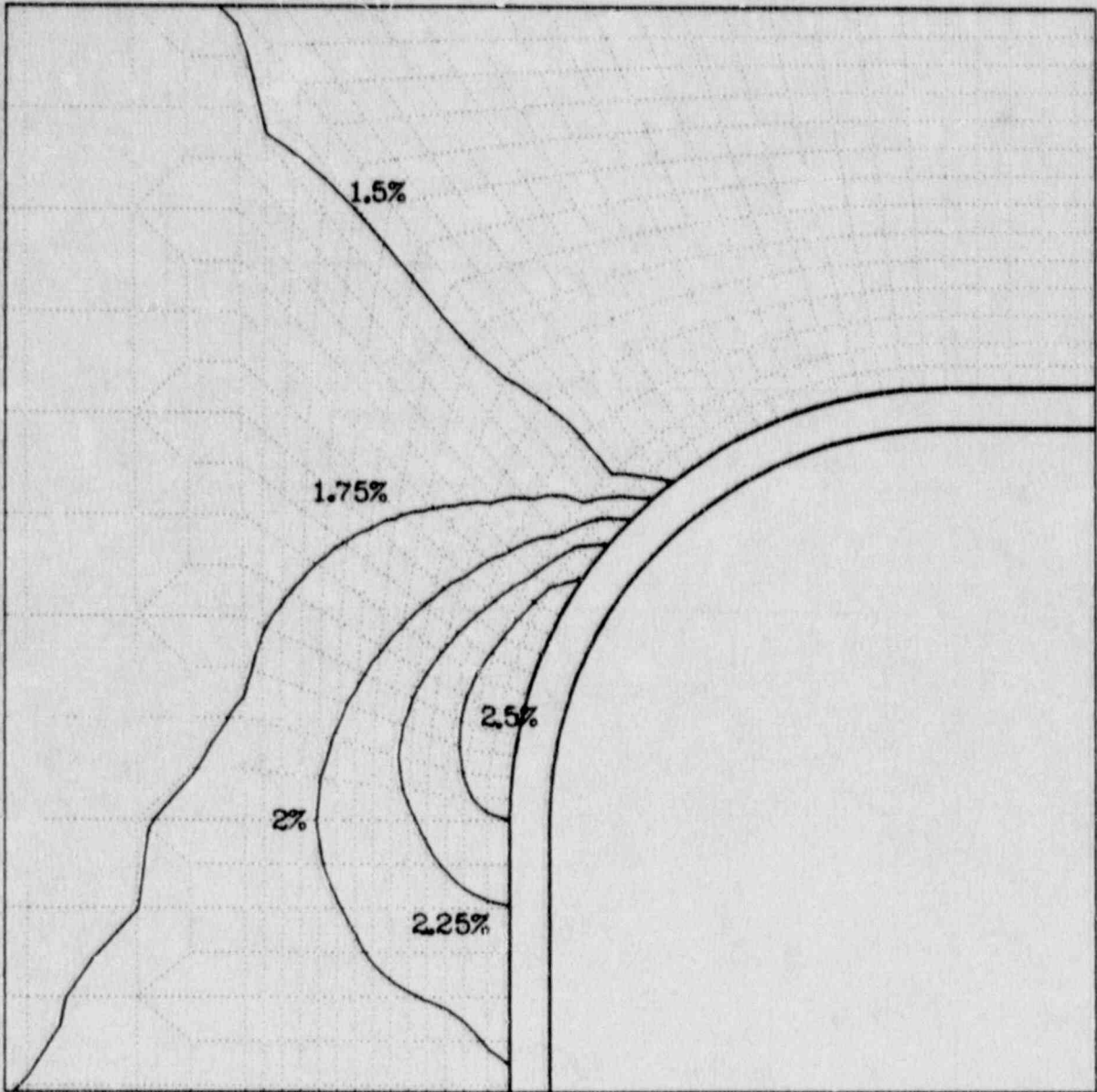
Figure 5.1.27  Equivalent Plastic Strain in the Penetration Region
at 145 psig (1.0 MPa) (Results From Anchorage-Free Analysis)
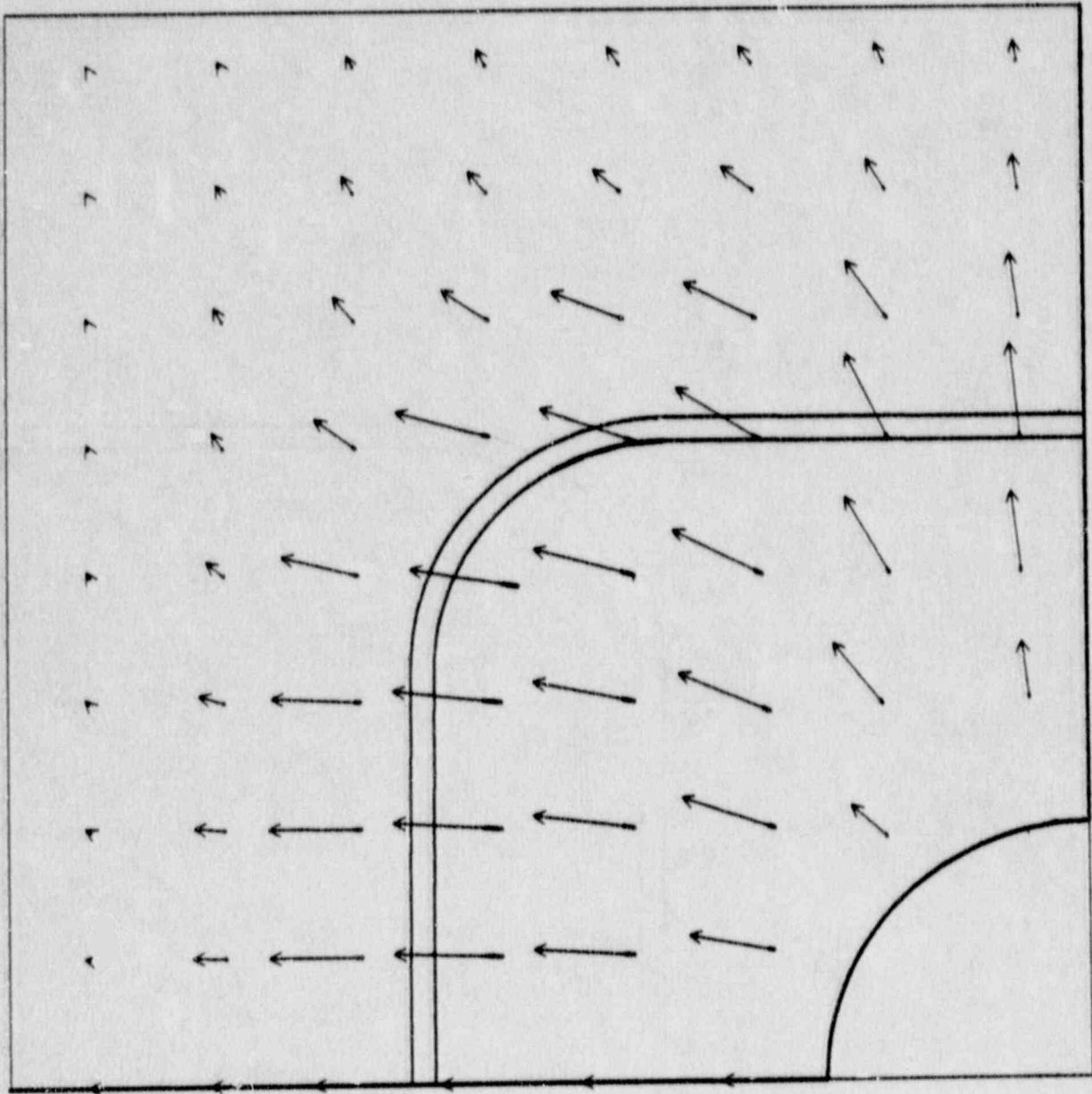
Figure 5.1.28 Relative Magnitudes and Directions of the Forces Acting
on the Liner From the Stud Anchors (145 psig (1.0 MPa))
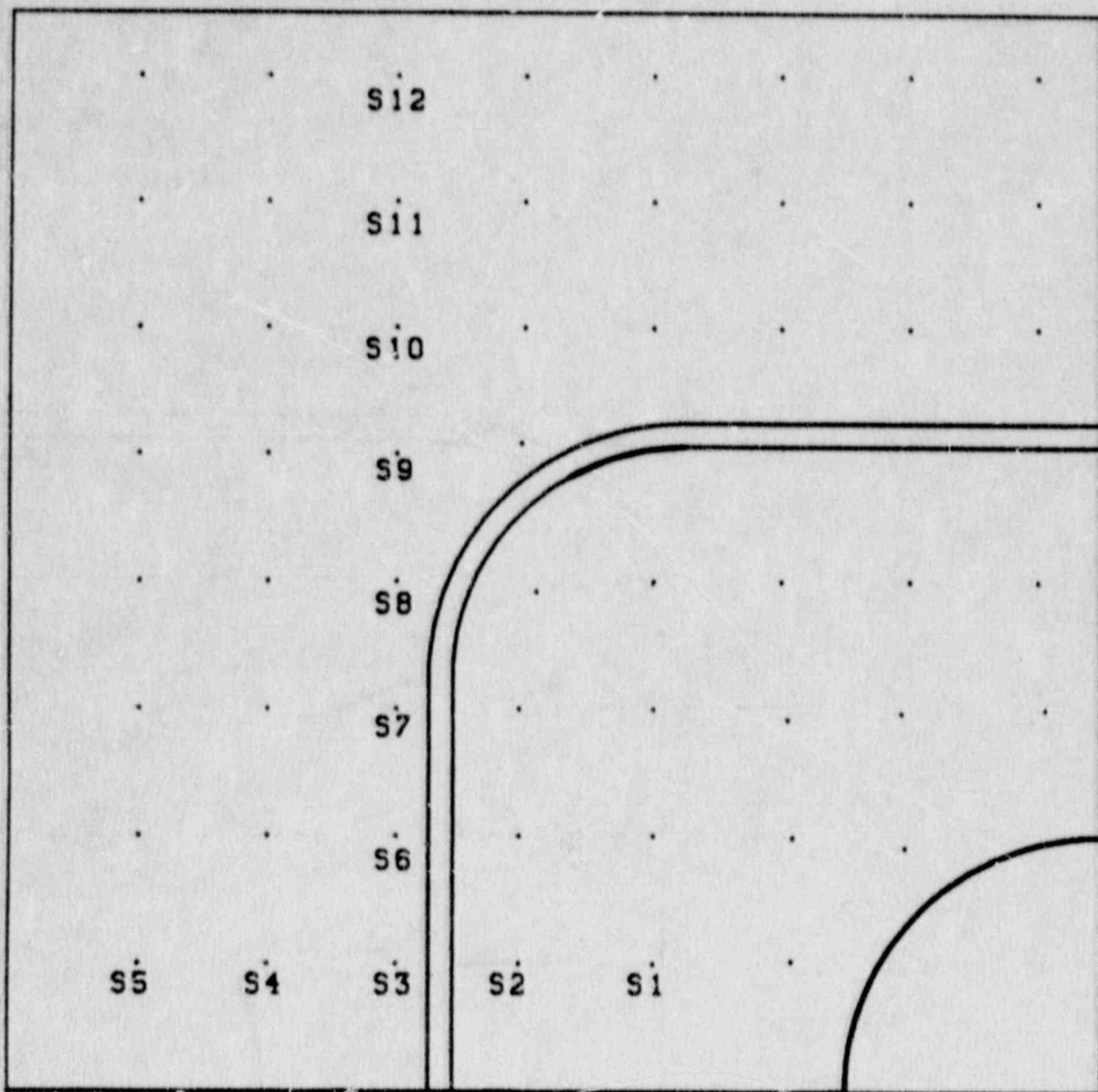
Figure 5.1.29 Stud Designations for Plots in Figures 5.1.30 and 5.1.31
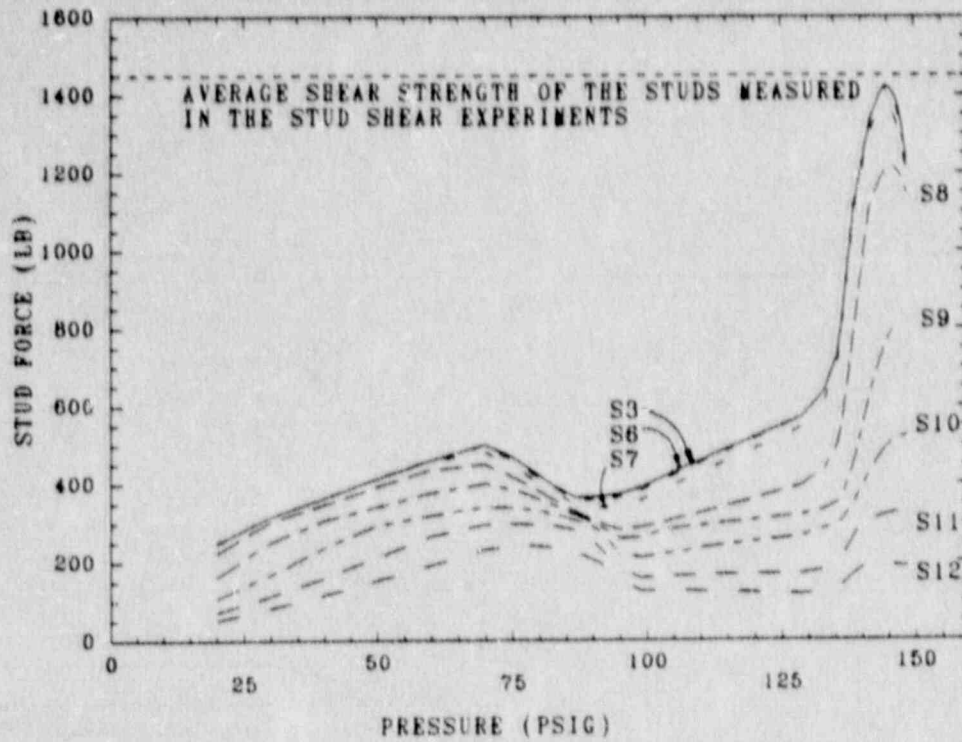
Figure 5.1.30 Forces in the Studs Located Along the Vertical Edge
of the 3/16 in. (4.76 mm) Plate (See Figure 5.1.29)
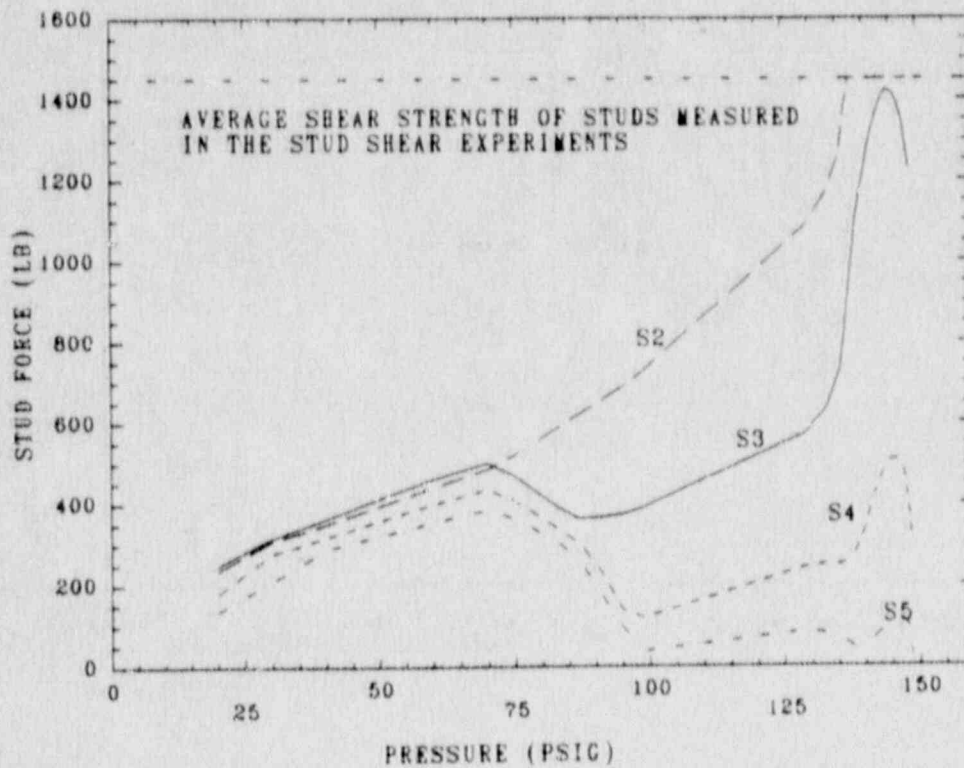


Figure 5.1.31 Forces in Studs Near in the Penetration Region
as a Function of Internal Pressure
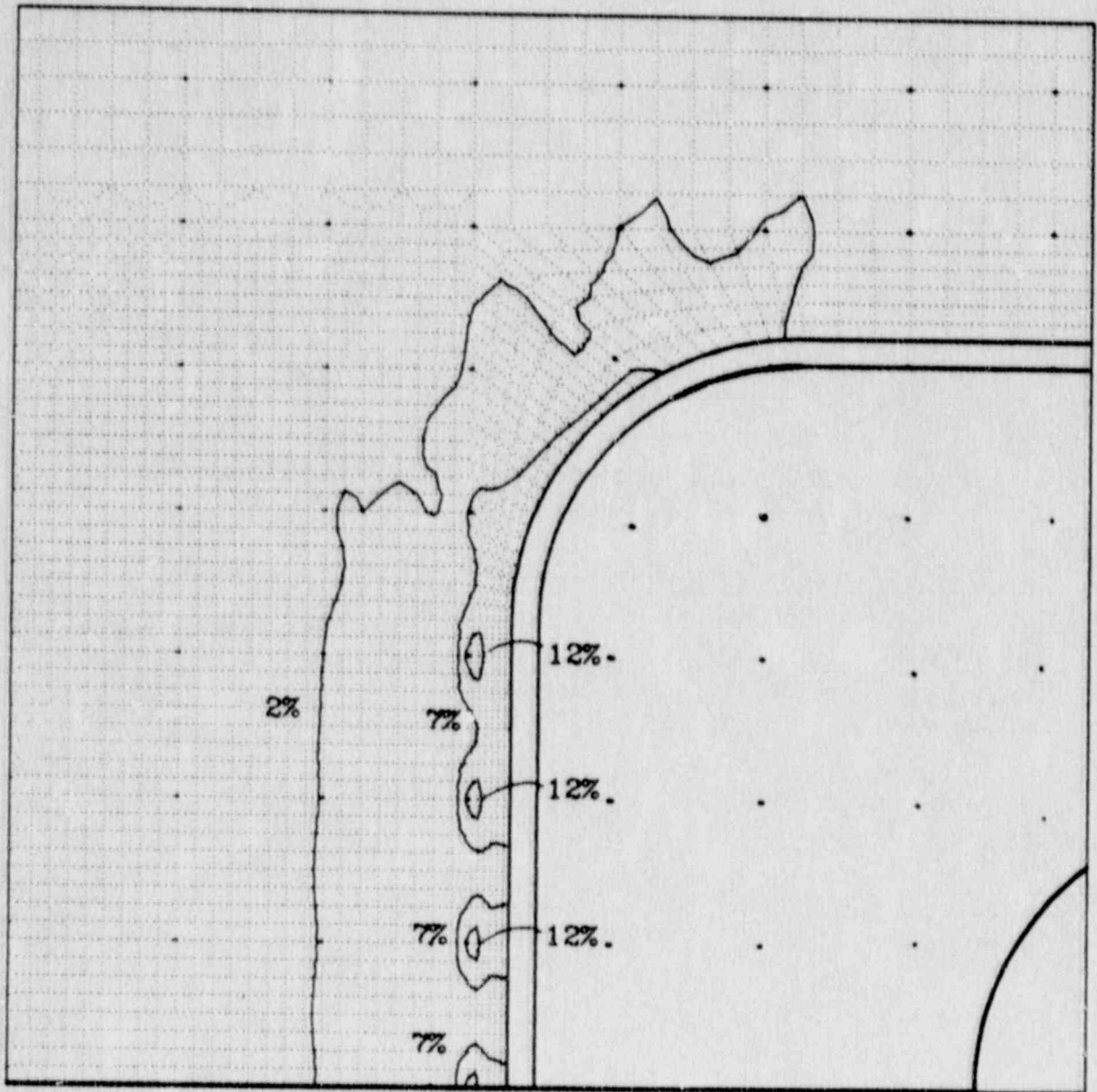
Figure 5.1.32 Equivalent Plastic Strain in the Penetration Region
at 145 psig (1.0 MPa) (Results from Point-Anchorage Analysis)
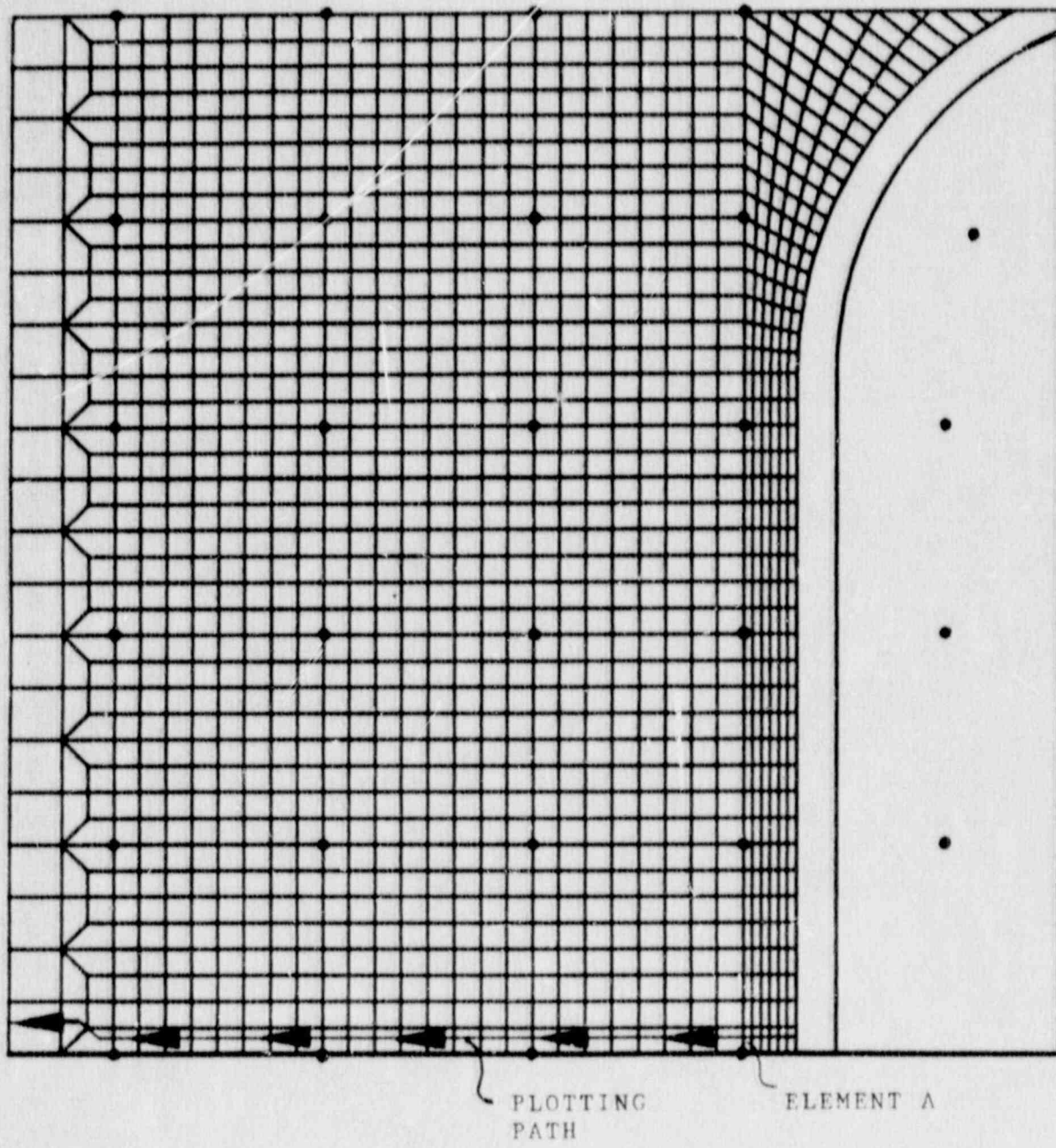
Figure 5.1.33  Definition of Plotting Path for Figure 5.1.34
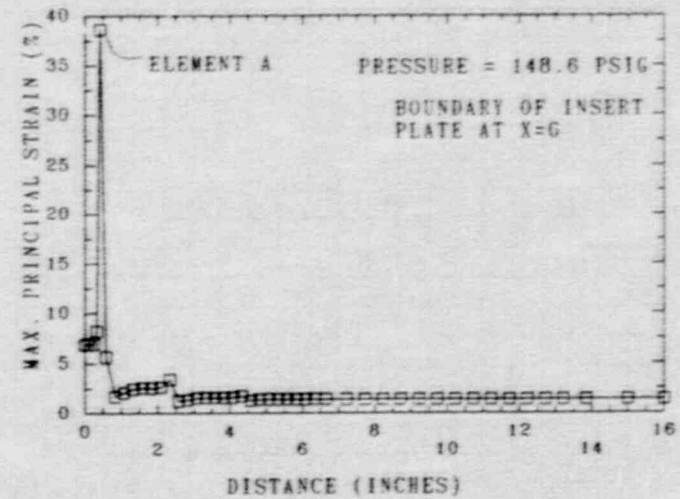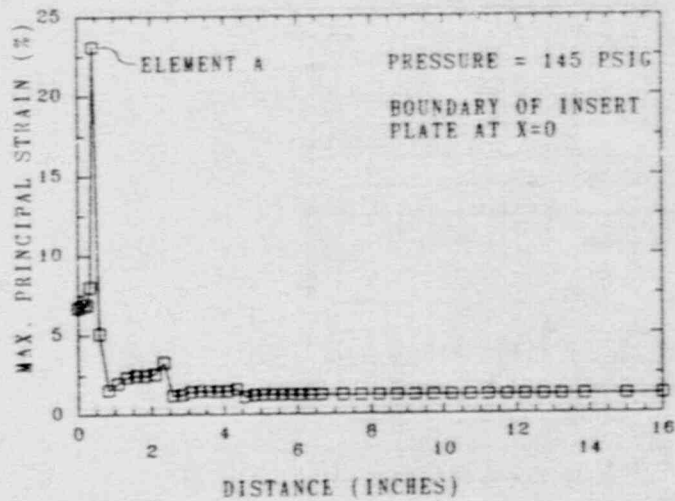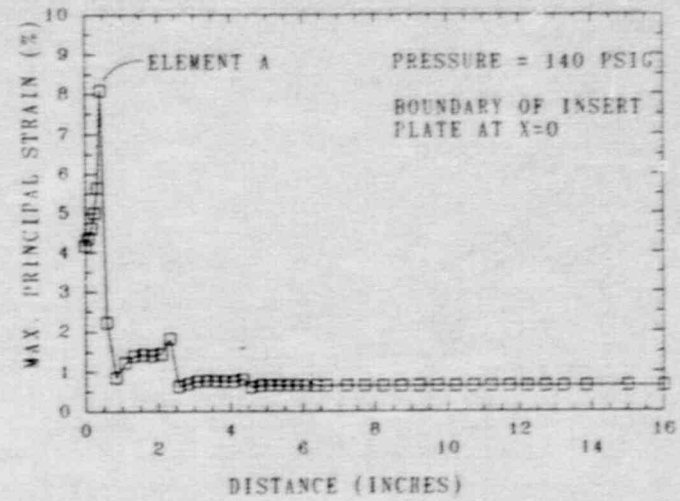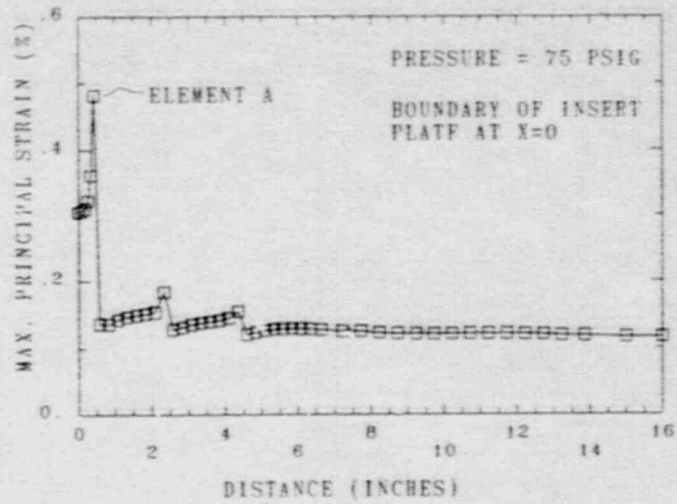
Figure 5.1.34 Maximum Principal Strain as a Function of Position Along the Path Shown in Figure 5.1.33

STRAIN CONCENTRATION FACTOR BASED ON MAXIMUM STRAIN
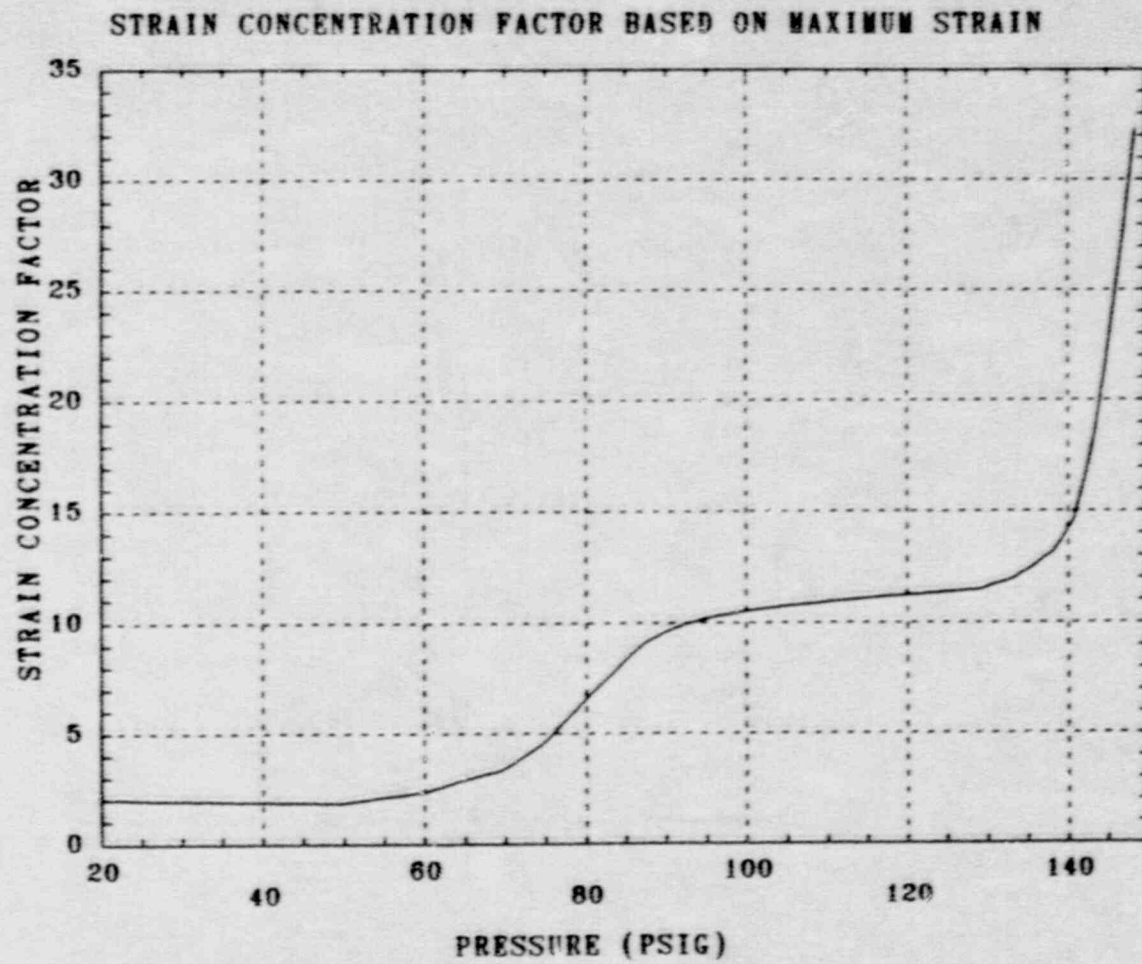
Figure 5.1.35  Strain Concentration Factor for Element A (See Figure 5.1.33) as a Function of Internal Pressure

5-51
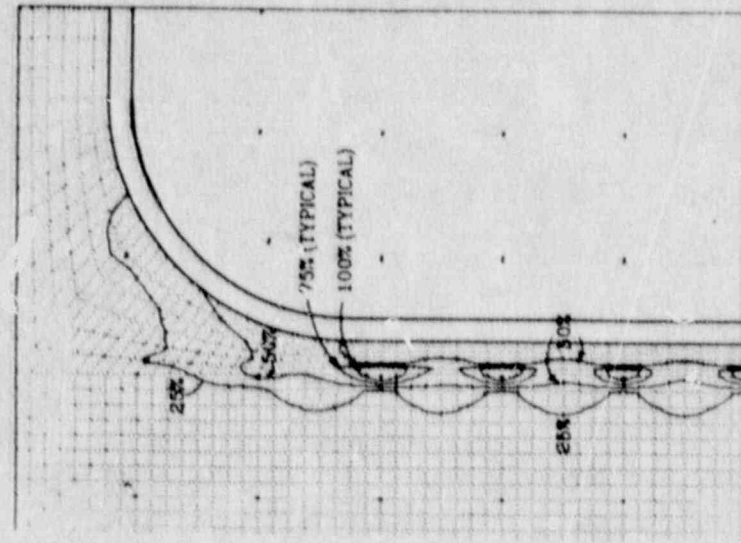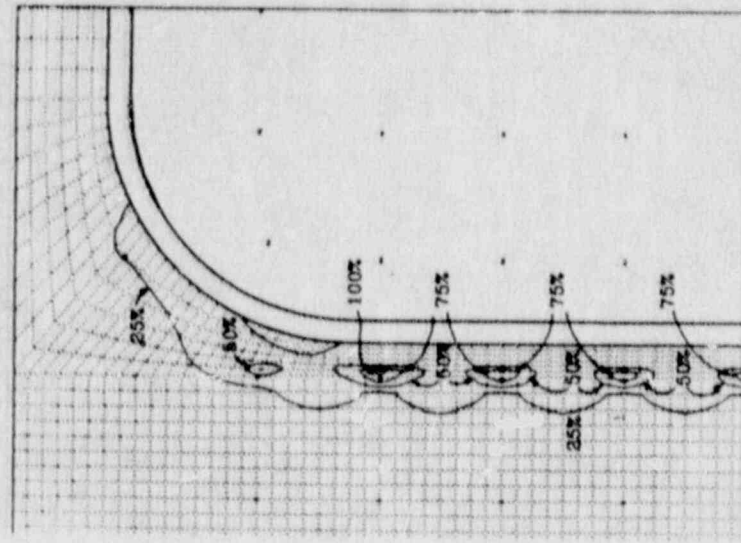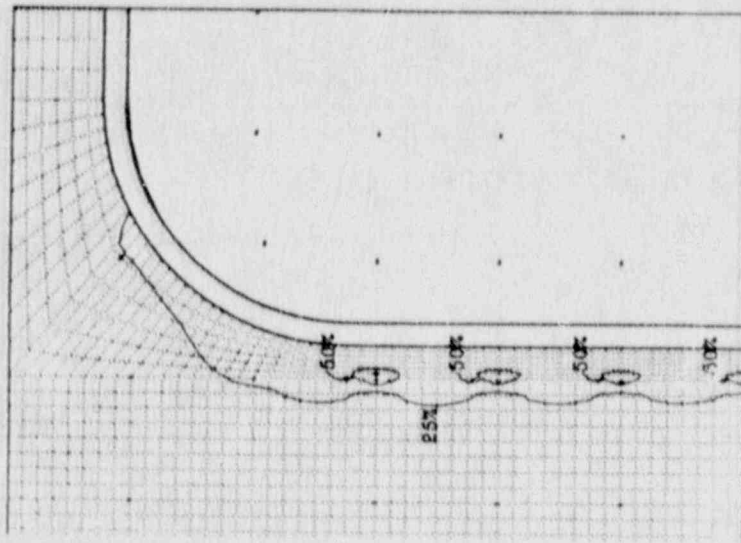
143.5 psig        145.5 psig        147.7 psig

Figure 5.1.36  Ratio of the Equivalent Plastic Strain ($\bar{\varepsilon}_p$) to the Fracture Strain ($\varepsilon_f$) at Three Different Levels of Internal Pressure
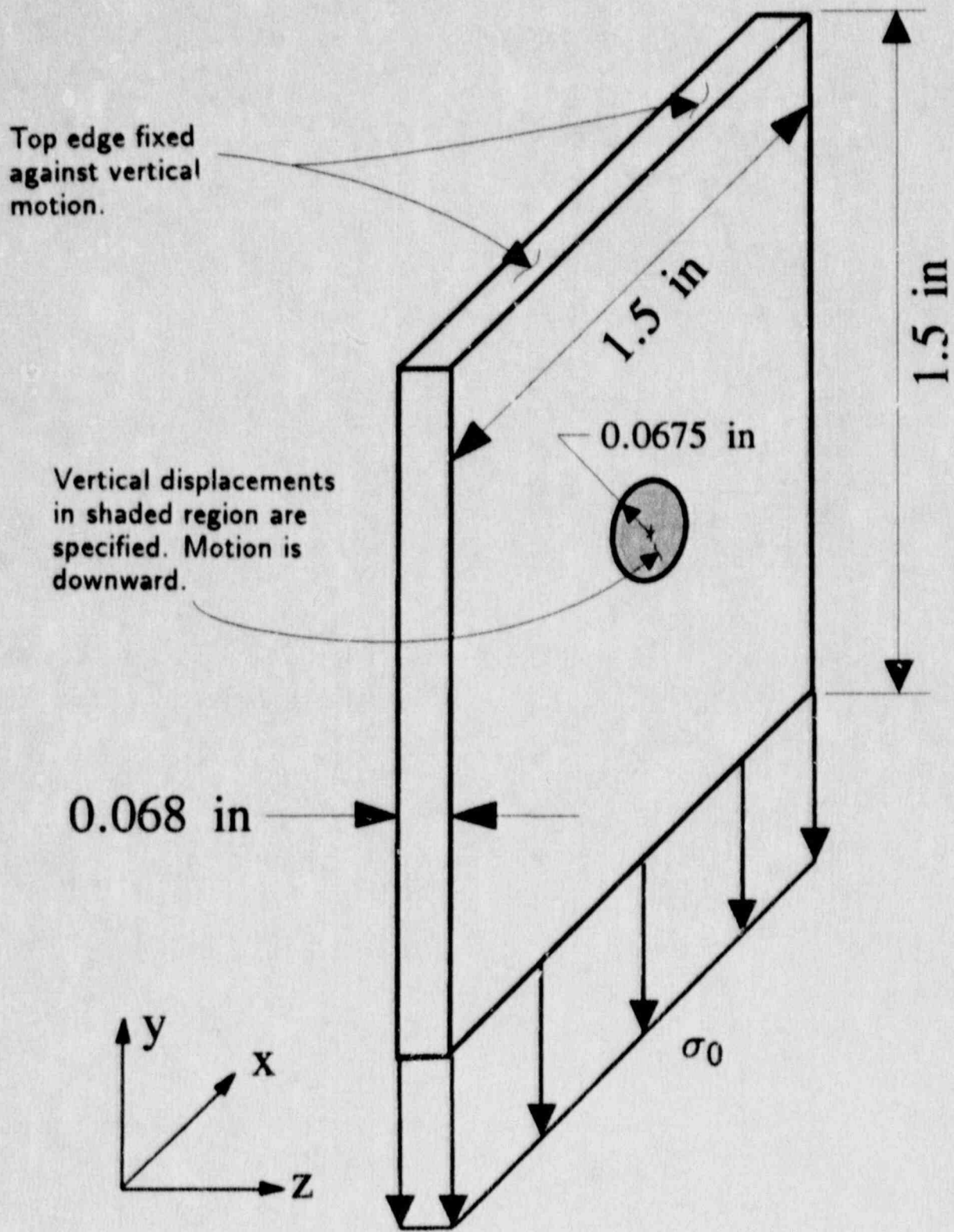
Figure 5.1.37 Model Problem for Studying Strains in the Liner
Near a Stud Loaded in Shear
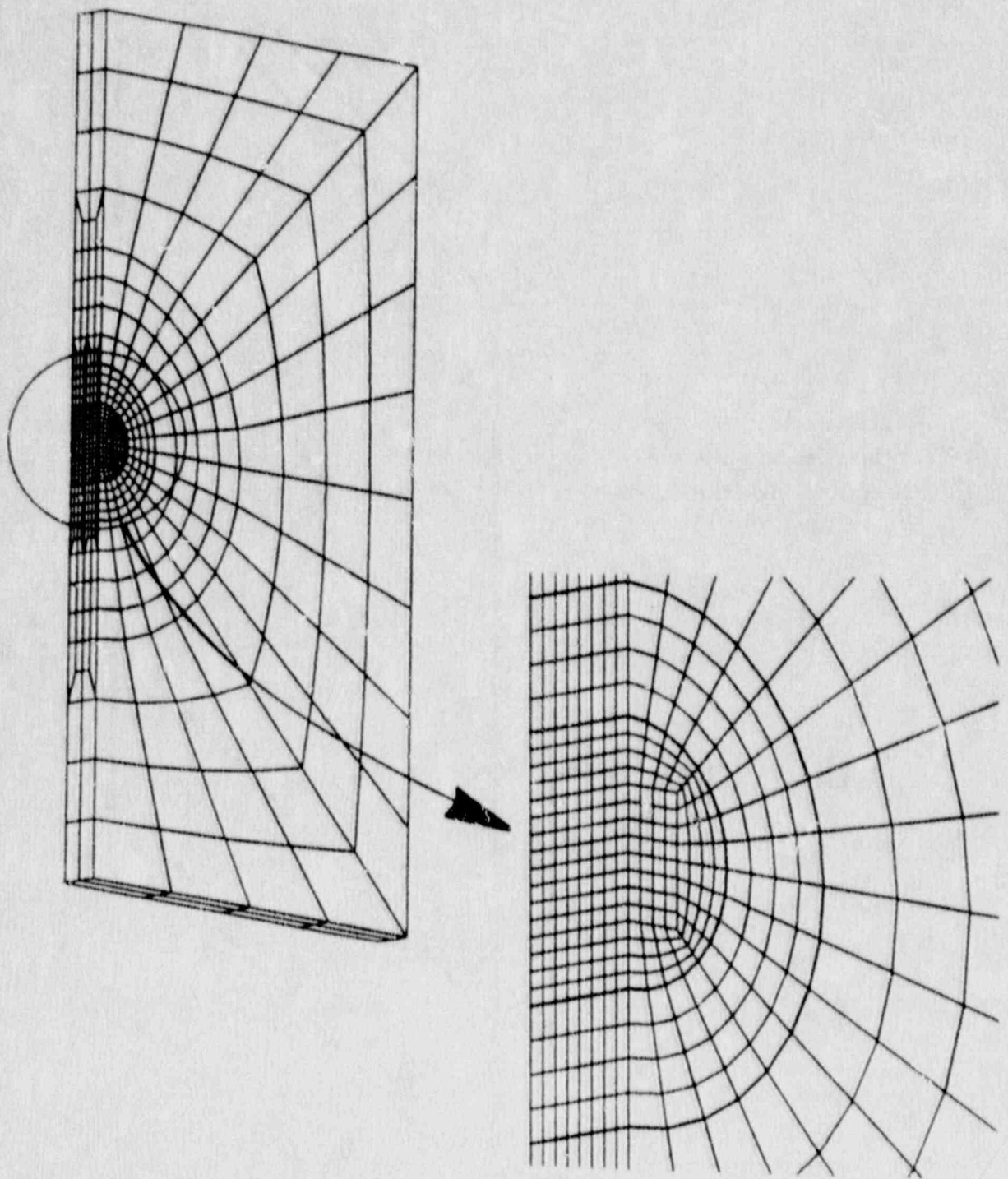
Figure 5.1.38 Three-Dimensional Finite Element Models
Used to Analyze the Stud-Shear Model Problem
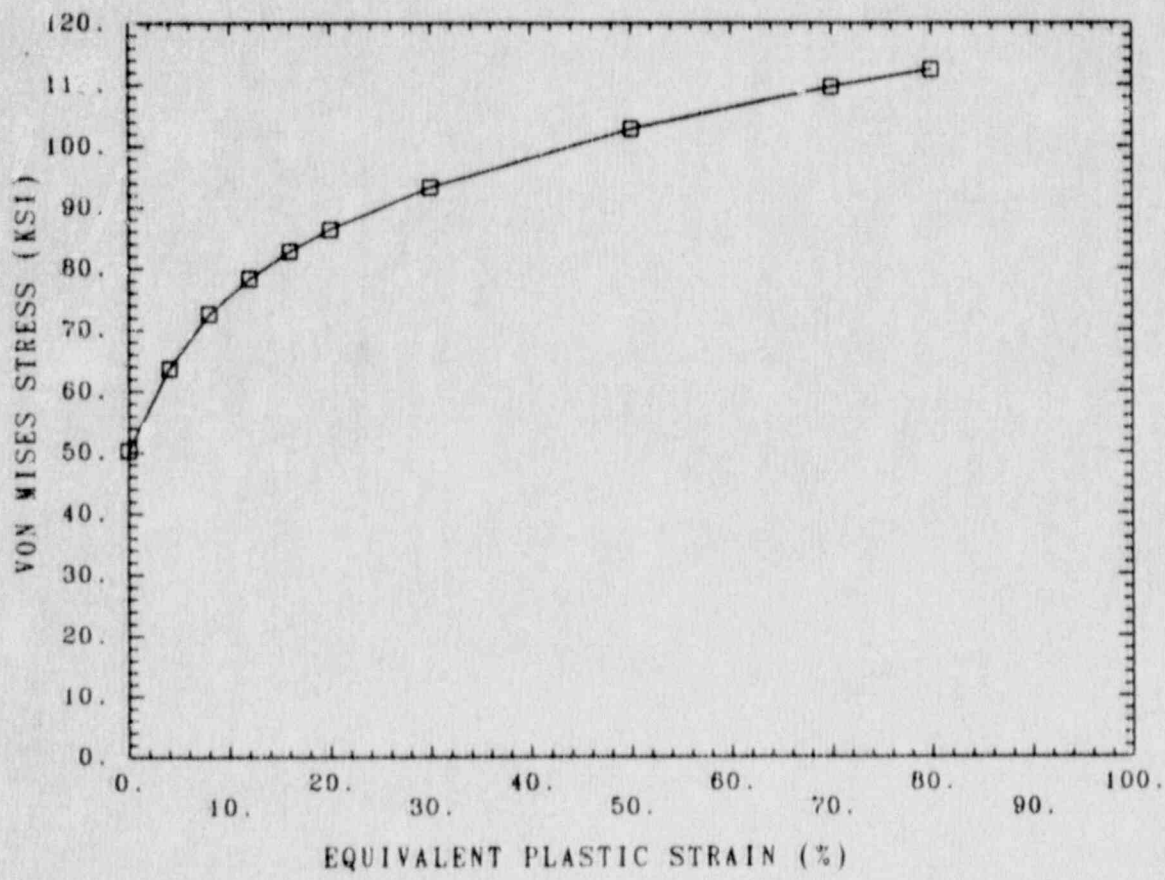
Figure 5.1.39 Effective Stress-Equivalent Plastic Strain Curve
Used for the Liner in the Analysis of the Stud-Shear Model Problem

**STUD DIAMETER**

Stud Force = 985 lb.          Stud Force = 1135 lb.

Stud Force = 1225 lb.          Stud Force = 1530 lb.
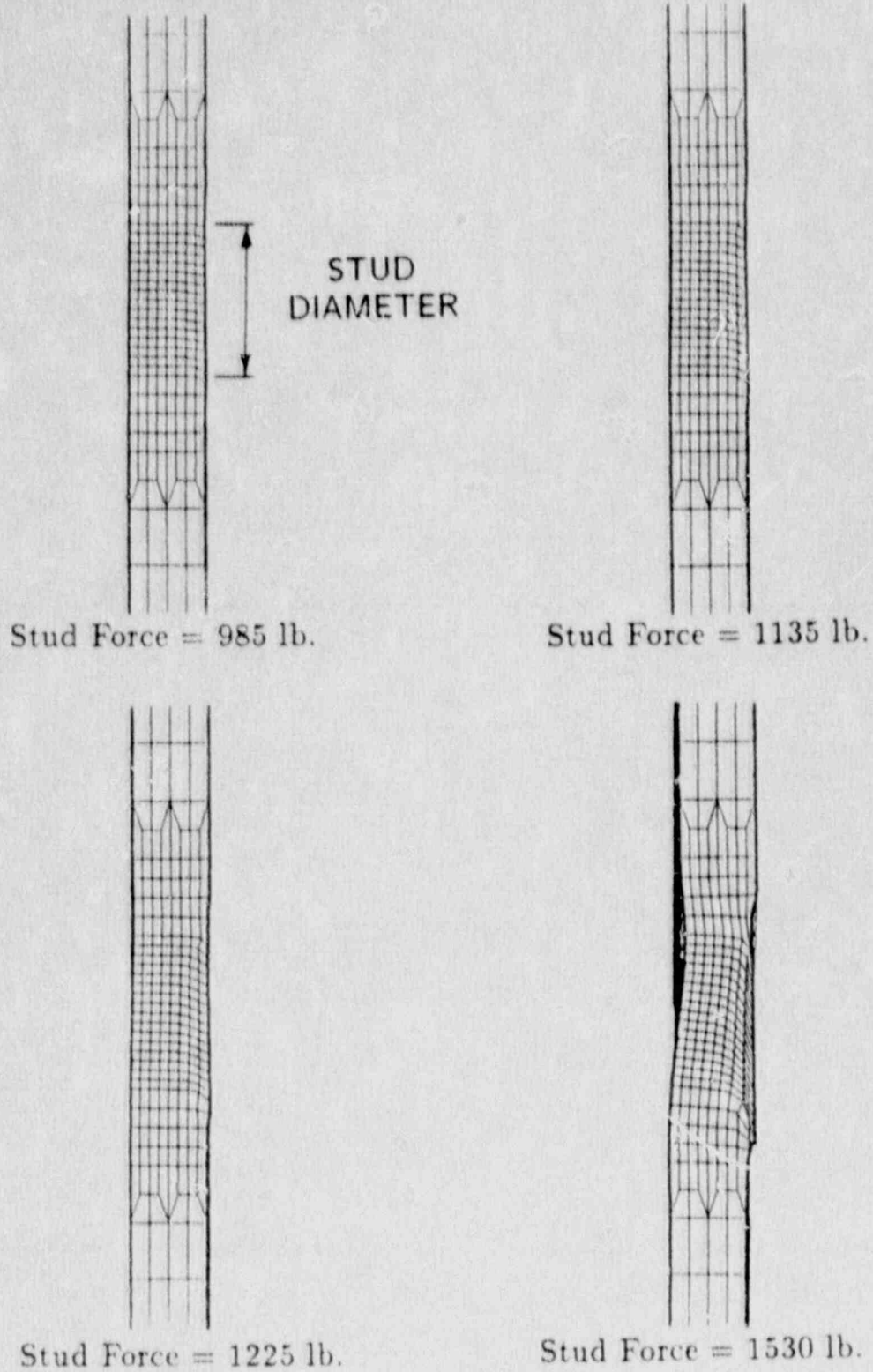
Figure 5.1.40 Side View of Deformed Shape of the Liner
in the Stud-Shear Problem Without Initial Membrane Tension (Analysis 1a)
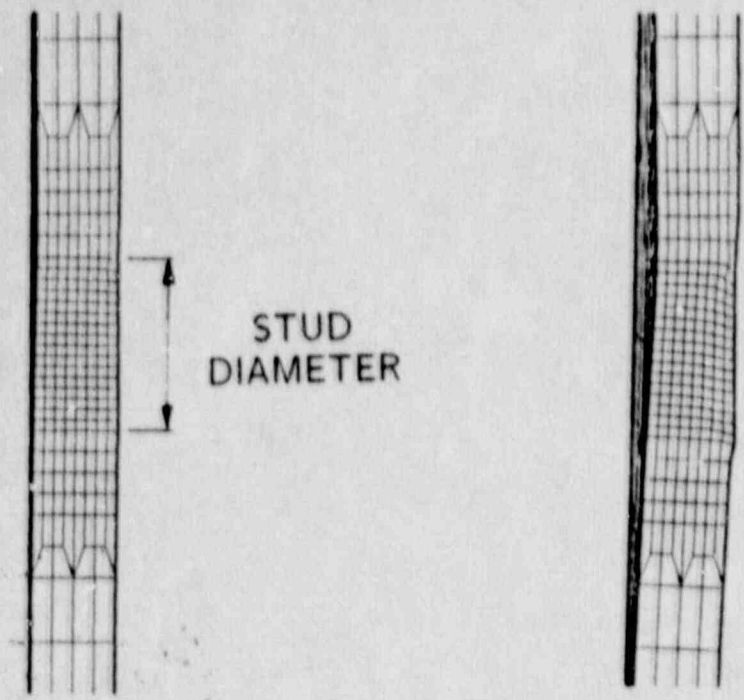
STUD
DIAMETER

Stud Force = 860 lb.                Stud Force = 973 lb.

Stud Force = 1125 lb.               Stud Force = 1230 lb.

Figure 5.1.41  Side View of Deformed Shape of the Liner
in the Stud-Shear Problem With Initial Membrane Tension (Analysis 1b)

Stud Force = 985 lb.
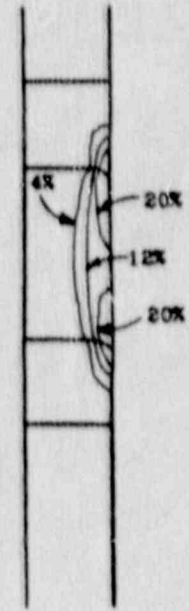
Stud Force = 1135 lb.
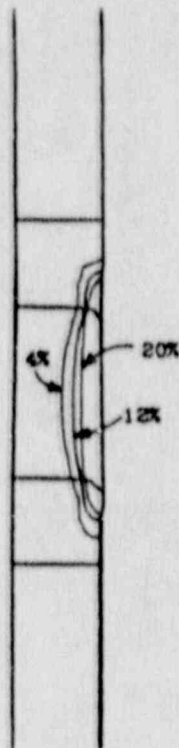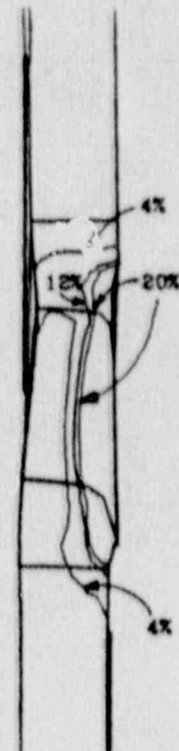
Stud Force = 1225 lb.

Stud Force = 1530 lb.

Figure 5.1.42 Equivalent Plastic Strain in the Liner at Four Different Stud Loads-
Stud Shear Problem Without Initial Membrane Tension (Analysis 1a)
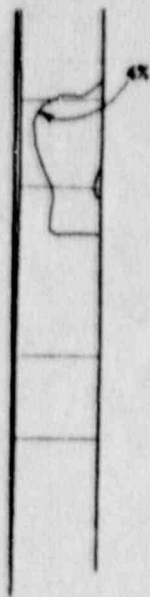
Stud Force = 860 lb.

Stud Force = 973 lb.
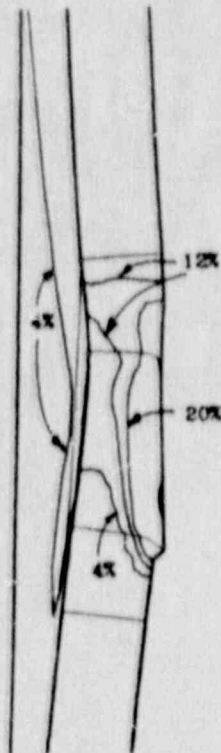
Stud Force = 1125 lb.
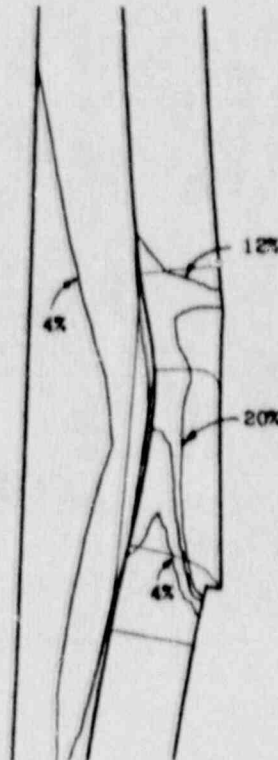
Stud Force = 1230 lb.

Figure 5.1.43 Equivalent Plastic Strain in the Liner at Four Different Stud Loads-
Stud Shear Problem With Initial Membrane Tension (Analysis 1b)
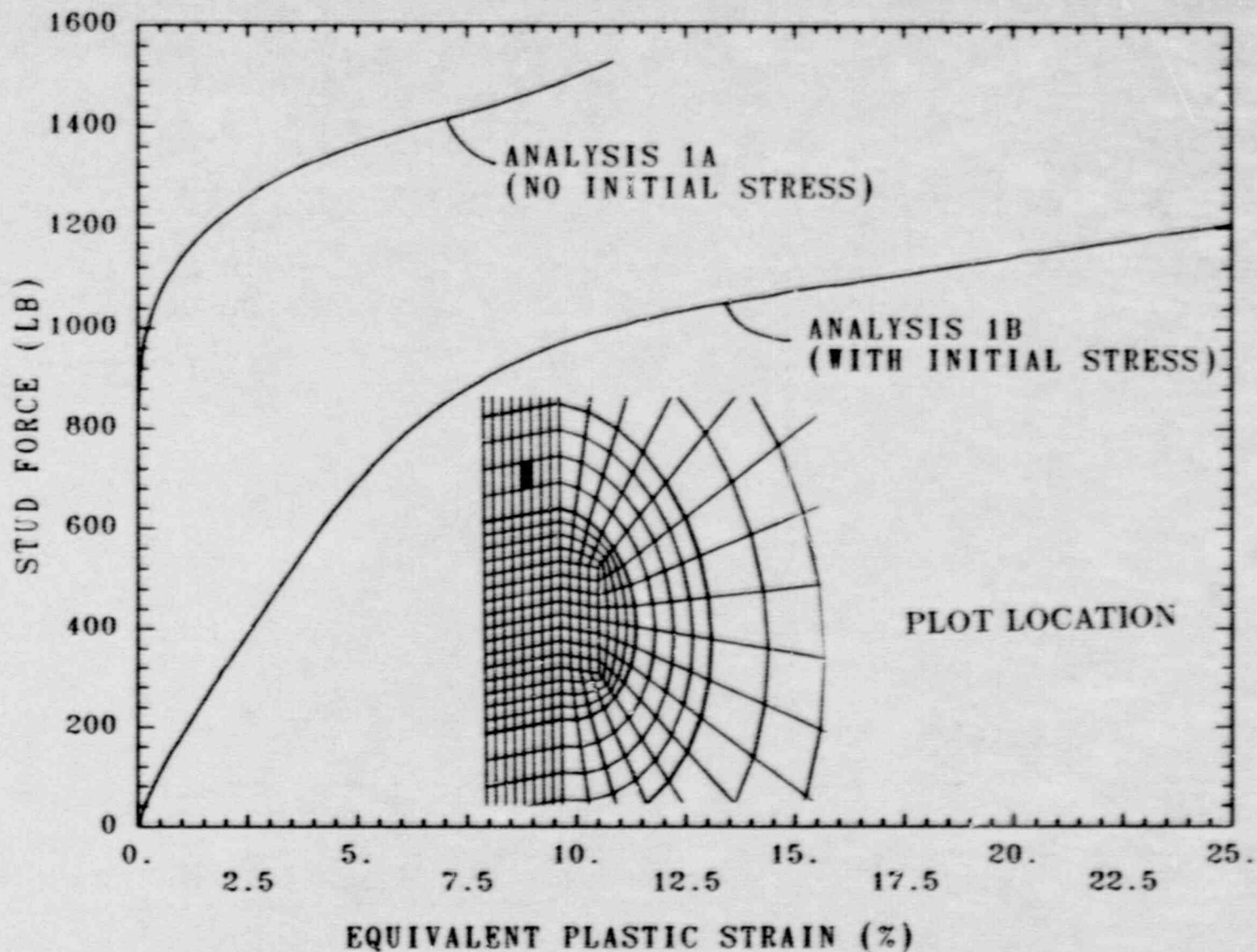
Figure 5.1.44 Stud Force as a Function of the Equivalent Plastic Strain
at the Midthickness of the Liner (Analysis 1a and Analysis 1b)
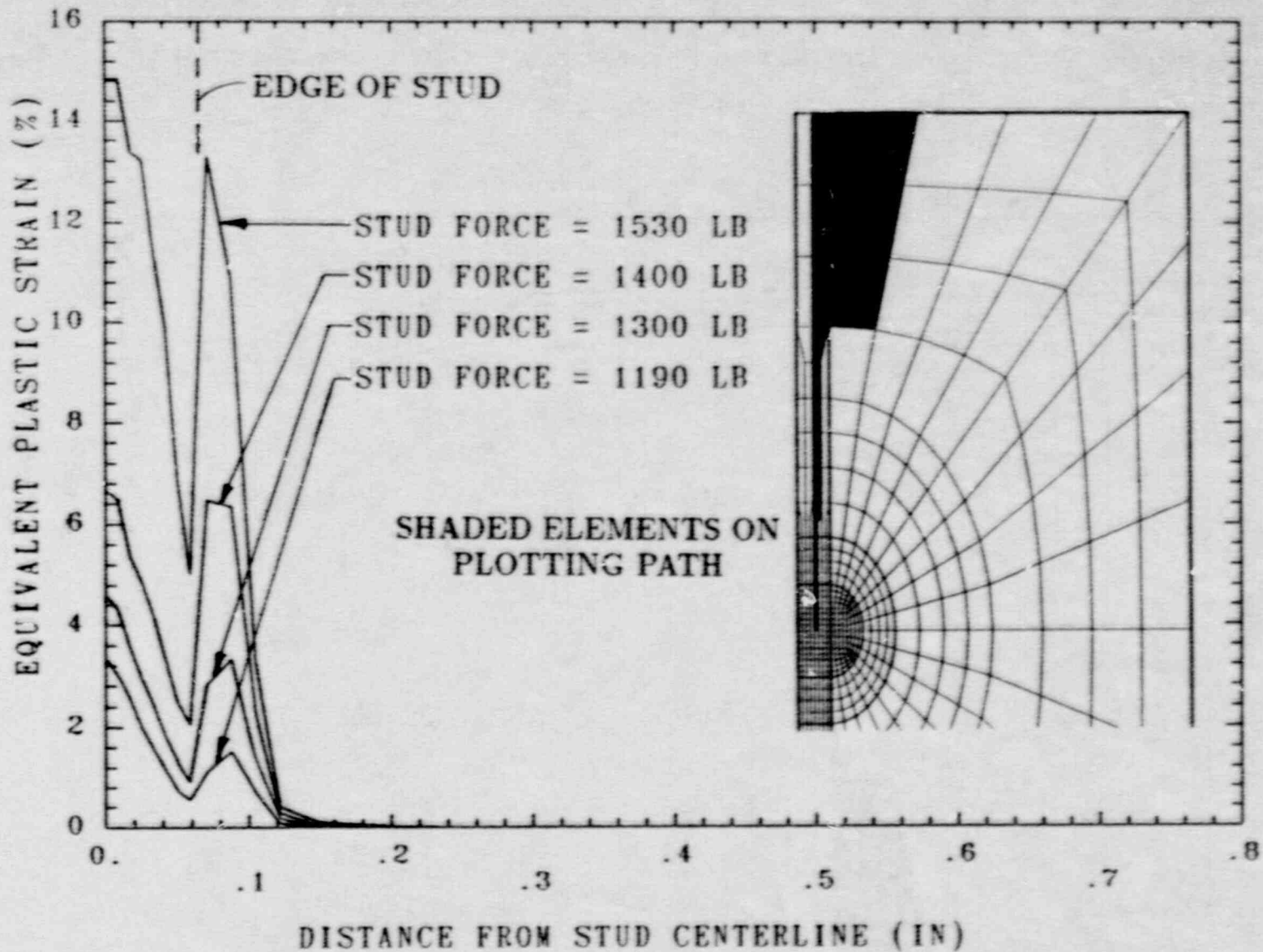
Figure 5.1.45 Equivalent Plastic Strain as a Function of Distance From the Center of the Stud (Analysis 1a)
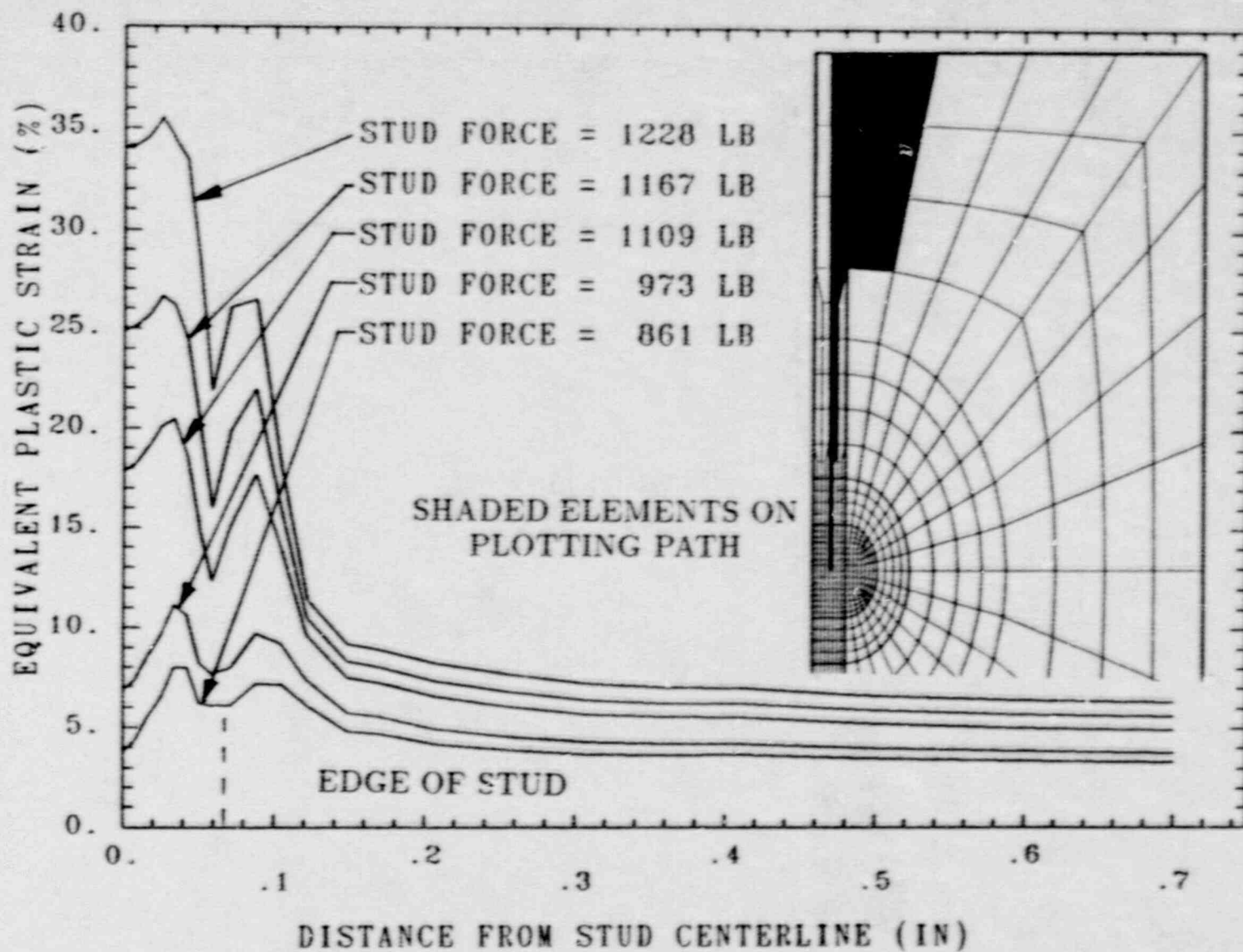
Figure 5.1.46 Equivalent Plastic Strain as a Function of Distance From the Center of the Stud (Analysis 1b)

Vertical displacements of nodes in this circular region are specified. The direction of motion is downward.

$2R$

$R =$ STUD SHANK RADIUS

50.3 ksi
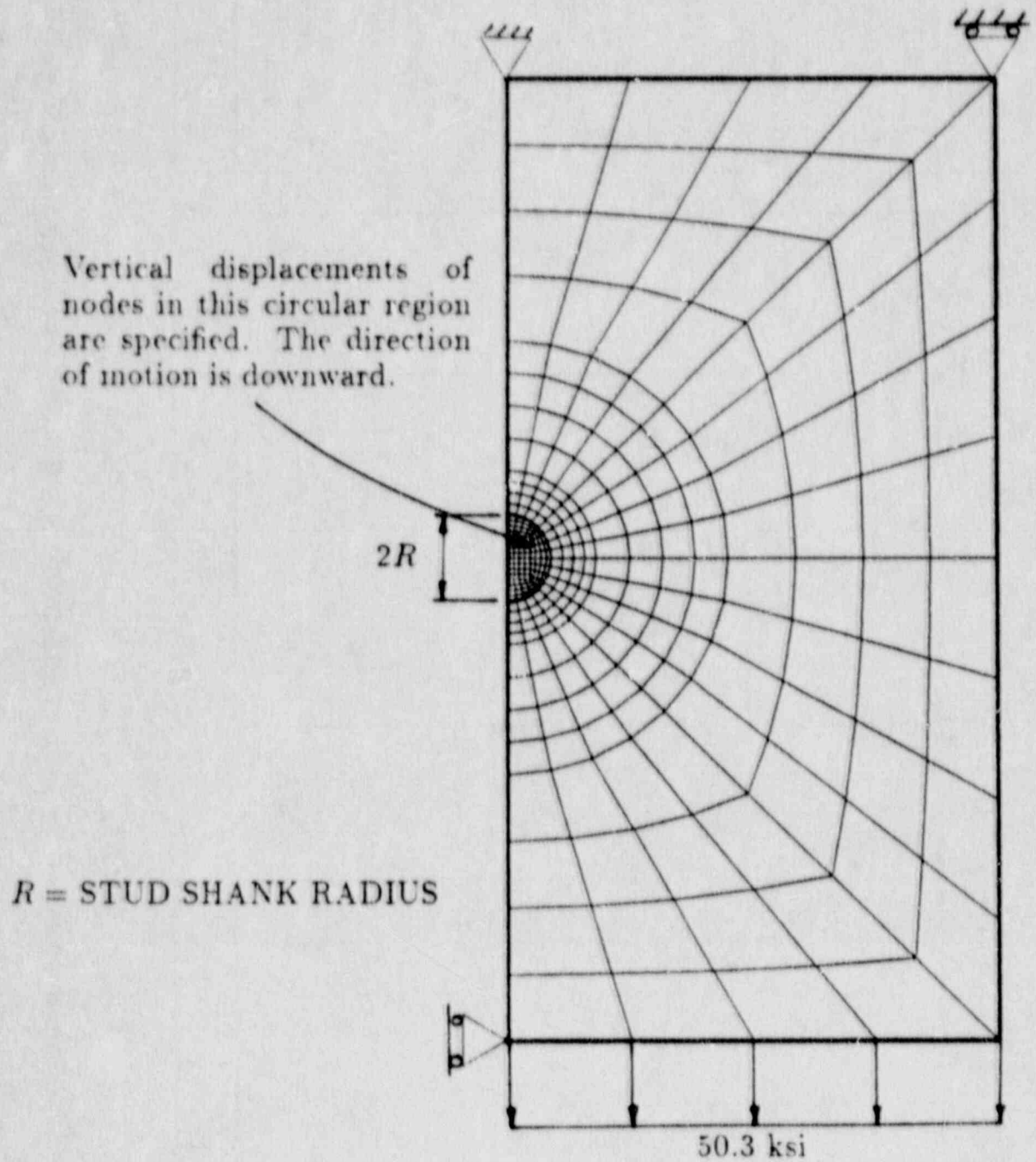
Figure 5.1.47 Two-Dimensional Plane Stress Finite Element Model With Stud Force Distributed Over a Circular Area (Analysis 2)

ANALYSIS 3
$h = 2R$

ANALYSIS 4
$h = R$

ANALYSIS 5
$h = R/2$

DOTTED LINE IS PERIMETER OF STUD SHANK
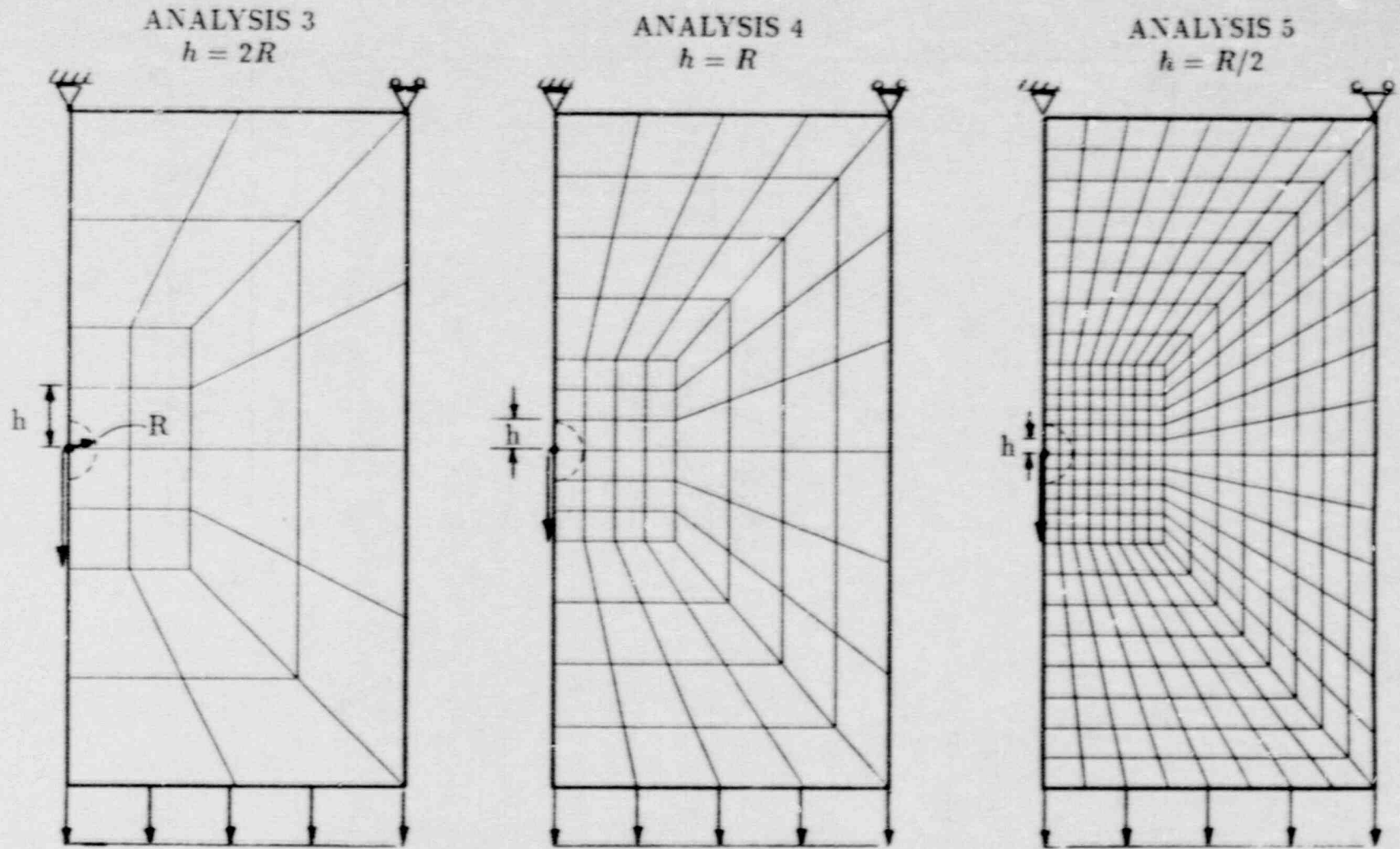
Figure 5.1.48 Two-Dimensional Plane Stress Finite Element Models With Stud Forces Applied at a Single Point (Analyses 3-5)
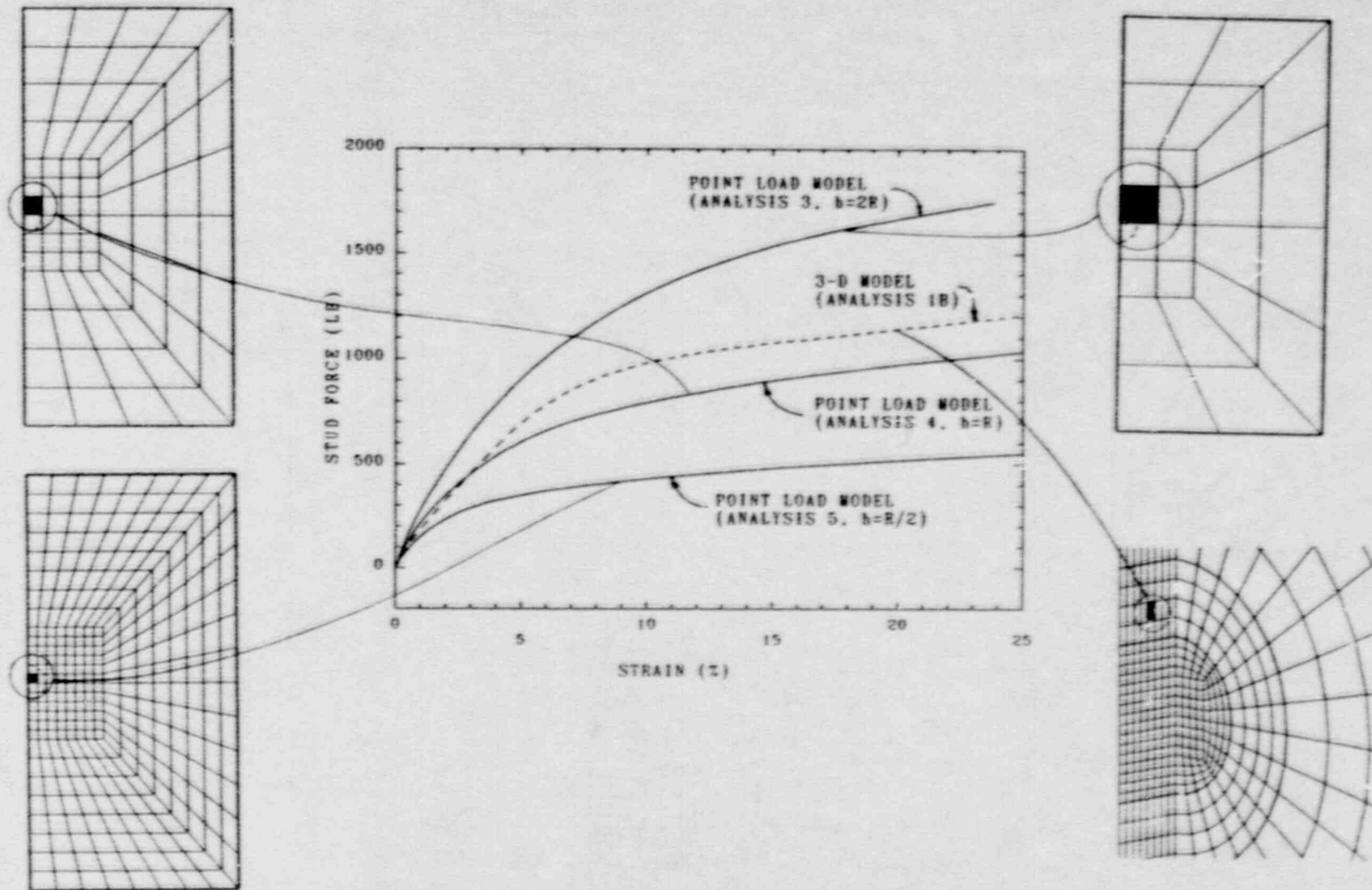
Figure 5.1.49 Stud Force as a Function of the Equivalent Plastic Strain
Near the Edge of the Stud - Comparison of 2-D Point-Load Results and 3-D Results
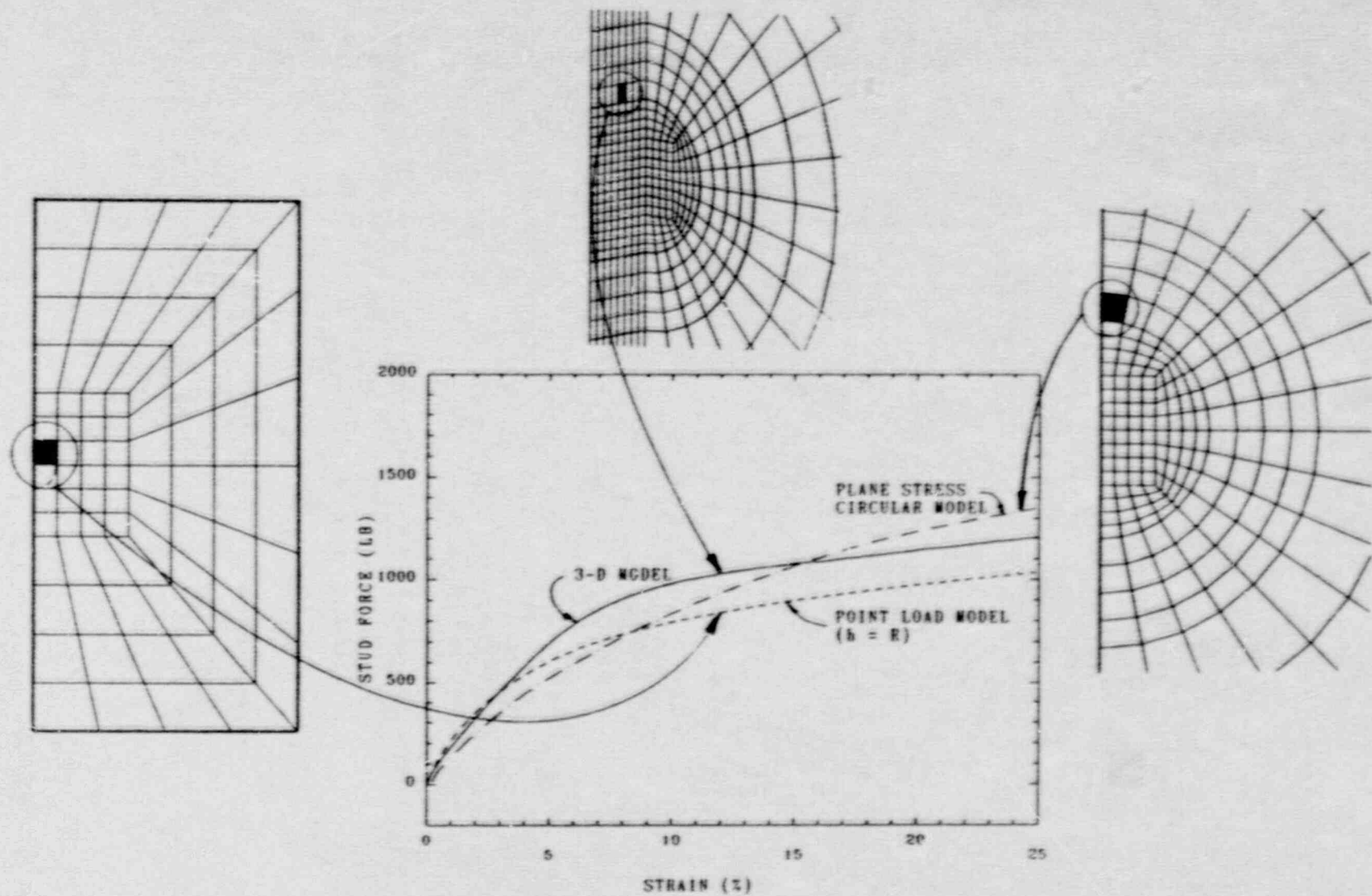
Figure 5.1.50  Stud Force as a Function of the Equivalent Plastic Strain
Near the Edge of the Stud - Comparison of 2-D and 3-D Results
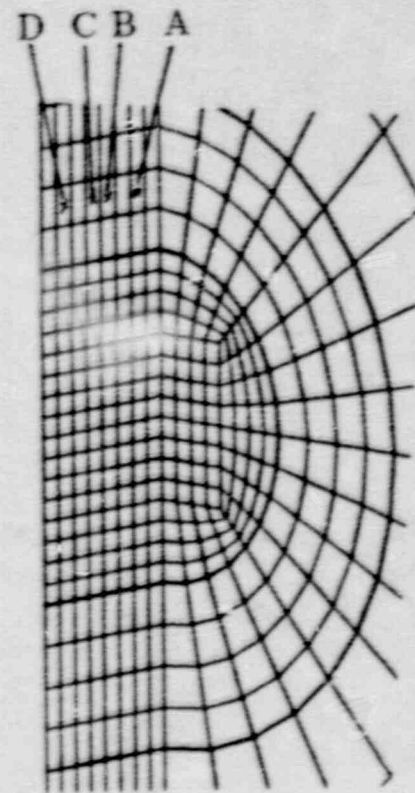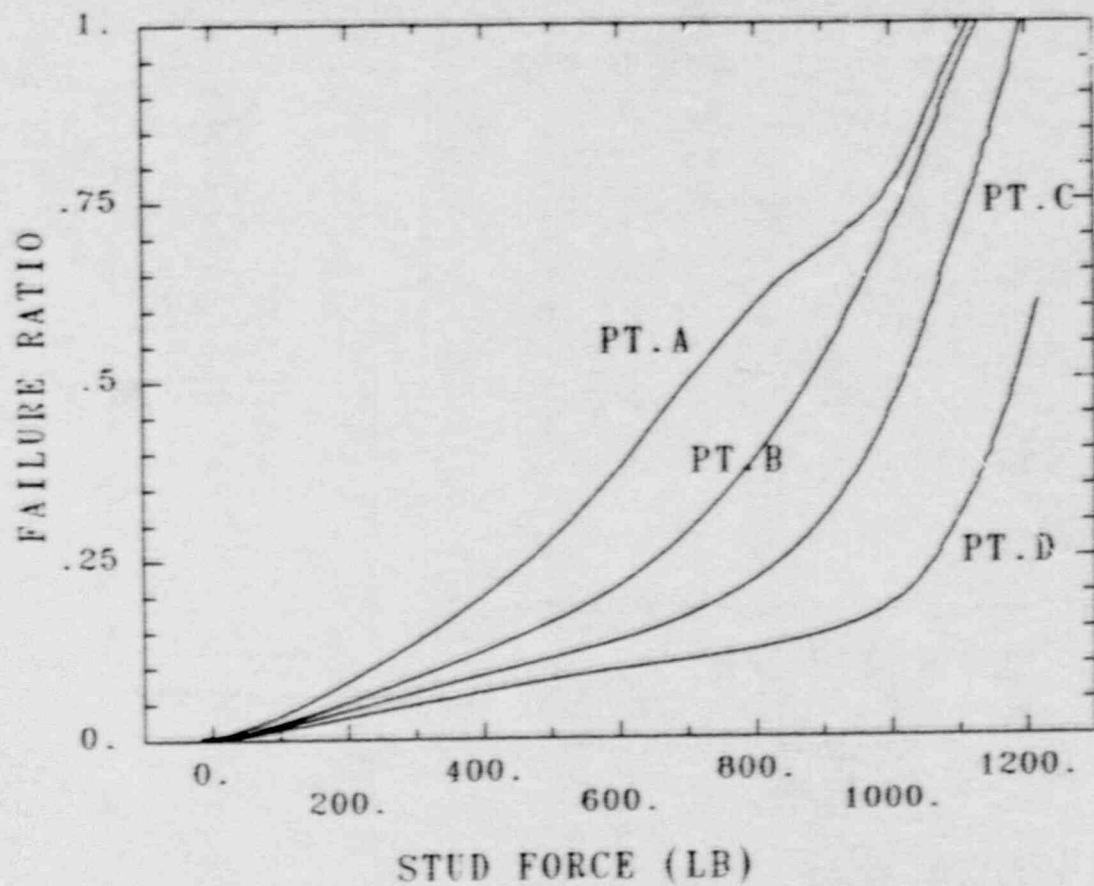
Figure 5.1.51  Failure Ratio ($\bar{\epsilon}_p/\epsilon_f$) as a Function of Stud Force
at Four Locations Through the Thickness of the Liner in the Three-Dimensional Analysis.
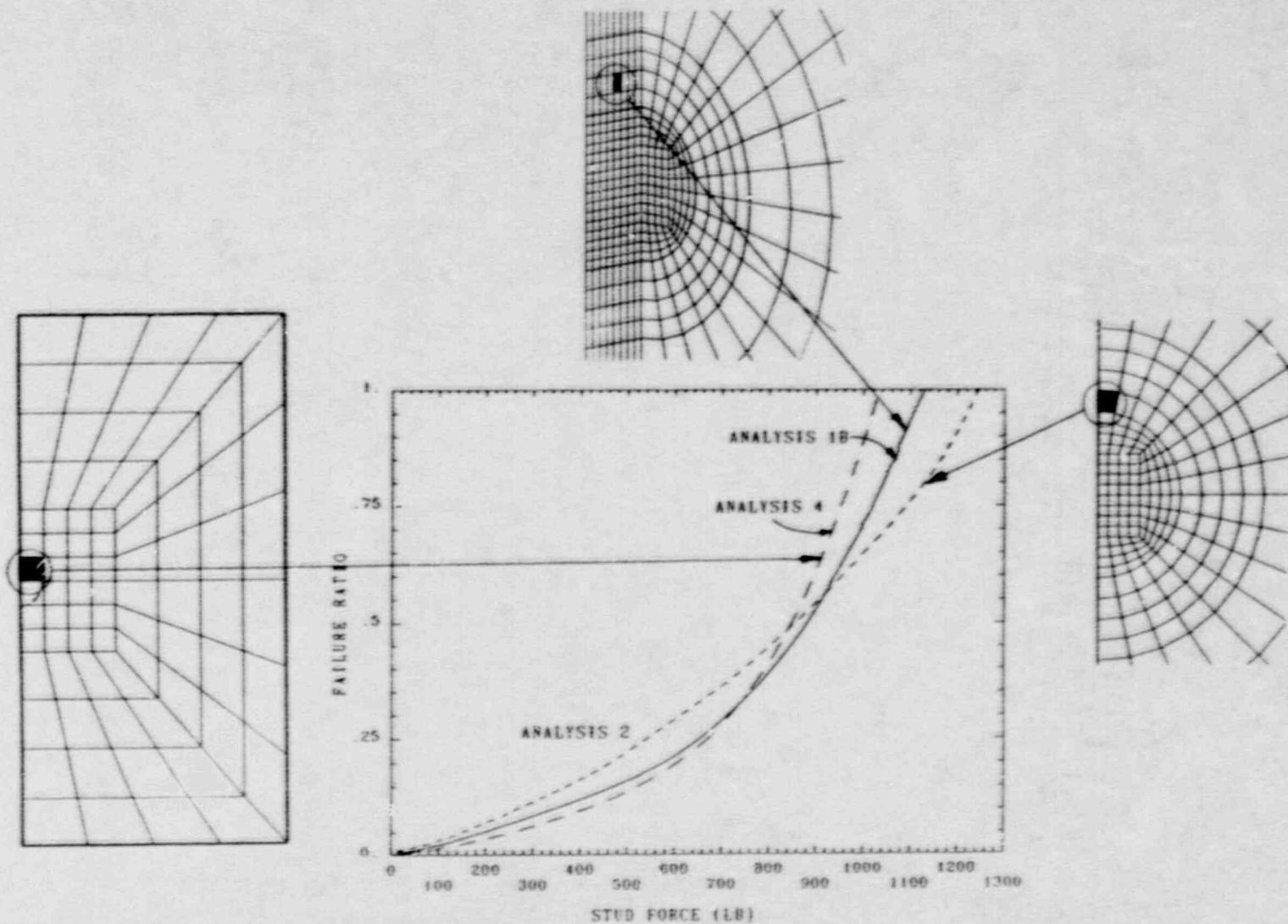
Figure 5.1.52  Failure Ratio ($\bar{\epsilon}_p/\epsilon_f$) in the Two-Dimensional and Three-Dimensional Analyses as a Function of the Stud Force

## 5.2 Argonne National Laboratory

This section was authored by P. A. Pfeiffer and J. M. Kennedy of the Reactor Analysis and Safety Division at Argonne National Laboratory and A. H. Marchertas of the Mechanical Engineering Department at Northern Illinois University.

### 5.2.1 Introduction

A prediction of the response of the Sandia National Laboratories 1:6-scale reinforced concrete containment model test was made by Argonne National Laboratory (ANL). ANL along with nine other organizations performed a detailed nonlinear response analysis of the 1:6-scale model containment, which was subjected to overpressurization in July 1987. The two-dimensional code TEMP-STRESS [15-19] and the three-dimensional NEPTUNE [20-22] code were utilized (1) to predict the global response of the structure, (2) to identify global failure sites and the corresponding failure pressures, and (3) to identify some local failure sites and corresponding pressure levels. A series of axisymmetric models was studied with the two-dimensional computer program TEMP-STRESS. A three-dimensional model of a cylindrical sector, including one penetration, was analyzed with NEPTUNE. The comparison of these pretest computations with test data from the containment model has provided a test for the capability of the respective finite element codes to predict global failure modes, and hence serves as a validation of these codes. Only the two-dimensional analyses will be discussed in this section.

Three axisymmetric models have been analyzed [23] and are displayed in Figures 5.2.1-5.2.3. The first (Figure 5.2.1) is a simplified model which only represents the cylindrical and spherical containment shell and omits the basemat. The basemat is included in the two more complex models (Figures 5.2.2 and 5.2.3). The complex models also include representations of the foundation and sliding interfaces which permit separation and sliding between components of the basemat and the basemat and foundation. The purpose of this third model (Figure 5.2.3) was to investigate the potential for failure of the wall and basemat juncture in detail.

The three two-dimensional models all indicated failure at 180-185 psig (1.24-1.28 MPa). However, the three models predicted three different failure mechanisms: (1) hoop failure of the vessel at midheight following failure of a splice in this area, (2) failure of a weld in the liner near the basemat due to excessive strains, and (3) failure of the liner just above the knuckle due to compression failure of the concrete. In reality, simultaneous failure in more than one mechanism is unlikely since the onset of failure in any one mechanism will reduce the pressure and therefore reduce the stress on other possible sites of failure.

The two-dimensional models all predicted similar sequences of initial damage: meridional cracking commences at the vessel base at 25 psig (0.17 MPa); yielding of the liner begins at the midpoint of the cylinder at 100 psig (0.69 MPa) and propagates up and down; yielding of the hoop reinforcement starts at 120-125 psig (0.83-0.86 MPa). More detail is available in Reference 23.

### 5.2.2 Comparison of Computed Results with Experiments

Low and high pressure tests of the containment were completed in July 1987. The low pressure test was a structural integrity test (SIT), in which the containment was subjected to 53 psig (0.37 MPa). This is 1.15 times the design pressure of 46 psig

(0.32 MPa). No leakage of the structure was observed at 53 psig (0.37 MPa). Crack mapping, displacements, and strains were recorded at various pressures. The purpose of the high pressure test was to determine the ultimate failure pressure. As in the SIT, displacements and strains in the containment were recorded at various pressures.

The experimental results of the high pressure test indicated a maximum internal pressure of 145 psig (1.0 MPa). Failure occurred due to the liner ripping at various locations, which resulted in the release of internal gases through the concrete and decrease in internal pressure. The locations of failure are around equipment hatches and penetration insert plates that are at the midheight of the vessel. This agrees with the results of the analyses, which indicated that the concrete is heavily cracked at these locations; once the liner rips, the pressure will decrease.

The models employed for the analyses all indicated failure at 180 to 185 psig (1.24 to 1.28 MPa). The major reason that the analyses predicted a higher failure pressure than observed was that the axisymmetric models only capture the global response. Details of hatches and insert plates, which cause the stress concentrations, would have to be analyzed through local models. However, the global models do predict the experimental displacement and strain response in the free-field (away from the penetrations) of the vessel quite well.

Displacement and strain gages were distributed throughout the containment and data were obtained during the internal pressurization. A comparison of the uniform response data and the pretest predictions is given in Figures 5.2.5 through 5.2.53. Most of the comparisons are for the first model, shown in Figure 5.2.1, which is titled "R. C. SHELL" in these figures. In cases where this model was inappropriate for a reasonable comparison, the second model, shown in Figure 5.2.2 was used and titled "R. C. SHELL AND BASEMAT". No comparisons are given for the third model, shown in Figure 5.2.3, because it gave essentially the same results as the second model.

Displacement Response

Table 5.2.1 cross-references the figure number with the data channel number, azimuthal angle and elevation of the measuring point. For a reference point, the elevations and azimuthal angles are given in Figure 5.2.4. The radial displacements of the liner are given in Figures 5.2.5 through 5.2.10 for elevations of 6, 11.2, 13, 15.4, 17.9 and 20.1 ft, respectively. Vertical displacements of the liner are given in Figures 5.2.11 through 5.2.16 for elevations of 6, 11, 15 ft, the springline and the dome apex, respectively. Figure 5.2.17 is the basemat uplift. A couple of remarks about the vertical displacement plots should be noted. In Figure 5.2.13 the original experimental data indicated the displacement gage was not zeroed out, so all the data points were adjusted downward by 0.086 in. In Figure 5.2.15, the "R. C. SHELL" (pretest) and "STEEL SHELL" (zero tensile strength concrete) results give the relative displacement between the dome apex and the junction of the basemat and wall (see Figure 5.2.1). Therefore the experimental data in Figure 5.2.15 was adjusted by subtracting the basemat uplift (Channel 169) from the dome apex displacement (Channel 205). No adjustment on the experiment data was needed for Figure 5.2.16, because the "R. C. SHELL AND BASEMAT" models the basemat uplift. In Figure 5.2.17, the original experimental data indicated the displacement gage was not zeroed out, so all the data points were adjusted upward by 0.0338 in.

A very good comparison between the experimental and numerical results is obtained for the radial displacements. The nonlinear response due to plasticity in the rebar and liner is modelled quite well and is evident after 125 psig (0.86 MPa) in the plots. Figures 5.2.5 through 5.2.10 show a distinct jump between 40 and 50 psig (0.28 and 0.34 MPa) in the pretest predictions. This jump is attributed to pronounced hoop crack formation in the concrete throughout the structure's thickness with very little softening, that is, the cracks open up completely and develop fully. (Note: Softening was included in the analysis, see Reference 23 for details). However, the experimental results do not indicate this type of behavior. A reasonable agreement for the vertical displacements is obtained only after the pressure reaches about 125 psig (0.86 MPa), although the numerical results are significantly shifted to the right of the experimental data. This discrepancy probably originates from the same cause as the jump in the numerical results in the radial displacements.

In the vertical response, it was observed numerically that concrete cracking in the meridional (axial) direction occurred for pressures of approximately 40 to 115 psig (0.28 to 0.79 MPa). The experimental data does not support this observation. This lack of observed cracking will be further discussed in Section 5.2.3. The basemat uplift, which was depicted in Figure 5.2.17, indicates that this absence of observed cracking could explain many of the differences in results. However, in spite of those caveats, the overall agreement is sufficiently good for most engineering purposes.

Liner Strains

Table 5.2.2 cross-references the figure number with the data channel number, and azimuthal angle and elevation of the measuring point. Maximum principal strains of the liner are given in Figures 5.2.18 through 5.2.34 for elevations of 4.1, 5.2, 8, 8.9, 9.9, 10.7, 11.6, 13.1, 14.1, 15.5, 16.2, 17, 17.8, 19.2, 20.1, 20.7 and 23.9 ft (springline), respectively. When the maximum principal strain is compared, the direction of the strain cannot be easily depicted in the plots. In most cases the dominant strain is the hoop strain, however some axial strain effects near the springline are present (Figure 5.2.34). The dominance of the hoop strain can be observed from the figures because the strain jumps between 40 and 50 psig (0.28 and 0.34 MPa) just like the radial displacements of the liner. After the strain jump, the experiment and the pretest predictions for the maximum principal strains compare favorably.

In Figures 5.2.19, 5.2.21 and 5.2.25 the pretest results are at approximately the mean of the experimental results. For Figures 5.2.18, 5.2.26, 5.2.27, 5.2.28, 5.2.29, 5.2.30, 5.2.31, 5.2.32, and 5.2.33 the comparison is very good; even the nonlinear response above 125 psig (0.86 MPa) is modelled quite well. The results in Figures 5.2.20, 5.2.22, 5.2.23, 5.2.24, and 5.2.34 did not compare very well. In Figures 5.2.20 and 5.2.34 the pretest results underpredict the experiment response, and in Figures 5.2.22, 5.2.23, and 5.2.24 the pretest results overpredict the experimental response. No reasonable explanation can be given. Overall, the results of the liner strains look good.

Rebar Strains

Table 5.2.3 cross-references the figure number with the data channel number, azimuthal angle and elevation, and rebar layer of the measuring port. The rebar layers are illustrated in Figure 5.2.54. The hoop rebar strains are given in Figures 5.2.35 through 5.2.43, for elevations of 13.4, 4.2, 6.75, 9.5, 12.8, 13.8, 16.25, 19 and 21.4 ft respectively. Figure 5.2.35 is for layer 1 and Figures 5.2.36 through 5.2.43

are for layer 6. The pretest predictions and the experimental hoop rebar strains compare very well. The nonlinear response due to plastic strains in the rebar was successfully modelled. The nonlinear behavior is pronounced after about 125 psig (0.86 MPa). As before in the radial displacement and maximum principal liner strains, there is a jump in strain for the pretest results at 40 through 50 psig (0.28 through 0.34 MPa). This behavior was attributed to the predicted hoop cracking at 40-50 psig (0.28-0.34 MPa).

The meridional rebar strains are given in Figures 5.2.44 through 5.2.53, for elevations of 4, 10.9, 13, 16.7, 20 and 21.6 in layer 2 rebar and for elevations of 7.3, 13.2, 19.1 and 20.1 in layer 5 rebar, respectively. In general, the vertical rebar strains agree only after the pressure reaches about 125 psig (0.86 MPa). Even after this pressure the numerical results are shifted to the right of the experimental data. This trend was also noticed in the vertical displacement response discussed earlier for the pretest results. Discussion of these discrepancies is given in the following section.

### 5.2.3 Precracked Behavior

In general, good agreement was observed between the analytical prediction and the test results regarding the global behavior of the structure. A number of notable discrepancies between the analysis and test data were observed, the most apparent of which was in the vertical displacement, meridional rebar strains and in the uplift of the basemat for the containment.

One possible explanation for the discrepancy is that the test structure was "pre-cracked" before the test. This possibility was pursued by analyzing a shell model (Figure 5.2.1) that completely neglected the tensile strength of the concrete. This model assumed that the tensile strength of the reinforced concrete was solely due to the reinforcement. It was found that this analytical model yielded significantly better agreement with the test data on vertical displacements and strains. The results of the analysis, labeled "STEEL SHELL," are plotted in Figures 5.2.5 through 5.2.53.

The main observations of the "STEEL SHELL" results when compared to the pretest results and the experimental data are the following:

1. In the radial displacements (Figures 5.2.5 through 5.2.10) the displacement jump between 40 and 50 psig (0.28 and 0.34 MPa) is absent for the "STEEL SHELL" analysis. This is because the concrete is modelled as pre-cracked. In the higher pressure analysis (125 psig (0.86 MPa) and up) of the "STEEL SHELL" the results are shifted to the left of the pretest analysis. Thus, the "STEEL SHELL" analysis provides a better comparison with the experimental data.

2. In the vertical displacements (Figures 5.2.11 through 5.2.15) the "STEEL SHELL" results are shifted up for the whole pressure range and shifted to the left for the higher pressure (125 psig (0.86 MPa) and up) when compared to the pretest results. Also, the "STEEL SHELL" analysis compares very well with the experimental data, whereas the pretest analysis did not.

3. In the liner strains (Figures 5.2.18 through 5.2.34) the strain jump between 40 and 50 psig (0.28 and 0.34 MPa) is absent for the "STEEL SHELL" analysis. The higher pressure results are shifted to the left of the

pretest result. Other than the strain jump, the "STEEL SHELL" analysis compares as well as the pretest analysis against the experimental data.

4. In the hoop rebar strains (Figures 5.2.35 through 5.2.43) the strain jump between 40 and 50 psig (0.28 and 0.34 MPa) is absent for the "STEEL SHELL" analysis. The higher pressure results are shifted to the left of the pretest results. Other than the strain jump, the "STEEL SHELL" analysis compares as well as the pretest analysis against the experimental data.

5. In the meridional rebar strains (Figures 5.2.44 through 5.2.53) the "STEEL SHELL" results, in general, are shifted up for the whole pressure range and shifted to the left for the higher pressures (125 psig (0.86 MPa) and up) when compared to the pretest results. Also, the "STEEL SHELL" analysis generally compares very well with the experimental data, whereas the pretest analysis did not.

It was believed initially that prooftesting (structural integrity test) of the containment model to 53 psig (0.37 MPa) pressure was responsible for cracking of concrete or the loss of tensile strength. It was noted, however, that the vertical displacement discrepancy in that test was of the same magnitude. Thus, the loss of tensile strength of the model could not be attributed to the prooftesting (SIT) phase.

Because of the excellent agreement of the "STEEL SHELL" model results with the experiment, an explanation was sought for the low tensile strength of the concrete before the tests. Several reasons were suggested, namely:

a) Shrinkage cracking, which takes place during the curing process of the concrete.

b) Cracking during the diurnal thermal cycling as well as seasonal temperature changes.

In order to investigate the cracking possibility of the concrete structure due to diurnal temperature fluctuations, a shell model (Figure 5.2.1) for a thermomechanical analysis was set up. A sinusoidal temperature variation was imposed on the outside wall of the model with an assumed amplitude of 20°F for a 24 hour cycle. The inside temperature of the containment (liner) was initially at 70°F and allowed to change with transient thermal analysis. In the heat conduction analysis only the concrete was modeled. The thermal properties are given in Table 5.2.4. The coefficient of thermal expansion for both the steel and concrete were assumed to be $1.0 \times 10^{-5}$ in/in/°F ($5.6 \times 10^{-6}$ m/m/°C). The resulting damage (hoop and meridional cracking) due to the outside temperature varying from a high of 90°F (32°C) to a low of 50°F (10°C) on the outside (see Figure 5.2.55 for thermal loading) results in the damaged areas (shaded) in Figure 5.2.56. In general the concrete is cracked (hoop and meridional) 2/5 of the thickness from the outside surface in the cylinder and cracked 1/5 of the thickness from the outside surface in the dome. Although the structure is not completely damaged from this one day hypothetical thermal cycle, there is no doubt that actual daily temperature fluctuations and seasonal changes will cause the structure to be somewhat precracked or damaged. This precracking will also enhance shrinkage cracking, by providing pathways for the moisture in the concrete to escape. We believe that the temperature effect and shrinkage are mainly responsible for the concrete being in a precracked state.

Other reasons for the containment exhibiting a precracked state might be due to differential thermal expansion between the reinforcing steel and the concrete; and/or poor (no) bonding of rebar with the concrete. These areas should also be examined but were not evaluated here.

### 5.2.4 Summary

The reason that the vertical displacements and meridional strains of the pretest predictions and the experimental data did not compare well was due to the actual structure being softer or less stiff. Even the SIT test (in which the structure was not cracked beforehand) exhibited the same trend. This indicates that the concrete was precracked or the concrete and reinforcement bond was very low or even nonexistent. As a check, the two-dimensional model was re-run with zero tension concrete, with only the steel liner and rebar having tension strength capacity. The liner displacements and strains and rebar strains of this altered model check very well with the experimental results.

As for the failure of the containment, the pretest global analysis performed would have to be used as input for localized models in order to predict the failure pressure of 145 psig (1.0 MPa). There seem to be no obvious remedies for the shortcomings of global analysis of reinforced concrete structures. In light of the liner failure, which limits the maximum pressure of the vessel, analytical effort should shift somewhat to focus on the local failures. The prediction of local failure of the vessel is not so much restricted by the limitation of the present analytical capabilities but rather the knowledge of local physical constraints. It appears that if the anchorage of the liner to the concrete vessel were well defined, and the physical parameters known, the present day analytical methods (would be able) are adequate to predict the range of liner failure. Much more experimental data on the specific types of anchorages would need to be available to the analyst for the failure prediction.

The situation would seem more hopeful if the types of anchorages could be standardized - limiting the number of experimental data to be generated. With the limited number of anchorage types, experimental data could be generated for needed input to the analytical computational programs. With such information available, rather simple computational methods could be utilized for the prediction of liner failure.

In general, a very good comparison between the experimental and pretest predictions was obtained for much of the global behavior of the structure. Strain and displacement responses where major discrepancies existed between the analysis and observed test data could be explained by precracking.

### 5.2.5 Acknowledgements

Table 5.2.1 Displacement Locations of Liner

| Figure | Data Channel | Azimuthal Angle (Deg.) | Elevation (ft) | Measurement |
|---|---|---|---|---|
| 5.2.5 | 215 | 228.37 | 5.98 | Radial |
| 5.2.6 | 218 | 228.57 | 11.21 | Radial |
| 5.2.7 | 206 | 134.10 | 13.00 | Radial |
| 5.2.7 | 219 | 228.57 | 13.00 | Radial |
| 5.2.7 | 228 | 315.01 | 13.00 | Radial |
| 5.2.8 | 220 | 228.48 | 15.41 | Radial |
| 5.2.9 | 221 | 228.27 | 17.93 | Radial |
| 5.2.10 | 222 | 227.85 | 20.07 | Radial |
| 5.2.10 | 225 | 289.43 | 20.09 | Radial |
| 5.2.11 | 214 | 225.20 | 5.97 | Vertical |
| 5.2.12 | 217 | 227.62 | 10.98 | Vertical |
| 5.2.13 | 223 | 222.97 | 17.97 | Vertical |
| 5.2.14 | 224 | 225.95 | 23.93 | Vertical |
| 5.2.15 | 205 | -- | 35.00 | Dome Apex |
| | minus | | | minus |
| | 169 | 83.72 | 2.00 | Basement Uplift |
| 5.2.16 | 205 | -- | 35.00 | Vertical for Dome Apex |
| 5.2.17 | 169 | 83.72 | 2.00 | Basement Uplift |

Table 5.2.2 Liner Maximum Principal Strain Locations

| Figure | Data Channel | Azimuthal Angle (Deg.) | Elevation (ft) |
|--------|--------------|------------------------|----------------|
| 5.2.18 | 1323 | 44.18 | 4.10 |
| 5.2.19 | 1326 | 45.03 | 5.49 |
| 5.2.19 | 1480 | 315.00 | 5.18 |
| 5.2.19 | 1429 | 228.33 | 5.30 |
| 5.2.20 | 1442 | 228.47 | 7.69 |
| 5.2.20 | 1483 | 314.92 | 8.31 |
| 5.2.21 | 1341 | 44.95 | 8.84 |
| 5.2.21 | 1422 | 221.85 | 8.93 |
| 5.2.21 | 1445 | 228.30 | 8.88 |
| 5.2.22 | 1344 | 45.08 | 9.83 |
| 5.2.22 | 1448 | 228.60 | 10.02 |
| 5.2.23 | 1347 | 44.30 | 10.68 |
| 5.2.24 | 1527 | 44.90 | 11.63 |
| 5.2.25 | 1540 | 45.07 | 13.37 |
| 5.2.25 | 1606 | 133.65 | 12.93 |
| 5.2.25 | 1685 | 228.37 | 13.08 |
| 5.2.25 | 1729 | 314.88 | 13.02 |
| 5.2.26 | 1543 | 45.1 | 14.12 |
| 5.2.27 | 1688 | 228.37 | 15.46 |
| 5.2.28 | 1546 | 45.52 | 16.20 |
| 5.2.29 | 1701 | 228.36 | 16.98 |
| 5.2.30 | 1549 | 45.88 | 17.82 |
| 5.2.31 | 1562 | 46.32 | 19.15 |
| 5.2.32 | 1802 | 112.67 | 20.07 |
| 5.2.32 | 1867 | 292.05 | 20.13 |
| 5.2.33 | 1748 | 44.47 | 20.75 |
| 5.2.33 | 1826 | 224.65 | 20.71 |
| 5.2.34 | 1761 | 44.53 | 23.88 |
| 5.2.34 | 1887 | 134.20 | 23.91 |
| 5.2.34 | 1840 | 228.30 | 23.93 |
| 5.2.34 | 1808 | 315.43 | 23.88 |

Table 5.2.3 Rebar Strain Locations

| Figure | Data Channel | Azimuthal Angle (Deg.) | Elevation (ft) | Layer |
|--------|--------------|------------------------|----------------|-------|
| 5.2.35 | 1104 | 135.00 | 13.38 | 1 |
| 5.2.36 | 680  | 45.33  | 4.15  | 6 |
| 5.2.37 | 681  | 45.50  | 6.75  | 6 |
| 5.2.38 | 682  | 46.00  | 9.54  | 6 |
| 5.2.39 | 1107 | 135.00 | 12.82 | 6 |
| 5.2.40 | 1109 | 46.50  | 13.75 | 6 |
| 5.2.41 | 1120 | 45.50  | 16.25 | 6 |
| 5.2.42 | 1048 | 242.00 | 19.04 | 6 |
| 5.2.42 | 1029 | 46.00  | 19.21 | 6 |
| 5.2.43 | 683  | 44.50  | 21.90 | 6 |
| 5.2.44 | 562  | 44.10  | 4.00  | 2 |
| 5.2.45 | 563  | 45.50  | 10.88 | 2 |
| 5.2.46 | 1105 | 134.00 | 12.98 | 2 |
| 5.2.46 | 529  | 305.50 | 13.08 | 2 |
| 5.2.47 | 564  | 46.00  | 16.71 | 2 |
| 5.2.48 | 540  | 305.00 | 20.04 | 2 |
| 5.2.49 | 565  | 46.50  | 21.58 | 2 |
| 5.2.50 | 1040 | 45.50  | 7.33  | 5 |
| 5.2.51 | 1041 | 45.50  | 13.42 | 5 |
| 5.2.51 | 1106 | 134.50 | 13.04 | 5 |
| 5.2.51 | 620  | 305.50 | 13.08 | 5 |
| 5.2.52 | 1042 | 47.00  | 19.13 | 5 |
| 5.2.53 | 622  | 331.50 | 20.08 | 5 |

Table 5.2.4 Concrete Thermal Properties

| | | |
|---|---|---|
| Specific Heat | = | 949 J/kg/$^\circ$C<br>$8 \times 10^5$ in$^2$/s$^2$/$^\circ$F |
| Thermal Conductivity | = | 1.85 J/m/s/$^\circ$C<br>0.2771 lb-in/s$^3$/$^\circ$F |
| Mass Density | = | $2.25 \times 10^{-4}$ lbf-s$^2$/in$^4$ |
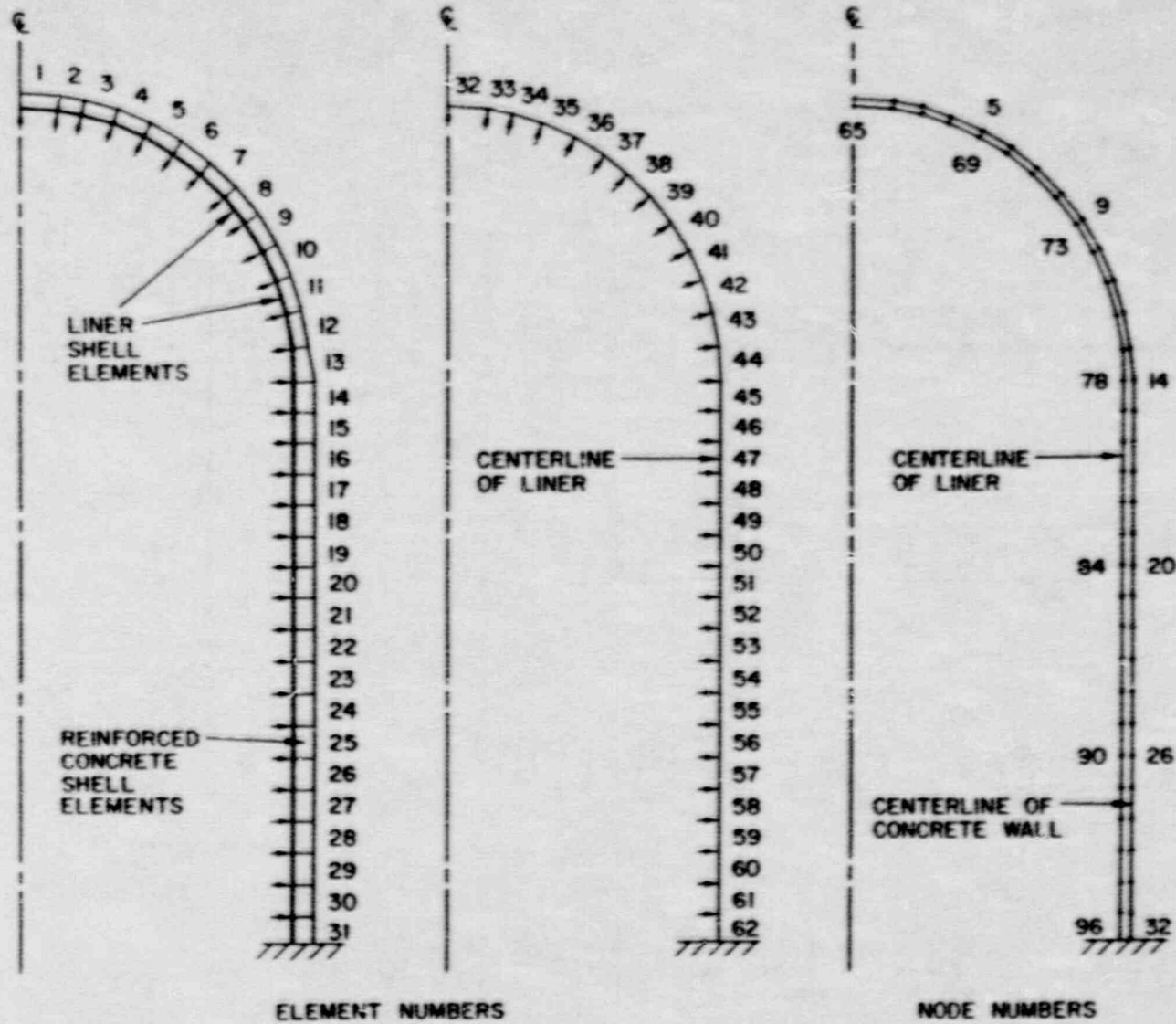
Figure 5.2.1 Discretization of Shell Model

ELEMENT NUMBERS

NODE NUMBERS

5-78
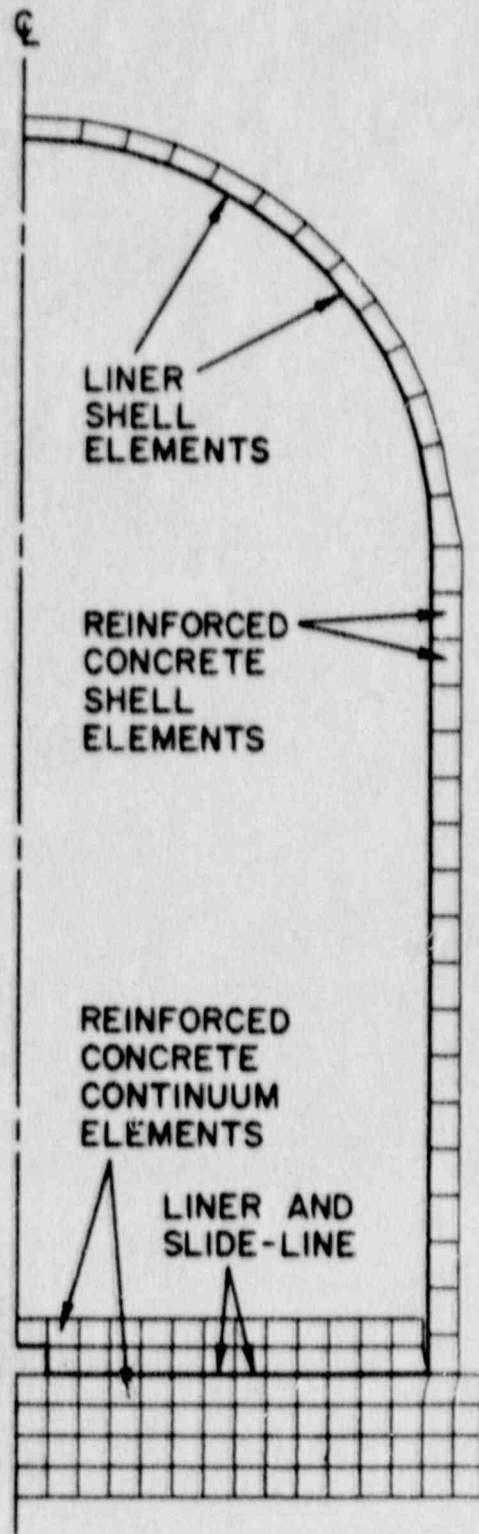
Figure 5.2.2 Discretization of Shell and Slab Model
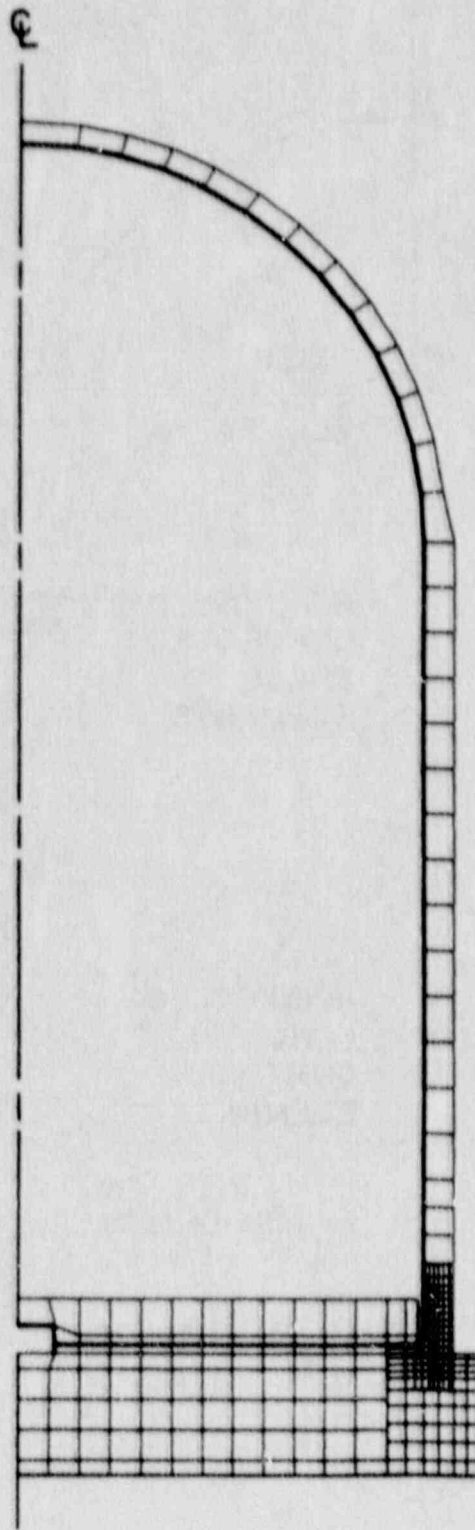
Figure 5.2.3  Discretization of Refined Shell and Slab Model
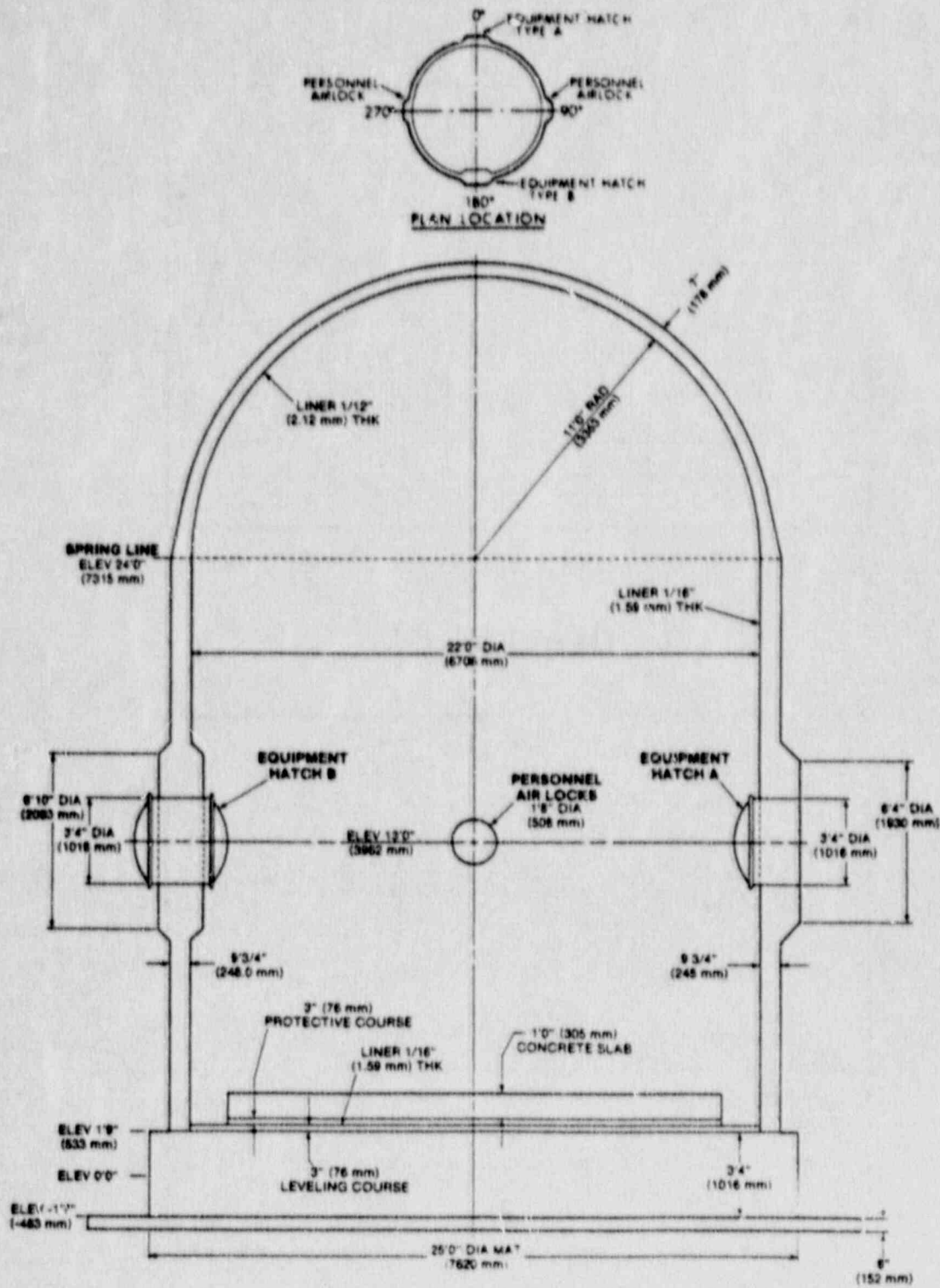
Figure 5.2.4  Schematic of the Containment Model
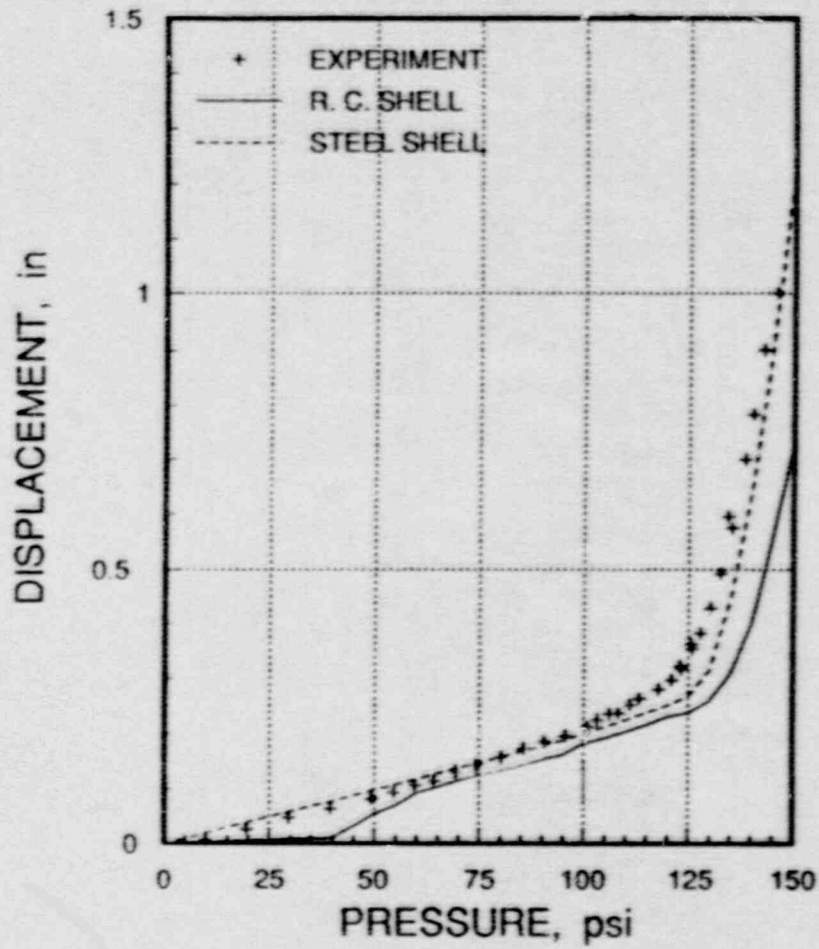
Figure 5.2.5
Radial Displacement of Liner at EL 6.0 ft
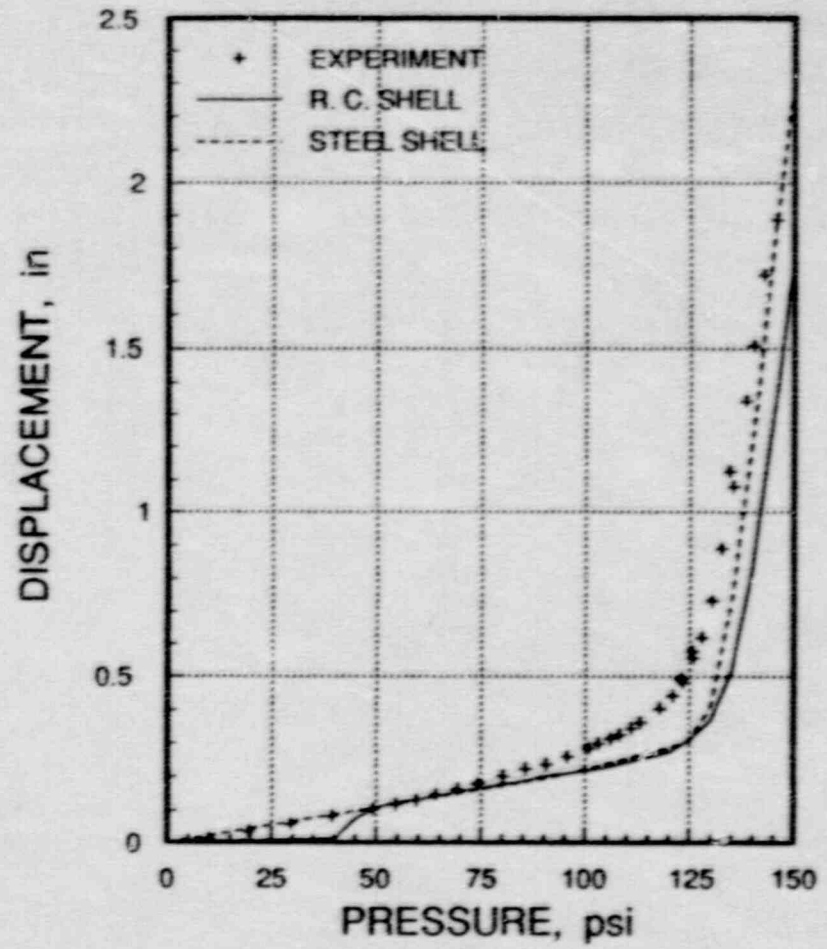


Figure 5.2.6
Radial Displacement of Liner at EL 11.2 ft
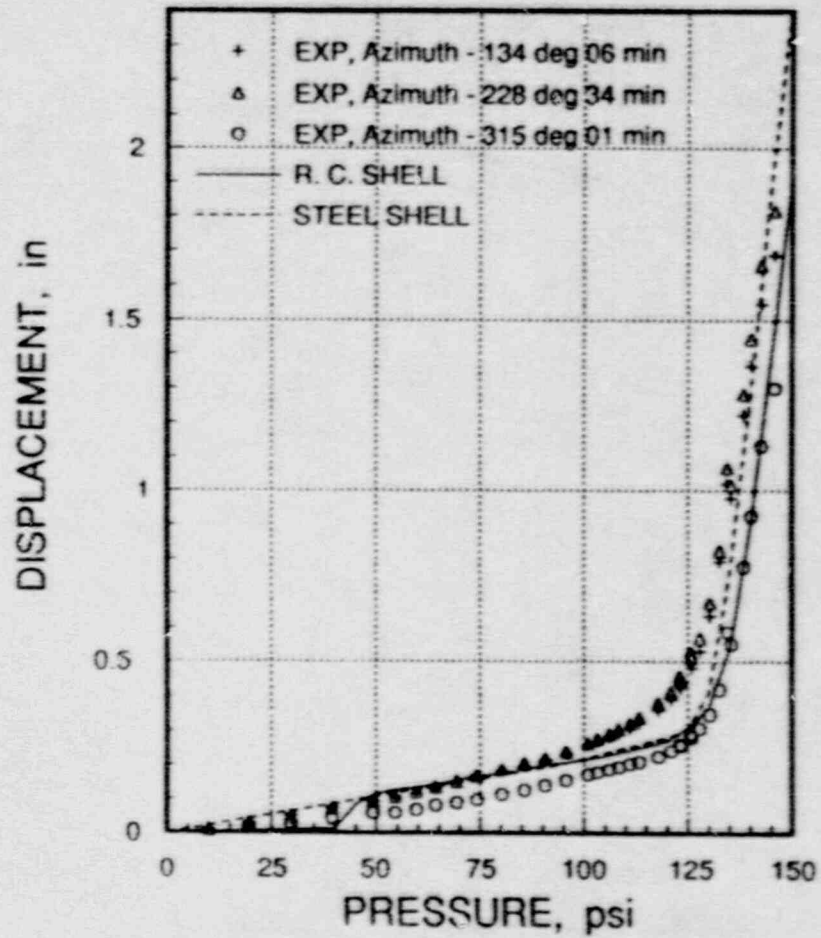
Figure 5.2.7
Radial Displacement of Liner at EL 13.0 ft
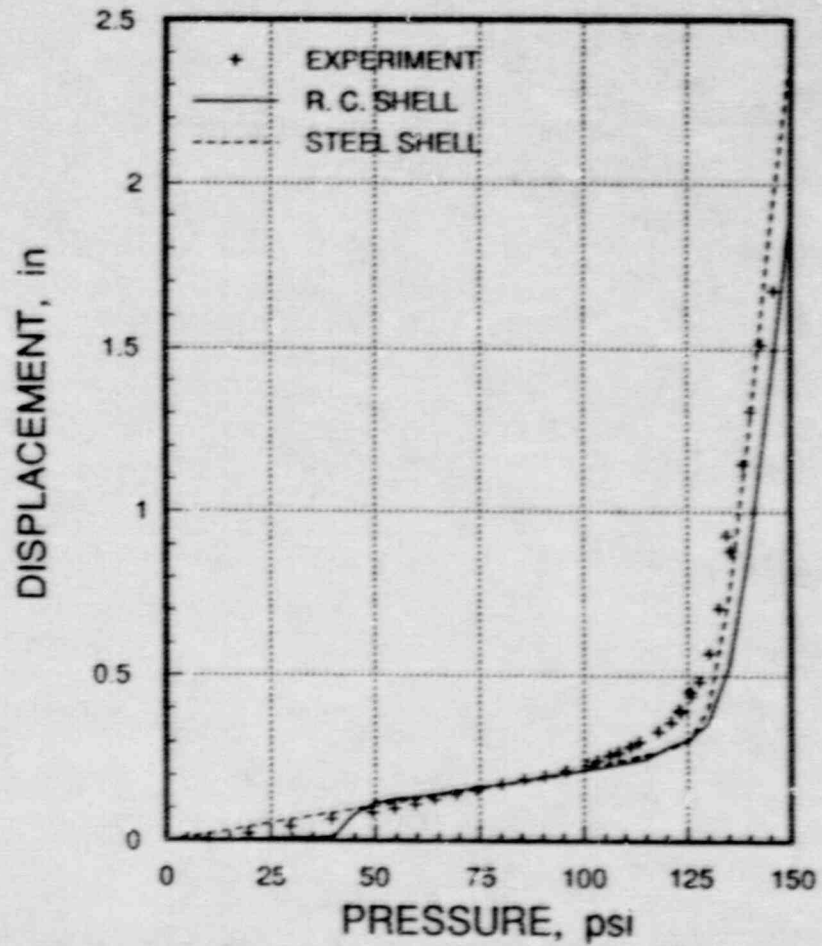


Figure 5.2.8
Radial Displacement of Liner at EL 15.4 ft
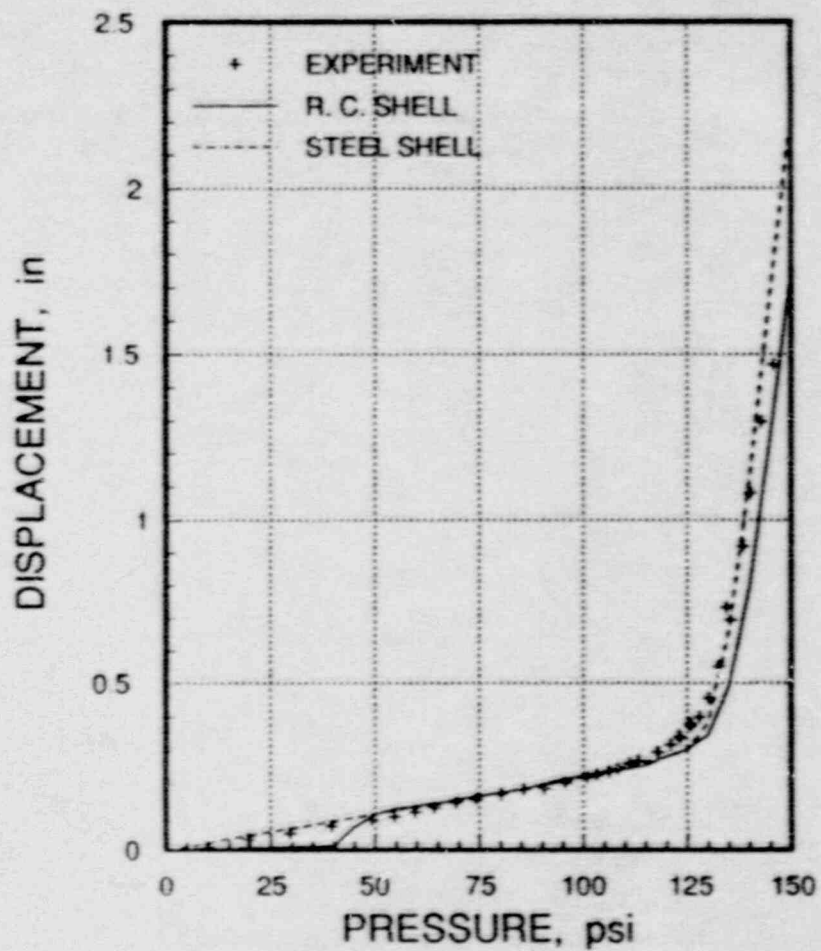
Figure 5.2.9
Radial Displacement of Liner at EL 17.9 ft
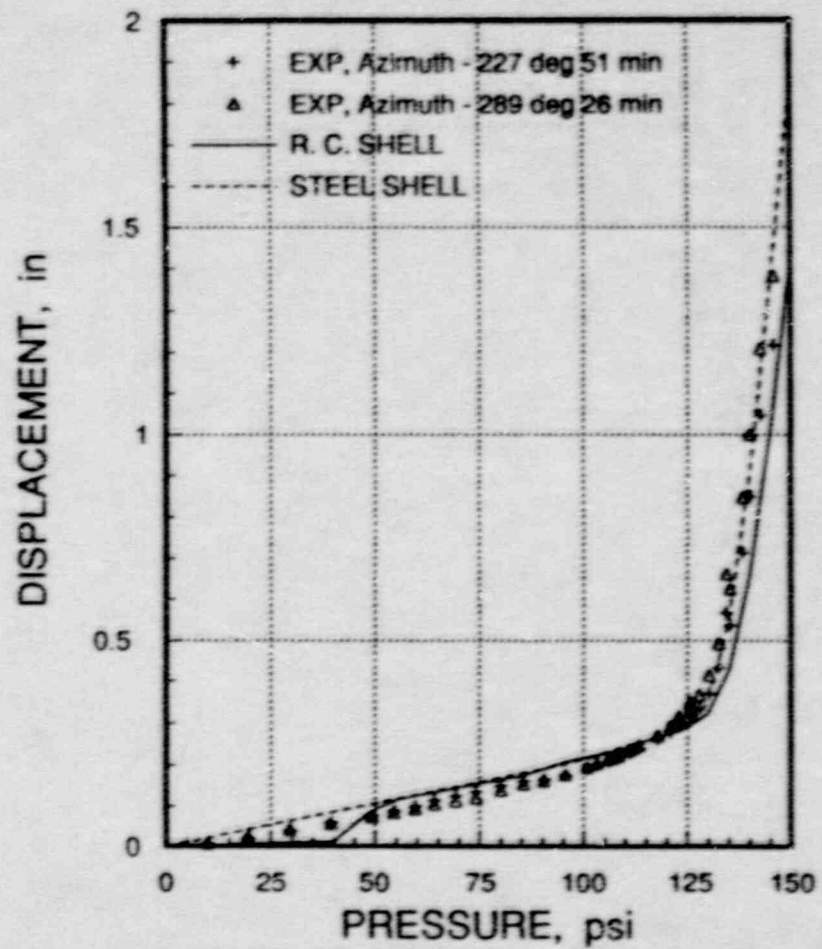
Figure 5.2.10
Radial Displacement of Liner at EL 20.1 ft
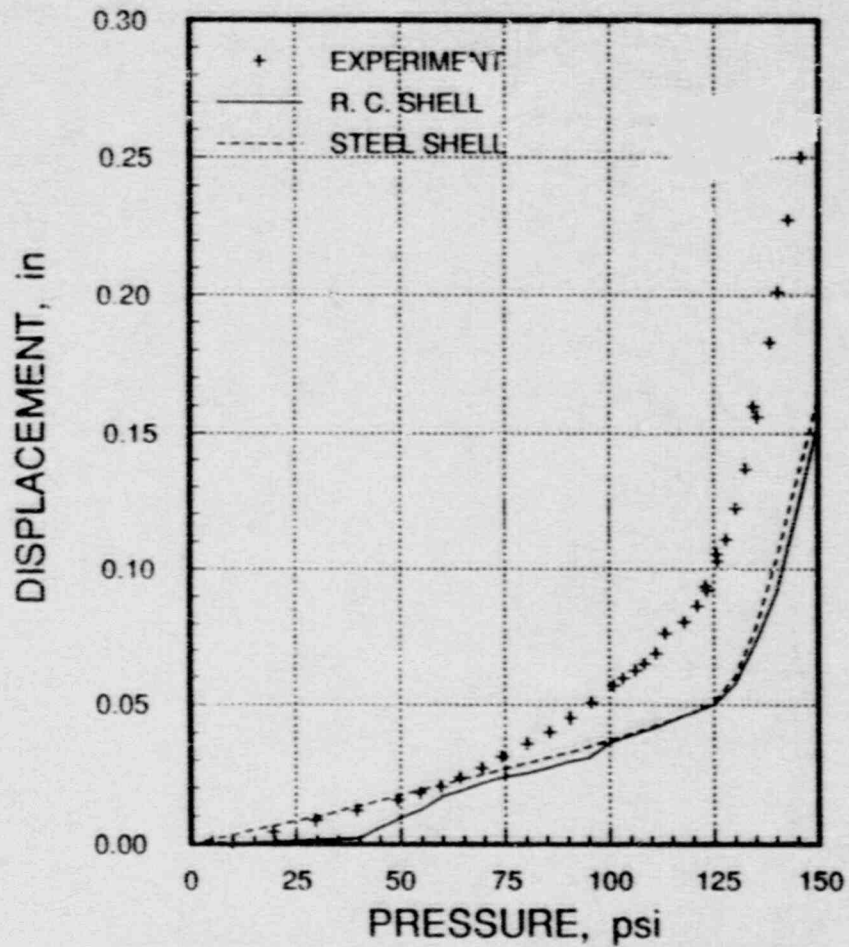
Figure 5.2.11
Vertical Displacement of Liner at EL 6.0 ft
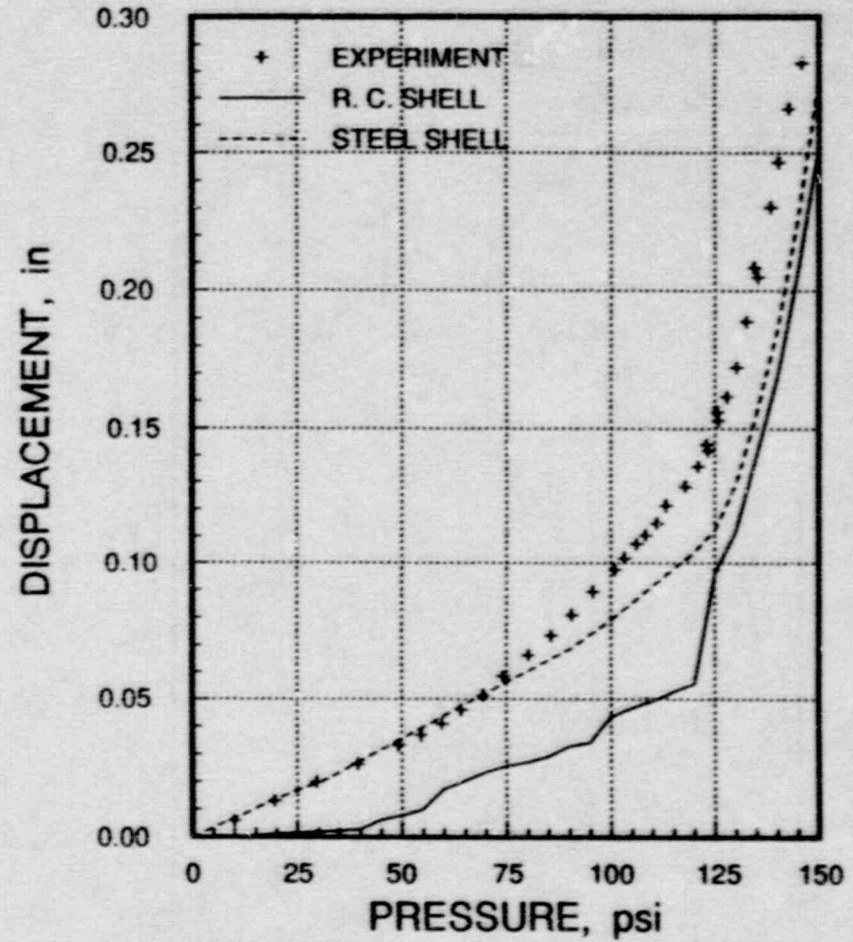
Figure 5.2.12
Vertical Displacement of Liner at EL 11.0 ft
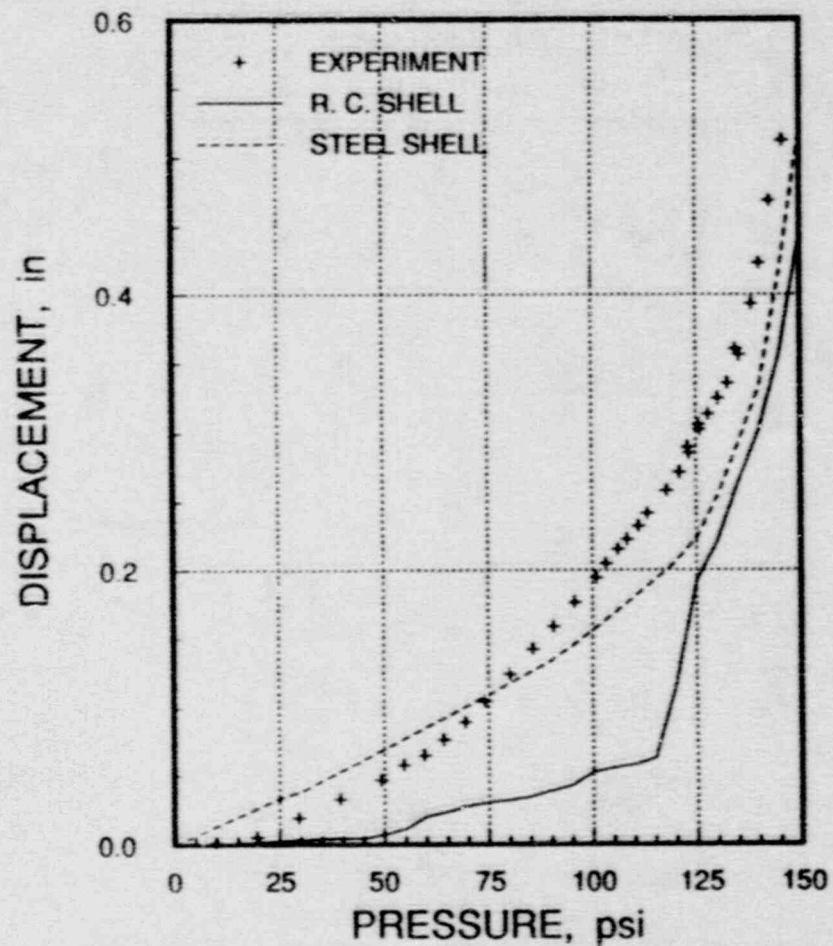
Figure 5.2.13
Vertical Displacement of Liner at EL 18.0 ft
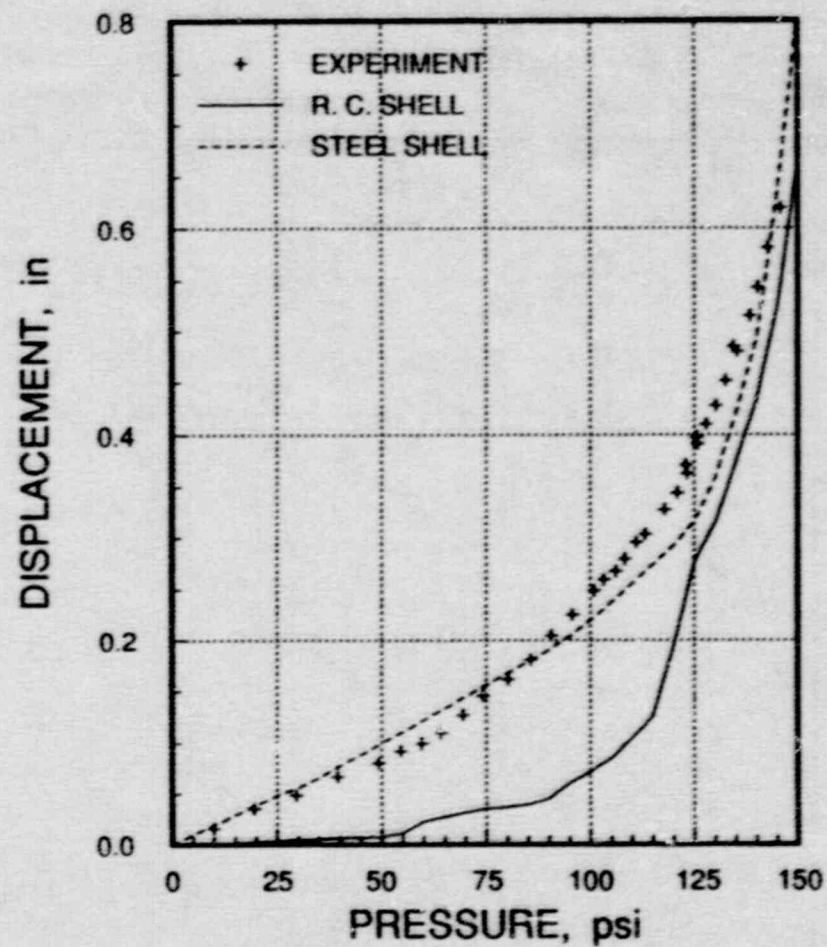


Figure 5.2.14
Vertical Displacement of Springline
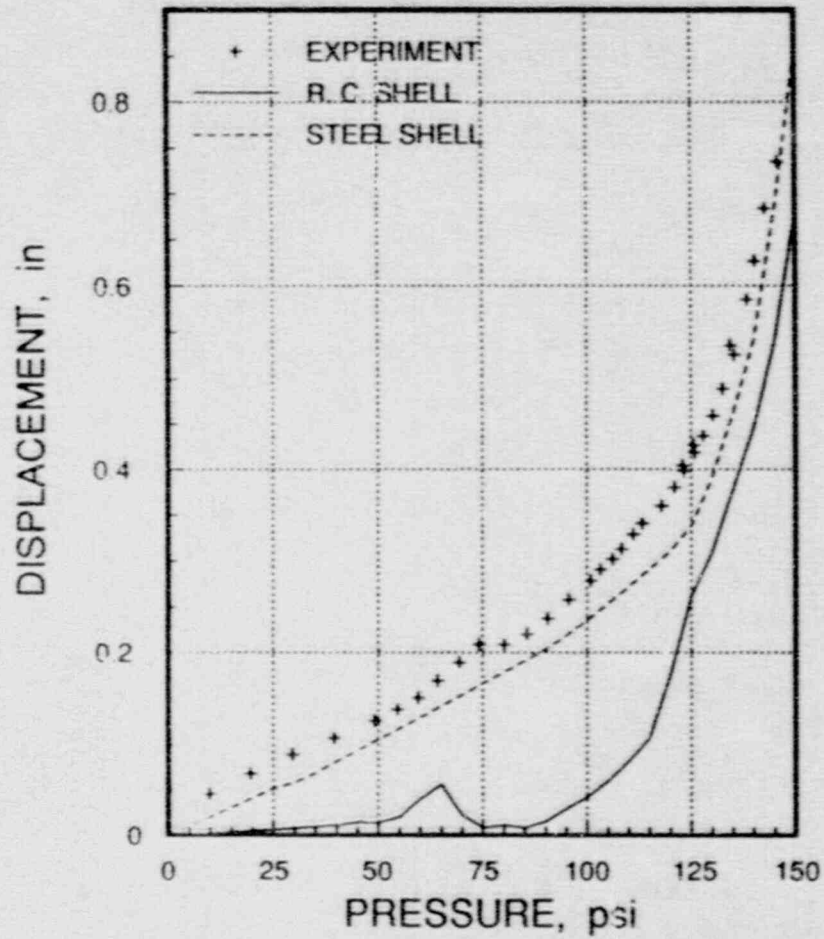
Figure 5.2.15
Relative Vertical Displacement of Dome Apex to Basemat Uplift
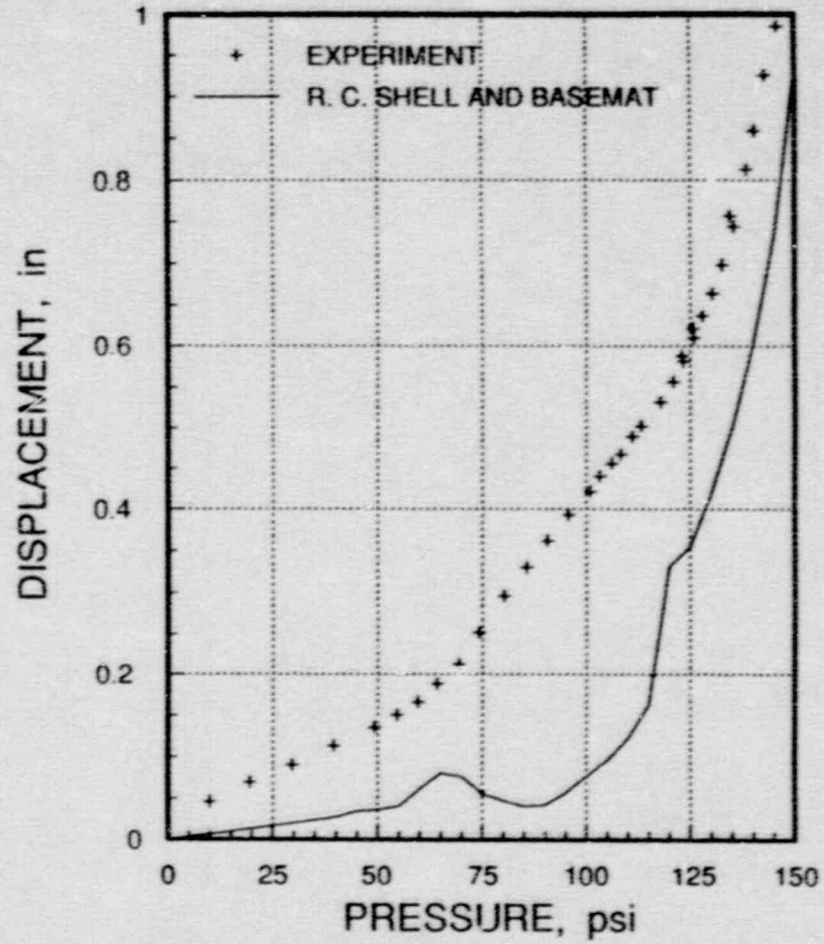
Figure 5.2.16
Vertical Displacement of Dome Apex
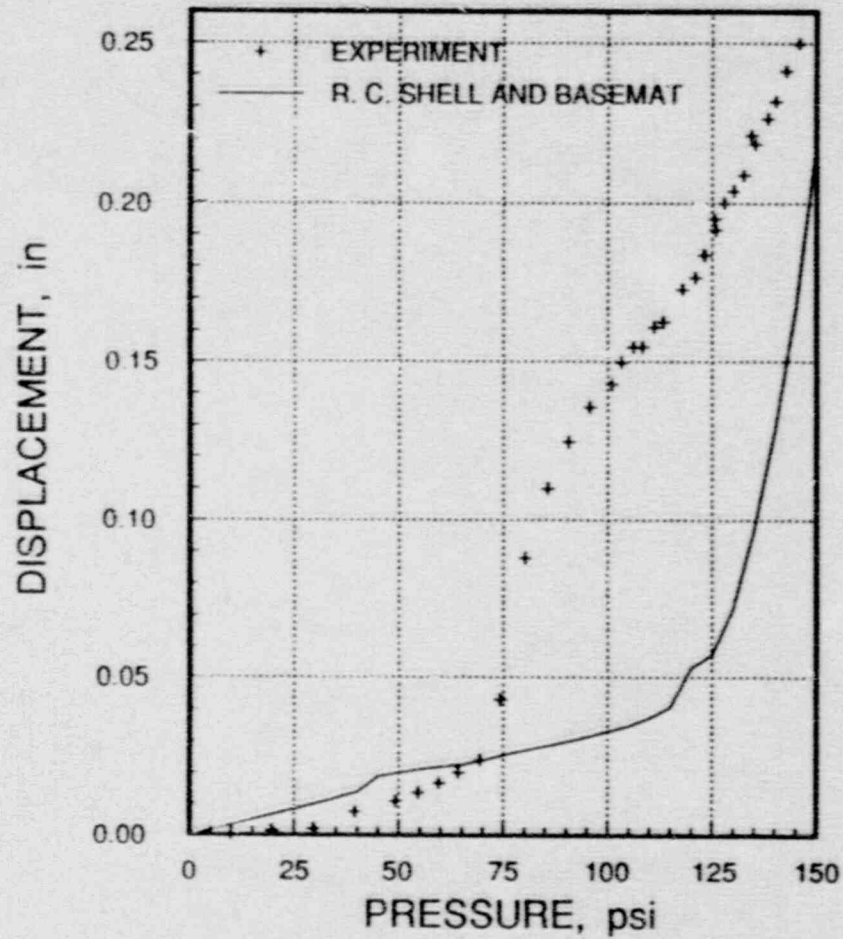
Figure 5.2.17
Vertical Displacement of Basemat Uplift
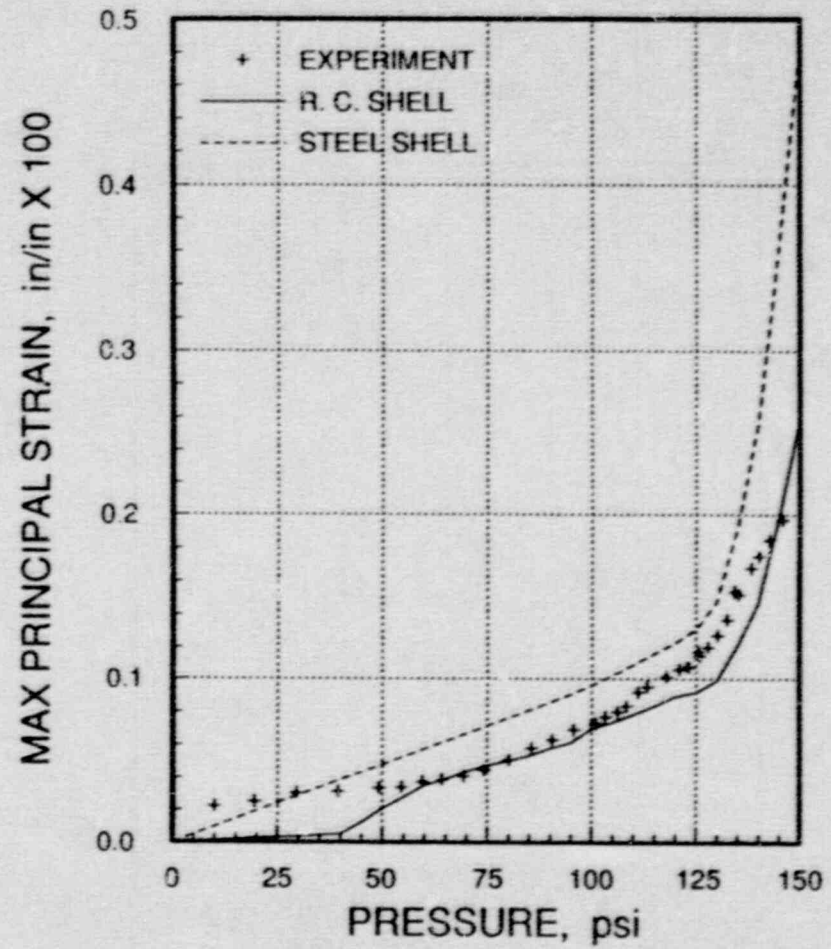
Figure 5.2.18
Maximum Principal Liner Strain at EL 4.1 ft
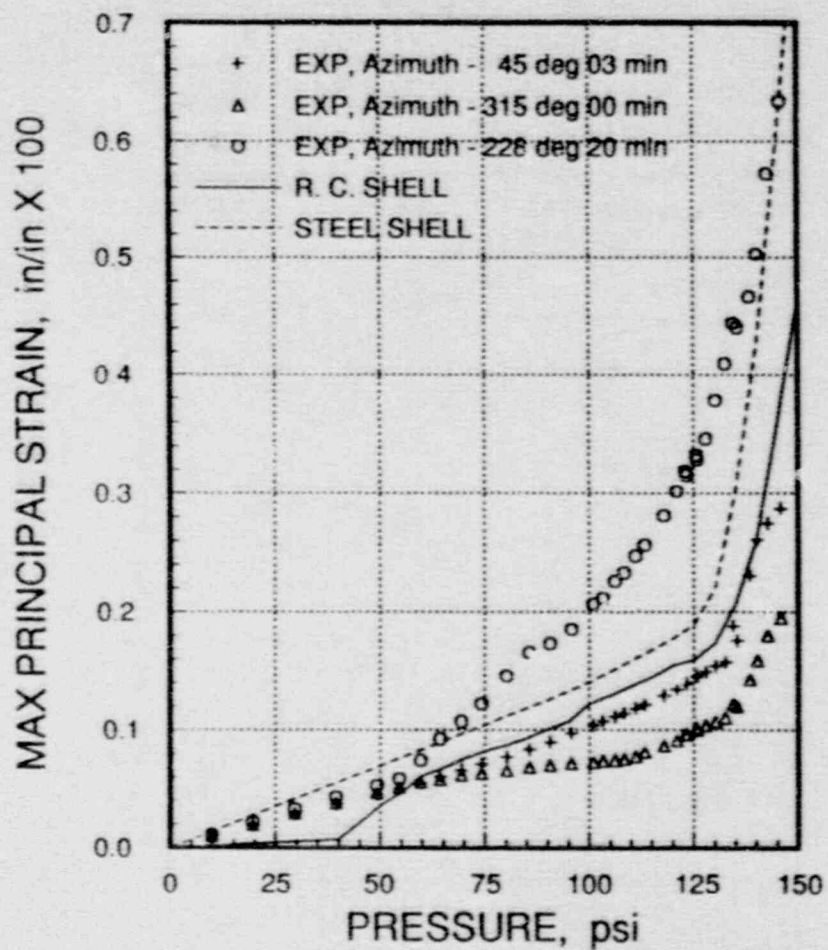
Figure 5.2.19
Maximum Principal Liner Strain at EL 5.2 ft
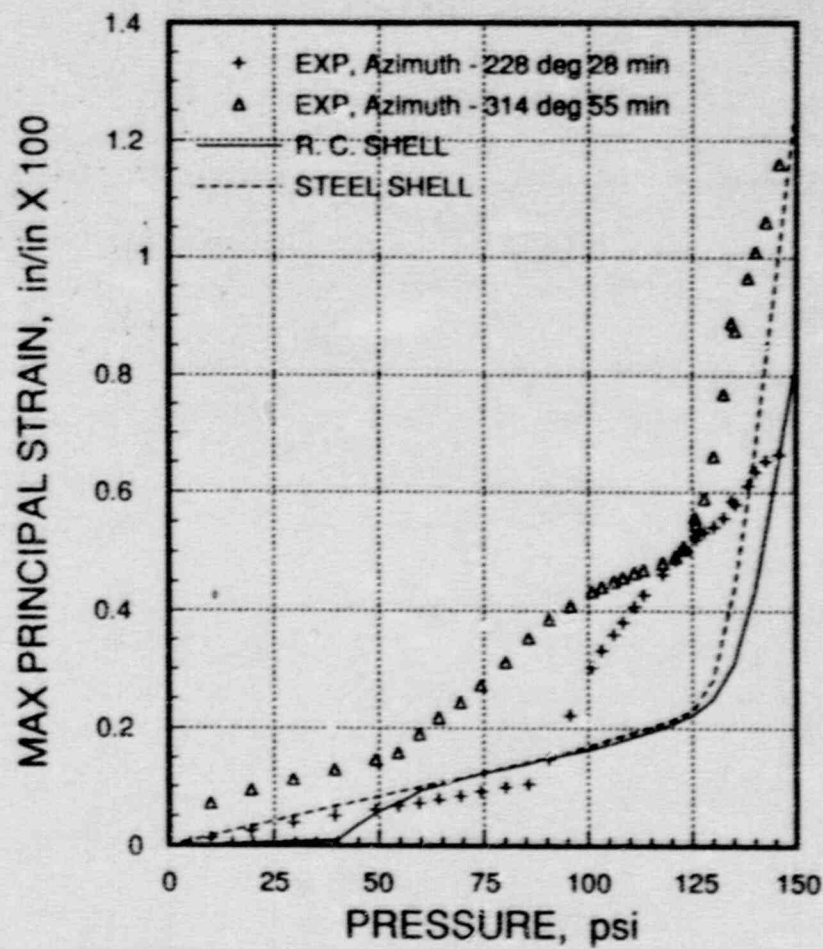


Figure 5.2.20
Maximum Principal Liner Strain at EL 8.0 ft

MAX PRINCIPAL STRAIN, in/in X 100

| | |
|---|---|
| + | EXP, Azimuth - 44 deg 57 min |
| △ | EXP, Azimuth - 221 deg 51 min |
| ○ | EXP, Azimuth - 228 deg 20 min |
| —— | R. C. SHELL |
| ----- | STEEL SHELL |
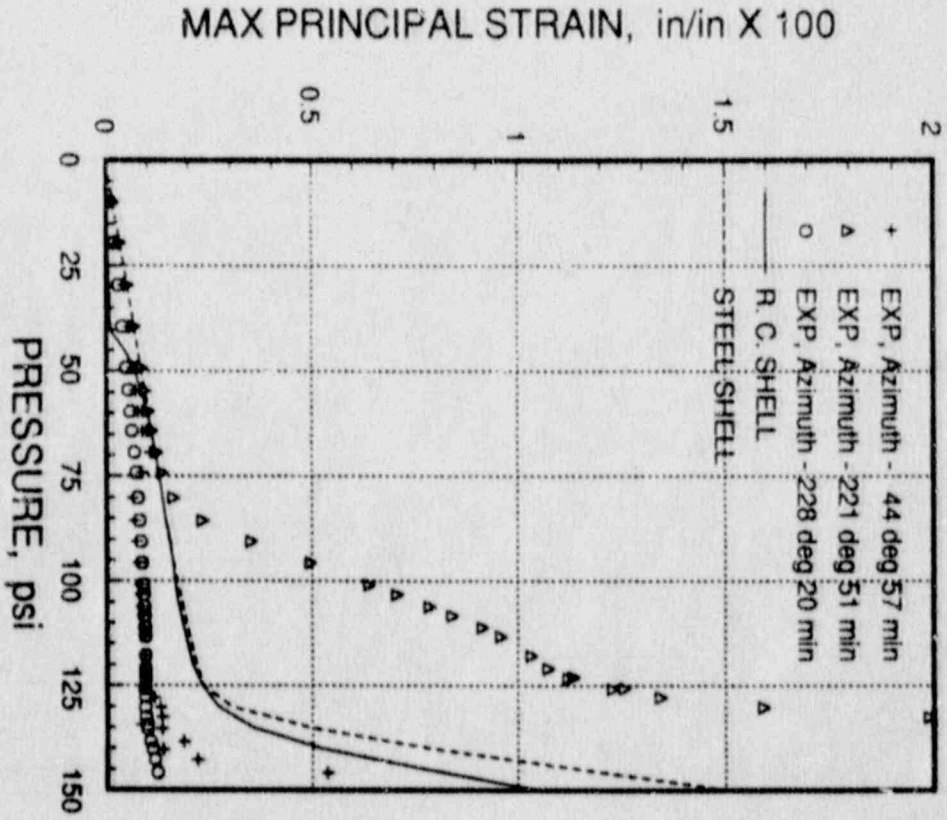
Figure 5.2.21
Maximum Principal Liner Strain at EL 8.9 ft

MAX PRINCIPAL STRAIN, in/in X 100

| | |
|---|---|
| + | EXP, Azimuth - 45 deg 05 min |
| △ | EXP, Azimuth - 228 deg 36 min |
| —— | R. C. SHELL |
| ----- | STEEL SHELL |
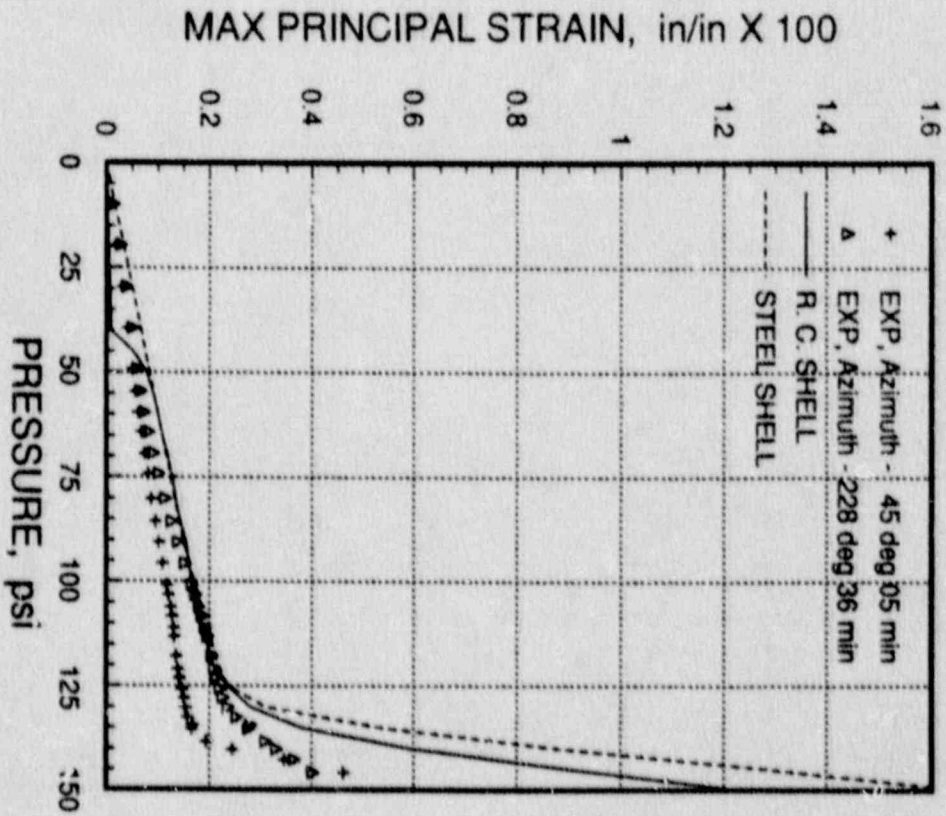
Figure 5.2.22
Maximum Principal Liner Strain at EL 9.9 ft
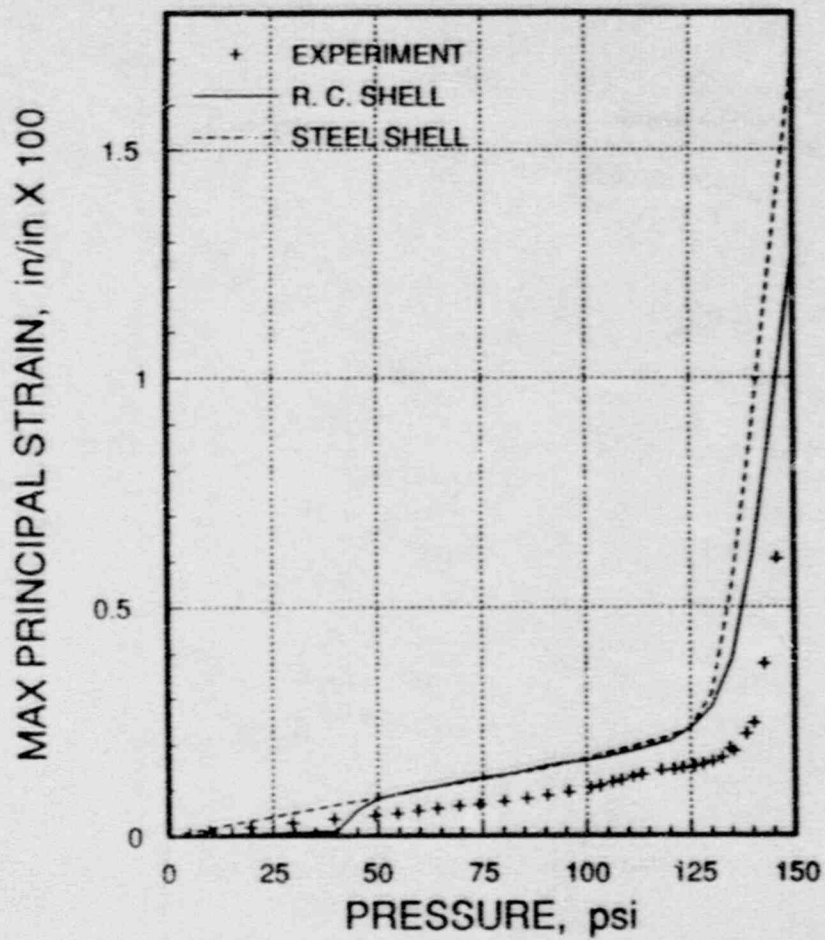
Figure 5.2.23
Maximum Principal Liner Strain at EL 10.7 ft
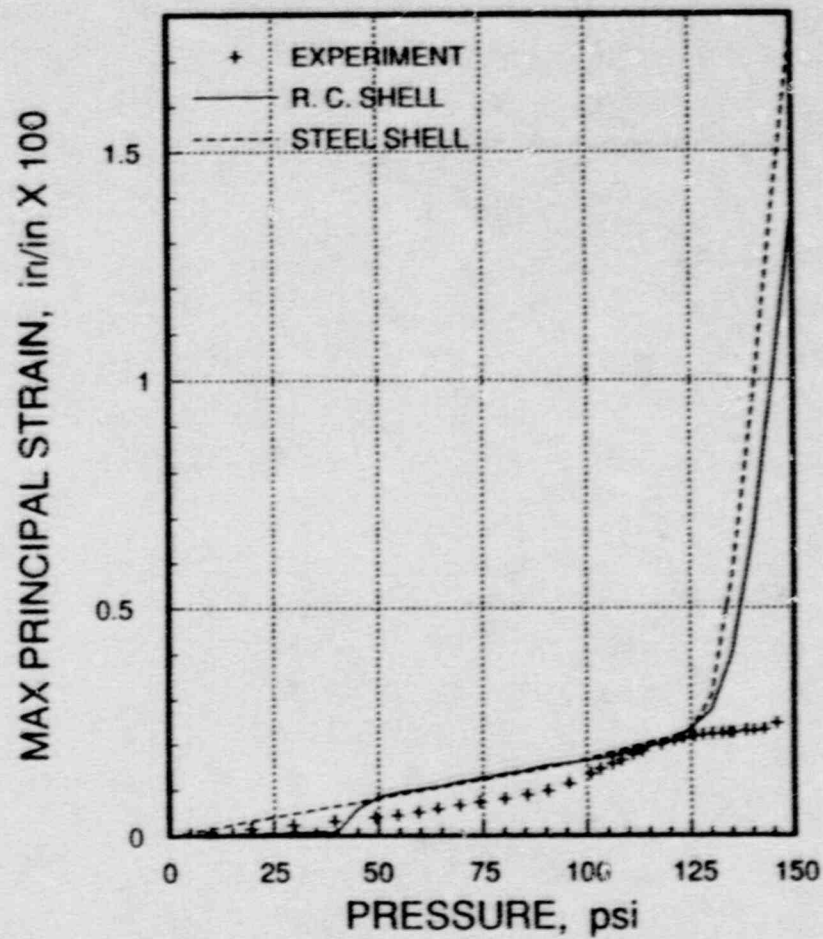
Figure 5.2.24
Maximum Principal Liner Strain at EL 11.6 ft
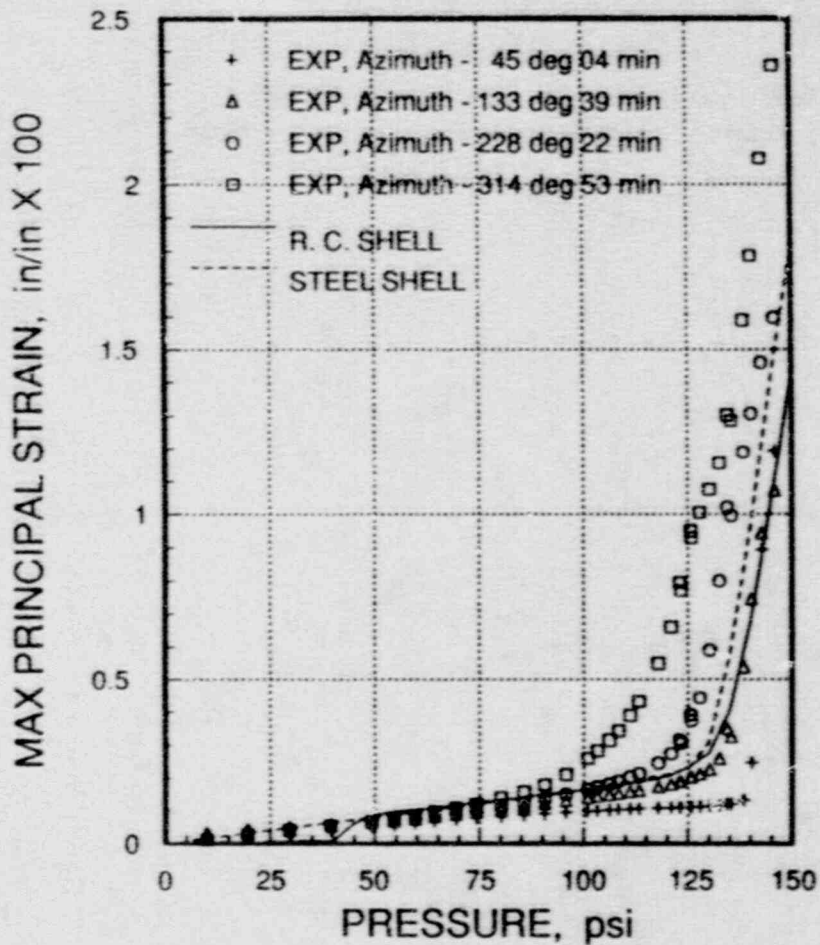
Figure 5.2.25
Maximum Principal Liner Strain at EL 13.1 ft
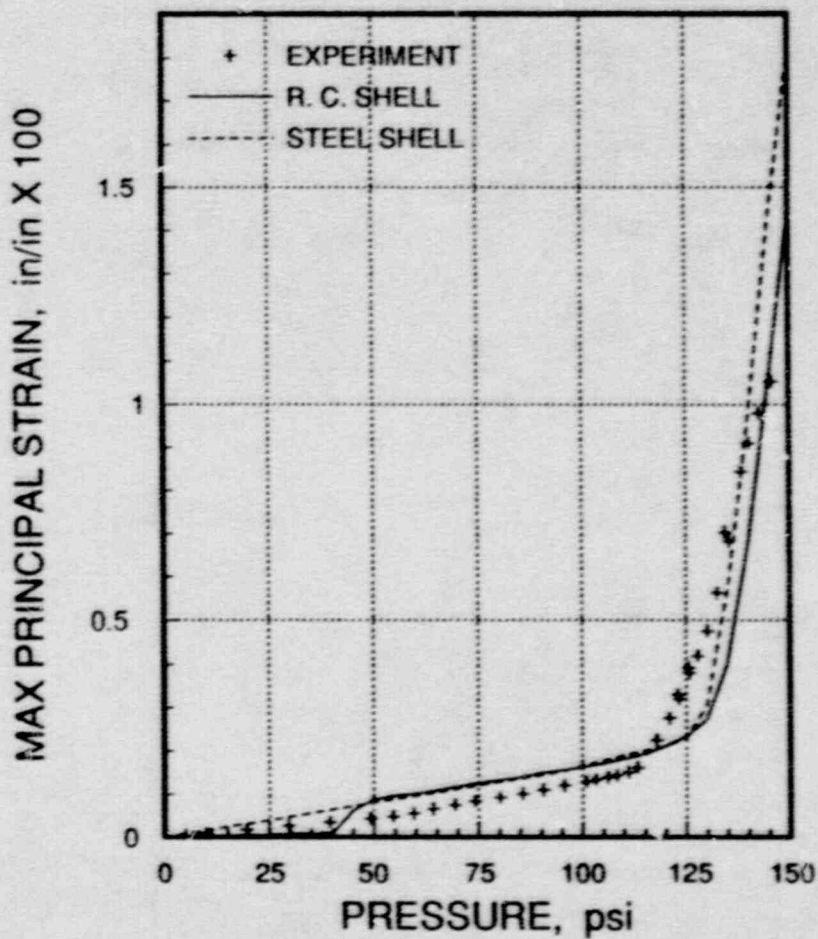
Figure 5.2.26
Maximum Principal Liner Strain at EL 14.1 ft

MAX PRINCIPAL STRAIN, in/in X 100

+ ........ EXPERIMENT
——— R. C. SHELL
------- STEEL SHELL

PRESSURE, psi
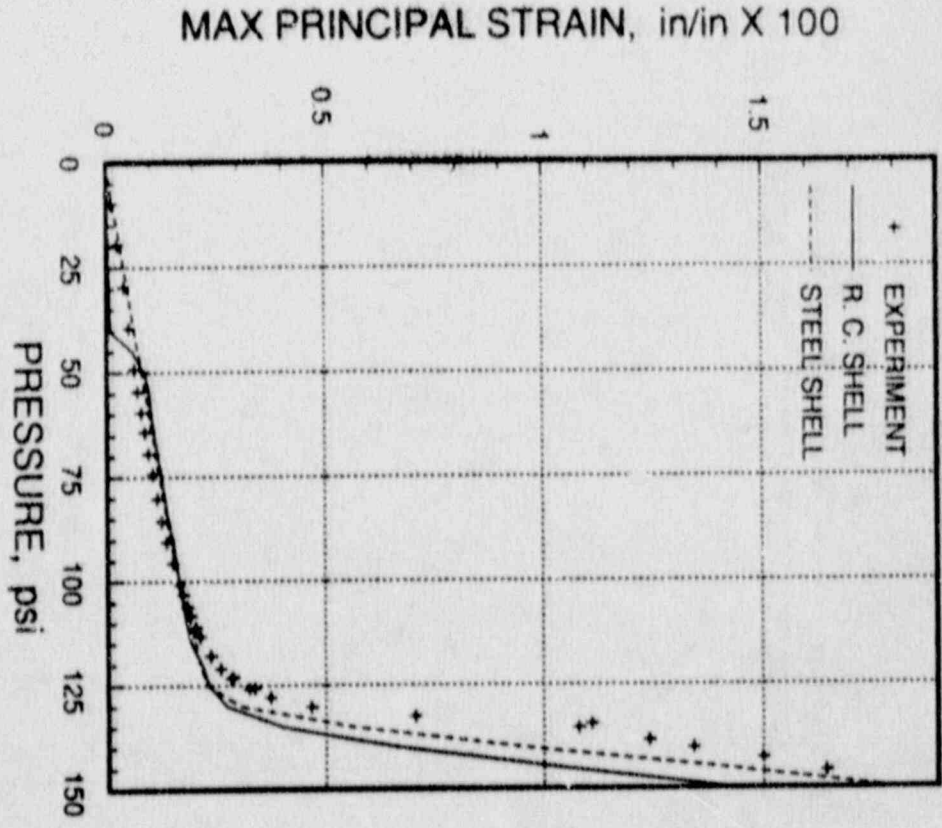
Figure 5.2.27
Maximum Principal Liner Strain at EL 15.5 ft

MAX PRINCIPAL STRAIN, in/in X 100

+ ........ EXPERIMENT
——— R. C. SHELL
------- STEEL SHELL

PRESSURE, psi
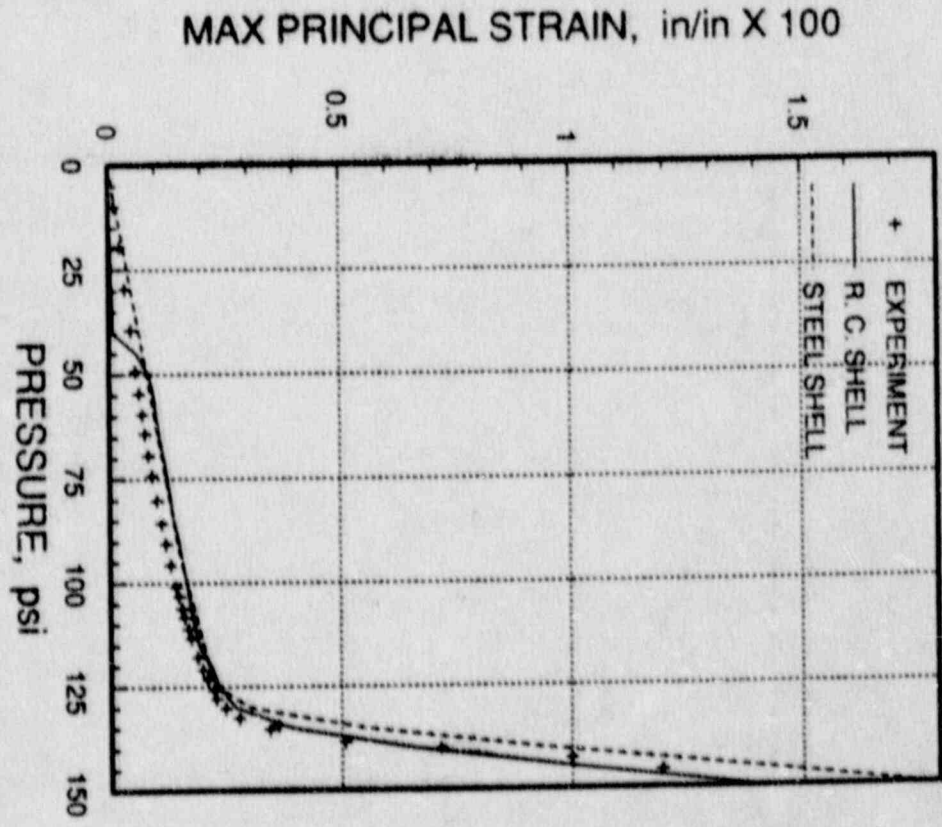
Figure 5.2.28
Maximum Principal Liner Strain at EL 16.2 ft
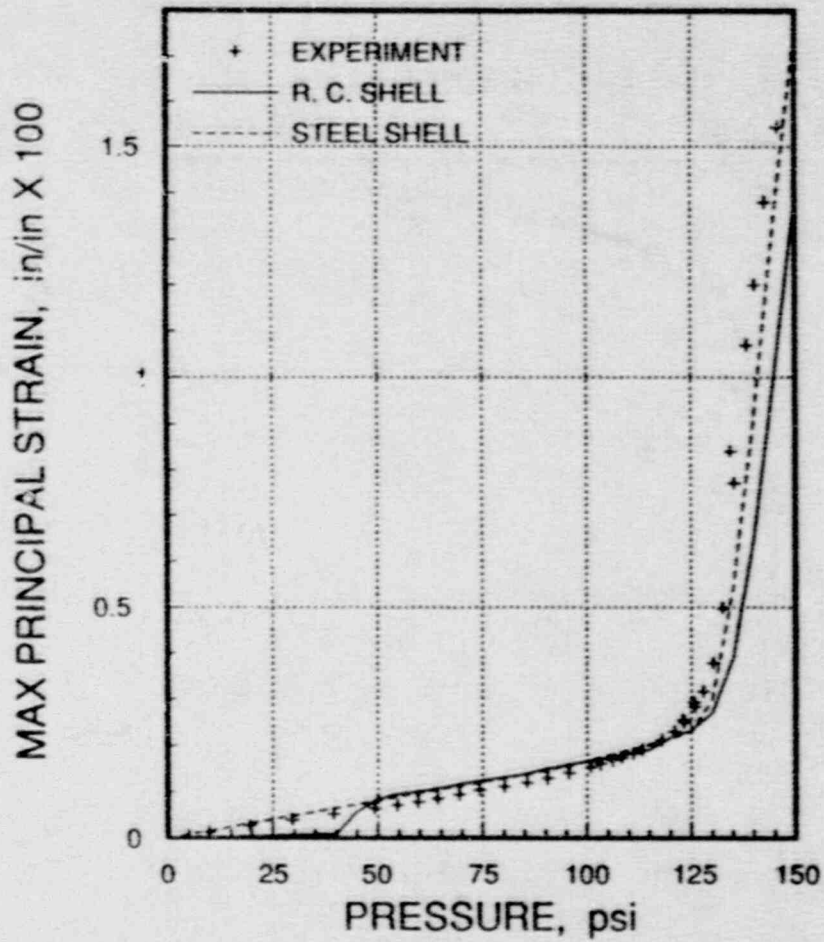
Figure 5.2.29
Maximum Principal Liner Strain at EL 17.0 ft
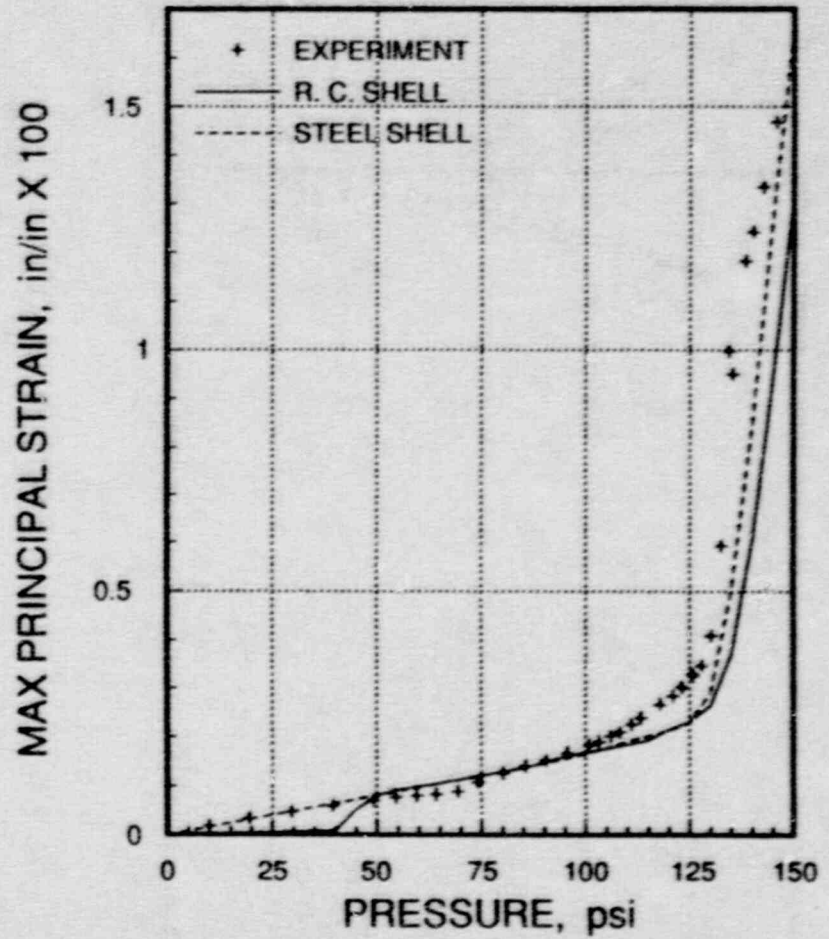


Figure 5.2.30
Maximum Principal Liner Strain at EL 17.8 ft
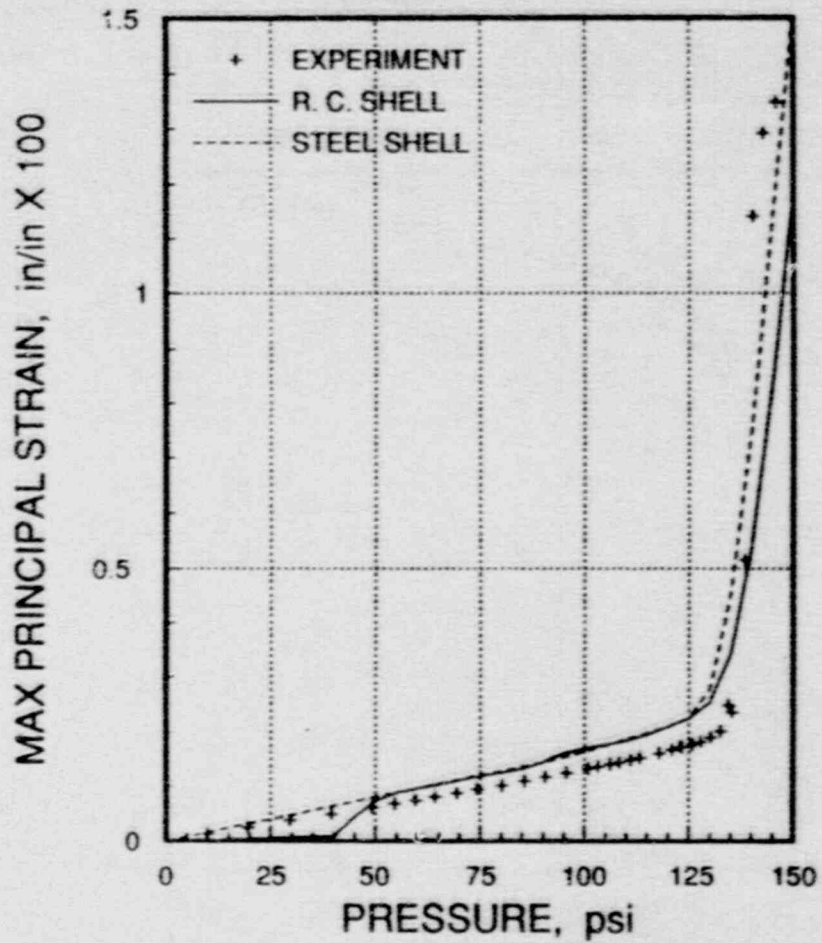
Figure 5.2.31
Maximum Principal Liner Strain at EL 19.2 ft
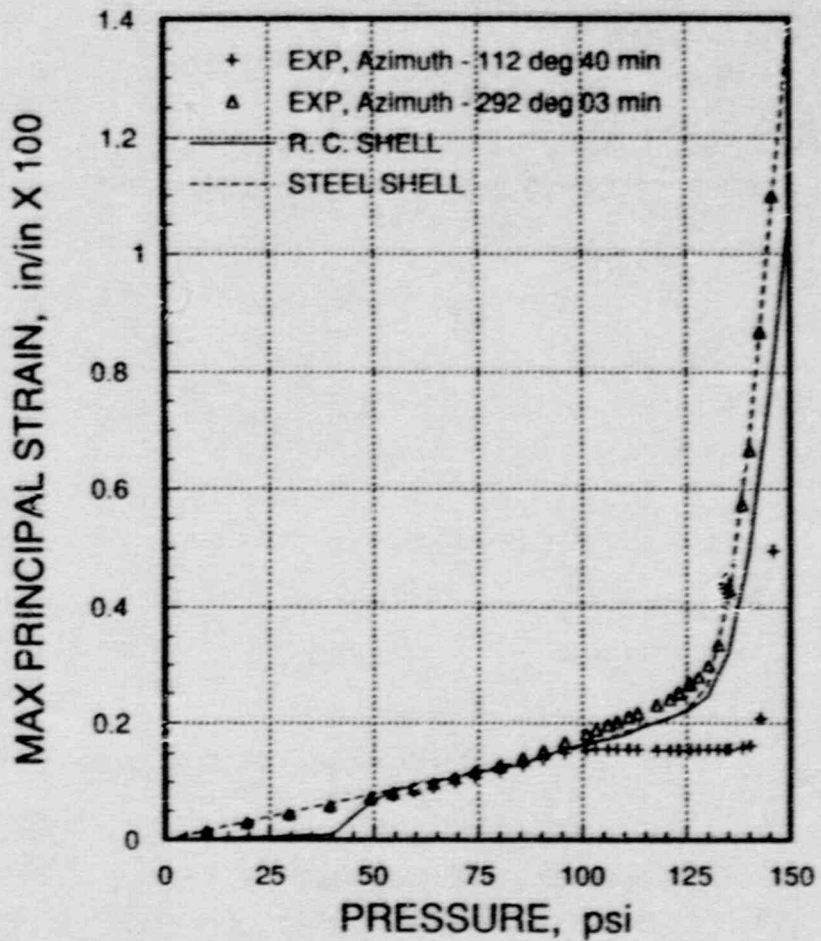


Figure 5.2.32
Maximum Principal Liner Strain at EL 20.1 ft
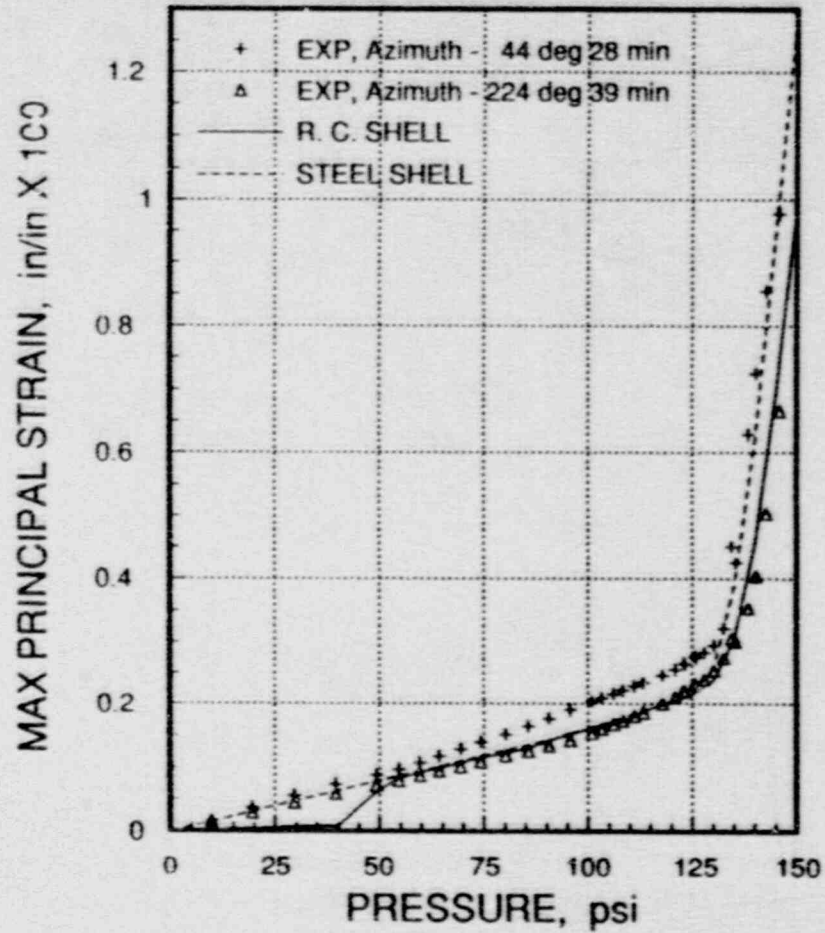
Figure 5.2.33
Maximum Principal Liner Strain at EL 20.7 ft
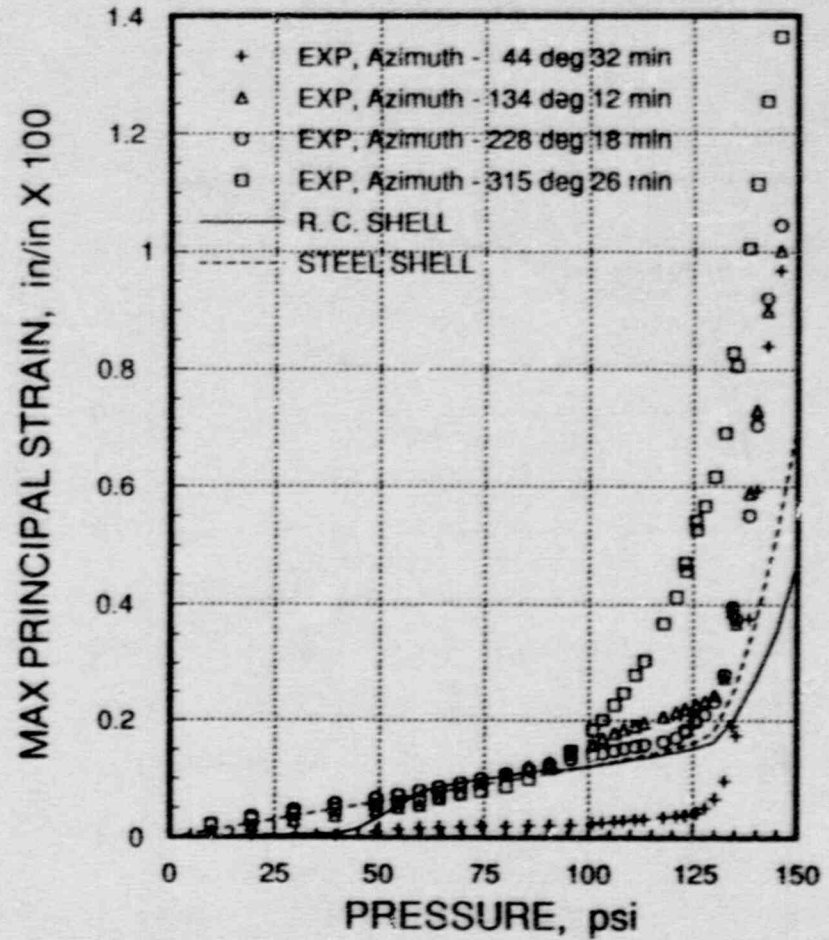
Figure 5.2.34
Maximum Principal Liner Strain at Springline
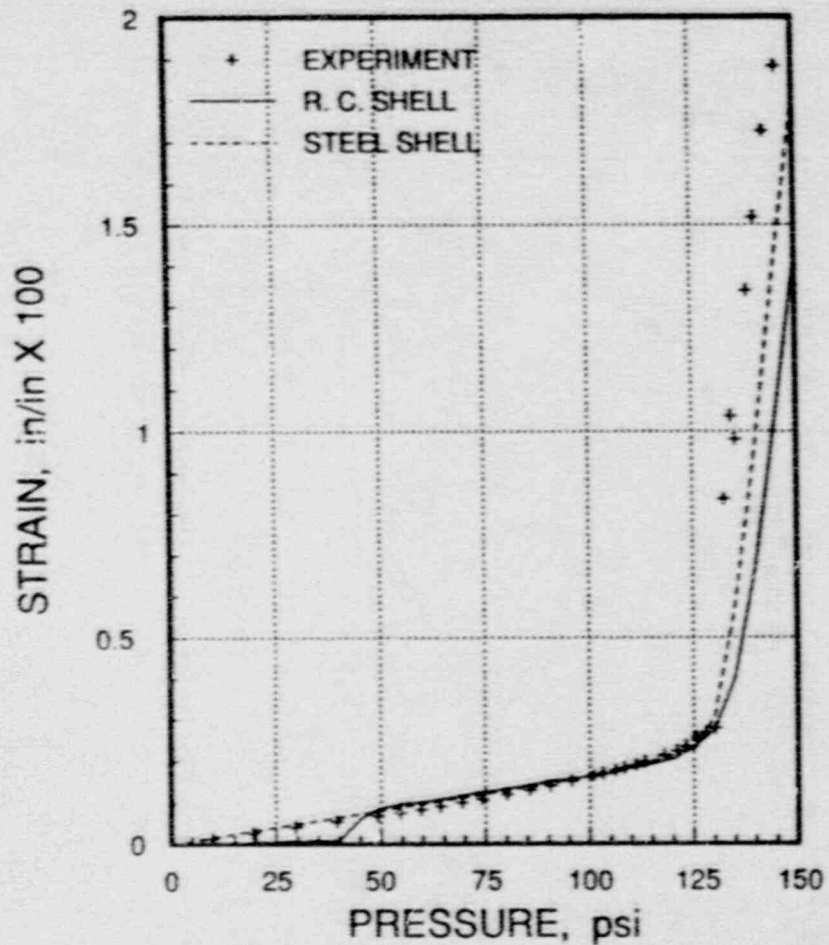
Figure 5.2.35
Hoop Rebar Strain at Eʼ. 13.4 ft
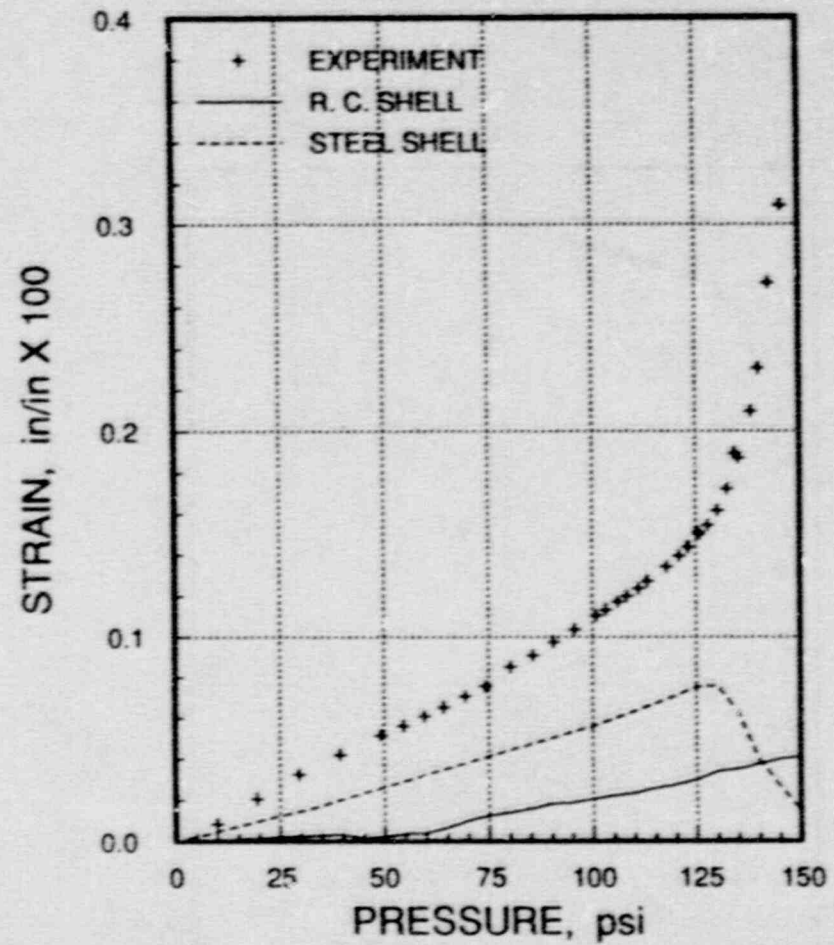
Figure 5.2.36
Hoop Rebar Strain at EL 4.2 ft

5-97
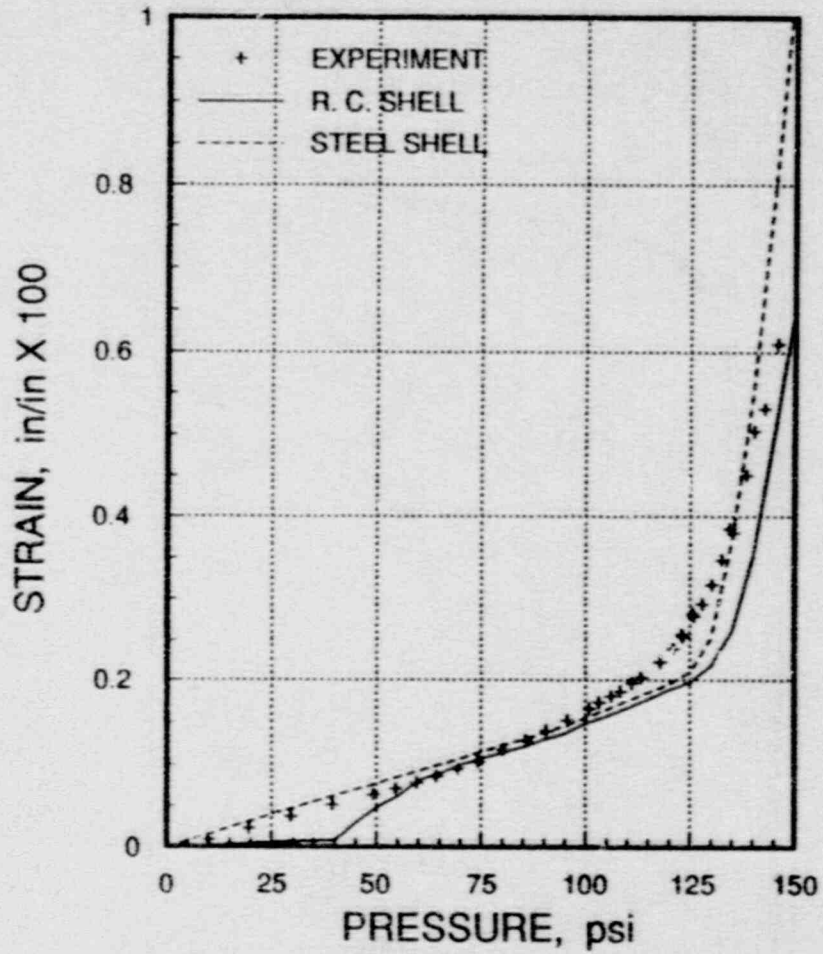
Figure 5.2.37
Hoop Rebar Strain at EL 6.8 ft
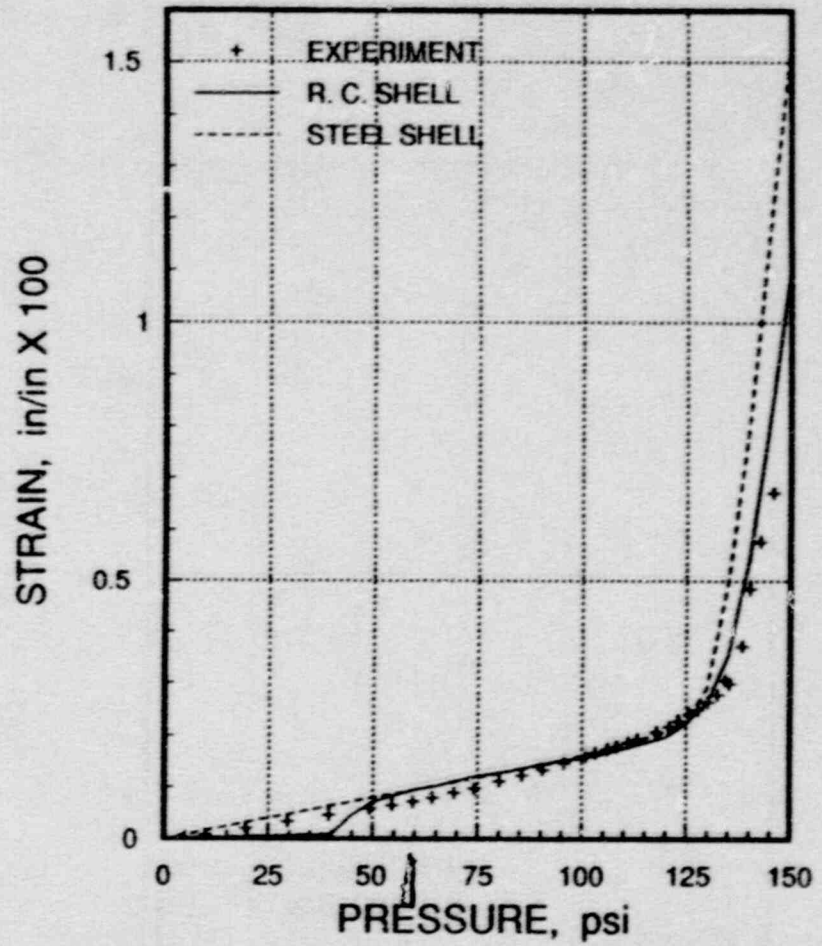


Figure 5.2.38
Hoop Rebar Strain at EL 9.5 ft
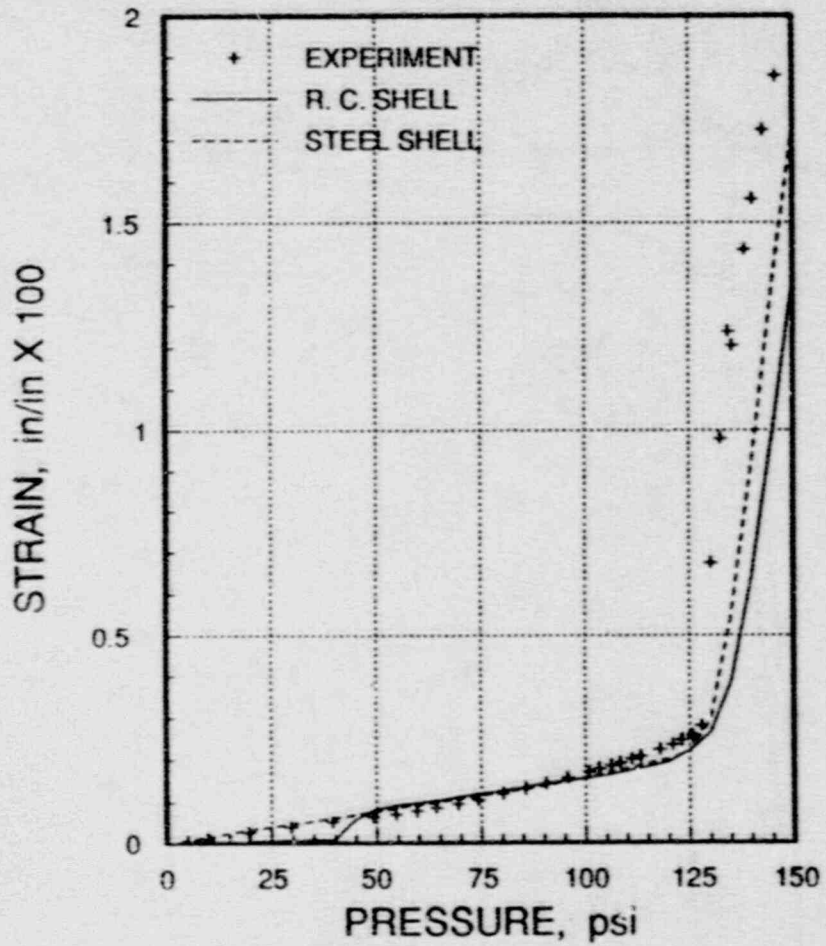
Figure 5.2.39
Hoop Rebar Strain at EL 12.8 ft
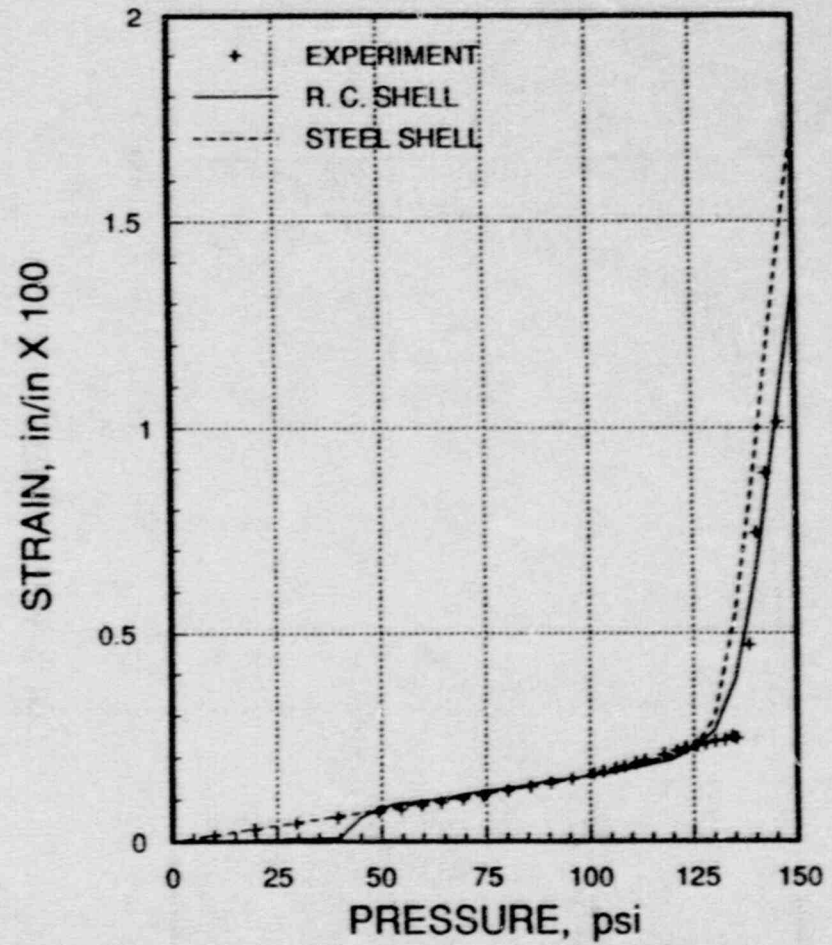
Figure 5.2.40
Hoop Rebar Strain at EL 13.8 ft
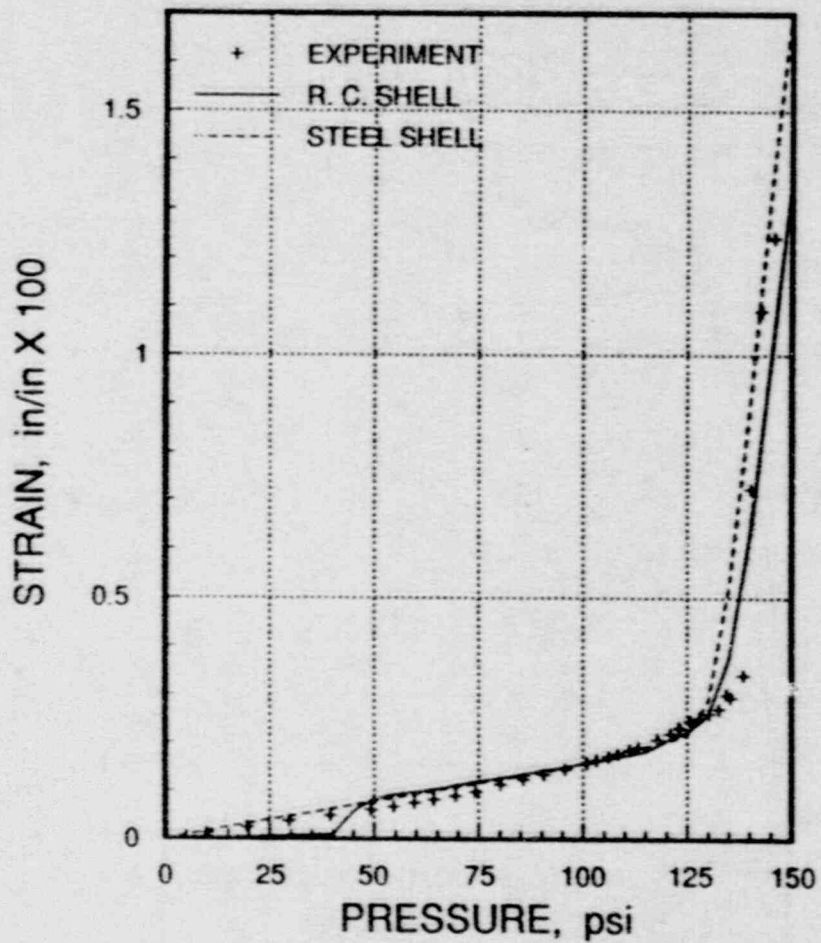
Figure 5.2.41
Hoop Rebar Strain at EL 16.3 ft
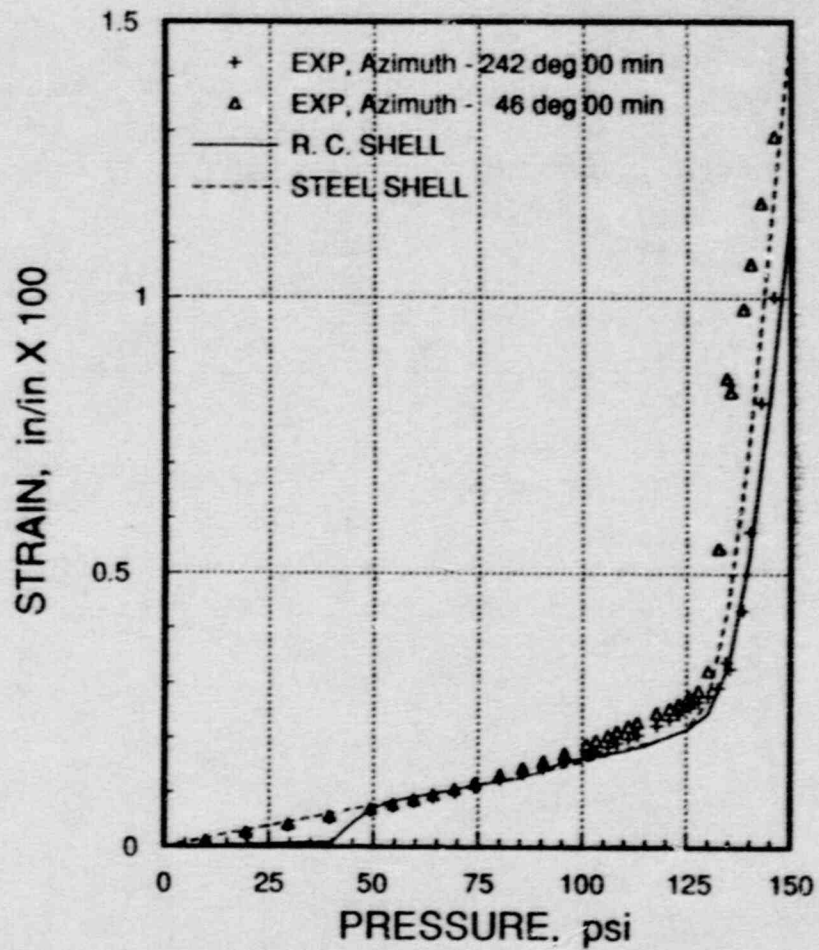


Figure 5.2.42
Hoop Rebar Strain at EL 19.1 ft
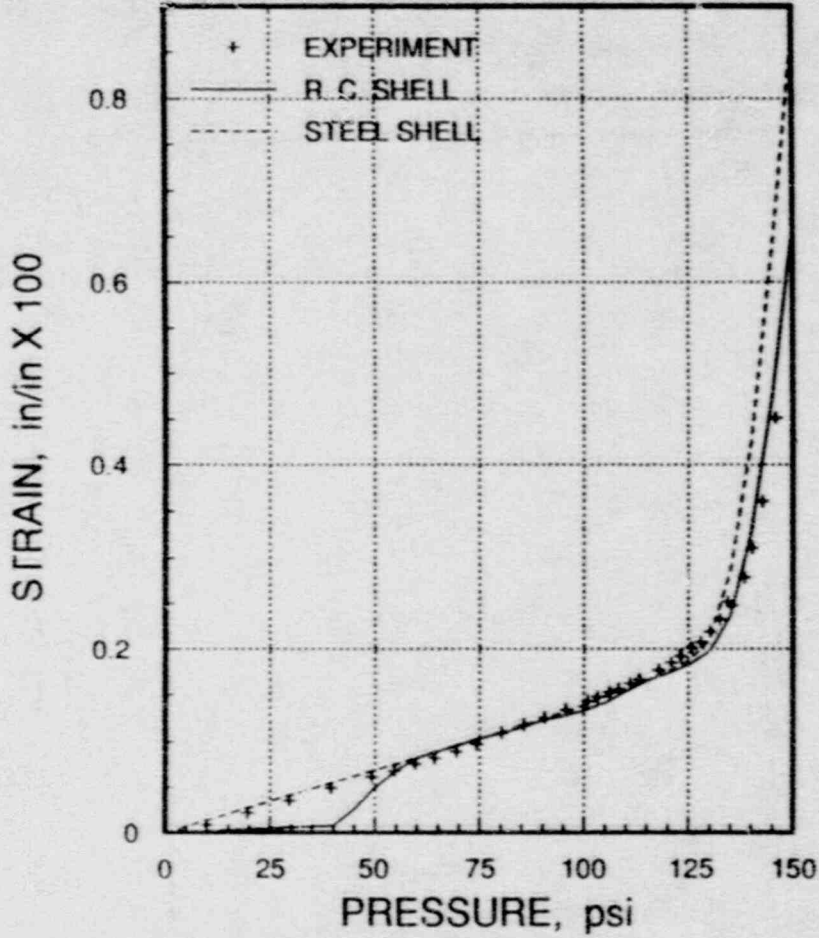
Figure 5.2.43
Hoop Rebar Strain at EL 21.9 ft
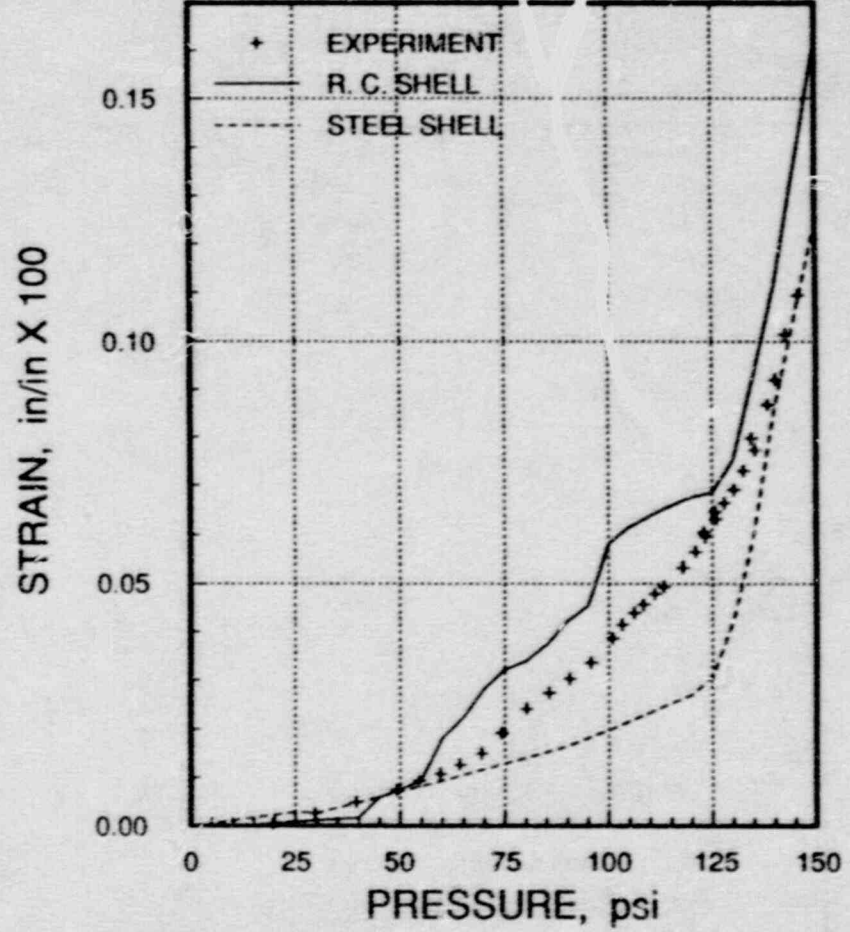
Figure 5.2.44
Meridional Rebar Strain at EL 4.0 ft
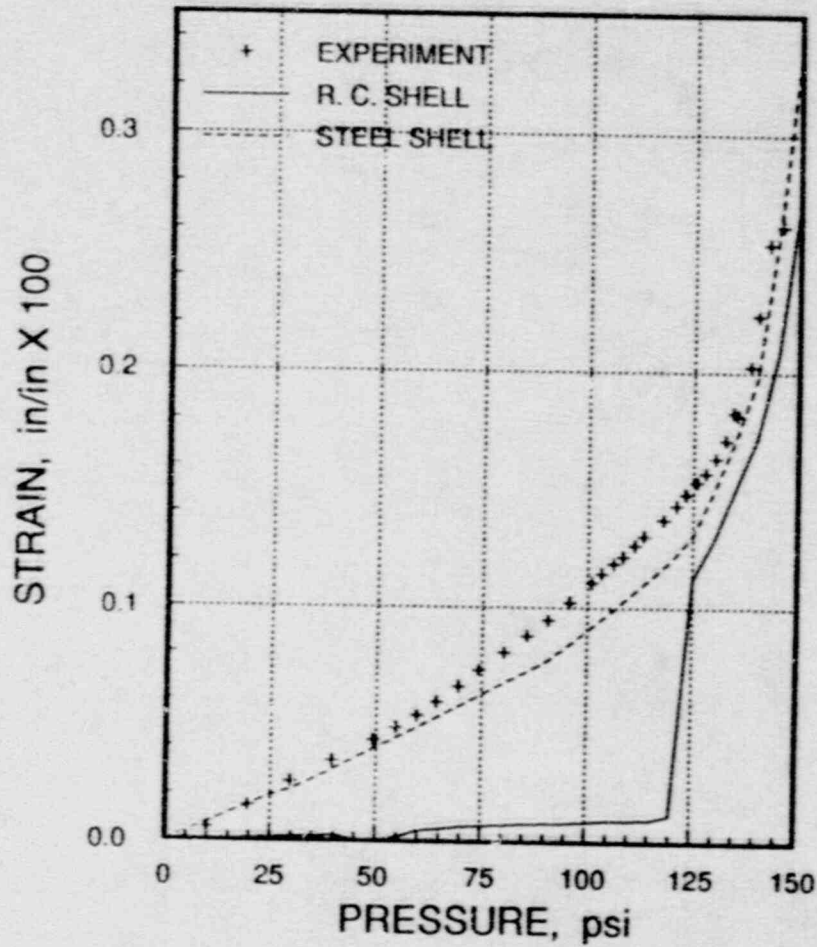
Figure 5.2.45
Meridional Rebar Strain at EL 10.9 ft
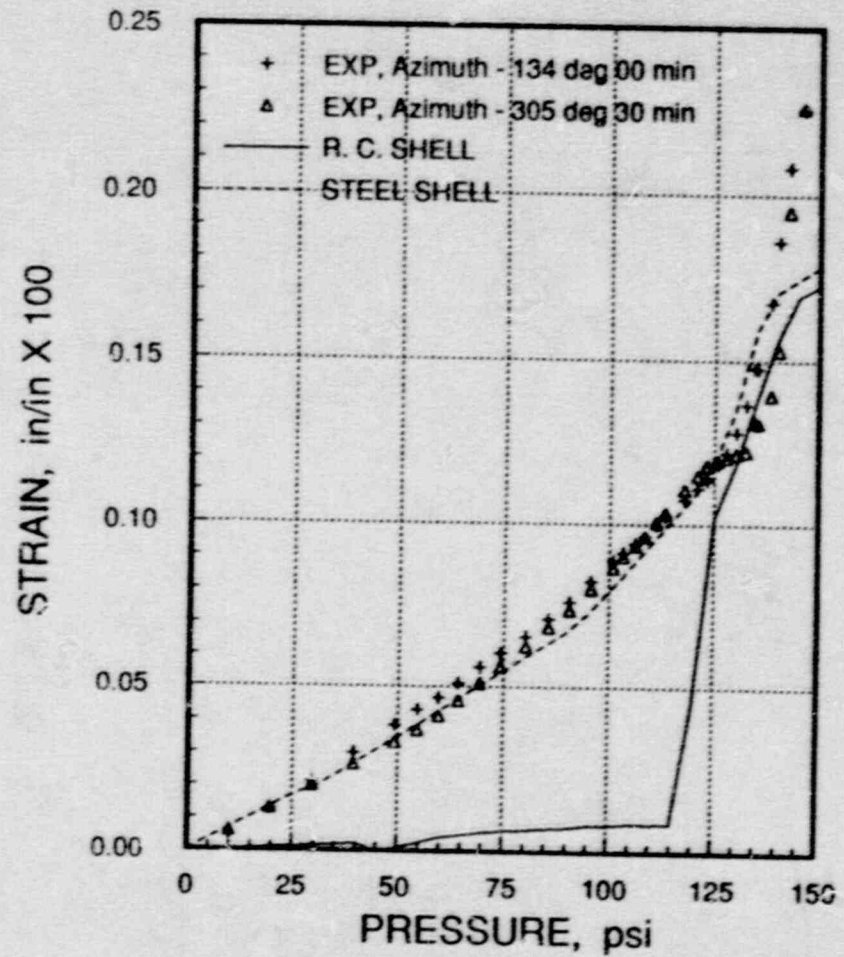


Figure 5.2.46
Meridional Rebar Strain at EL 13.0 ft
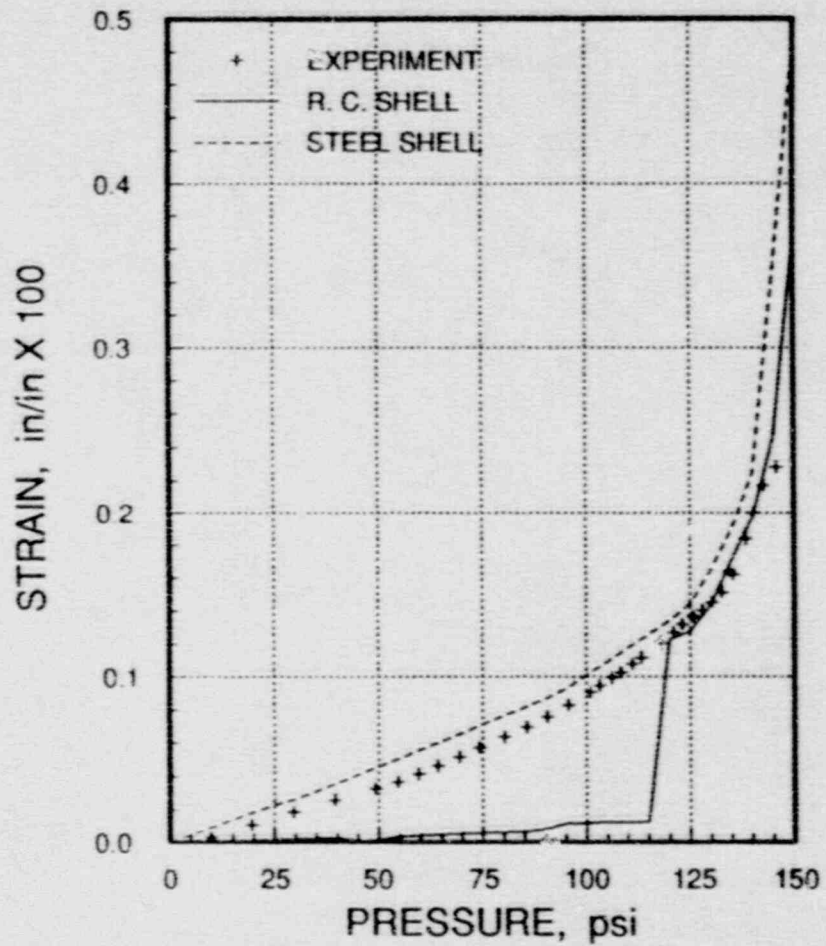
Figure 5.2.47
Meridional Rebar Strain at EL 16.7 ft
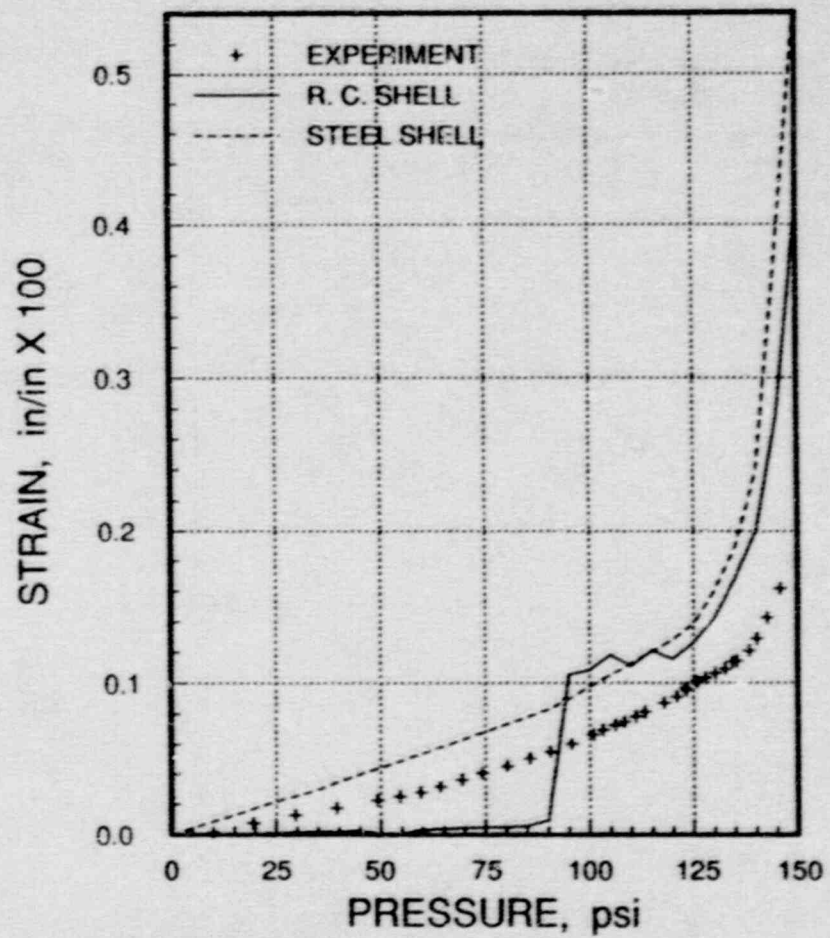
Figure 5.2.48
Meridional Rebar Strain at EL 20.0 ft

5-103
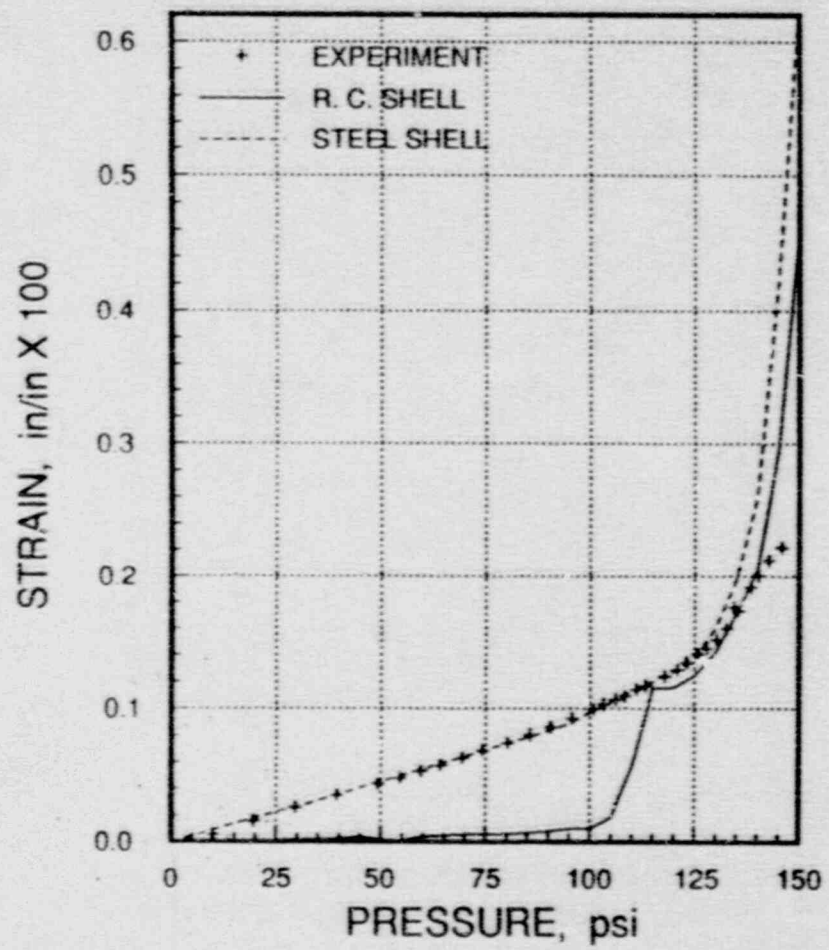
Figure 5.2.49
Meridional Rebar Strain at EL 21.6 ft
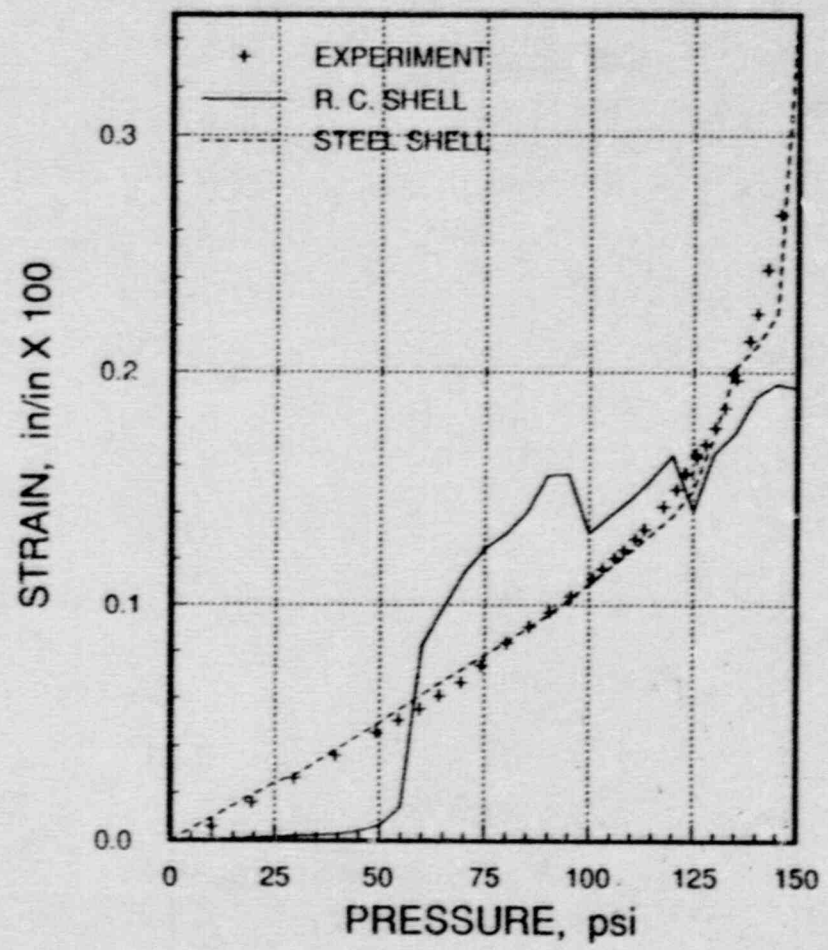


Figure 5.2.50
Meridional Rebar Strain at EL 7.3 ft
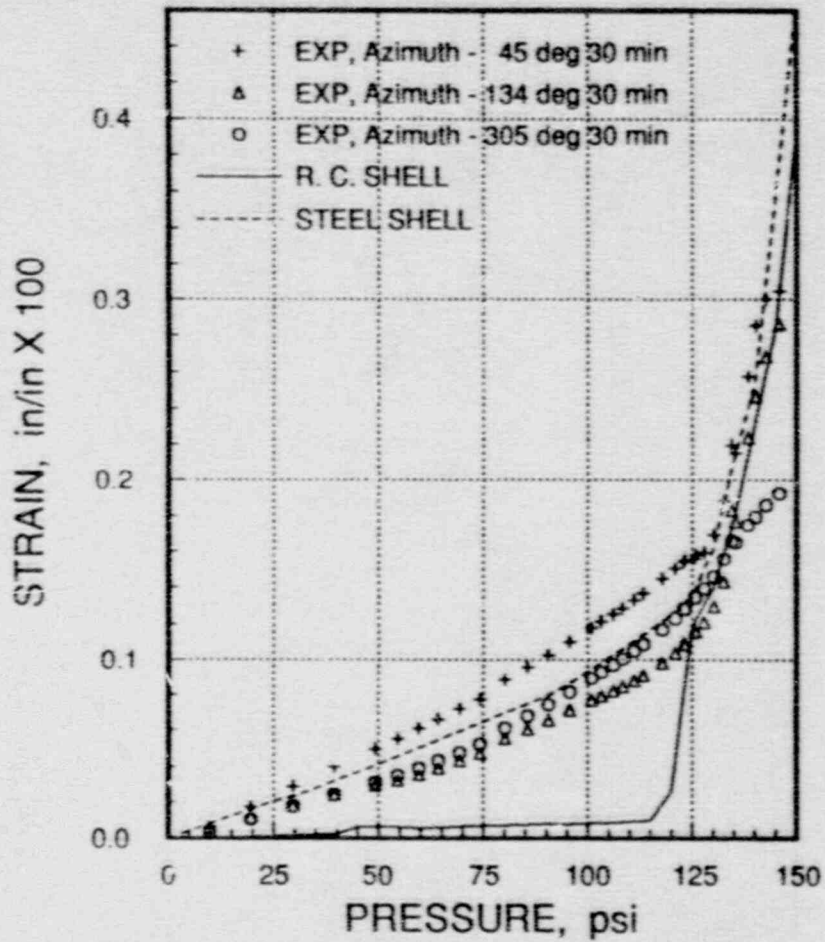
Figure 5.2.51
Meridional Rebar Strain at EL 13.2 ft
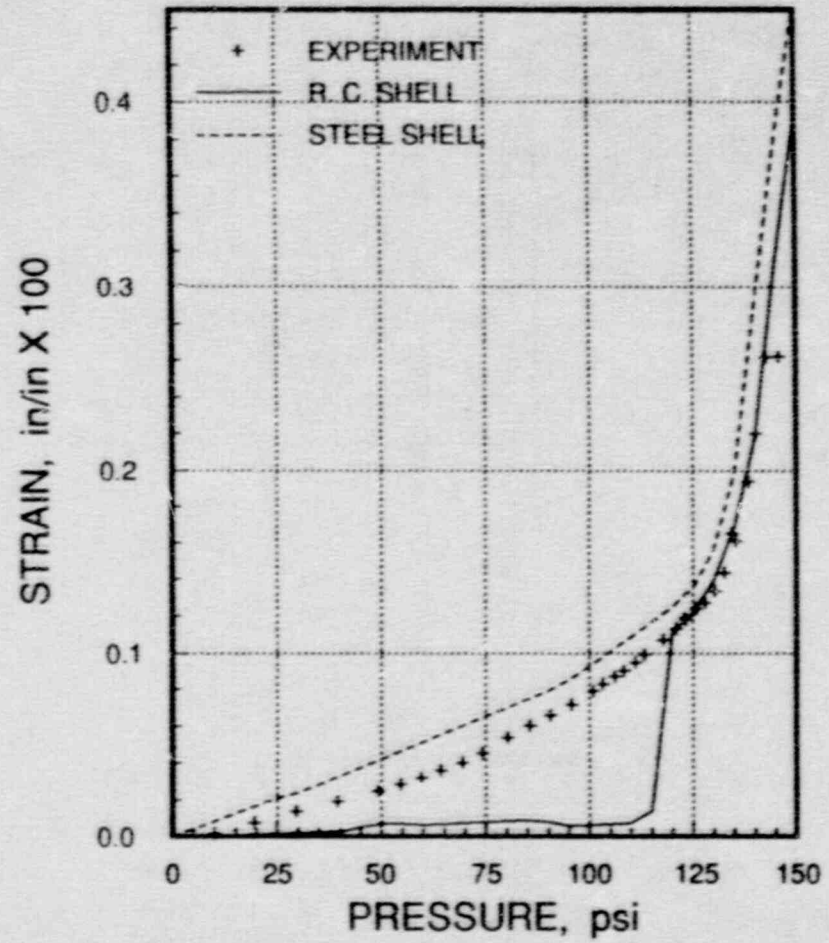


Figure 5.2.52
Meridional Rebar Strain at EL 19.1 ft
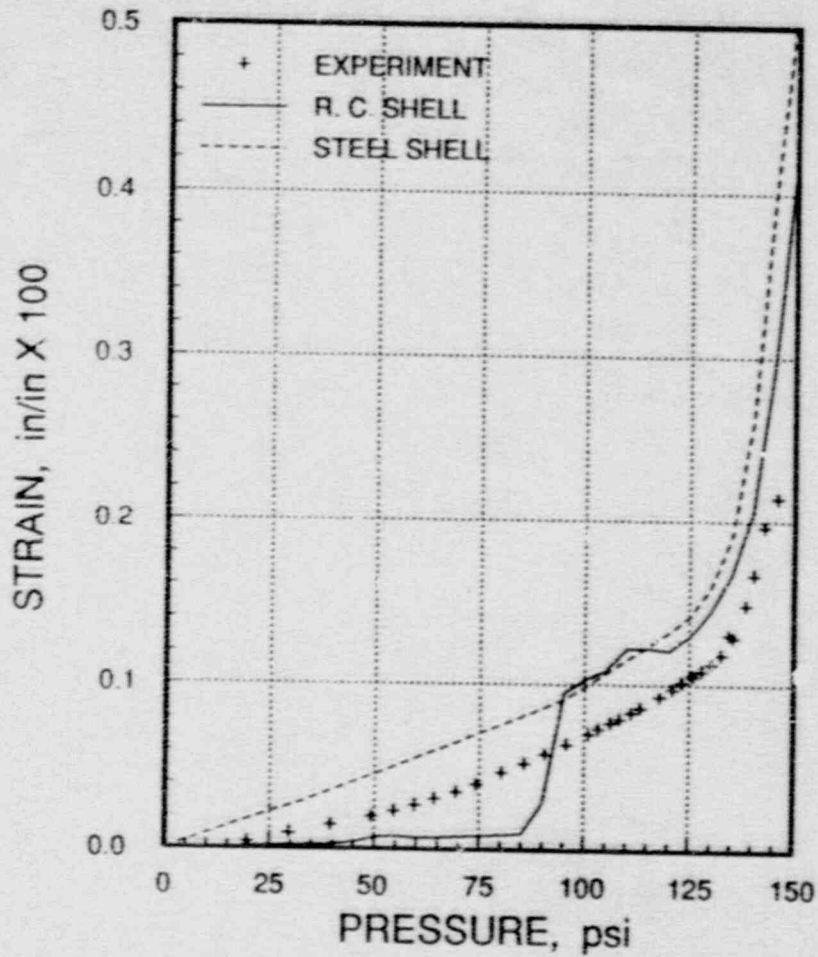
Figure 5.2.53
Meridional Rebar Strain at EL 20.1 ft
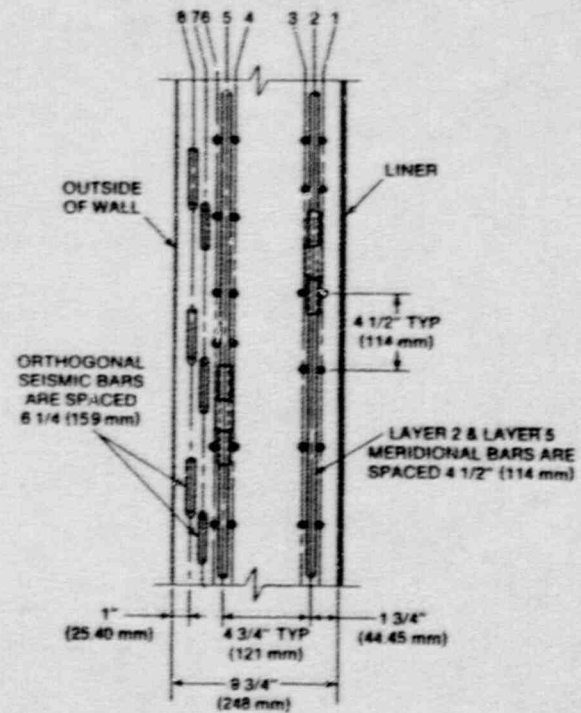


Figure 5.2.54
Reinforcement in the Free-Field Cylinder
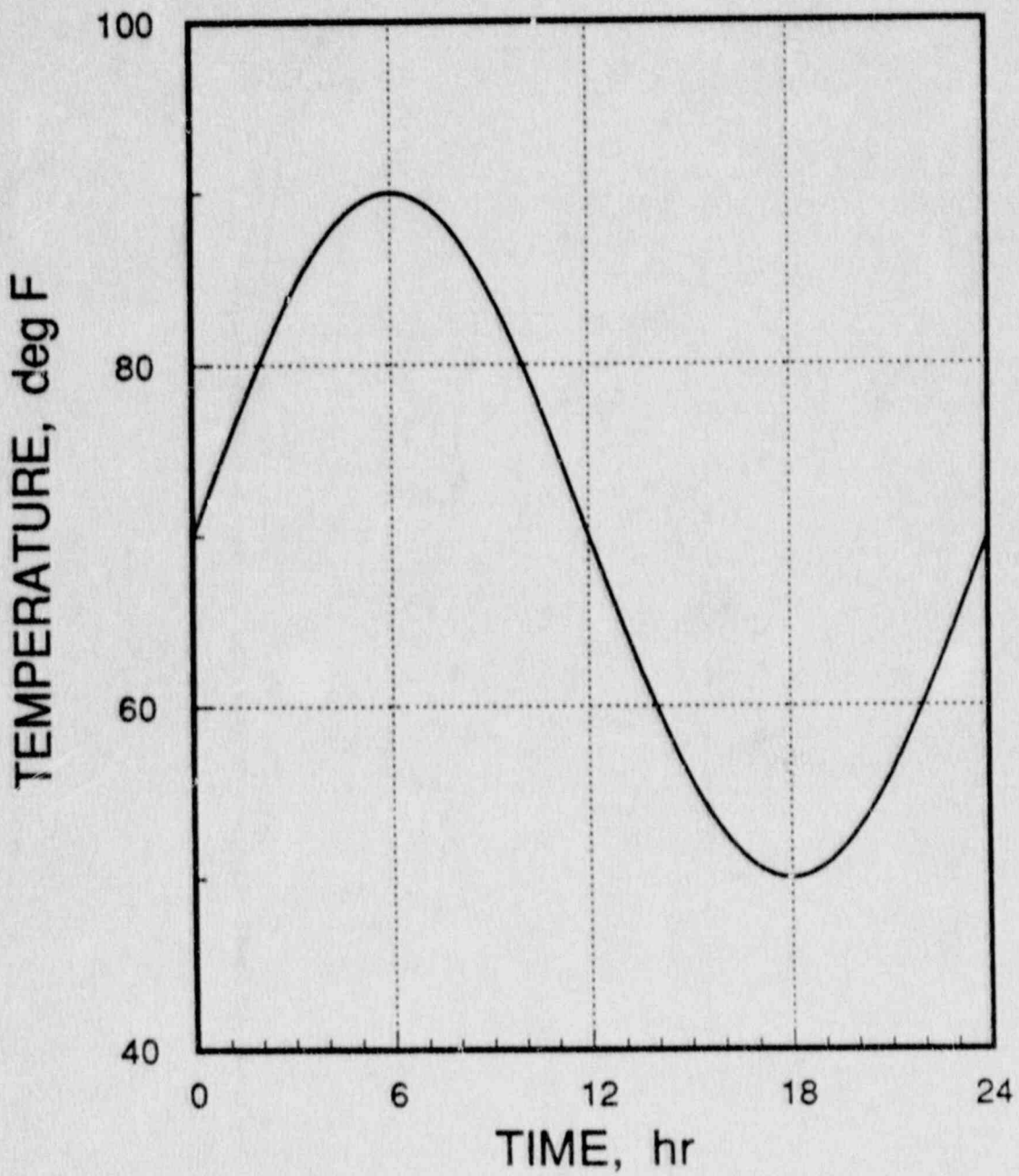
Figure 5.2.55 Prescribed Temperature for Outside Containment Wall

5-107
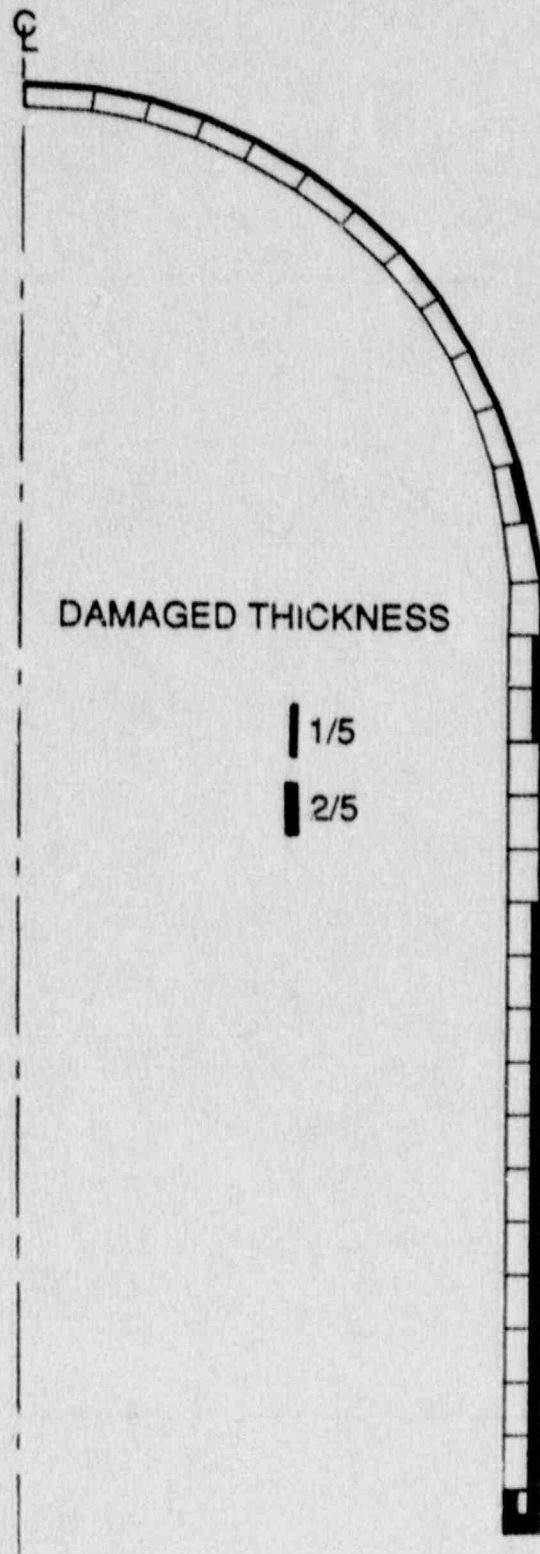
Figure 5.2.56  Damage of Containment Due to One Day Thermal Cycle

5-108

## 5.3 Electric Power Research Institute

This section was prepared by ANATECH Research Corp. (formerly ANATECH International). The principal investigators were R. A. Dameron, R. S. Dunham, Y. R. Rashid, and M. F. Sullaway. The work was conducted for the Nuclear Power Division of the Electric Power Research Institute (EPRI), where the project manager was H. T. Tang.

### 5.3.1 Summary

This EPRI/ANATECH contribution to this report describes work done by ANATECH after the test to compare pretest predictions to measured results, fine-tune analysis techniques based on the measured results, and to study the largest liner tear/leakage location in detail. The text to follow is a condensed version of an EPRI publication [24]. This work represents much of the analysis portion of the Third Phase of EPRI's research program "Methods for Ultimate Load Analysis of Concrete Containments". An important objective of the program was to establish criteria and guidelines for predicting liner tearing and leakage in concrete containments. The development and justification of these guidelines is the topic of the EPRI Third Phase Report [25], in which many of the posttest comparisons made here are described in more detail. In parallel to the development of the leakage prediction methodology, advanced analytical techniques, particularly in the area of 3D continuum modeling, have continued to be developed and compared with experiments. To this end, the Sandia 1:6-scale model has offered a unique opportunity to test these new analytical techniques; the authors of this Section gratefully acknowledge the efforts of all those involved with sponsoring and running the test.

The pretest analysis published in Reference 11 predicted leakage failure and the correct leakage pressure that occurred in the test, namely a leakage pressure range of 140 to 150 psig (0.96 to 1.03 MPa) was predicted, which bracketed the final test pressure of 145 psig (1.0 MPa). The posttest comparisons with experiment that were conducted show good correlation between global results such as cylinder displacements, rebar strains, far-field liner strains, etc. In fact, most of the pretest analysts who participated in the pretest prediction program showed very good agreement in these categories. However, in the bending areas of the cylinder, namely at the springline and at the wall-base juncture, the round-robin pretest predictions showed a wide variation and significant departure from the test results, while ANATECH's predictions generally speaking track the experiment well in these bending regions. It is felt that this demonstrates the validity of the analytical methodology for computing global response components. This is important since the computation of the global response with standardized two-dimensional analysis was a goal of the current research phase, forming the framework for the newly developed EPRI guidelines for predicting containment leakage.

The calculation of local response, on the other hand, is much more difficult, and involves significant labor and computer time intensive efforts to develop and analyze fine local grids with advanced constitutive and material interaction modeling techniques. Several local regions of the 1:6-scale model were analyzed by ANATECH in the pretest work and this resulted in a list of potential liner rupture locations in which the regions horizontally adjacent to thickened liner inserts around penetrations were given a high probability of developing leakage. As can be seen in Figure 5.3.1, these locations agreed with the liner tears that were observed after the

test. The liner-knuckle connection at the wall-base juncture was predicted to tear several psi earlier than at other locations, so it was listed as the location most likely to tear and leak. With the aid of hindsight from the test, the liner tearing criteria has since been modified to require membrane strains to exceed the tearing criteria rather than bending strains; the predicted tear at this location was based on a very localized bending strain at the knuckle (on the order of 6 to 7%), while membrane strain remained less than 1%. At the same pressure, the pretest analysis predicted some local liner membrane strains to reach between 4 and 6%. Based on a membrane strain tearing criteria, these locations become the most likely candidates for liner tearing and this was exhibited in the test. The current work looks into the local liner tearing in further detail including a 3D local analysis of the mechanical/electrical feedthrough penetration where the largest tear occurred.

The two global response parameters that showed significant variation among analysts (including ANATECH) and between analyses and experiment are the effect of the concrete tensile strength cutoff and basemat uplift response. At lower pressures (below 100 psig, 0.69 MPa), where the concrete tensile strength significantly affects the response, most analyses overpredicted the strength of the concrete in tension. The calculated quantities such as hoop rebar strain and radial displacement typically show a sharp jump when the concrete cylinder cracks (between 40 and 50 psig, 0.28 and 0.34 MPa), but test gages did not show this sharp jump. Analysis predicts very small early response for displacement, rebar strain, etc. in the uncracked structure; then all the curves jump and match the measured data after the analytically predicted cracking occurs. The measured data would indicate that the structure makes a smoother transition in stiffness from the before-cracked to the after-cracked response. Reasons that have been put forth for this include (1) low in-situ concrete cracking strength, (2) pre-existing micro-cracks due to curing conditions and exposure to weather, (3) close bar spacing and small amounts of cover over outer bars causing pre-cracking during curing, and 4) small bars (1/2 in. (12.7 mm) diameter) susceptible to a loss of bond in a purely tension structure. All four reasons contribute to the phenomenon, but the cracking strength is the only adjustable parameter which can be incorporated into the constitutive model. Moreover, in ANATECH's view a constitutive model for use with general purpose finite element codes should deal only with plain concrete in order to separate the constitutive modeling from the modeling complexity associated with the concrete/reinforcement interaction. Accounting for bond strength, pre-cracking due to curing and crack/bar interaction requires special constitutive formulation of the bond characteristics which depend on bar sizes, bar spacings, and development length (the length required to develop the full strength of the bar through rebar to concrete bond stress). This level of modeling becomes impractical for global analysis, although it has been attempted for special local effects earlier in the EPRI research program [26,28]). Concrete strength, on the other hand, can easily be adjusted to better match the experimental results, and there is much experimental evidence supporting the occurrence of low in-situ concrete tensile strengths. Taking these results into consideration, a cracking strain of $50 \times 10^{-6}$ in/in was chosen as a best estimate for the actual in-situ concrete cracking strain in the test. With this input to the constitutive model, posttest axisymmetric analysis produced improved correlation of global response in the low pressure range, including basemat uplift.

Basemat uplift was investigated with a series of posttest correlation analyses that demonstrate the sensitivity of this response component to various parameters. It is important to note, however, that the behavior of the cylinder at high pressure, including liner tearing and leakage near the penetrations, was largely unaffected by

fine-tuning the basemat parameters. The first discrepancy in the pretest grid that was rectified was to add the 12 in. (0.3 m) thick unreinforced fill slab[6], which was previously ignored on the basis that an unbonded, unreinforced concrete layer would not contribute significantly to the basemat bending stiffness. In the posttest analyses, this slab was included by way of an interface layer facilitated through ANATECH's UMAT (use of UMAT and the EPRI-sponsored finite element code, ABAQUS-EPGEN is described in the pretest report [11]). The interface layer was given the same properties as ordinary concrete, except that cracks were introduced in the plane of the interface a priori. The next modeling parameter subject to varying interpretation was soil stiffness. It was found by varying this parameter that softer soil causes uplift to occur 10 to 15 psi (0.07 to 0.10 MPa) earlier than with stiffer soil. However, by far the most significant improvement to basemat uplift prediction was to lower the concrete tensile strength for the reasons cited above. Progressive reduction in concrete cracking strain caused the uplift to turn up at lower and lower pressures. With $\epsilon_{cr} = 50 \times 10^{-6}$, the uplift turned up at around 72 psig (0.5 MPa), and this curve matched the measured results the best.

Because of the major hatches that were located every 90° at the cylinder mid-height, the model showed behavior that varied significantly with azimuth (measured around the model's circumference). Displacements were somewhat less at the heavily reinforced hatches than the free-field containment wall. Liner strains also showed wide variations with azimuth because of varying effects from the hatches in the four quadrants. At the end of the test (145 psig (1.0 MPa) pressure), the measured free-field strains in the four quadrants ranged from 0.8% to 2%. These results clearly demonstrate the inadequacy of axisymmetric analysis alone to predict the variation of response around the circumference, and comparisons are made between the test and the 3D pretest global quarter model that was used to drive local submodels with displacement boundary conditions.

Important correlations have been made between the liner strain measurements and the local 3D predictions near penetrations which have helped validate the liner strain concentration factors being used in EPRI's concrete containment leakage prediction criteria. Gage locations did not always coincide with peaks of strain concentrations, but in some cases illustrated herein, gage placement was such that the experimental data could be used to establish general strain concentration trends and to validate the analysis.

A final posttest study was performed for a grid that was similar to the pretest local effects grids, but that was much finer than before in the peak strain region. The latest grid also utilized discrete stud modeling and an interface element layer to allow the liner-concrete-stud interaction to enter into the results. The grid is a local quarter model of the mechanical/electrical feedthrough penetration cluster. The analysis shows sharp strain concentration in the first two inches out from the edge of the insert plate, which coincides with the long tear that occurred in the experiment, and it further validates the conclusions from the pretest local analyses which showed similar strain concentrations. The analysis also showed locally elevated strains at the first welded stud line adjacent to the 3/16 in. (4.76 mm) insert, but it is not felt that the

---

6. After the analysis was completed, it was realized that the fill slab is actually mildly reinforced. However, this would not be expected to change the results significantly because the fill slab is in compression and therefore almost all its stiffness is due to the concrete.

studs by themselves caused the tear; however, within a region of generally high local strain, they may have directed the tear, i.e., from stud to stud. Strain contours developed from the analysis show that the strain field is constant all along the edge of the insert, making it easy for a small tear to propagate until reaching a lower strain field near the corners of the insert. This is consistent with what was observed in the test.

A vast amount of information has been compiled as a result of the 1:6-scale model test for analysis code validation and for assessing reinforced concrete containment response to overpressure conditions. Experimental verification of the notion that concrete containments leak before they burst catastrophically was an important objective that was realized. For ANATECH's analytical support of the test, the research has been valuable in verifying the EPRI-sponsored concrete containment leakage prediction criteria that have been developed. In terms of general analytical lessons learned from this work, it has been shown that, because of insufficient grid refinement, 2D models alone cannot predict the detailed response and the local liner behavior near stiffness discontinuities in the structure, and highly detailed 3D models are much better suited for this purpose. Further, two-dimensional analysis can be significantly improved by using a detailed concrete model with a verifiable in-situ concrete tensile strength and by following certain guidelines that have been established in the EPRI research for grid density and other modeling parameters.

### 5.3.2 Introduction

During the EPRI research program, the concrete analysis methodology that has been developed has continued to be refined and extended to more challenging problems and complex computational grids. The first analyses [26] modeled simple panel specimens without liner plate as tested at Construction Technology Laboratories [27] in order to validate the newly developed concrete constitutive model. In Phase 2 of the program [28], the methodology was extended to more complex laboratory specimens with liners, stiffness discontinuities and penetrations [29] and to global containment analysis of typical reinforced and prestressed concrete containments subjected to overpressure and to various temperature/pressure combinations. Detailed enhancements to the concrete model were made to investigate liner-concrete and rebar-concrete interaction and their effect on liner tearing mechanisms. Extensive analytical support was provided for various specimen tests. All of these analyses, however, were performed in two dimensions. It was not until a detailed investigation of all aspects of a particular containment was required that three-dimensional analysis became a necessity. Of course, this computational advancement carries with it a manyfold increase in grid development time and computation time.

Three-dimensional modeling was undertaken because of the challenge presented by the Sandia 1:6-scale model. While analyses of containment prototypes had been conducted before, never had comprehensive detailed prediction calculations been performed for an as-built structure with the recently developed methodology. The posttest work described herein builds on what was reported in the pretest study and therefore begins by comparing the pretest results with test results. The new analyses include a 2D global parameter study to assess the sensitivity of concrete tensile strength and other parameters, and a detailed 3D analysis of the mechanical/electrical feedthrough penetration. All analytical tools, namely ABAQUS-EPGEN with ANATECH's UMAT concrete model are the same as those described in the pretest work, so this information need not be repeated here.

### 5.3.3 Pretest Analyses Compared with 1:6-Scale Model Results

### 5.3.3.1 General Conclusions from Posttest Inspection

Upon posttest inspection, many small tears were discovered in addition to the one large tear; they were all located in the narrow strain concentration region associated with penetrations, as predicted by ANATECH in pretest local effects analyses. (See Figure 5.3.1 introduced in the summary section). The cause of the strain concentrations appears to be due partly to the change in liner thickness that occurs next to the liner insert plates and partly due to out-of-plane dislocation motion through the thickness of the liner due to the difference in wall and liner stiffness at the penetrations compared to away from the penetrations. The latter effect causes shearing strains, and this was evidenced in ANATECH's pretest and posttest analyses. At the largest tear adjacent to the mechanical/electrical feedthrough penetration, there is a set difference in radial displacement of about 1/4 in. (6.4 mm) or 4 liner thicknesses across the tear, with the free-field side of the tear showing the larger radial displacement than the penetration side. However, this may simply be a product of unloading behavior and may only show the trend of differential radial displacement rather than a measure of the total dislocation. The liner appears to have buckled and shifted somewhat upon unloading.

At 140 psig (0.97 MPa), the total measured leakage has been reported to be 13% mass/day. Between 140 and 145 psig (0.97 and 1.0 MPa), leakage measurements of 234% mass/day and 354% mass/day were recorded. By holding the pressure as steady as possible at 145 psig (1.0 MPa) for approximately one hour and continuing to increase the pumping rate, the large (22 in. (0.56 m) long) tear next to the mechanical/electrical feedthrough combined with other smaller tears caused leakage to become very large (approximately 4000 scfm of nitrogen). In ANATECH's view, the large increase in leakage after 140 psig (0.97 MPa), posttest examinations of the liner, and local leak rate tests conducted by Sandia tend to support the conclusion that all the liner tears occurred between 140 and 145 psig (0.97 and 1.0 MPa), and that minor leakage below 140 psig (0.97 MPa) can probably be attributed to leakage through hatch seals.

All of the tears near penetrations and corresponding high strain locations predicted by analysis occur just outside of the thickened liner except at equipment hatch B. There, the highest calculated and measured strain occurs at the root of the embossed concrete due to the liner attempting to straighten itself across a corner. (Note, equipment hatch A and the personnel airlocks have embossed concrete on the outside only, so liner corners do not exist at those locations.) The only structural components acting to prevent this motion are the studs, and with this liner deformation they are subjected to direct pullout. This is offered as an explanation of why the tears near hatch B appear to be more of a puncture related to stud pullout rather than an extensional tear. The analysis of this region predicts elevated strain at this liner corner, but not as high as the strains near other penetrations. However, the 3D pretest analyses did not model the studs discretely, so this puncturing action that was exhibited would not be predicted by the analysis. The other tear locations appear to be true extensional tears caused by the liner being stretched to its ductility limit. However, the long tear at the mechanical/electrical feedthrough appears to have run from stud to stud. Thus, the studs may act as very localized strain risers. Posttest analysis described herein and an independent analysis performed at Sandia (described earlier in this report) demonstrate the very localized strain around the base of studs. However, ANATECH feels that the studs in these locations are not

the direct cause of the tearing; rather, their presence vis-a-vis positive liner anchorage is a necessary condition for the large strain field to occur at points of differential radial displacement.

The conditions for liner tearing that the EPRI leakage criteria attempts to predict are large peak strains which occur irrespective of studs, provided that positive liner anchorage exists to concentrate the strain. Therefore, the addition to the strain field of very localized stud effects around the root of the stud is not addressed by these criteria, nor can it be with the experimental evidence that is currently available. For the purposes of these criteria, this eliminates the questions that arise regarding the adequacy of the stud scaling in the 1:6-scale model. Clearly, the studs that were chosen provided enough anchorage to elevate the strain and cause tearing mechanisms to occur, similar to tears that have also been demonstrated by analysis.

### 5.3.3.2 Two-Dimensional Axisymmetric Analysis Comparisons

As described in the pretest report, 2D global pretest analyses consisted of an axisymmetric grid convergence study and several axisymmetric grids. The computational grid is shown in Figure 5.3.2 to support the pretest analysis comparison discussion and the posttest analysis discussion. Detailed description of grid development and convergence studies may be found in References 11 and 24. Concrete was modeled with 8-node axisymmetric continuum elements (3 elements through the wall thickness), rebar with ABAQUS *REBAR sub-elements, and the liner with 3-node shell elements. The basemat-soil interface was modeled using nonlinear no-tension springs.

Several quantities and locations have been selected for comparison with experiment from the set of standardized prediction plots requested by Sandia early in 1987. The few plots presented in the allowed space are not necessarily those with the "best fit", but they are a variety of quantities and locations to present an overview of global response comparison. Figure 5.3.1 also shows the locations of the comparisons and serves as a reference chart for the figures that follow. Each figure shows the experimental measurements of the High Pressure Test (HPT) shown as crosses (+) and the pretest prediction shown as a line. Figure numbers, locations, and quantities are given below. Units are indicated on the plots.

| Figure # | Quantity | Location |
|---|---|---|
| 5.3.3 | Radial Displacement | z = 11 ft |
| 5.3.4 | Vertical Displacement Relative to Basemat | z = 11 ft |
| 5.3.5 | Radial Displacement | z = 18 ft |
| 5.3.6 | Maximum Principal Inside Surface Liner Strain | z = 13.75 ft, $\theta$ = 45° |
| 5.3.7 | Axial Strain Layer 6 Hoop Rebar | z = 13.75 ft, $\theta$ = 45° |
| 5.3.8 | Maximum Principal Inside Surface Liner Strain | z = 22 ft, $\theta$ = 45° (springline) |
| 5.3.9 | Axial Strain Layer 8 Seismic Bar | z = 22 ft, $\theta$ = 45° (springline) |
| 5.3.10 | Maximum Principal Inside Surface Liner Strain | $\phi$ = 72°, $\theta$ = 90° (dome) |
| 5.3.11 | Axial Strain Layer 5 Meridional Rebar | $\phi$ = 72°, $\theta$ = 90° (dome) |

The agreement for these global results quantities is generally good. Most of the computed quantities show a significantly stiffer structure prior to concrete cracking than was exhibited in the experiment; therefore, there is consistent deviation of the measured and computed values below 50 to 60 psig (0.34 to 0.41 MPa). This aspect of response is explored in detail in the next subsection. In the high pressure range, which is felt to be the most important part of the response, the strains and displacements were predicted very well. Comparison of basemat uplift has been left out of this set of plots since it is also a subsection topic.

The computed radial and vertical displacements of the shell wall (Figures 5.3.3 to 5.3.5) generally lag the measured response by 5 to 10 psi (0.03 to 0.07 MPa). This observation can also be made for most of the other pretest analyst's predictions. Since this is consistently true for vertical and horizontal displacements, but not for rebar or liner strains, the explanation may lie in the displacement measurement technique. The shapes of the curves are still reasonably close. Rebar and liner strains show very good agreement at the cylinder midheight (Figures 5.3.6 and 5.3.7) and at the springline (Figures 5.3.8 and 5.3.9). This not only validates the constitutive model and computational grid but also the ABAQUS-EPGEN plasticity algorithm and the nonlinear material data that was input for the various steels based on Sandia's coupon tests. Global quantities in the dome (Figures 5.3.10 and 5.3.11) are more susceptible to the influence of the apparently low concrete tensile strength discrepancy as mentioned earlier in this section, and this is evidenced in the comparison plots.

The global comparisons are very encouraging for validation of the containment global analysis guidelines that have been established in EPRI's leakage criteria development report [25].

### 5.3.3.3 Investigation of Effects of Varying Concrete Tensile Strength

As was seen in the previous discussion, global response parameters predicted by pretest analyses matched the measured response very well at high pressures. However, at lower pressures (below 100 psig, 0.69 MPa), where the concrete tensile strength significantly affects the response, most analyses, including ANATECH's, overpredicted the strength of the concrete in tension. The calculated quantities such as hoop rebar strain and radial displacement typically show a sharp jump when the concrete cylinder cracks between 40 and 50 psig (0.34 and 0.41 MPa), but test gages did not show this sharp jump. Consider, for example, the low pressure portions of Figures 5.3.7 and 5.3.9 as illustrated in Figures 5.3.12 and 5.3.13. The crosses are the high pressure test (HPT) gage data, as before, and the triangles are the same gages from the Structural Integrity or Low Pressure Test (SIT). The reason for including both is that the SIT is assumed to begin with an uncracked structure, but the SIT itself goes beyond hoop cracking. Thus, the HPT begins with a cracked structure. It should be noted, however, that the gages were all "re-zeroed" after the SIT, so comparisons of the SIT with the HPT should be made with caution.

The analysis concrete material properties were chosen based on standardized test data, reported by Sandia [11].

$f_c'$ = 6500 psi (44.8 MPa)
$E$ = 4.8x10$^6$ psi (33 GPa)

$\nu$ = 0.2
$f_t$ = 500 psi (3.45 MPa), maximum tensile stress

Using $f_t$ = 500 psi (3.45 MPa) and E = 4.8x10$^6$ psi (33 GPa) gave a tension cutoff strain of $\epsilon_{cr}$ = 105x10$^{-6}$ in/in

$\epsilon_{cr}$ is the primary tensile strength input parameter to the concrete model developed by ANATECH for use with ABAQUS. The stress vs. strain failure surface also predicts cracking based on the strength cutoff, $f_t$; this depends on the stress and strain state in the problem.

In Figures 5.3.12 through 5.3.14, $\epsilon_{cr}$ = 105x10$^{-6}$ corresponds to the dashed line, which was the pretest analysis result. These figures and the previous figures (5.3.3 through 5.3.11) show that analysis predicts very small early response for rebar strain, etc. in the uncracked structure; then all the curves jump and match the measured data after the analytically predicted cracking occurs. The measured data would indicate that the structure makes a smoother transition in stiffness from the before-cracked to the after-cracked response. Possible reasons for this behavior that have been collectively put forth by the pretest analysts include:

1.   The cracking strength (and strain) of the in-situ concrete is lower than that measured by cylinder tests.

2.   The concrete in the model may contain micro-cracks due to curing conditions and exposure to weather, whereas cylinders cured in a controlled environment would not.

3.   The close bar spacing and the small amount of cover over the outer bars in the model may have caused pre-cracking during curing due to the bars themselves. Some surface micro-cracks were reported at 45° angles (the orientation of the outer seismic bars) prior to either pressure test. This argument is particularly important to evaluate since it would probably not occur in a full scale containment where spacing and cover are comparatively very large.

4.   The small bars (1/2 in. (12.7 mm) diameter) are susceptible to a loss of bond in a purely tension structure. This also would be prevalent in the scale model rather than at full scale. This is a particularly strong argument to explain the lack of a sharp meridional cracking cutoff. The existence of the meridional bars at 4.5 in. (0.11 m) intervals serve as hoop crack (vertically oriented cracks) initiators, so hoop cracking would coincide with the meridional bars. Given this condition, as the hoop cracks open up, the meridional bars begin to lose bond. The development of bond stress is a gradual process, hence, so is the development of bar stress. This would result in a gradual stiffness change from a fully bonded condition where the bar stress is a function of the effectiveness of the bond to a fully cracked condition where the bar stress is independent of the bond. This behavior is apparent in the structure and cannot be predicted in analyses that do not account for bond stress history.

ANATECH attributes the phenomenon to all four reasons, but in particular to reasons 1 and 4. However, ANATECH's ultimate goal is to incorporate this experience into a reinforced concrete analysis methodology as has been done in the

leakage criteria development report [25]; hence, the cracking strength (or strain) is the only adjustable parameter which can be incorporated into the constitutive model. It is important to point out in this regard that a constitutive model for use with general purpose finite element codes should deal only with plain concrete in order to separate from the constitutive modeling the modeling complexity associated with the concrete/reinforcement interaction. Accounting for bond strength, pre-cracking due to curing, and crack/rebar interaction requires special constitutive formulation of the bond characteristics which depend on bar sizes, bar spacings, and development length (the length required to develop bar stress through rebar to concrete bond stress), and this level of modeling becomes impractical for global analysis.

On the other hand, concrete strength can easily be adjusted to better match the experimental results, and there is much experimental evidence that supports the occurrence of low in-situ concrete strengths. Raphael demonstrated in a study of concrete tensile strength in concrete gravity dams that in-situ tensile strengths were actually about half of the usual assumption of $0.1f_c'$ [30]. He points out three typical causes for the occurrence of lower tensile strengths than that measured in test cylinders. (It should be noted that his findings are for plain concrete without rebar.) First, curing conditions for the actual structure are different than the cylinders that are poured at time of construction. Part drying and exposure to weather have adverse effects on tensile strength. Second, basing tensile strength estimates on cylinder splitting tests can produce results that are too high, even accounting for the usual knockdown factors applied to split cylinder data. Split cylinder tests are normally used because the cylinder sample is the same as that used for the compressive tests, and the data has much less scatter than typical direct tension tests of unreinforced concrete samples. While textbooks such as Reference 31 advise that direct tension tests produce tensile strengths of 75% to 80% of split cylinder tests because of the mechanics of the stress state in the test, Raphael gives data that shows that in laboratory direct tension tests where sample end effects are carefully controlled, direct tension strengths can be as low as half that of split cylinder results. For the round-robin pretest analyses, both types of tests were used to choose the $f_t = 500$ psi (3.45 MPa); however, Raphael's work would suggest choosing a much lower number. The third effect involves the duration of the test. Loading rates seem to have an even larger effect on tensile strength than on compressive strength. Most split cylinder tests are conducted on the order of seconds, but tests extended to hundreds of seconds can give significantly lower tensile strengths.

Taking these results into consideration, a cracking strain ($\epsilon_{cr}$) of $50 \times 10^{-6}$ in/in was chosen as a best estimate for the actual in-situ concrete cracking strain that existed in the model at the time of the test. With this input to the constitutive model, posttest axisymmetric analysis produced the solid curves in Figures 5.3.12 through 5.3.14. The most significant improvement occurs for meridional response as can be seen in Figure 5.3.14 showing meridional rebar strain. Since meridional cracking occurs later than hoop cracking (i.e., ideal elastic cylinder meridional stress is 1/2 that of elastic cylinder hoop stress), the shift in cracking pressure is more significant. Low pressure response in the dome was also significantly improved by using the lower cracking strain. The effect on the basemat response was the most significant of all, as will be seen in the paragraphs below. The remaining variance between analysis and experiment below 30 psig (0.21 MPa) is attributed to pre-existing cracking for the reasons (numbered 1 to 4) cited previously. While one may argue that the test results might be matched even better with zero tensile strength concrete, many full-scale panel tests in the EPRI-sponsored test program [27,29] gave results that show a sharp jump in response related to cracking; there, the cracking model tracked experimental

results very closely. It is felt that any further modifications to the model to match the 1:6-scale model results would be an overspecialization of a general purpose concrete model.

### 5.3.3.4 Basemat Uplift Behavior and Soil Stiffness Sensitivity

Basemat uplift was significantly overpredicted by many of the pretest predictions including ANATECH's. It has been the topic of many of the posttest discussions including SMiRT 9 Session J, the November 1987 posttest meeting at Sandia, and the 4th Containment Integrity Workshop. The pretest predictions of the ten organizations who participated in [11] are all shown compared to the measured value in Figure 5.3.15. The curve patterns for each organization are indicated, but it is not intended to judge any of the predictions on this basis; the importance of the figure is to show the scatter in the predictions for this particular quantity. There was generally very little scatter for the prediction of many global response parameters in the cylinder, such as radial displacement and hoop rebar strain, but because the basemat uplift quantity showed widely varying analysis results, it was investigated by ANATECH with a series of posttest correlation analyses that demonstrate the sensitivity of this response component to various parameters. It should be stated at the outset, however, that the behavior of the cylinder at high pressure, including liner tearing and leakage near the penetrations, was unaffected by fine-tuning the basemat parameters. The axisymmetric grid used for these analyses was shown in Figure 5.3.2, and an enlarged view of the basemat modeling is shown in Figure 5.3.16. The measured basemat uplift is plotted compared to the results of five different ANATECH analyses with varying treatments of the basemat in Figure 5.3.17. The parameters that were varied in this study are outlined in Table 5.3.1 to help identify the curves in the figure.

Table 5.3.1 : Basemat Edge Displacement Labeling
(See Figure 5.3.17)

| Curve Number | 12 in. Fill Slab Modeled | Foundation Stiffness (ksf/ft) | Concrete Tensile Cracking Strain |
|---|---|---|---|
| 1 | -------------- Experimental Results ---------------- | | |
| 2 | No | 13,400 | $105 \times 10^{-6}$ |
| 3 | Yes | 13,400 | $105 \times 10^{-6}$ |
| 4 | Yes | 1,340 | $70 \times 10^{-6}$ |
| 5 | Yes | 1,340 | $50 \times 10^{-6}$ |
| 6 | Yes | 1,340 | $105 \times 10^{-6}$ |

Basemat uplift occurs because of the upward force exerted by the wall on the outer edge of the mat, which causes radial bending near the center of the mat. The analysis must handle the nonlinear shifting of the contact pattern as it shrinks radially inward along the bottom of the mat. The first discrepancy in the pretest grid that was

rectified was to add the 12 in. (0.3 m) thick unreinforced fill slab (Figure 5.3.16)[7], which was previously ignored on the basis that an unbonded, unreinforced concrete layer would not contribute significantly to the basemat bending stiffness. Curve number 3, which shows large reduction in uplift, includes the 12 in. (0.3 m) concrete layer along with an interface layer facilitated through UMAT with the same properties as ordinary concrete, except that cracks were introduced in the plane of the interface a priori. The interfacial shear friction between the concrete and liner was modeled by limiting the shear stress to:

$$\tau_{max} = 0 \qquad \text{for } \epsilon_n > 0 \text{ or } \sigma_n > 0$$

$$= 50 \text{ psi} \qquad \text{for } -100 < \sigma_n < 0 \text{ psi}$$

$$= |0.5 \sigma_n| \qquad \text{for } \sigma_n < -100 \text{ psi}$$

where $\sigma_n$ and $\epsilon_n$ are the stress and strain normal to the crack; 0.5 is the coefficient of friction. Negative stress or strain represents compression, i.e., stress or strain acting to close the interface. Note that the sign of $\tau_{max}$ is always positive, but $\tau_{max}$ is used as an absolute maximum on shear stress; whether positive or negative, the sign of the shear stress is unchanged. The algorithm for the shear stress subject to the $\tau_{max}$ condition is:

$$\tau < 0 \qquad \tau = \text{MAX}(\tau, -\tau_{max})$$
$$\tau > 0 \qquad \tau = \text{MIN}(\tau, \tau_{max})$$

The shear modulus was also modified as follows:

$$G = E/(1 + \nu) \qquad \text{for } \sigma_n < -100 \text{ psi}$$

$$= |\sigma_n| E/100(1 + \nu) \text{ for } -100 \text{ psi} < \sigma_n < 0$$

$$= 1 \qquad \text{for } \sigma_n > 0$$

The purpose of setting $G = 1$ is to set G to a relatively small number without causing an ill-conditioned stiffness matrix.

The next modeling parameter subject to varying interpretation was soil stiffness. The value reported by the soil testing firm (Western Technology, Inc.) retained by Sandia was 390 ksf/ft (61.26 MPa/m). Since this was recognized as a foundation design value and represents a relatively soft value for analysis, ANATECH's pretest analysis was given a foundation stiffness of 13,400 ksf/ft (2100 MPa/m) based on an assumption of 0.001 in. (0.025 mm) displacement under the structural dead load. This was a convenient assumption for purposes of analysis. The justification for this assumption was based on past experience, which showed that soil stiffness has little effect on the eventual contact pattern of the basemat at high pressure. It is interesting to note that this conclusion is supported by the 1:6-scale model test and the posttest analysis results plotted in Figure 5.3.17 (i.e. by comparing curves 3 and

---

7. After the analysis was completed, it was realized that the fill slab is actually mildly reinforced. However, this would not be expected to change the results significantly because the fill slab is in compression and therefore almost all its stiffness is due to the concrete.

6). It was found that the softer soil causes significant uplift to start 10 to 15 psi (0.07 to 0.10 MPa) earlier than with stiffer soil, but the concrete tensile strength cutoff has a much more significant effect on the results. The soil stiffness for ANATECH's posttest analyses was chosen by re-examining Western Technology's plate test data. The stiffness selected was $K_s$ = 1340 ksf/ft (210 MPa/m), which is 3.4 times the design value and represents a dead load displacement of 0.01 in. (0.25 mm).

The final modification to the analytical model was to lower the concrete tensile strength for reasons discussed in detail in the previous subsection. The reduction in concrete cracking strain caused the uplift to turn up at lower pressures. With $\epsilon_{cr}$ = $70 \times 10^{-6}$, the uplift response turns up at around 95 psig (0.66 MPa). With $\epsilon_{cr}$ = $50 \times 10^{-6}$, the uplift response turns up at around 72 psig (0.5 MPa), and this curve (curve 5) matches the measured results the best. Of the changes that were made, the soil stiffness appears to be the least important, i.e., there is not much change moving from curve 3 to curve 6.

### 5.3.4 Investigation of Wall Base Juncture and Cylinder Wall Bending

This subsection is aimed at discussing the complex subject of bending and shear behavior in the containment cylinder wall. It is complex because not only has shear and bending in concrete structures proved to be difficult to calculate, but it also has been difficult to formulate failure criteria for shearing mechanisms from an analytical and a design code standpoint. At the analytical level, calculation of bending and shear response is a globally driven phenomenon (as opposed to very localized liner tearing) but the mechanics of a bending or shear failure are highly dependent on the numerical representation of the details within the wall section. While smeared computational models have been shown to be very accurate for the "breathing" mode of the shell, they do not provide the detail necessary to model shear and bending at a section. Bending response is captured fairly well by discretizing several concrete elements with individual rebar layers at various depths in the section, as was done by ANATECH for the 1:6-scale model (discussed below). However, the rebars in this model do not alone carry any shear or bending so dowel effects are ignored; in the actual structure, concrete-rebar interaction across a shear crack plays a major role in governing a potential shear failure. Detailed calculation of the mechanics occurring within a significant shear transfer zone would require very fine local grids with rebar modeled as beam or continuum elements and concrete-rebar bond transfer modeling incorporated into the constitutive model.

At the design-code level the issue is presumed to be solved with conservatism, but no insight is provided into the mechanics of failure. Codes governing concrete structures for nuclear power applications such as ACI 349-86 establish allowable shear stress values for concrete or steel dowels acting alone, but these values are based on testing of conventional beams and slabs where the mechanics of shear failure are much different than shear failure in a containment wall. It is well known that shear capacities of sections are significantly influenced by the effectiveness of the shear reinforcement, the crack opening size, the stress field around the crack, etc. The ACI code even recognizes one aspect of these effects in its Section 12.1.1 governing shear in "deep beams". Application of this section of the code to massive concrete structures can lead to increases in the allowable concrete shear stress by a factor of two or more. While, by following the code, containment designers and analysts can be sure that the shear capacity of their structures can withstand pressures well in excess of design pressure, they cannot, with currently available methods, predict when shear failure will occur and what sort of breach of the containment will result. Of

utmost importance is to predict whether or not a shear failure will occur before a leakage failure. Those analysts who predicted shear failure in the 1:6-scale model test [11] did so because of numerical instabilities that occurred at the wall-base juncture late in their analysis and not because a specific shear failure criterion had been met. The discussion below is not intended to fully answer these questions, but by examining the calculated shear and bending response for the 1:6-scale model we begin to focus attention on this aspect of behavior that heretofore has not been addressed in the pretest work. The lack of conclusive analytical or experimental evidence as to if or when shear failure was imminent in the test further identifies the shortcomings of the current state of the art in shear failure prediction.

### 5.3.4.1 Cylinder Wall Bending

As mentioned earlier, an important part of the leakage prediction guidelines being developed in the EPRI-sponsored work is to standardize an accurate but computationally efficient global results model. A variety of axisymmetric grids and constitutive models were used by the pretest analysts as reported in [11]; the grids chosen included various numbers of concrete elements through the cylinder wall thickness. Although shell element models with composite properties have been used by some analysts, ANATECH has found such models to be inadequate in the shear and bending regions. In our methodology guidelines, we recommend the use of discrete liner and concrete elements. At least three concrete continuum elements through the wall thickness are required to adequately separate the rebar/concrete layers and properly simulate the cylinder wall bending response. Through several years of experience with containment global analysis, we have found that shell element representations of the entire wall do not properly predict the shear flow and shear distribution in bending regions of the wall. Moreover, shell elements make it more difficult and less reliable to post-process individual rebar and liner stress and strain histories.

Figures 5.3.18 through 5.3.20 have been included to illustrate the response prediction in regions with bending. With regard to global response in the containment, the only bending that typically occurs in the cylinder wall is at the springline and at the wall-basemat juncture. Figures 5.3.18 and 5.3.19 show analysis vs. experiment strain history comparisons for the two meridional rebar layers at the springline. The difference in strain in these rebar layers, which are separated by 4.5 in. (114 mm), indicates the bending present at this section (refer to Figure 5.3.24 for typical wall cross-section). The first plot in each figure shows the pretest result from all the analysts compared to experiment results as reported by Sandia. Here again the purpose of the plots are to show the relatively wide variation in computed results. In contrast, at cylinder wall sections where there was no bending, results were predicted more uniformly by all the analysts, and with good agreement with the experiment. As shown in the figures, the ANATECH/EPRI pretest and posttest analyses predicted the bending fairly well with some improvement in the low pressure prediction gained with the reduced concrete tensile strength used in the posttest analysis. It is felt that this agreement, in light of the wide variation of results produced by other grids and constitutive models, validates the global containment analysis guidelines that have been developed in the EPRI Research. A similar comparison is made in Figure 5.3.20 for layer 2 rebar at the severe bending region at the base of the wall on the pressure side.

### 5.3.4.2 Wall-Basemat Juncture Liner Connection

As has been reported in previous papers and reports, ANATECH's failure prediction consisted of a list of potential liner tearing locations which were predicted to occur between 140 and 150 psig (0.97 and 1.03 MPa). These included the wall-basemat juncture liner connection (the knuckle region as shown in Figure 5.3.21) and the liner thickness transitions at the 3 o'clock and 9 o'clock positions of most of the penetration inserts. Surface strain at the wall-base liner connection was predicted to exceed strains near penetrations, so the wall-base juncture was predicted to develop the first leak. With the exception of the wall-base location, the predicted locations and leakage pressure agreed very closely with the experiment. It has been concluded that the lack of agreement between the failure prediction and the test results for the wall-basemat juncture is due to the fact that the liner strain at that location is predominantly bending strain. The liner tearing criterion developed in the EPRI program has since been modified to distinguish between membrane strain concentrations and bending strain concentrations. The modified criteria has since been re-applied to the 1:6-scale model which resulted in a liner tearing prediction at the wall-base juncture of approximately 154 psig (1.06 MPa).

To examine what ANATECH believes actually occurred in the test, an "as-built" sketch of the knuckle detail is shown in Figure 5.3.22, which is a modified version of the idealized detail shown in ANATECH's pretest reports. Next, consider the idealized displacement mechanism predicted by the pretest analysis as shown in Figure 5.3.23 (also taken from earlier pretest reports). The pretest prediction analysis allowed the knuckle to slip free from the surrounding concrete, and the thin liner just above the knuckle gave little resistance to bending. This modeling resulted in large uplift and rotation of the knuckle itself, which clearly is the cause for the large bending strains predicted in the pretest analysis at the top of the knuckle.

By re-examining the construction detail sketch in Figure 5.3.22, one can envision two key factors that would serve to keep the knuckle in the actual experiment from lifting up and causing the large bending strains predicted in the pretest analysis. First is the effectiveness of the bond or "sticking" between the knuckle and the concrete. The pretest analysis used springs to approximately model the stud behavior, and this modeling probably did an adequate job at the studs (the first stud is about 2 in. (51 mm) above the top of the knuckle). But below the first stud, the liner and knuckle elements were modeled with no connectivity at all to the concrete. In retrospect this was probably a poor assumption. Second is the size and irregularity of the weld bead at the top and bottom of the knuckle, which was information unavailable to ANATECH at the time of the pretest analysis (drawings indicated a butt weld which was assumed to be ground smooth). The extra thick sections at both of these severe bending locations significantly impede possible upward rotation of the knuckle. These reasons can possibly account for the lack of any observed liner distress at the wall-base juncture. No posttest analysis was conducted to further evaluate the effect of these two factors, because assumptions used in modeling the "sticking" of the knuckle and the shape and behavior of the weld beads cannot be analytically justified other than to guess and hope to match the test behavior.

Because of the proximity to the weld bead, it was impossible for Sandia to place gages any closer than about 0.5 in. (12.7 mm) away from the top of the knuckle. However, the strain profiles from the pretest analysis indicate that the bending strain concentration is only 0.25 in. (6.4 mm) wide; thus, elevated strains associated with the top of the knuckle were not recorded in the gages. This (combined with the factors

discussed in the preceding paragraph that serve to restrain the knuckle from rotating) explains the lack of any significantly elevated strain measurements in the test near the wall-base juncture.

This location is still considered a point of concern in reinforced concrete containments because of the shear transfer and the knuckle rotation phenomenon exhibited in ANATECH's analysis (albeit an analysis based on modeling assumptions that perhaps exaggerated this rotation). Unfortunately, little more can be learned from the test measurements to add to the liner tearing database to be used for general containments. To further study reinforced concrete containment wall-base liner junctures, detailed local analysis and further experimentation is needed.

### 5.3.4.3 How Close was the Model to Wall-Base Shear Failure?

Posttest examination of the model indicates that minor concrete crushing may have occurred on the outer edge of the base of the wall, but other than this, the model gives no indication of significant distress at the wall base juncture. However, this is the nature of shear and brittle failures in general; they give no early warning before massive failure occurs. Several of the pretest analysts have proposed that the model may have been close to a wall-base juncture shear failure, but little or no analytical or experimental evidence has been offered to date to support this hypothesis. This subsection attempts to draw some conclusions on this subject based on analysis results.

The construction geometry of the cylinder wall at the wall-base juncture is shown by the idealized sketch in Figure 5.3.24. The shear transfer and moment at the wall base can be approximated by hand calculations as follows. Assume the basemat provides a rigid clamped edge to the base of the cylinder (deformed grid plots indicate this is approximately true). For a clamped cylinder with internal pressure.

$$M_0 = \frac{P}{2\beta^2} \tag{5.3.1}$$

$$Q_2 = \frac{-P}{\beta} \tag{5.3.2}$$

$$M_x = -D \frac{d^2w}{dx^2} \qquad Q_x = -D \frac{d^3w}{dx^3} \tag{5.3.3}$$

$$D = \frac{Et^3}{12(1-\nu^2)} \tag{5.3.4}$$

$$\beta^4 = \frac{3(1-\nu^2)}{r^2t^2} \tag{5.3.5}$$

where E is Young's modulus, t is the idealized cylinder thickness and $\nu$ is Poisson's ratio, P is cylinder Pressure, M is meridional moment in lb.-in/in and Q is shear through the cylinder wall in lb/in. Reference 32 also gives:

$$w = \frac{-1}{2\beta^3 D} [\beta M_0 \psi(\beta x) + Q_0 \theta(\beta x)] \tag{5.3.6}$$

$$\frac{d^2w}{dx^2} = \frac{-1}{2\beta D} [2\beta M_0 \phi(\beta x) + 2Q_0 \xi(\beta x) \tag{5.3.7}$$

$$\frac{d^3w}{dx^3} = \frac{1}{D} [2\beta M_0 \xi(\beta x) - Q_0 \psi(\beta x)] \tag{5.3.8}$$

where $\psi$, $\theta$, $\phi$, and $\xi$ are tabulated. This completely determines the displacement of the wall and the bending moment, moving up from the clamped edge for a homogeneous elastic cylinder. Of course, the problem is significantly complicated by the fact that the wall is highly inhomogeneous and inelastic, and the effective thickness t varies with the response. At high pressures, however, let us assume that the effective t is the transformed thickness of the cracked wall section. Using this approach for estimating meridional bending is a reasonable assumption because, for the first one or two feet (0.3 to 0.6 m) above the wall base, the basemat confines the cylinder to little or no cracking in the hoop direction. A more detailed explanation of the transformed bending thickness calculation may be found in Reference 24. For the cement abbreviated discussion, the hand calculation methods produce

$t_{tr}$ = 6.1 in. (155 mm) at p = 100 psig (0.69 MPa).

Using this thickness and Eqs. 5.3.1 through 5.3.4 gives

$\beta$ = 0.044

At p = 100 psig (0.69 MPa)

$M_0(100)$ = 25,826 lb-in/in

$Q_0(100)$ = 2,273 lb/in (0.4 MN/m)

taking positive shear outward. By 140 to 150 psig (0.97 to 1.03 MPa), analysis demonstrated that the inner steel showed significant yielding at the wall-base bending section (e.g., see strain history in Figure 5.3.20). Consequently, the joint rotates so much that the outermost concrete at the wall base becomes somewhat effective at carrying compression and contributing to the moment carrying stiffness of the section. Based on this the effective transformed thickness was assumed to increase to approximately 8 in. (203 mm). It is important to note that, because of the extensive reinforcement and the diagonal shear ties, the concrete that does contribute will be highly confined and will exhibit high residual strength. With this change,

$\beta$ = 0.039

$M_0(150)$ = 49,800 lb-in/in

$Q_0(150)$ = 3,863 lb/in (0.68 MN/m)

Then using Eqs. 5.3.5 and 5.3.6 and the tables in Reference 32, one may solve for $d^2w/dx^2$ and $d^3w/dx^3$ and

$$M(x) = \frac{Et^3}{12(1 - \nu^2)} \frac{d^2w}{dx^2} \qquad (5.3.9)$$

$$Q(x) = \frac{Et^3}{12(1 - \nu^2)} \frac{d^3w}{dx^3} \qquad (5.3.10)$$

This exercise has been performed to compare with the finite element results and thereby establish a basis for discussion of the possibility of shear failure at the wall-base juncture. The finite element results were reported in [11] as part of the standardized plot package requested by Sandia prior to the test. For these plots, total section moment and shear were plotted versus wall elevation starting at the inside

base of the wall and extending up five feet (1.5 m). To our knowledge, these plots have not been extensively used in posttest analysis discussions. Total moments and shears were computed based on the finite element nodal point force output available in ABAQUS-EPGEN. The results of Eqs. 5.3.9 and 5.3.10 are plotted versus those pretest prediction results in Figures 5.3.25 and 5.3.26. These plots show a reasonable correlation (given the crudeness of the hand calculations) between the finite element model and a closed form solution where assumptions of transformed thickness were made according to the above discussion.

There is no known data available on specific levels of shear required to cause failure in this type of structure. To evaluate how close the structure was to shear failure, the only option available is to look at the individual meridional bars and assume that before shear failure occurs enough shifting of concrete must occur so that the bars are all acting in pure dowel action. This would probably quantify the limit state of a massive shear failure. However, before this happens, a substantial shift of the concrete at the shear crack must occur, and this would probably be enough to tear the liner and cause leakage. This supports the leak-before-break failure scenario even for a shear failure location. (For a detailed study of liner strain concentrations due to dislocations at major cracks, see Reference 26.) If the bars, through dowel action, have plenty of reserve shear capacity once this shift takes place, then the leak-before-break scenario is likely to occur.

Pursuing the question of ultimate shear capacity even further, however, one must investigate the behavior of the individual dowels. From the transformed section calculations in Reference 24 the distance to the centroid of the transformed section, $y_t$ = 3.83 in. (97 mm) from the outside concrete surface; $I_t$ = 18.6 $in^4$ (774 $cm^4$). Therefore, the stress in the bar layers can be found by

$$\sigma_x = (N_u/A_s) + M_0(150)(y_{bar} - y_t)/I_t \qquad (5.3.11)$$

This gives component stresses of

| | | |
|---|---|---|
| liner: | $\sigma_x$ | = 30,114 + 15,850 = 46,000 psi (317 MPa) |
| layer 2: | $\sigma_x$ | = 41,300 psi (285 MPa) |
| layer 5: | $\sigma_x$ | = 28,560 psi (197 MPa) |
| layer 10: | $\sigma_x$ | = 38,270 psi (264 MPa) |
| seismic: | $\sigma_x$ | = 23,200 psi (160 MPa) |

$$(5.3.12)$$

It is clear from the strain gage histories (and analysis strain histories) for the liner and the meridional bars at this section (see Figure 5.3.20) that the innermost bars (layer 2) and the liner have reached yield by the end of the test, while the outer bars (e.g., layer 5) are still well below yield. These strain results can be shown to be consistent with the approximate component stress results above by considering the Von Mises yield condition that is assumed for the bars:

uniaxial $\sigma_{yield} = [1/2 \{(\sigma_x - \sigma_y)^2 + (\sigma_y - \sigma_z)^2 + (\sigma_x - \sigma_z)^2\} + 3\tau_{xy}^2 + 3\tau_{yz}^2 + 3\tau_{zx}^2]^{0.5}$ (5.3.13)

Assuming that in the rebar (acting in combined tension and dowel action) the only non-zero stresses are $\sigma_x$ and $\tau_{xy}$, we can solve for $\tau_{xy}$ in terms of $\sigma_x$

$$\tau_{xy} = \frac{1}{\sqrt{3}} \sqrt{\sigma_{yield}^2 - \sigma_x^2} \qquad (5.3.14)$$

If we then establish the criteria for catastrophic shear failure of the section to be the yield of all the bars (acting in tension plus dowel action), we can solve for what the shear stress would have to be at $p = 150$ psig (1.03 MPa) in order to meet the criteria. Using Eqs. 5.3.12 and 5.3.14 and yield stresses of 50.2 ksi (346 MPa) for the liner and 66.6 ksi (459 MPa) for the bars, we get

| | | |
|---|---|---|
| liner: | $\tau_{xy}$ | = 11,600 psi (80 MPa) |
| layer 2: | $\tau_{xy}$ | = 30,160 psi (208 MPa) |
| layer 5: | $\tau_{xy}$ | = 34,750 psi (240 MPa) |
| layer 10: | $\tau_{xy}$ | = 31,460 psi (217 MPa) |
| seismic: | $\tau_{xy}$ | = 36,043 psi (249 MPa) |

When dowel action initiates, it is impossible to tell from the data available what the distribution in shear is between the layers; however, because of the bending of the section, one can assume that dowels will start carrying shear from the inside moving out. (The concrete will be less likely to slip and create dowel action on the outside where the bending component of stress is compressive.) If the total shear (as computed earlier) is 3863 lb/in (0.68 MN/m), then the available contribution from the different layers is

$$V_{liner} = (1/16)\text{in. x } 11,600 \text{ psi} = 725 \text{ lb/in } 0.13 \text{ (MN/m)}$$
$$V_{layer\ 2} = (0.2/4.5)\text{in. x } 30,160 \text{ psi} = 1340 \text{ lb/in (0.23 MN/m)}$$
$$V_{layer\ 10} = (0.44/4.5)\text{in x } 31,460 \text{ psi} = 3076 \text{ lb/in (0.54 MN/m)} \qquad (5.3.15)$$
$$V_{layer\ 5} = 1544 \text{ lb/in (0.27 MN/m)}$$
$$V_{seismic} = 2403 \text{ lb/in (0.42 MN/m)}$$
$$V_{total\ dowel\ capacity} = 9088 \text{ lb/in (1.59 MN/m)}$$

With the assumption that the dowel action becomes effective from the inside out, it is clear that at a minimum, the liner and layer 2 bars are at maximum capacity (and therefore yielding, which is consistent with the measured strain results) and the remaining shear can be carried entirely by the large (0.75 in. (19 mm) diameter) layer 10 bars,

$$V_{layer\ 10} = 3863 - 725 - 1340 = 1798 \text{ lb/in (0.31 MN/m)} \qquad (5.3.15)$$

To calculate the pressure at which massive shear failure would be reached would require several more iterations even using the very approximate methodology given here because the x values continue to change as the pressure increases and so do the wall section properties ($t_{tr}$, y, I, etc.). However, the conclusion that can be reached is that at 150 psig (1.03 MPa), which was itself unreachable in the test due to leakage elsewhere, there is still substantial reserve shear capacity considering dowel action of the rebar. The total capacity from Eq. 5.3.14, 9088 lb/in (1.59 MN/m) is more than twice the shear at the section at 150 psig (1.03 MPa), 3863 lb/in (0.68 MN/m).

### 5.3.5 3D Analysis Comparisons

Many of the 1:6-scale model test measurements and analyses that have been performed show results that have emphasized the need for three-dimensional analysis. To name a few examples of 3D dominated behavior:

1.  "Far-field" liner strain measurements (away from penetrations) showed widely varying results in the four different azimuthal quadrants of the model, indicating the non-axisymmetric nature of the response.

2. Displacement gradients and "dimpling" at the major hatches show the effect that the hatches have on global behavior.

3. "Hatch ovalization" requires local 3D modeling.

4. Liner strain concentrations that resulted in leakage require local 3D modeling.

This section summarizes the global and local 3D pretest analyses that ANATECH performed and compares them to the test.

### 5.3.5.1 Brief Summary of 3D Pretest Analyses

The main response component that cannot be determined with certainty by 2D analysis is the interaction between hoop and meridional deformations around the hatches. The modeling must include local rebar details built in complex patterns sweeping around hatches, and the analysis must be capable of capturing the difference in the hoop direction stress state and the meridional direction stress state and the interaction between the two. In order to compute displacement boundary conditions to drive local 3D models, a relatively coarse quarter model geometry of the wall and dome was analyzed from azimuth 270° to 0°. "Hidden-line" plots of this grid with examples of rebar layers were plotted in the pretest work [11]. The rebar layers were constructed in the computational grid with a spatial rebar generation program ANATECH developed for use with ABAQUS-EPGEN. By searching the finite element grid for bars that intersect element faces, ABAQUS *REBAR input is generated. The rebar generation program has recently been released in a proprietary EPRI report [33].

Following the global analysis, local 3D grids of the equipment hatches and two smaller penetrations, an 8 in. (203 mm) and a 4 in. (102 mm), were analyzed with edge displacement boundary conditions from the parent grid. The local 3D grids were finer than the global grid, and the liner was modeled with two layers of continuum elements rather than with a single layer of shells as in the global grid in order to better calculate the liner shearing and liner strain concentration response due to the difference in out-of-plane displacement of the penetration relative to the free-field shell displacement. Unfortunately, because of the complexity of the multiple penetration clusters at the mechanical/electrical feedthrough penetrations (as will be seen in a later Subsection), none of these small penetration groups were analyzed prior to the test, and one of these is where the largest liner tear occurred.

### 5.3.5.2 Global Quarter Model Comparisons

As discussed in Section 5.3.2, most of the measured quantities showed good agreement with the quantities predicted by global axisymmetric analysis. These include liner and rebar strain versus pressure histories away from stiffness discontinuities (referred to as "free-field" quantities) and most displacement histories. However, because of the major hatches which are located every 90° at the cylinder midheight, the model showed behavior that varied significantly with azimuth (measured around the model's circumference).

Displacements were somewhat less at the heavily reinforced hatches than the free-field containment wall. In a Containment Integrity Workshop paper on synopsis of

the test results [34], Horschel compares the radial displacements of the cylinder wall midheight at various azimuths, including free-field and hatch locations. Those comparisons indicate that the free-field displacements exceeded the average hatch location radial displacement by about 40%. The maximum displacements at 145 psig (1.0 MPa) at these locations reported by Horschel are:

| Location | Radial Displ. at 145 psig | Calculated in 3D Global Analysis |
|---|---|---|
| Free-Field, Azimuth 315° | 1.81 in. | 1.83 in. |
| Free-Field, Azimuth 134° | 1.70 in. | |
| Free-Field, Azimuth 229° | 1.31 in. | |
| At Personnel Airlock "A" | 1.35 in. | |
| At Equipment Hatch "B" | 1.17 in. | |
| At Equipment Hatch "A" | 1.12 in. | 0.71 in. |

Unfortunately, there was no series of gages at the 270° to 0° quadrant for direct comparison of the displacement profile; however, a qualitative comparison of the general behavior can be made in Figure 5.3.27, which shows a deformed grid (section-plan view) of the pretest global quarter model at 145 psig (1.0 MPa). Two of the displacements from the above table above are indicated on the figure. The 315° azimuth displacement matches the calculated result very well, but the hatch A radial displacement exceeds the calculated value. For this coarse quarter-model grid, the stiffness of the hatches is apparently somewhat exaggerated compared to the free-field shell.

As expected from the displacement variation, liner strains also showed wide variations with azimuth because of varying effects from the hatches in the four quadrants. Liner principal strain measurements from gages well away from penetrations are shown in Figure 5.3.28 compared to the 2D axisymmetric pretest analysis results. At the end of the test (145 psig (1.0 MPa) pressure), the measured strains in the four quadrants range from 0.8% to 2%; all of those measurements presumably represent free-field measurements. These results clearly demonstrate the inadequacy of axisymmetric analysis alone to predict the variation of response around the circumference.

The 3D pretest analysis procedure has been further validated by additional comparisons made in Reference 24 between global response parameters of the 3D quarter model, the 2D analyses, and the experiment. Displacement history comparisons and far-field rebar strain comparisons show a close agreement between the 3D results, 2D results, and the test. The quarter model grid is too coarse, however, to make local rebar and liner strain comparisons with localized measured results.

### 5.3.5.3 3D Local Effects Analysis Comparisons

Important correlations have been made between the liner strain measurements and the local 3D predictions near penetrations that have helped validate the liner strain concentration factors being used in simplified concrete containment leakage prediction criteria. These local 3D analyses were the key to leakage prediction in the 1:6-scale model pretest analyses.

Prior to the test, computer time, manpower, and schedule commitments allowed four grids to be developed and their analyses to be completed. These were equipment hatches A and B, an 8 in. (203 mm) penetration and a 4 in. (102 mm) penetration. The first three of these represented three very different penetration geometries; the personnel airlocks were not analyzed but had very similar geometries to that of equipment hatch A. The fourth analysis (4 in. (102 mm) penetration) had a geometry similar to the 8 in. (203 mm) penetration; thus, it required a similar grid and did not represent extensive additional grid generation effort. That analysis was used to make a direct comparison between smaller and larger penetration sizes (of otherwise similar geometries) and also to investigate the effect of the location of the penetration occurring lower on the wall and nearer the wall bending zone. As mentioned earlier the clustered mechanical/electrical feedthrough penetrations could not be analyzed in the pretest scope of work; as will be seen in the next subsection, the grid development and analysis effort for this was significantly more extensive than any of the pretest grids.

The analyses that were chosen did provide useful and diverse results for the different hatch and penetration types. The trend for equipment hatch A and the small penetration was for a severe strain concentration to develop in the thinner liner material immediately adjacent to the thickened liner insert. This theme has been a recurring one in many of the posttest observations, analyses, and correlations made by various groups, but it was first introduced in the ANATECH/EPRI pretest work (e.g., see Reference 11). It was also observed and studied earlier in ANATECH's support of the Construction Technology Laboratory specimens with penetrations. After significant study, analysis, and discussion of the subject at posttest meetings of the analysts, there appears to be a consensus of those participating in the experiment that we shall take the liberty of summarizing: the level of strain concentration appears to be caused and governed to varying degrees by at least three competing mechanisms. These mechanisms are illustrated in Figure 5.3.29.

1) The first is the strain concentration that would exist in a plain, flat piece of liner with no concrete and no anchorage, simply due to the transition from the thick material to the thin material. This effect is partly due to the sudden stress transfer from the thick to the thin material and partly due to the eccentricity of the midplanes of each material (see the figure) causing shear and bending. From simple 2D approximate analysis of a flat plate, the concentration factor from this effect alone ranges from about 2.5 to 3.5.

2) The second is caused by radial displacement differential between the free-field and the penetration assemblage as shown in the figure. The presence of the heavy penetration sleeve (to which the liner is rigidly attached) and the increased steel area of the wall section at the penetration versus that at the free-field can cause significant radial displacement differential, with the free-field displacing more than the penetration. This combined with

the fact that this displacement differential (or out-of-plane dislocation motion) tries to occur across a major crack that is likely to occur within the first one or two inches of the penetration insert can highly concentrate the strain in the liner. The strain due to this out-of-plane dislocation has a large shear component. The magnitude of this concentration varies from one penetration to the next, and it even has some randomness to it because of unpredictability of precise crack locations.

3) The third effect is a highly localized strain at the root of welded studs in the vicinity of where the strain is already elevated for reasons 1 and 2 above. This mechanisms's effect on the liner was demonstrated in the early stud-pullout and shear tests conducted by Meinheit [35] with the same stud and liner sizes and geometry in preparation for designing the model. In direct shear loading, the 1/2 in.-long (12.7 mm) studs all bent over and pulled out of the concrete with little distress to the liner. The 3/4 in. (19 mm) studs, which were used throughout the upper parts of the cylinder, including around all penetrations, showed different results. Exactly half of the tests "failed" due to liner plate tearing at the root of the stud. The other half failed by stud pullout or shearing of the stud shank. ANATECH is of the opinion that the liner strain peak associated with this mechanism has a width limited to approximately the diameter of the stud plus approximately one liner thickness. This highly localized stud effect was demonstrated by analysis by Weatherby (see an earlier section in this report) as it occurs in conjunction with the "in-plane" strain concentration, i.e., the first strain concentration type described above. However, Weatherby's 2D analysis ignored reason 2 in the preceding paragraph and perhaps overestimated the stud's effect on the liner due to the overly "harsh" nature of his assumed displacement boundary conditions. As his analysis demonstrates, however, this third effect can only be predicted by analysis with an extremely fine grid, finer than practical for a 3D continuum analysis that includes the concrete.

The local 3D pretest analyses conducted by ANATECH predicted strain concentrations with large shear component with contribution from both the first and second strain concentration effects described above. The posttest analysis discussed in the next subsection combined more refined calculation of both of these with the addition of the welded stud effects, although not with the grid refinement or stud degrees of freedom that is probably necessary to completely define the welded stud effects. The results of the pretest calculations indicated varying levels of strain concentrations due to the varying geometries of the penetrations, and these results were validated by the test. Gage placements were generally not extensive enough nor closely spaced enough to give precise validation of strain concentration peaks, but families of gages that were placed near several of the major penetrations have agreed with the analysis strain concentration trends. Maximum principal strain profiles at 145 psig (1.0 MPa) compared to gages are shown for the 8 in. (203 mm) penetration, equipment hatch A and equipment hatch B in Figures 5.3.30 through 5.3.32, respectively. These are the only penetrations that have a number of gages arranged in a closely spaced line for a profile comparison. A detailed breakdown of what ANATECH considers to be the most useful liner strain gages and their locations is listed in Reference 25.

In Figure 5.3.30, the largest gage measurement is about 4.5%, whereas the peak calculated strain is 6%. Note that the same peak strains were measured next to two

identical penetrations separated 180° opposite each other on the model, thus giving even more credibility to the strain measurement. The closest gage to the insert plate is about 3/4 to 1 in (19 to 25 mm) from its edge, and it remains unclear whether a somewhat higher strain may actually have occurred between the gage and the insert plate. Horschel at Sandia independently reached this same conclusion in his posttest "synopsis of results" paper [34]. In that paper, he also took a closer look at the stud's effect on liner strains by plotting expanded profiles of "strip" gages that were placed across studs. In the case of the strip gage placed near penetration "R-2" (one of the two 8 in. penetrations), seven channel readings are available that span a length of about 1.5 in. (38 mm). These show a downward trend moving out from the penetration insert (moving away from the peak strain) reading from 3.9% down to about 3%. Between the second and fourth reading, however, is a reading on the underside of a stud location; this reading shows a sharp drop from about 3.8% down to 3.4% at the stud then back up again to 3.7%. Because the range along the strip gage is not very large, and because the x-axis in Figure 5.3.30 is expanded to show the peak strain versus far-field strain, the strip gage has been shown as a point (average strain of 3.5%) in this figure. The calculated strain concentration trend is generally in close agreement with the measured results.

In Figure 5.3.31 for equipment hatch A, the comparison benefits from having a closely spaced line of gages along a line moving horizontally from the center of the penetration (the 3 o'clock line). Here again, the strain concentration trend is in good agreement, while the peak strain is slightly higher in the analysis (3.5%) than in the gage closest to the insert plate (2.9%). The lower overall strain next to the equipment hatch seems to indicate that, since the thicker embossed concrete on the outside of the shell extends beyond the edge of the 3/16 in. (4.76 mm) insert plate, it may help to spread out and diffuse the strain concentration associated with both in-plane and out-of-plane effects. The transition in stiffness of the overall shell wall is made more gradually than in the smaller penetrations, thus, the strain concentration next to the insert plate is lower.

Equipment hatch B shows even more convincing evidence supporting this explanation of the diffusing of the strain concentration associated with the insert plate. The embossed concrete on the inside surface of the wall makes it so that the liner material next to the insert plate never sees elevated strains, or in fact, has lower strains than in the far field. Instead, the liner problems here occur at the root of this embossed concrete (or as Horschel describes [34] at the intersection of the conical surface with the cylinder wall). Here again a strip gage result has been condensed to a point. The complex local behavior is predicted reasonably well by the pretest analysis. The liner goes into tension and bending as the cylinder expansion forces the liner to straighten across the re-entrant corner at the root of the embossed concrete. The studs act to prevent the liner from straightening and are thus put into direct pullout by the liner. One of the tears that occurred near equipment hatch B appears to be associated with stud pullout. Another strain profile in Reference 34 has an expanded x-axis and shows the readings from a strip gage near a stud. Because of the local bending at this re-entrant corner, part of the liner actually shows compressive strain, even at the end of the test.

More insight into the liner strain distribution near these penetrations has been gained with strain contours and other plots in Reference 24, but space does not allow them to be included here.

### 5.3.6 3D Study of Mechanical/Electrical Feedthrough Penetration

A final posttest study was performed for a grid that was similar to the pretest local effects grids discussed in the previous subsection, but that was much finer than before in the peak strain region. The latest grid also utilized discrete stud modeling and an interface element layer to allow the liner-concrete-stud interaction to enter into the results. The grid development and analysis represent a significant level of effort, and many difficulties were encountered, particularly because of the numerical behavior of the 3D interface element layer. Nevertheless, the completed analysis showed sharp strain concentration in the first two inches out from the edge of the insert plate, which coincides with the long tear that occurred in the experiment, and it further validates the conclusions which have been drawn from the pretest local analyses.

#### 5.3.6.1 Computational Model

A perspective view of the posttest local grid is shown in Figure 5.3.33. The grid detail in the high strain region is best viewed in elevation, as shown in Figure 5.3.34. The 3/16 in. (4.76 mm) thickened insert plate is a rectangular shape with rounded corners. Note that in these figures, the 3D plotter being used does not include the midside nodes, which greatly improves the efficiency of the plotter. If the midside nodes were plotted, however, the rounded corners and edges of the grid would appear much smoother and appear to more accurately model the structure. These nodes are, in fact, present in the analysis in their appropriate positions to produce the properly curved element boundaries.

The liner, interface, and concrete elements are ABAQUS C3D2OR elements, 20 node bricks with "reduced" 2x2x2 integration. The penetration sleeves were initially modeled as 8-node shells (S8R), but in the course of the work it was discovered that the presence of even a few shell elements in a 3D "continuum" grid causes ABAQUS to construct a stiffness with an excessively large solver front width, thus the solution time was much higher than what should have been necessary for a problem of this size. When the shell elements were removed, the frontwidth and solution time dropped significantly. They were subsequently replaced with beam elements that at least provided the same equivalent stiffness in the plane of the cylinder wall. The out-of-plane stiffness was not of much concern since the concrete wall is reasonably stiff in this direction anyway. It is felt that these grid approximations had little effect on the peak liner strain area, which was the primary focus of the analysis.

The concrete was modeled with the same 3D constitutive model developed prior to the pretest work. The same concrete properties were used as in the posttest 2D global analysis discussed in Section 5.3.2 with a tensile cracking cutoff strain of $50 \times 10^{-6}$. The liner and rebar were modeled the same as in all the pretest and posttest analyses. The rebar input is shown graphically in the grid of Figure 5.3.33, rebar input is generated by the FORTRAN program mentioned earlier that checks the intersections of the input bars with the existing element faces and generates ABAQUS rebar input accordingly.

The studs were modeled in several different ways before arriving at the final scheme. A detailed report of the stud pullout and shear behavior was provided by Sandia [35], and this formed the basis for the final stud modeling. The use of beam elements to model studs added unnecessary complexity and degrees of freedom to the grid, and a way could not be devised to handle the rotational boundary conditions at the ends of these beams in order to accurately model the studs. Note that the continuum

elements have no rotational degrees of freedom so the studs modeled as beams would have to have some type of slope restraints at their ends. To avoid making these approximating assumptions, the studs were modeled as springs between the nodes on either side of the interface layer, separated by the interface thickness (3/4 in., 19 mm), which corresponds to the length of the studs. The test results in Reference 35 produced force displacement histories for the studs in pullout and shearing modes, and these were input in piecewise linear fashion for the spring equations. The average maximum forces and displacements achieved by the 3/4 in. (19 mm) studs in the tests [35] were 934 lb (4.16 kN) and 0.018 in. (0.457 mm) in tension (direct pullout) and 1408 lb (6.27 kN) and 0.156 in. (3.96 mm) in shear. The stud spring equations in the computational model were specified accordingly. The compressive stiffness of the studs was modeled as zero because the concrete carries the compressive force transfer from the liner.

Boundary and force conditions applied to the grid are similar to that used for the pretest local effects analyses. Although the mechanical/electrical feedthrough penetration does not lie in the 270° to 0° quadrant, it was assumed as such, and the displacement conditions were taken from the 3D quarter model analysis as shown in Figure 5.3.35. Displacement boundary conditions between nodes in the parent grid were approximated by quadratic interpolation.

The interface concrete proved to be the most significant modeling difficulty, primarily because of numerical problems. A 3D interface element was developed for this research and is described in more detail in Reference 24.

Because of this behavior, the interface was eventually modeled with elastic properties with a comparatively weak Young's modulus, 1x10⁶ psi (6.9 GPa) (compared to 4.8x10⁶ psi (33 GPa) for the rest of the concrete). This largely improved the stability of the solution because the oscillatory behavior described above was eliminated as well as any unconverged force residuals due to cracking in the interface layer. The drawbacks and potential solution uncertainties introduced with this modeling are:

1. The response transition from the uncracked structure to the cracked structure will be influenced, as well as the amount of tensile stress carried by the concrete wall. However, this effect can be quantified, and it is not very significant.

2. The compressive behavior of the interface will also be "soft." This is probably not overly significant since the stresses in this direction are only approximately as large as the pressure, which is relatively small compared to the model stresses.

3. The studs probably will not build up as much shearing or pullout force as in the actual structure because the as-modeled interface concrete will always transmit some force between the liner and the main concrete. In the actual structure there will be a tendency for the liner and concrete to slip in zones of changing relative wall stiffness; this is what causes stud forces that impose higher strains on the liner near the root of the studs. Unfortunately, it is difficult to quantify this modeling discrepancy. Since the modulus used is only 2% of the original modulus (Young's modulus and shear modulus), it is assumed that the model still allowed significant relative movement between the liner and the primary concrete and, thus, approximated the buildup of stud shearing forces fairly well.

## 5.3.6.2 Results

Deformed structure plots in Figures 5.3.36 and 5.3.37 at 120 psig (0.83 MPa) pressure show the displacement response of the mechanical/electrical feedthrough grid. Note that the last two rows of elements at the right-hand edge of the grid have been removed for ease in post-processing. The figures show that the free-field side of the grid has larger radial displacement than the penetration side of the grid. This helps to drive the dislocation type of liner strain concentration discussed earlier (mechanism 2 in Figure 5.3.29). Displacement gages were not placed closely enough on the model to validate this behavior near the small penetrations, but this type of behavior was validated at most of the large hatches. The deformed shapes throughout the post-cracking regime look about the same, but have progressively larger displacement magnification factors. Figure 5.3.36 is a perspective and top views of the entire grid, and Figure 5.3.37 shows the liner only.

A good summary of the analysis results may be ascertained from a liner strain contour plot at 145 psig (1.0 MPa), the end of the analysis, as shown in Figure 5.3.38. The contours represent percent strains (1%, 2%, ... 7%) for the calculated effective plastic strain. As expected, the highest strains occur along the edge of the insert plate, and there are a few local strain risers around welded stud locations (shown as large dots on the figure). The effective strain band all along the insert (along the model tear location) is uniform at about 5%. The highest strain in the grid occurs within this zone at a stud; there the strain reaches about 7.3%. The plot shows the attenuation pattern next to the top of the insert plate. Detailed strain profiles of the strain components given in Reference 24 are similar to the liner strain profiles reported near other penetrations in the pretest analyses. This helps to validate those earlier analyses that used coarser grids than the current model. The primary difference in the profiles are the effects of the studs. Multiple peaks in the strain profiles correspond to the welded stud locations at which the strain is further concentrated.

## 5.3.6.3 Conclusions of Mechanical/Electrical Feedthrough Study

Comparison of the strain contour (Figure 5.3.38) to strain contours for the local pretest analyses of other penetrations (see Reference 24) shows why, even though tears occurred near many penetrations, the longest tear occurred next to a rectangular penetration. The long lines of equal strain along the edge of the rectangular insert serve to guide or orient the tear and make it easier for a tear to extend in an equipotential strain field. As soon as the tear reached a significantly lower strain field (at the top of the insert), the tear stopped. Next to the circular penetrations, on the other hand, the strain ahead of a liner crack tip is much more diffused making it difficult for a tear to run. Earlier research in the EPRI sponsored program [28,29] has examined the crack propagation potential for concrete containment liner tears, and it has been ascertained both experimentally and analytically that the concrete backing and anchorage redundancy allow only ductile tearing; in other words, crack extension occurs only under increasing load rather than brittle tearing where a crack can run once a critical pressure is reached. However, the tear next to the 1:6-scale model mechanical/electrical feedthrough indicates that a tear at least as long as the vertical edge of a rectangular insert plate may occur in an actual containment, even under gradually increasing overpressure conditions.

To summarize, the posttest detailed analysis has helped to evaluate the causes for the large liner tear that depressurized the 1:6-scale containment model. Strain concentration effects can be traced to three mechanisms: (1) the strain concentration that would exist at the junction of the thin and thick material, regardless of the penetration geometry; (2) the strain concentration occurring due to differential radial displacement (and probably coinciding with a major concrete crack); and (3) the highly localized strain rise at the base of welded studs. The cause of the uniform elevated strain field is the first two mechanisms, and the welded studs may serve to help initiate and guide the tear from stud to stud. The tear can rapidly extend to the full height of the edge of the thick insert plate because the strain contours are parallel and uniform over this range. At round insert plates, the strain field around liner tear is not so conducive to liner crack extension.
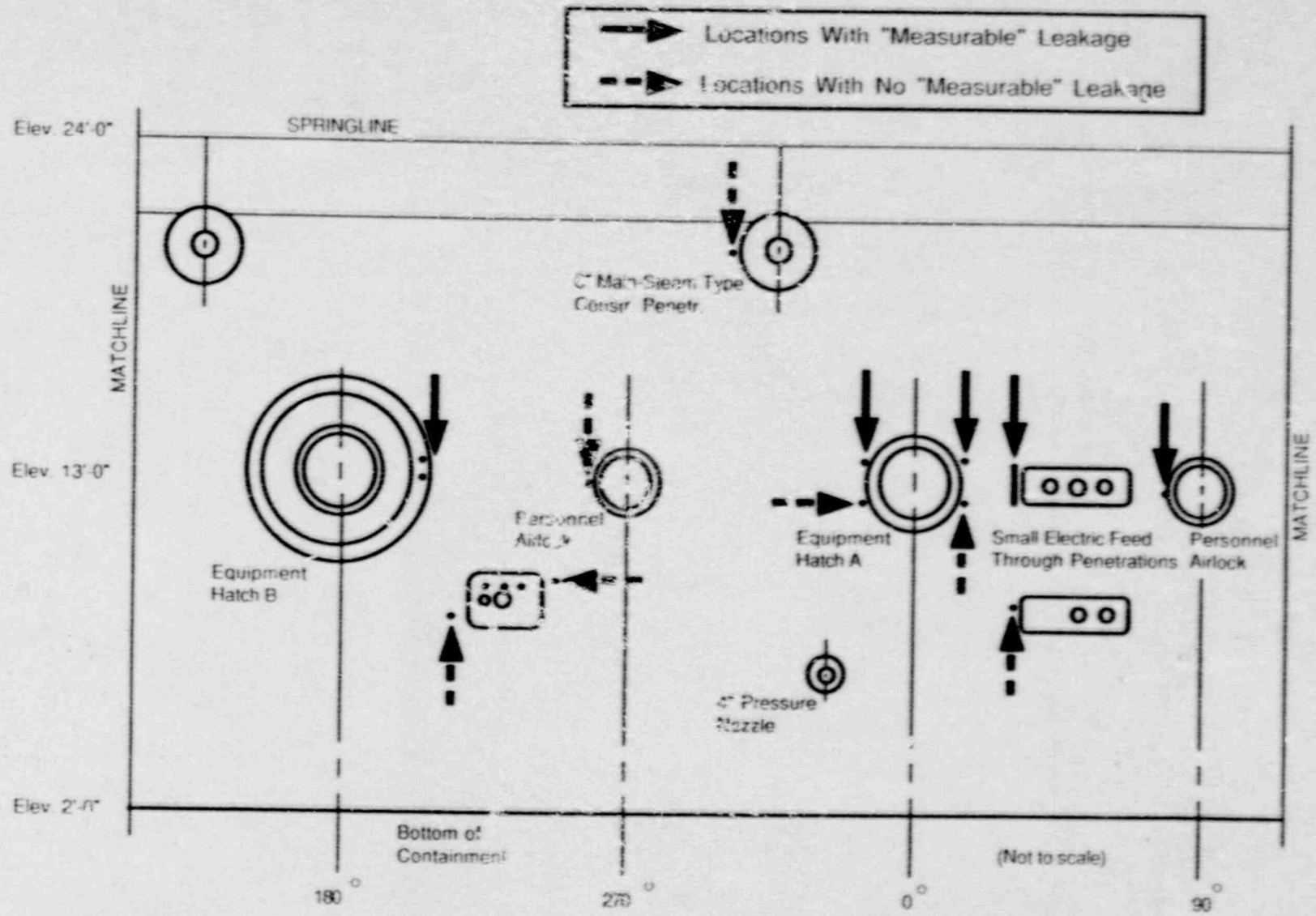
Figure 5.3.1  1:6-Scale Model Liner Stretchout Showing Tears with "Measurable and "Immeasurable" Leakage

S-136

CENTERLINE

FIGURE 2-13, 14
LINER & MERID.
REBAR STRAIN ───────

FIGURE 2-11, 12
LINER & SEISMIC REBAR ─────── ── z = 22'-0"
STRAIN

FIGURE 2-7
RADIAL DISPLACEMENT ───────

FIGURE 2-8, 9, 10
LINER, HOOP & MERID.
REBAR STRAIN ───────

FIGURE 2-5, 6
DISPLACEMENTS ───────

CYLINDER
MID-HEIGHT
z = 11'-0"

CONSTRAINT
EQUATION
BOUNDARY ───────

FINE GRID AT
WALL-BASE
JUNCTURE

12" UNREINFORCED
FILL SLAB
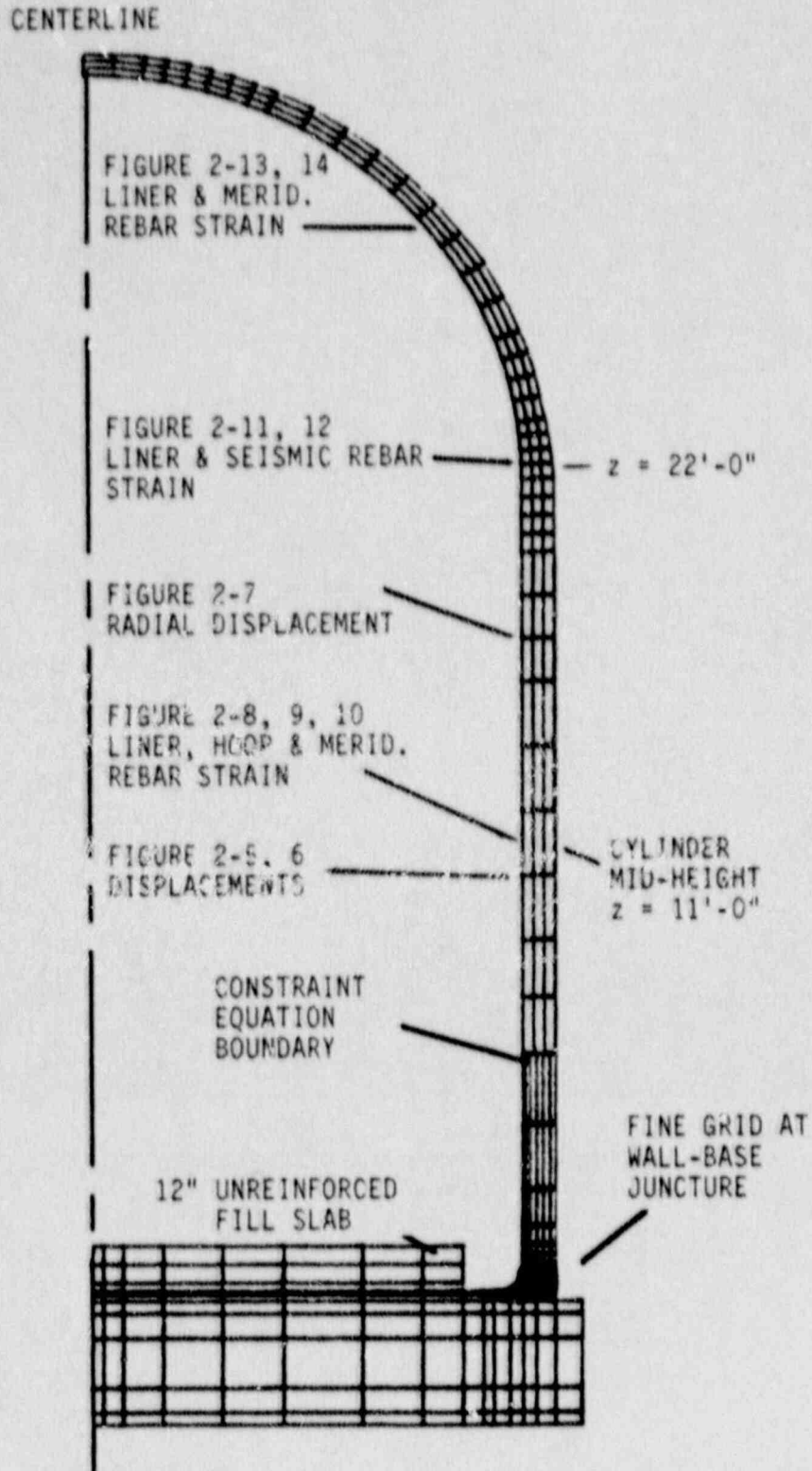
Figure 5.3.2  Pretest/Posttest Computation Grid Showing Plot Locations
for Figures 5.3.3 to 5.3.11
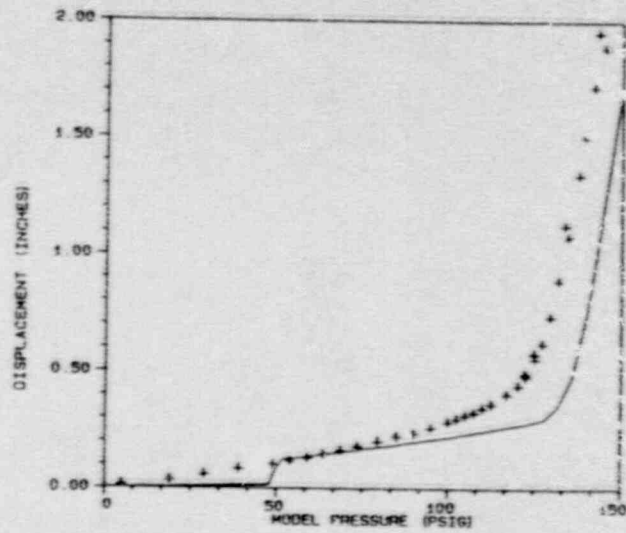
Figure 5.3.3 Pretest Global Axisymmetric Analysis vs. Experiment: Radial Displacement at z=11 ft
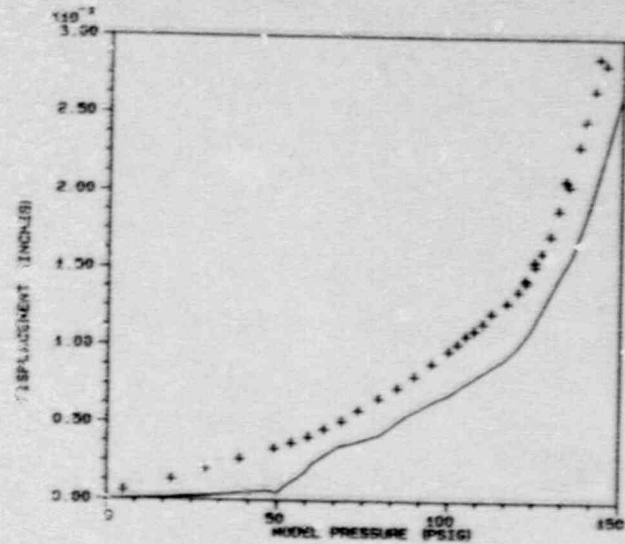


Figure 5.3.4 Pretest Global Axisymmetric Analysis vs. Experiment: Vertical Displacement Relative to Basemat at z=11 ft
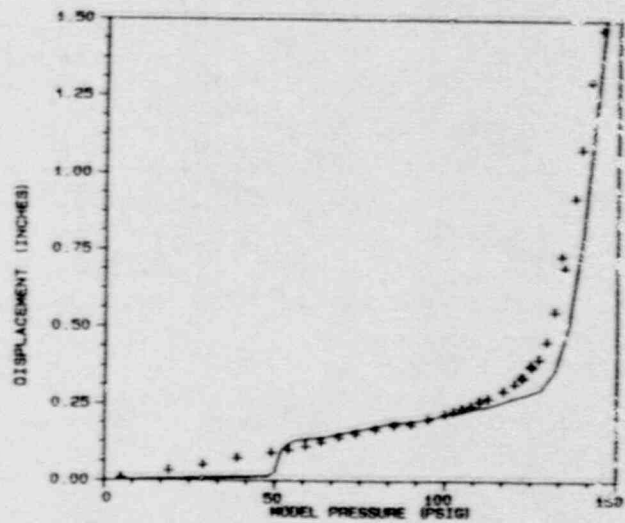


Figure 5.3.5 Pretest Global Axisymmetric Analysis vs. Experiment: Radial Displacement at z=18 ft
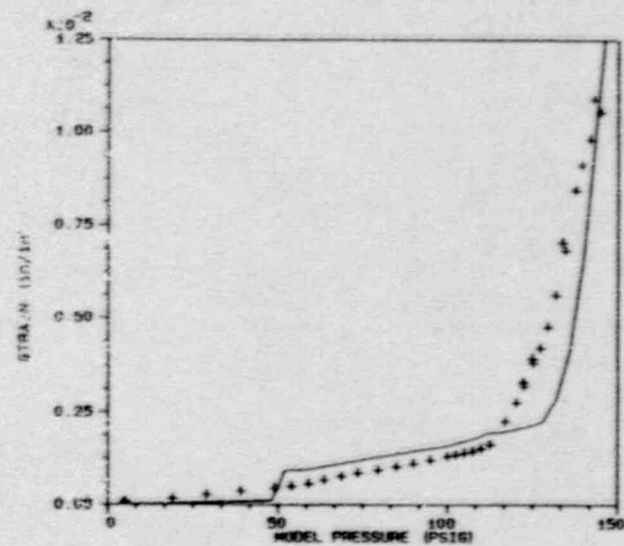


Figure 5.3.6 Pretest Global Axisymmetric Analysis vs. Experiment: Max Principal Inside Surface Liner Strain at z=13.75 ft, $\theta$=45°
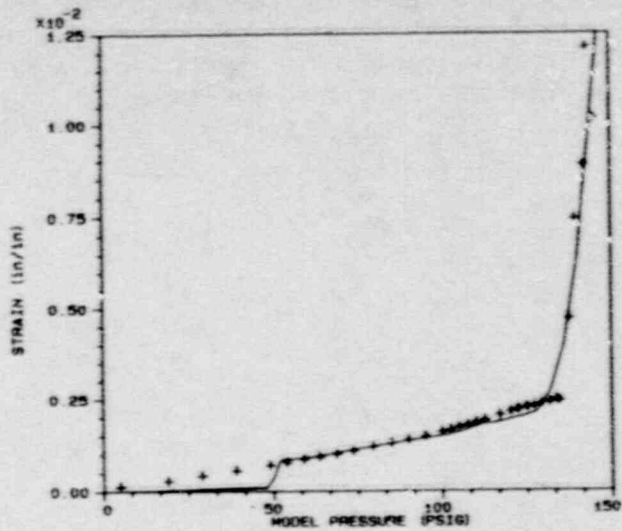
Figure 5.3.7  Pretest Global Axisymmetric Analysis
vs. Experiment: Axial Strain Layer 6 Hoop Rebar
at z=13.75 ft, θ=45°
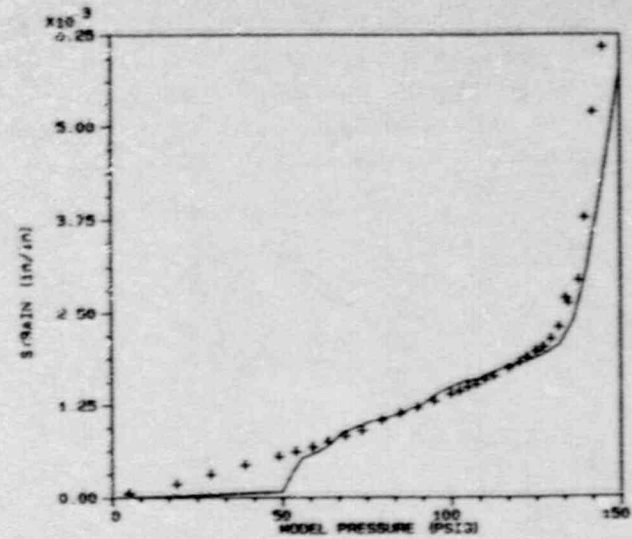


Figure 5.3.8  Pretest Global Axisymmetric Analysis
vs. Experiment: Max Principal Inside Surface Liner Strain
at z=22 ft, θ=45° (springline)
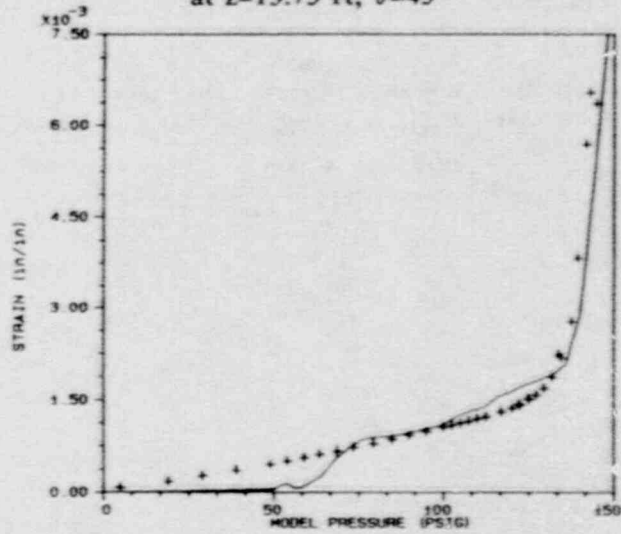


Figure 5.3.9  Pretest Global Axisymmetric Analysis
vs. Experiment: Axial Strain Layer 8 Seismic Rebar
at z=22 ft, θ=45° (springline)
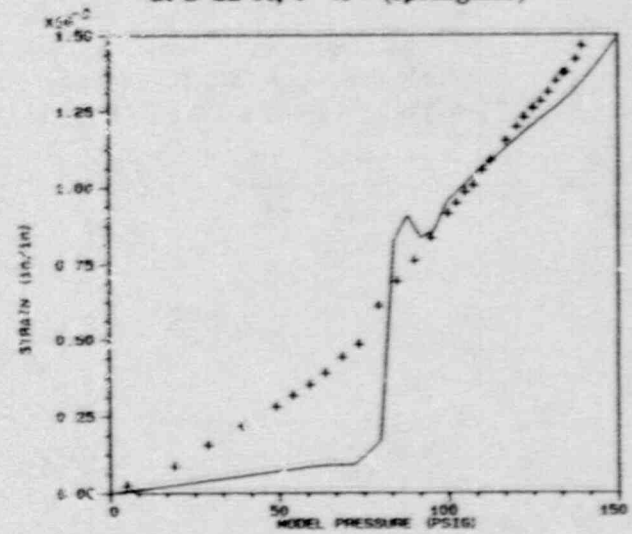


Figure 5.3.10  Pretest Global Axisymmetric Analysis
vs. Experiment: Max Principal Inside Surface Liner Strain
at φ=72°, θ=90° (dome)
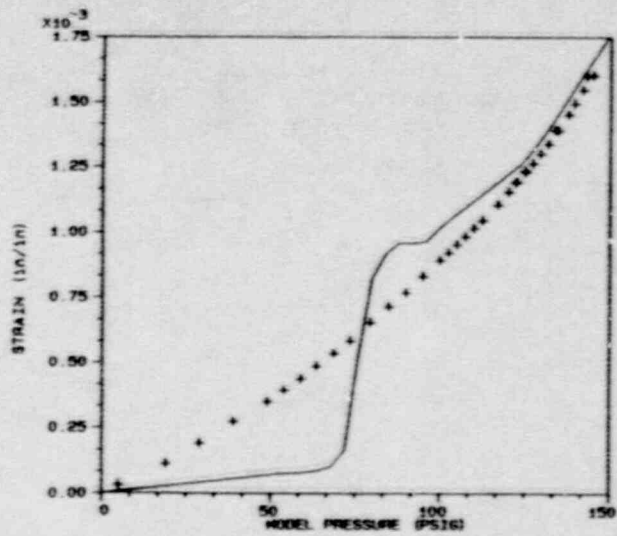
Figure 5.3.11  Pretest Global Axisymmetric Analysis
vs. Experiment: Axial Strain Layer 5 Meridional Rebar
at $\phi=72°$, $\theta=90°$ (dome)
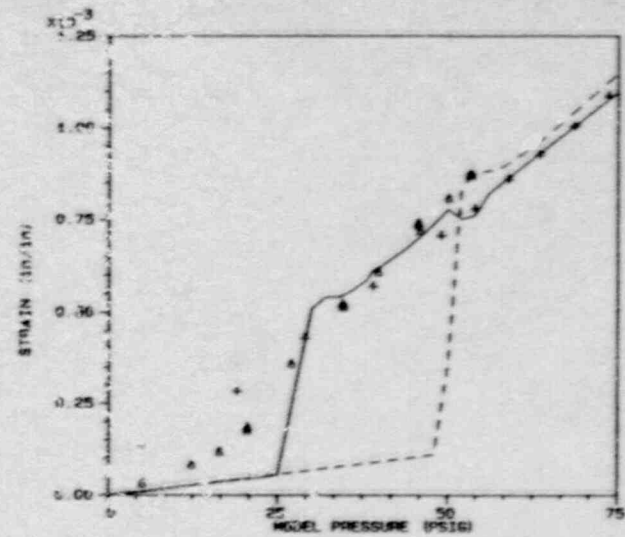
Figure 5.3.12  Pretest and Posttest Analysis
vs. Experiment: Layer 6 Hoop Rebar Strain History
at z=13.75 ft
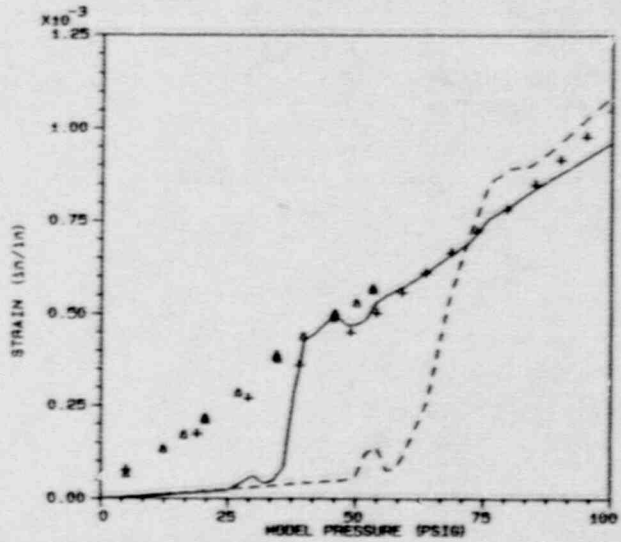
Figure 5.3.13  Pretest and Posttest Analysis vs. Experiment:
Layer 8 Seismic Rebar Strain History at z=22 ft
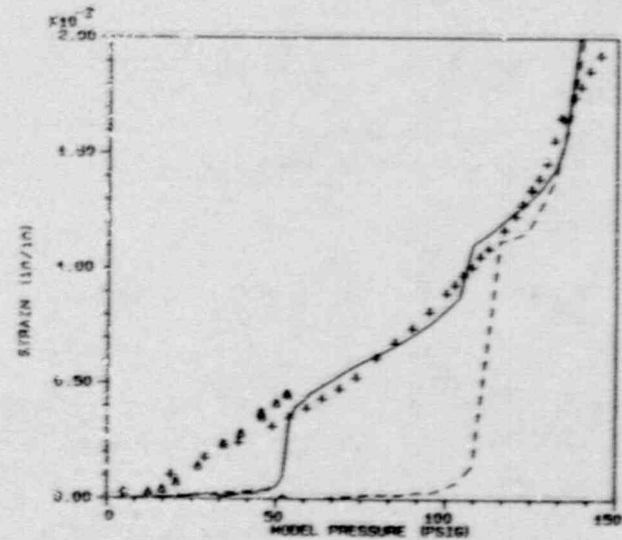
Figure 5.3.14  Pretest and Posttest Analysis vs. Experiment:
Layer 5 Meridional Rebar Strain History at z=13.75 ft
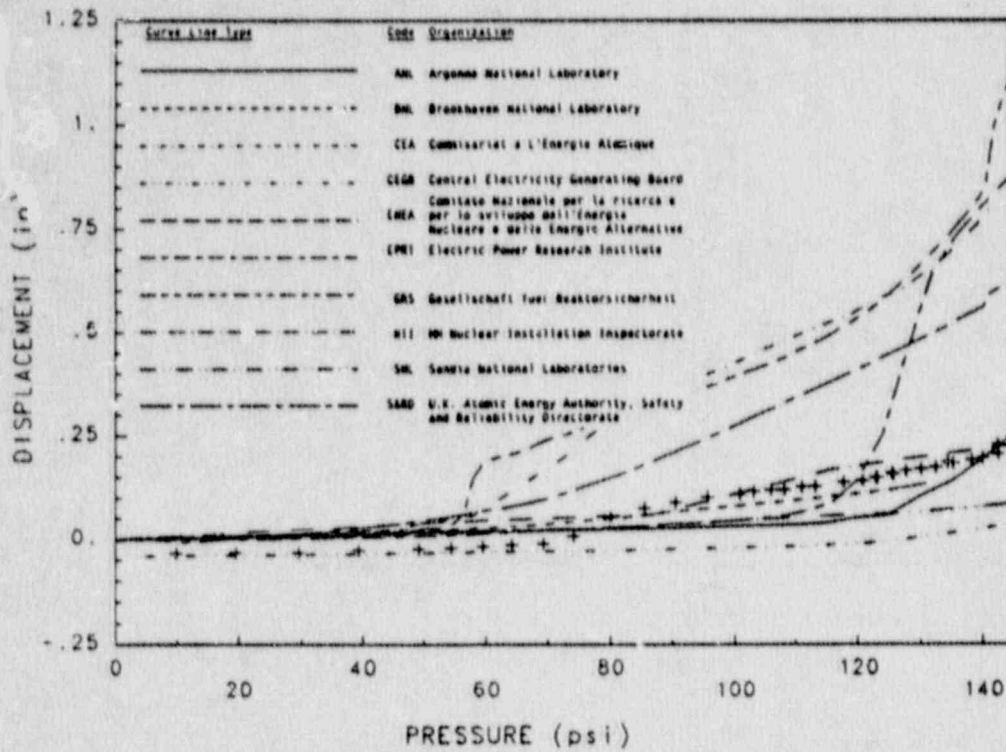
Figure 5.3.15  Comparison of All Pretest Round-Robin Analyst Predictions
to Experiment, Basemat Edge Uplift Displacement
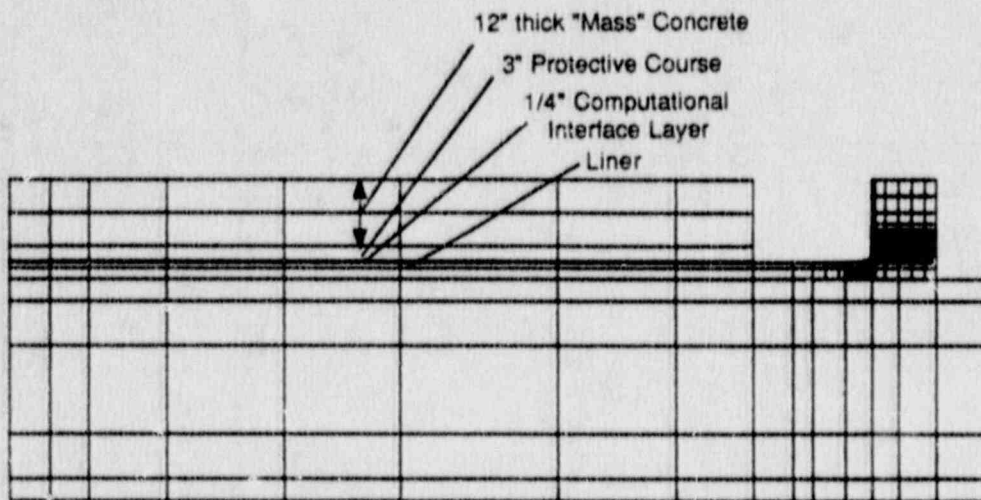


Basemat Axisymmetric Computational Grid

Figure 5.3.16  Enlarged View of Basemat Portion of Axisymmetric Posttest Grid
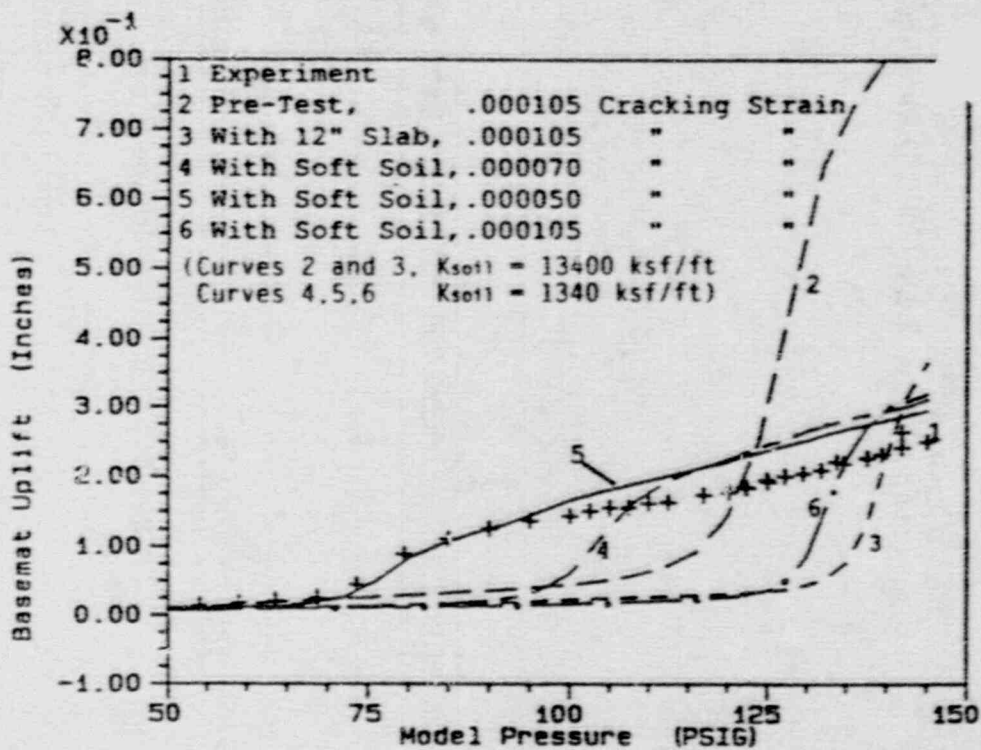
Figure 5.3.17  Basemat Uplift Parameter
Study Results vs. Experiment
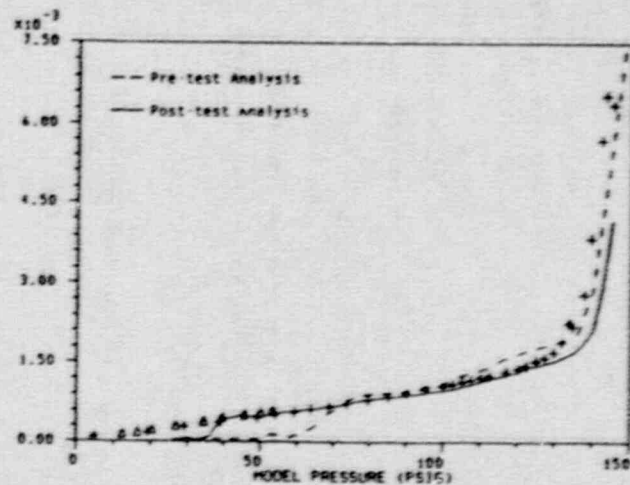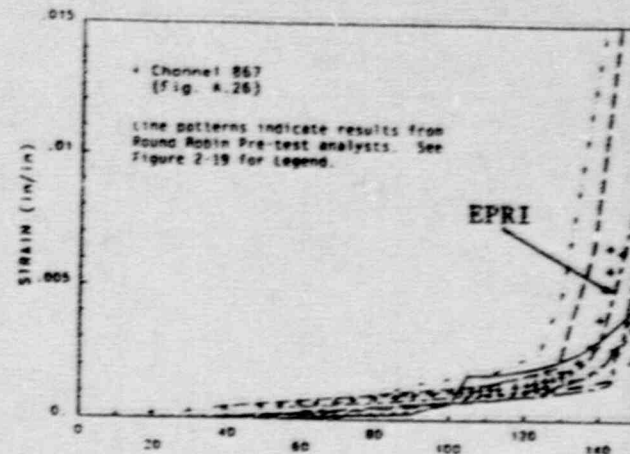


Figure 5.3.18
Comparison of Analysis and Experiment:
Axial Strain in Layer 2
Meridional Rebar at z=23.92 ft, θ≈90°
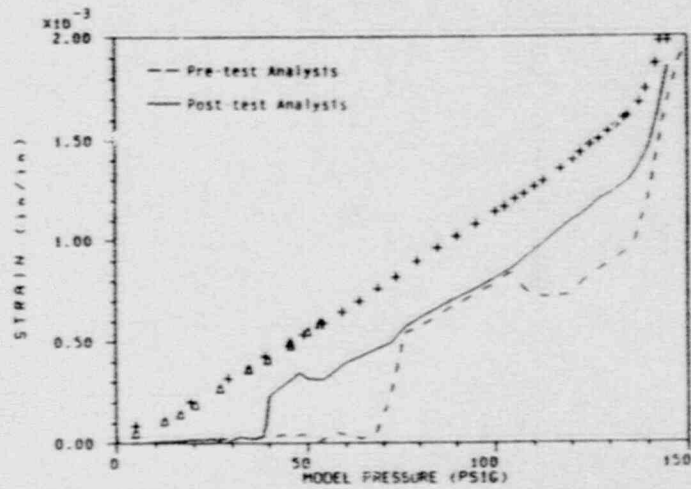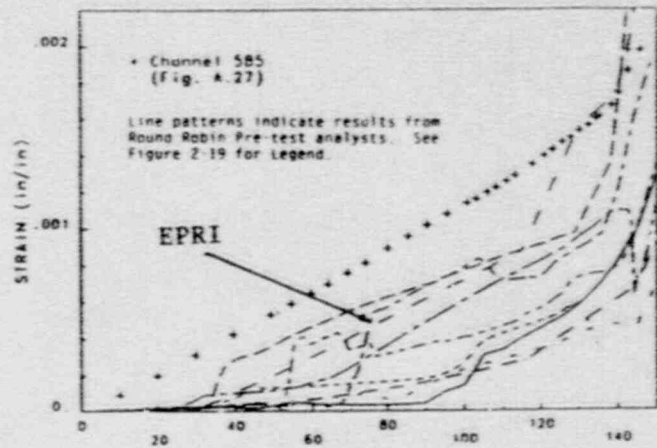
Figure 5.3.19 Comparison of Analysis and Experiment:
Axial Strain in Layer 5 Meridional Rebar at z=23.92 ft, θ=90°
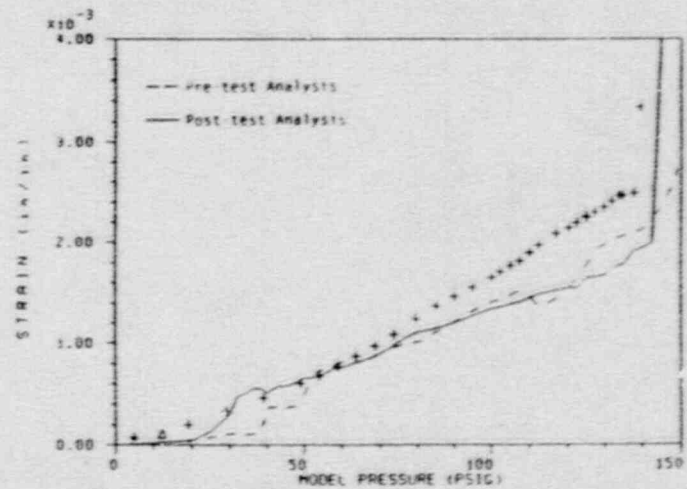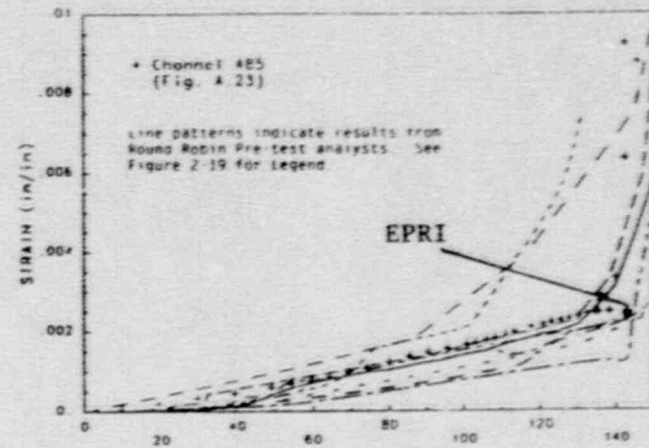
Figure 5.3.20 Comparison of Analysis and Experiment:
Axial Strain in Layer 2 Meridional Rebar at z=2.10 ft, θ=90°
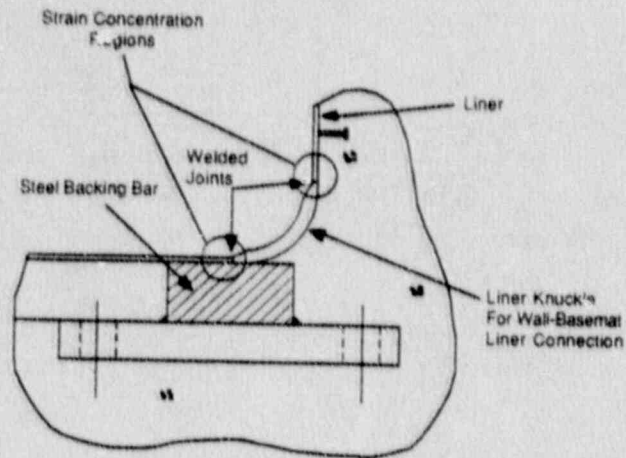
Figure 5.3.21 Assumed Construction Geometry Near Wall-Basemat Juncture Liner Knuckle
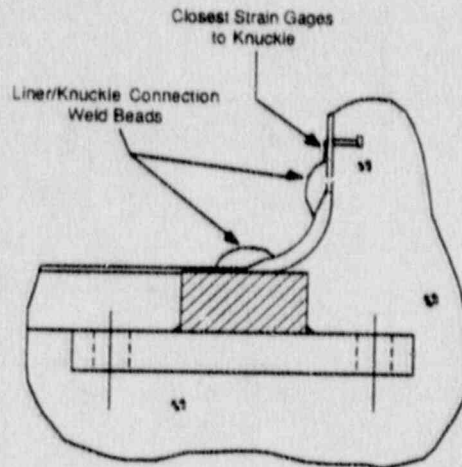


Figure 5.3.22 As-Built Construction of Knuckle Region (Weld Beads Exaggerated)
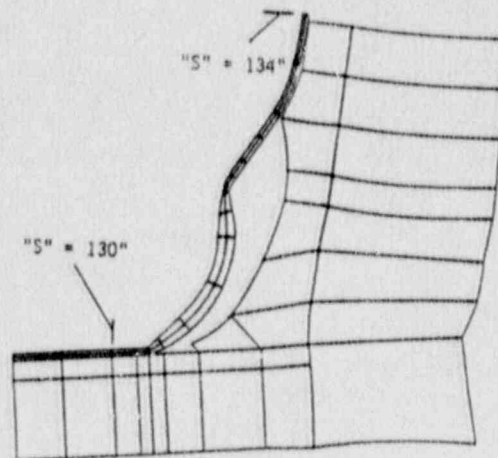


Figure 5.3.23 Knuckle Rotation and Displacement from Pretest Analysis

11'-0" R INSIDE FACE OF WALL

LINER

1
2
3
10

**TYPICAL SECTION THRU WALL**

4
5
6
7
8

9.75"

(SHEAR TIES NOT SHOWN)

1" .75" 1.5" 4.75" 1.75"

4

5

3

#6 @ 4.5"
(TOP EL 6'-6")

2

6

1

7

#4 @ 4.5"

8

10

#4 @ 4.5"

(LINER KNUCKLE GEOMETRY NOT SHOWN)

1" CLEAR

**TYPICAL SECTION OF MAIN REINFORCING AT WALL-BASE JUNCTURE**
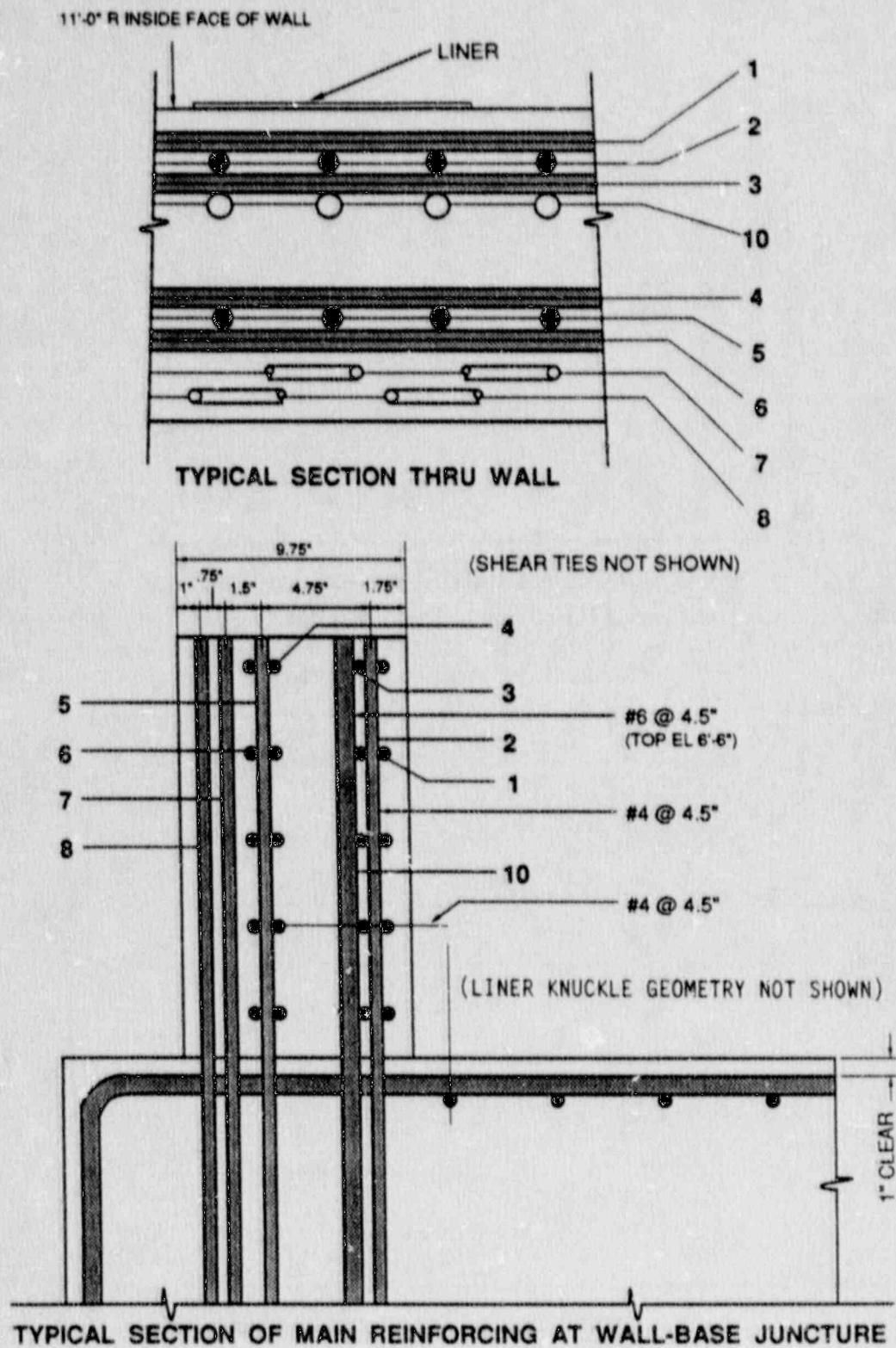
Figure 5.3.24  1:6-Scale Model Typical Wall Cross-Section
with Identification of Rebar Layers
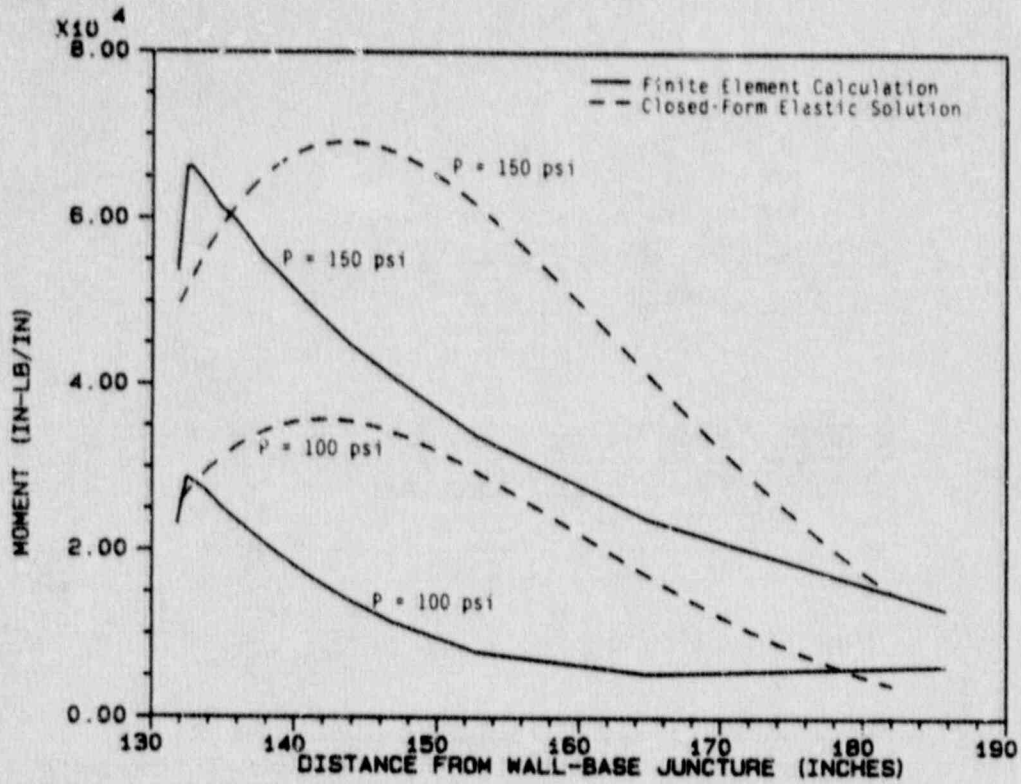
Figure 5.3.25  Comparison of F.E. Calculation of Radial Moment from [25] with Closed-Form Elastic Solution Using Transformed Wall Section Properties. (X=132 in. at the Wall-Base Juncture)
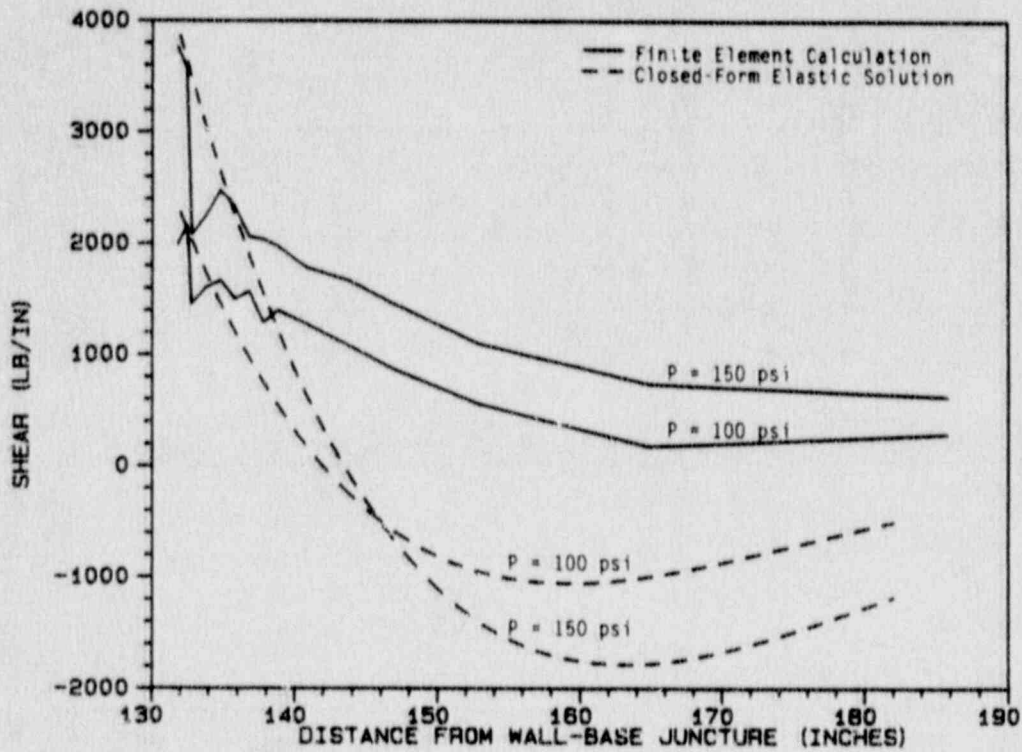


Figure 5.3.26  Comparison of F.E. Calculation of Radial Shear from [25] with Closed-Form Elastic Solution Using Transformed Wall Section Properties. (X=132 in. at the Wall-Base Juncture)

PERSONNEL
AIRLOCK

EXPERIMENTAL MEASUREMENT
1.81"(X10) AT AZIMUTH 315°

EQUIPMENT
HATCH A

EXPERIMENTAL MEASUREMENT
1.12" (X10) AT
EQUIPMENT HATCH A
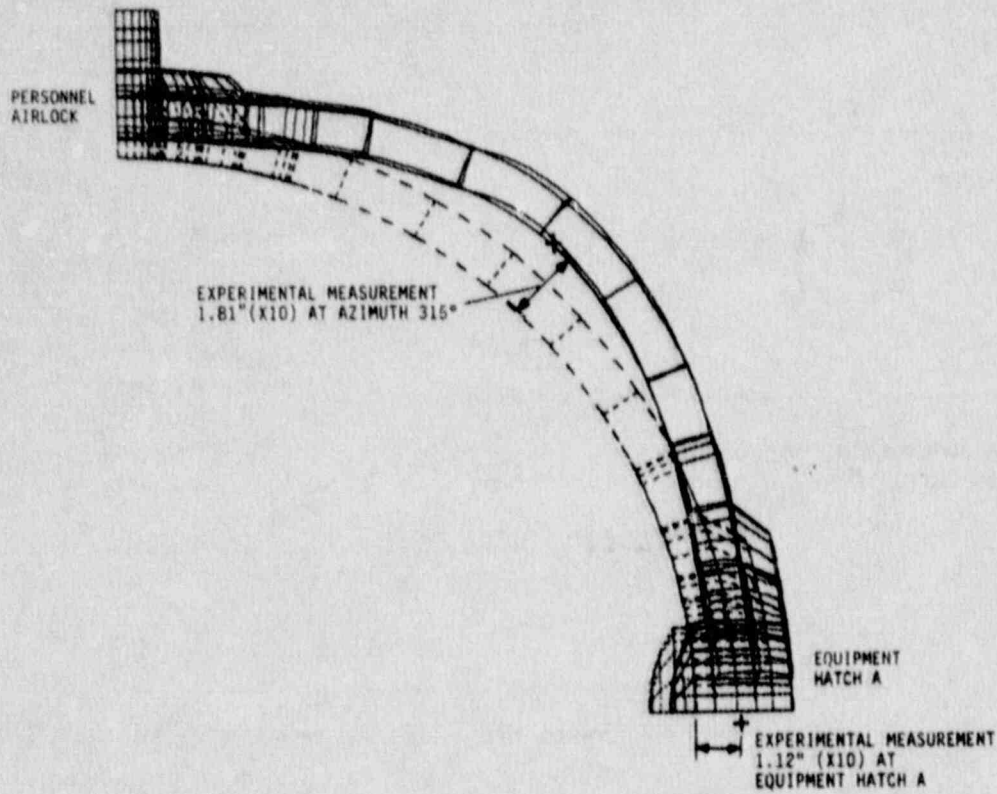
Figure 5.3.27  Deformed Slice at Belt-Line of Cylinder at 145 psig, Displacements X10
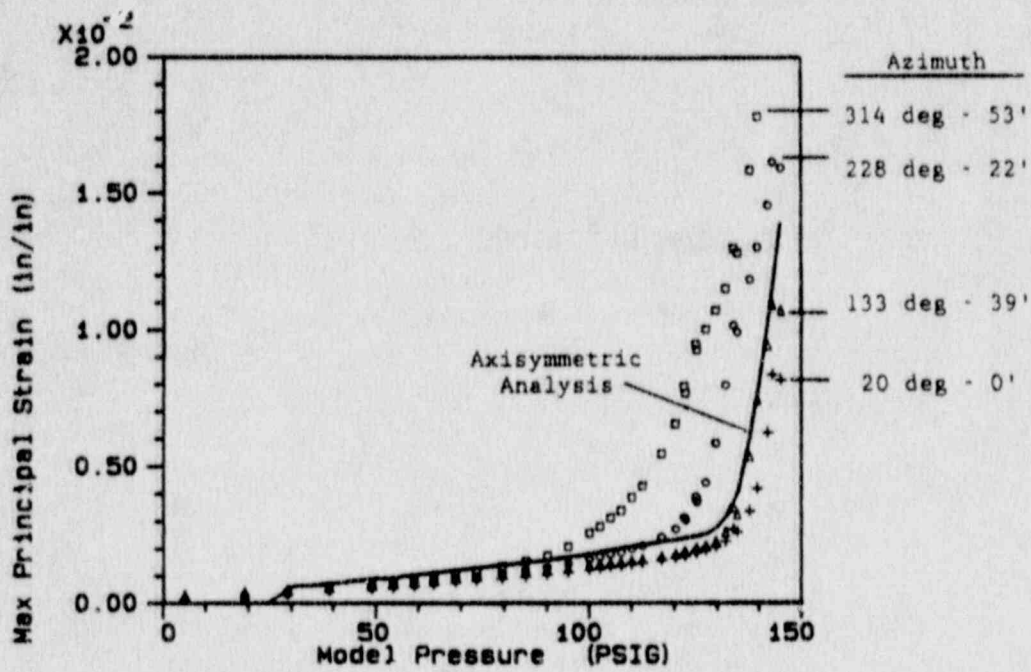


Figure 5.3.28  Free-Field Liner Maximum Principal Strain Measurements
in Four Azimuthal Quadrants vs. Axisymmetric Analysis

Flat piece of
steel plate

Strain Concentration of
Approx. 2.5 to 3.5

Mid plane of thicker material

Strain
Concentration

Mid plane of
thinner material

eccentricity

Section A-A

## 1. Thickness Transition

Penetration C̸

Major Crack

Thickened Insert
Plate
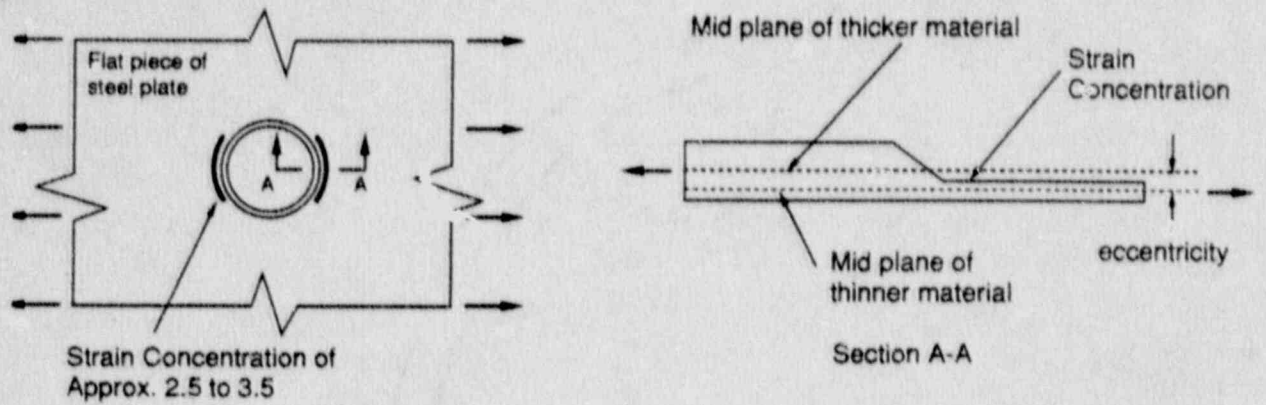
Undeformed
Position

## 2. Shear Dislocation

Very Localized Liner Strain Concentration Due to Stud
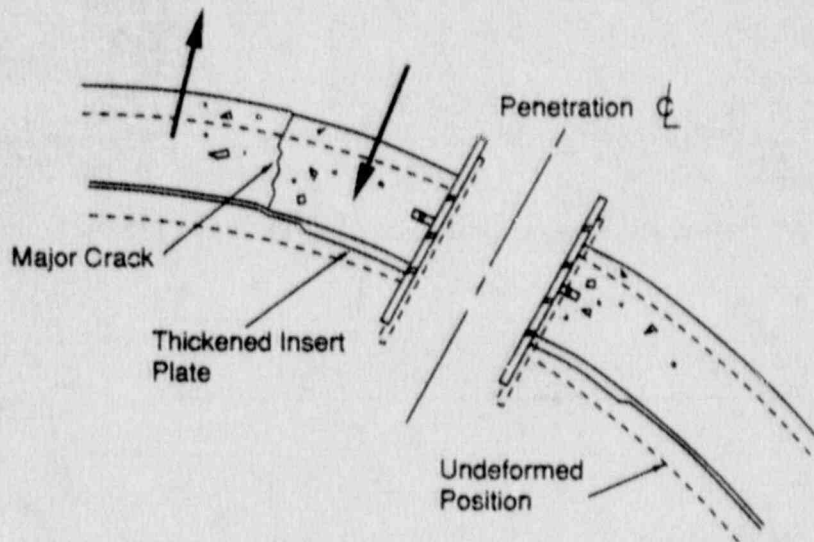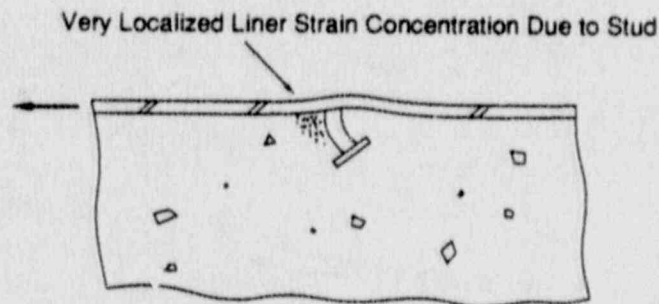
## 3. Crimping Due to Stud

Figure 5.3.29  The Three Primary Liner Strain Concentration Mechanisms
that Occur Near Penetrations

Exper. vs. Analysis Strain Profile, 8 in. Penetr.

$X10^{-2}$

MAXIMUM PRINCIPAL STRAIN

ANALYSIS

EXPERIMENT GAGE NUMBERS

R121
R110
ST7

R110 LOCATED NEXT TO THE 135° PENETRATION
ALL OTHERS LOCATED NEXT TO THE 315°
PENETRATION

R120

R109

Distance From CL of Penetr., Inches

Exper. vs. Analysis Strain Profile, Eq. Hatch A

$X10^{-2}$

MAXIMUM PRINCIPAL STRAIN

ANALYSIS

EXPERIMENT GAGE NUMBERS

R1

R14
R2

R3
R17  R5
R16   R4          R18

Distance From CL of Hatch, Inches

Figure 5.3.30  Principal Strain Profile Comparisons at 145 psig
Moving Out Horizontally from the 8" Constrained Penetration
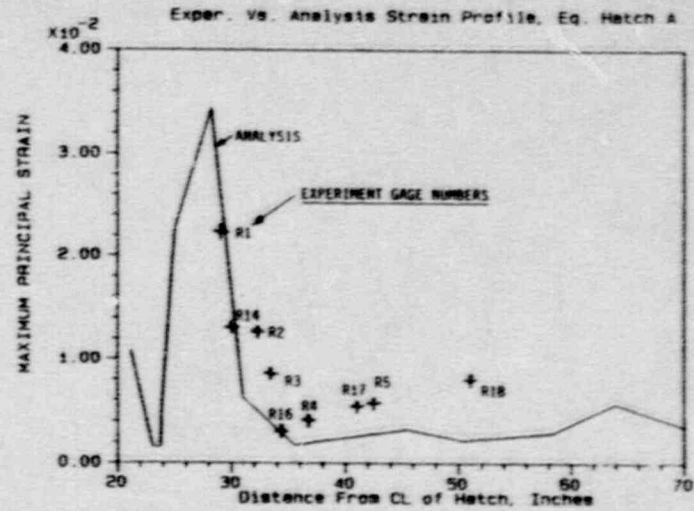
Figure 5.3.31  Principal Strain Profile Comparisons at 145 psig
Moving Out from Equipment Hatch A

Analysis Vs. Exp. Strain Profile at Eq. Hatch B

$X10^{-2}$

MAX PRINCIPAL STRAIN

R78

ANALYSIS

R77

STRAIN GAGE
NUMBERS

R80
R79

Distance From CL of Hatch  Inches
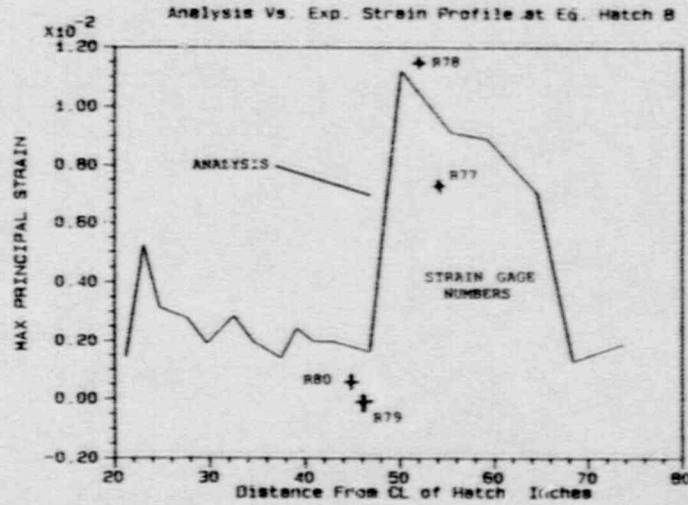
Figure 5.3.32  Principal Strain Profile Comparisons at 145 psig at Equipment Hatch B
Root of Embossed Concrete at 50"; Edge of Hatch at 20.5"
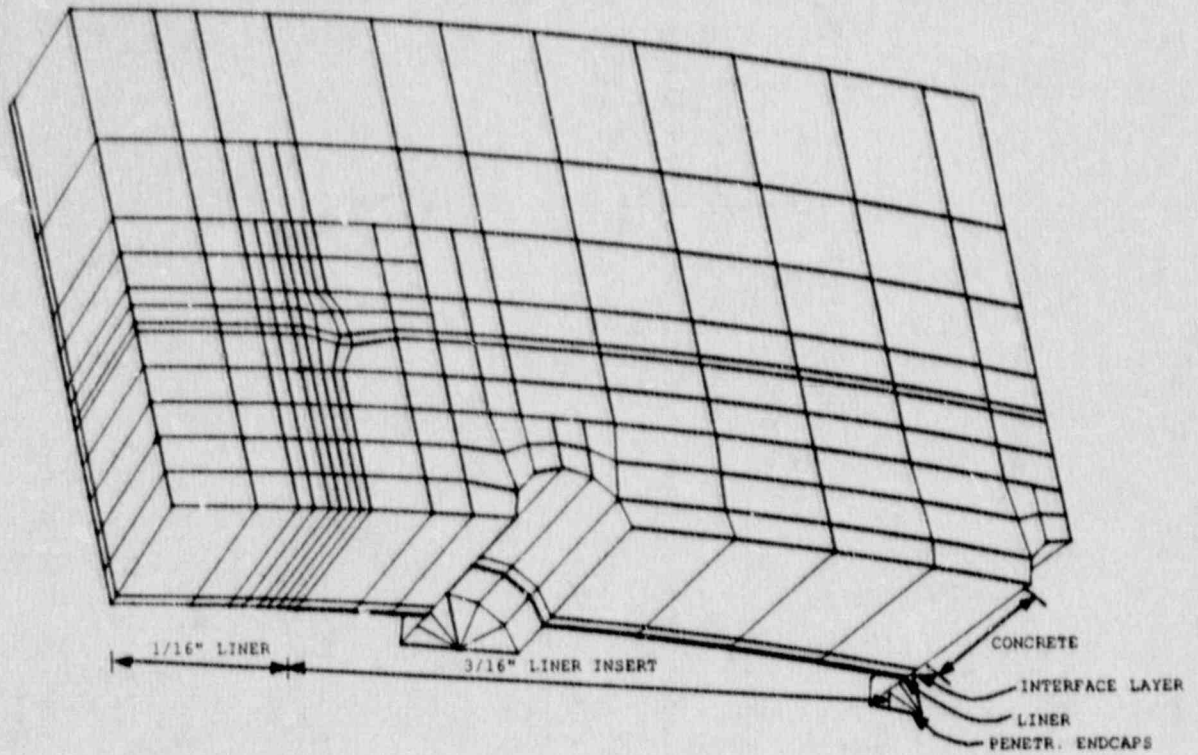
Figure 5.3.33  1/4-Symmetry Grid for Mechanical/Electrical Feedthrough Penetration Analysis - Symmetry Planes on Lower and Right Edges
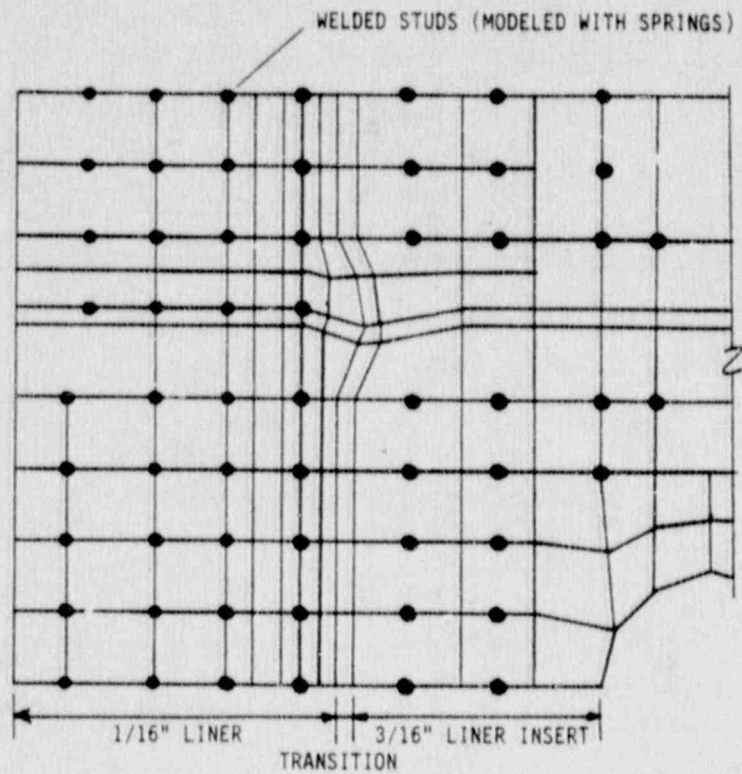


Figure 5.3.34  Enlarged View of Critical Region Around Edge of 3/16" Insert Plate
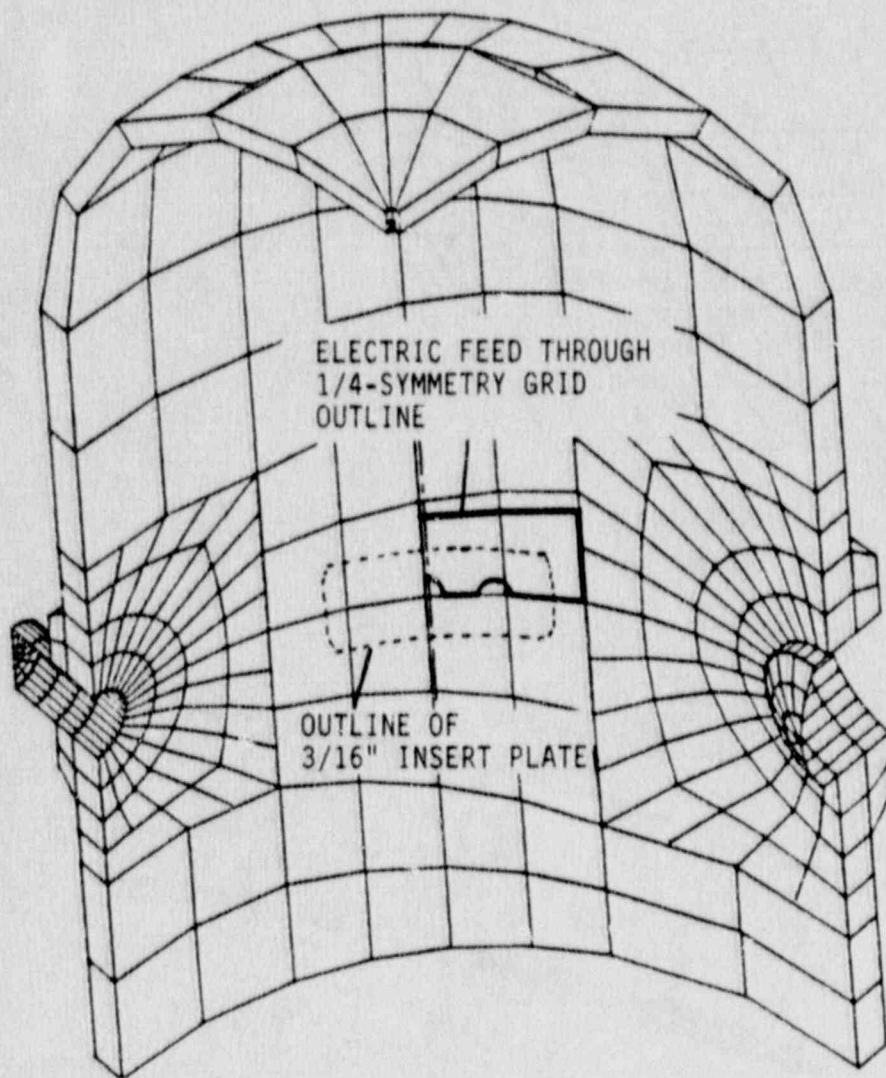
Figure 5.3.35  Old Quarter Model Grid Showing Boundaries of Feedthrough Grid
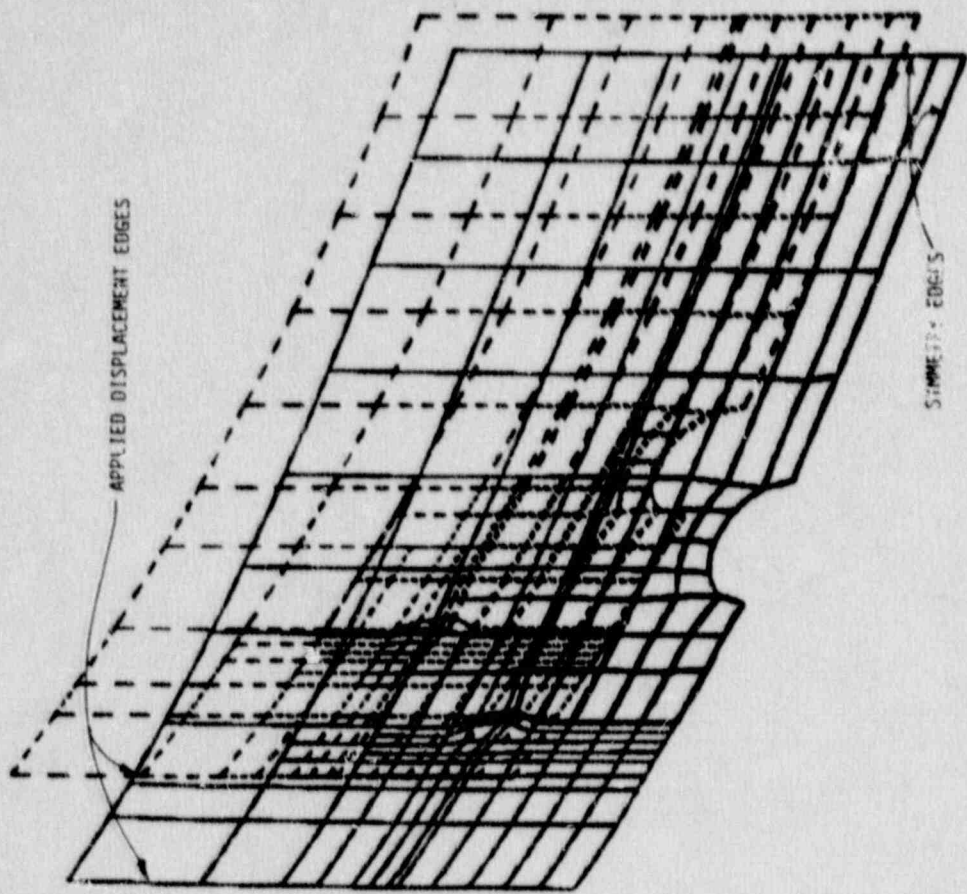
Figure 5.3.37 Perspective View (Liner Only) at 120 psig, Displacements X10
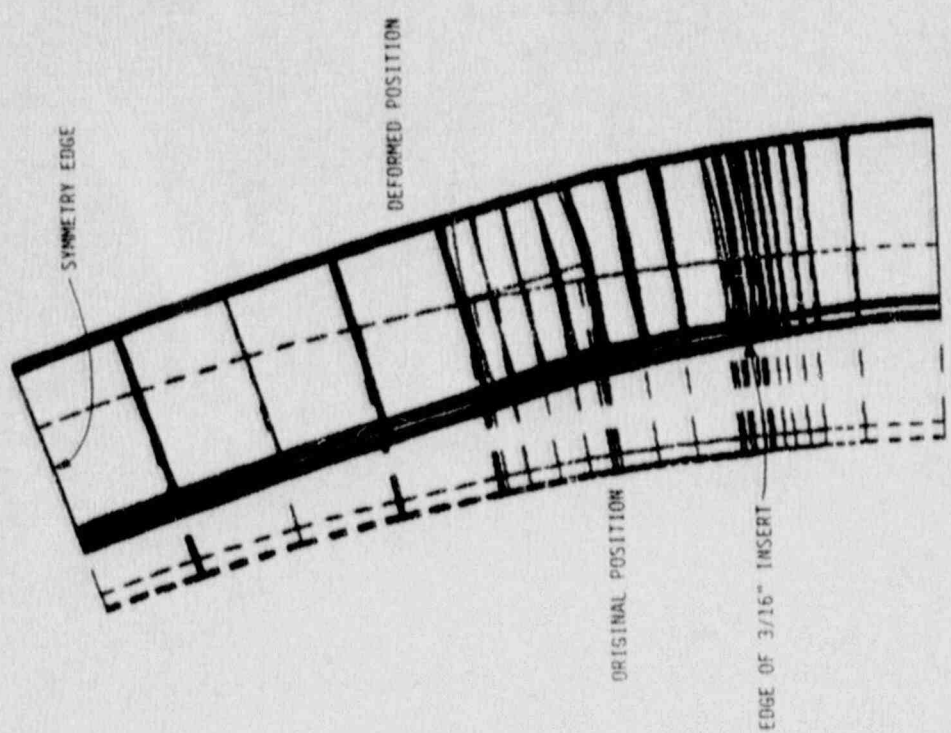


Figure 5.3.36 Top View of Deformed Feedthrough Grid at 120 psig, Displacements X10
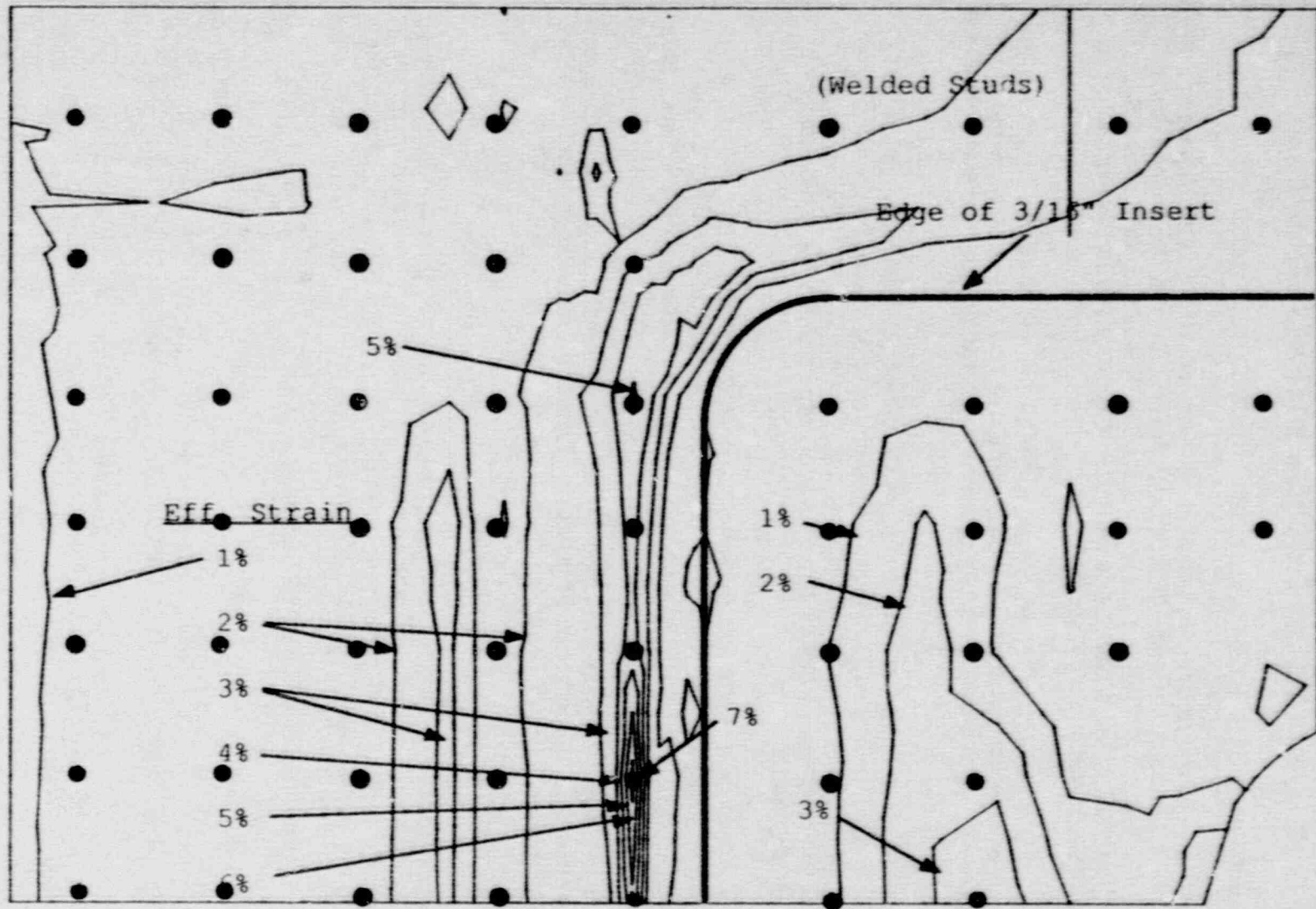
Figure 5.3.38 Effective Strain Contour Plot With Locations of Welded Studs and Edge of 3/16" Insert Plate Also Shown

## 5.4 Commissariat a L'Energie Atomique

This section was authored by J. Rivière and B. Barbé (CEA/IPSN/DAS), A. Millard and Ph. Jamet (CEA/IRDI/DEMT), and V. Koundy (CISI/INGENIERIE)

### 5.4.1 Introduction

Forecasting the behavior under pressure of the 1/6-scale model has already been the subject of two axisymmetric finite element calculations. In one, the foundation soil was considered to be infinitely rigid and in the other it was assigned a modulus of 61.26 MPa/m (390 ksf/ft). In these calculations, the fill slab and protective course at the bottom of the basemat were disregarded.

Agreement of the theoretical and experimental results was found to be generally satisfactory, except for lifting of the outer edge of the basemat, for which the calculated values were some three times greater than those measured experimentally [11,36].

Subsequent to this initial study, several other calculations were made [37], particularly, with allowance made for the additional rigidity caused by the fill slab at the upper surface of the basemat, of the sensitivity of the results to the value of the modulus of the soil, and of more accurate values of the thickness of the leak-tight liner supplied by Sandia.

All these theoretical results are reviewed in this report and are systematically compared to the experimental results. Also, the accuracy of the calculation results is evaluated by examining the effect of the convergence tests used in the INCA code calculation algorithm.

Lastly, it is explained how, as indicated in the experimental results, the leak-tight liner in the vicinity of a mechanical penetration is subjected to sufficient plastic strain to cause it to be torn.

### 5.4.2 Overall Behavior of the Containment

After having described the different calculations with the basic data and hypotheses, a comparison is made of the different numerical results, both for global deformed shape and for cracking of the concrete. Finally, these results are set against the experimental values obtained with the scale model.

#### 5.4.2.1 Description of the different calculations

In this report, the following nomenclature is used:

- Calculation 1 - Calculation carried out earlier [11,36] with a ground modulus of 61.26 MPa/m (390 ksf/ft) and in the absence of the fill slab.

- Calculations 2 and 3 - Calculations made with allowance for the additional rigidity caused by the fill slab and soil modulus considered to be 61.26 MPa/m (390 ksf/ft) and then 10 MPa/m (64 ksf/ft), respectively.

These calculations are summarized in Table 5.4.1. In Figure 5.4.1, the grid for calculations 1, 2, and 3, as well as the numbers of certain nodes corresponding to the positions of the measurement points, are shown.

## Table 5.4.1 - Summary of Calculations

|  | Calculation 1 | Calculation 2 | Calculation 3 |
|---|---|---|---|
| Basemat | Without fill slab | With fill slab without slip | With fill slab without slip |
| Concrete - Ultimate tensile strength | 3.45 MPa (0.50 ksi) | 3.16 MPa (0.46 ksi) | 3.16 MPa (0.46 ksi) |
| Concrete - Ultimate compression strength | 46.90 MPa (6.8 ksi) | 43.44 MPa (6.3 ksi) | 43.44 MPa (6.3 ksi) |
| Thickness of leak-tight liner at cylindrical section and basemat | 1.59 mm (0.0625 in.) | 1.73 mm (0.068 in.) | 1.73 mm (0.068 in.) |
| Thickness of leak-tight liner at dome | 2.12 mm (0.083 in.) | 2.29 mm (0.090 in.) | 2.29 mm (0.090 in.) |
| Stiffness of soil | 61.26 MPa/m (390 ksf/ft) | 61.26 MPa/m (390 ksf/ft) | 10 MPa/m (64 ksf/ft) |

## Calculation 1

The finite element model generated by the GIBI code consists of:

- 1,162 nodes,

- 3,826 three-node triangular elements,

- 688 two-node shell elements, and

- 419 one-node cable elements.

The mechanical calculation, which allows for damage to the concrete and plasticity of the reinforcing steel, is carried out using the INCA code. Post-processing of the results is carried out using the ALICE code.

The properties of the materials used are the following:

Concrete:
| | |
|---|---|
| Young's modulus | 33,100 MPa (4800 ksi) |
| Poisson's coefficient | 0.2 |
| Density | 2,300 kg/m³ (144 lb/ft³) |
| Ultimate tensile strength | 3.45 MPa (0.5 ksi) |
| Ultimate compression strength | 46.90 MPa (6.8 ksi) |

Reinforcement:
| | |
|---|---|
| Young's modulus | 214,000 MPa (31000 ksi) |
| Poisson's coefficient | 0 |
| Density | 7,800 kg/m³ (486 lb/ft³) |
| Yield point | 459 MPa (66.6 ksi) |
| Ultimate stress | 682 MPa (98.9 ksi) |
| Ultimate strain | $4.57 \times 10^{-2}$ |

Leak-tight liner:
| | |
|---|---|
| Young's modulus | 207,000 MPa (30000 ksi) |
| Poisson's coefficient | 0.3 |
| Density | 7,800 kg/m³ (485 lb/ft³) |

Basemat Liner:
| | |
|---|---|
| Yield point | 346 MPa (50.2 ksi) |
| Ultimate stress | 482 MPa (69.9 ksi) |
| Ultimate strain | $16.4 \times 10^{-2}$ |

Cylinder and Dome Liner:
| | |
|---|---|
| Yield point | 354 MPa (51.3 ksi) |
| Ultimate stress | 489 MPa (70.9 ksi) |
| Ultimate strain | $14.9 \times 10^{-2}$ |

Ground:

The stiffness of the ground is taken to be 61.26 MPa/m (390 ksf/ft) in calculations 1 and 2 and 10 MPa/m (64 ksf/ft) in calculation 3.

Calculation 2

Here, the three layers of concrete covering the upper part of the basemat are added to the model. Its thickness is 0.457 m (18 in.), which is roughly half that of the basemat itself, of which the thickness is 0.978 m (38.5 in.). We assume that the fill slab and protective course, which necessitate adding 78 nodes and 300 triangular elements, do not slide on the upper part of the basemat.

The properties of the materials, on the basis of the indications given by Sandia, are modified as follows:

Concrete:
| | |
|---|---|
| Ultimate tensile strength | 3.16 MPa (0.5 ksi) |
| Ultimate compression strength | 43.44 MPa (6.3 ksi) |

Leak-tight liner (thickness):
| | |
|---|---|
| Cylindrical section and basemat | 1.73 mm instead of 1.59 mm (0.068 in. instead of 1/16 in.) |

Calculation 3

The third calculation is identical to the second, except that in this case the stiffness of the soil is taken to be 10 MPa/m (64 ksf/ft)

**5.4.2.2 Results of calculations**

The results of the different calculations are successively compared for global deformed shape, cracking of the concrete and vertical movement of the basemat.

Comparison of deformed shape

The displacement amplification coefficient is taken to be 30 in all cases. Figure 5.4.2, which shows the strain of the scale model subjected to its own weight alone for the three calculations, shows that:

- The weight of the fill slab with a ground modulus of 61.26 MPa (390 ksf/ft) as used in calculations 1 and 2 has little effect on the initial settling.

- Settling is roughly six times greater with the ground modulus of 10 MPa (64 ksf/ft) used in calculation 3, i.e., 6 mm (0.24 in.)

Figures 5.4.3 to 5.4.6 give the deformation of the scale model under the effect of internal pressure (excluding its own weight) varying between 0.4 MPa (58 psig) and 1.05 MPa (152 psig). These figures require the following comments:

- When P = 0.4 MPa (58 psig), deformation is very similar in all three calculations.

- When P = 0.5 MPa (72 psig), the radial displacement of the containment is substantially identical with all three calculations. On the other hand, the vertical displacement is greater with calculation 1 due to the lifting of the basemat, which is absent when the rigidity introduced by the fill slab is taken into consideration (calculations 2 and 3).

- When P = 0.98 MPa (142 psig), radial displacement is slightly less extensive with calculations 2 and 3 than with calculation 1. There is no doubt a relationship between this and the increase in the thickness of the leak-tight liner. The lifting of the edge of the basemat, as measured relative to its center, is some three times greater withcalculation 1 than with calculations 2 and 3.

- When P = 1.05 MPa (152 psig), displacement rapidly increases in the cylindrical section and the dome. On the other hand, no additional flexing of the basemat than in the previous pressure step appears to occur.

Comparison of cracking

Development of cracking as a function of pressure, in meridional plane RZ, is shown in Figures 5.4.7 to 5.4.12. The cracked zones are plotted in the outline of the strained structure. It is found that:

- The first cracks appear in the three calculations at P = 0.2 MPa (29 psig) where the cylindrical section joins the basemat.

- When P = 0.4 MPa (58 psig), cracking is observed to appear at the center of the basemat with calculation 1; this cracking, which occurs earlier than in calculations 2 and 3, is due to the bending of the basemat (see Figure 5.4.3).

- When P = 0.5 MPa (73 psig), the basemat begins to crack with calculation 3 whereas this is not the case with calculation 2; this difference in behavior is no doubt attributable to the rigidity of the soil in calculation 3, which is six times lower than in calculation 2.

- Above P = 0.6 MPa (87 psig), the dome and the cylindrical section are completely cracked with all three calculations, while cracking of the basemat continues to increase.

Vertical displacement of bottom of basemat

Displacement of the inner surface of the basemat as a function of pressure is given for the three calculations in Figures 5.4.13 to 5.4.15. It is found that:

- The rigidity introduced by the fill slab (calculation 2) reduces the sinking of the center of the basemat (calculation 1).

- Using a lower ground modulus in calculation 3 increases the sinking of the center of the basemat, which becomes comparable to that in calculation 1.

- The area of contact between the soil and the basemat increases from calculation 1 to calculation 3. This area depends both on the stiffness of the basemat and the stiffness of the soil. It will be noted that in calculation 3, the basemat bends about the same point as when the pressure increases.

- When pressure P = 0.98 MPa (142 psig), the displacement of the end of the basemat as measured relative to its center is respectively 25, 9.6 and 10.6 mm (0.98, 0.38, and 0.42 in.) with calculations 1, 2 and 3.

### 5.4.2.3 Comparison of numerical and experimental results

The displacement transducers and the corresponding nodes are shown in Figure 5.4.1.

Before the comparison is made, it must be remembered that the scale model has undergone an initial design pressure test which has in all probability already cracked the concrete. This being the case, the theoretical results, which do not account for this initial cracking, are not directly comparable with the experimental results. This reservation explains that the theoretical curves, unlike the experimental curves, show a sudden discontinuity in slope in the vicinity of the design pressure.

Radial displacement

Comparison of the radial displacement obtained with calculations 2 and 3, along a generatrix of the cylinder, with that obtained by experimental measurement with

transducers D96, D97, D100, D101, D102 and D103 (Figure 5.4.1) is given in Figures 5.4.16 to 5.4.23.

These figures require the following remarks:

- Firstly, it is found that there is no significant difference between calculations 2 and 3; this means that radial displacement is independent of the value of the soil modulus.

- As a general rule, the theoretical curves show a plastic step which appears with pressure values approximately 0.1 MPa (14.5 psi) above that of the experimental curves. This systematic shift is partly due to the measurement accuracy and basic data, but above all to the convergence criteria used in the calculation algorithm.

Vertical displacement

A comparison of the vertical displacement between the measurements and calculations 2 and 3 is given in Figures 5.4.24 to 5.4.27. The measured values are all higher than the calculated values. The displacement at transducers D95, D98 and D104 is slight. For sensor D104, a significant difference appears between the theoretical curve and the experimental curve, no doubt due to incorrect adjustment of the zero point of the sensor.

For transducer D105 (Figure 5.4.27), which is located at the point where the cylindrical section joins the dome, the displacement is more significant. Agreement between the experimental and numerical values is good.

The discontinuity in the slope of the theoretical curves at between 0.5 and 0.6 MPa (73 and 87 psig) corresponds partly to cracking of the basemat and to a lesser degree to cracking of the cylindrical section (Figures 5.4.10 and 5.4.11). This slope discontinuity is not found in the experimental curves as the cracking is more gradual.

Lifting of the basemat

Figure 5.4.28 represents the lifting of the periphery of the basemat relative to its center. The displacement values at close to 1 MPa (145 psig) are:

- measured               8.6 mm     (0.34 in.)

- calculation 1        24.0 mm    (0.94 in.)

- calculation 2        9.6 mm     (0.38 in.)

- calculation 3        10.6 mm    (0.42 in.)

These values thus show that allowance for the rigidity caused by the fill slab results in an improvement in the numerical results. On the other hand, the stiffness of the soil has little effect on the intensity of the lifting, as is shown with calculations 2 and 3.

## Vertical movement of center of dome

Vertical movement of the center of the dome as a function of pressure is shown in Figure 5.4.29. The analysis of the curves of this figure indicates that:

- The displacements obtained with calculations 2 and 3 vary only slightly.

- The experimental curves and those obtained with calculations 2 and 3 are in close agreement.

- Up to a pressure of 0.5 MPa (73 psig), displacement is virtually identical whatever the calculation model. Above 0.5 MPa (73 psig), the differences become significant between calculations 2 and 3 on one hand and calculation 1 on the other. Indeed, the maximum displacement values are of the order of 45 mm (1.77 in.) with calculation 1 and of the order of 27 mm (1.06 in.) with calculations 2 and 3 and with the experimental curve.

## Strain

Total strain as a function of pressure is given in Figures 5.4.30 to 5.4.40. Figures 5.4.30 to 5.4.37 relate to the vertical reinforcement of the cylindrical section and Figures 5.4.38 to 5.4.40 relate to the circumferential reinforcement. The position of the nodes and the intensity of the strain obtained with a pressure of 1.05 MPa (152 psig) are given in Table 5.4.2.

### Table 5.4.2

| Mesh node | Elevation (ft) | Strain (%) for inner reinforcement | Strain (%) for outer reinforcement | Figure | Remarks |
|---|---|---|---|---|---|
| | | ------- Vertical Reinforcement ------- | | | |
| 363 | 23.92 | | 0.17 | 30 | |
| 366 | 23.92 | 0.23 | | 31 | |
| 435 | 20.00 | | 0.2 | 32 | Plastification |
| 543 | 13.75 | | 0.24 | 33 | from |
| 558 | 13.00 | 0.17 | | 34 | 1.05 MPa |
| 665 | 6.75 | | 0.17 | 35 | |
| 815 | 2.10 | | 0.12 | 36 | |
| 818 | 2.10 | 0.18 | | 37 | |
| | | ------- Horizontal Reinforcement ------- | | | |
| 435 | 20.00 | | 0.63 | 38 | Plastification |
| 543 | 13.75 | | 0.9 | 39 | from |
| 665 | 6.75 | | 0.53 | 40 | 0.925 MPa |

The table shows that maximum total strain of the vertical reinforcement bars is slight compared to that of the circumferential reinforcing bars (between 3 and 3.75 times less). The high strain value is recorded at node 543, and is of the order of 0.9%.

Overall, the measured and calculated strain of the vertical reinforcement bars are comparable except for the nodes located between the lower part of the cylindrical section (Figures 5.4.36 and 5.4.37). The slope discontinuity observed in the curves corresponds to cracking of the concrete (compared with Figures 5.4.7 to 5.4.12: the reinforcement picks up the loading up to the point to which the concrete cracks).

For the circumferential bars, in which the strain values are higher, the calculated and measured values are in closer agreement, the measured values being significantly higher than the calculated values.

### 5.4.2.4 Evaluation of stress

Figures 5.4.41 to 5.4.43 give curves showing stress as a function of pressure respectively in the concrete, the leak-tight liner and the outer reinforcement. Stress levels are given for nodes 553, 554, 555, 556, 557, and 558, which are all located at the same height at the middle of the cylindrical section where the radial displacement is greatest. The positions of these nodes are shown in the following diagram:

Thickness

| $R_i \rightarrow$ | 556 | 558 | 557 | 555 | 554 | 553 |

Middle of cylindrical section →

| Leak-tight liner | Inner reinforcement | Outer Reinforcement | Seismic Reinforcement | Outer facing |
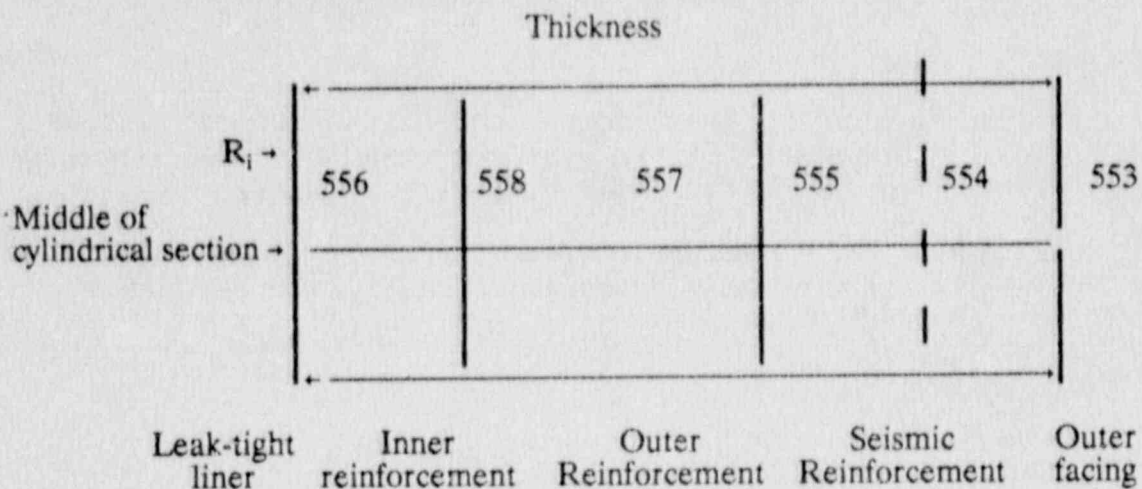
In the mesh, these nodes (except 557) belong to both the concrete and the reinforcement.

Stress in concrete

Figure 5.4.41 shows that the axial stress is practically uniform throughout the thickness. The concrete attains the tension damage criterion at 0.55 MPa (80 psig) for the vertical direction and at 0.2 MPa (29 psig) for the circumferential direction.

Stress in liner and reinforcement

The curve in Figure 5.4.42 shows a decrease in vertical stress in the leak-tight liner corresponding to an increase in the vertical stress of the vertical bars located close to the outer liner of the wall (see Figure 5.4.43).

### 5.4.3 Accuracy of Calculation

In the nonlinear calculations made with the INCA code, the convergence of the iterative method can be tested in two different manners.

### 5.4.3.1 Global criterion

As a general rule, the tests are carried out with global variables, i.e., variables such as nodal displacement, nodal force or event energy.

In the case of the INCA code, this test is carried out at all the nodes of the grid and concerns the increment in $\Delta q$ displacement for the loading step considered.

$$\frac{||\Delta q\,(n+1) - \Delta q\,(n)||}{||\Delta q\,(n+1)||} < P$$

where n is the index of iteration and $P = 0.01$ is the accuracy criterion adopted.

### 5.4.3.2 Local criterion

The tests on local variables are more stringent as they relate to quantities defined at certain points of the element (integration points) for which there is frequently a less accurate approximation than for the global variables from which they are derived.

In practice, with the INCA code, these tests are made on equivalent plastic strain increment $\Delta \varepsilon^*$ and on plastic energy W dissipated at all integration points of the grid and for each load increment considered.

$$\frac{||\Delta \varepsilon^*(n+1) - \Delta \varepsilon^*(n)||}{||\Delta \varepsilon^*(n+1)||} < P$$

$$\frac{||\Delta W^t(n+1) - \Delta W^t(n)||}{||\Delta W^t(n+1)||} < P'$$

where $\Delta W^t = \overline{\sigma_{ij}} \Delta \varepsilon^P_{ij}$ with $\overline{\sigma_{ij}} = \frac{\sigma^0_{ij} + \sigma^f_{ij}}{2}$

and $\sigma^0_{ij}$ = stress at start of increment

$\sigma^f_{ij}$ = stress at end of increment

n = iteration index

P and P' = accuracy criteria adopted = 0.01

### 5.4.3.3 Application to scale model

Calculation of behavior of the model under pressure is repeated with allowance for the local criteria. The results obtained are compared to those made (calculation 1) using the global criterion.

Global strain

Figures 5.4.44 and 5.4.45 show that:

- For pressures of 0.3 and 0.4 MPa (44 and 58 psig), axial displacement is virtually identical. On the other hand, vertical displacement is considerably greater when the local criterion is used.

- When $p = 0.4$ MPa (58 psig), lifting of the basemat is observed to start only above 0.5 MPa (73 psig) in calculation with the global criterion (Figure 5.4.4 - calculation 1).

Cracking

The cracks in plane RZ are indicated in Figure 5.4.46 which shows that:

- Distribution of cracks in the cylindrical section is denser when $P = 0.3$ MPa in calculation with the local criterion than with the global criterion.

- Tipping and cracking of the basemat is more extensive at a given pressure (Figure 5.4.47), when the local criterion is used.

Conclusion

As a general rule, use of the local criterion indicates that, at a given pressure, the structure shows significantly more damage than when the calculation is made with the global criterion. Overall, this tendency for damage to occur in the structure at an earlier stage results in better correlation between the experimental and theoretical results.

The difficulty in using the local criterion in the numerical convergence process is due to the considerable number of iterations necessary to attain collapse of the containment. For this reason, the calculations have been limited to a pressure of 0.4 MPa (58 psig).

### 5.4.4 Local Study in the Vicinity of a Penetration

The pressurization test of the 1/6-scale containment model was limited to a pressure in the vicinity of 1.0 MPa (145 psig) due to the appearance of tears in the leak-tight liner. The largest tear, which was 0.55 m (22 in.) in length, was located at midheight of the containment close to the edge of a insert plate surrounding a set of three penetrations (Figure 5.4.48).

### 5.4.4.1 Goals

Global analysis of the containment using axisymmetric finite element calculation codes does not allow modelling of special features such as penetrations. Thus, determination of the rupture mechanisms was investigated by a local approach.

Indeed, the results of the experiment showed that the tear phenomena were due to stress concentrations near studs. These secure the liner to the containment concrete to avoid buckling in the event of heavy thermal loading.

The goals of the following study are firstly to determine by finite element calculation the behavior of the liner in the vicinity of the insert plate and secondly to show the role of the studs in the appearance of the tear.

### 5.4.4.2 Geometry

The system consisting of the insert plate, the leak-tight liner, the studs and the wall of the containment is shown in Figure 5.4.49. The thickness of the liner is 1.5875 mm (1/16 in.), that of the insert plate is three times greater, i.e., 4.7625 mm (3/16 in.).

The studs are approximately 20 mm (3/4 in.) long and are 3.43 mm (0.135 in.) in diameter. In typical areas, the studs are welded to the liner in a 152.4 x 152.4 mm (6 x 6 in.) grid pattern. In the vicinity of the insert plates, the grid density is increased to 50.8 x 50.8 mm (2 x 2 in.).

### 5.4.4.3 Modelling

The leak-tight liner and the insert plate are modelled over a length of 78 cm (30 7 in.) and allowance is made for 13 studs providing a link with the concrete.

The grid used (Figure 5.4.49) comprises:

· 633 nodes,

· 144 isoparametric 8-node elements, and

· 6 isoparametric 6-node elements.

The liner and insert plate behavior law is given in Figure 5.4.50, the maximum ductility being 16%.

The stud behavior law (Figure 5.4.51) is calculated using the shear tests carried out by Sandia.

### 5.4.4.4 Loading

Three types of loading are applied:

· pressure on inside surface,

· tangential displacement ($u_y$) imposed at the studs, and

· imposed vertical strain.

## Pressure

The pressure imposed on the inner surface of the model is that corresponding to pressurization of the containment. This pressure which is relatively low compared to the other forms of loading will oppose any tendency for the liner to separate from the insert plate. The nodes in contact with the concrete have unilateral links that allow separation of the insert plate and the liner.

## Tangential displacement $U_y$

To simplify the local study, the curvature of the containment is disregarded and it is considered that the studs move with the concrete. This hypothesis provides freedom from the need to model the concrete by imposing on each stud the tangential displacement calculated on the basis of the experimental strain of the concrete (Figure 5.4.52) which is evaluated in the following manner:

$$U_{Gi} = Y_i . \varepsilon_\theta$$

where $U_{Gi}$ is the tangential displacement of stud i, $Y_i$ is the distance of a stud relative to the fixed nodes, and $\varepsilon_\theta$ is the tangential strain of the concrete wall.

## Vertical deformation

The calculation is based on generalized planar strain obtained by imposing the experimental vertical strain of the concrete (Figure 5.4.52) at all the mesh nodes.

### 5.4.4.5 Results

Two calculations are made:

- one under the exact conditions of the scale model under pressure,

- one with the stud (G4) welded to the liner in the immediate vicinity of the insert plate deleted.

## Calculation 1

This calculation is made at up to 0.95 MPa (138 psig). At this pressure, the maximum equivalent Von Mises strain is located in the liner close to the insert plate (Figure 5.4.53). The strain is of the order of 15% making it possible to assume that the conditions of tearing of the liner are reached, especially if allowance is made for the residual stresses induced by the weld bead. Furthermore, it is found that bending of the insert plate involves separation of around 0.4 mm (Figures 5.4.54 and 5.4.55).

The Von Mises stress in the studs, located on either side of the liner-insert plate joint, reaches the plasticity level at a pressure of 0.95 MPa (138 psig), as shown in Figure 5.4.56.

Calculation 2: Deletion of stud G4

Deletion of a stud gives lower Von Mises strain than in the preceding case. Indeed, the maximum strain at 0.95 MPa (138 psig) is roughly 7.3% (Figure 5.4.57), as compared to 15% calculated in the presence of the stud.

Strain at 1 MPa (145 psig) is close to 10% (Figure 5.4.58). The liner has therefore not yet reached its breaking point (approximately 16%).

The strain at a pressure of 0.95 MPa (138 psig), Figure 5.4.59, shows that there is less separation of the liner than in the preceding case.

The stresses in the studs (Figure 5.4.60) are of the same order of size.

### 5.4.4.6 Conclusion

This analysis indicates that the mechanisms responsible for tearing of the liner are effectively represented. The tear is caused by the combined action of the following two factors:

- Firstly, the difference between the stiffness of the insert plate and that of the leak-tight liner,

- Secondly, the stud at the edge of the insert plate induces a major stress concentration by limiting displacement.

Deletion of a stud reduces the strain, nevertheless, it remains to be determined whether its deletion is compatible with the design basis accident thermal loading.

### 5.4.5 General Conclusion

Study of the behavior of the 1/6-scale model of a pressurized water reactor containment under pressure indicates that the theoretical and experimental results for the structure, which is assumed to be perfectly axisymmetric, are in good general agreement:

- The maximum strain and displacement occur at mid-height of the containment. If it is assumed that liner integrity is preserved, collapse of the containment would only occur when the horizontal reinforcement ductility limit is reached under a pressure of the order of 1.05 MPa (152 psig), which is about 3.3 times the design pressure.

- The rigidity of the soil has no significant effect on the overall behavior on the containment.

- Flexing of the basemat and the resulting cracking and lifting of the outer edge vary greatly with the rigidity value used in calculation. In particular, the hypothesis that there is no relative movement between the basemat itself and the fill slab appears to be realistic.

- The overall convergence criterion used in the calculation algorithm gives a perceptibly stiffer structure than the experimental structure. The use of a more constraining local criterion tends to make the structure more flexible,

but its use for pressures corresponding to substantial cracking of the concrete raises numerical convergence problems.

Study of the behavior of the leak-tight liner in the vicinity of a mechanical penetration indicates that:

- In view of the method used to secure the liner to the concrete and the additional rigidity introduced by the insert plate, plastic strain in the vicinity of a vertical line close to the penetration reaches a level that can explain the tearing of the liner.

- Deletion of the stud closest to the insert plate reduces plastic strain by about half. It remains to be determined whether such deletion is compatible with the design basis accident thermal loading.

As a whole, this study bears out the calculation code used (INCA) and makes it possible to envisage moving on to study the behavior of a prestressed containment with greater confidence.
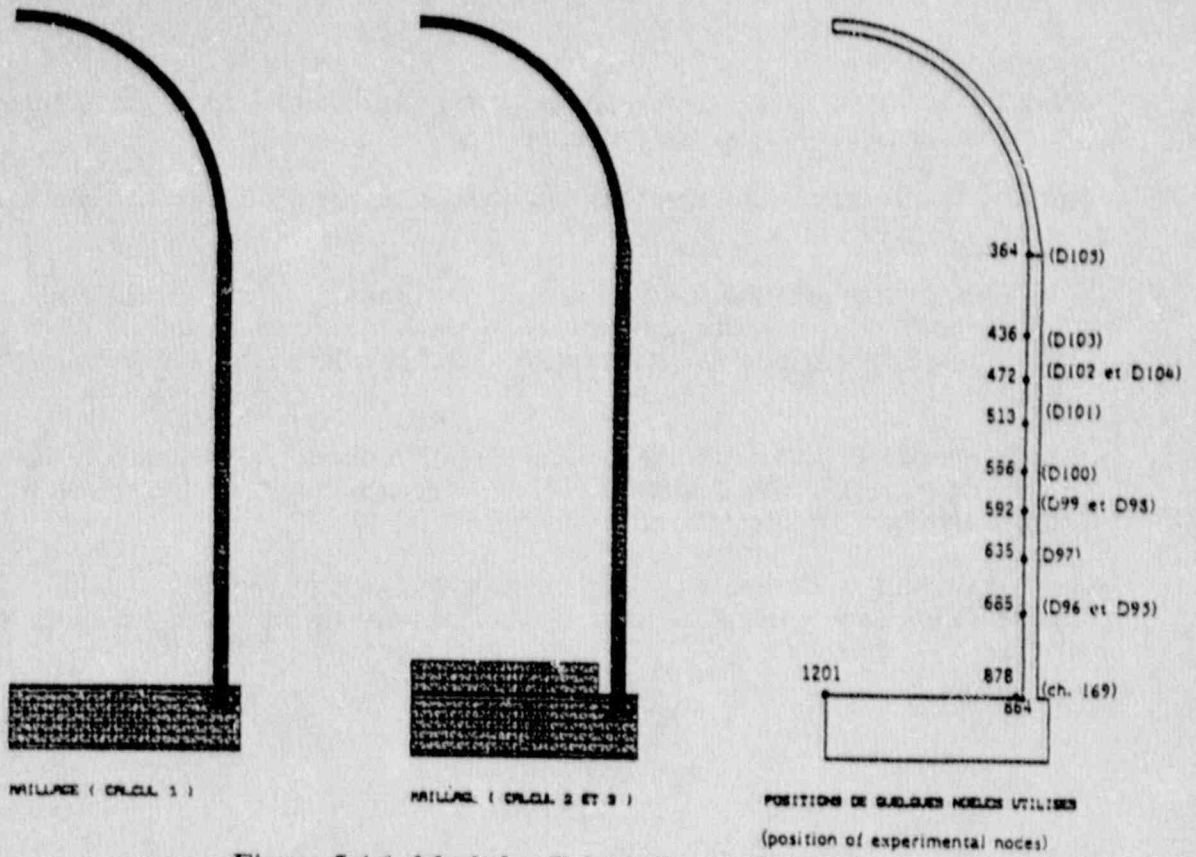
Figure 5.4.1  Mesh for Calculations 1, 2, and 3
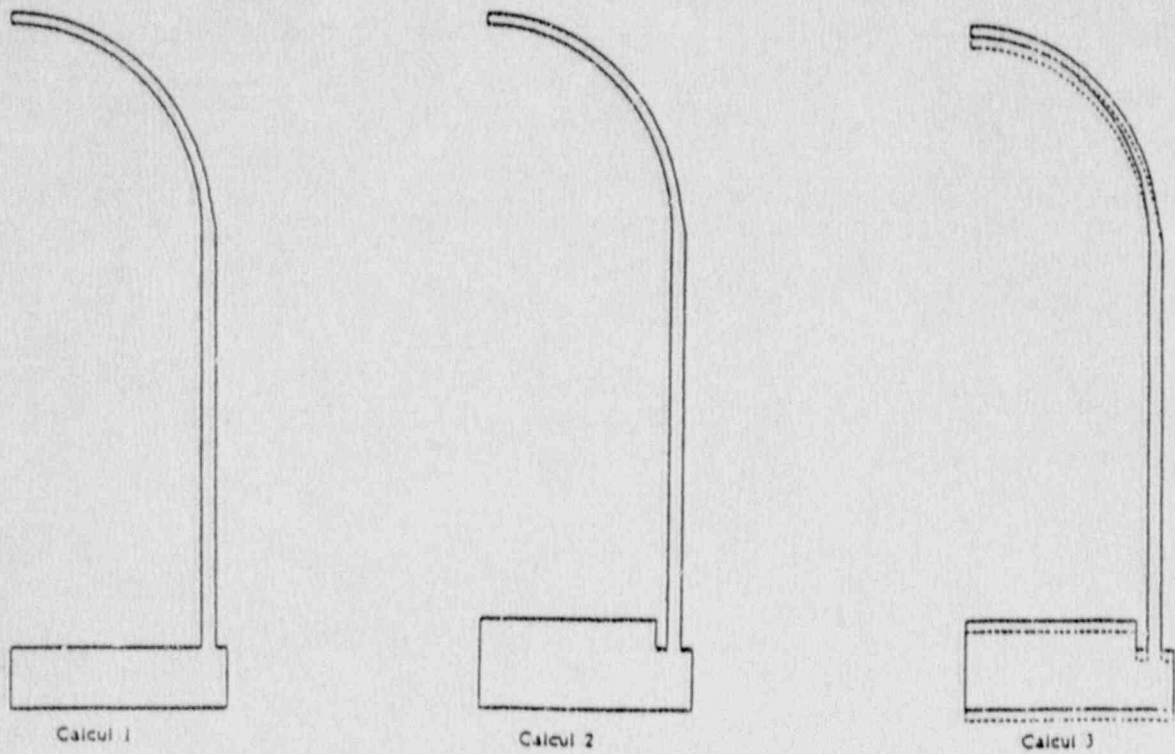


Figure 5.4.2  Deformed Mesh Under Dead Weight

Calcul 1        Calcul 2        Calcul 3
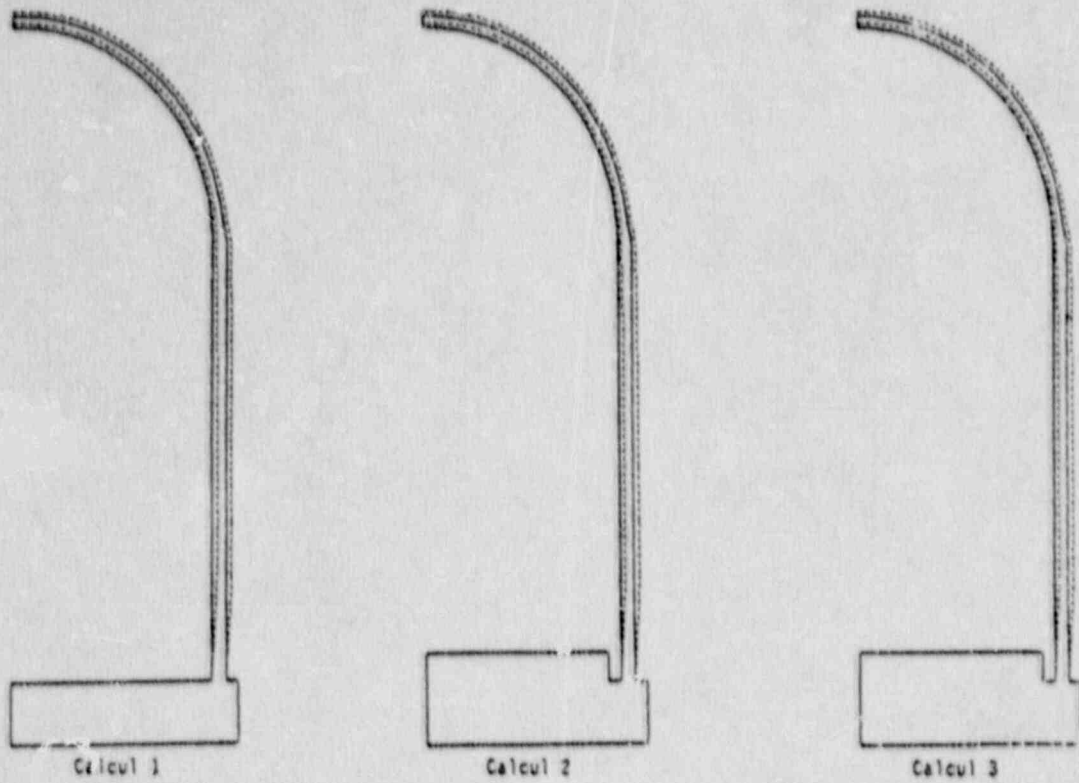
Figure 5.4.3  Deformed Mesh at 0.4 MPa (58 psig)



Calcul 1        Calcul 2        Calcul 3
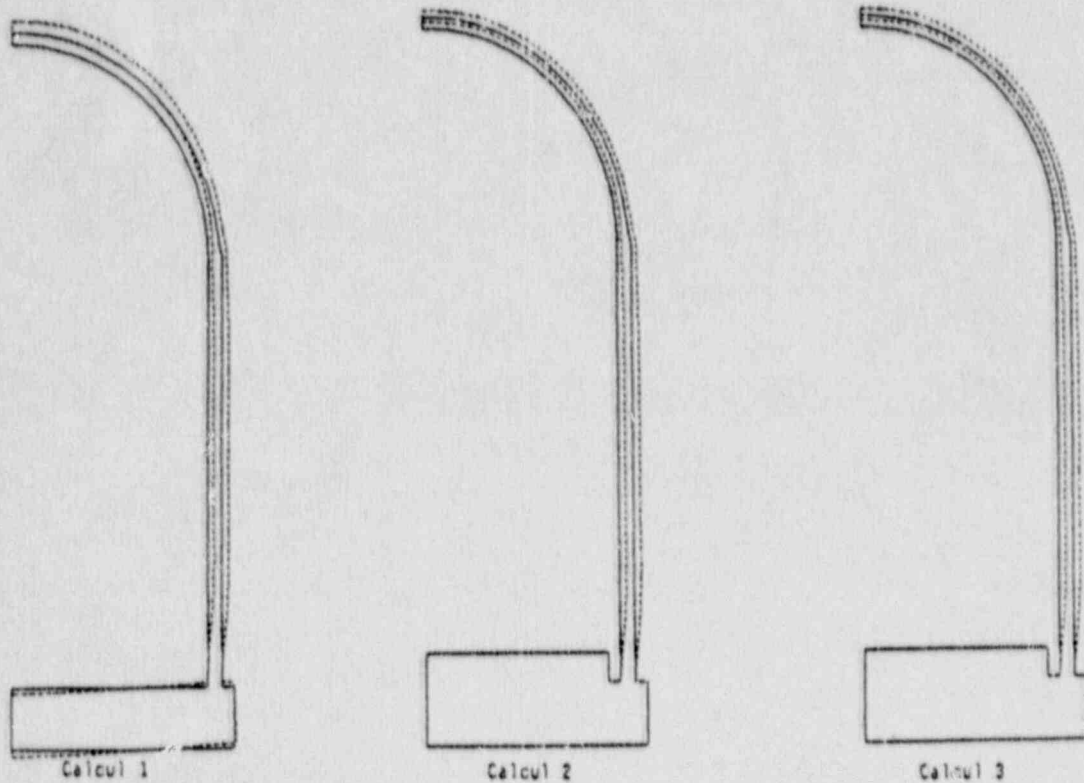
Figure 5.4.4  Deformed Mesh at 0.5 MPa (73 psig)
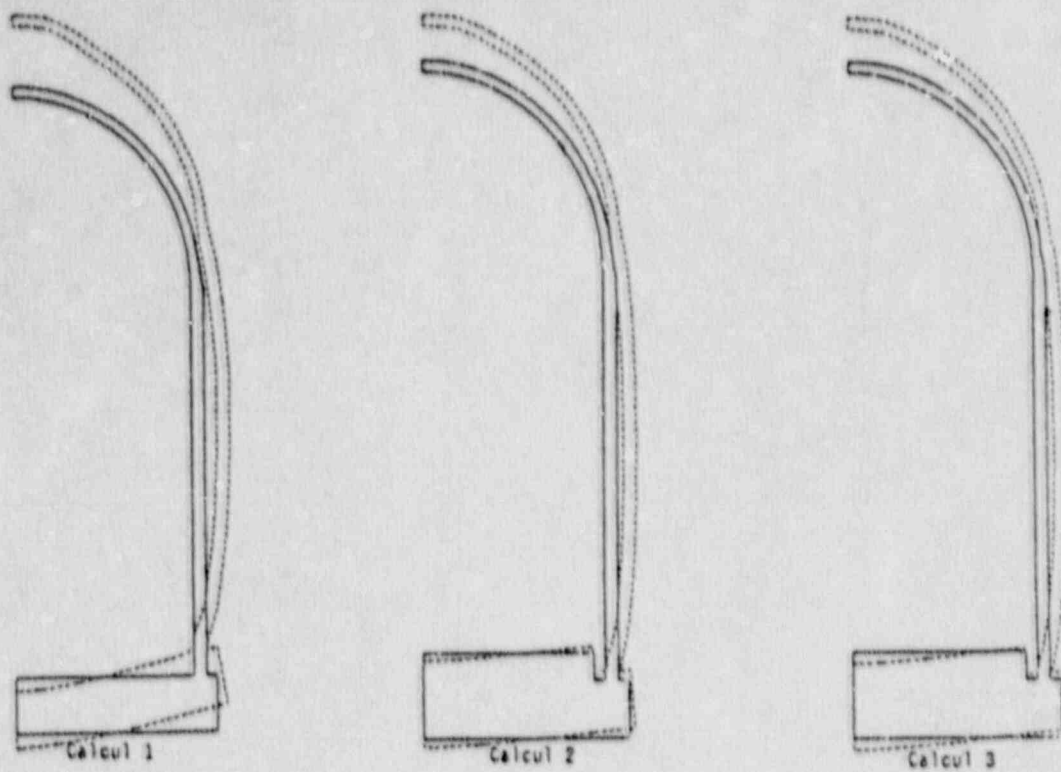
Figure 5.4.5  Deformed Mesh at 0.98 MPa (142 psig)
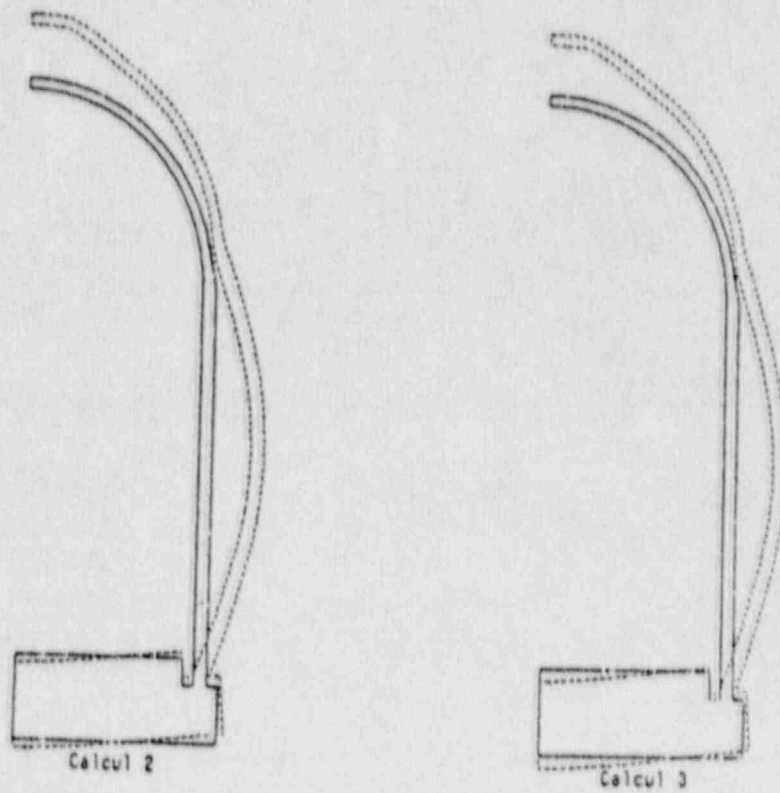


Figure 5.4.6  Deformed Mesh at 1.05 MPa (152 psig)

Calcul 1    Calcul 2    Calcul 3
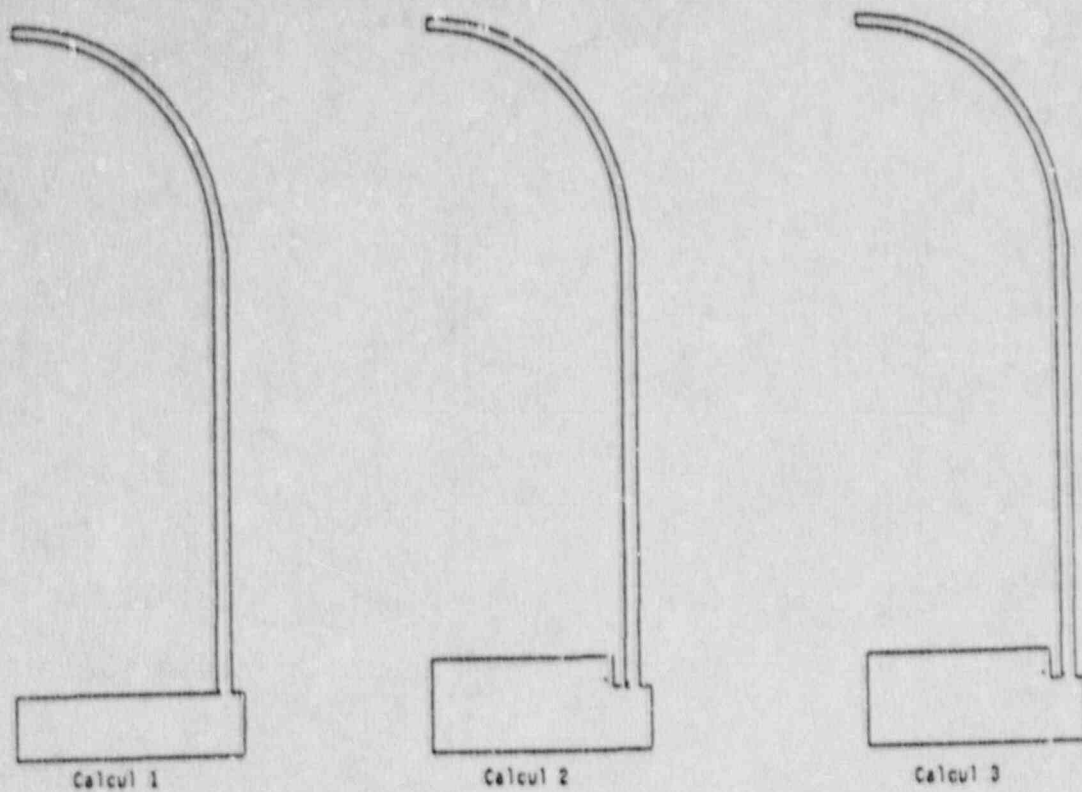
Figure 5.4.7  Meridional Crack Pattern at 0.2 MPa (29 psig)

Calcul 1    Calcul 2    Calcul 3
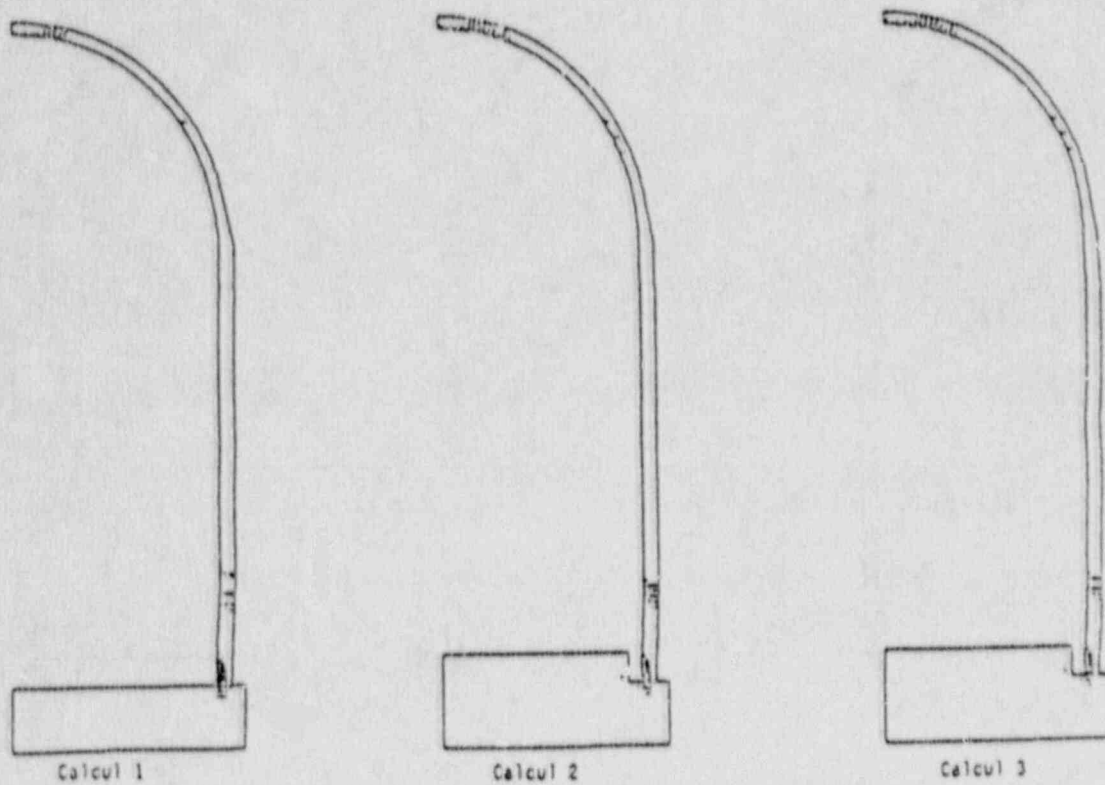
Figure 5.4.8  Meridional Crack Pattern at 0.3 MPa (44 psig)

Calcul 1    Calcul 2    Calcul 3
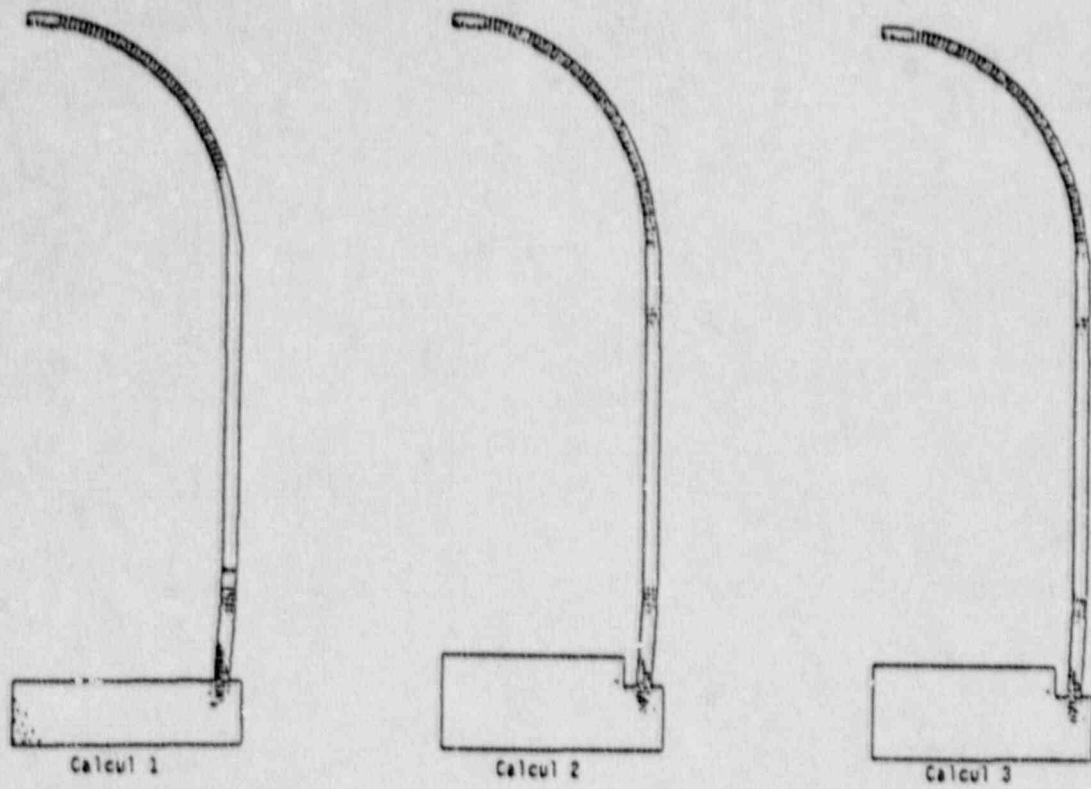
Figure 5.4.9  Meridional Crack Pattern at 0.4 MPa (58 psig)



Calcul 1    Calcul 2    Calcul 3
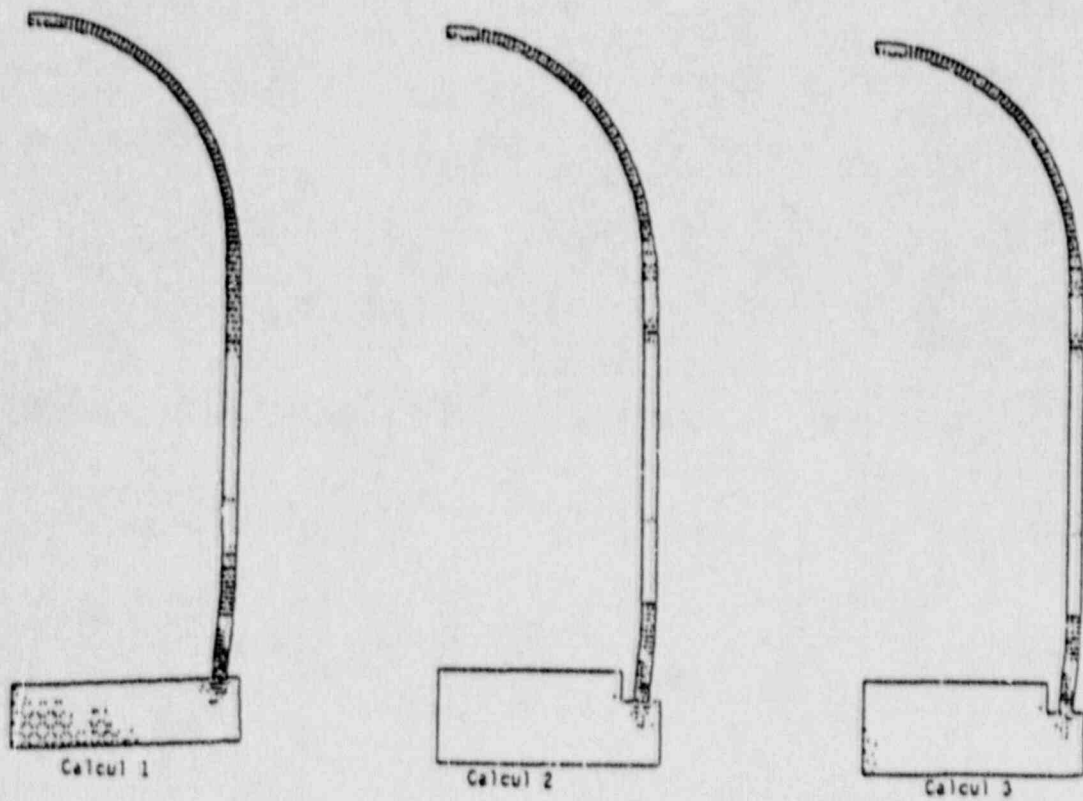
Figure 5.4.10  Meridional Crack Pattern at 0.5 MPa (73 psig)

Calcul 1                    Calcul 2                    Calcul 3
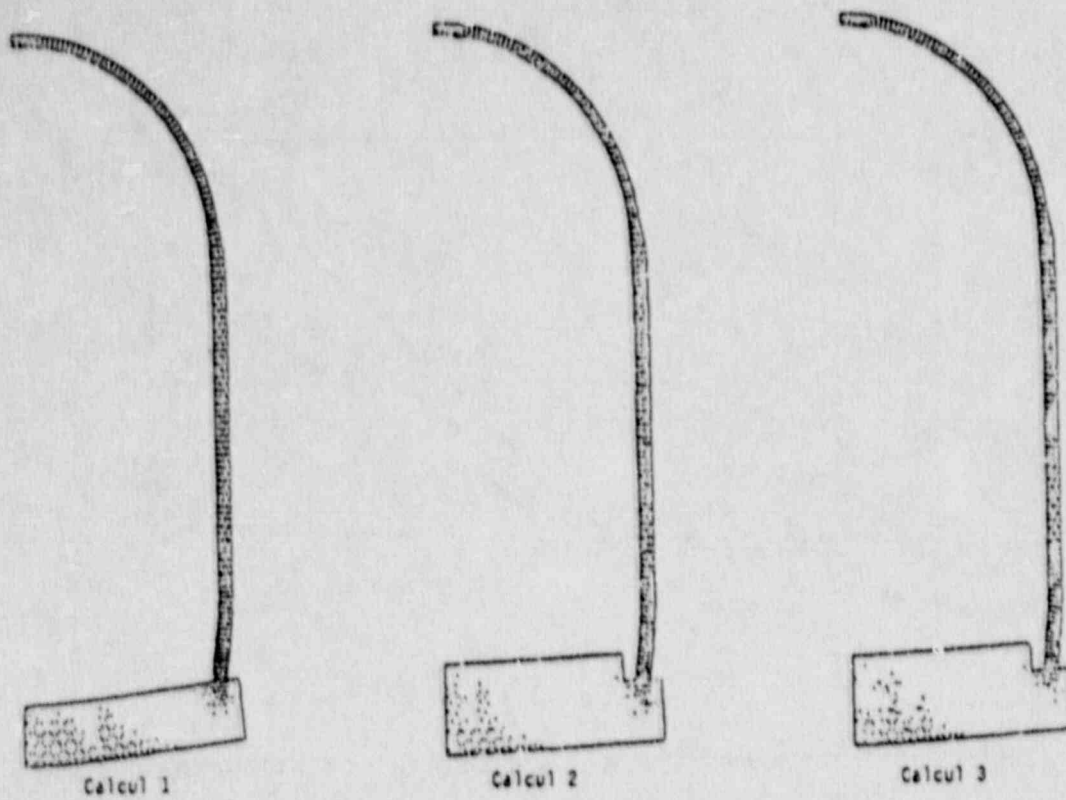
Figure 5.4.11  Meridional Crack Pattern at 0.6 MPa (87 psig)

Calcul 1                    Calcul 2                    Calcul 3
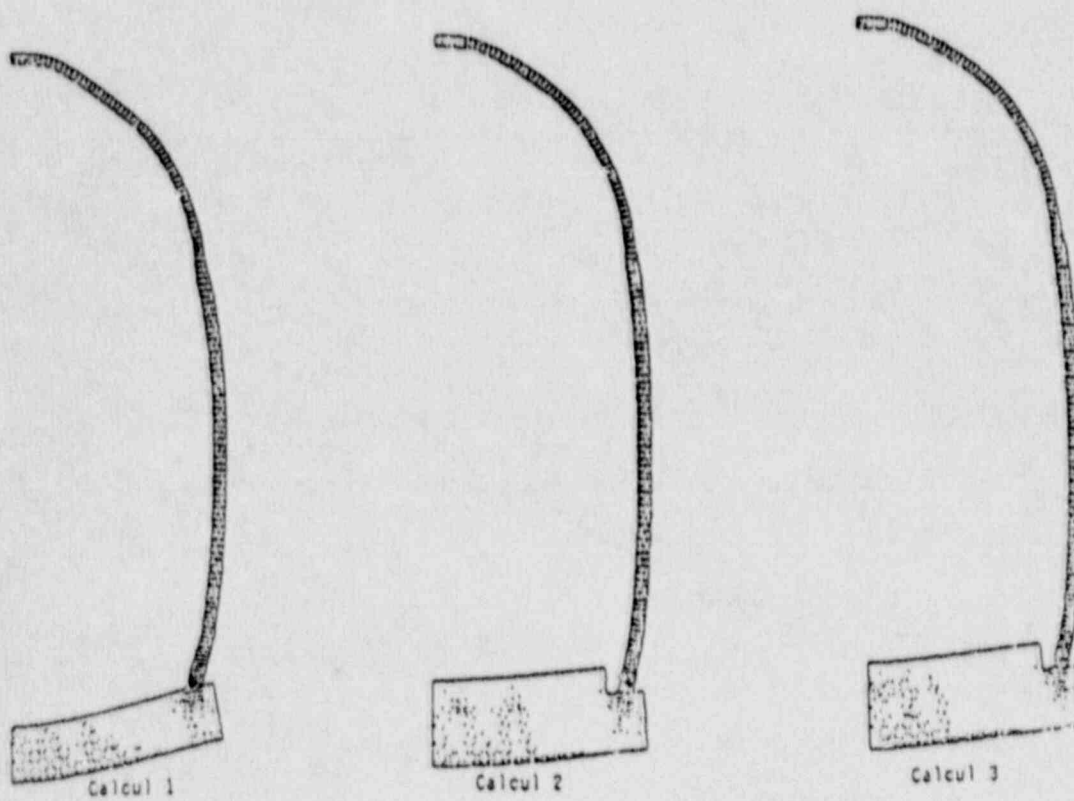
Figure 5.4.12  Meridional Crack Pattern at 0.98 MPa (142 psig)
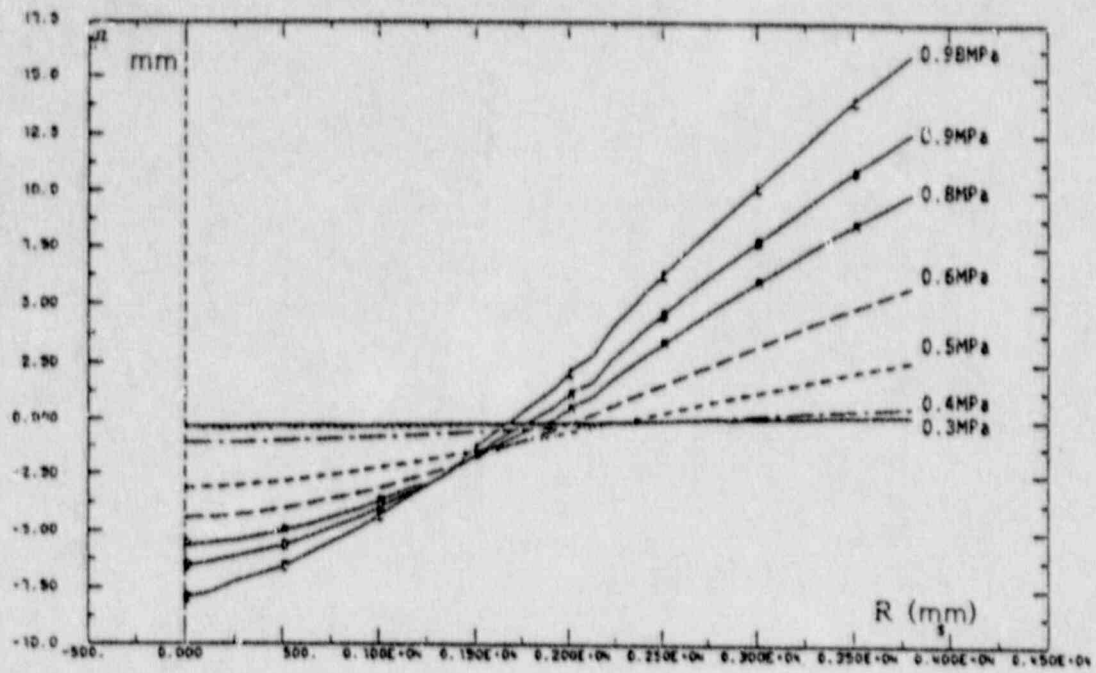
Figure 5.4.13  Vertical Displacement of Basemat - Calculation 1
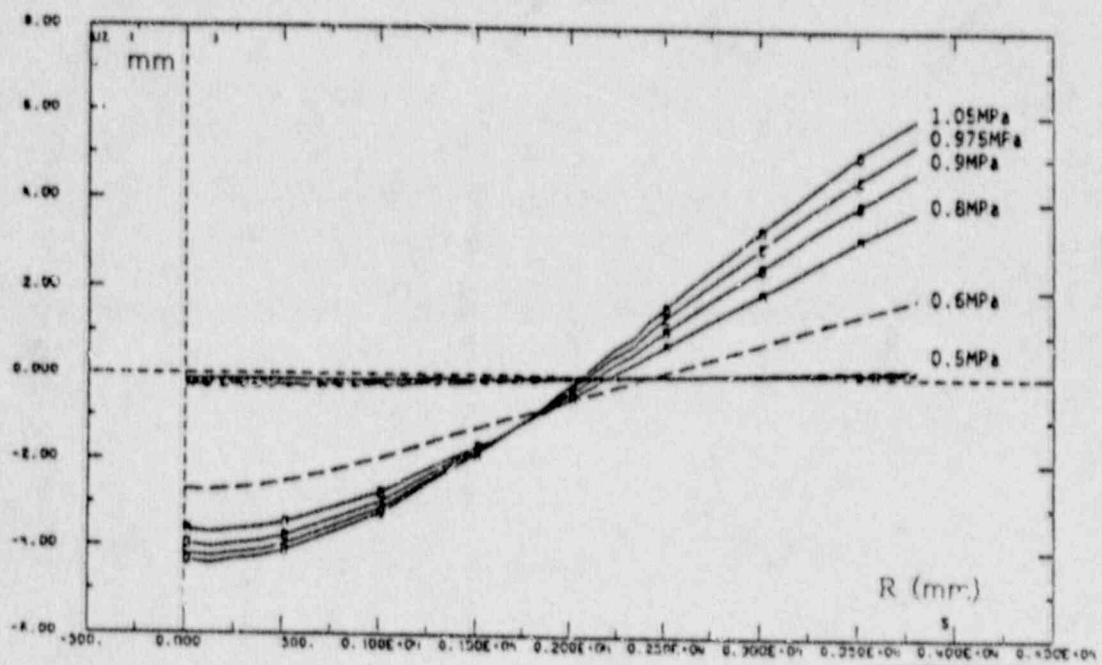


Figure 5.4.14  Vertical Displacement of Basemat - Calculation 2
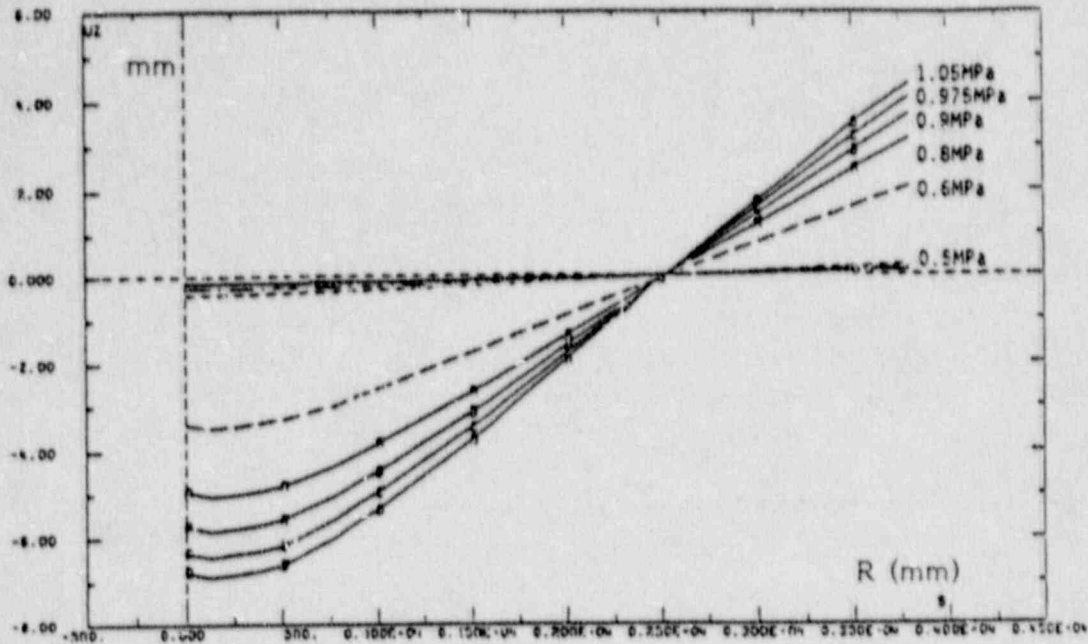
Figure 5.4.15  Vertical Displacement of Basemat - Calculation 3
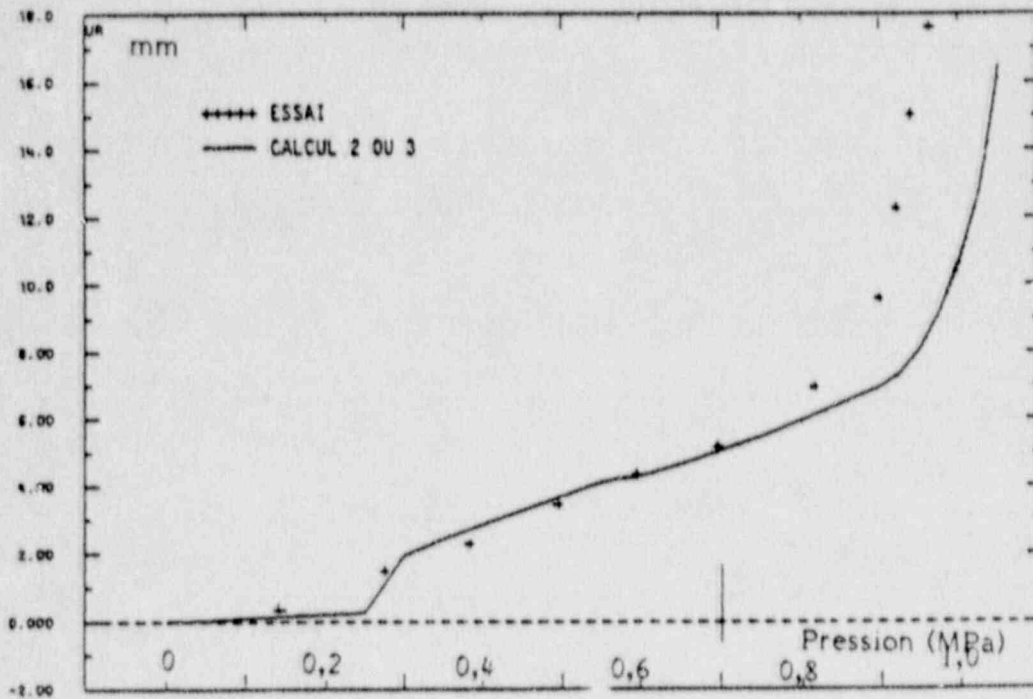


Figure 5.4.16  Radial Displacement at Node 685 - Transducer D96
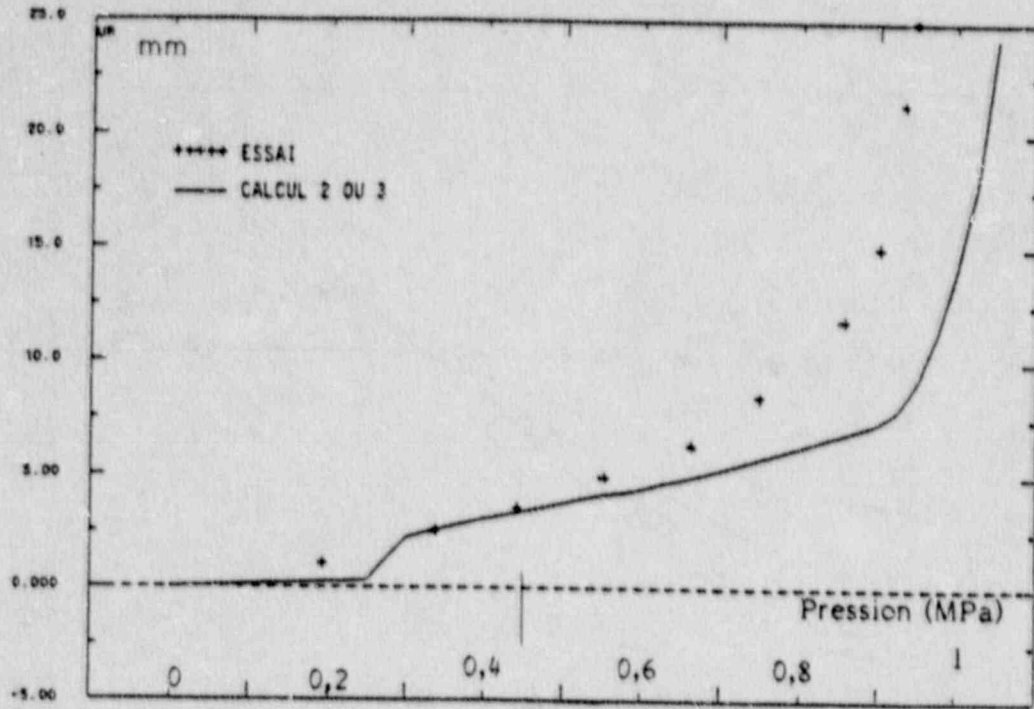
Figure 5.4.17  Radial Displacement at Node 635 - Transducer D97
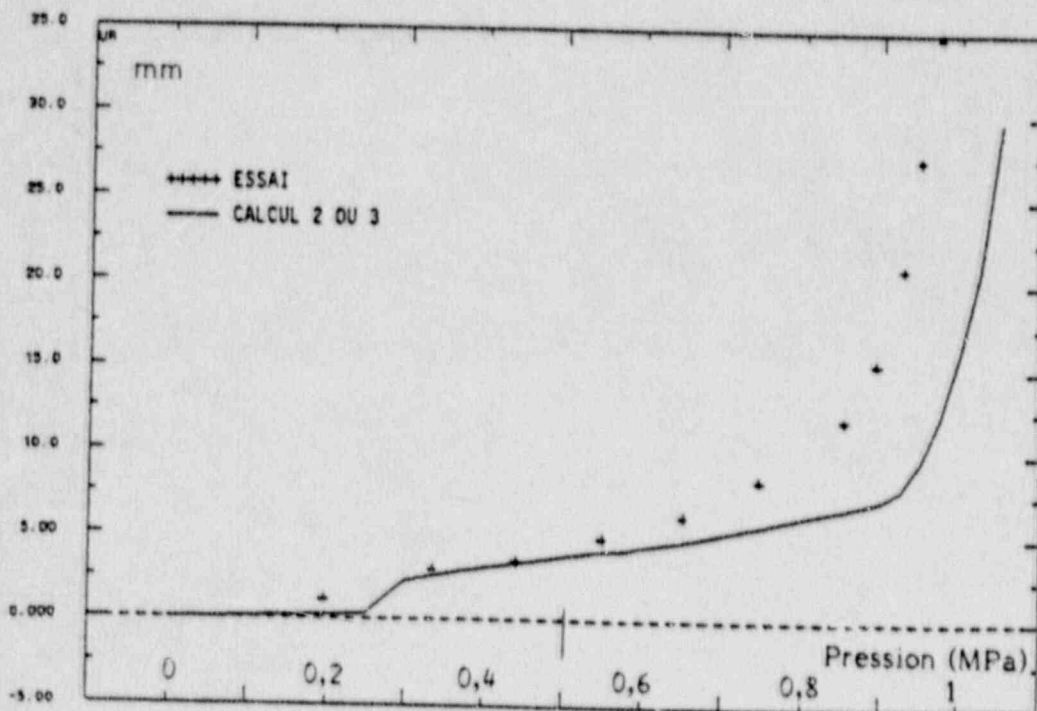


Figure 5.4.18  Radial Displacement at Node 592 - Transducer D99
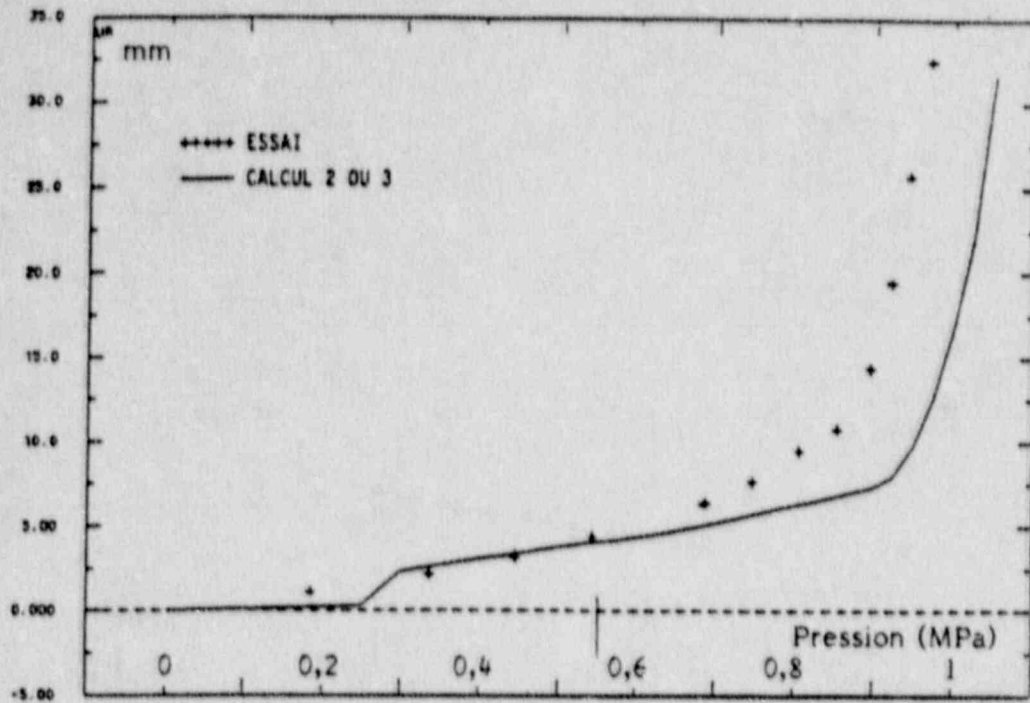
Figure 5.4.19  Radial Displacement at Node 556 - Transducer D100
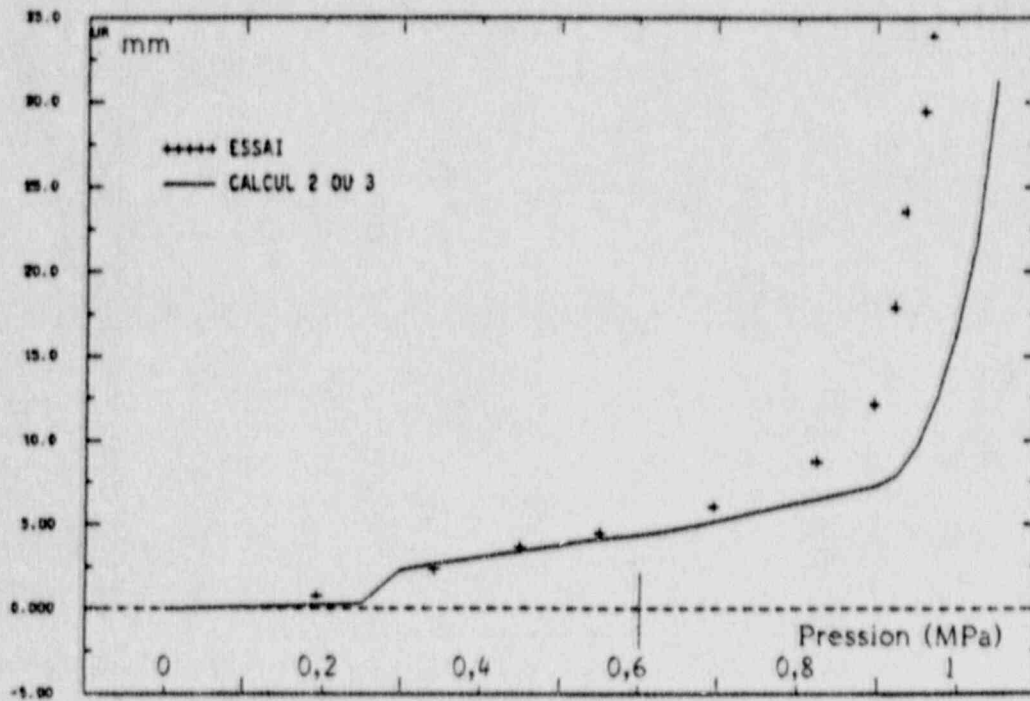


Figure 5.4.20  Radial Displacement at Node 513 - Transducer D101
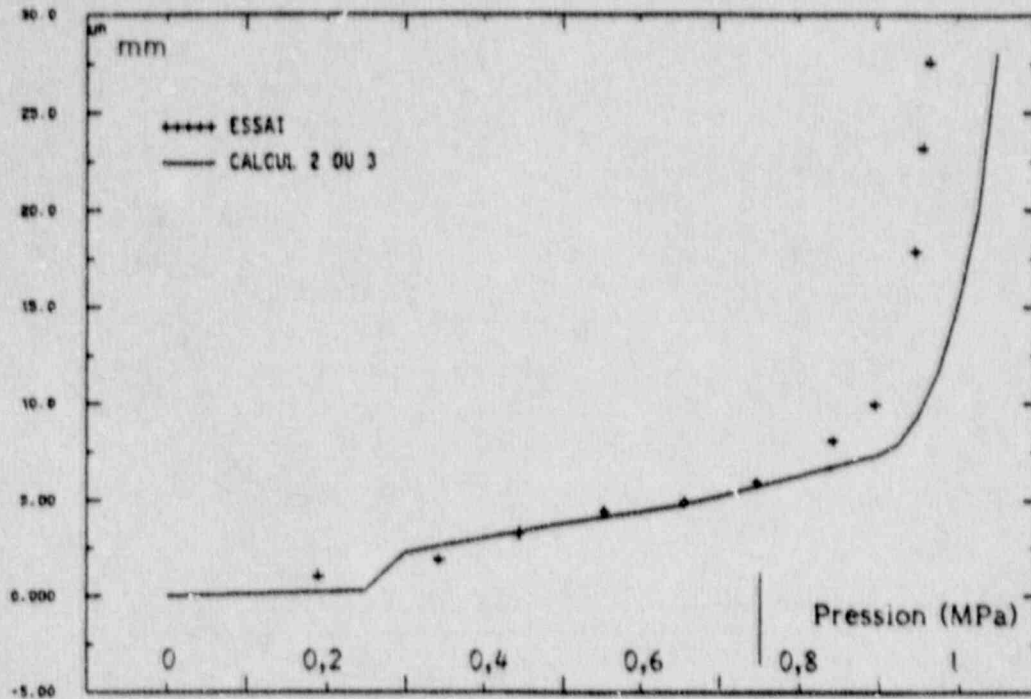
Figure 5.4.21  Radial Displacement at Node 472 - Transducer D102
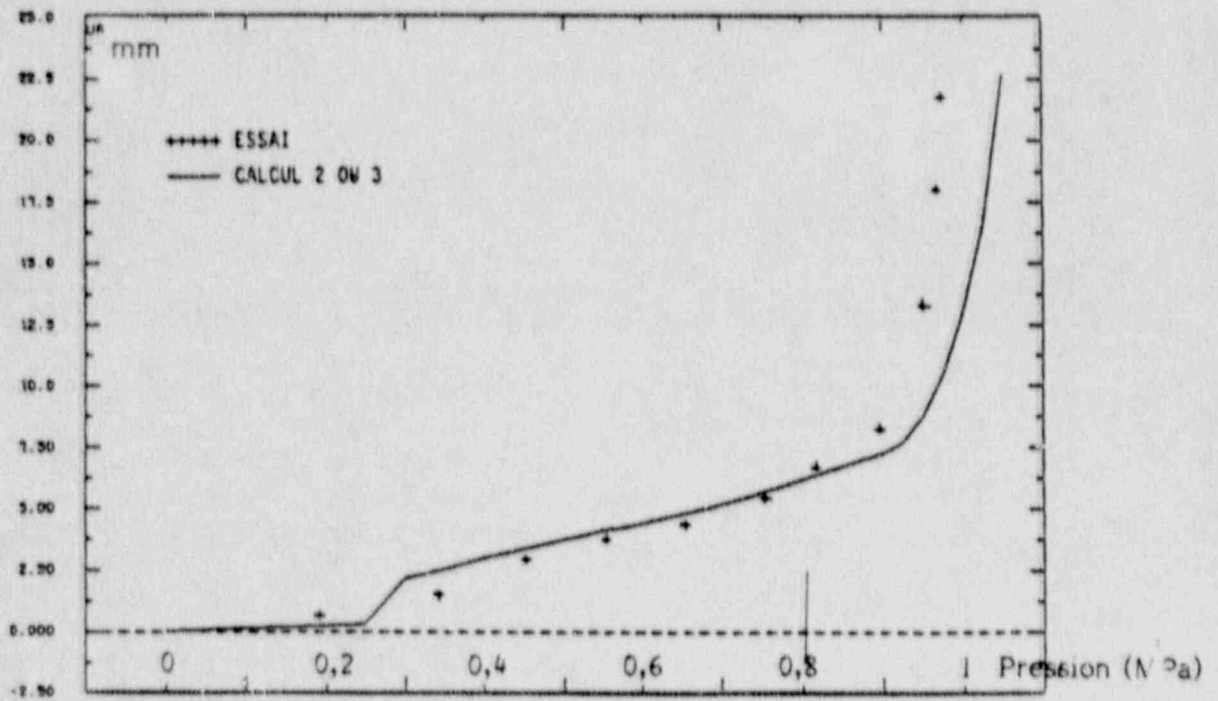


Figure 5.4.22  Radial Displacement at Node 436 - Transducer D103
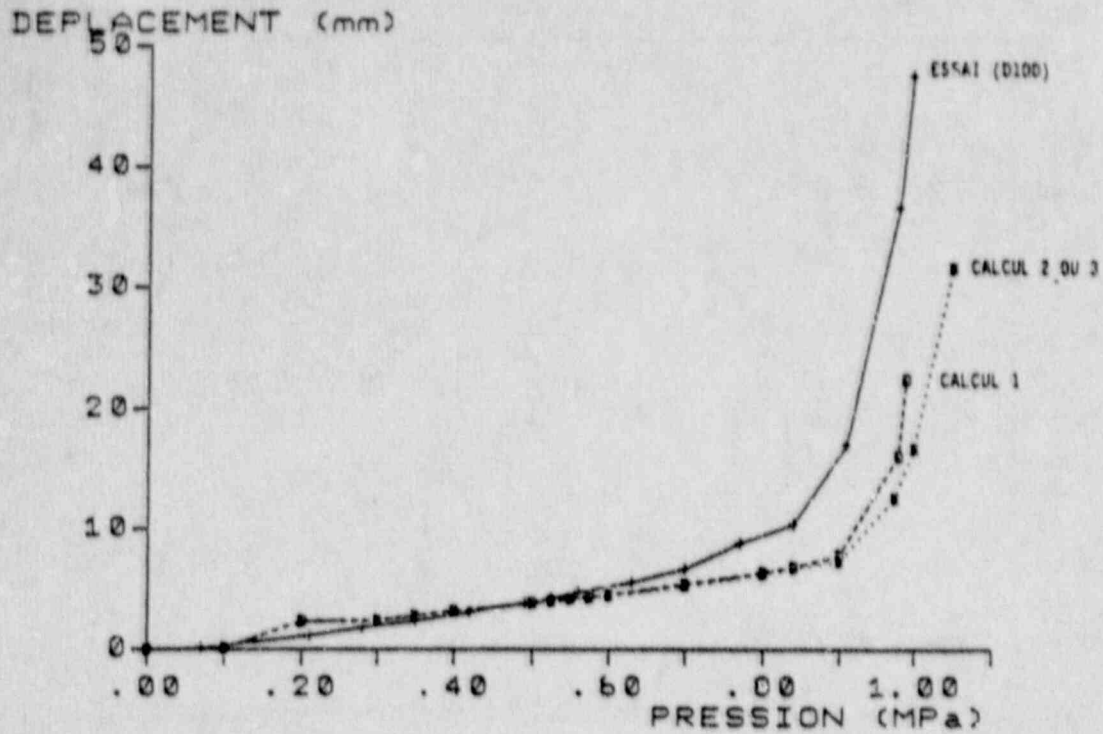
Figure 5.4.23 Radial Displacement at Cylinder Midheight - Transducer D100
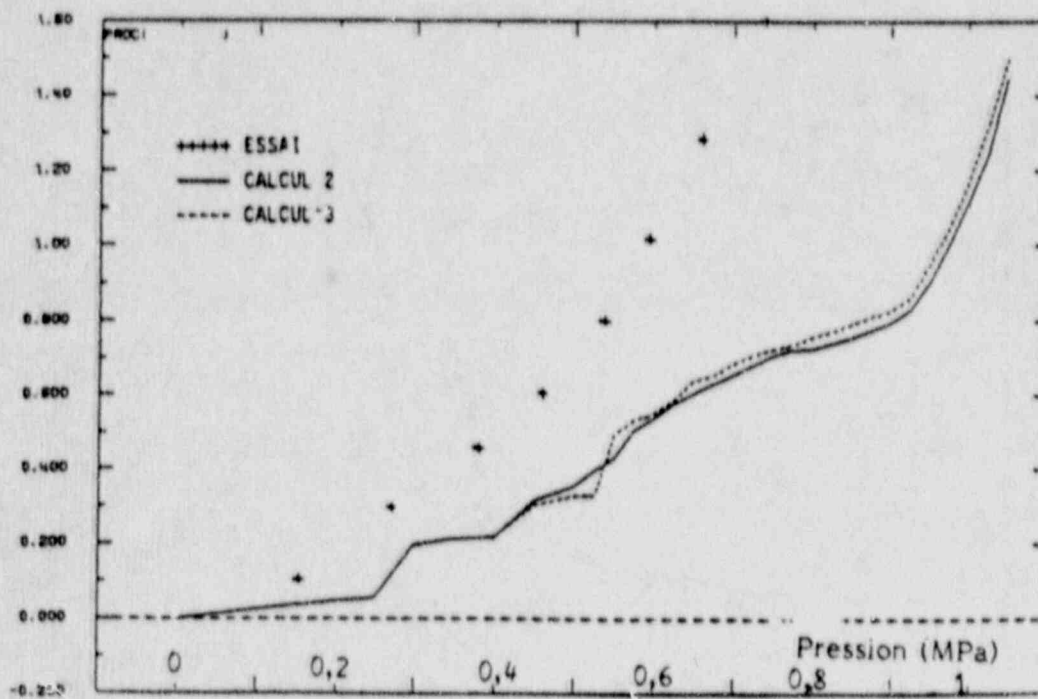


Figure 5.4.24 Axial Displacement at Node 685 Relative to Node 864 - Transducer D95
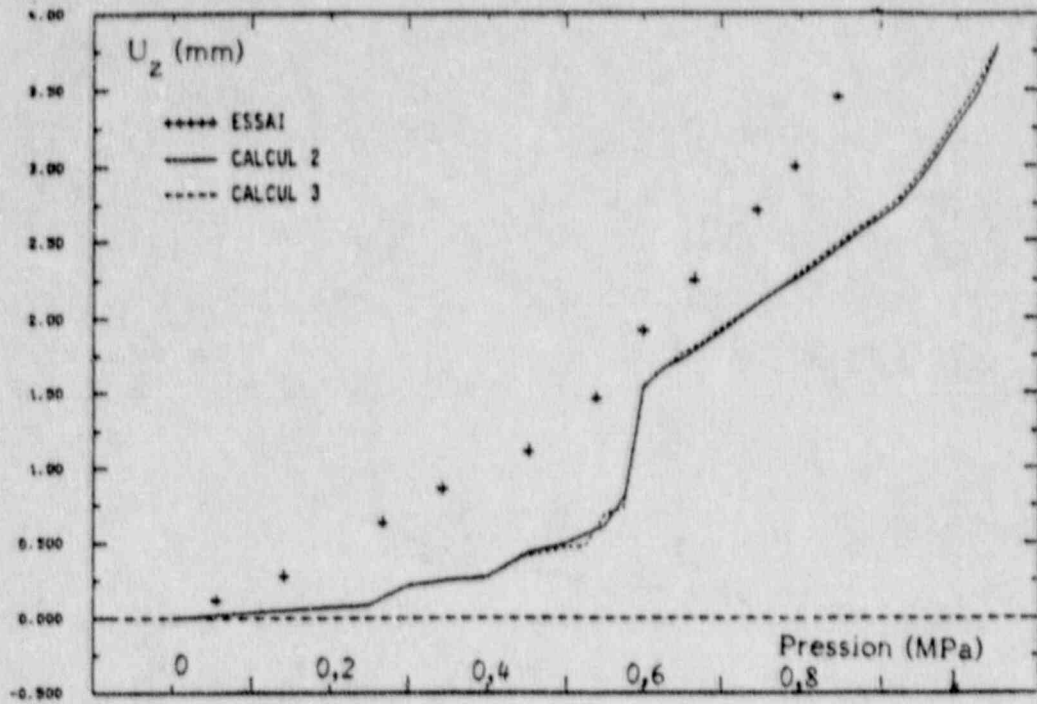
Figure 5.4.25  Axial Displacement at Node 592 Relative to Node 864 - Transducer D98
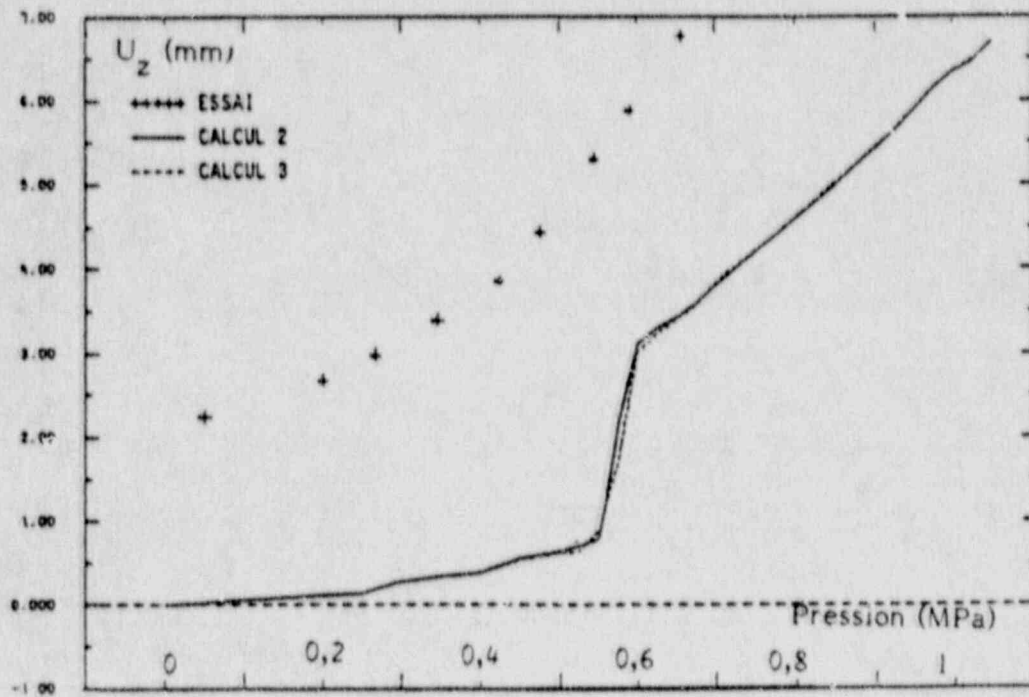


Figure 5.4.26  Axial Displacement at Node 472 Relative to Node 864 - Transducer D104
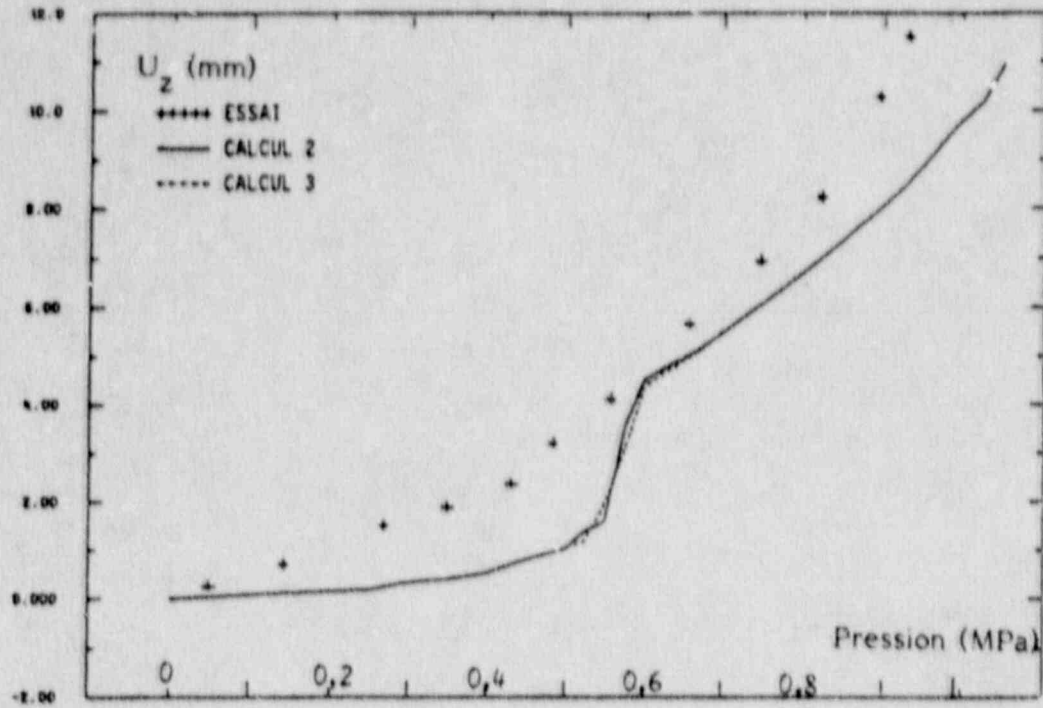
Figure 5.4.27 Axial Displacement at Node 364 Relative to Node 864 - Transducer D105
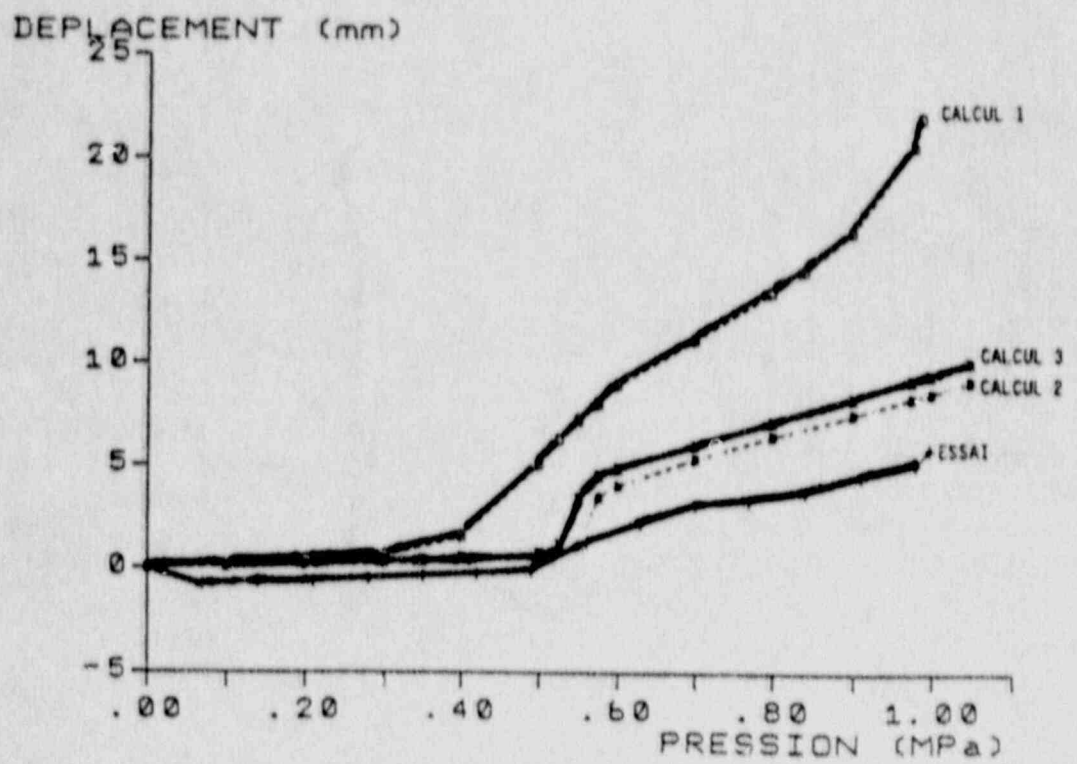


Figure 5.4.28 Basemat Uplift (Node 878 Relative to Node 1201) - Channel 169
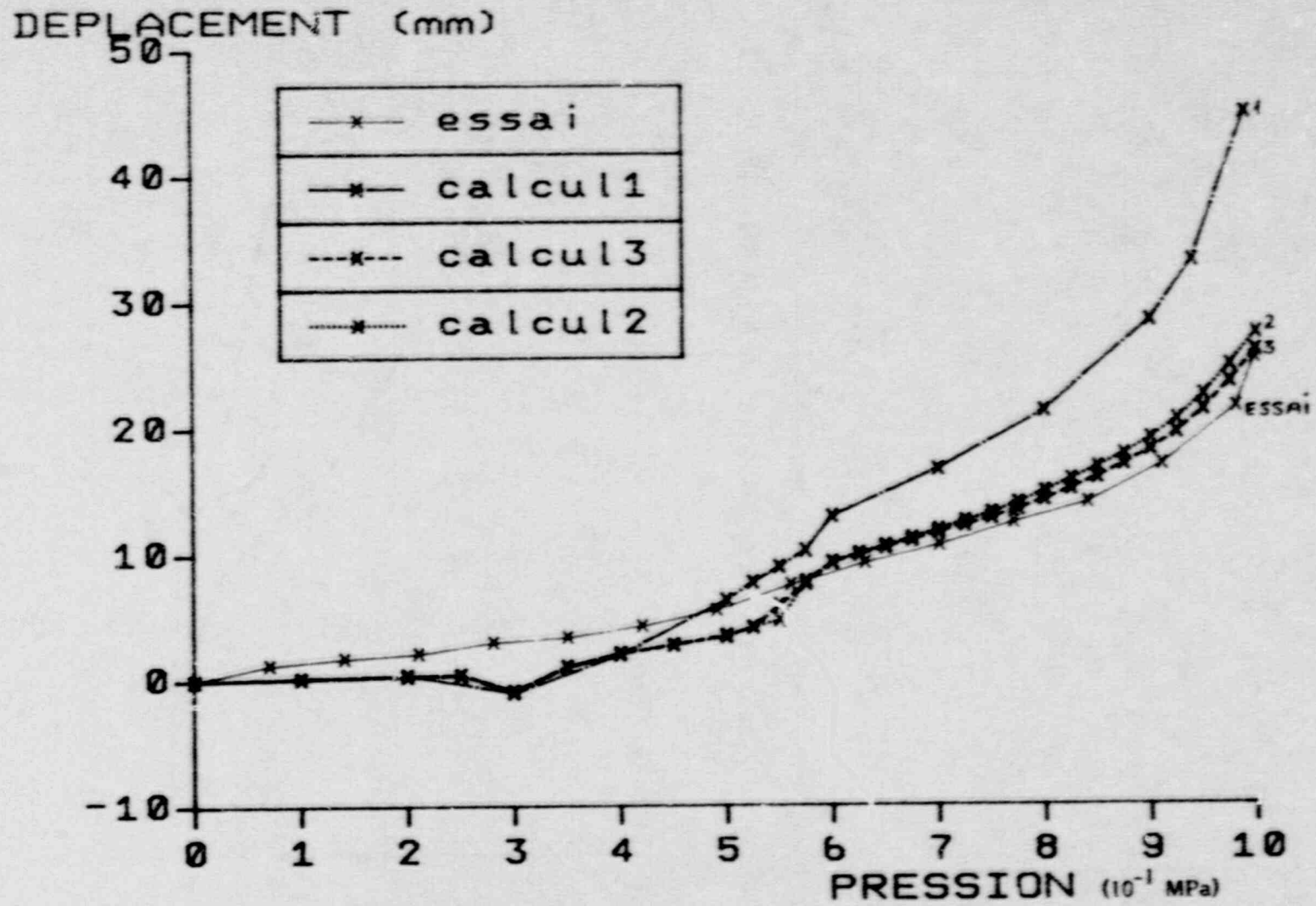
Figure 5.4.29  Axial Displacement at Dome Apex
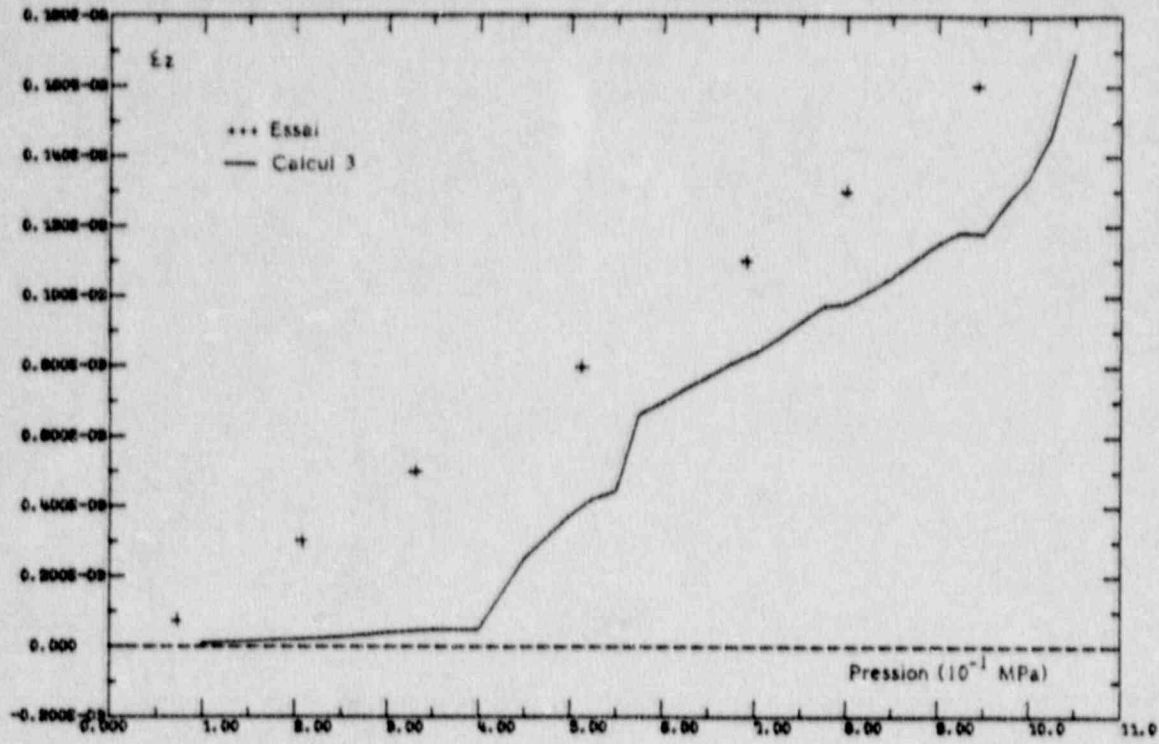
Figure 5.4.30  Strain in Layer 5 Meridional Bar at El 23.92 ft (Node 363)
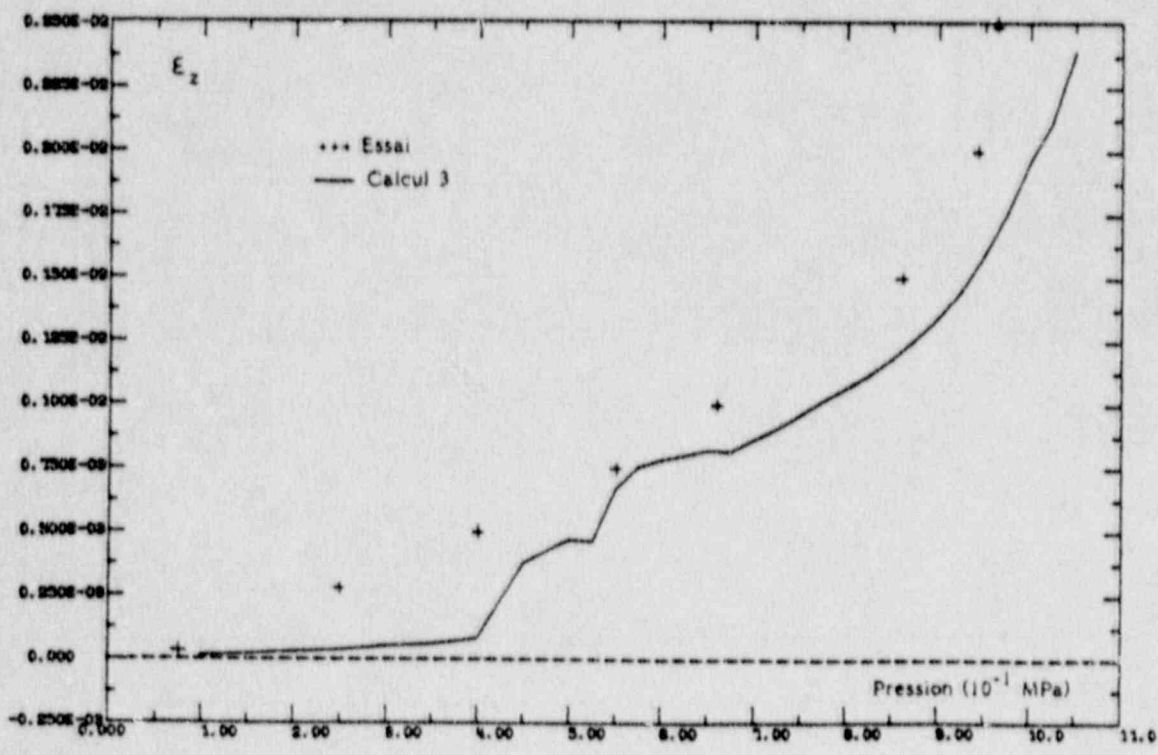


Figure 5.4.31  Strain in Layer 2 Meridional Bar at El 23.92 ft (Node 366)
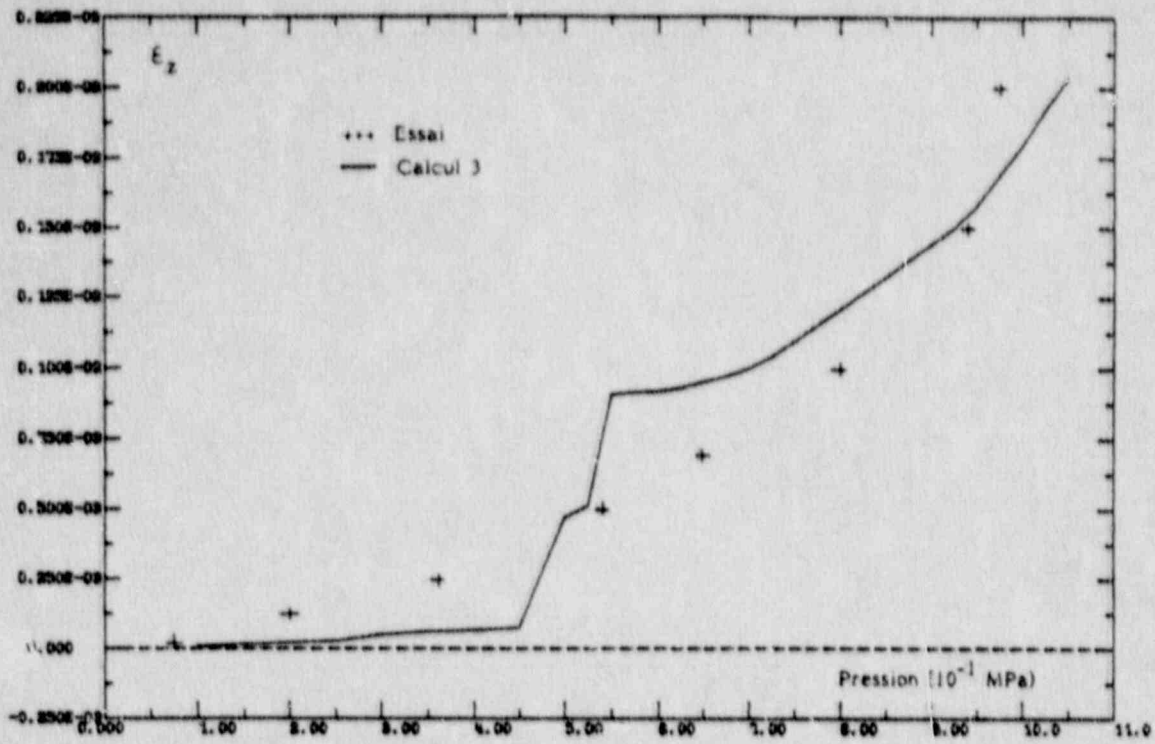
Figure 5.4.32  Strain in Layer 5 Meridional Bar at El 20 ft (Node 435)
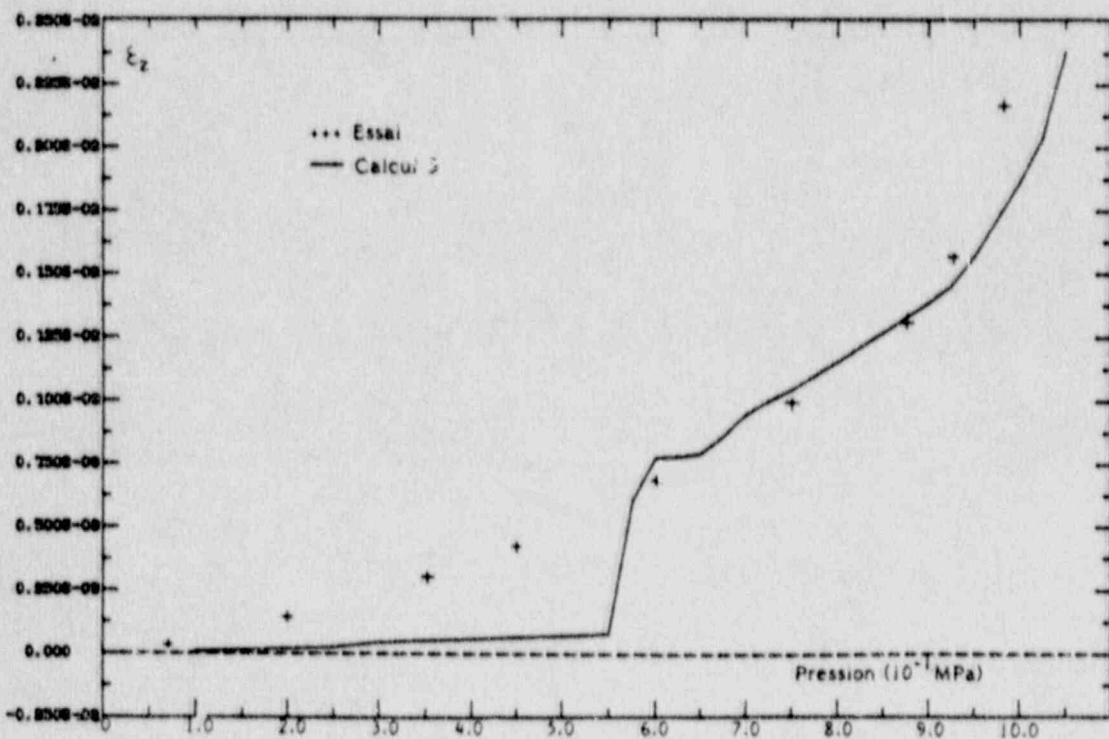


Figure 5.4.33  Strain in Layer 5 Meridional Bar at El 13.75 ft (Node 543)
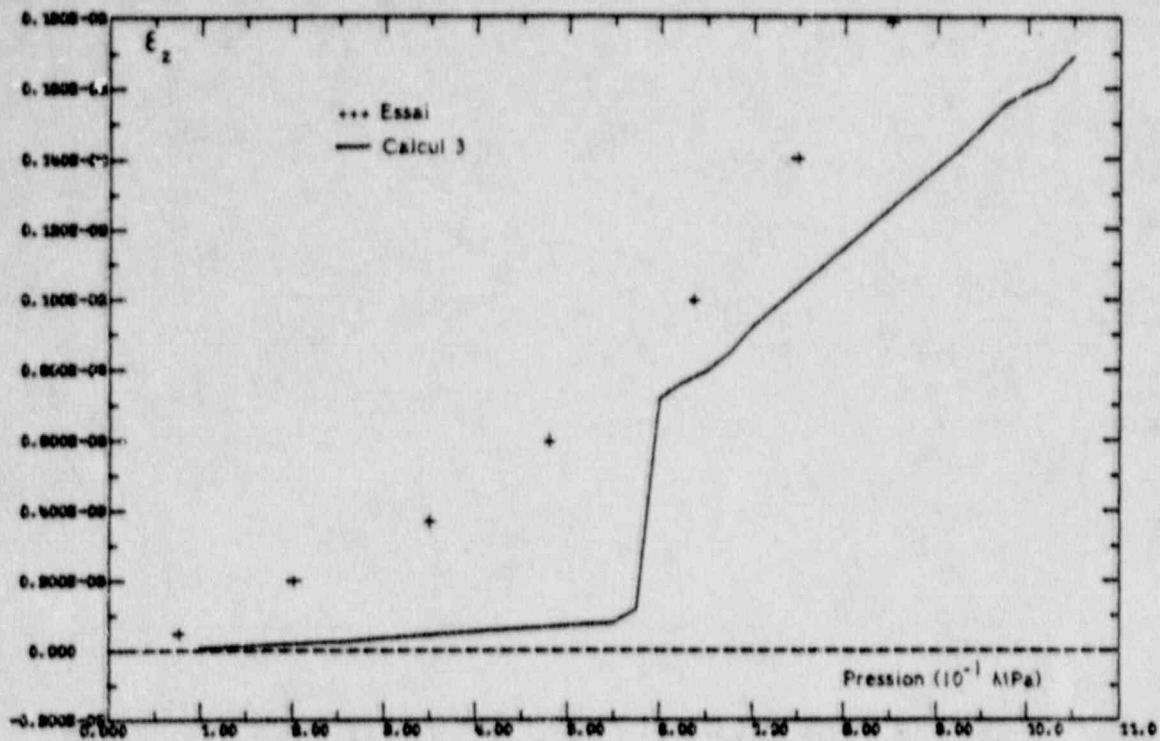
Figure 5.4.34  Strain in Layer 2 Meridional Bar at El 13 ft (Node 558)
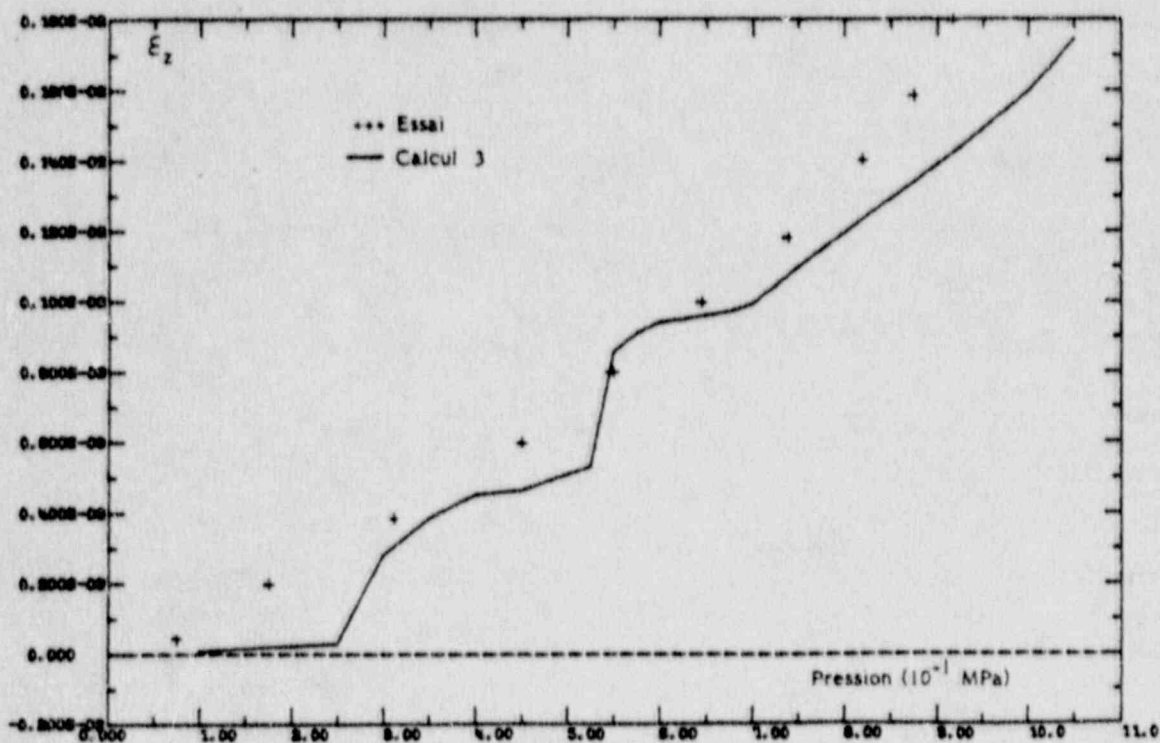


Figure 5.4.35  Strain in Layer 5 Meridional Bar at El 6.75 ft (Node 665)
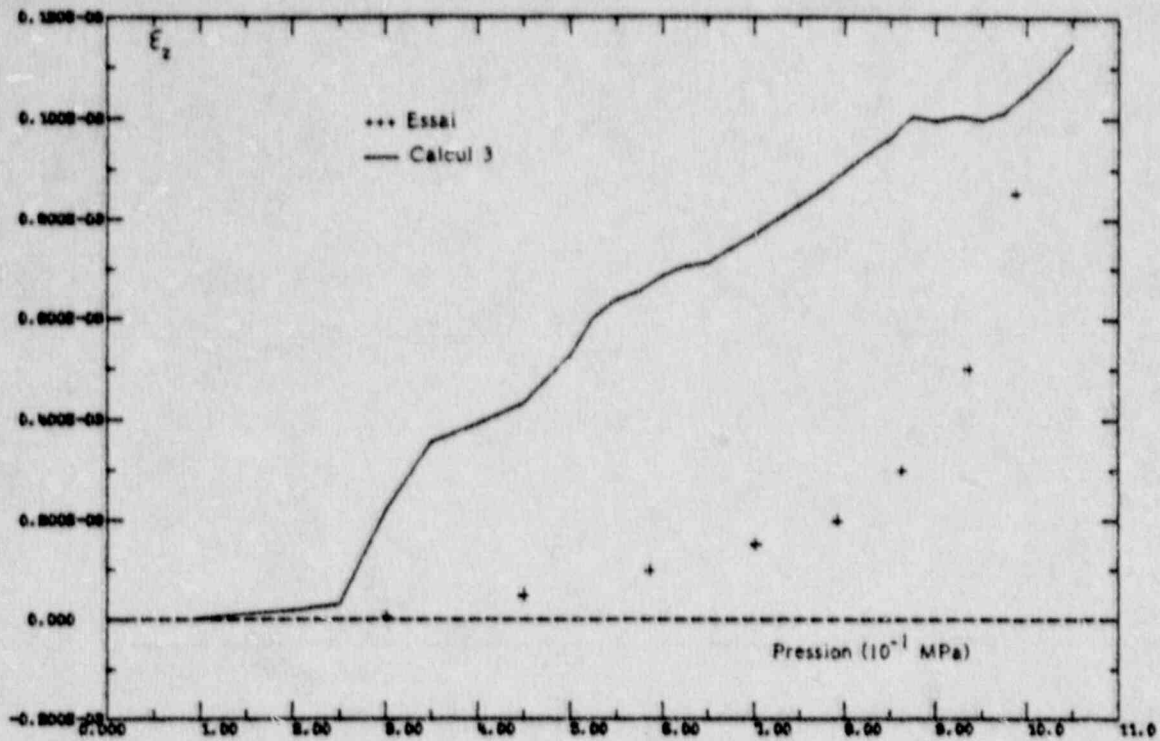
Figure 5.4.36  Strain in Layer 5 Meridional Bar at El 2.10 ft (Node 815)
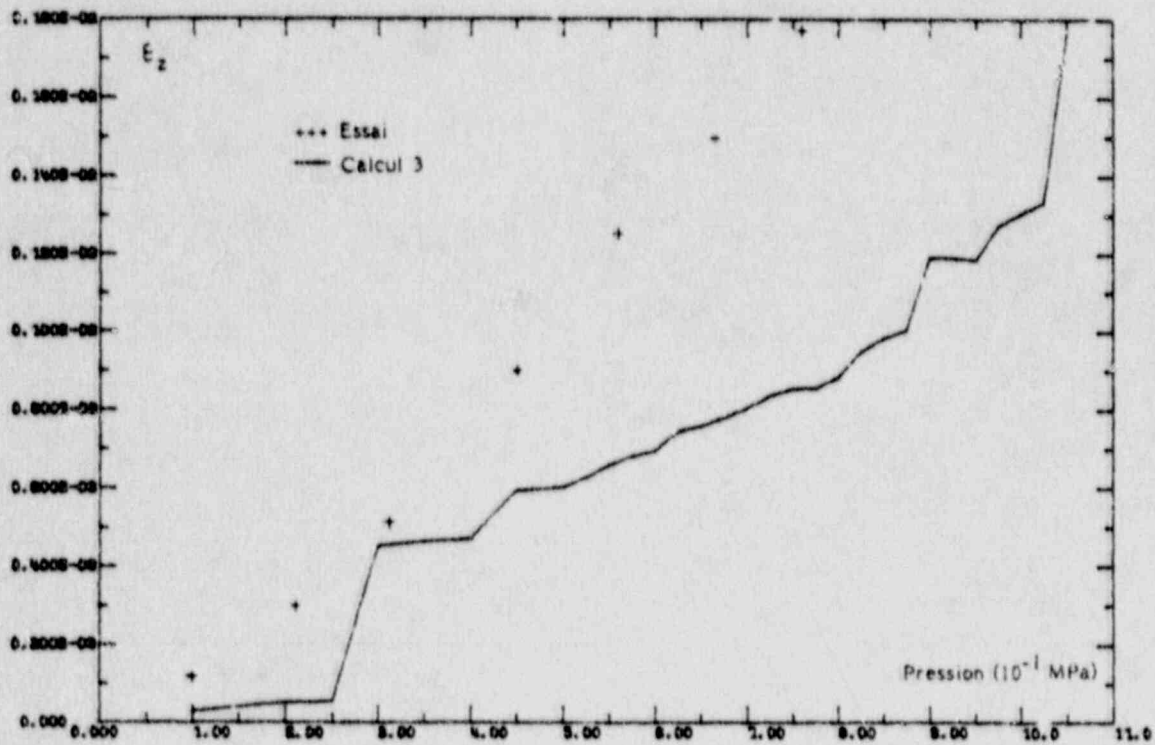


Figure 5.4.37  Strain in Layer 2 Meridional Bar at El 2.10 ft (Node 818)
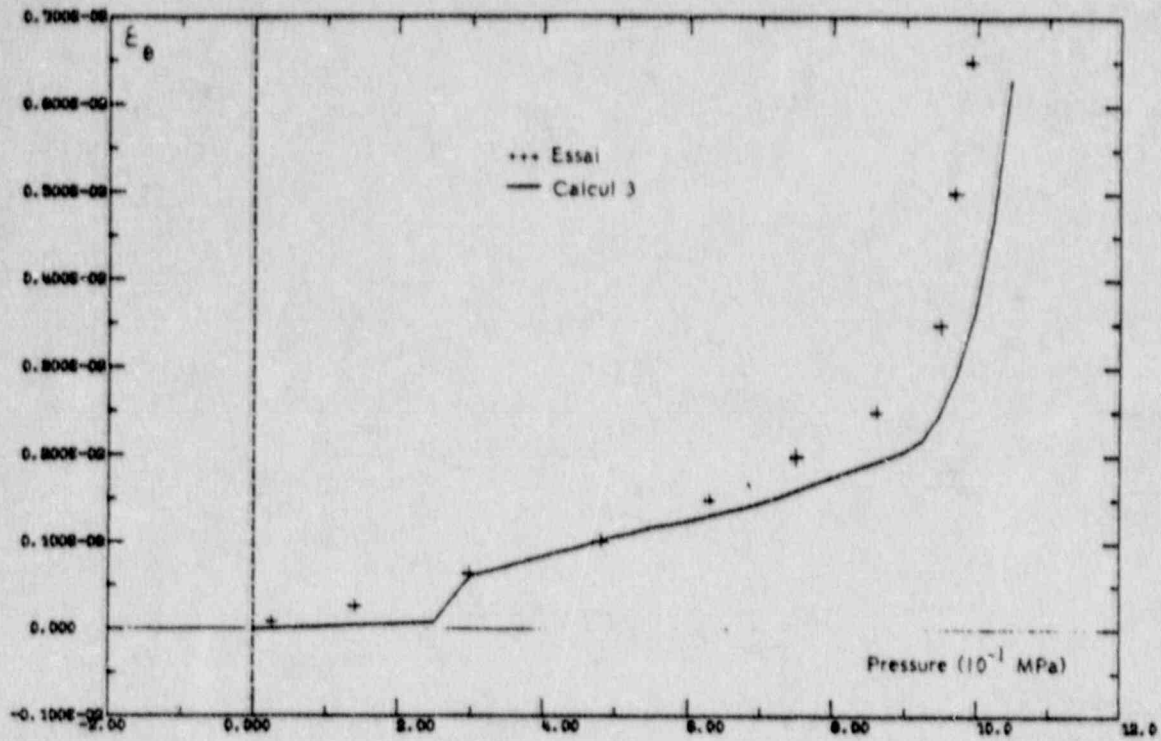
Figure 5.4.38  Strain in Layer 6 Hoop Bar at El 20 ft (Node 435)
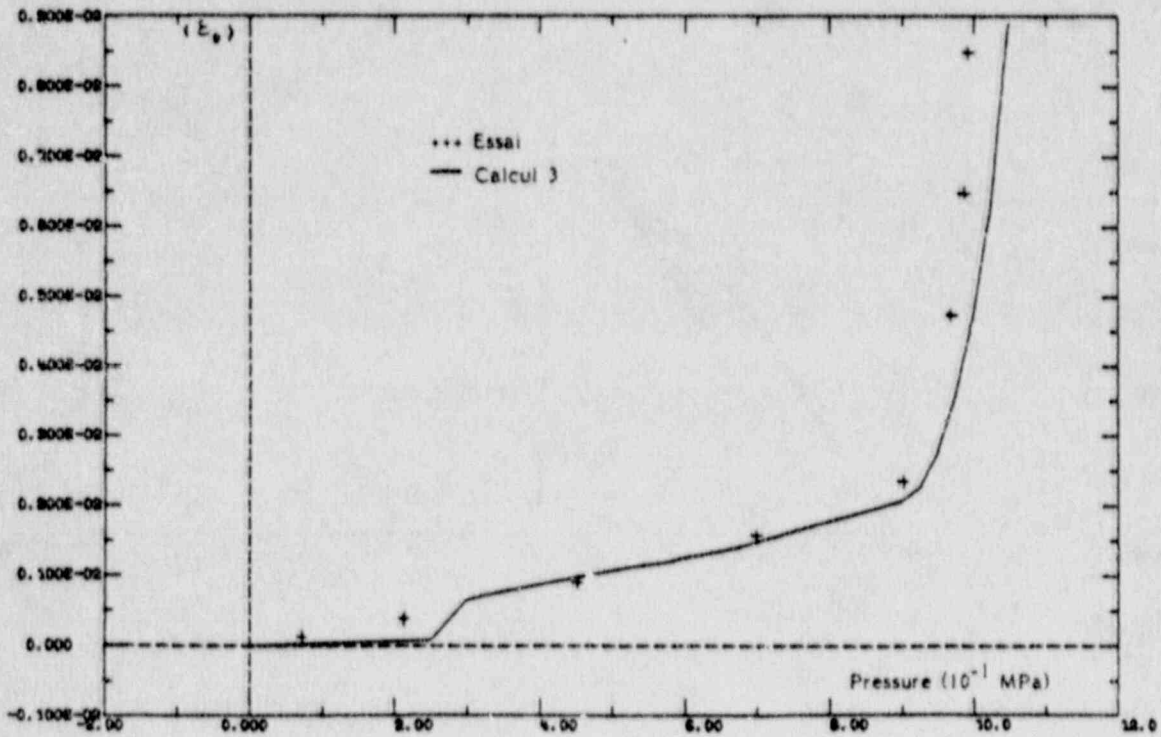


Figure 5.4.39  Strain in Layer 6 Hoop Bar at El 13.75 ft (Node 543)
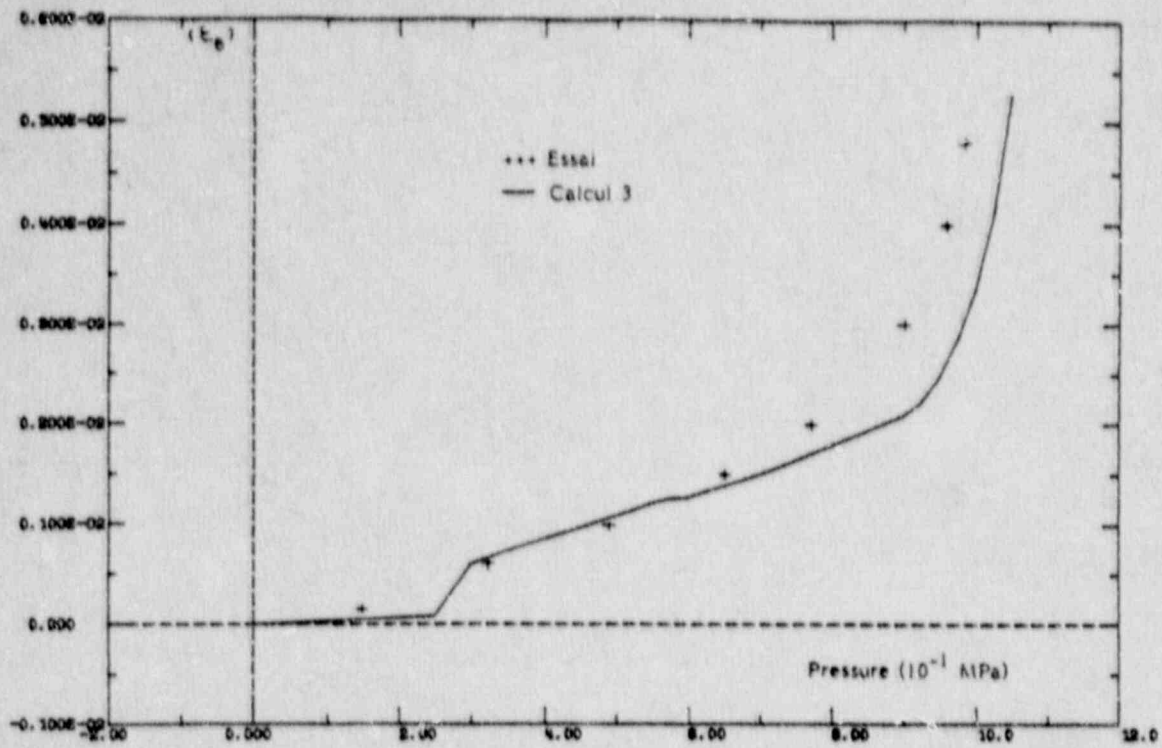
Figure 5.4.40 Strain in Layer 6 Hoop Bar at El 6.75 ft (Node 665)
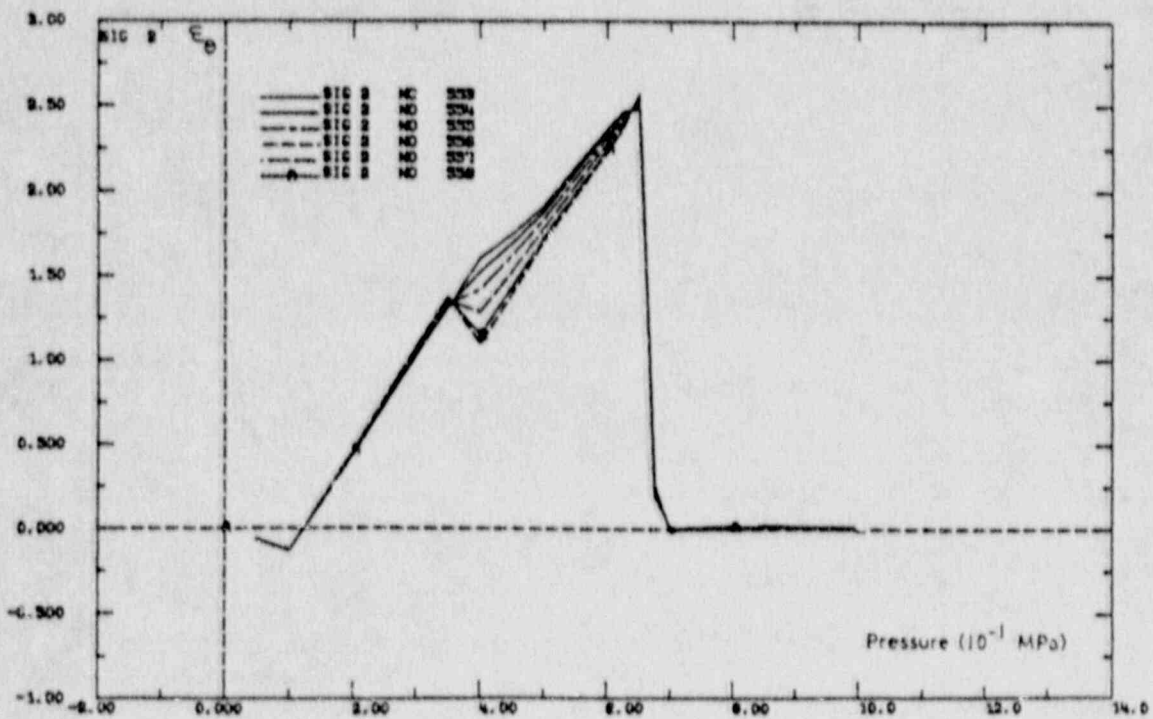


Figure 5.4.41 Vertical Stress in Concrete at Cylinder Midheight (Node 553 to 558)
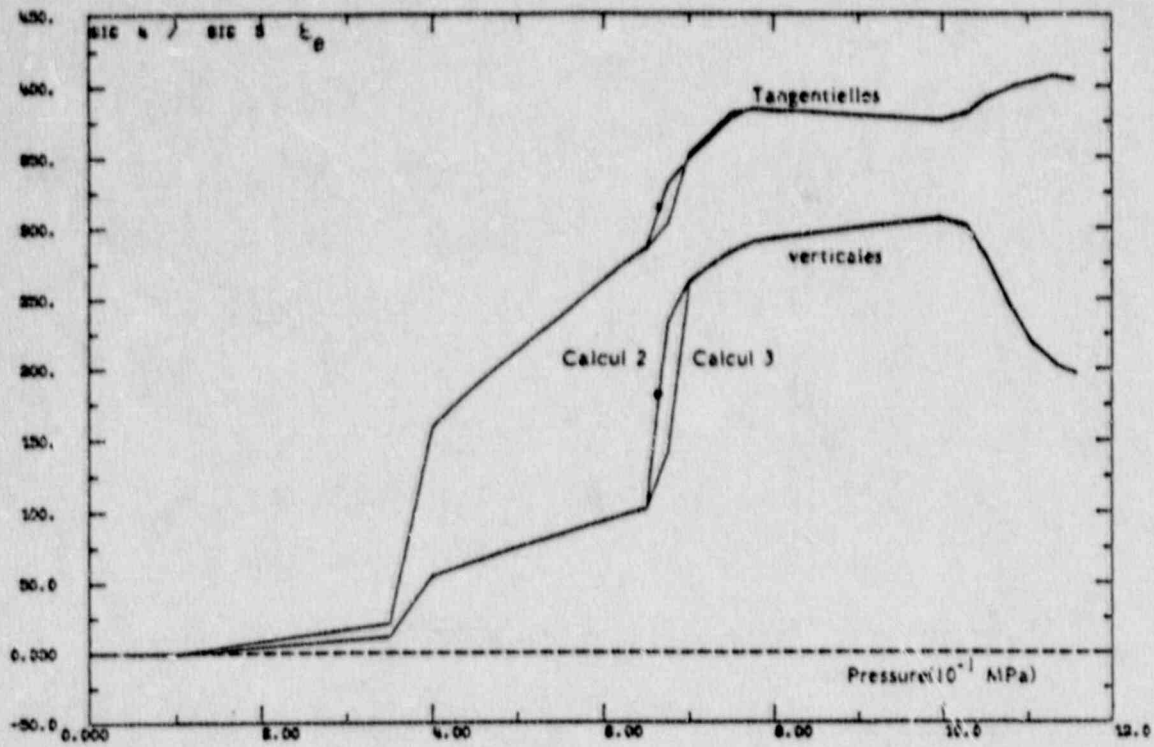
Figure 5.4.42  Axial and Hoop Stress in Liner at Cylinder Midheight
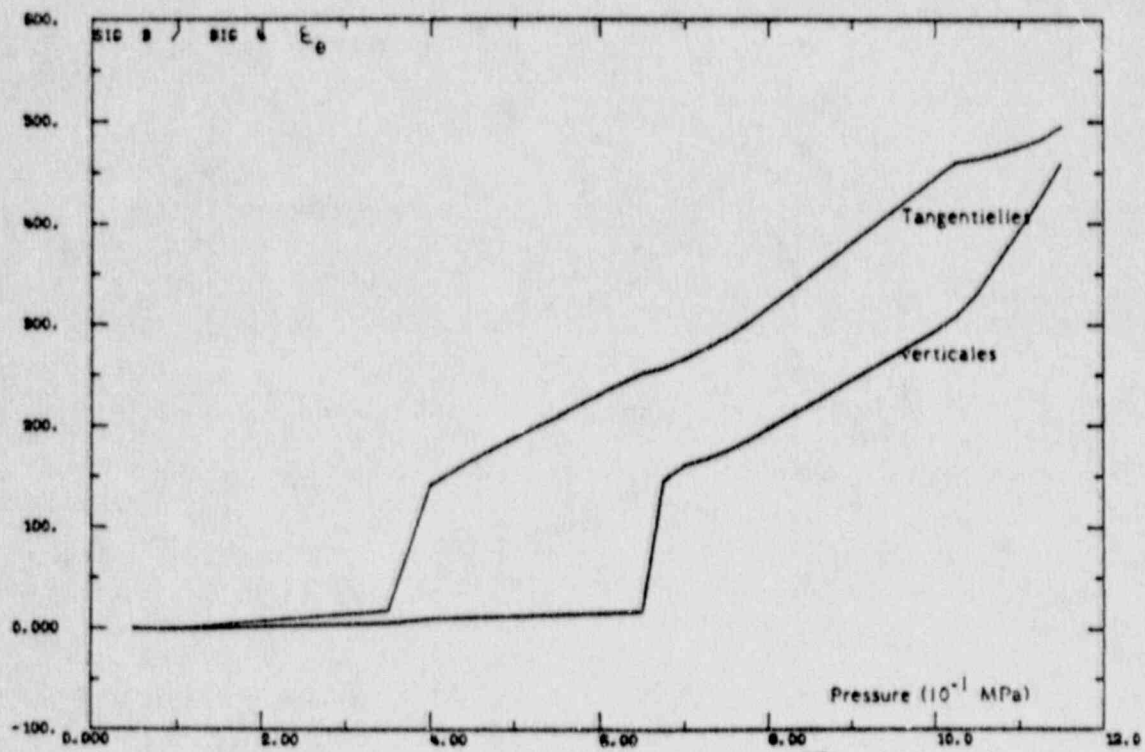


Figure 5.4.43  Stress in Hoop Rebars and Vertical Rebars at Cylinder Midheight

1. Without local criterion    2. With local criterion
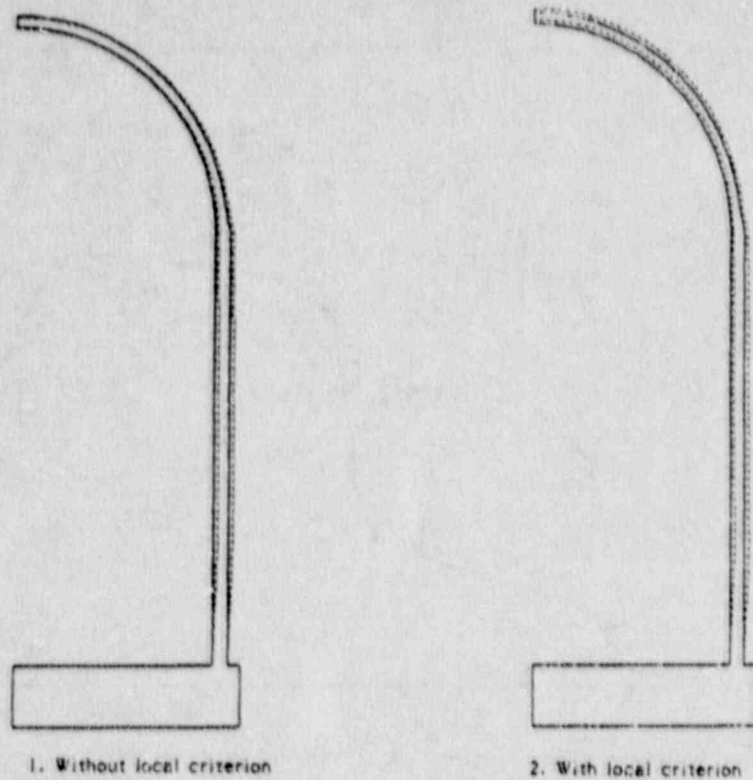
Figure 5.4.44  Deformed Structure at 0.3 MPa - Global and Local Criterion



1. Without local criterion    2. With local criterion
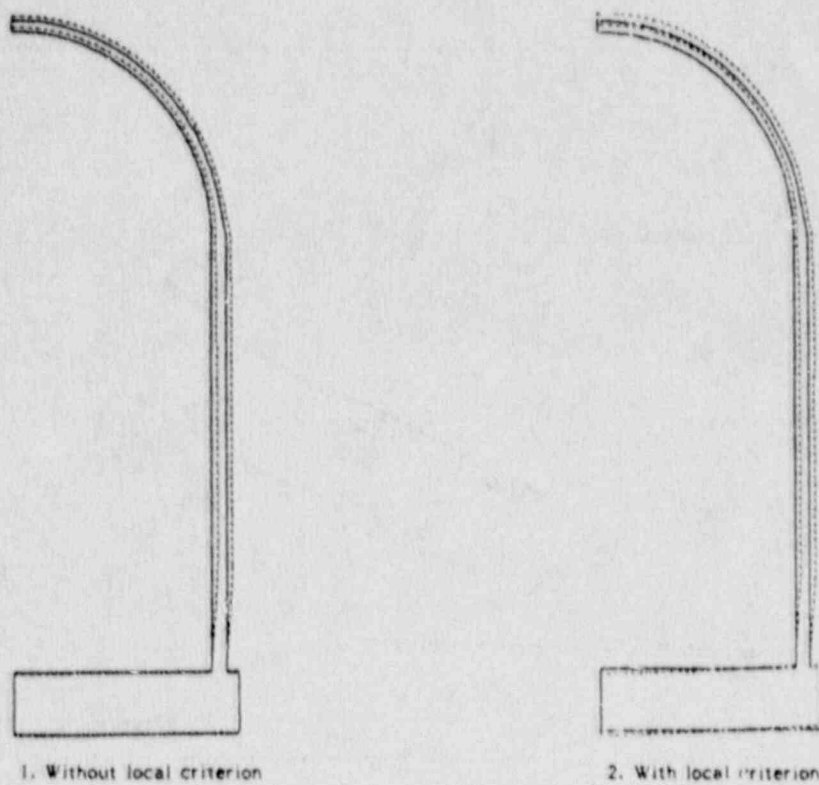
Figure 5.4.45  Deformed Structure at 9.4 MPa - Global and Local Criterion

1. Without local criterion    2. With local criterion
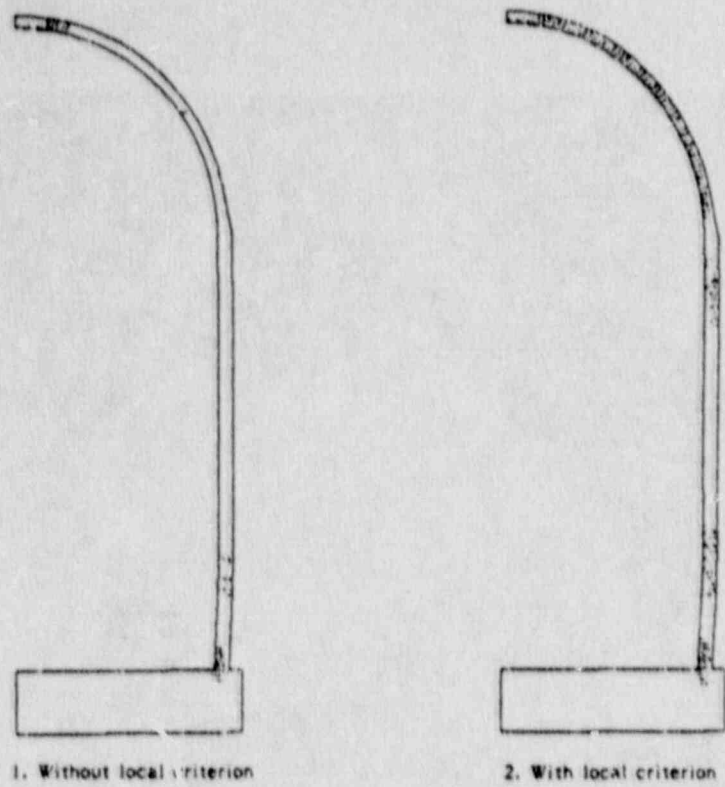
Figure 5.4.46  Meridional Crack Pattern at 0.3 MPa - Global and Local Criterion



1. Without local criterion    2. With local criterion
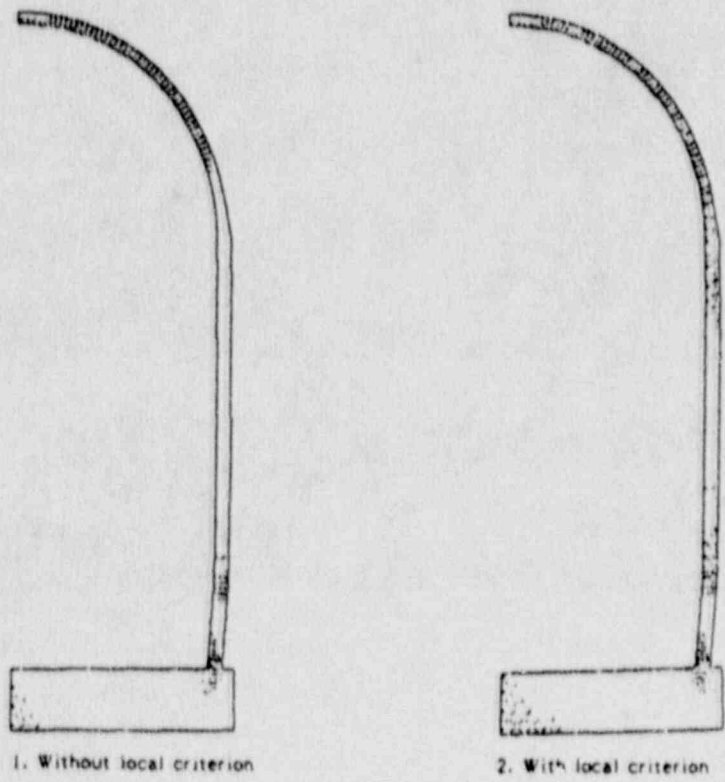
Figure 5.4.47  Meridional Crack Pattern at 0.4 MPa - Global and Local Criterion
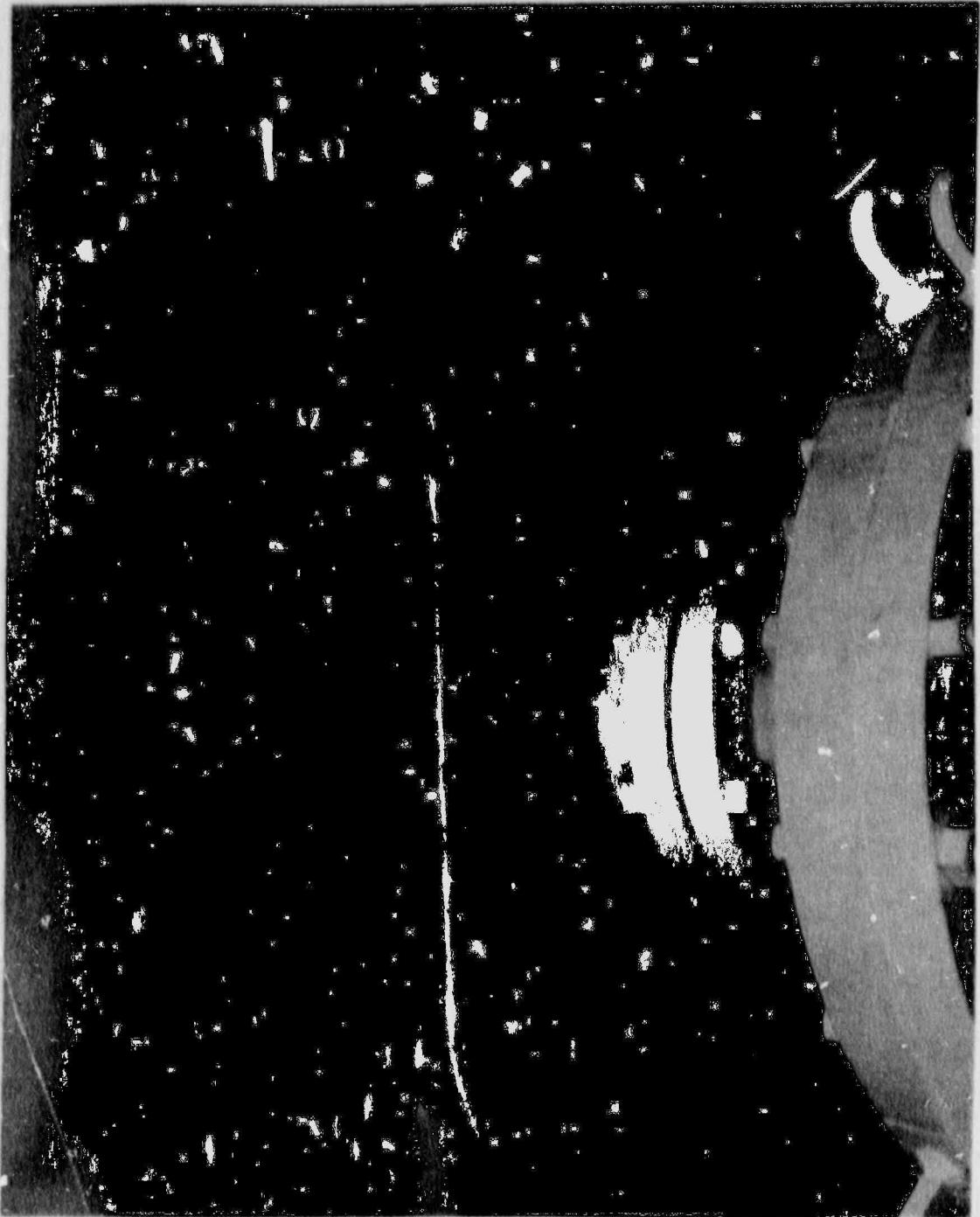
Figure 5.4.48  22-Inch Liner Tear Located Near a Piping Penetration

liner
(e = 1,59 mm)

stud anchors

concrete
(e = 247 mm)

G13

G6

G5

G4

G3

Insert plate
(e' = 4,76 mm)

G2

G1

Circumferential
direction

⊙ Vertical
direction

Radial
direction

penetration
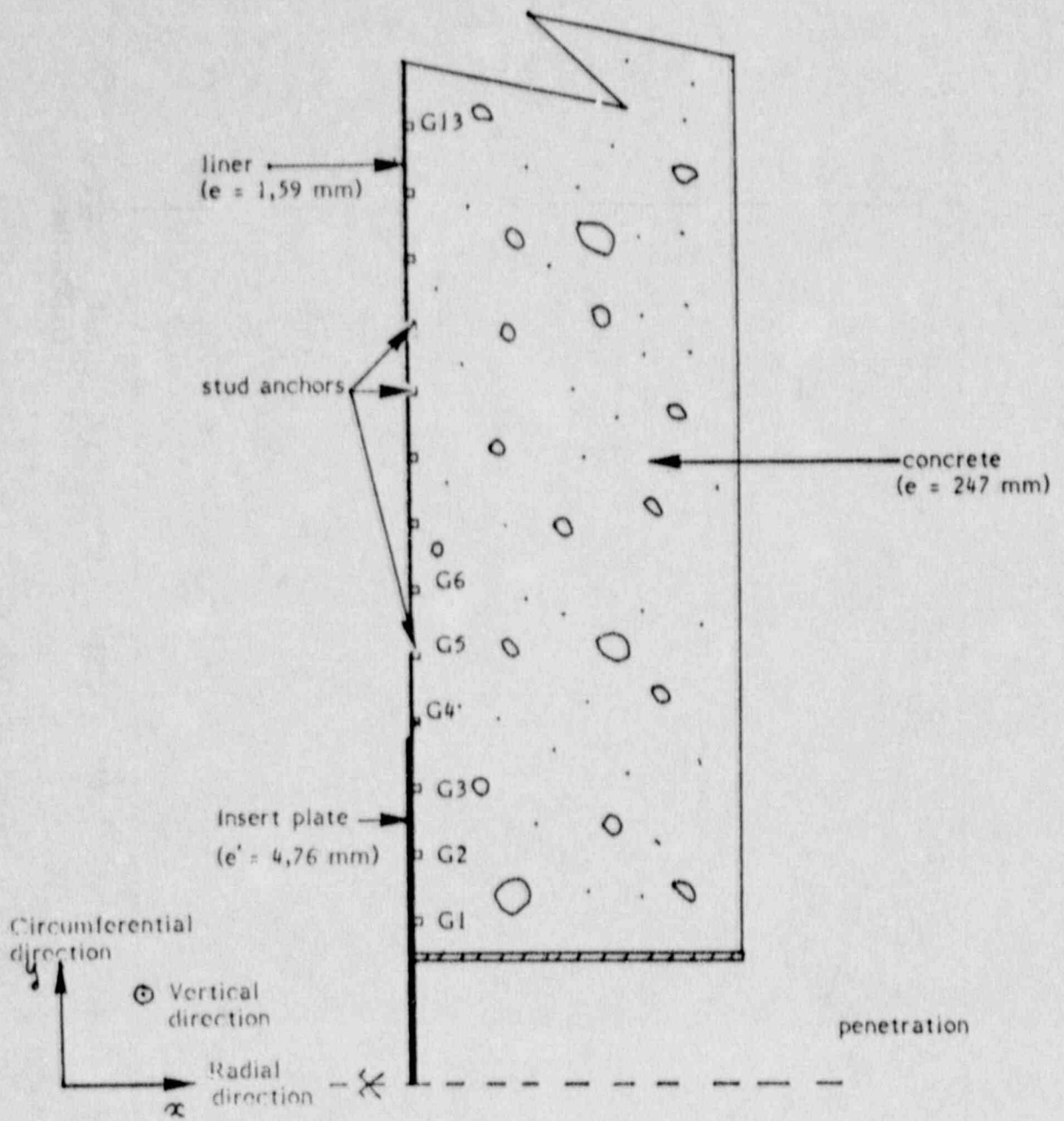
**••• ETUDE LOCALE •••**

Figure 5.4.49  Model of the Liner and Insert Plate
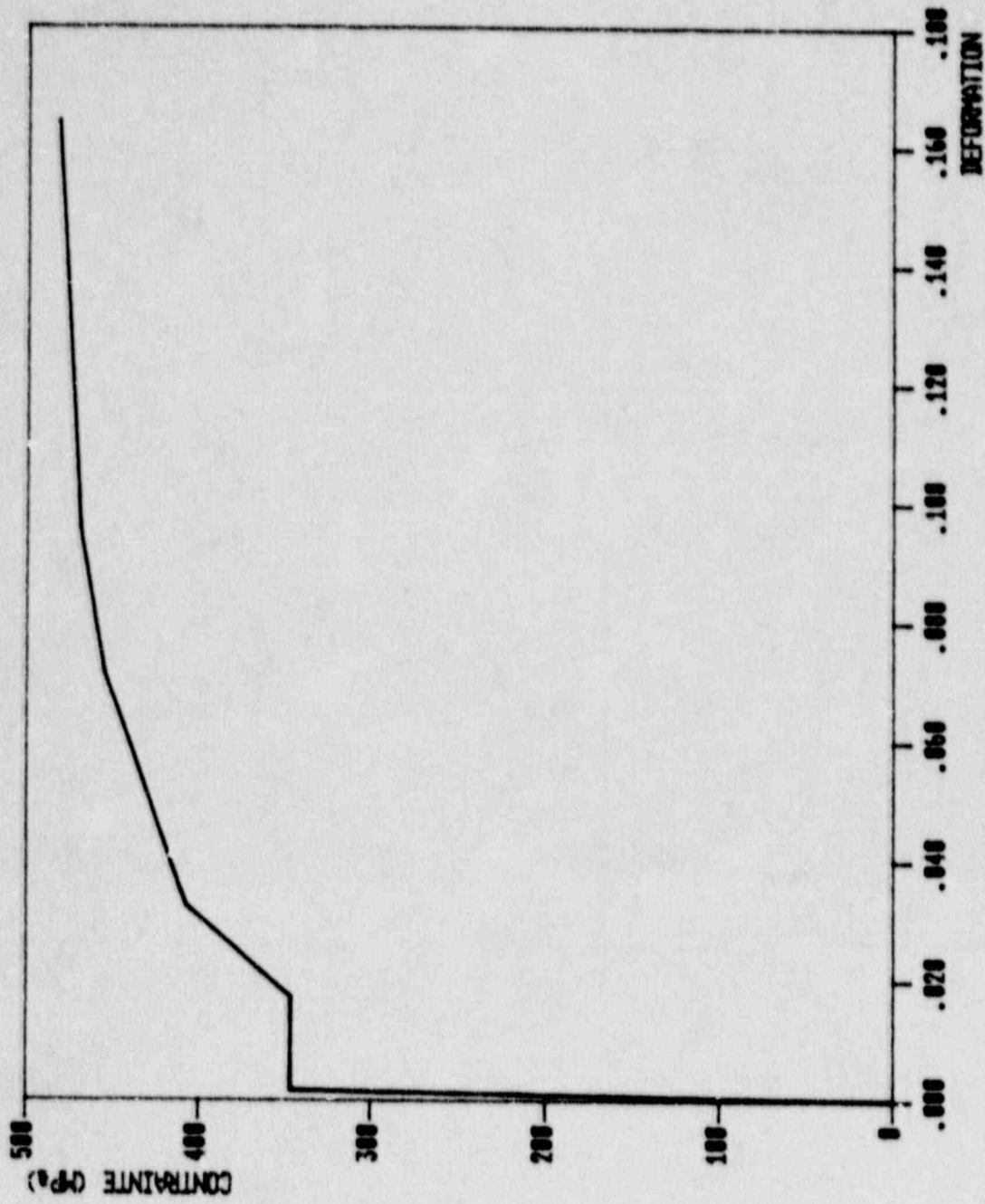
Figure 5.4.50 Stress-Strain Curve for the Liner
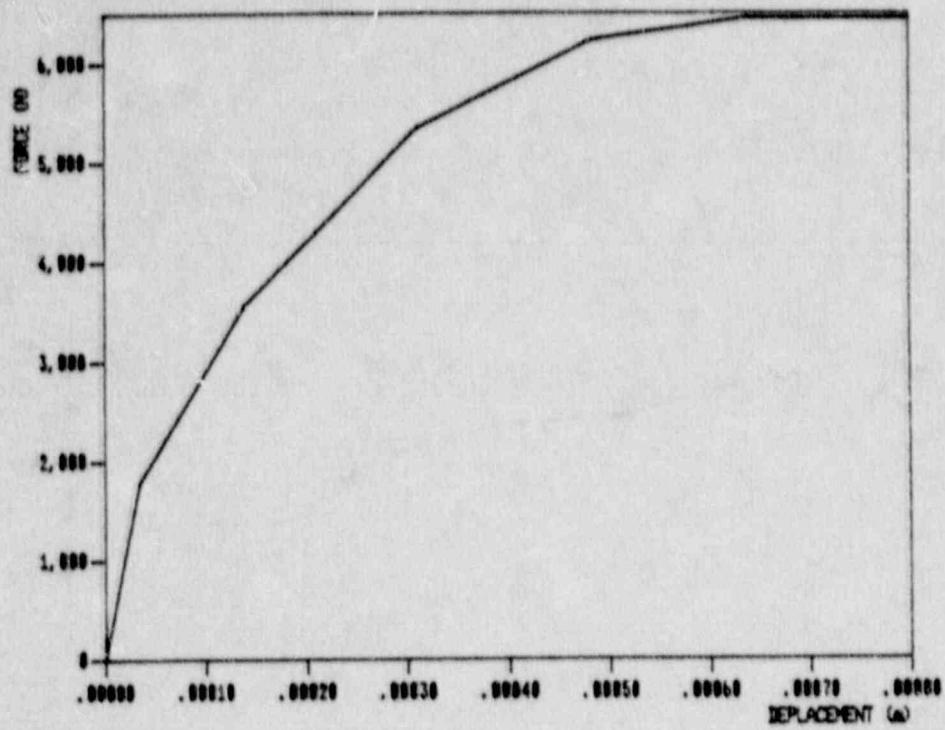
(a) Shear Force - Displacement Curve
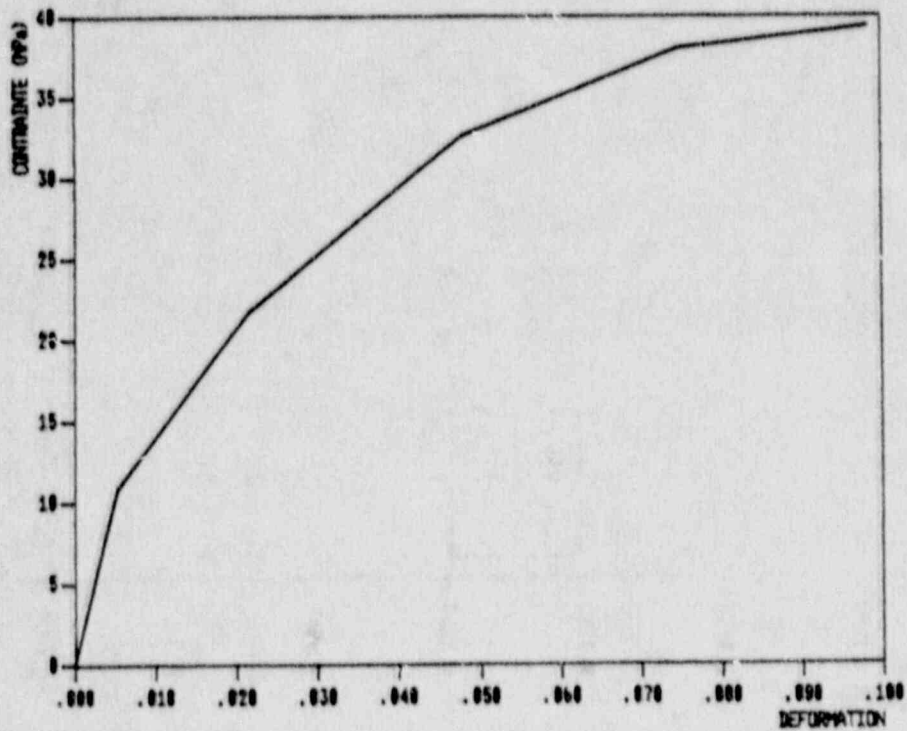


(b) Von Mises Stress-Strain Curve
Figure 5.4.51  Material Behavior for Studs
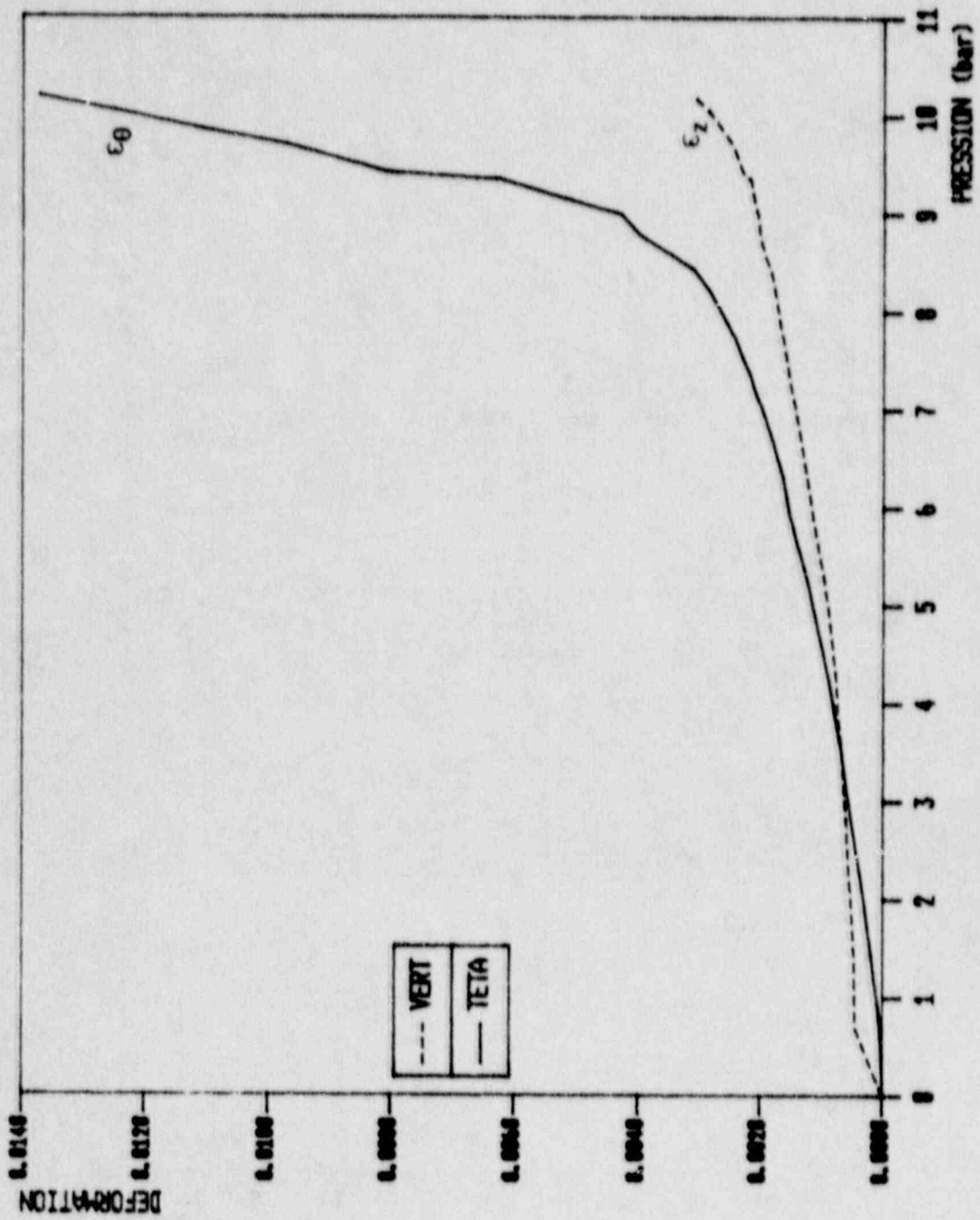
Figure 5.4.52 Axial and Hoop Strains at Cylinder Midheight

UNITES:

0.4698659E-03

0.1748354E-01

0.3449711E-01

0.5151089E-01

0.6852456E-01

0.8553823E-01

0.1025519

0.1195656

0.1365793

0.1535929
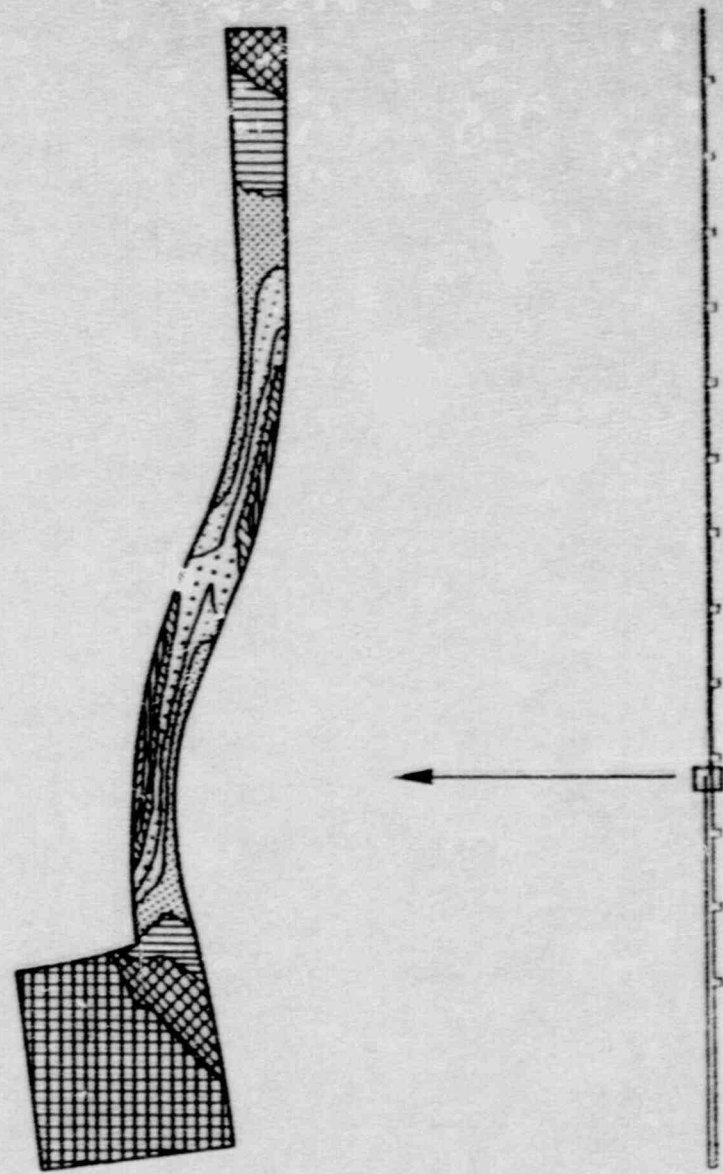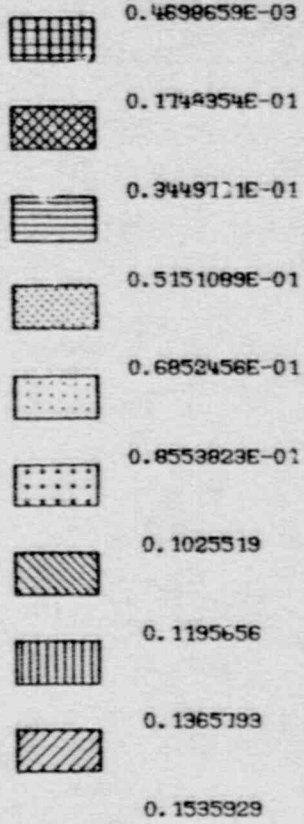
Figure 5.4.53  von Mises Strain Contours at 0.95 MPa

Figure 5.4.54 Uplift of the Insert Plate
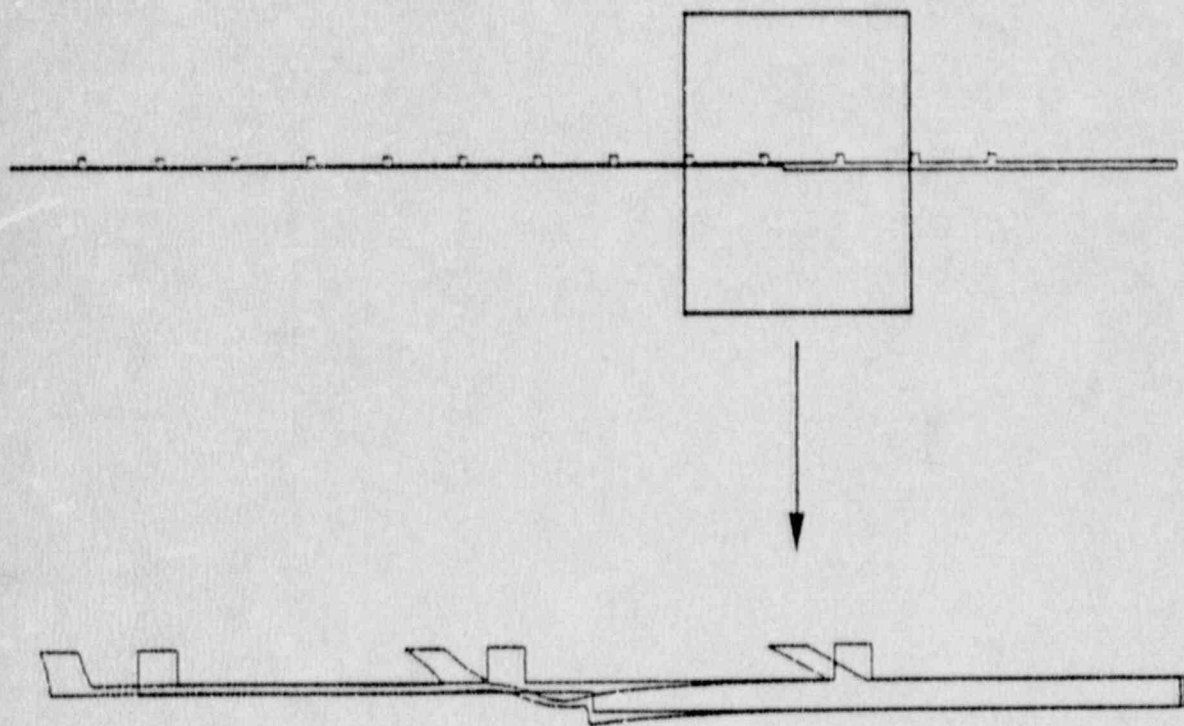
Figure 5.4.55  Deformed Mesh at 0.95 MPa
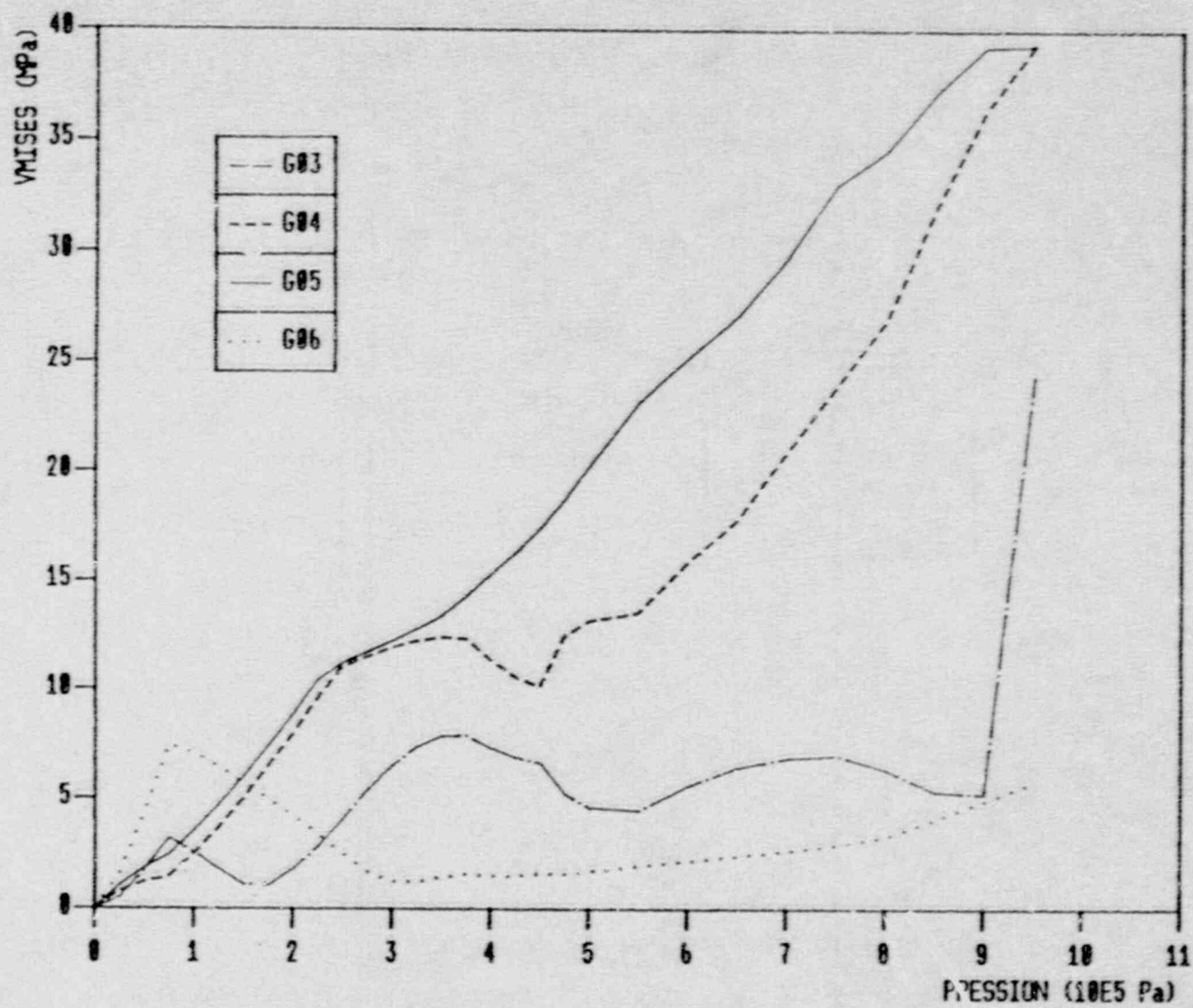
Figure 5.4.56  von Mises Stress in Studs 3-4-5-6

UNITES:

| | |
|---|---|
| ▦ | 0.5502222E-03 |
| ▨ | 0.8592296E-02 |
| ▤ | 0.1663431E-01 |
| ▥ | 0.2487844E-01 |
| ▥ | 0.3271952E-01 |
| ▥ | 0.4076059E-01 |
| ▧ | 0.4880266E-01 |
| ▥ | 0.5684474E-01 |
| ▥ | 0.6488681E-01 |
| ▨ | 0.7292888E-01 |
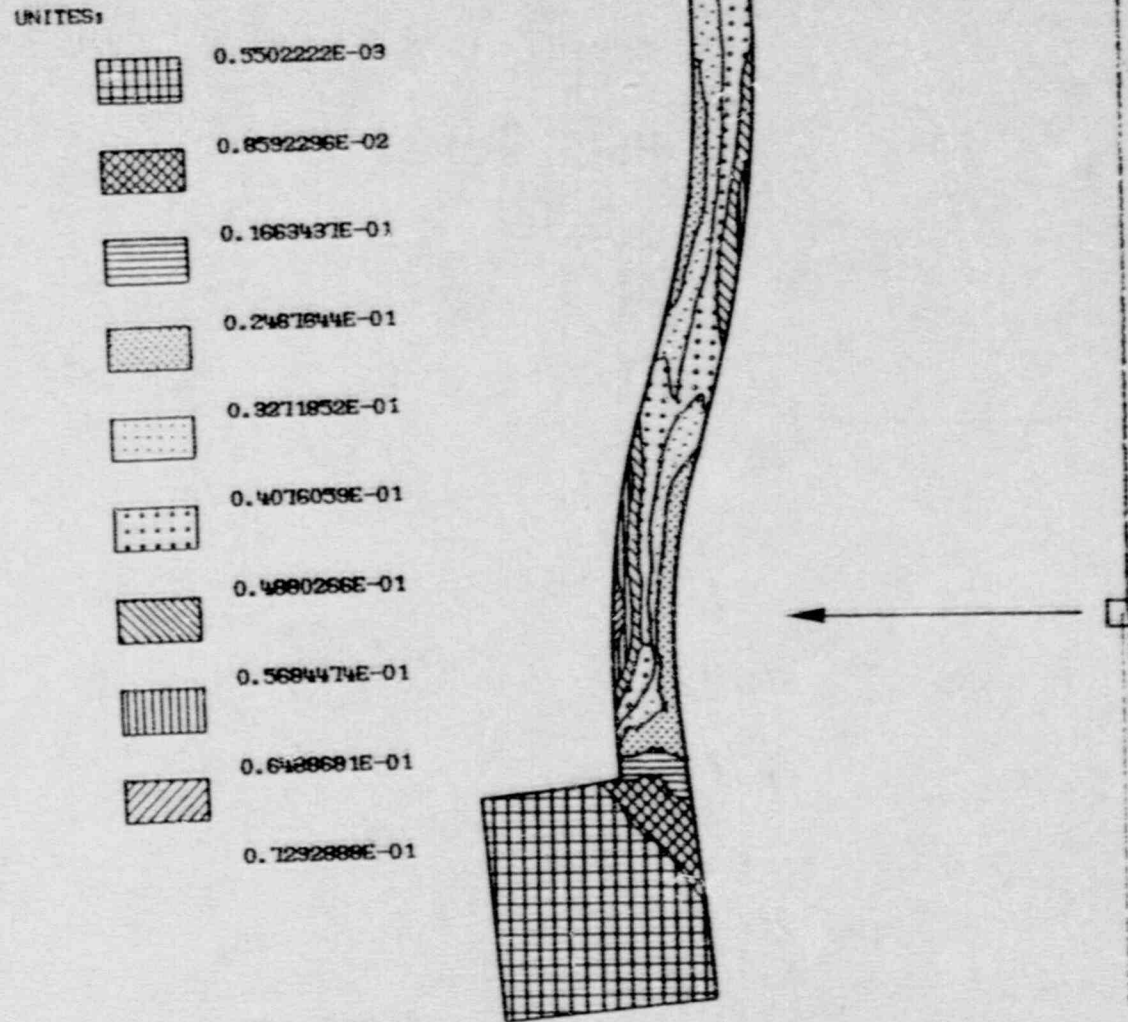
Figure 5.4.57  von Mises Strain Contours in Model without Stud G4 at 0.95 MPa

UNITES:

| Pattern | Value |
|---------|-------|
| | 0.6450638E-03 |
| | 0.1217518E-01 |
| | 0.2370531E-01 |
| | 0.3523543E-01 |
| | 0.4676555E-01 |
| | 0.5829567E-01 |
| | 0.6982579E-01 |
| | 0.8135591E-01 |
| | 0.9288603E-01 |
| | 0.1044162 |
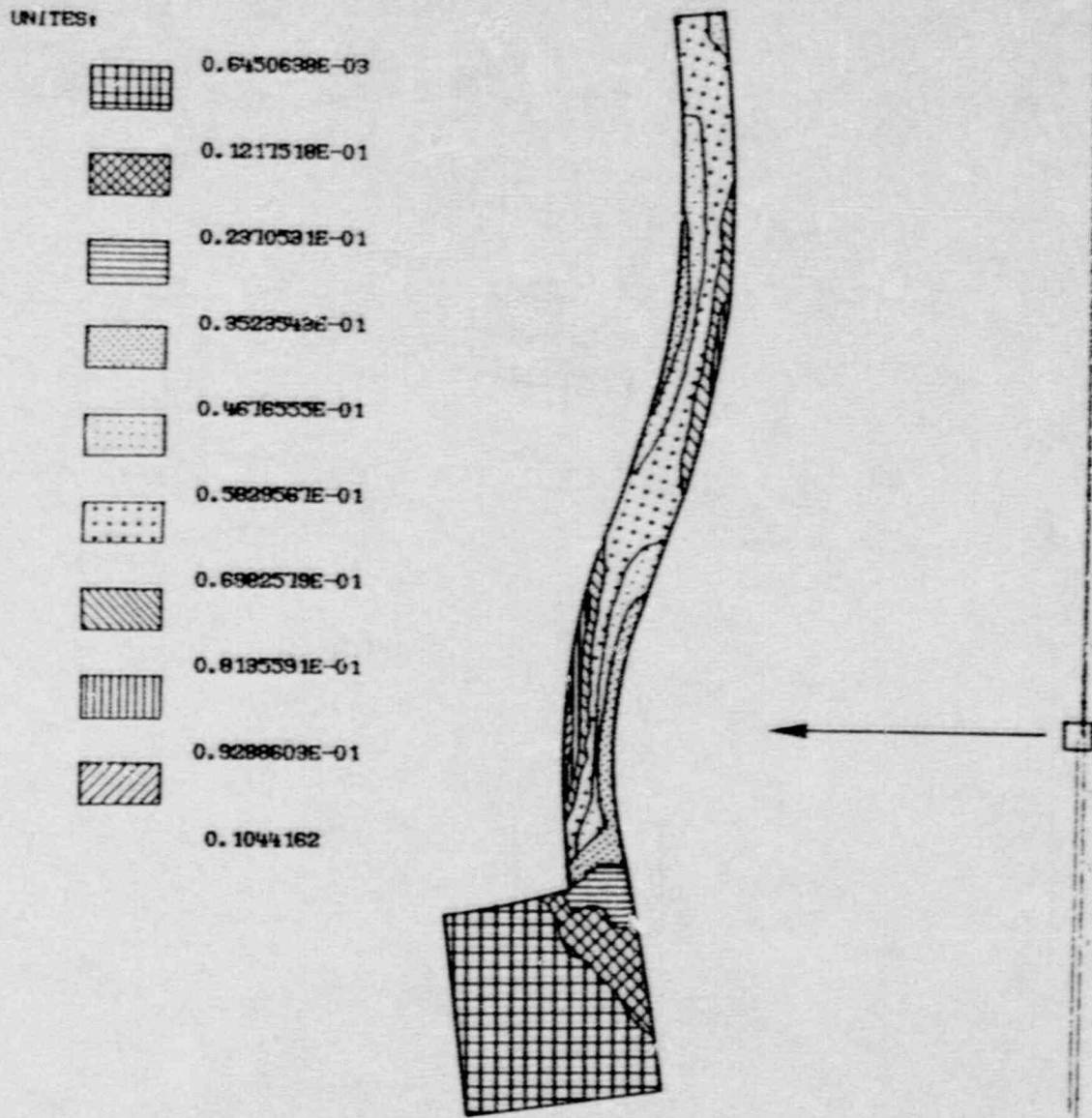
Figure 5.4.58  von Mises Strain Contours in Model without Stud G4 at 1.0 MPa
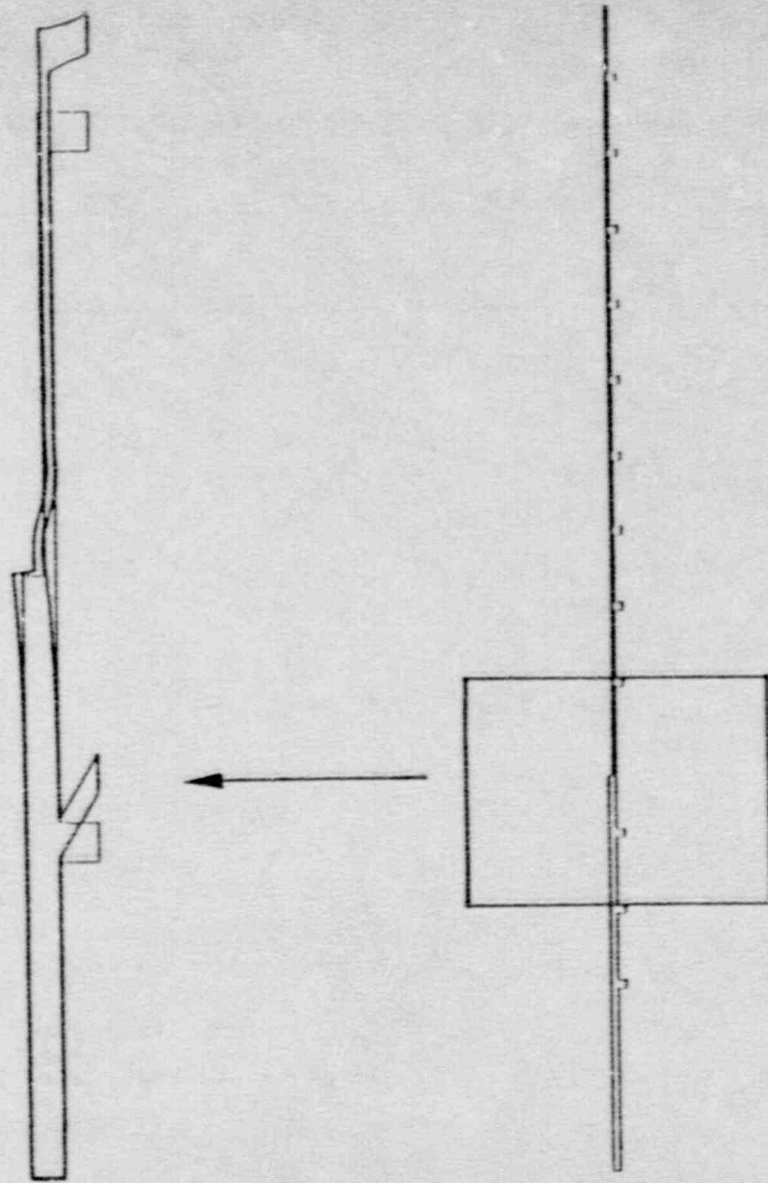
Figure 5.4.59 Deformed Mesh (without Stud G4) at 0.95 MPa
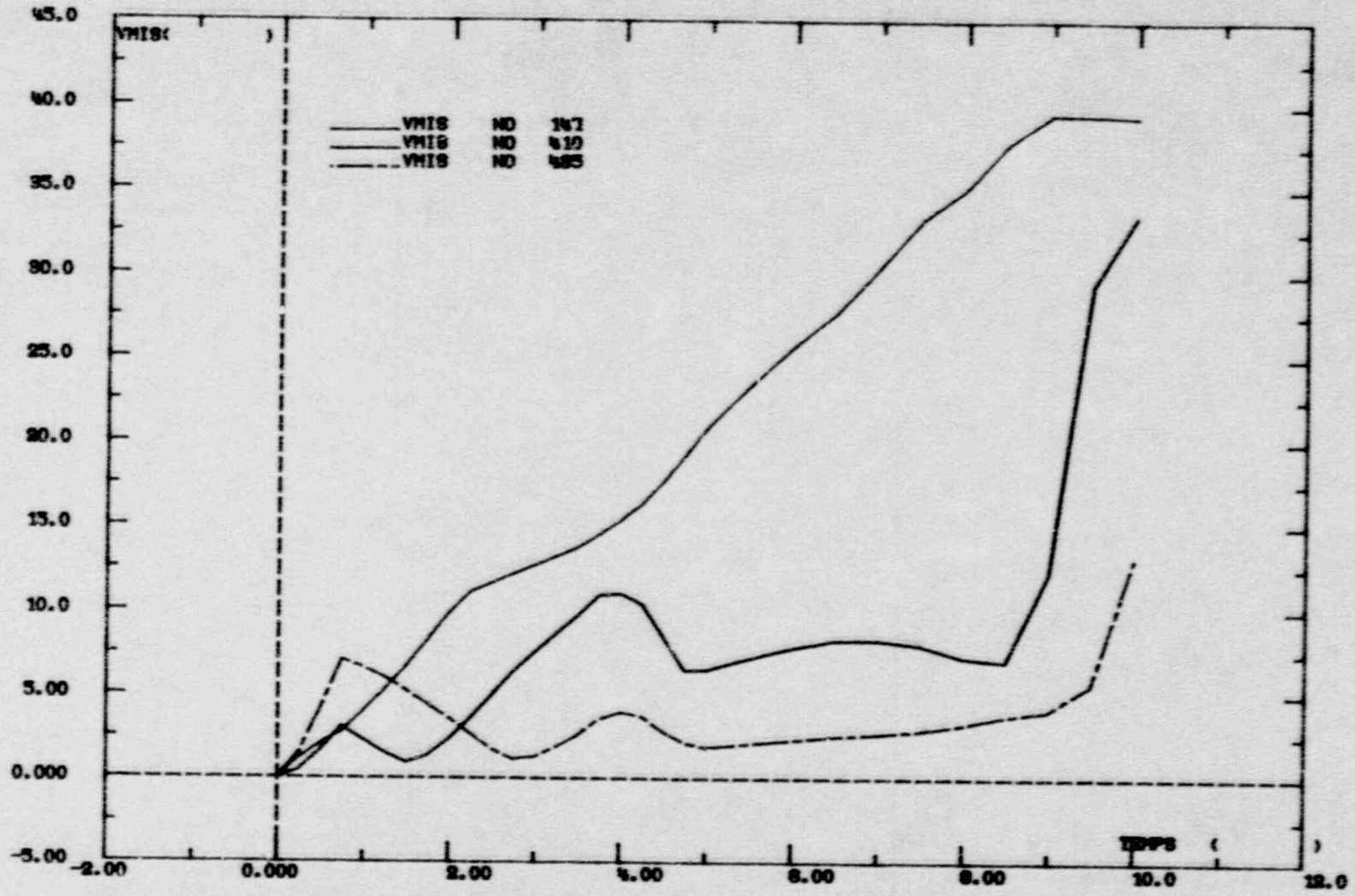
Figure 5.4.60 von Mises Stress in Studs 3-5-6 (Model without Stud G4)

## 5.5 H.M. Nuclear Installations Inspectorate

The authors of this section are I. W. Todd and R. J. Stubbs of HM Nuclear Installations Inspectorate and B. Walker and D. Collier of Ove Arup and Partners, United Kingdom.

### 5.5.1 Introduction

The regulation of nuclear installations in the United Kingdom is achieved by means of a licensing system administered by HM Nuclear Installations Inspectorate. For some years, the Inspectorate has been assessing a modified SNUPPS design for the introduction of a PWR system to the UK. Part of this work has involved the analysis of the prestressed containment structure proposed for the Sizewell B site; this and the present study have been carried out on behalf of the Inspectorate by consultants Ove Arup and Partners (OAP).

The requirements of the Inspectorate with regard to structural analysis are rather different to those of the licensee. The licensee is responsible for ensuring that the structure complies with statutory requirements, and is also economical. The regulator, on the other hand, is concerned less with the detail of the design than with the adequacy of its approach. Such analysis therefore tends to concentrate on sensitivity studies, and to take a somewhat broader view. For this reason, the approach adopted for the Sizewell structure was not a full nonlinear analysis, but a more simplified approach. Basically, a linear analysis is performed, to which nonlinearity is added only at those locations and at those load levels at which it is required. The method is therefore highly economical, requires a greater level of engineering judgement, and in addition, provides a diverse check on the more sophisticated analyses submitted by the licensee.

It is this technique that was used for the pretest predictive calculations of the behavior of the Sandia model containment, incorporating some improvements since the Sizewell work. For example, nonlinearity was introduced by the use of pseudo-loads rather than softening of the element stiffness; this is more economical in terms of computer time and allows a greater number of variables to be modified. The technique is, however, fundamentally the same, and the Inspectorate was interested to see how its predictions compared with those of more advanced techniques.

The comparison of the pressure test results with the OAP predictions is given in Section 5.5.3. In Section 5.5.4, a number of recommendations for further study are made.

The method adopted by OAP was seen to perform well when compared with the sophisticated nonlinear methods used by the other participants. However, the method overestimated the axial stiffness of the cylindrical wall and the pressure required to yield both the hoop and meridional bars. It was decided that investigations should be made into the effect of altering i) the concrete shear stiffness and ii) the foundation stiffness of the soil. Section 5.5.5 of this report contains the results from these two parametric studies.

At a latter stage it was discovered that the stiffness of the seismic reinforcement had been overestimated in the original pretest analysis. The containment with the revised seismic reinforcement was re-analyzed, and the results from this are reported in

Section 5.5.6. Also reported in this section are the results from a third parametric study, in which the tensile strength of the concrete was assumed to be zero.

Finally in Section 5.5.7 an investigation into the strains in the liner around the major liner tear is reported. The analysis in this section was performed using the nonlinear finite element code NIKE2D.

### 5.5.2 Containment Structure

A brief description of the 1:6 scale reinforced concrete containment model is presented in this section. A more detailed description of the structure can be found in [11].

The containment consists of three basic structural elements; a foundation mat, cylindrical shell and hemispherical dome (Figure 5.5.1). The foundation mat is a 1.016m (40 in.) thick circular base, 3.810m (25 ft) in diameter. The cylindrical shell is 0.2476m (9.75 in.) thick, with an internal radius of 3.3528m (11 ft) and a height of 6.7m (22 ft) from the foundation mat to the spring line at the base of the dome. The hemispherical dome wall is slightly thinner than that in the cylinder, being 0.1778m (7 in.) thick. The containment has an internal mild steel liner anchored to the concrete walls by shear studs, which are 3.75 mm (0.148 in.) in diameter. The liner plates have a nominal thickness of 1.59 mm (1/16 in.) except for those in the dome where the thickness is 2.12 mm (1/12 in.). The reinforcement arrangement in the cylinder wall is shown in Figure 5.5.2.

### 5.5.3 Comparison of Results

#### 5.5.3.1 Introduction

The pretest predictions at a number of positions are compared with those of the other participants and the measured results in Figures 5.5.3 through 5.5.30. It can be seen that for nearly all plots there is a significant scatter of results. The best agreement is shown in hoop strains, and the widest divergence in axial strains. On average most participants overpredicted the stiffness of the containment vessel, especially in the meridional direction.

#### 5.5.3.2 Comparison of OAP Predictions and the Test Results

Basemat

The stiffness of the basemat was not iterated in the analysis. At each pressure level the stiffness of each element in the base was calculated depending on the moment present and whether the basemat was cracked or uncracked.

It appears that the approach adopted, which included modelling the stiffness of the foundations using nonlinear springs, is satisfactory. The uplift at the edge of the basemat was accurately predicted in the OAP calculations (Figure 5.5.3).

Radial Displacement and Hoop Rebar Strain

From the plots of radial displacement of the liner in the cylindrical section of the containment (Figures 5.5.4-5.5.7) it can be seen that although the initial slope was reasonably predicted, the initiation of nonlinear behavior was consistently predicted

late. This phenomenon is also shown on the plots of the axial strain in the hoop rebar (Figures 5.5.8-5.5.10).

It also appears that the bending and/or shear stiffness used in the analysis for the cylindrical wall was too high. Figure 5.5.4 shows the radial displacement of the liner close to the wall base. At this point, the analysis indicated a delayed onset of yielding due to the stiffness of the wall. However the results of the test indicate no delayed yield and if anything the reverse.

Vertical Displacement and Meridional Rebar Strain

A comparison was made of the vertical displacement of the liner relative to the cylinder base at a number of heights up the wall (Figures 5.5.11-5.5.14). It can be seen that the OAP analysis consistently underpredicted the axial displacement.

The analysis also underpredicted the meridional rebar strains (Figures 5 5.15-5.5.20) apart from those at the wall base where there was a large curvature. A useful point to note is that in the meridional direction there is a similar area of steel (reinforcement and liner) as in the hoop direction but only half the stress. This means that the concrete in tension plays a much greater role in determining the axial stiffness of the section.

Tension stiffening (not to be confused with geometric tension stiffening) was introduced in the analysis (see 3.7, [39]) to better represent the behavior of concrete in tension and to overcome some numerical problems. It is possible that either the tensile stiffening adopted was incorrect and overestimated the effect, or the tensile capacity of the reinforced concrete as built was not correctly represented by the material tests carried out.

Liner Strain

A comparison of maximum strains in the liner up the height of the cylinder are shown in Figures 5.5.21-5.5.25 and as expected they follow the strains in the hoop reinforcement (with the exception of Figure 5.5.22). The problem with the liner is that it is in a state of biaxial strain, which has to be interpreted into elastic or plastic biaxial stresses. Therefore to obtain, for example, the correct hoop stress it is necessary not only to predict the correct hoop strain but also the correct meridional strain and, if yielding, the strain history.

Figure 5.5.21 shows the maximum principal strain on the inside surface of the liner at the knuckle. This shows that, as predicted, the wall base has insufficient restraint to generate any significant strain in the vertical direction.

Figure 5.5.24 compares the maximum principal strain in the liner at the springline with the predictions. Again the onset of nonlinearity was predicted late, due probably to the restraint of the dome being overpredicted.

Seismic Rebar

Figure 5.5.26 shows the axial strain in layer 8 seismic rebar in the cylindrical wall compared with the predictions. The seismic bars are at 45°, therefore the strain in the bars is half the sum of the meridional and hoop strains in the wall. As the

meridional strain in the wall was underpredicted, this is reflected by a slight underprediction in the seismic bars.

Dome

The vertical displacement of liner at the dome apex is shown in Figure 5.5.27. Although the figure shows that the displacement is significantly underpredicted it is attributable entirely to the underprediction of the displacement in the wall (see Figure 5.5.14). The displacement of the apex of the dome relative to the springline was correctly predicted.

Figures 5.5.28, 5.5.29, and 5.5.30 show the comparison of the maximum principal strain on the inside surface of the dome liner and the meridional rebar strain in the dome with the analytical predictions. It can be seen that OAP predictions fit very well to the experimental results, which indicates that the decision to treat the dome as a membrane structure and not soften on every iteration was justified.

### 5.5.4 Recommendations for Posttest Study

#### 5.5.4.1 Introduction

The method adopted by OAP to carry out the pretest analysis for the NII was seen to perform well when compared with the sophisticated nonlinear methods used by the other participants. Although it overestimated the axial stiffness of the cylindrical wall, it correctly predicted overall behavior of the containment and the range of the failure pressure.

The main conclusion to be drawn from the pretest work is that although the different analytical methods adopted predicted the overall behavior of the containment vessel in general with reasonable accuracy, there are a number of areas where modelling techniques could be improved and areas where more experimental testing is required. For example:

- The concept of tension stiffening needs to be investigated more thoroughly to assess if it is a real or artificial phenomenon.

- The interaction between the liner and the concrete is not fully understood. For example, how does the size and shape of the studs affect the performance of the liner, and how well is the liner tied to the concrete?

- Methods to establish the ultimate strength of the liner require development, including the local strength of the liner around the studs.

- Experimental work is required to establish the ultimate limit strength of reinforced concrete under biaxial tension and bending moment. Also more work is required to establish the loss of shear stiffness of reinforced concrete under high biaxial tension.

The following recommendations for further study were made. These are split into three parts: firstly, recommendations for posttest analysis work to be carried out by OAP; secondly, posttest analysis work to be carried out by Sandia; and finally, work by others.

### 5.5.4.2 Posttest Analysis by OAP

Posttest analyses to investigate the following five areas were recommended;

(i) The overestimate of axial stiffness in the cylindrical wall, particularly with regard to the effectiveness of the liner, and the tensile strength of the concrete.

(ii) The effect of reduced shear stiffness on hoop forces.

(iii) The effect of soil spring stiffness on basemat movement.

(iv) The strain distribution at the major liner tear.

(v) The effect of studs on the ultimate strength of the liner.

Items (ii) and (iii) above were conducted as a series of parametric studies and are presented in Section 5.5.5. The results from an investigation into item (i) are covered in Section 5.5.6. The strain distribution at the major liner tear, item (iv), was investigated using the nonlinear finite element code NIKE2D. The results from this analysis are reported in Section 5.5.7. At this stage no investigation into local effects around the shear studs has been performed.

### 5.5.4.3 Work by Sandia

Consideration was also given to further tests that could be carried out on the 1:6 scale containment. The possibilities include repressurization using an internal bladder to try and produce a failure at the wall base, internal explosion, and detailed sectioning for further examination. Although the idea of repressurization is an interesting one, the problems involved in producing liner failure, and interpretation of the results, probably exceeds its usefulness. The most cost-effective tests would be to section the wall at a number of locations (for example; at the wall base, at the penetrations, and at the tears in the liner) to obtain information about the state of the concrete, whether the concrete has delaminated, the behavior of the studs, and where cracks initiated.

### 5.5.4.4 Work by Others

Although the predicted failure at the wall base did not occur, there was evidence of concrete crushing and the general consensus was that a failure at the wall base was imminent. It is therefore important that a reliable method of predicting ultimate shear failure in conjunction with high axial tensile forces and bending moments is developed. This is probably only possible with an experimental test program. Other areas where experimental programs are required to provide data include;

- individual stud tests

- panel tests to assess the interaction between liners and reinforced/prestressed concrete

- panel tests to investigate loss of rebar bond stress under biaxial tensile stress.

### 5.5.5 Parametric Studies

#### 5.5.5.1 Introduction

In this section two parametric studies are reported. The first study investigates the sensitivity at the structure to the foundation stiffness. In the second study the effect of varying the concrete shear modulus is investigated. In both of these studies the pretest analysis reported in [39] is used as the base case.

The pretest analysis was performed over five pressure steps, with internal pressures of 0.365, 0.6, 0.8, 1.0 and 1.2 MPa (53, 87, 116, 145, and 174 psig) being considered. For the two parametric studies reported here the same five pressure steps were used.

#### 5.5.5.2 Subgrade Modulus Variation

In the original analysis of the containment a Winkler-type foundation was assumed with a sub-grade modulus of 40 MN/m²/m (255 ksf/ft). This value was obtained from plate bearing test results supplied by Sandia [38]. For this sensitivity study the analysis was repeated using sub-grade moduli of 20 MN/m²/m and 80 MN/m²/m (128 ksf/ft and 510 ksf/ft).

The response of the structure was found to be very insensitive to changes in the subgrade modulus. This is illustrated in Figures 5.5.31 and 5.5.32, which show the radial displacement and the vertical displacement measured relative to the cylinder base at an elevation of 3.3528m (11 ft). At the lower pressure levels there is no difference between the analyses, and only a small difference is noticeable at the highest pressure case. This insensitivity to the sub-grade modulus arises from the massive nature of the foundation mat, which is very stiff in bending. The only noticeable effect of changing the sub-grade modulus is in the global meridional displacements. This is illustrated in Figure 5.5.33, which shows the meridional displacement at the outer radius of the basemat, a positive displacement indicating that uplift from the foundation has occurred. It can be seen that at an internal pressure of 1.2 MPa (174 psig) the basemat has lifted up from the foundation in all three cases.

The greatest uplift is 3.5 mm (0.138 in.) for a sub-grade modulus of 80 MN/m²/m (510 ksf/ft) and this reduces to 0.01 mm (0.00039 in.) for a modulus of 20 MN/m²/m (128 ksf/ft). However, when the meridional displacement at the wall base measured relative to the centre of the basemat is considered, the three analyses produce similar results (Figure 5.5.34). This shows that the amount of dishing experienced by the foundation mat is relatively unaffected by the sub-grade modulus. Thus, a change in sub-grade modulus produces only a rigid body type movement to the structure and has no effect on the stress within the structure.

#### 5.5.5.3 Concrete Shear Modulus Variation

In the original analysis the following approach was used to calculate the shear modulus of the concrete. The three orthogonal elastic moduli $E_M$, $E_H$, and $E_R$ (subscripts M: meridional, H: hoop, R: radial) are calculated from the previous load case. The shear moduli are then calculated from [39];

$$E_{ij} = \frac{(E_i E_j)^{1/2}}{2(1 + Pr)}$$

where Pr is Poisson's ratio, taken to be 0.15 for an uncracked section or zero for a cracked section. A section is judged to have cracked in a particular direction when an axial tensile strain of 0.0007 is reached.

The above method for calculating the shear modulus is uncertain, but owing to the lack of conclusive data, is a reasonable assumption to make. In order to test the importance of the value used for the concrete shear modulus the containment was re-analyzed using shear moduli 0.5 and then 2.0 times the values used in the original analysis. All other values in the analyses were kept the same.

The shear modulus was found to have negligible effect on the results, with values changing by generally less than 0.1%. This is illustrated in Figures 5.5.35 and 5.5.36, which show the radial and vertical displacements at an elevation of 3.3528 m (11 feet). Thus, the method employed to calculate the shear modulus of the containment wall is not critical as the structural response is relatively unaffected by its value.

### 5.5.6 Re-Analysis

### 5.5.6.1 Introduction

After completion of the parametric studies it was discovered that the stiffness of the diagonal seismic reinforcement had been overestimated. The effect of this was to stiffen the structure in both the meridional and hoop directions. In this section two re-analyses of the containment using the revised seismic reinforcement are reported.

In the first analysis the method used in the pretest analysis is used to model the tensile capacity of the concrete [39]. In this model it is assumed that, due to tension stiffening, the tensile strength of the concrete reaches its peak valve at a tensile strain of 55 per cent of the split cylinder failure strain. The strength then decreases linearly to zero at a tensile strain of 0.0007. In the second analysis the tensile capacity of the concrete was ignored and assumed to be zero.

For these two analyses the number of pressure steps was increased to six, with internal pressures of 0.365, 0.6, 0.8, 0.9, 1.0 and 1.1 MPa (53, 87, 116, 130, 145, and 160 psig) being used.

### 5.5.6.2 Re-Analysis with Tensile Concrete Strength

As expected, the change to the stiffness of the diagonal reinforcement produced a considerable improvement in the results obtained. This is illustrated in Figures 5.5.37 to 5.5.42, which show the results from the re-analysis compared with pretest analysis and model test results.

The radial displacement of the liner at an elevation of 3.3528m (11 ft) is shown in Figure 5.5.37, and the meridional displacement of the liner at the same elevation measured relative to the cylinder base is shown in Figure 5.5.38. At the lower pressures there is great improvement in the agreement with the test results, especially in the meridional direction. The point of yielding of the structure is also reduced and agrees more closely with the test results.

Similar improved agreement between the re-analysis and test results is shown in Figures 5.5.39, 5.5.40 and 5.5.41, which show the axial strains in selected reinforcing

bars. Figure 5.5.39 shows the axial strain in a layer 5 meridional rebar at an elevation of 4.119m (13.75 ft), and Figure 5.5.40 shows the axial strain in a layer 6 hoop rebar at the same elevation. The axial strain in a layer 8 seismic rebar at an elevation of 6.096m (12 ft) is shown in Figure 5.5.41. Finally Figure 5.5.42 shows the maximum principal strain in the liner at an elevation of 4.191m (13.75 ft), where a similar improvement is again obtained.

A further improvement that could be introduced is to model the increase in hoop force that occurs when the radial displacements become large. However this large displacement effect is not considerable and for the final pressure case considered (1.1 MPa) the hoop force is increased by only 2% at the mid-cylinder position.

### 5.5.6.3 Re-Analysis with Zero Tensile Strength Concrete

In the previous analysis the structure is still too stiff in the meridional direction at the lower pressures. This was clearly illustrated in Figures 5.5.38 and 5.5.39. However, in the hoop direction there is better agreement between the analytical and test results. Figures 5.5.38 and 5.5.39 are repeated in Figures 5.5.43 and 5.5.44 with inclusion of the results from the zero tensile concrete strength re-analysis. It is noticed that by removing the tensile capacity of the concrete the structure is less stiff at the lower pressures. However, above 0.9 MPa (130 psig) there is very little difference between the two re-analyses, since the concrete is almost fully cracked at this pressure. At the lower pressures the test results fall between the two re-analyses showing the concrete to have some tensile strength, indicating that this was possibly overestimated in the original analysis.

The hoop strains are approximately twice the meridional strains and consequently the concrete cracks considerably earlier in the hoop direction than in the meridional direction. Hence the tensile strength of concrete is less critical in the hoop direction. This is shown in Figure 5.5.45 which gives the radial displacement at 3.3528m (11 ft); very little difference between the two re-analyses can be seen.

The reason for the lower concrete tensile strength is uncertain and can be attributed to a number of possible reasons. For example:

(i) concrete was cracked by the structural integrity test

(ii) shrinkage cracking during the curing of the concrete [30]

(iii) test used to obtain the UTS over estimated the strength of the concrete.

(iv) test specimen in UTS test stronger than concrete in structure

### 5.5.7 Analysis of Liner Strains

### 5.5.7.1 Introduction

It was reported in Section 5.5.4.3 that the main tear in the liner occurred next to an insert plate containing instrumentation ports. The position of this tear is illustrated in Figure 5.5.46, from which it can be seen that it extends along the entire height of the insert plate. The actual length of the tear was measured to be 0.51m (20 inches). From the axisymmetric analyses reported in Section 5.5.7, the maximum hoop and

meridional liner strains at mid-cylinder height were found to be 1.6% and .15% respectively. This level of strain is not considered to be great enough to initiate a liner tear. However, it is probable that the insert plate acts as a stress raiser and the strain levels in the vicinity of the plate are consequently much higher. An investigation of the liner strain around the insert plate was undertaken using the finite element code NIKE2D [40].

NIKE2D is a two-dimensional implicit finite element code that can model such nonlinear features as thinning of shells, finite deformation and nonlinear material properties. It is the combination of these three features that made the code suitable for the present analysis.

### 5.5.7.2 Liner Finite Element Model

The liner was modelled as a 2-D flat sheet, assuming a state of plane stress, and loaded by applying edge displacements obtained from the previous axisymmetric analysis. The area of liner modelled had to extend far enough from the insert plate and penetrations for the free-field displacements applied to be correct. The section of the liner modelled is shown in Figure 5.5.47. Symmetry boundary conditions were applied along two edges and calculated displacements corresponding to the state of strain in the axisymmetric analysis were applied along the other two. The liner was discretized using four node quadrilateral elements. Figure 5.5.48 shows the finite element mesh and boundary conditions. Also shown on the figure are the four areas of different thickness. Area 1 corresponds to the standard liner thickness of 1.5875 mm (1/16 in.). Areas 2 and 3 correspond to the thickened liner plate around the instrumentation ports and equipment hatch A, where the liner is 4.7625 mm (3/16 in.) thick. Area 4 has been added to model the equipment hatch tube.

Before proceeding with the main analysis, an initial verification analysis was undertaken to demonstrate that the non-uniform mesh would not influence the strain results. In this analysis the thickness of the whole model was set to 1.5875 mm (1/16 in.). The boundary displacements to be used in the main analysis were then applied to the model, along with additional displacements around the penetrations, so that every node on the boundary was either restrained or given a specified displacement. The displacements were such that a uniform strain field over the whole model should result. Thus if the elements in the mesh were to behave in a non-uniform manner or to lock up (that is, to induce areas of local stiffness), it would be shown in this analysis. This was not found to be a problem, as the variation of equivalent plastic strain across the model was from 1.72% to 1.73%.

Having established the validity of the mesh a thickness for area 4, the tube within equipment hatch A, had to be determined. The tube is 12.7 mm (1/2 in.) thick and consequently this is the width of the ring of elements in the 2-D analysis, and over 0.5m (19.7 in) long. In determining the thickness to use in the analysis, the reduction of the tube thickness from 12.7 to 6.35 mm (1/2 to 1/4 in.) and stiffness of the end cover were both considered. A thickness of 140 mm (5.5 in.) was calculated and used in the analysis.

The strains applied to the liner boundaries, as calculated from the axisymmetric analysis, are given in the following table.

| Pressure (MPa) | Meridional Strain (%) | Hoop Strain (%) |
|---|---|---|
| 0.365 | 0.004 | 0.088 |
| 0.600 | 0.072 | 0.133 |
| 0.800 | 0.106 | 0.188 |
| 0.900 | 0.129 | 0.220 |
| 1.000 | 0.139 | 0.600 |
| 1.100 | 0.147 | 1.600 |

The NIKE2D analysis was performed using 15 load steps, one step between each of the first five pressures and 10 steps between 1.0 and 1.1 MPa (145 and 160 psig). The 10 steps between the last two pressures was found to be necessary as the liner becomes highly nonlinear at this stage.

### 5.5.7.3 Results

The effective plastic strains in the liner, obtained after the fifteenth load step are shown in Figures 5.5.49-5.5.51. Figure 5.5.49 shows the distribution of strain over the whole area analyzed, and Figures 5.5.50 and 5.5.51 show the strains in the region of the insert plate and equipment hatch, respectively.

It can be seen that around the insert plate a peak strain of 7.0% is obtained and around the equipment hatch the peak strain is 5.7%. The location of these peak strains correspond well with the positions of the tears in the liner shown in Figure 5.5.46. It is noted though that the strains are considerably less than the 16% obtained in the uniaxial test on the liner plate. However, other work has shown that, in a biaxial state, failure strains of 5% are not uncommon in steel plates [41].

### 5.5.8 Conclusions

(i) The method adopted by OAP to carry out the pretest analysis for the NII was seen to perform well when compared with the sophisticated methods used by other participants of the round-robin pretest analysis.

(ii) The method correctly predicted the overall behavior of the containment and the range of the failure pressure.

(iii) The axial stiffness of the cylindrical wall was found to be overestimated in the analysis.

(iv) An investigation into varying the sub-grade modulus has shown that the response of the structure is relatively insensitive to this parameter, owing to the massive nature of the foundation mat. The only noticeable effects were in the amount of lift-off shown by the foundation mat and the global displacement of the whole structure.

(v) An investigation into varying the concrete shear modulus has shown the structure to be insensitive to this parameter.

(vi) At a later stage it was discovered that the stiffness of the seismic reinforcement had been overestimated in the original pretest

analysis. A re-analysis of the structure using a new model for the seismic reinforcement produced considerably better agreement with the test results.

(vii) A further re-analysis was undertaken ignoring the tensile strength of the concrete. This analysis showed that the best agreement with test results would be obtained by assuming the concrete to have some tensile capacity, but this capacity had been overestimated by the method originally used to model the tension stiffening.

(viii) A nonlinear analysis of the liner has been performed which predicts large strains in the areas where tears formed in the test.
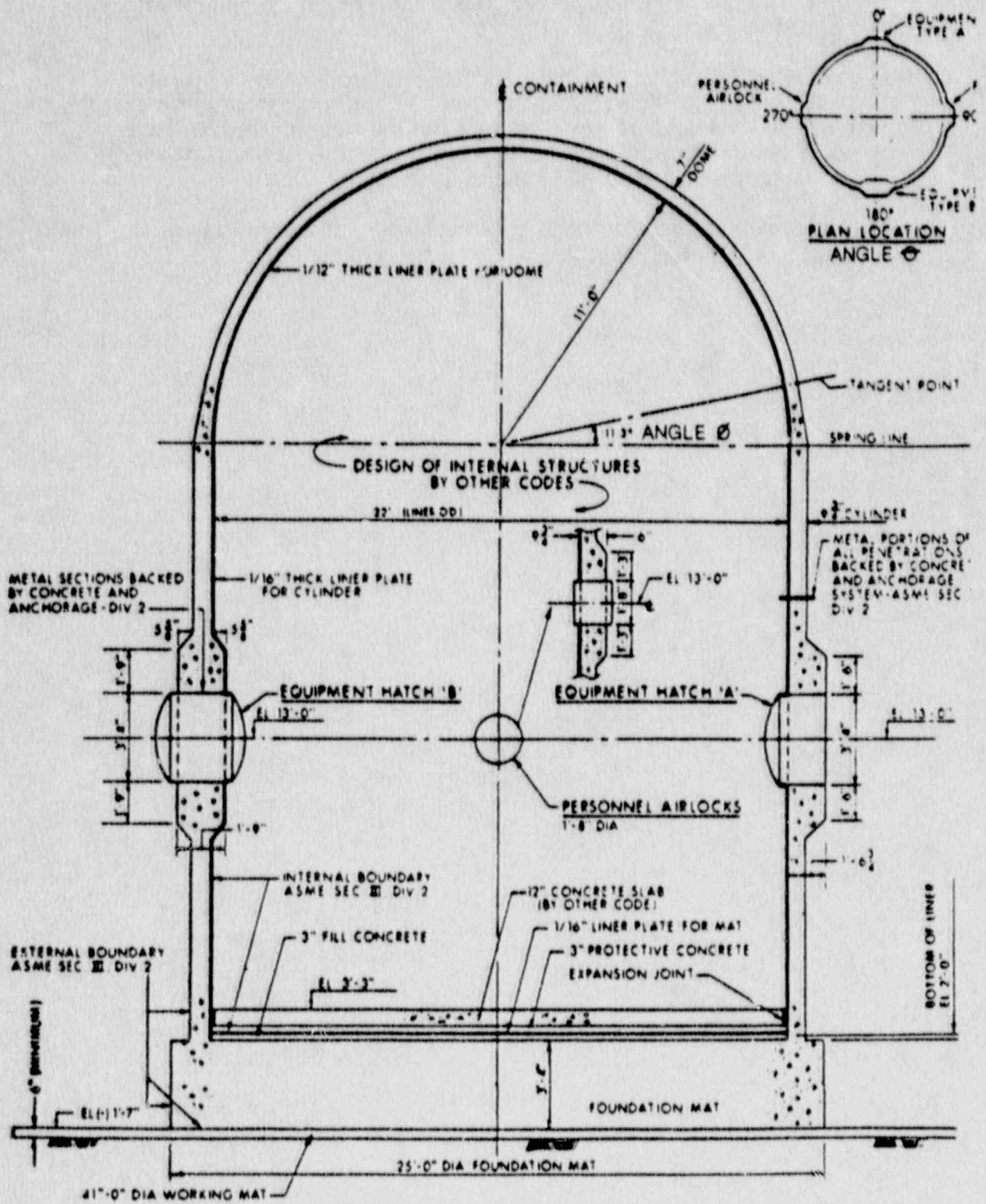
Figure 5.5.1 Typical Section Through 1/6-Scale LWR Reinforced Concrete Model

**REINFORCING BAR DETAILS**

| LAYER | TYPE | SIZE |
|-------|------|------|
| 1 | HOOP | #4 |
| 2 | MERIDIONAL | #4 |
| 3 | HOOP | #4 |
| 4 | HOOP | #4 |
| 5 | MERIDIONAL | #4 |
| 6 | HOOP | #4 |
| 7 | SEISMIC (45° DIAG) | #4 |
| 8 | SEISMIC (45° DIAG) | #4 |
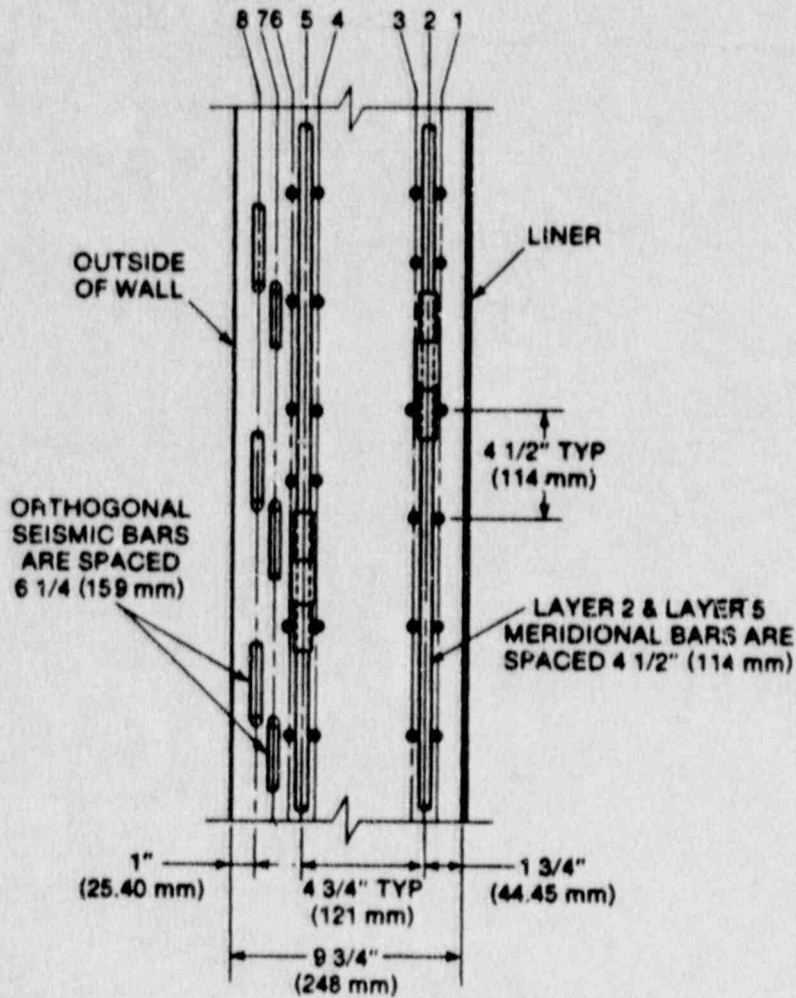
Figure 5.5.2 Reinforcement in the Cylinder
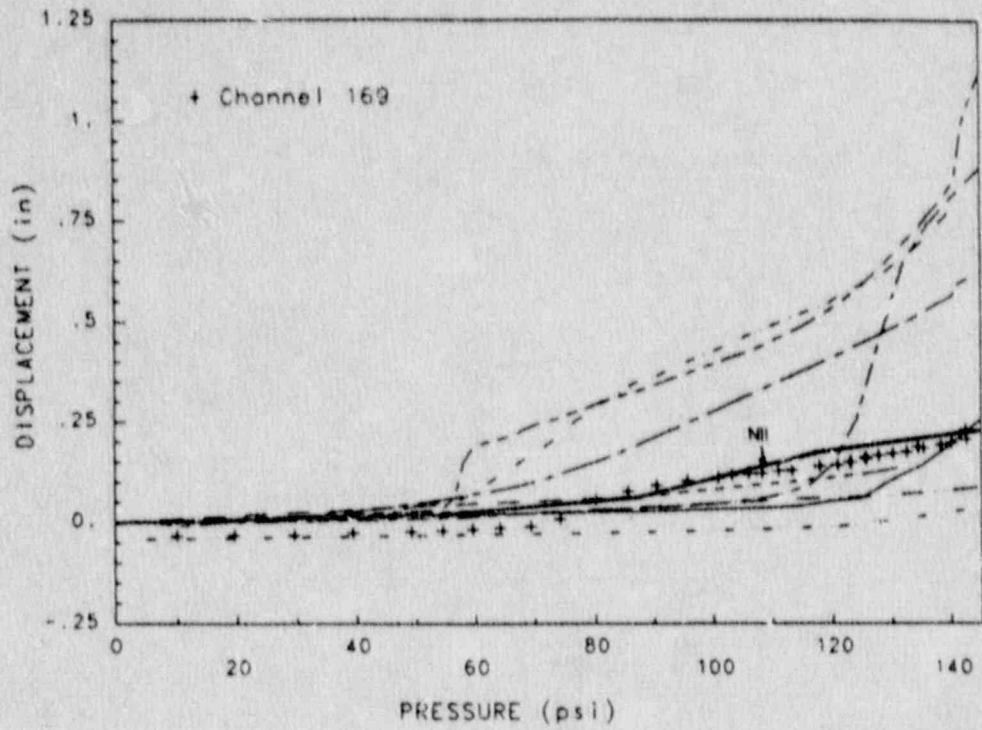
Figure 5.5.3  Basemat Uplift Relative to Center of Basemat
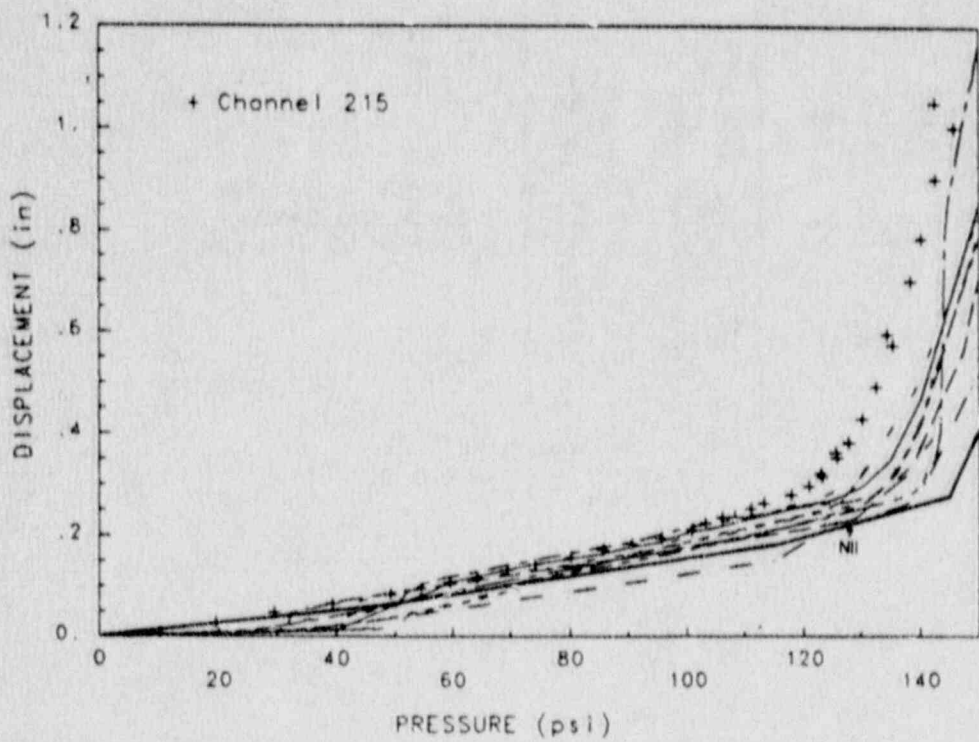


Figure 5.5.4  Radial Displacement of Liner at El 6 ft
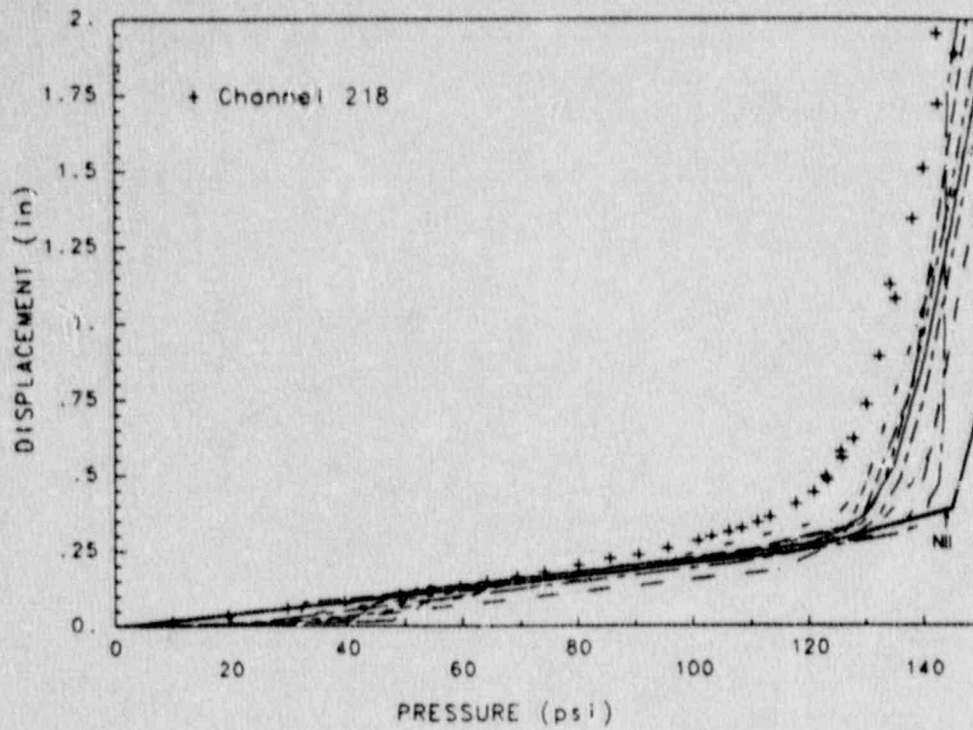
Figure 5.5.5  Radial Displacement of Liner at El 11 ft
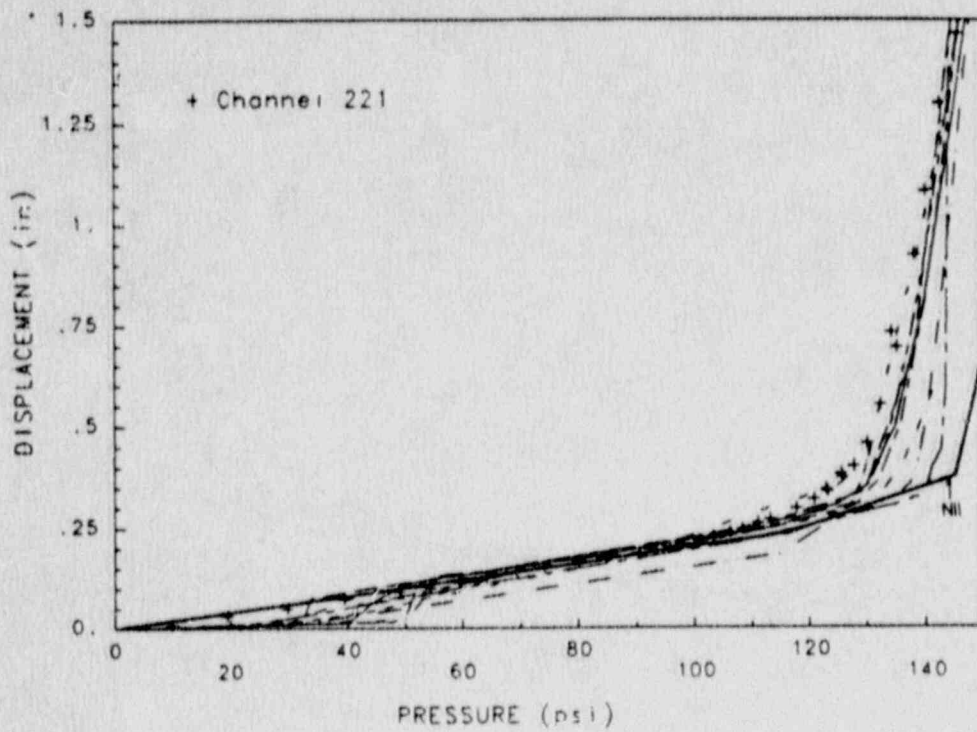


Figure 5.5.6  Radial Displacement of Liner at El 18 ft
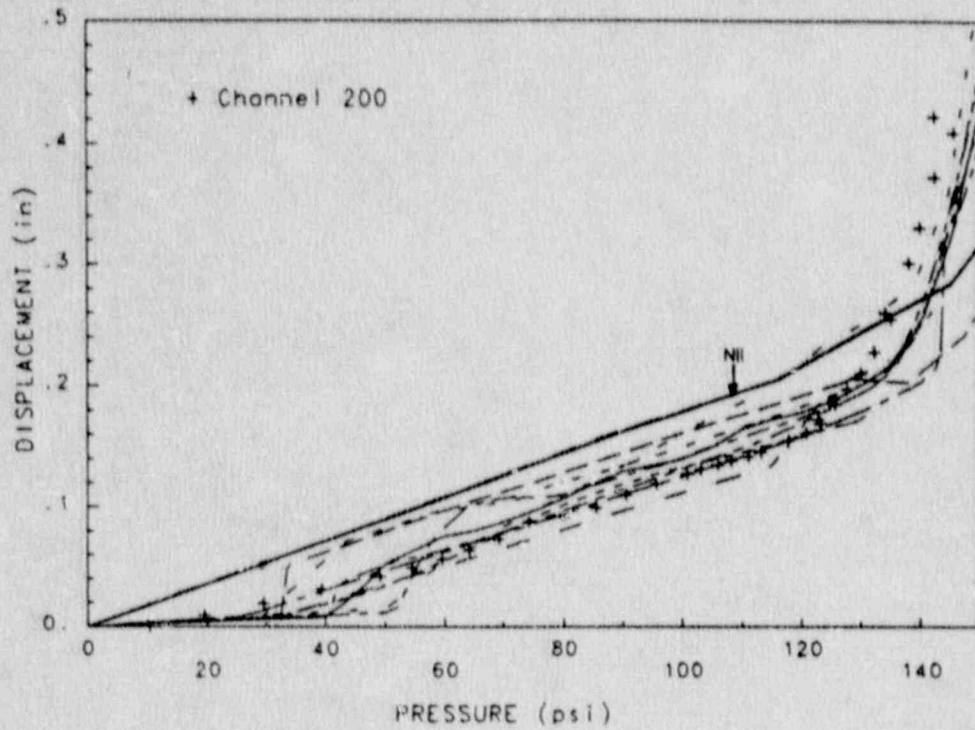
Figure 5.5.7  Radial Displacement of Liner at El 24 ft
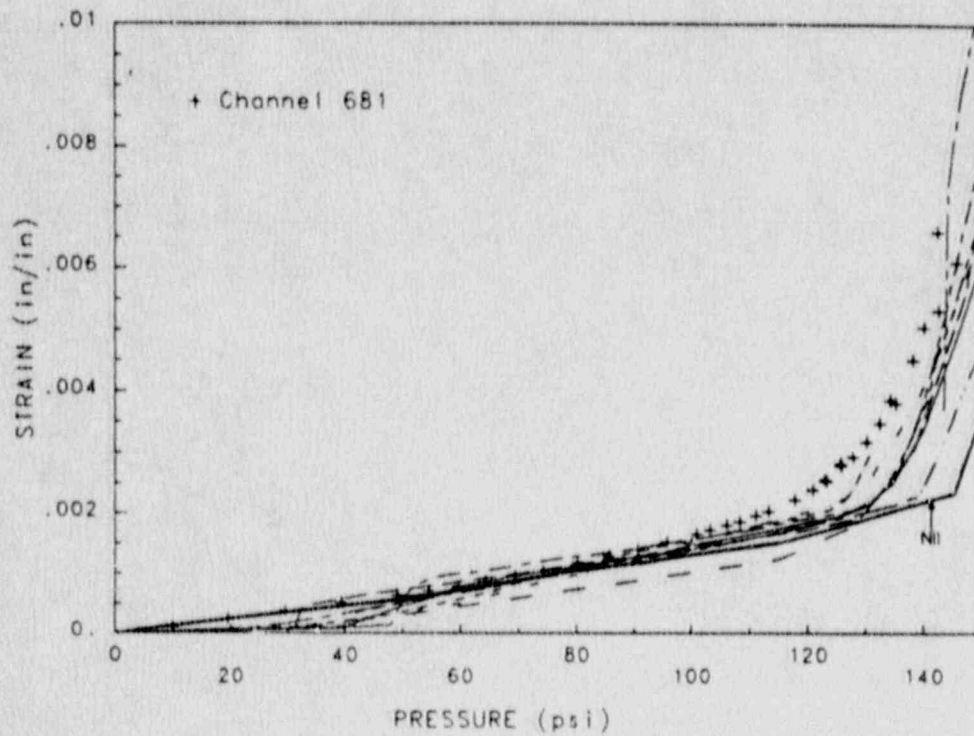


Figure 5.5.8  Axial Strain in Layer 6 Hoop Rebar at El 6.75 ft
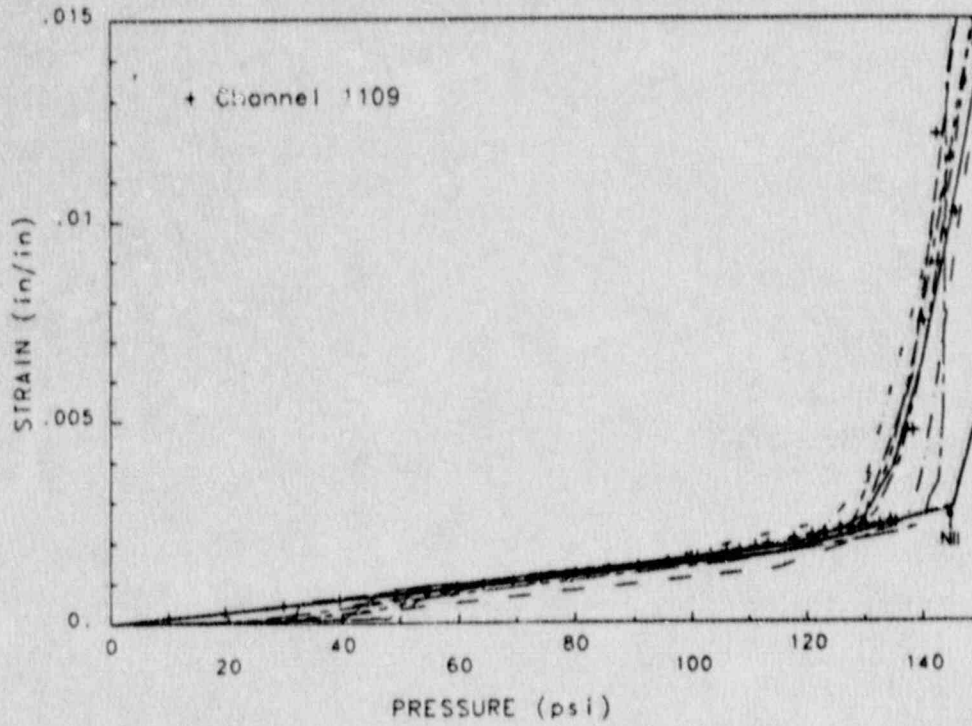
Figure 5.5.9  Axial Strain in Layer 6 Hoop Rebar at El 13.75 ft
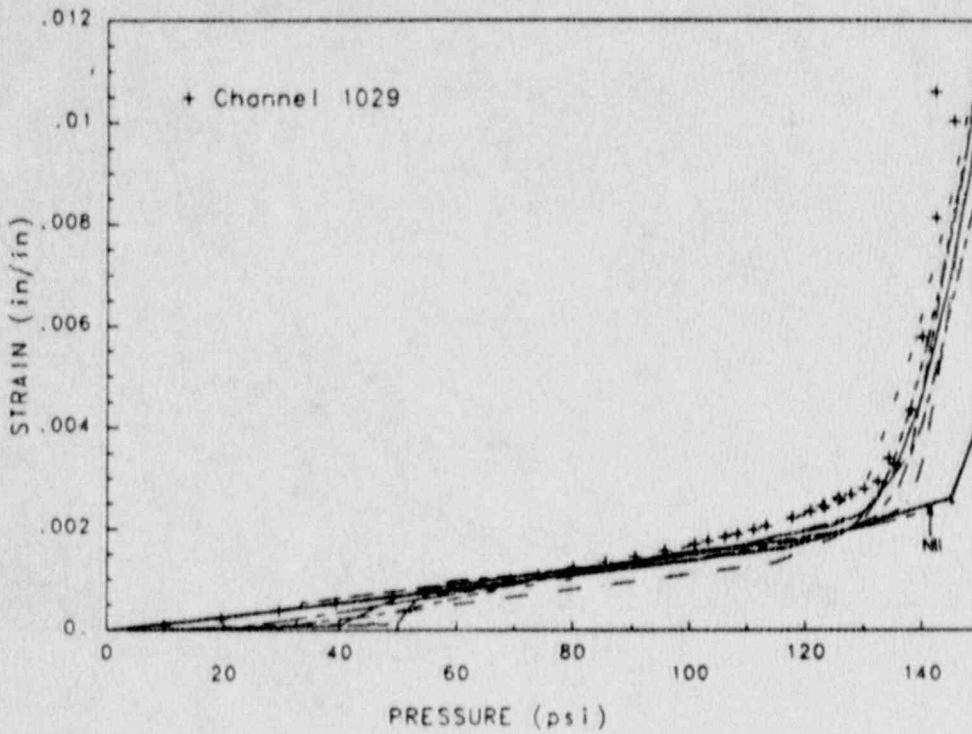


Figure 5.5.10  Axial Strain in Layer 6 Hoop Rebar at El 20 ft
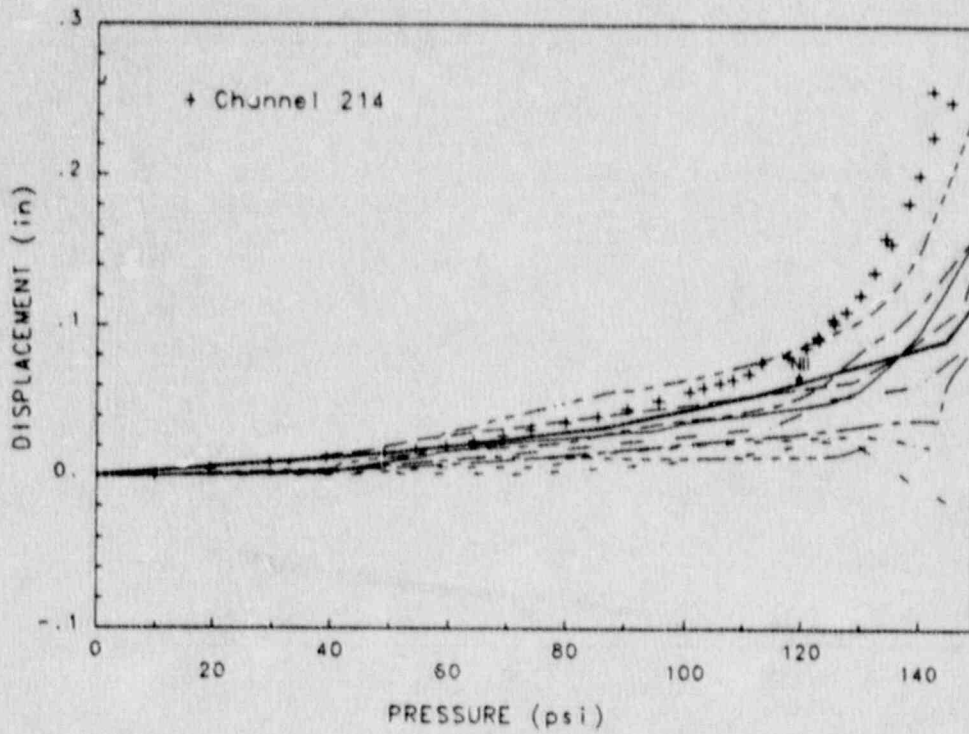
Figure 5.5.11 Vertical Displacement of Liner
Relative to Cylinder Base at El 6 ft
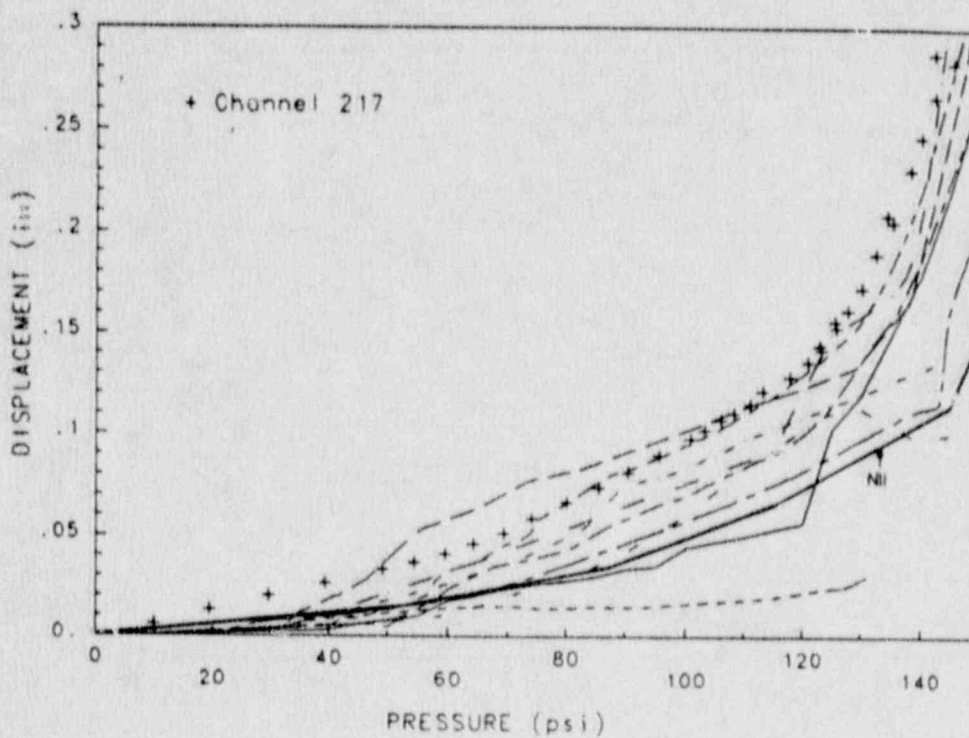


Figure 5.5.12 Vertical Displacement of Liner
Relative to Cylinder Base at El 11 ft
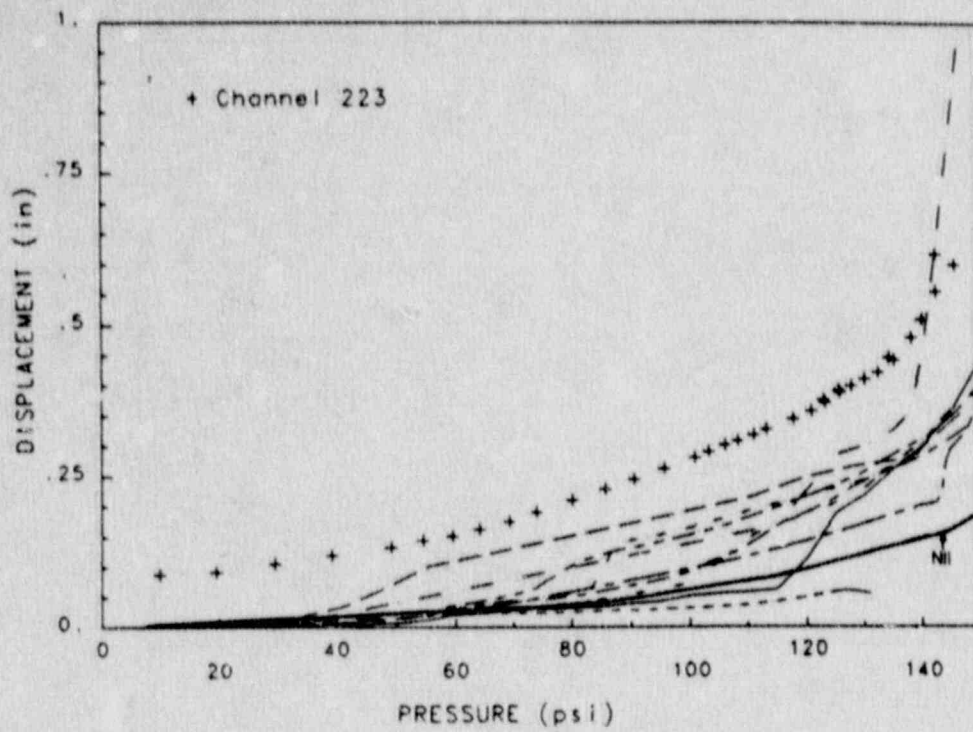
Figure 5.5.13 Vertical Displacement of Liner
Relative to Cylinder Base at El 18 ft
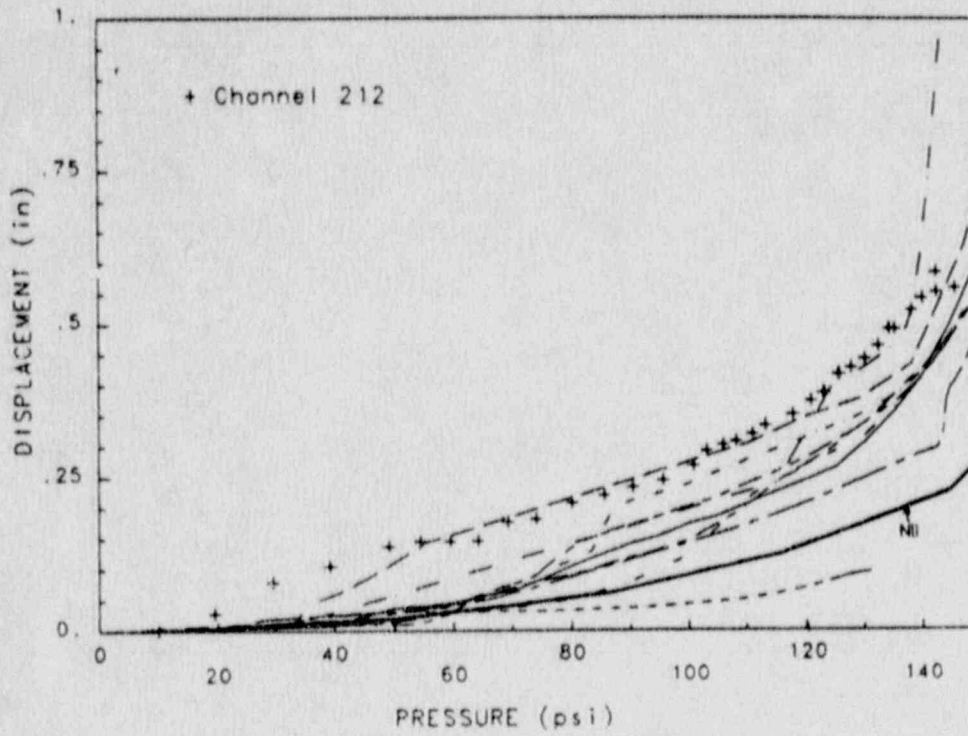


Figure 5.5.14 Vertical Displacement of Liner
Relative to Cylinder Base at El 24 ft
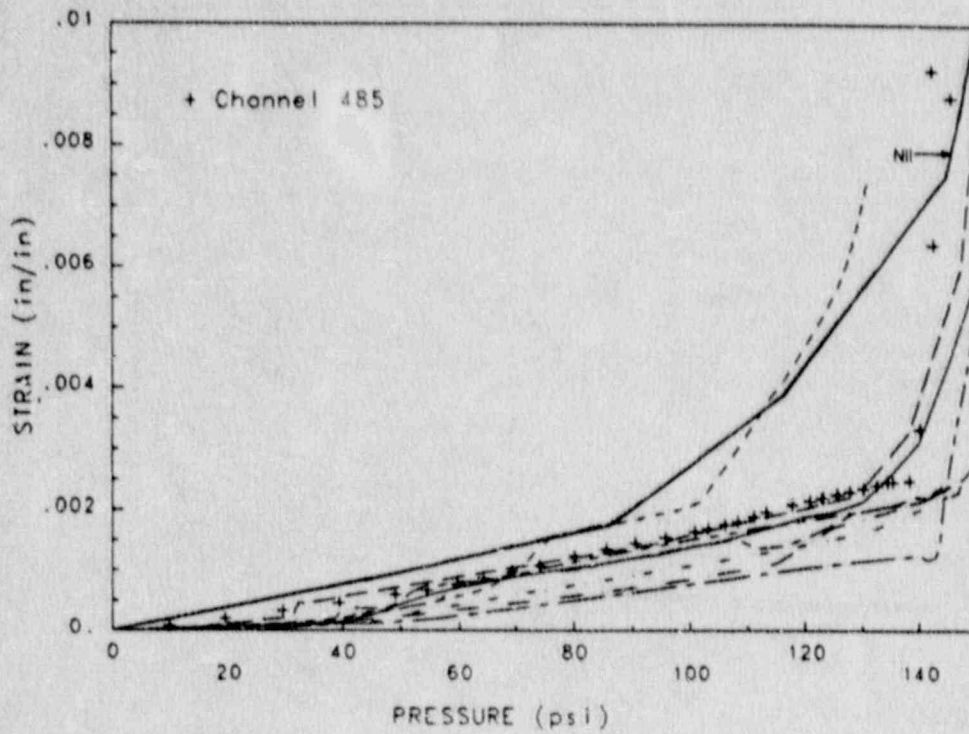
Figure 5.5.15  Axial Strain in Layer 2 Meridional Rebar at El 2.10 ft
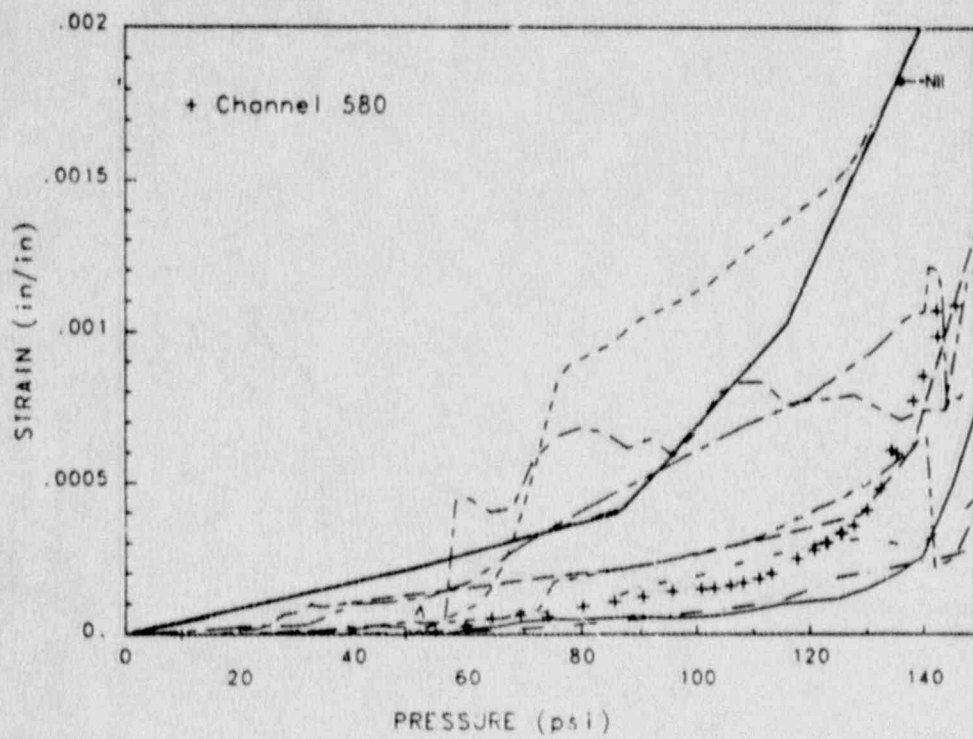


Figure 5.5.16  Axial Strain in Layer 5 Meridional Rebar at El 2.10 ft
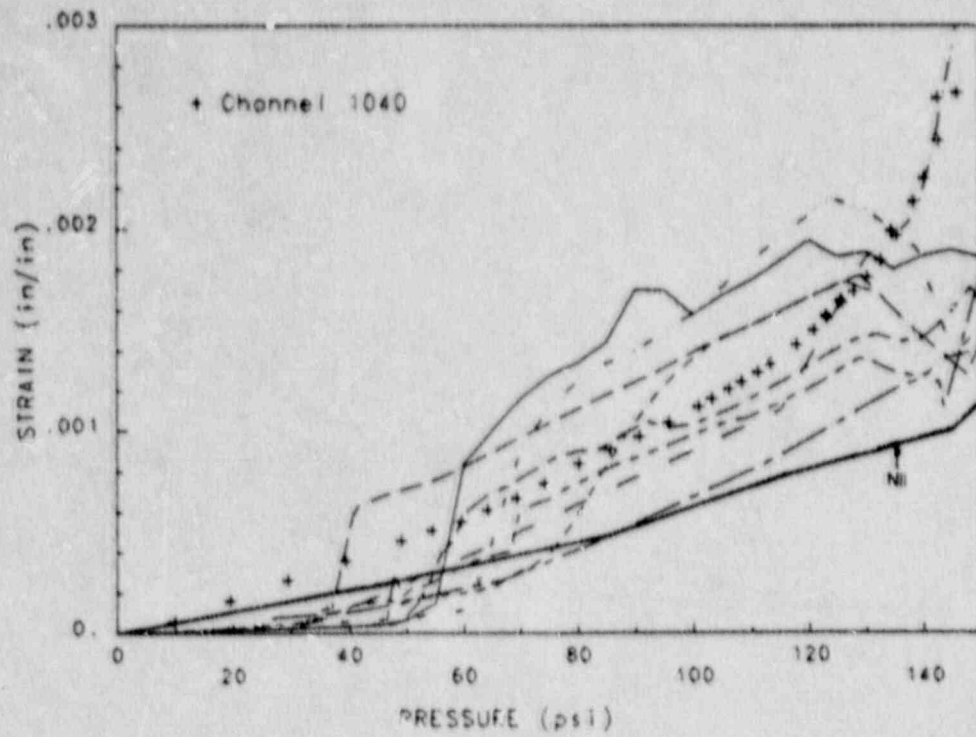
Figure 5.5.17  Axial Strain in Layer 5 Meridional Rebar at El 6.75 ft
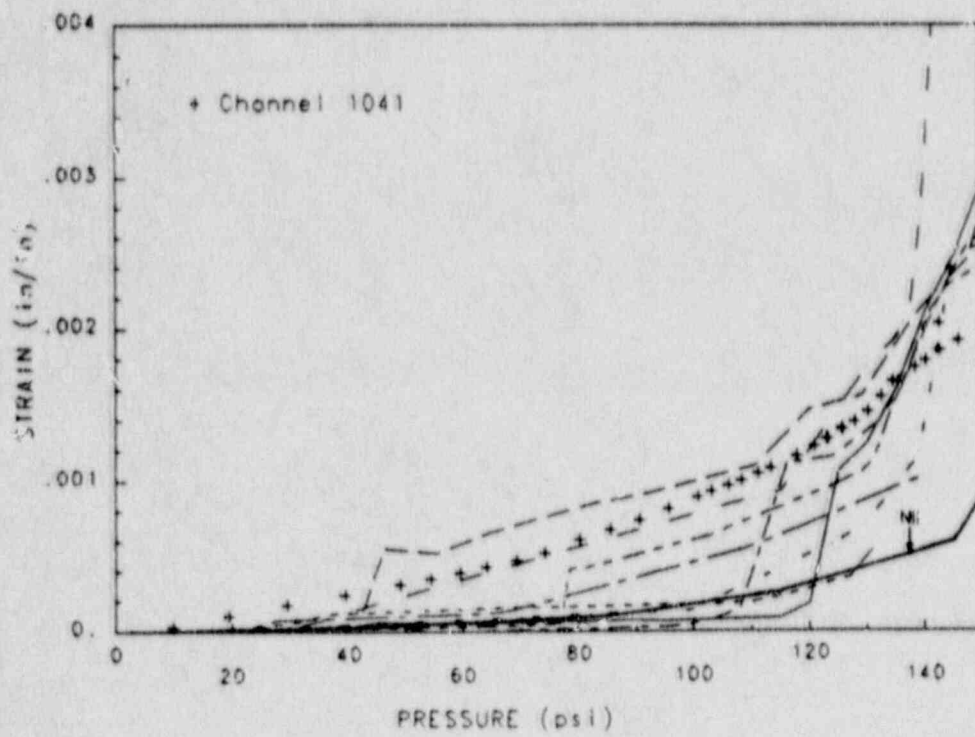


Figure 5.5.18  Axial Strain in Layer 5 Meridional Rebar at El 13.75 ft
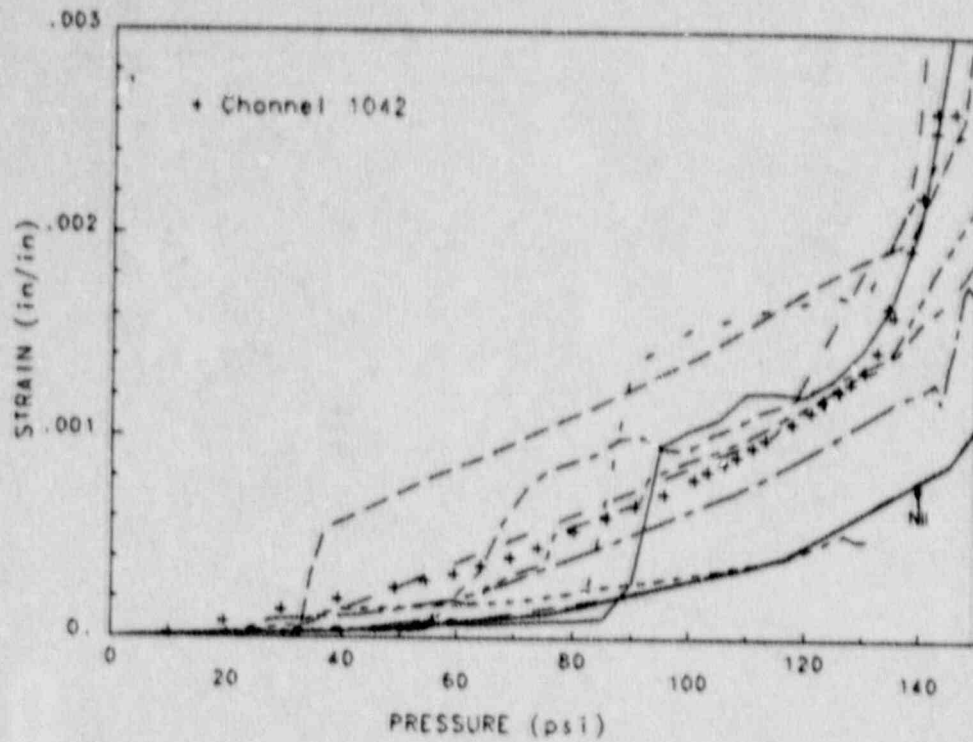
Figure 5.5.19 Axial Strain in Layer 5 Meridional Rebar at El 20 ft
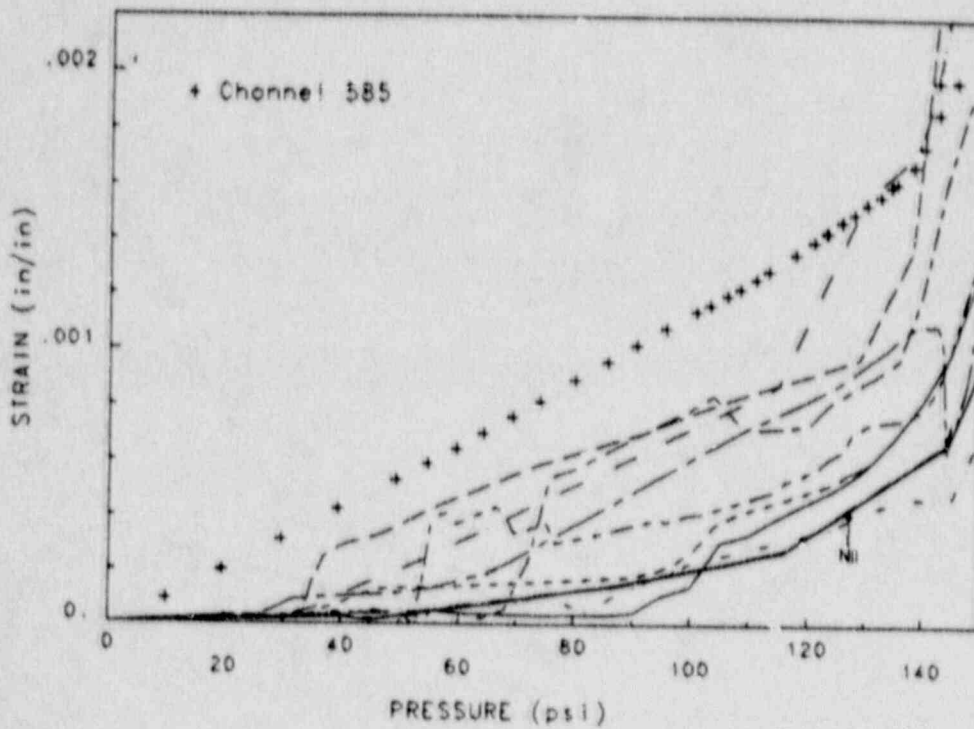


Figure 5.5.20 Axial Strain in Layer 5 Meridional Rebar at El 23.92 ft
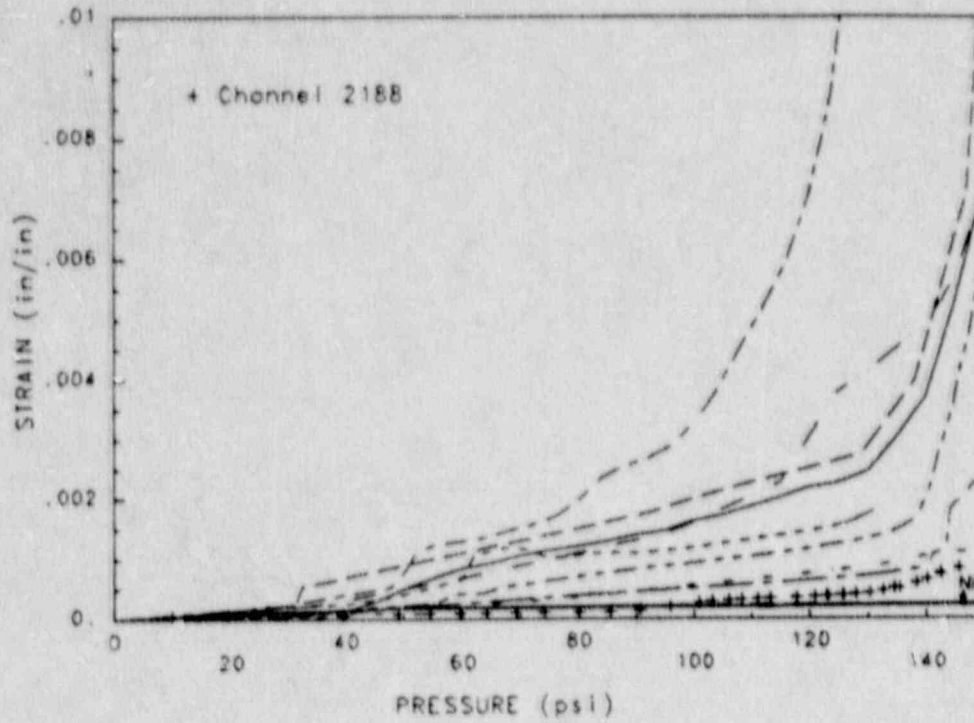
Figure 5.5.21  Maximum Principal Strain
on Inside Surface of Liner at El 2.10 ft
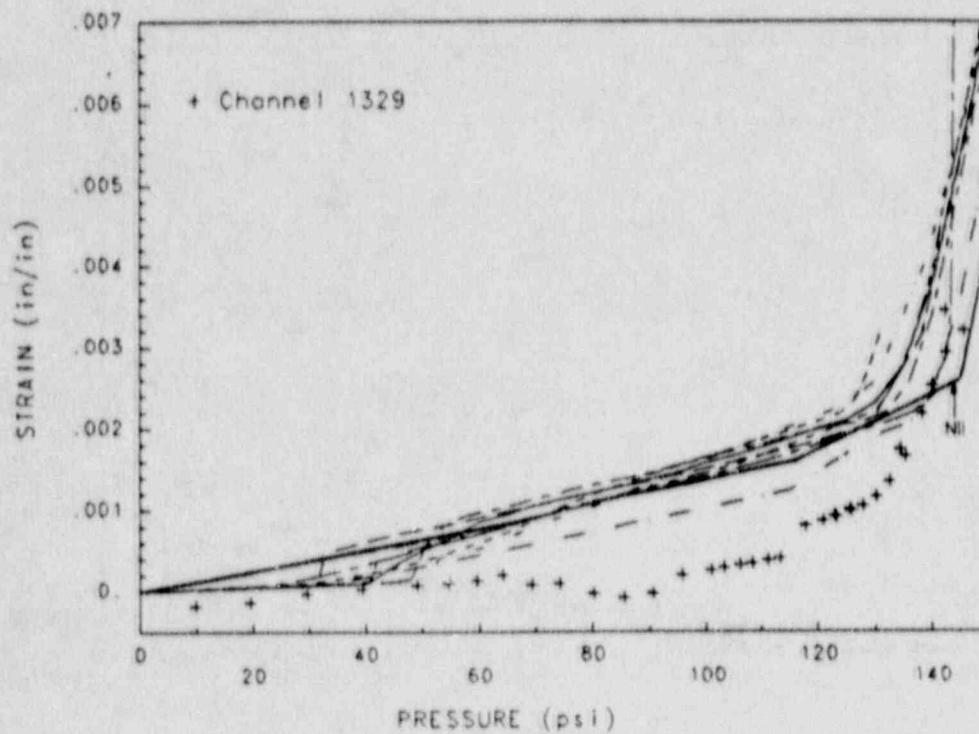


Figure 5.5.22  Maximum Principal Strain
on Inside Surface of Liner at El 6.75 ft

5-227
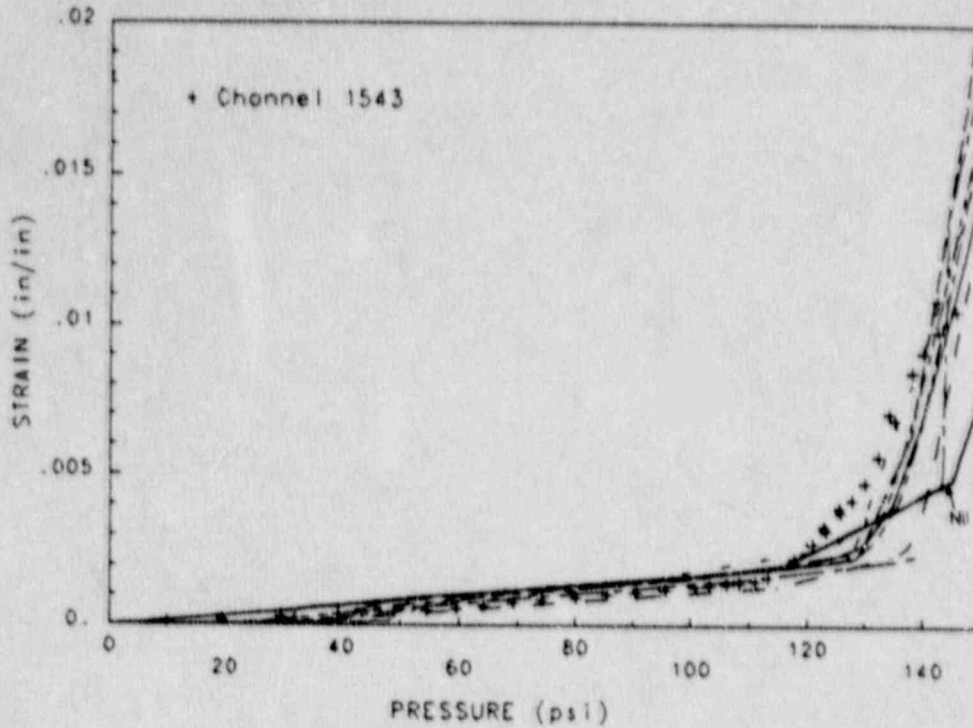
Figure 5.5.23 Maximum Principal Strain
on Inside Surface of Liner at El 13.75 ft
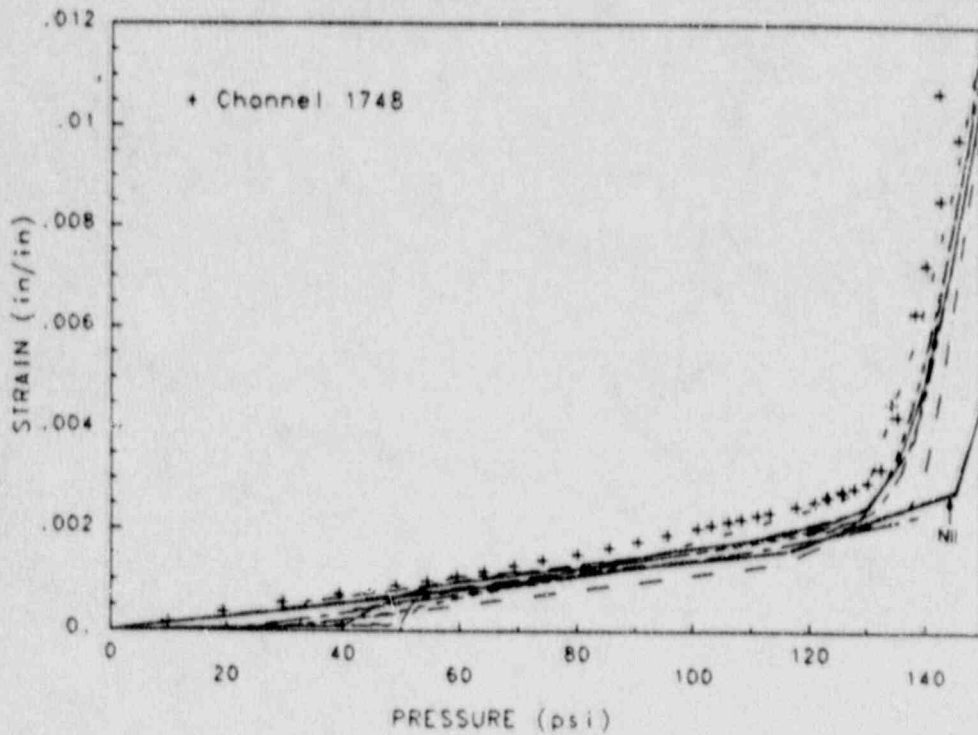


Figure 5.5.24 Maximum Principal Strain
on Inside Surface of Liner at El 20 ft
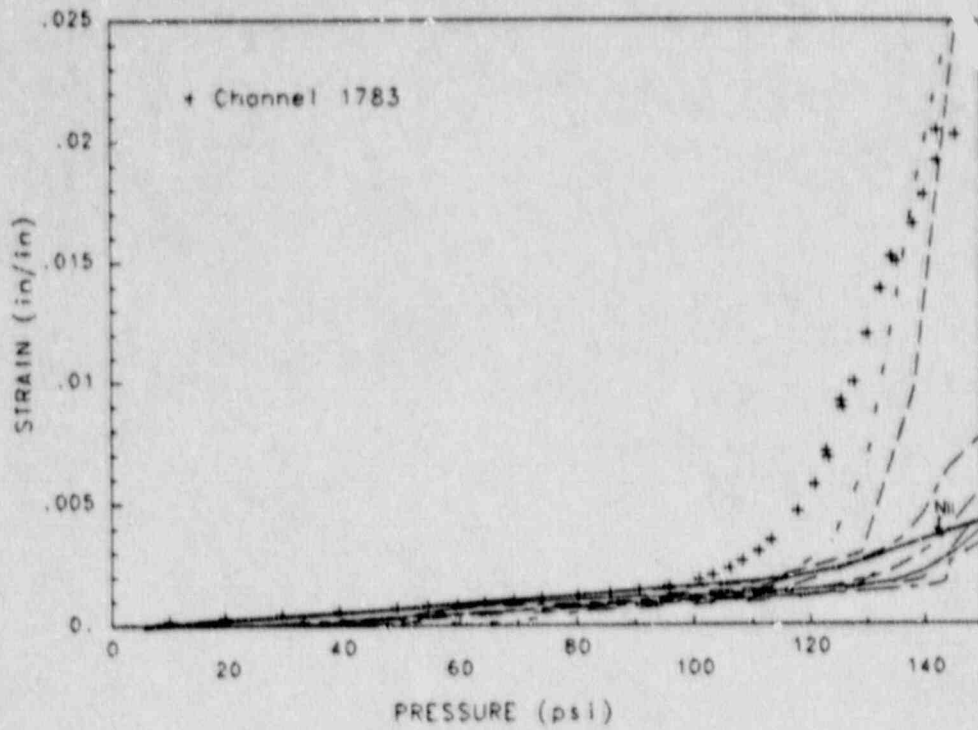
Figure 5.5.25  Maximum Principal Strain
on Inside Surface of Liner at El 23.92 ft
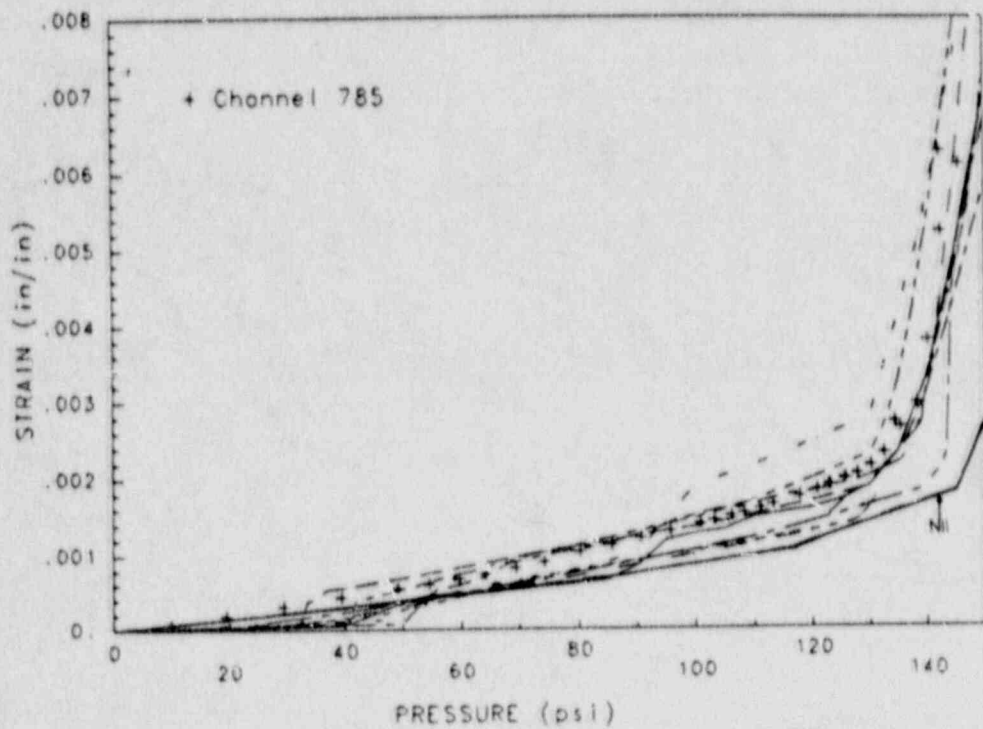


Figure 5.5.26  Axial Strain in Layer 8 Seismic Rebar at El 20 ft
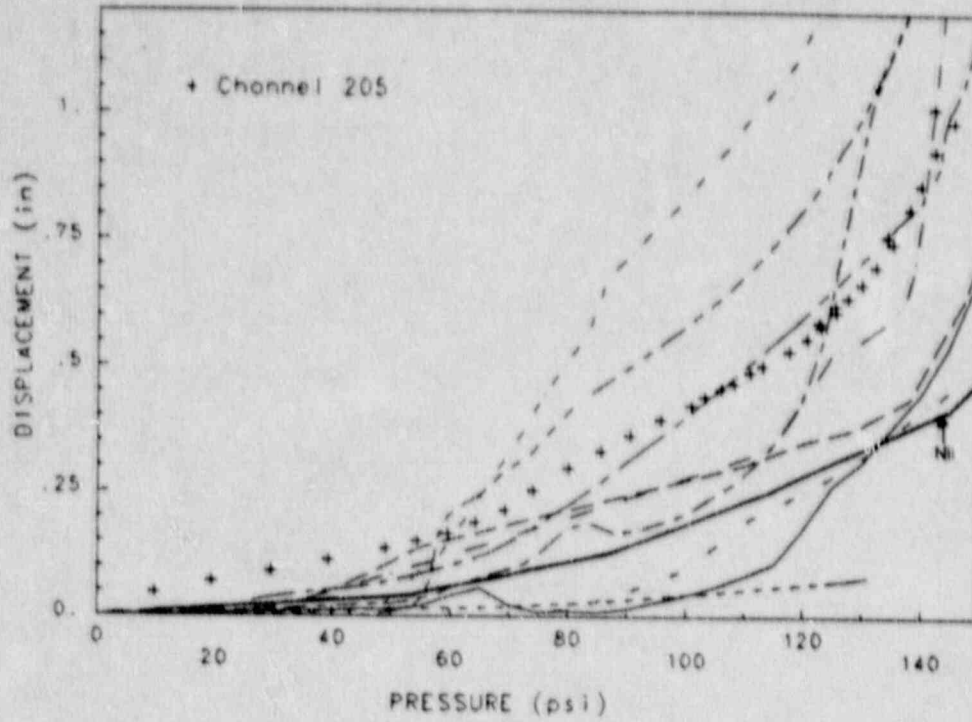
Figure 5.5.27 Vertical Displacement of Liner at Dome Apex ($\phi = 90°$)
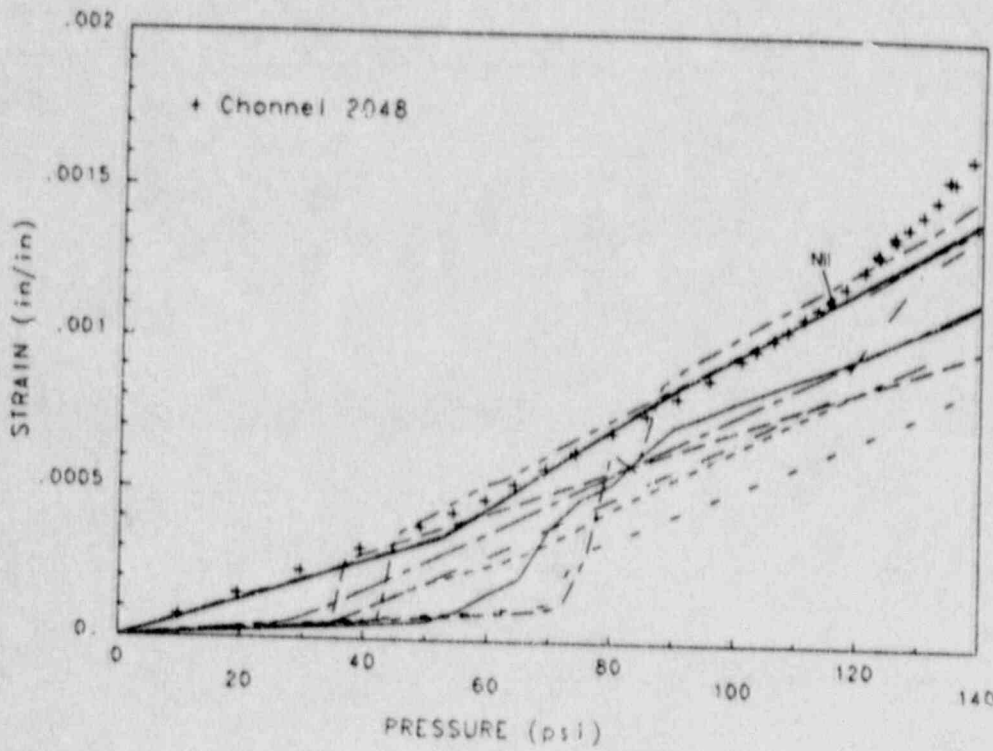


Figure 5.5.28 Maximum Principal Strain
on Inside Surface of Liner at $\phi = 72°$ (Dome)
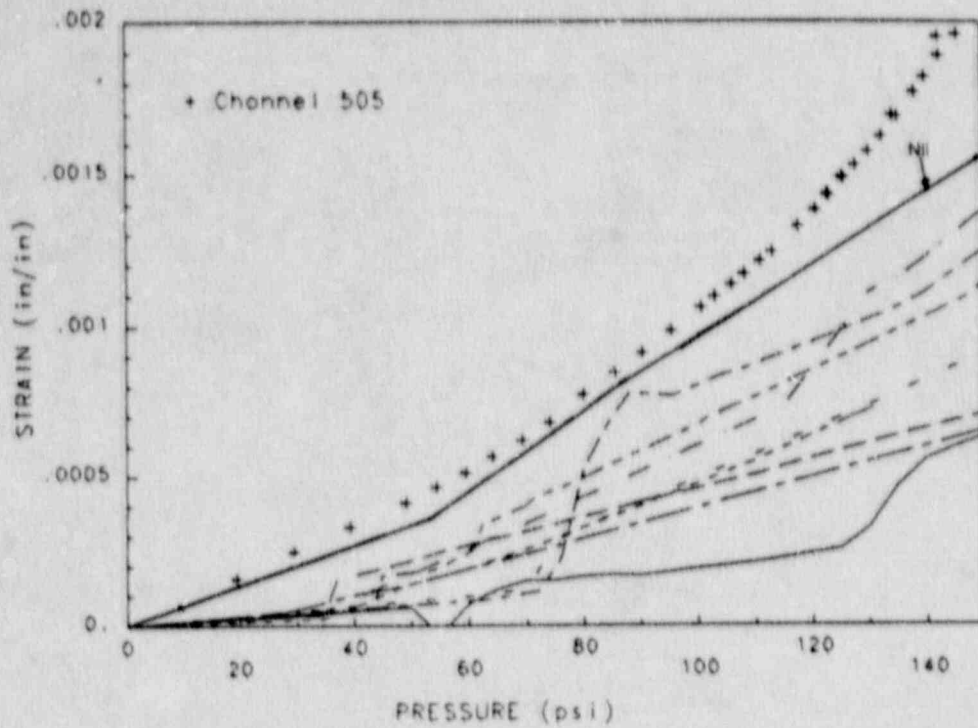
Figure 5.5.29 Axial Strain in Layer 2 Meridional Rebar at $\phi = 72°$ (Dome)
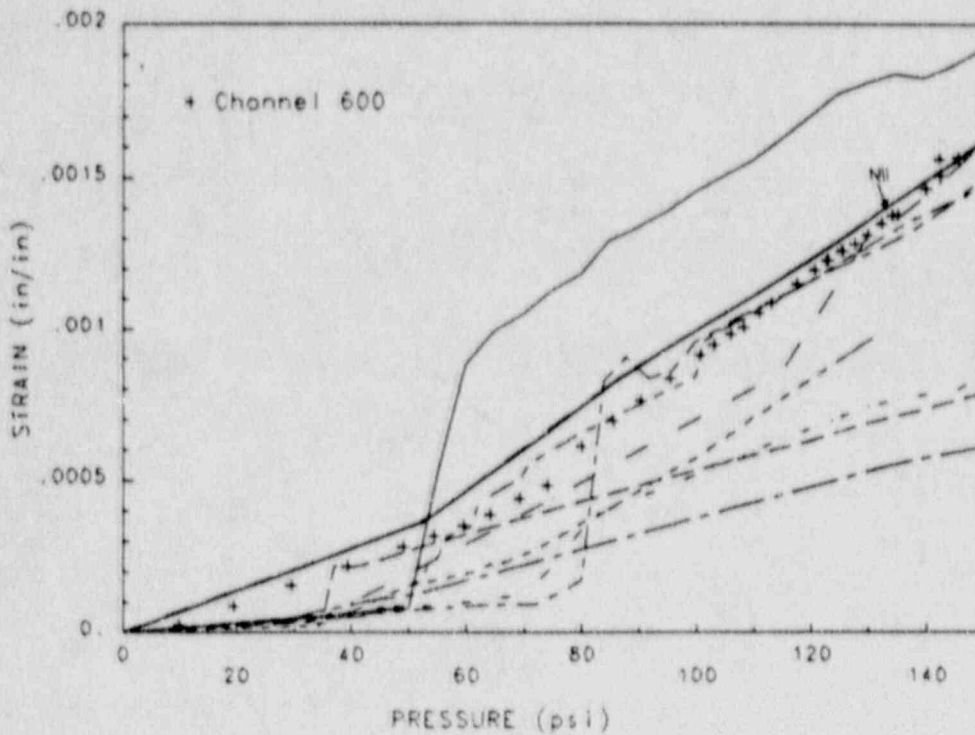


Figure 5.5.30 Axial Strain in Layer 5 Meridional Rebar at $\phi = 72°$ (Dome)
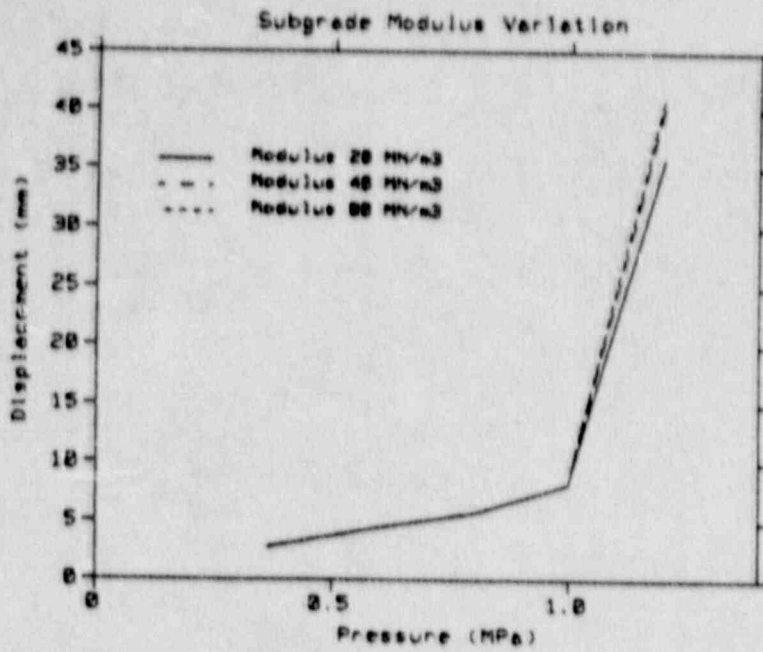
Figure 5.5.31 Effect of Subgrade Modulus
on Radial Displacement of Liner at El 11 ft
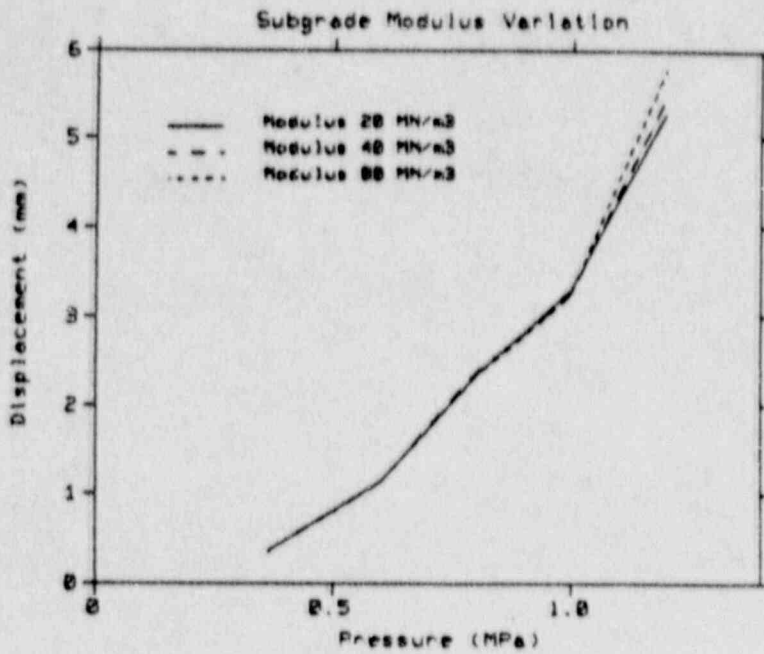


Figure 5.5.32 Effect of Subgrade Modulus
on Vertical Displacement of Liner Relative to Cylinder Base at El 11 ft
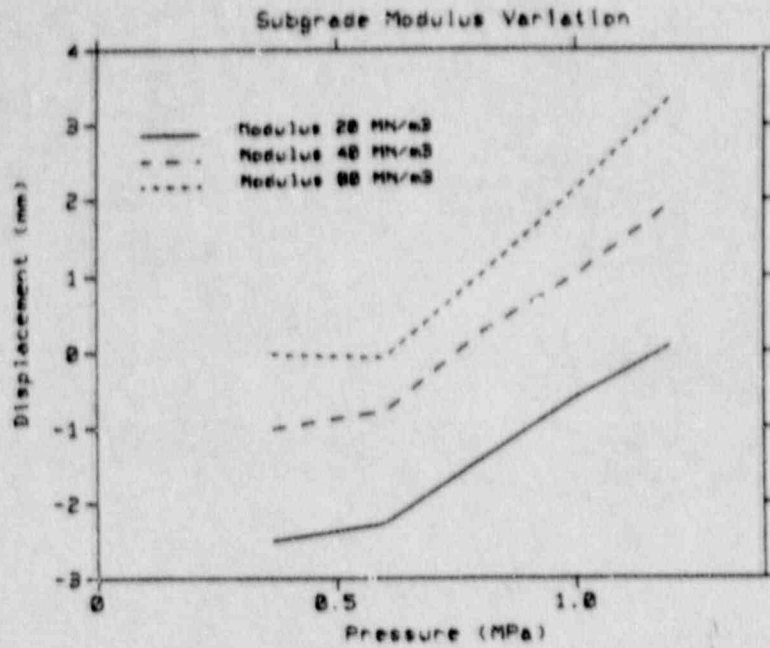
Figure 5.5.33  Effect of Subgrade Modulus on Uplift of Basemat
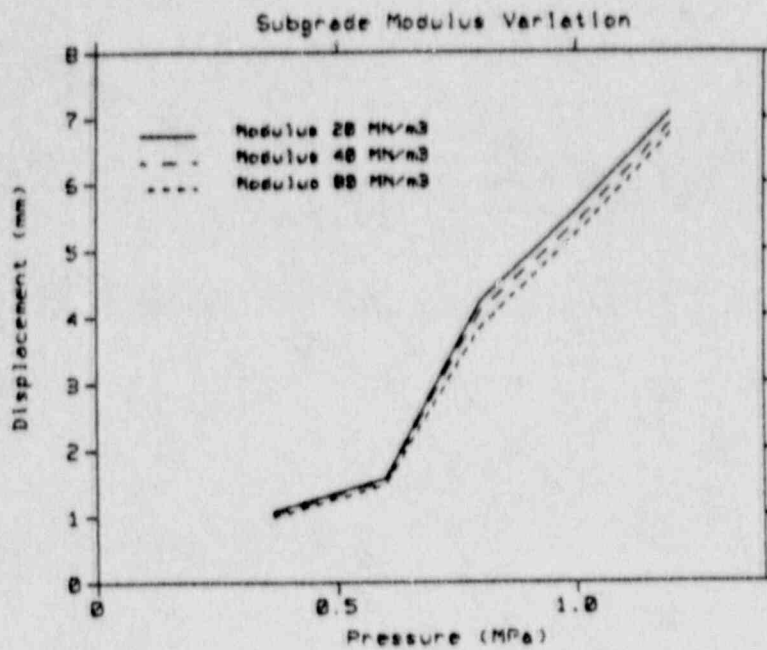


Figure 5.5.34  Effect of Subgrade Modulus
on Basemat Uplift Relative to Center of Mat
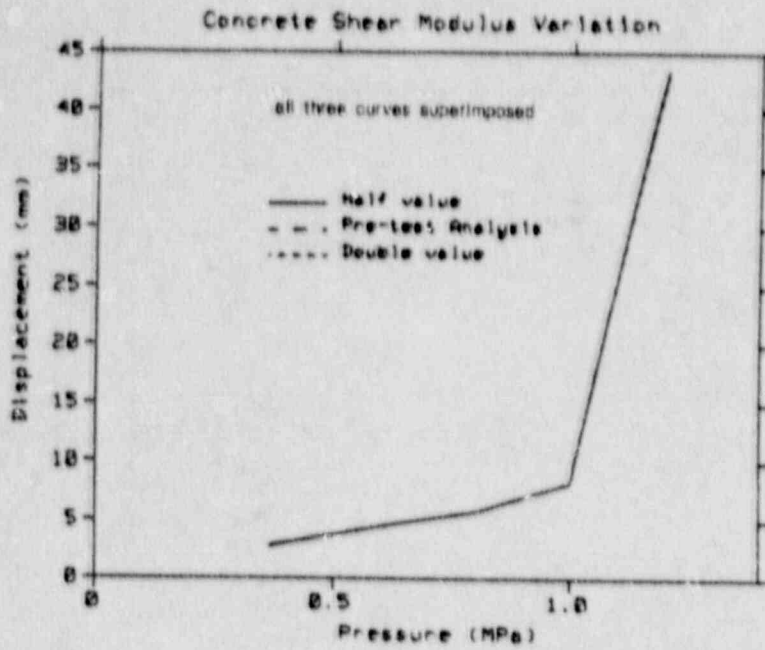
Figure 5.5.35  Effect of Concrete Shear Modulus
on Radial Displacement of Liner at El 11 ft
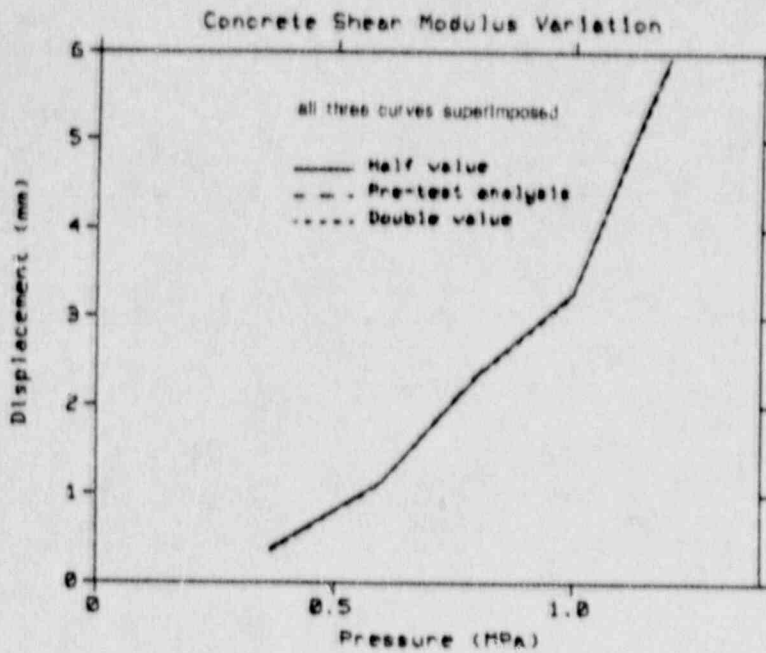


Figure 5.5.36  Effect of Concrete Shear Modulus
on Vertical Displacement of Liner Relative to Cylinder Base at El 11 ft
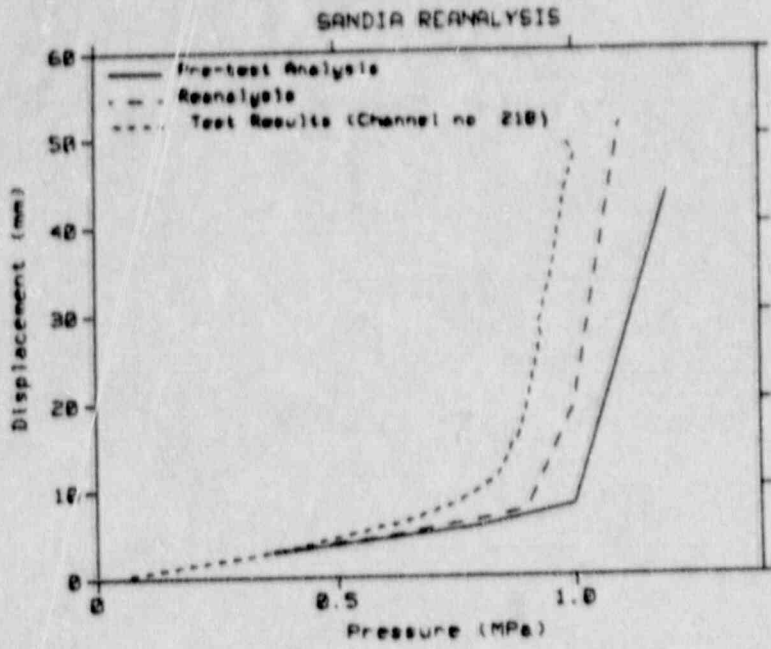
Figure 5.5.37  Radial Displacement of Liner at El 11 ft (Re-Analysis)
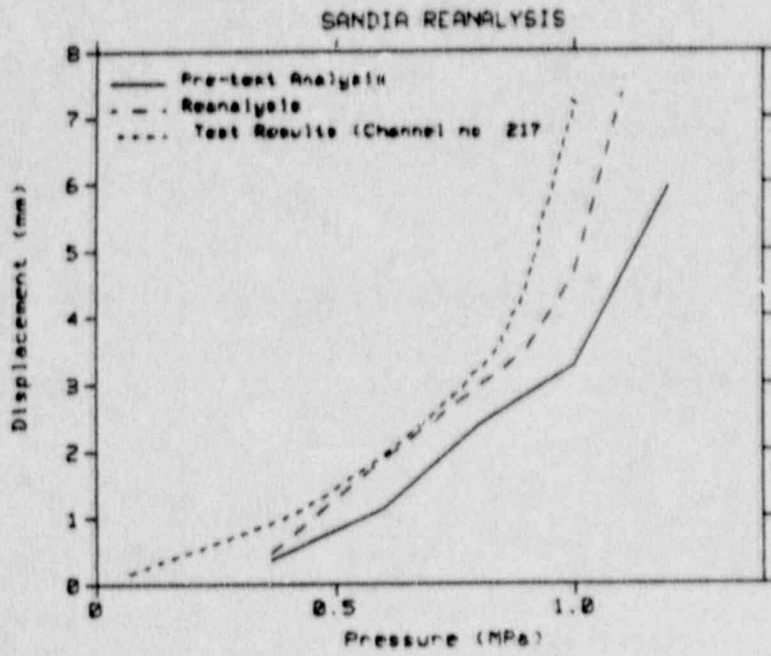


Figure 5.5.38  Vertical Displacement of Liner
Relative to Cylinder Base at El 11 ft (Re-Analysis)
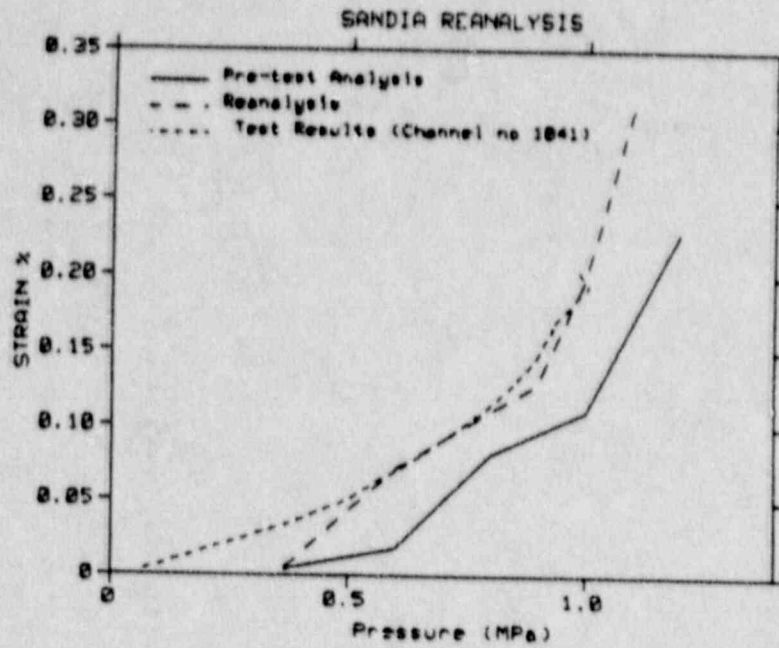
Figure 5.5.39  Axial Strain in Layer 5 Meridional Rebar
at El 13.75 ft (Re-Analysis)
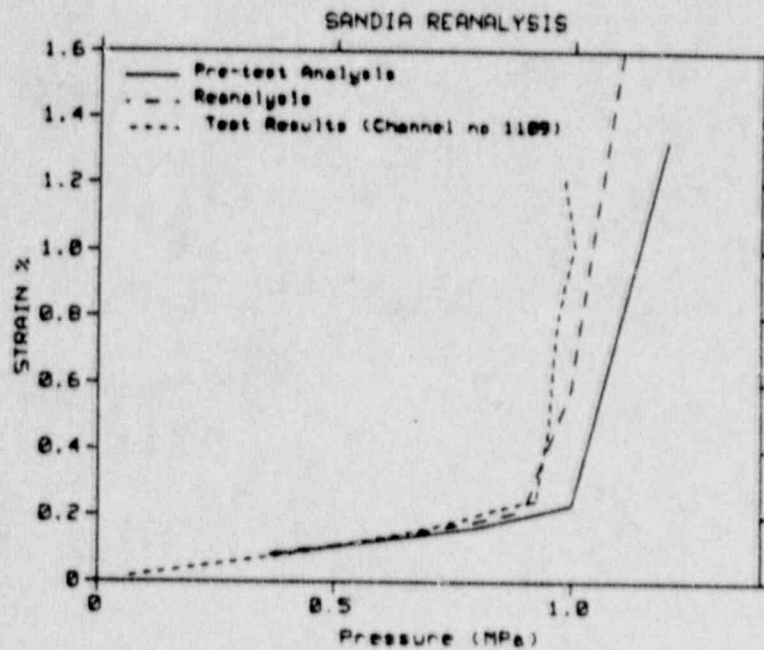


Figure 5.5.40  Axial Strain in Layer 6 Hoop Rebar
at El 13.75 ft (Re-Analysis)

SANDIA REANALYSIS
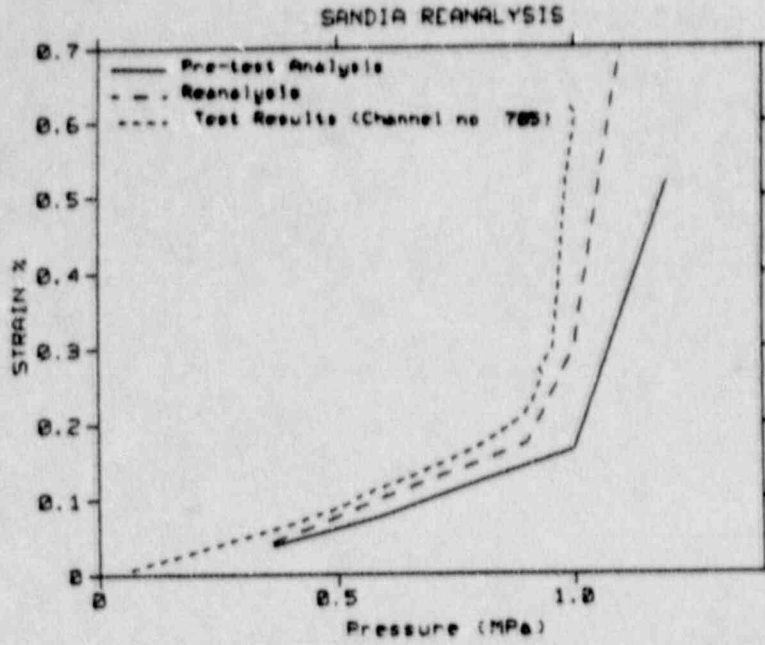


Figure 5.5.41  Axial Strain in Layer 8 Seismic Rebar
at El 20 ft (Re-Analysis)

SANDIA REANALYSIS
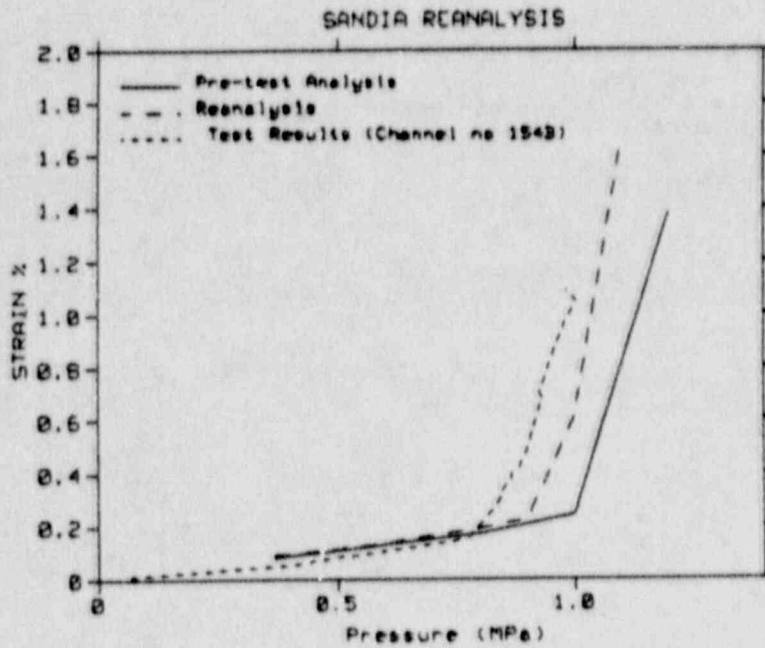


Figure 5.5.42  Maximum Principal Liner Strain
at El 13.75 ft (Re-Analysis)

SANDIA REANALYSIS
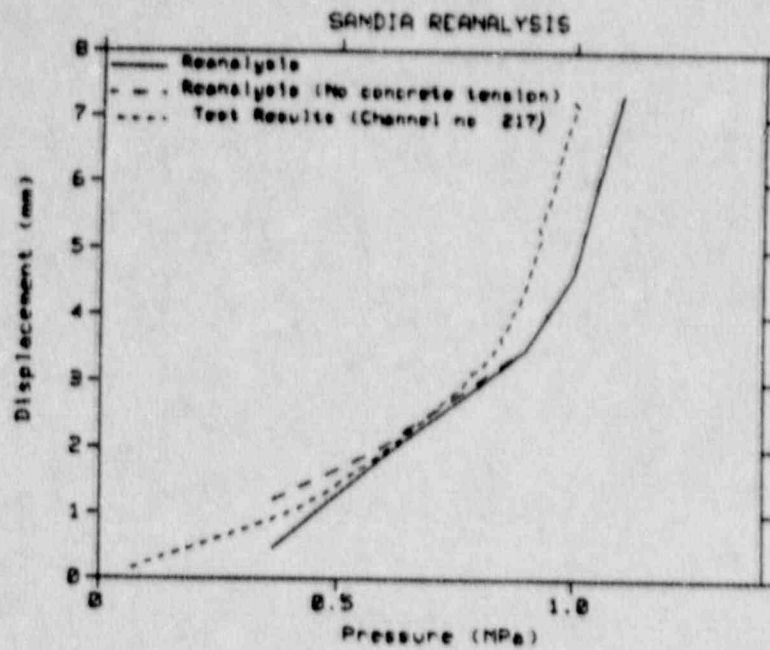


Figure 5.5.43  Vertical Displacement of Liner
Relative to Cylinder Base at El 11 ft
(Re-analysis with no-tension concrete)

SANDIA REANALYSIS
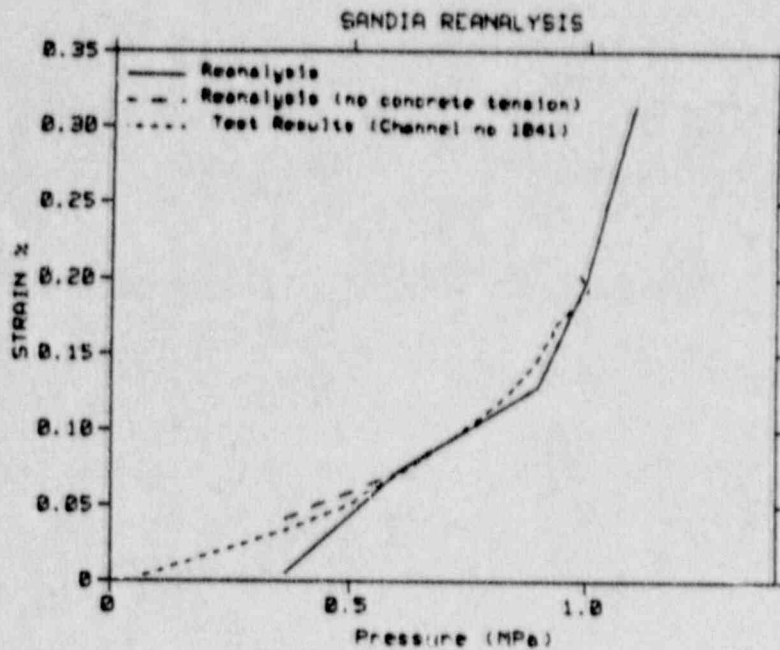


Figure 5.5.44  Axial Strain in Layer 5 Meridional Rebar at El 13.75 ft
(Re-analysis with no-tension concrete)
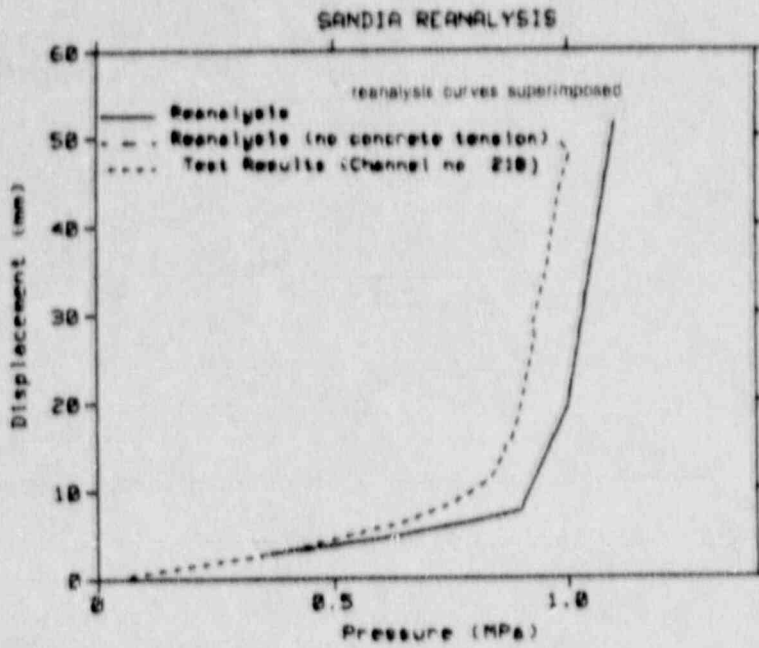
Figure 5.5.45 Radial Displacement of Liner at El 11 ft
(Re-analysis with no-tension concrete)
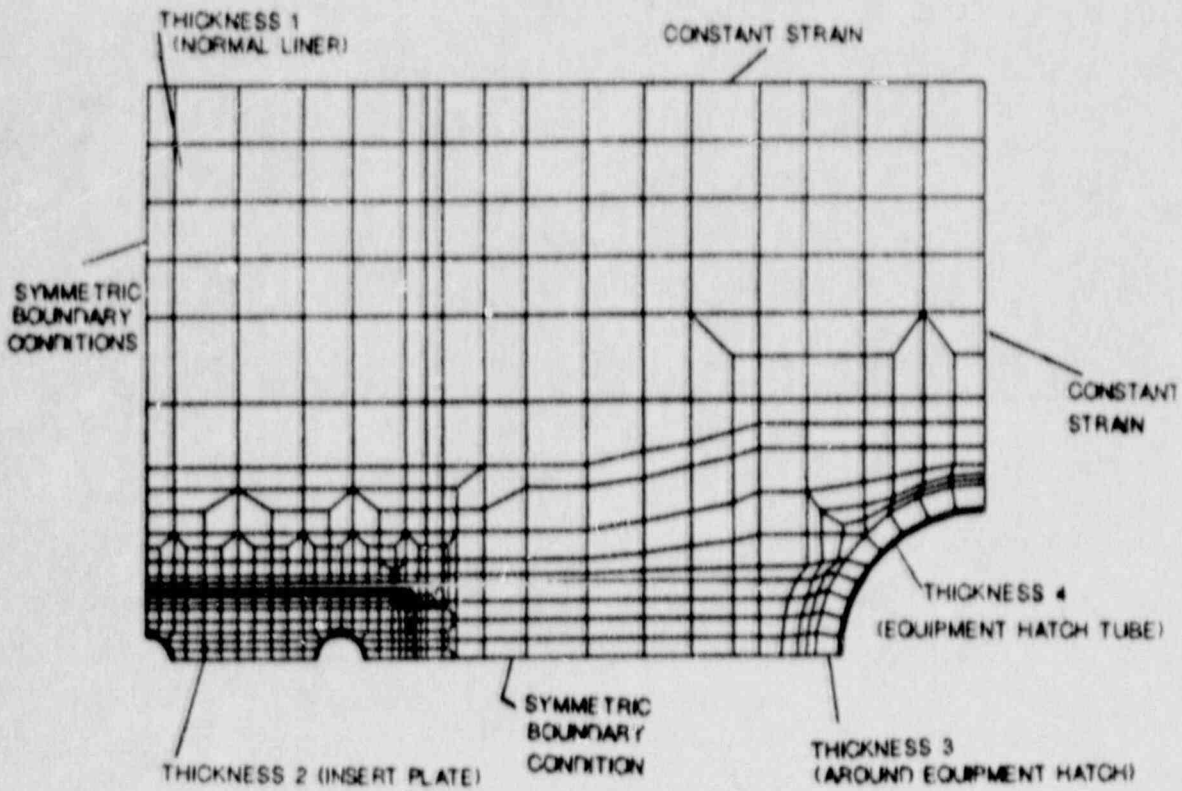


Figure 5.5.46 Liner Showing Locations of Main Tears
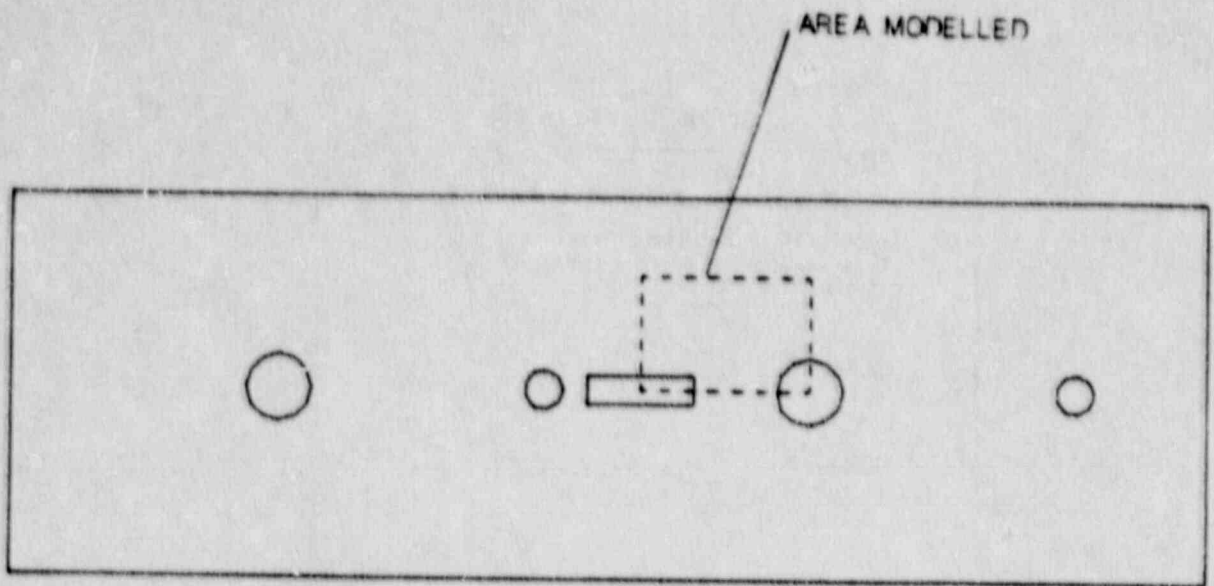
Figure 5.5.47  Area of Liner Modelled
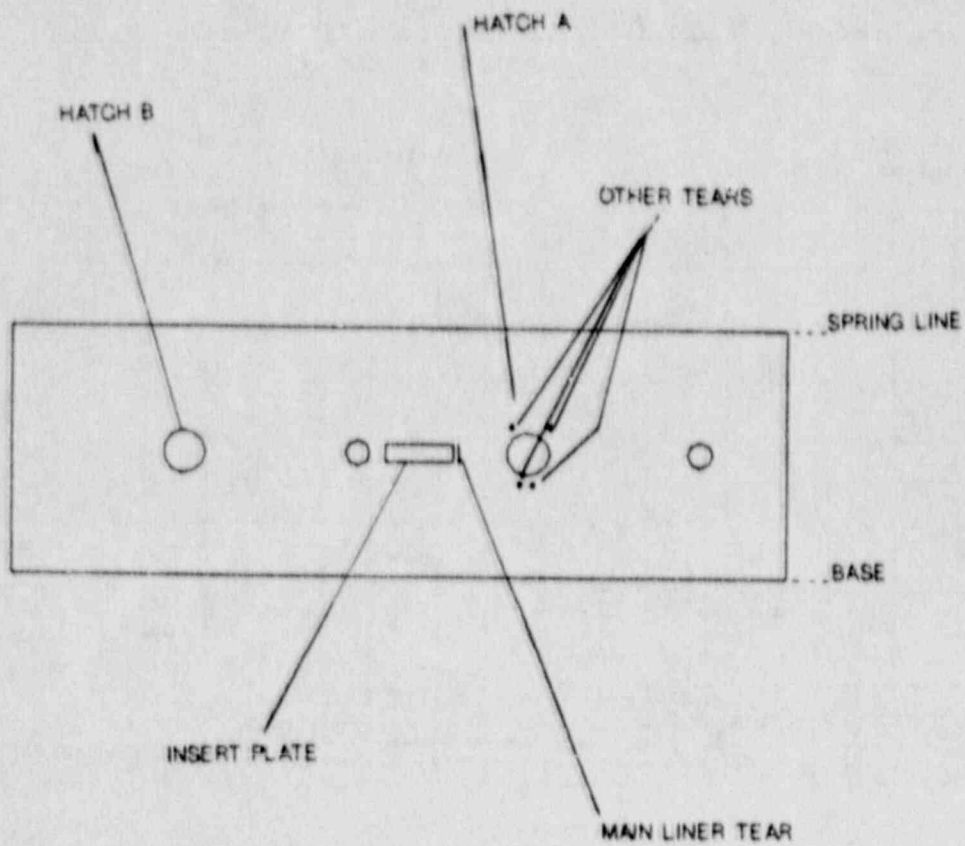


Figure 5.5.48  Finite Element Mesh and Boundary Conditions
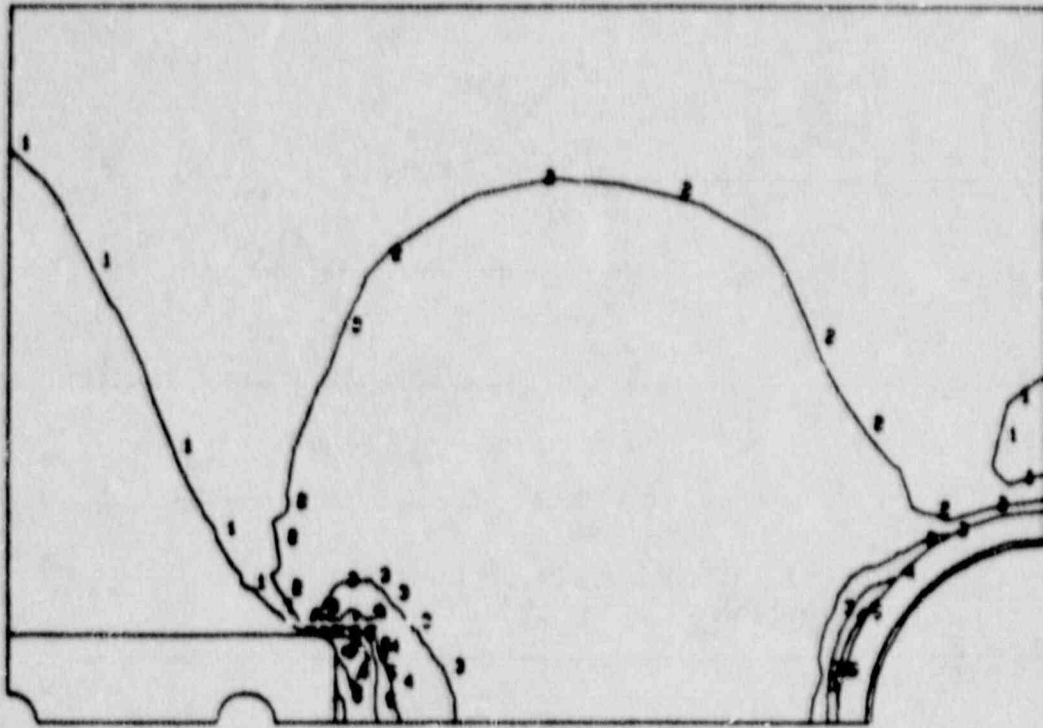
| 1 | 2 | 3 | 4 | 5 | 6 | 7 |
|---|---|---|---|---|---|---|
| 1.00E-02 | 2.00E-02 | 3.00E-02 | 4.00E-02 | 5.00E-02 | 6.00E-02 | 7.00E-02 |

Figure 5.5.49  Effective Plastic Liner Strains at 1.1 MPa (160 psig)
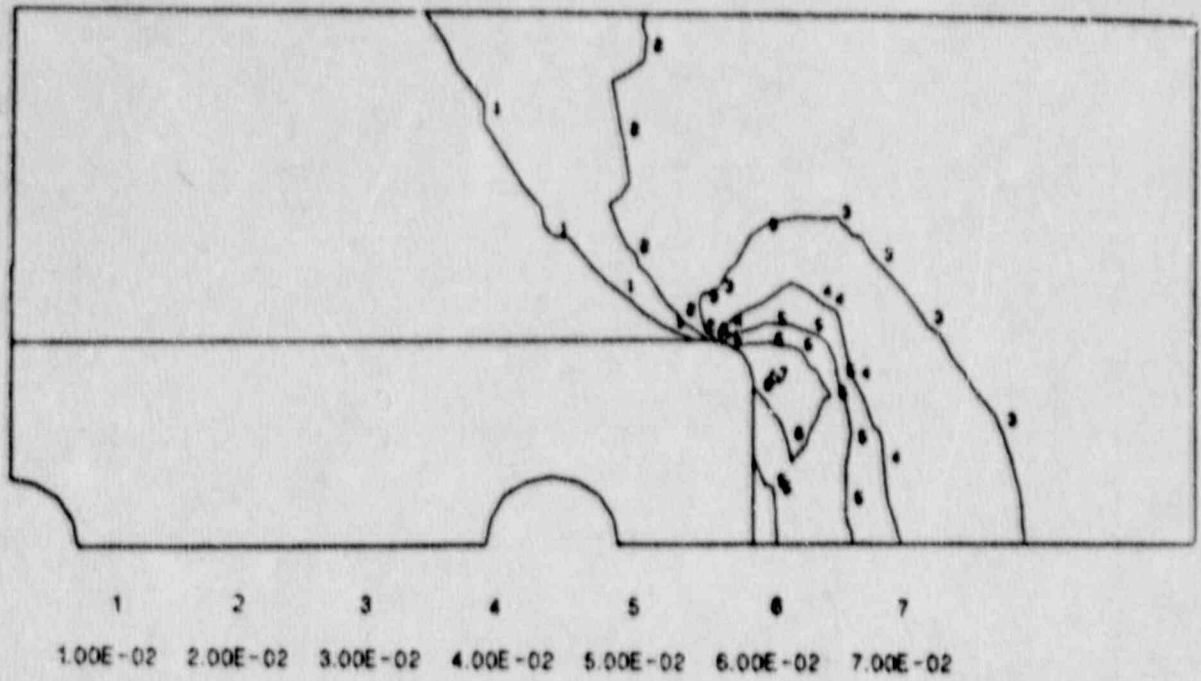
Figure 5.5.50  Effective Plastic Liner Strains
Around Insert Plate at 1.1 MPa (160 psig)
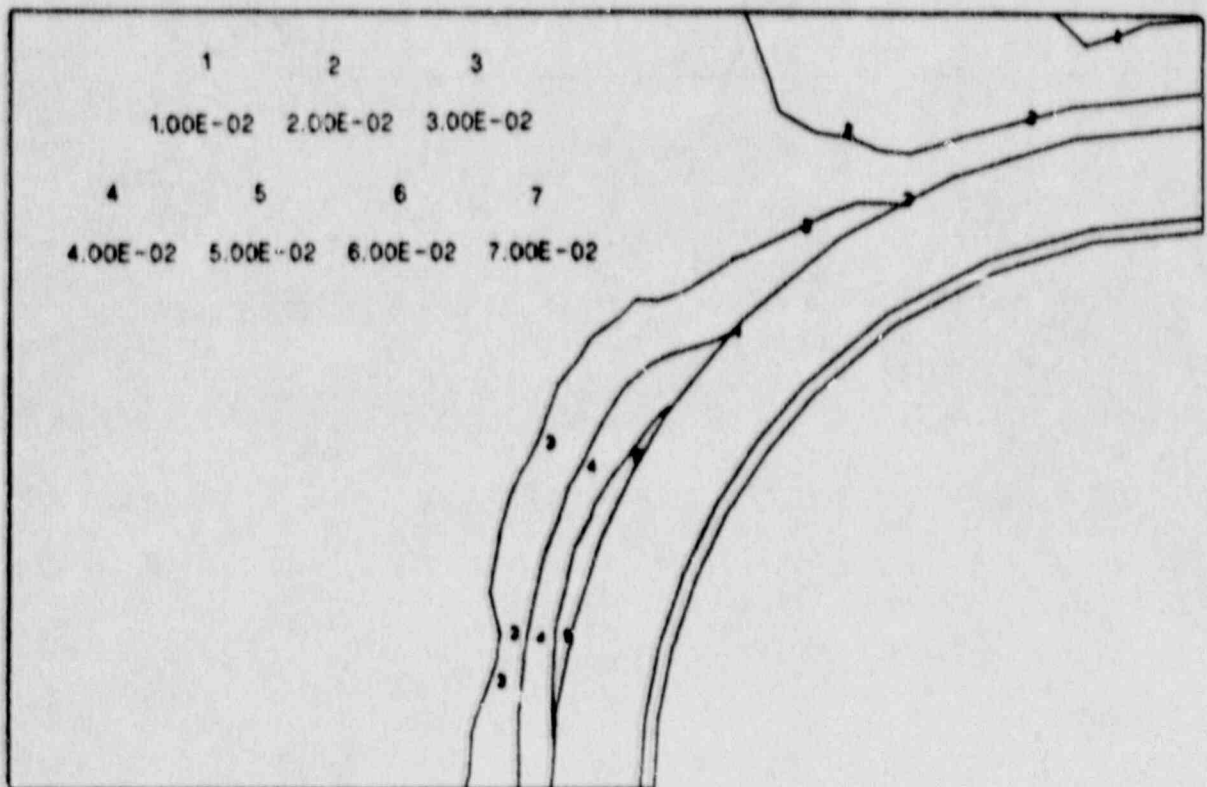


Figure 5.5.51  Effective Plastic Liner Strains
Around Equipment Hatch A at 1.1 MPa (160 psig)

## 5.6 ENEA-DISP

This section was prepared by G. Orsini and G. Pino.

### 5.6.1 Summary

Pretest analysis results obtained at ENEA-DISP are compared with test measures, looking mainly at the critical sections where global structural failure might have initiated if the liner had not leaked. Also, major differences between analytical and test results are presented. Finally, results of posttest analyses for examining the liner tearing and the effects influencing basemat deformation are discussed.

### 5.6.2 Pretest Analyses vs. Test Results

### 5.6.2.1 Finite Element Models

An extensive description of the finite element model used with the ADINA code for pretest analysis is reported in [11]. The main feature of this model is to have neglected the basemat, having firmly clamped the cylinder wall bottom. The finite element model is an axisymmetric continuum model, consisting of 300 concrete eight-node isoparametric elements, 252 ring elements representing the hoop rebars, and 283 two-node truss elements representing hoop, meridional, diagonal and shear resisting rebars. In addition, the liner was modeled by equivalent truss elements (99 ring elements and 100 two-node meridional elements). The number of nodes is 1109 with 2197 degrees of freedom (DOF).

After the model test, a second finite element model that included the basemat and soil-structure interaction, which was represented by Winkler springs with no-tension strength, was analyzed (Figure 5.6.1). The number of nodes is 1448 with 2854 DOF. In this second finite element model, the contribution to the basemat stiffness provided by the mildly reinforced concrete fill slab above the liner was neglected. The contribution of the fill slab to the model stiffness appears to be one of the major cause of disagreement between analytical predictions and test results and it will be discussed later on.

The material model for concrete in both finite element models has been represented by the model implemented in the ADINA code. The main parameters are:

    initial tangent modulus = 5700 ksi (39300 MPa)
    Poisson's ratio = 0.15
    uniaxial cut-off tensile stress = 0.4 ksi (2.7 MPa)
    uniaxial maximum compressive stress = -6.5 ksi (-44.8 MPa)
    after cracking, normal stiffness reduction factor (STIFAC) = 1x10$^{-4}$
    after cracking, shear stiffness reduction factor (SHEFAC) = 0.5

The material model for steel is elastic-plastic with isotropic hardening:

|        | initial tangent modulus | yield stress | post-yielding tangent modulus |
|--------|--------------------------|--------------|-------------------------------|
| rebars | 30000 ksi<br>(209000 MPa) | 69 ksi<br>(476 MPa) | 470 ksi<br>(3200 MPa) |
| liner  | 30000 ksi<br>(209000 MPa) | 51.5 ksi<br>(355 MPa) | 110 ksi<br>(700 MPa) |

In solving the finite element system, equilibrium iterations were used until extensive cracking of concrete occurred at about $p = 0.67\,P_d$ ($P_d = 46$ psig or 0.32 MPa, which is the design pressure). Above this pressure level, it was impossible to obtain solution convergence. Thus, a small pressure increment was used ($0.005\,P_d$) without equilibrium iterations; however the stiffness matrix was reformed at every step. The results requested by Sandia in terms of displacements and strains were reported in [11] based on the first finite element model, which neglected the basemat. Results of the second finite element model were presented at the 4th Workshop on Containment Integrity [42] along with test results, and will be further discussed in what follows.

### 5.6.2.2 Analytical Predictions vs. Test Results

The test was concluded at 145 psig (1.0 MPa) when high leakage developed, due primarily to a large tear in the liner adjacent to a thicker plate of a penetration cluster. In the pretest analyses, local potential liner failures around penetrations were not examined because we wanted, at first, to look at the capability of getting reliable results on global ultimate structural behavior using a nonlinear computer program. Our prediction of the structural failure mode was bending rupture due to concrete crushing at the cylinder wall base at an internal pressure $\geq 3.5\,P_d$ (161 psig, 1.15 MPa). In the tested model, clear evidence of crushed concrete at the wall base was not observed after having reached the pressure of 145 psig (1.0 MPa). Nevertheless, looking at material strains measured during the test, it is possible to say that the section at the wall base was going to be a critical point together with the wall midheight section. Therefore, we deem it interesting to compare computed and measured strains and displacements in these locations. When comparing rebar strain, the strain variation between adjacent cracks must be taken into account. A maximum value is reached at positions where cracked surfaces cross the rebar, and a minimum at half distance between cracks. In Figure 5.6.2, from [43], rebar strain variation from the average $\epsilon_m$ is indicated. In Figure 5.6.3, also taken from [43], it is shown that $\delta\epsilon_s$ represents the contribution of concrete in tension between the cracks (tension stiffening), which follows a hyperbolic relationship approaching the line $\epsilon_{s2}$ asymptotically for stresses in excess of $\sigma_{sr}$. It has been shown experimentally that $\epsilon_s$ can be represented by the relationship:

$$\delta\epsilon = \delta\epsilon_{smax}(\sigma_{sr}/\sigma_{s2}),$$

which in the specific case of the cylinder wall at midheight gives this scatter bandwidth:

| $p/P_d$ | 0.72 | 1.29 | 1.94 | 2.59 | 3.2 |
|---|---|---|---|---|---|
| $\sigma_{s2}$ (kg/cm²) | 1113 | 2000 | 3000 | 4000 | 5000 |
| $\delta\epsilon$ | $4.6\times10^{-4}$ | $2.6\times10^{-4}$ | $1.7\times10^{-4}$ | $1.3\times10^{-4}$ | $1.\times10^{-4}$ |

## Cylinder Wall Base

Strain in layer 2 meridional rebar (inner wall face), in layer 5 meridional rebar (outer wall face) and maximum principal liner strain were measured. Test results and finite element analyses results for Layer 2 meridional rebar are shown in Figures 5.6.4, 5.6.5, and 5.6.5a along with the scatter bandwidth calculated as before said:

$$\delta\epsilon = \delta\epsilon_{smax}(\sigma_{sr}/\sigma_{s2})$$

$\delta\epsilon_{smax}$ is computed using N, M from a simple hand analysis of the containment structure clamped at the cylinder wall base and considering the contribution to resistance of the vertical and diagonal rebars and of the liner. The results obtained are:

$$\epsilon_{s1r} = 5.1\times10^{-5}$$

$$\epsilon_{s2r} = 2.2\times10^{-4}$$

$$\delta\epsilon = (\epsilon_{s2r} - \epsilon_{s1r})(\sigma_{sr}/\sigma_{s2}) = (2.2\times10^{-4} - 5.1\times10^{-5})(450/\sigma_{s2})$$

| $p/P_d$ | 0.6 | 1. | 1.5 | 2. | 3.1 |
|---|---|---|---|---|---|
| $\sigma_{s2}$ (kg/cm²) | 750 | 1255 | 1900 | 2500 | 3927 |
| $\delta\epsilon$ | $1.\times10^{-4}$ | $6.1\times10^{-5}$ | $4.\times10^{-5}$ | $3.\times10^{-5}$ | $1.9\times10^{-5}$ |

Good agreement is observed in the range $0.7P_d$ - $2.8P_d$ (Figure 5.6.4). In the initial part of the graph, at $0.7P_d$, the effect of generalized concrete cracking in the finite element models is clearly indicated by the sharp strain increase in the rebar (Figure 5.6.5). Below $0.7P_d$, the test results show less stiffness than the analytical results, as though cracks were already present in the concrete mass. As a matter of fact, the containment model was subjected to the design pressure for the Structural integrity Test before High Pressure Test, which helps to explain the differences. In the final part of the graph (Figure 5.6.4), it can be seen that the yielding begins at $3P_d$, with a strain a little greater than 0.2% whereas in the finite element models the

elastic limit strain was input exactly as 0.2%. After this point the plastic strain increases following the same law for both test and analytical results, with a small gap with respect to the curve for the finite element model without the basemat. For the finite element model including the basemat, the plastic curve is shifted forward due to the basemat flexibility which lowers the bending moment at the wall-base junction. The maximum strain in the Layer 2 meridional rebar measured during the test was about 0.9% at 145 psig (1.0 MPa), which is still quite distant from the rebar material ultimate strain.

For the liner strain in this section, very different results are computed with the two finite element models (Figure 5.6.6). This fact can be explained by observing that in the finite element model clamped at the cylinder wall base, the liner and rebars were fixed in this section while in the second finite element model the liner was bent over the basemat, which is a better representation of the actual construction. The actual liner strain in this section shows flexibility of that liner restraint and this behavior is well represented by the finite element model with the basemat. It is also evident that the contribution of the liner to the section strength is small, due to the lack of sufficient anchorage, and the small strain measured indicates liner cracking is unlikely, unless it could come from local excessive strain due to the interaction with concrete largely cracked in this area.

For the layer 5 meridional rebar, located near the outside wall face, the analytical results closest to the test measures come from the finite element model not including the basemat and soil representation (Figure 5.6.7). Particularly in the higher pressure range, the agreement is good. These bars do not reach yielding. As for the layer 2 bars, the effect caused by concrete cracking at about $0.6P_d$ is also exhibited in the finite element model, but the experimental behavior does not show any sharp reduction of stiffness.

This section was predicted to be the location where failure would have started, owing to concrete crushing in the outside wall face, at a minimum internal pressure of $3.5P_d$. In the posttest inspection of the containment model, no evident crushing of concrete has been seen at the wall base caused from the internal pressure applied of $3.1P_d$ and no measures of concrete strain are available. To obtain a rough evaluation of how far the prediction was from the reality, we can use measured layer 2 and 5 rebar strain and, assuming a linear strain distribution through the thickness, the concrete strain at the outside face of the wall base can be determined as shown in Figure 5.6.8. Concrete strain at $3.1P_d$ comes out to be 0.45%, quite greater than the uniaxial ultimate compressive strain of 0.35%, which can be justified by considering the confinement effect of the basemat. This result shows the high risk of structural failure in this section, in accordance with the prediction.

Cylinder Wall Midheight Section

The section considered is at elevation 13.75 ft (4.12 m) and in this location the rebars reach the maximum strain, 1.2%. The stress state is membrane tension along hoop and meridional directions. The two finite element models give almost the same responses up to $2.8P_d$, when the beginning of yielding causes redistribution of forces (Figures 5.5.9, 5.5.11, 5.5.13). Liner and hoop rebar strains are of roughly the same value, showing the effectiveness of the liner as resisting element. In Figures 5.5.9 and 5.5.10, liner maximum principal strain is reported; the most significant points are:

- the finite element models' response is affected by concrete cracking at about $0.7P_d$ in the same way as previously noted, whereas the test results do not show any sharp change of stiffness;

- after $0.7P_d$ the responses of the two finite element models are practically the same and until $2.5P_d$ the gap with the test measures is small and constant ($\delta_\epsilon = 0.04\%$ maximum).

- The liner yields at $2.5P_d$ in the test and the computed response shows liner general yielding at about $2.8P_d$, even though yielding beginning is showed locally before $2.5P_d$ in the analysis.

- The final maximum liner strain reached in the test is about 1.1% and it compares well with the first finite element model response at $3.1P_d$. As already observed, in the second finite element model the foundation flexibility makes the response to shift a little forward, keeping however the same trend.

Judging the comparison among measured and computed values, one must remember that in the finite element models the liner has been represented with equivalent hoop and meridional truss elements, which neglects biaxiality effects on the stress-strain relationship. This explains the greater computed values in the elastic range and the anticipated general yielding. In fact, considering the biaxial stress-strain state of the liner and that the membrane stresses are:

$$\sigma_{hoop} = pR/t$$

$$\sigma_{mer} = \sigma_{hoop}/2$$

strains are computed by:

$$\epsilon_{hoop} = (\sigma_{hoop} - \nu\sigma_{hoop}/2)/E$$

assuming $\nu = 0.3$

$$\epsilon_{hoop} = 0.85\epsilon_{hoop,uniaxial}$$

Confirmation of this result could be inferred by observing in Figure 5.6.9 that test results are slightly below the analytical ones until $p = 2.5P_d$.

In Figures 5.6.11 and 5.6.12, the computed and measured strains in layer 6 hoop rebar near the cylinder midheight are compared. The agreement is good over the entire pressure range, and particularly for the finite element model without the basemat at the final pressure values. Observing the initial part of the graph in Figure 5.6.12, the concrete pre-cracking caused by the Structural Integrity Test can be noted as a gradual loss of stiffness whereas High Pressure Test results are more nearly linear in the low pressure range. As already observed, there is a small shift between the results of the two finite element models. In this case, the experimental general yielding is predicted better with the second finite element model but then, at $3-3.1P_d$, the test result is closer to that obtained with the first finite element model. It must be added that simple pretest hand calculation, using membrane stress-state formulas, gave as hoop yielding pressure the result of $2.9P_d$, which is very close to the experimental and analytical results. Further considerations should be made

observing test results of liner maximum principal strain, layer 6 hoop rebar axial strain, both at elevation 13.75 ft (4.19 m), and radial displacement at elevation 11 ft (3.35 m), slightly below the previous point of measure. The radial displacement should be the same for liner and rebar, thus one would expect equal strains, with increasing internal pressure, as resulted from the analyses of the finite element models. Test results show concordant behavior of liner and radial displacement (Figures 5.6.9 and 5.6.14), whereas hoop rebar behavior is stiffer (Figure 5.6.11) after $p = 2.5P_d$ and more in agreement with analytical results. Radial displacement is measured on the liner surface, thus good agreement with liner strain should be obvious, while some slipping between liner and concrete, and between concrete and rebars seems to take place after $2.5P_d$. The evidence of this slipping could be provided by a few small tears found in the liner adjacent to the studs, which attached the liner to the concrete wall.

For the layer 5 meridional rebar, placed at the outer wall-face, the results are compared in Figure 5.6.13. The finite element results that approach better the test results are those of the simpler model without the basemat and soil-structure interaction. Yielding is only just reached and meridional strains are well below hoop strains, as expected. Below $1P_d$ there is the effect, already seen, of concrete cracking in finite element models, in this case at noticeably different pressures.

Looking at the radial and vertical displacement, the latter relative to cylinder base, the agreement is good for the former one (Figure 5.6.14), showing differences at the beginning of general yielding (as already remarked), but then approaching the same final value at $3.1P_d$. The results of the two finite element model are virtually identical. The comparison of measured and computed vertical displacement is in Figure 5.6.15 and also in this case the simpler model gives better results.

The results so far discussed are related to the two sections indicated as more critical for the global structural stability. The comparison among finite element results and test measures shows a fairly good prediction of the experimental behavior. Maximum rebar strain, 1.2%, and maximum liner strain, 2% at springline (Figure 5.6.16), are far from the ultimate strain of materials used, therefore, as far as steel resistant elements are concerned, the containment structure is still capable of sustaining additional pressure.

Of course local liner failure due to strain concentration at discontinuities or due to interaction with studies is neglected in this respect. Extrapolating test measures up to $3.5P_d$, maximum hoop rebar strain reaches the value of 2.5%, which makes reasonable the prediction of structural failure at the cylinder wall base due to bending and crushing of concrete, subjected to a compression strain greater than 0.5%, as pointed out above.

In the dome of the containment model structure, pretest analysis results do not agree sufficiently with test measures. There are two points of strain measurement at $\phi = 72°$ and $\phi = 37°$ above the springline. At the first point, $\phi = 72°$, test measures diverge from finite element results (Figures 5.5.17 through 5.5.19). Analytical models show a stiffer behavior, which could be caused by not having adequately represented the meridional rebars whose actual total resisting area is reduced by 50% in this zone. Anyway, it must be observed that the maximum strain value is a bit less than 0.2% and thus this zone is not critical for structural stability. At the second point, at $\phi = 37°$, liner measured strain is in good agreement with computed strain, with the usual difference due to concrete cracking up to $0.7P_d$ (Figure 5.6.20), whereas the

strain in layer 5 meridional rebar (Figure 5.6.21) shows, at a less extent, similar difference observed in the previous point at $\phi = 72°$. The same conclusion reached for the point at $\phi = 72°$ (it is not a critical section for structural stability) holds also at $\phi = 37°$, because the maximum strain is below 0.14%.

Also the basemat uplift is a major point of disagreement between test measure and prediction of the analysis. This issue will be treated in the next section, which is dedicated to posttest analyses.

### 5.6.3 Posttest Analyses vs. Test Results

In the posttest analyses, two subjects have been treated: 1) the basemat uplift, considering the soil stiffness, the residual cracked concrete stiffness influence, and the contribution of the concrete layers above the foundation plate, and 2) the major liner tear observed in the test.

### 5.6.3.1 Basemat Uplift

In Figure 5.6.22, test measures and finite element model results of the basemat edge displacement relative to the basemat center are reported. Computed results have been obtained changing the Winkler modulus, represented by soil equivalent springs, and the value of two parameters of the ADINA code, STIFAC and SHEFAC, making an attempt to consider better the stiffness of uncracked concrete blocks in the basemat. Two soil stiffness values have been considered; for the first one, on the basis of site bearing plate tests, the Winkler modulus of 29 ksf/ft (4.56 MPa/m) was evaluated and equivalent truss elements as soil springs were introduced at the basemat bottom nodes; for the second case, the soil has been considered infinitely stiff by giving a high Young modulus to the trusses representing the soil. The disagreement between test result and finite element results showed in Figure 5.6.22 is very large, and change of soil stiffness and computer code parameters is not sufficient to approach more closely the experimental behavior. Observing the computed curves, it appears that stiffening the soil has limited influence after $1.5P_d$ and changing computer code parameters no influence at all, practically.

Based on the belief that the computer code gives a poor representation of the uncracked concrete contribution to the mat stiffness, a simplified method, which accounts for the "tension stiffening" effect in concrete, has been used to calculate displacements. This method, adopted by CEB [43], is known as the "bilinear method" and is based on the observation that, for the serviceability limit state, the moment-deflection relationship may be approximated by a bilinear relation (see Figure 5.6.23, from [43]).

The approach adopted is to calculate the limiting deflections $a_1$ and $a_2$, corresponding to state I and II respectively, from the basic deflection $a_c$ (calculated elastically using the appropriate stiffness of the concrete section alone, $EI_c$). In state I, uncracked sections are considered, with the contribution of the stiffness of the reinforcement, and in state II the concrete is only considered to be effective in compression. The appropriate formulas are given in Figure 5.6.23. The assumptions used in this method are the following: (a) the coefficient $n$, which in reality varies along the element, is replaced by a constant value $n_b$ calculated for the critical section (i.e., at the center of the plate in this case); (b) the limiting deflections $a_1$ and $a_2$, corresponding to states I and II, respectively, are calculated on the basis of the characteristics of the critical section alone. The effect of variations in the

reinforcement along the member is thus neglected. The other symbols in Figure 5.6.23 are:

$M_c = M_{cd} \approx W_c \cdot (f_{ct} - N/A_c)$, cracking moment for the critical section;

$W_c$ = section modulus of the concrete section alone;

$A_c$ = concrete section area; and

$M_d$ = moment of the critical section under the loading considered.

Calculations have been performed by hand, considering a simplified structure constituted of the circular foundation plate simply supported along the junction with the cylindrical wall, subjected to the internal overpressure and to forces and moment transmitted by the wall (Figure 5.6.24). $M_w$ and $N_w$ have been calculated considering a long cylinder clamped at the bottom and subjected to internal pressure.

Two resistant sections have been considered. The first one has thickness 40 in. (1016 mm), Figure 5.6.25A, and is the same adopted in the global finite element models. The second one is 58 in. (1475 mm) thick, Figure 5.6.25B, and comprises the unreinforced concrete slab above the liner. In Figure 5.6.26, results of hand calculations are compared with finite element analysis results. The first thing to observe is the extreme importance of the contribution of the unreinforced concrete slab above the mat, which makes experimental results and bilinear method results fit very well.

The second point of note is the small and constant gap between the first finite element model results and the bilinear method results, considering the mat section with thickness 40 in. (1016 mm). This gap of about 0.1 in. (2.5 mm) until $p = 2.5P_d$ should represent the effect of tension stiffening due to uncracked concrete and it appears not so large as it was thought at first. After $p = 2.5P_d$, the results begin to diverge; however, it must be considered that the bilinear method has been proposed only for deflection calculation in the elastic range.

In conclusion, it appears clearly that the correct analytical model must include the contribution of the unreinforced concrete layers above the mat. In this regard, the shear stress transfer at the contact surface of the top layers must be effective to enable the entire section of thickness 58 in. (1475 mm) to resist external forces. To investigate this subject, simplified hand calculations have been performed using the scheme in Figure 5.6.27.

The neutral axis is at about 6.7 in. (170 mm) from the top of the fill slab. According to classical theory for reinforced concrete sections, the shear stress is constant and equal to the maximum value below the neutral axis, in this case:

$\tau_{max} \approx T/(0.9 \times 1.44 \times 1.00)$

In the following table, shear forces and stresses related to the foundation plate model of Figure 5.6.27 are reported:

| Location in Fig. 5.6.27 | $p=P_d$ | | $p=1.5P_d$ | | $p=2.0P_d$ | | $p=3.1P_d$ | |
|---|---|---|---|---|---|---|---|---|
| | T ton | $\tau$ kg/cm² | T ton | $\tau$ kg/cm² | T ton | $\tau$ kg/cm² | T ton | $\tau$ kg/cm² |
| 1 | 56 | 4 | 83 | 6 | 111 | 9 | 174 | 13 |
| 2 | 37 | 3 | 56 | 4 | 74 | 6 | 116 | 9 |
| 3 | 19 | 2 | 28 | 2 | 37 | 3 | 58 | 5 |

The shear stresses calculated are sufficiently low, referring to friction between concrete layers and bond between liner and concrete, to not allow slip between the surfaces considered.

With the aim of evaluating the basemat behavior by a finite element analysis and checking the hand calculations, an axisymmetric finite element model of the basemat was developed. The mesh of the model is shown in Figure 5.6.28: It is a representation of the basemat alone, where, in contrast to the global model used in pretest analyses, the fill slab has been included too.

The analysis has been performed in order to evaluate the influence of the fill slab on the basemat uplift. About material models, a nonlinear elastic model for steel in tension has been used, with a particular stress-strain curve calculated to take into account tension stiffening effect (Figure 5.6.29). The model is made up of 186 2-D eight-node isoparametric elements with 9 integration points to represent the concrete and 102 truss elements representing rebars. The total number of nodes is 640 with 1211 DOF.

The standard ADINA concrete model has been used to model the concrete behavior with the same parameters used in the previous analyses. Steel rebars have been represented in two ways: for rebars in compression, the elasto-plastic model has been used, for rebars in tension, the material behavior has been modeled with an elastic-nonlinear relationship (Figure 5.6.29).

The necessity to operate in this way comes out because the ADINA Code does not allow the use of an elasto-plastic multilinear material model with different stress-strain relationships in tension and compression. Anyway, for the specific load path applied to the structure, there is no difference using nonlinear elastic or elasto-plastic model.

The stress-strain steel curve for the nonlinear elastic model has been calculated with the intent to evaluate the effect of the concrete between two cracks on the rebar stiffness. To do this, an analytical method has been employed according to [45]. That paper deals with the behavior of the reinforcement during the early second stage, which is characterized by very small values of crack opening and steel being in the elastic range. However, in this case, the gap evaluated at the end of the elastic range between the stress-strain curve of the naked bar and of the bar in a concrete member has been maintained beyond the reinforcement yield point extrapolating theoretical results into the plastic range. The typical stress-strain curve for a bar between two cracks is shown in Figure 5.6.30: it is possible to see the influence of the

steel ratios. As the steel ratio decreases, the influence of the concrete around a bar becomes more important.

A medium value for the steel ratio in the basemat of the Sandia 1:6-scale model is about 0.4%, which is the value used to determine the curve in Figure 5.6.29. With reference to the cracked section, the relationship between the steel stress and the corresponding displacement is:

$$\sigma = E \cdot (u/(l/2) + DS)$$

where $l$ is the crack spacing and DS is the strain increase with respect to the average strain $u/(l/2)$ close to the crack plane. The localized stress increase $E \cdot DS$ is due to bond stiffening effects. About the crack spacing, it is not an independent parameter. The formulation usually found in the literature takes into consideration the average bond stress $\tau$, the bar diameter $\phi$, the steel ratio, and the tensile strength of concrete. The following formulation has been assumed:

$$l = T (E_s/\tau^\circ) \phi/(n\mu) = T (E_c/\tau^\circ) \phi/\mu$$

where: $E_c$ and $E_s$ are the Young's moduli of the concrete and the steel respectively. $\tau^\circ$ is representative of the chemical adhesion: until the bond stress is smaller than $\tau^\circ$, slip between bar and concrete does not happen. The value of T is not subjected to large variation and can be assumed to be within the range $0.5-0.8 \times 10^{-5}$ [45].

In the present analysis the following values have been assumed, to obtain the stress stress curve shown in Figure 5.6.29:

    $\tau^\circ$ = 0.2 ksi (1.38 MPa)
    $\mu$ = 0.004 (steel ratio)
    T = $1. \times 10^{-5}$
    $E_s$ = 25850 ksi (178 GPa)
    $E_c$ = 5100 ksi (35 GPa)
    $\epsilon_t$ = $0.065 \times 10^{-3}$ (strain at concrete tension failure)
    n = $E_s/E_c$ = 5.1

These parameters have been chosen in order to agree with test results reported in [44]. Only the parameter T and the steel ratio $\mu$ have been independently set, using the appropriate values related to the basemat configuration.

Computed results are shown in Figure 5.6.26. To make a comparison in the same chart, results obtained without the fill mat, results from the original global model, and results from hand calculations are also shown. The agreement among analytical and test results is evident for the cases including the fill mat.

As a confirmation of the hand calculation results that were previously treated, the effect of the fill mat seems to be very important. On the other hand, the effect of the tension stiffening phenomenon does not seem important: only in correspondence of the transition zone from stage I to stage II, a better representation of the phenomenon in the material models can lead to a more stable and realistic solution. Moreover, the behavior of the model with the effect of tension stiffening taken into account seems to be too stiff with respect to test results at higher values of the internal pressure. The modifications introduced for the steel stress-strain curve,

evaluated as previously depicted, seem to be too large and a better refinement of the analytical method used should be done.

### 5.6.3.2 Liner Strain Concentration Analysis

Containment model pressurization stopped at 145 psig (1.0 MPa) owing to a vertical large tear of the liner very close to a thicker penetration cluster plate. Posttest analyses have been performed to study the importance of the perturbation caused by the stiffer plate welded to the liner, in terms of stress and strain concentration, using, in this phase, only plane stress finite element models and neglecting other contributions, such as from stud induced displacements by both in-plane and out-of-plane movements due to concrete cracking. Two finite element models with different mesh refinements have been used to test the sensitivity of the analysis. The first model is made up of 220 2-D eight-node isoparametric elements with 9 integration points and 1361 DOF. The second model consists of 419 2-D elements and 2575 DOF (Figures 5.6.31 and 5.6.32). Material properties are the same as those in the pretest analysis and the applied load consists of boundary nodes displacements as computed in the global finite element analysis. Elastic-plastic analyses using ADINA computer code were performed with step-by-step loading, equilibrium iterations, and stiffness reformation at every step. At about $1.1P_d$ yielding takes place near the corner of the thicker plate whereas in the global axisymmetric analysis the liner begins to yield after $2P_d$. At $3P_d$ the maximum effective strain in the liner is 6.3% near the penetration plate corner compared to boundary strains of 0.22% in the hoop direction and 0.16% in the meridional direction. In Figure 5.6.33 strain values through two section lines at the corner are plotted. Using the ductility criteria for failure proposed in [46], which provides the ratio of ultimate effective strain to uniaxial ultimate tensile elongation, $C_{TF}$, as a function of the Davis Triaxiality Factor, TF:

$$TF = \frac{\sqrt{2}(\sigma_1 + \sigma_2 + \sigma_3)}{[(\sigma_1-\sigma_2)^2 + (\sigma_2-\sigma_3)^2 + (\sigma_3-\sigma_1)^2]^{0.5}} = 2$$

The liner is in a plastic state, practically, considering the boundary strains of 0.22% and 0.16%. Thus, $\sigma_1 \approx \sigma_2$, $\sigma_3 = 0$ and

$$C_{TF} = 2^{1-TF} = 0.5$$

This means that the maximum effective strain bearable by the liner is about 50% of the test tensile elongation.

The uniaxial tensile elongation of the liner material should be in the range 20-30%, therefore the strain concentration due to the thicker plate is not yet sufficient, even though it is an important contribution, to initiate the tear and thus other probable contributions quoted before have also caused the definitive start of the rupture.

### 5.6.4 Concluding Remarks

The stop of the pressurization at $3.1P_d$ (145 psig, 1.0 MPa) due to a local liner tear did not allow the model to reach the global structural failure. Therefore definitive proof of accuracy of the finite element analysis predictions about global structural failure was not obtained. Nevertheless, it is possible to compare test measures and finite element analysis results over a wide range of pressure loading and a few interesting observations can be drawn:

a)  The most probable critical structural sections have been identified and their strain computed with a good approximation (i.e., the cylinder wall base and midheight wall sections);

b)  About the prediction of the behavior of the two critical    sections, the simpler finite element model with the cylinder wall clamped at the base gives good results; only the liner restraint at the base section must be better represented;

c)  Observing the strain measured during the test at the wall base, it is our opinion that the concrete in the outer face would have become crushed by further limited rising of internal pressure above $3.1P_d$, which would have led to structural failure at the wall base;

d)  The basemat deformation has been analyzed two ways; using CEB bilinear method, which accounts for tension stiffening effects in concrete by simple hand calculations, and using a partial finite element model of the basemat along with a modified stress-strain relationship for the rebars, considering the stiffness increment owing to the surrounding concrete.  More important, two thicknesses of the resistant section have been considered: the first one considers only the structural concrete below the basemat liner; the second one is thicker and includes the protective concrete layers above the liner and the fill slab. It appears that the contribution of these concrete layers is fundamental to make analytical results and test measure fit fairly well.  At first it was supposed that tension stiffening effect in concrete was not adequately simulated by the computer code, but the results obtained by the bilinear method show only a small gap from the finite element results, which is unable, by itself, to explain the disagreement of the pretest analyses;

e)  A local refined model of the liner around the penetration where the tearing took place, shows effective plastic strain concentration with a maximum value of 6.3%. Considering the biaxial state of deformation, the computed strain approaches the material limiting ductility. However, other contributions - mainly from interaction with the studs and, perhaps, a welding caused defect - must have also been present to start the rupture.
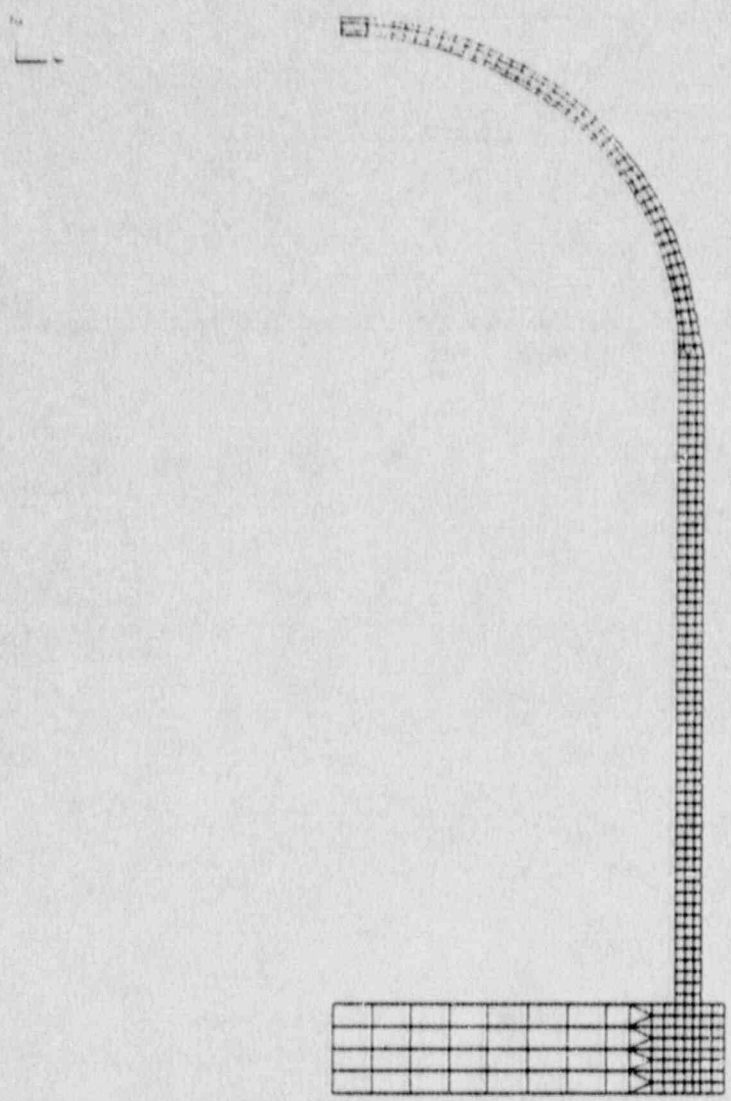
Figure 5.6.1  F.E. Mesh (2nd model includes basemat)
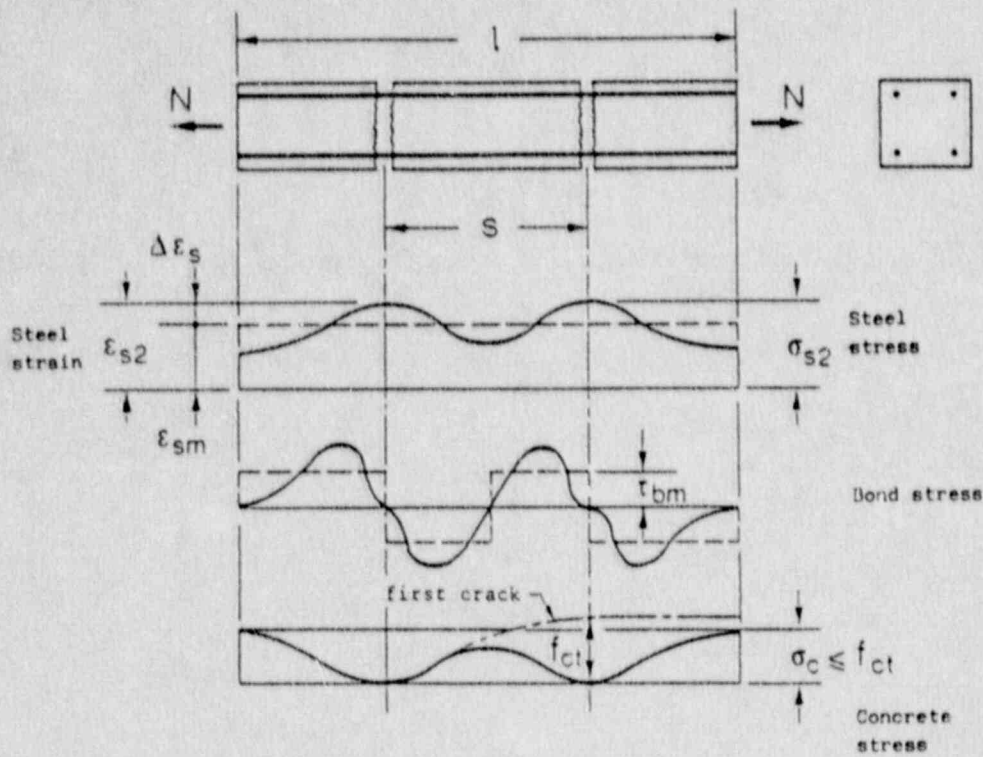
Figure 5.6.2 Cracking Mechanism in a Reinforced Concrete Member
Subject to Tension



$\sigma_{s2}$ = reinforcement stress at a
cracked section

$\sigma_{sr}$ = reinforcement stress compu
ted with the assumption of
cracked section (concrete
tension stress = $f_{ct}$)

$\varepsilon_{s1}$ = strain in the reinforcement
computed assuming sections
uncracked

$\varepsilon_{s2}$ = strain in the reinforcement
assuming all sections cracked
and neglecting concrete in
tension
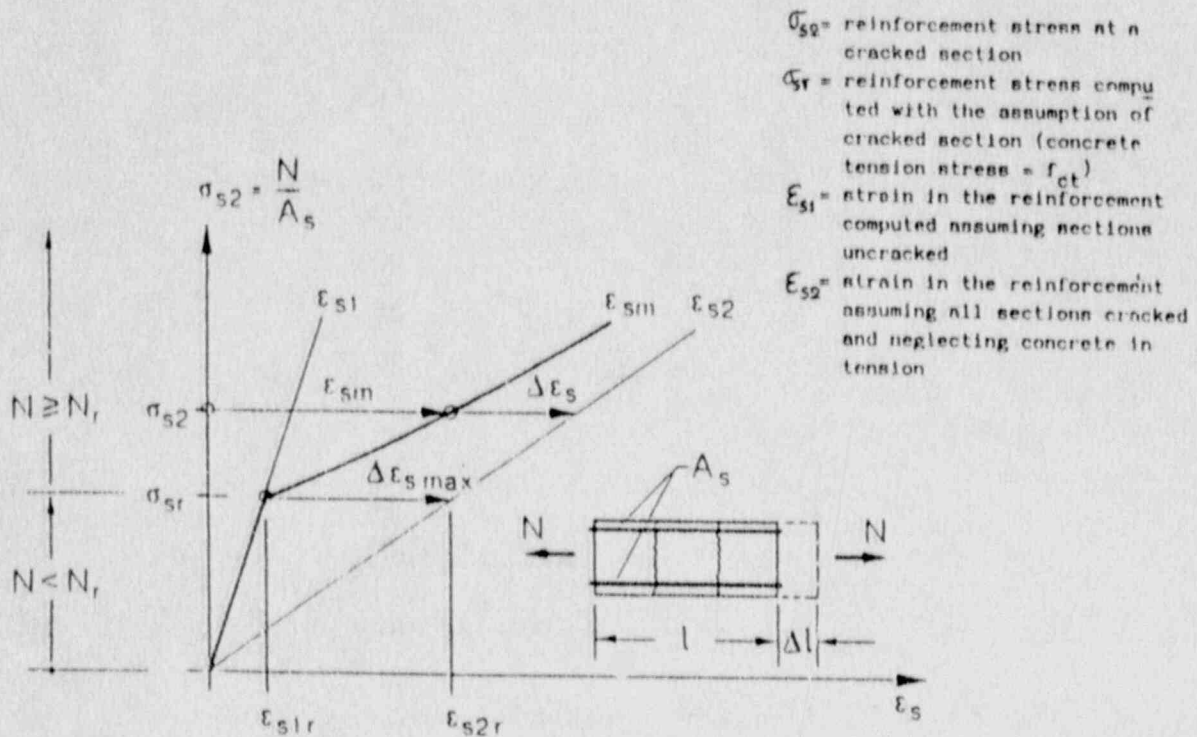
Figure 5.6.3 Strains in the Reinforcement
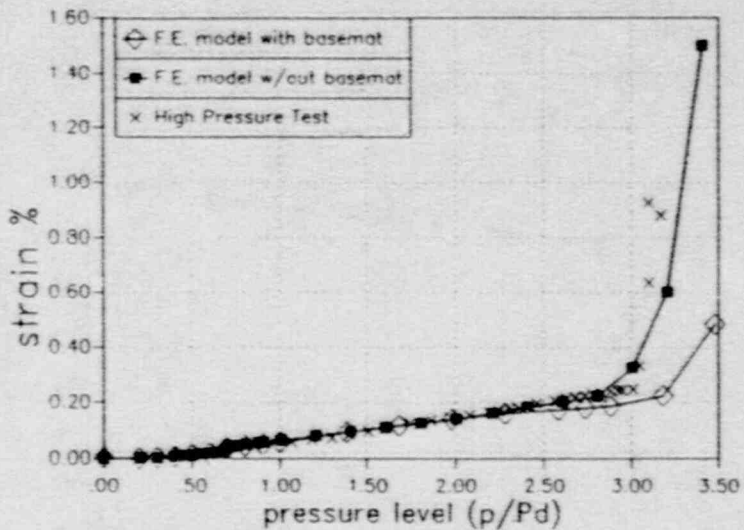
Figure 5.6.4   Axial Strain in Layer 2 Meridional Rebar at z=2.10 ft (Channel 485)
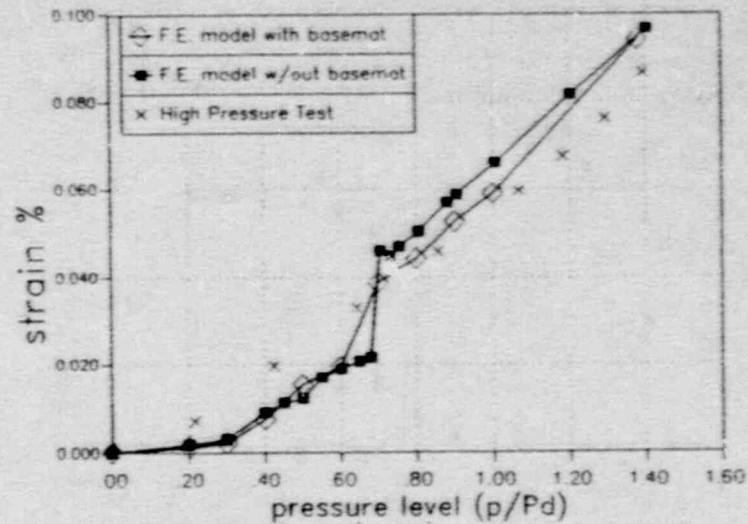


Figure 5.6.5   Axial Strain in Layer 2 Meridional Rebar at z=2.10 ft (Channel 485) – Low Pressure
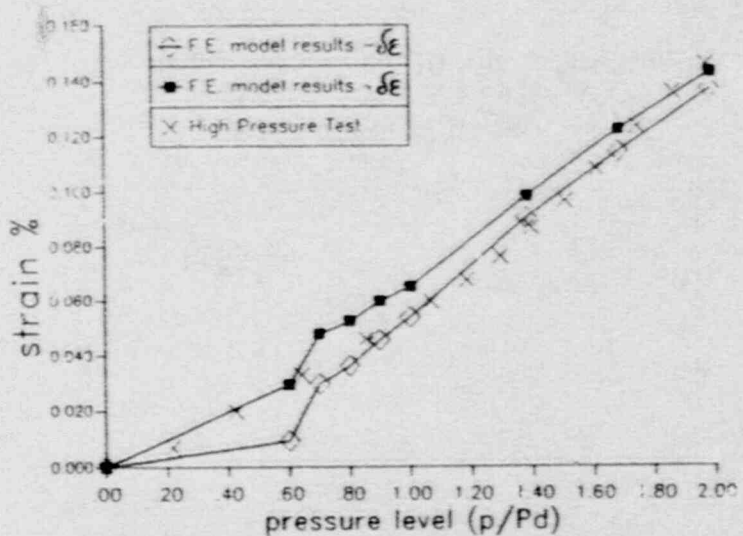


Figure 5.6.5a   Axial Strain in Layer 2 Meridional Rebar at z=2.10 ft (Channel 485) – Showing Scatter Band
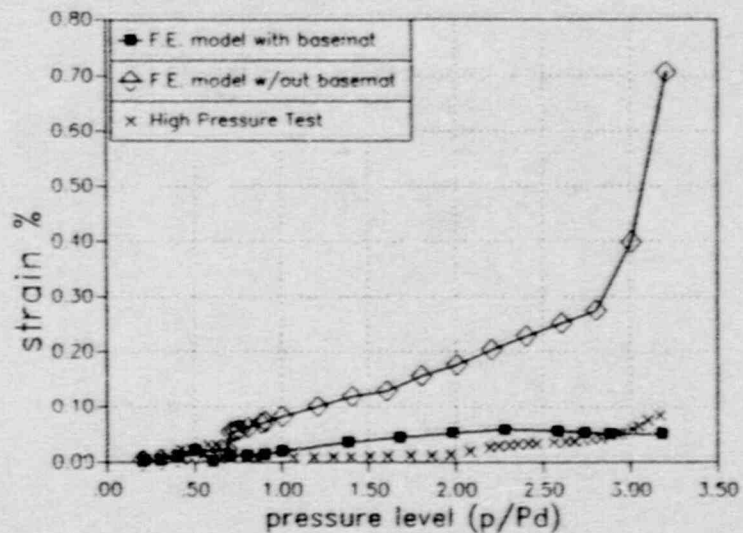


Figure 5.6.6   Maximum Principal Strain on Inside Surface of Liner at z=2.10 ft (Channel 2188)
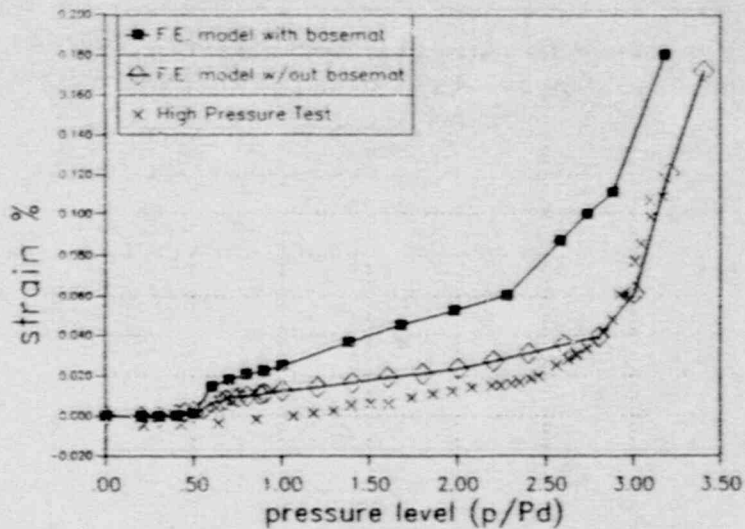
Figure 5.6.7  Axial Strain in Layer 5
Meridional Rebar at z=2.10 ft (Channel 580)
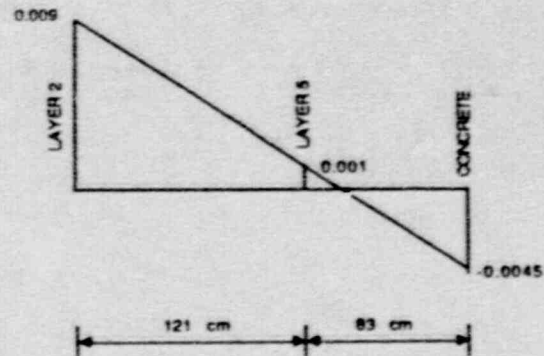


Figure 5.6.8  Strain Distribution
Through the Thickness at Wall Base
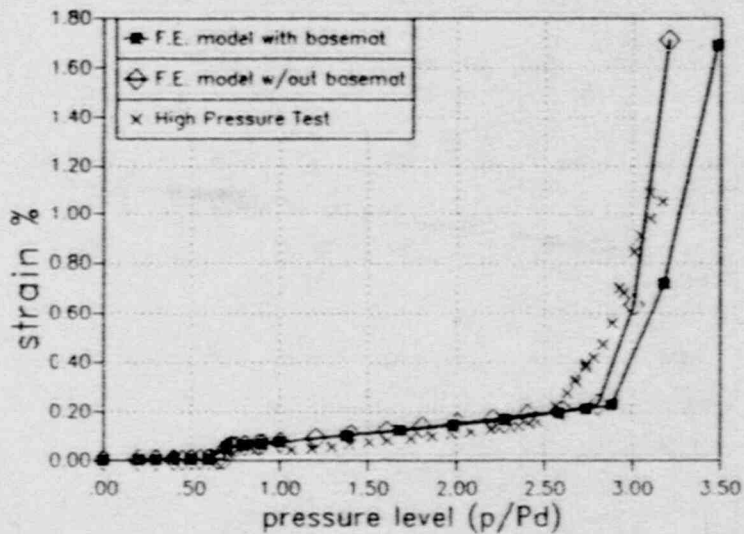


Figure 5.6.9  Maximum Principal Strain on Inside
Surface of Liner at z=13.75 ft (Channel 1543)
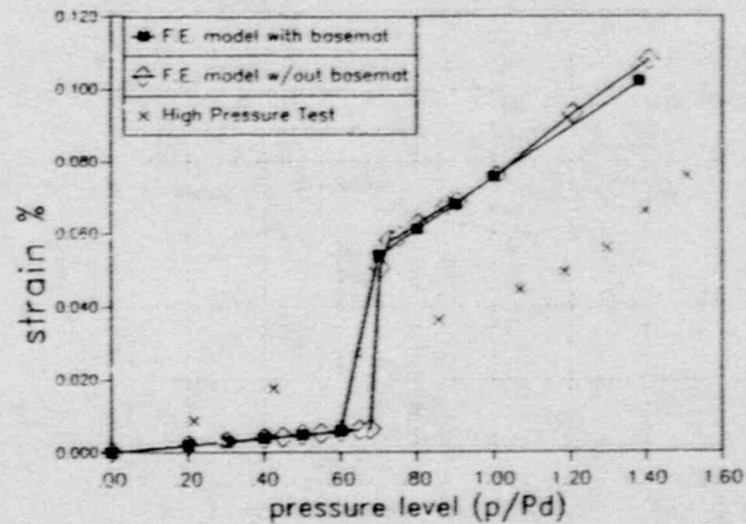


Figure 5.6.10  Maximum Principal Strain on Inside Surface
of Liner at z=13.75 ft (Channel 1543) – Low Pressure
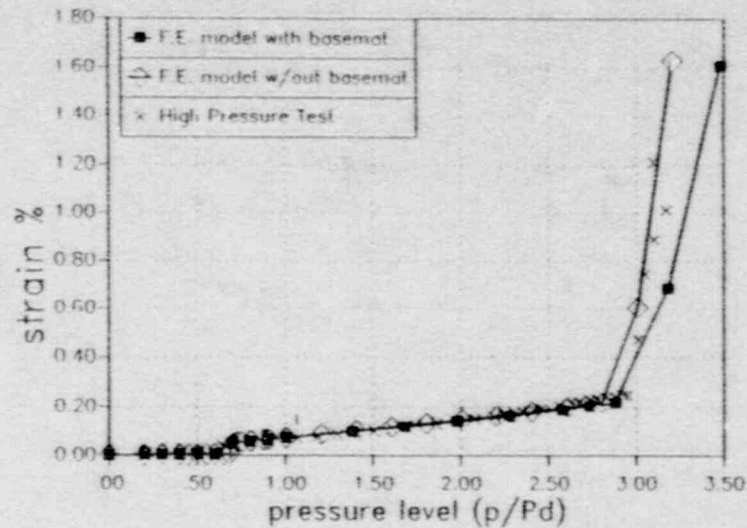
Figure 5.6.11  Axial Strain in Layer 6 Hoop Rebar
at z=13.75 ft (Channel 1109)
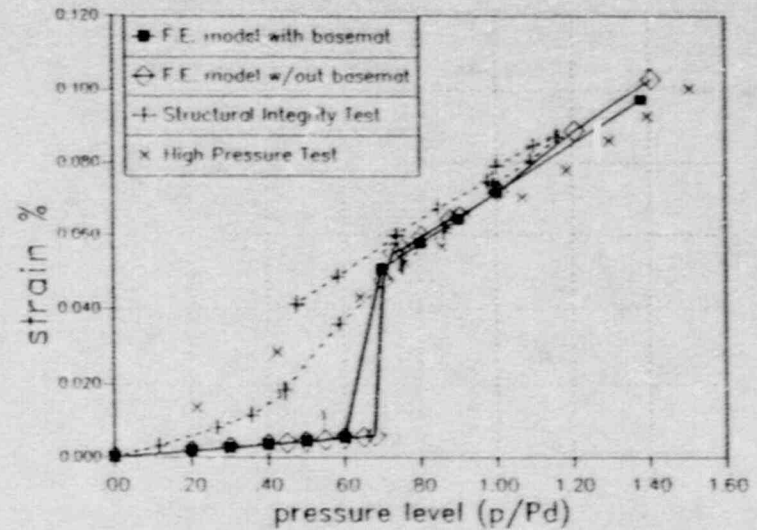


Figure 5.6.12  Axial Strain in Layer 6 Hoop Rebar
at z=13.75 ft (Channel 1109) - Low Pressure
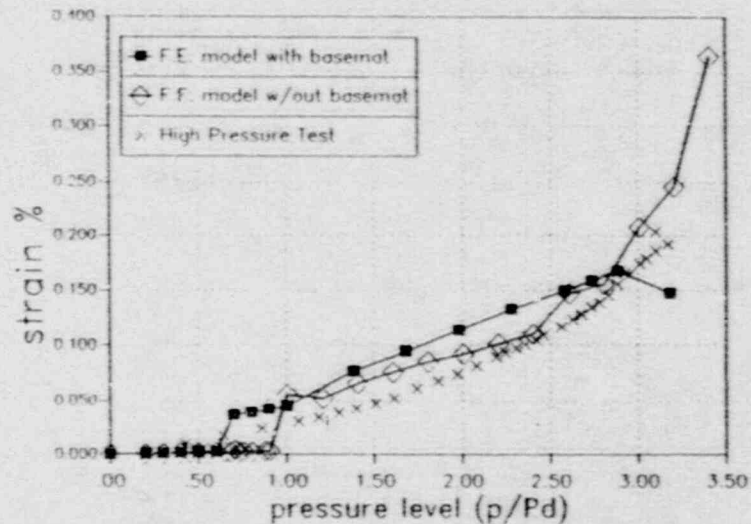


Figure 5.6.13  Axial Strain in Layer 5 Meridional Rebar
at z=13.75 ft (Channel 1041)
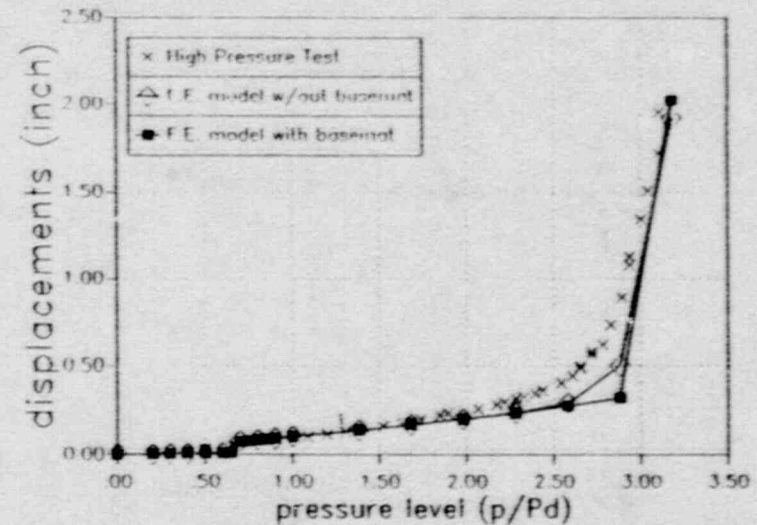


Figure 5.6.14  Radial Displacement at z=11 ft
(Channel 218)
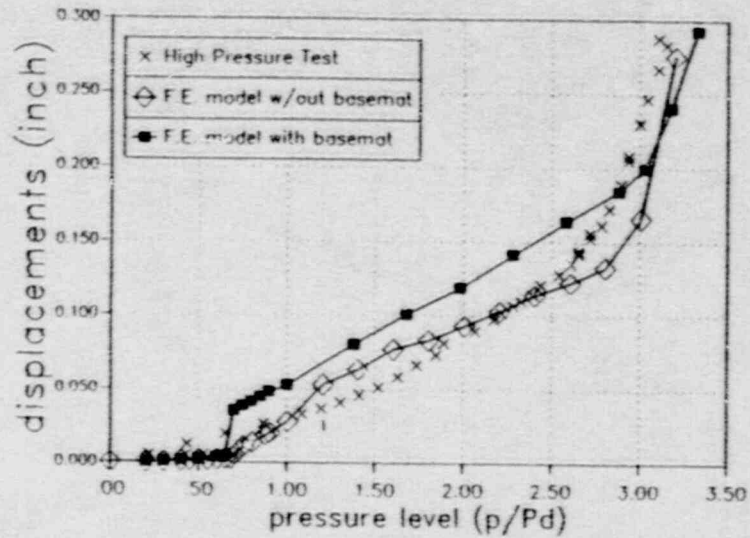
Figure 5.6.15  Vertical Displacement Relative
to Cylinder Base at z=11 ft (Channel 217)
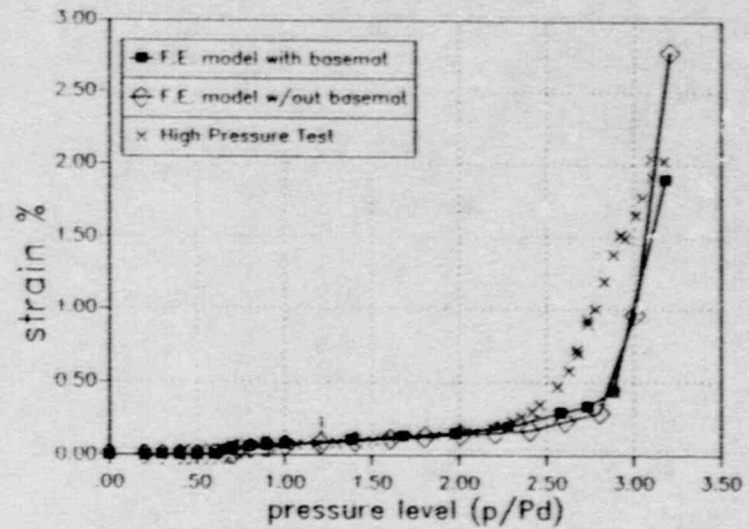
Figure 5.6.16  Maximum Principal Strain on Inside
Liner Surface at z=23.92 feet (Channel 1783)
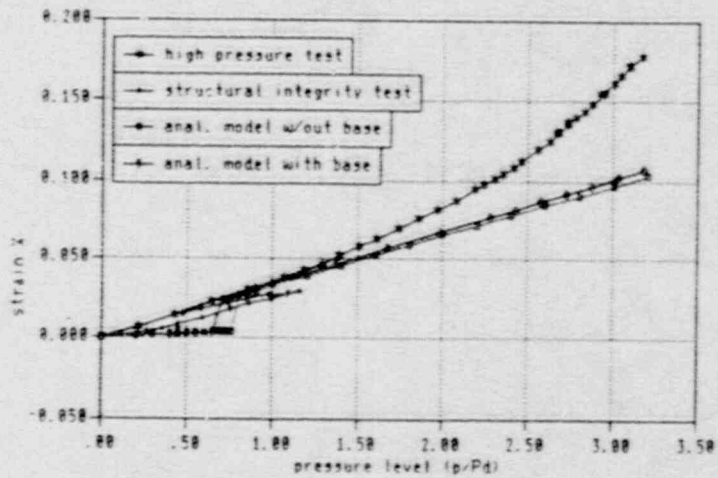
Figure 5.6.17  Maximum Principal Strain on Inside
Surface of Liner at $\phi$=72° (dome)
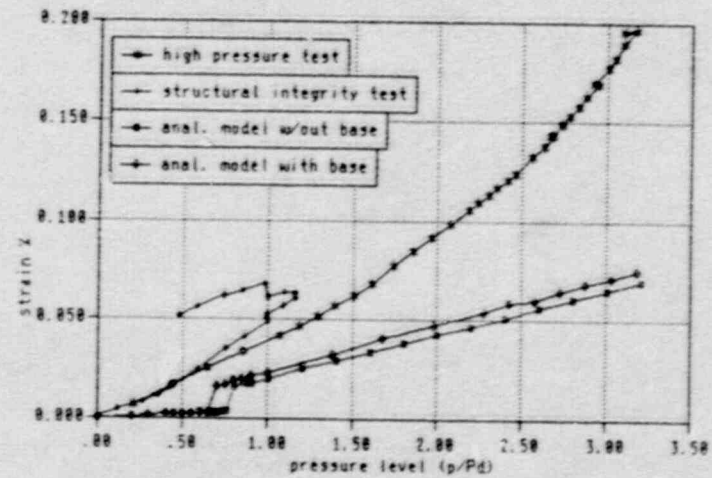
Figure 5.6.18  Axial Strain in Layer 2
Meridional Rebar at $\phi$=72° (dome)
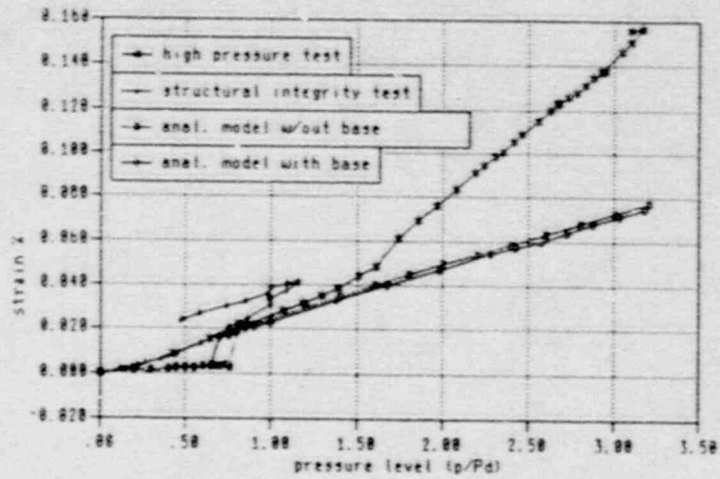
Figure 5.6.19  Axial Strain in Layer 5
Meridional Rebar at $\phi=72°$ (dome)
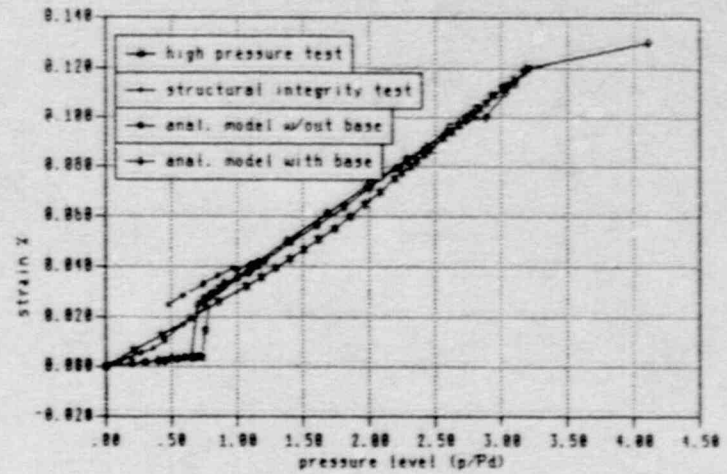


Figure 5.6.20  Maximum Principal Strain
on Inside Liner Surface at $\phi=37°$ (dome)
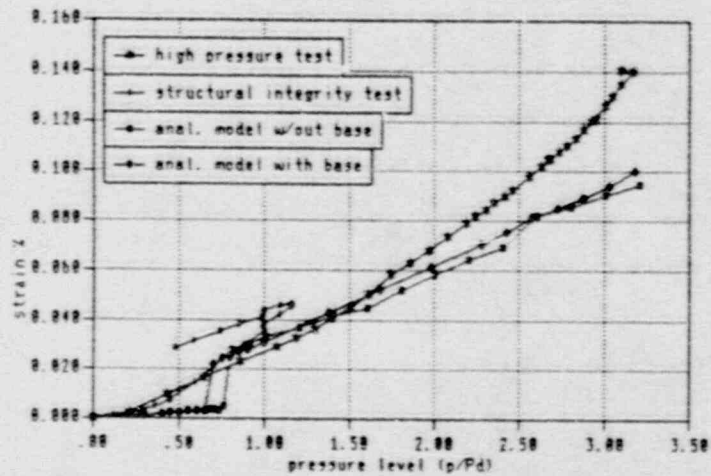


Figure 5.6.21  Axial Strain in Layer 5
Meridional Rebar at $\phi=37°$ (dome)
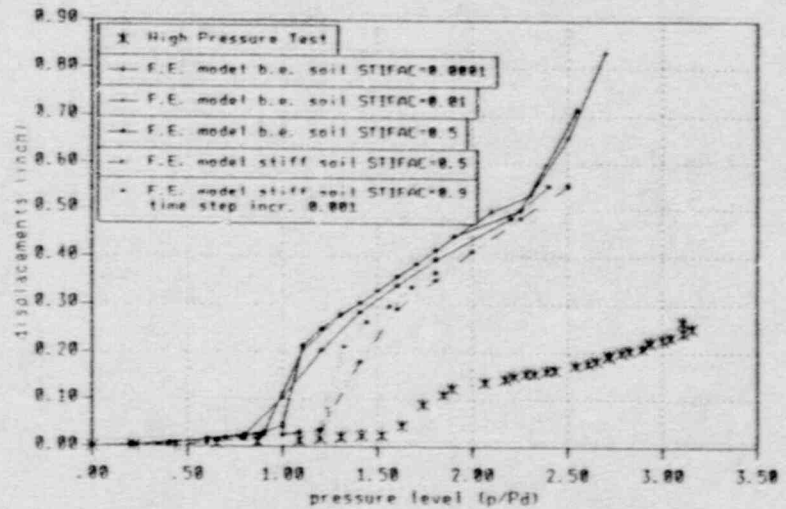


Figure 5.6.22  Basemat Uplift Relative
to Center of Basemat at z=2 feet (Channel 169)

$$(1-\Omega_b)\cdot(a_2-a_1)$$

tension stiffening

$$a = (1-\Omega_b)\cdot a_1 + \Omega_b \cdot a_2$$

$$\Omega_b = 1 - M_r / M_D$$
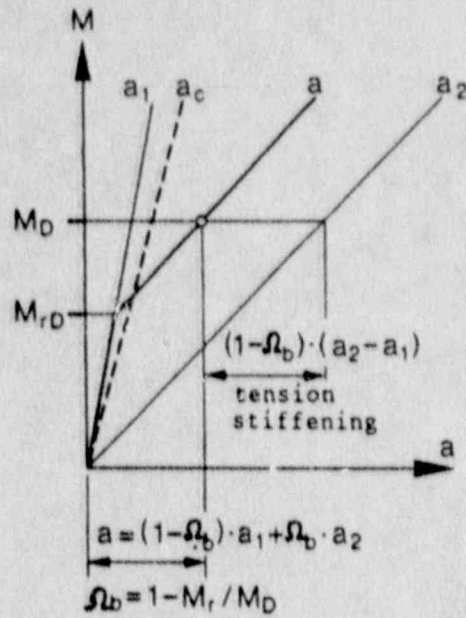
Figure 5.6.23  Deflection Due to Load



695.4 cm  (22' 9.75")
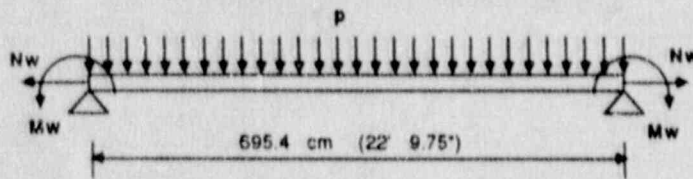
Figure 5.6.24  Simplified Scheme of the Foundation Mat



A1 = 22.4 sq. cm      A2=13.1 sq. cm      AL=15.9 sq. cm
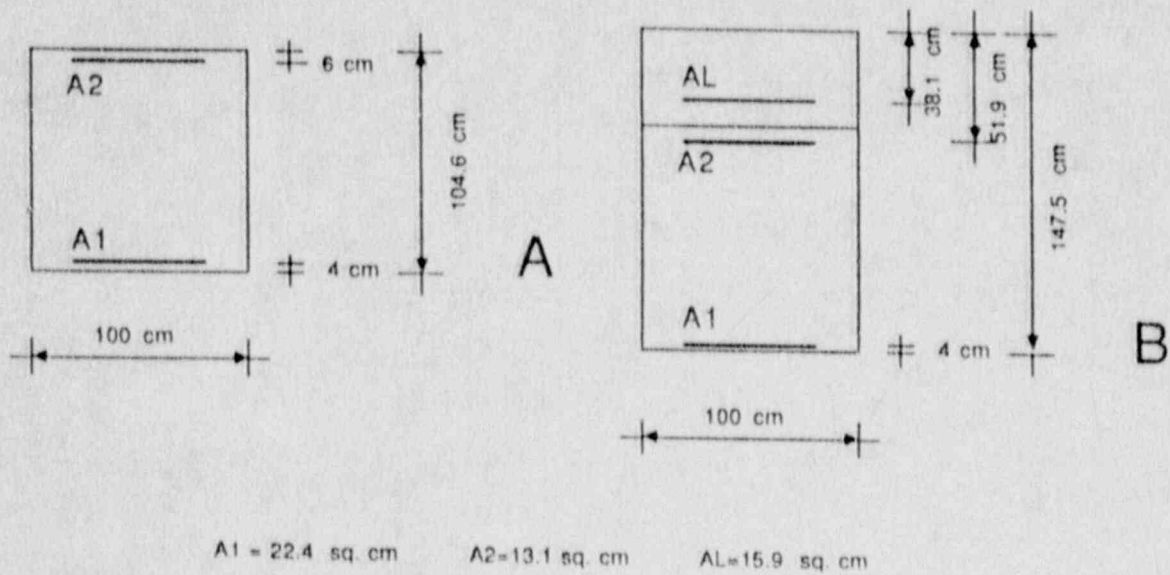
Figure 5.6.25  Basemat Sections Considered in Posttest Calculations
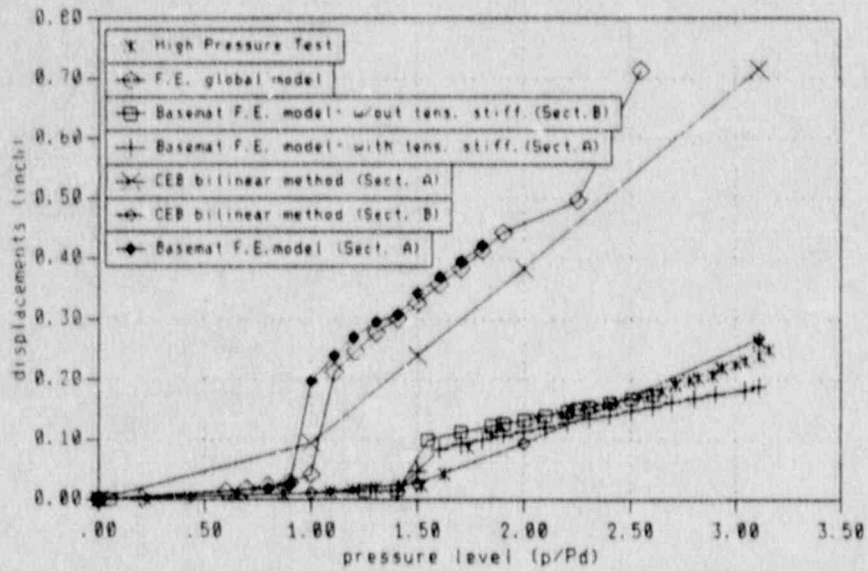
Figure 5.6.26  Posttest Analysis - Basemat Uplift Relative to Center of Basemat
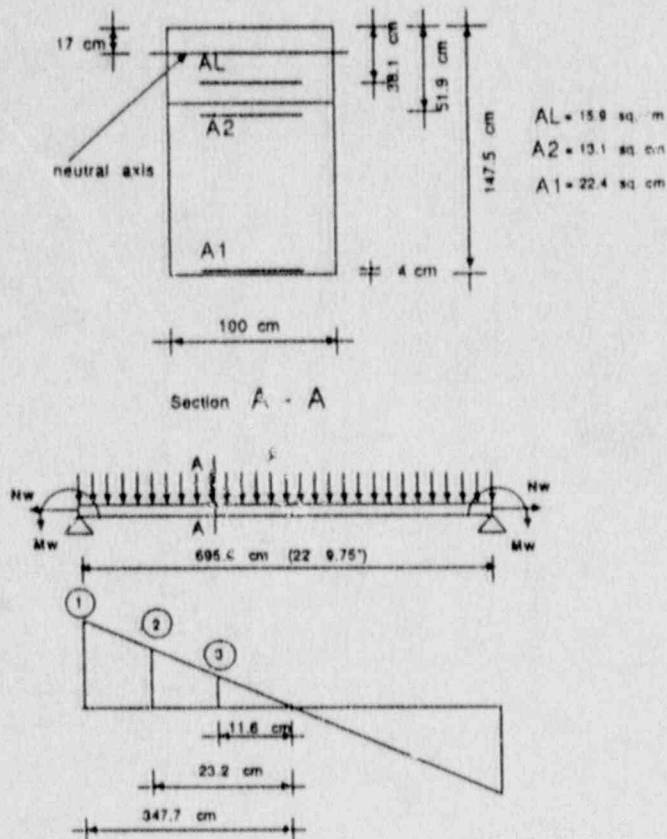


Figure 5.6.27  Shear Distribution in the Basemat
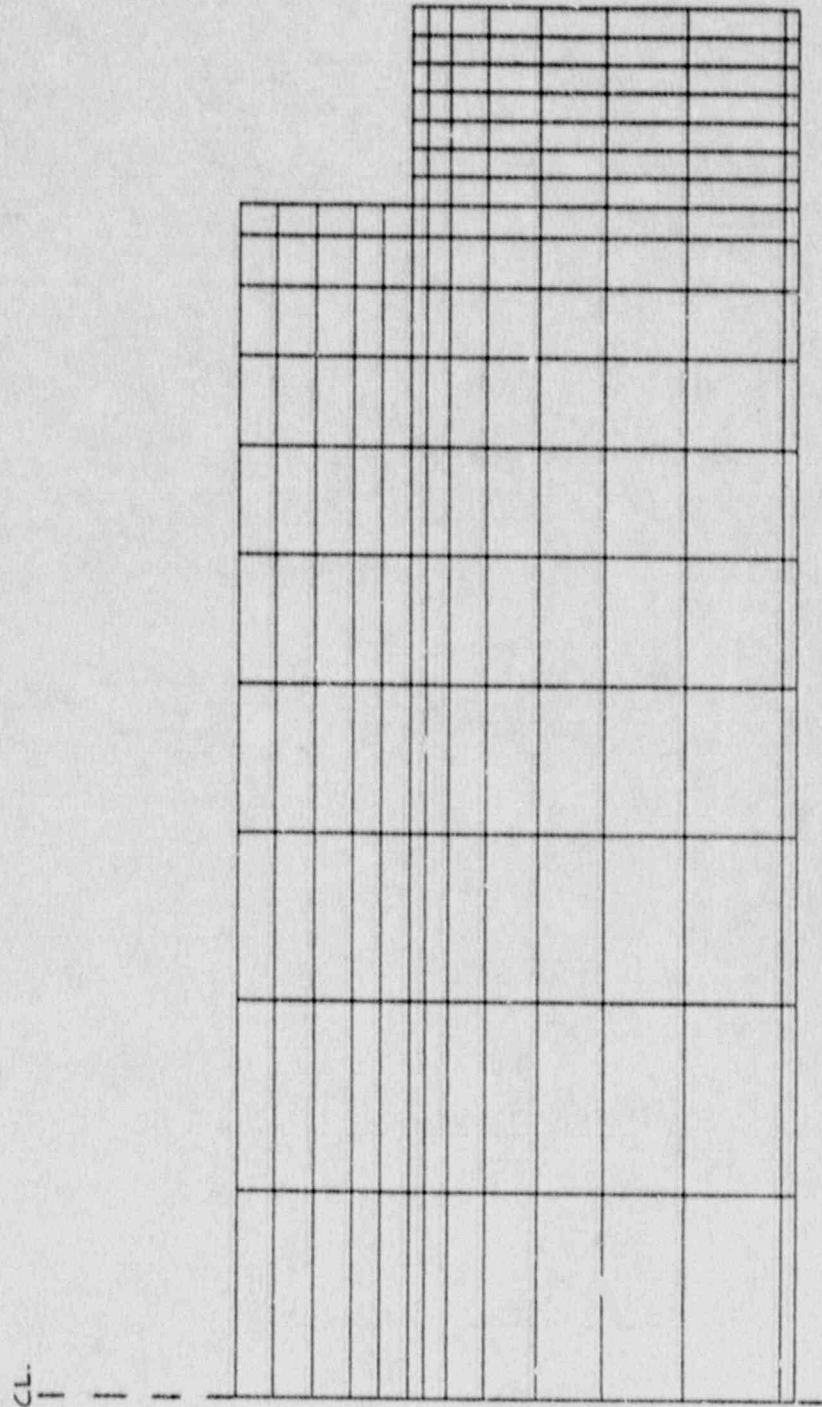
Figure 5.6.28 F.E. Mesh of Basemat - Posttest Analysis

CL.
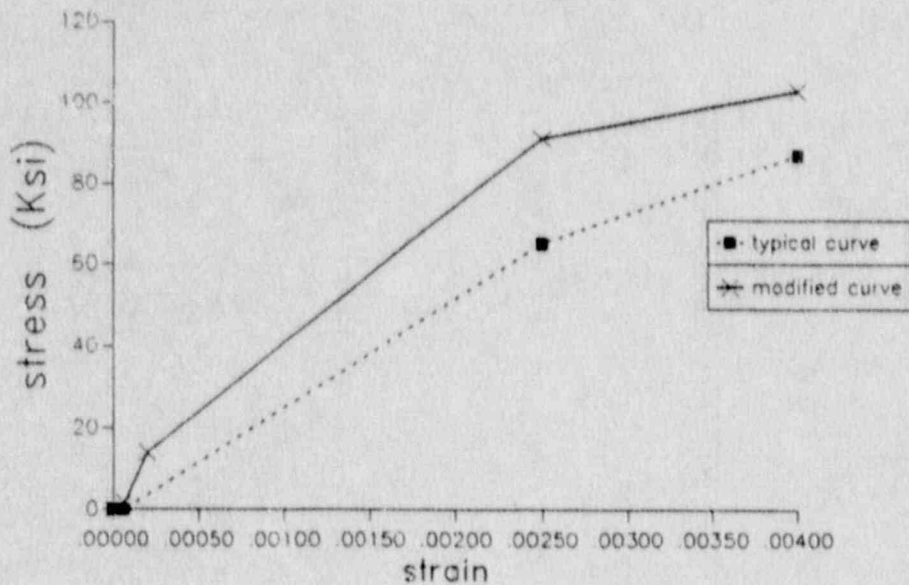
Figure 5.6.29  Steel Stress-Strain Curves
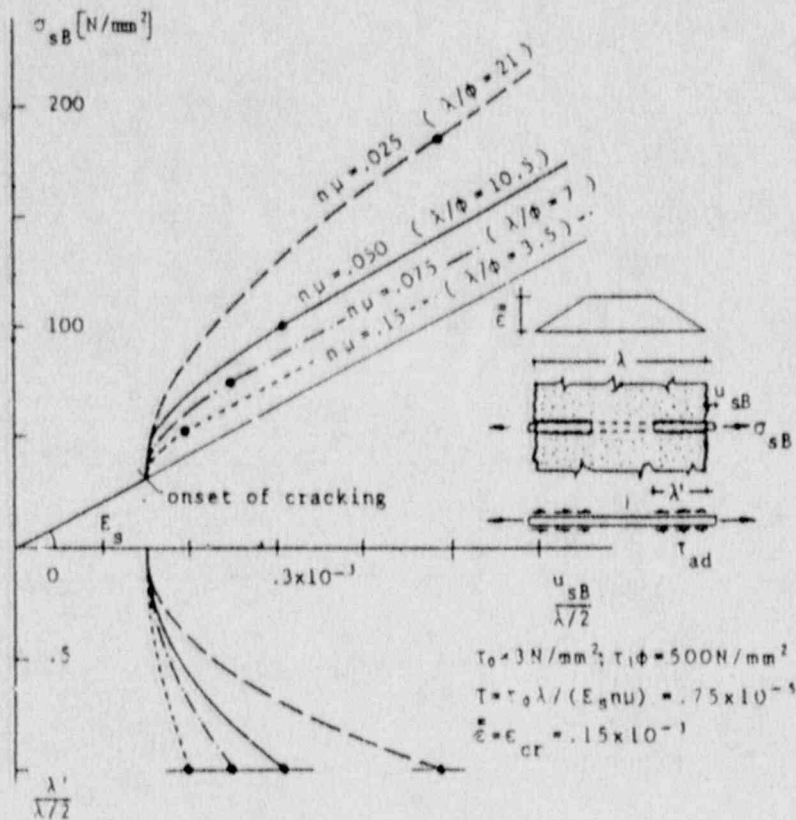


Figure 5.6.30  Curves of the Steel Stress (in the Crack Plane)
and of the Slip Bar Length for Different Steel Ratios
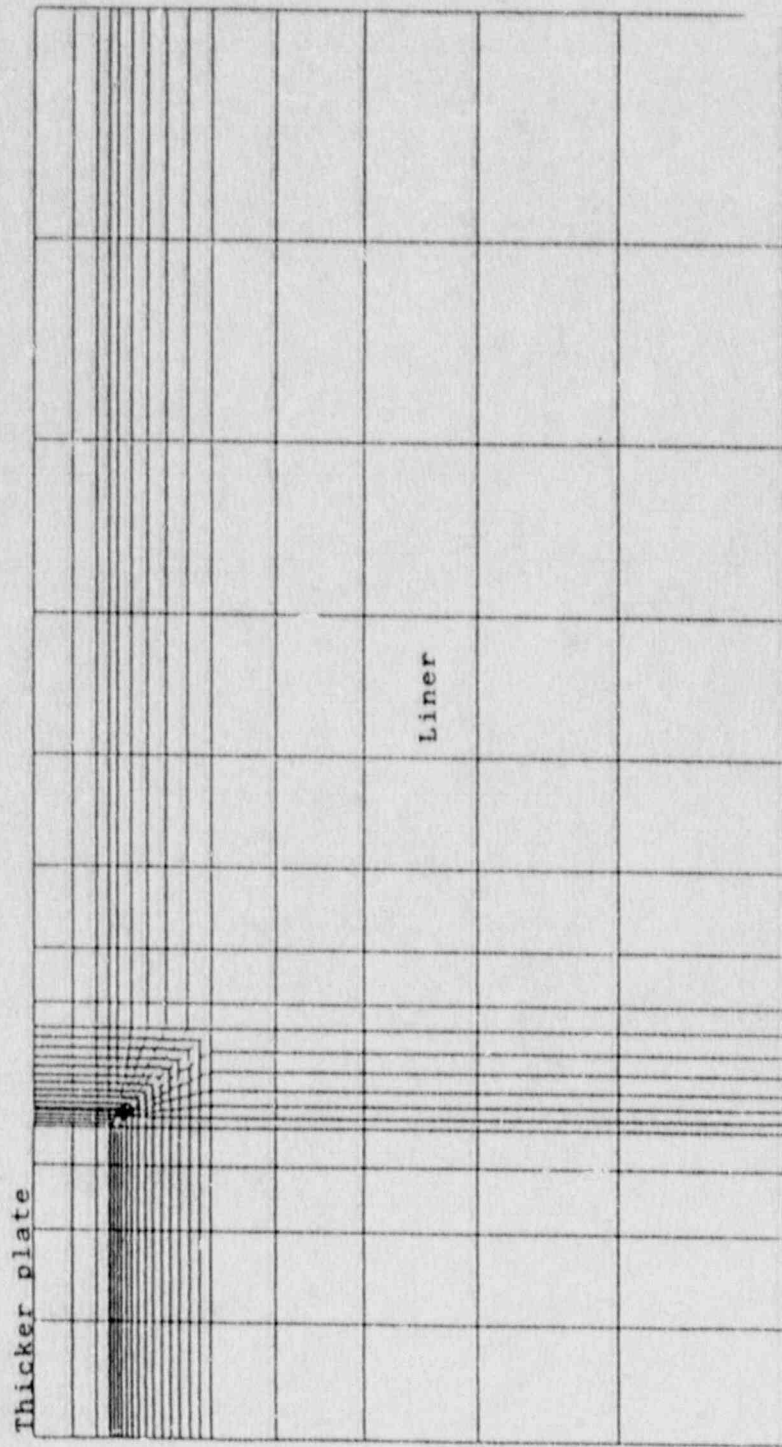
Figure 5.6.31  Penetration Insert Plate and Liner Mesh

LINER STRAIN CONCENTRATION

ORIGINAL ——— 0.830
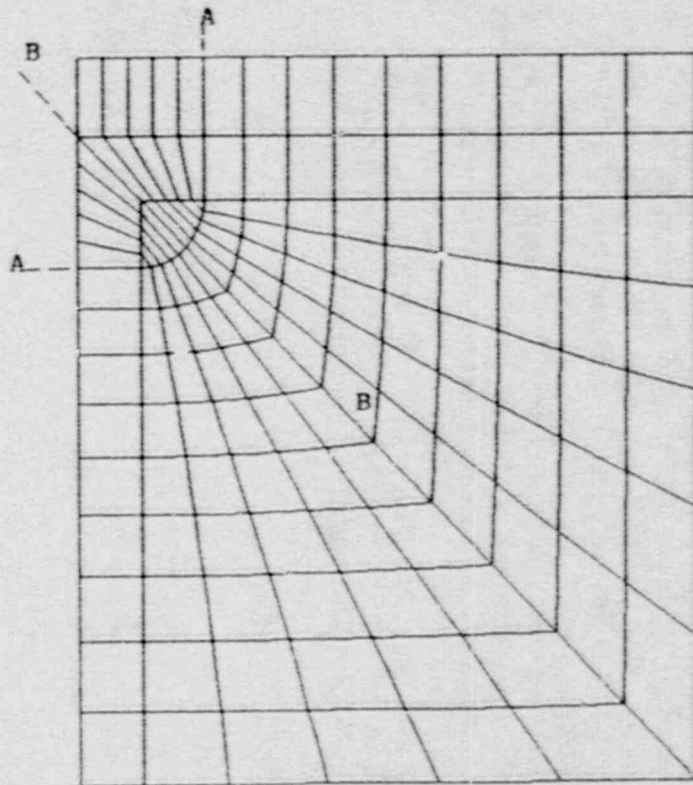


Figure 5.6.32  Refined Mesh
at the Insert Plate Corner

TIME 3.000

Line B-B

TIME 3.000

Line A-A
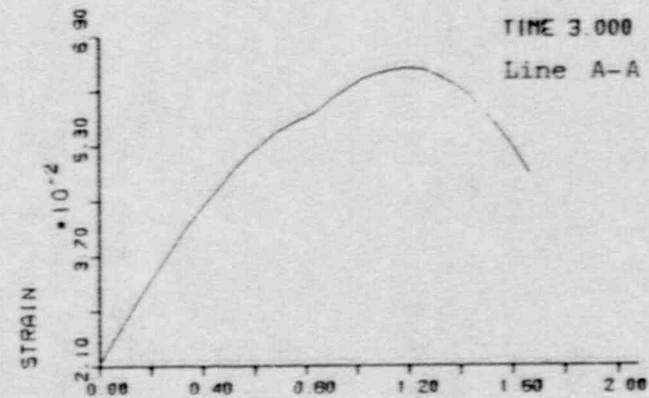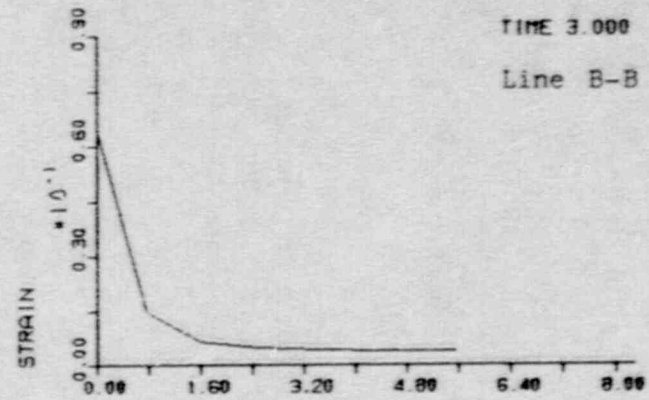
Figure 5.6.33  Calculated Liner Strain Profiles

## 5.7 Safety and Reliability Directorate, U.K. Atomic Energy Authority

This section was authored by M. H. Bleackley.

### 5.7.1 Summary

A posttest study on the major liner tear and the measured basemat uplift of the 1/6th scale Sandia reinforced concrete containment has been conducted. A 45 degree section of the containment wall in the region of the observed 22 in. (560 mm) liner tear has been analyzed. The basemat uplift has been investigated by modelling the 12 in. (305 mm) concrete floor slab lying on top of the basemat and modifying the uniaxial material properties of the concrete.

### 5.7.2 Introduction

In July 1987 the Sandia 1/6th scale reinforced concrete containment model (Figure 5.7.1) was internally pressurized by nitrogen gas to a maximum pressure of 145 psig (1.0 MPa). At this pressure major leakage of the gas was detected. Subsequent examination of the model showed a 22 in. (560 mm) vertical tear in the leak-tight membrane liner had occurred at mid-cylinder height, adjacent to an insert plate of a penetration cluster.

Prior to the actual experimental test, ten organizations participated in a numerical Round-Robin to predict the ultimate failure pressure of the containment. Although similar failure pressures were predicted amongst the participants as occurred experimentally, the location of the major liner tear was not.

There were major discrepancies amongst the participants in the prediction of basemat uplift; it was underestimated by a maximum of 4x and overestimated by 5x at the maximum test pressure. Seven participants had modelled soil-structure interaction with the soil stiffness value used varying by a factor of 15 between the participants. It has been suggested by Dameron et al. [47] and Bachmann et al. [48] that the discrepancies are partly due to lack of stiffness in the floor slab (see Figure 5.7.1) and how it interacts with the basemat. The actual floor slab is lightly reinforced and 'floats' on a 1/16 in. (1.6 mm) thick steel liner, atop the basemat. There is no mechanical connection between the liner and floor slab or basemat. In previous analyses of the containment response (e.g., [11]), it had generally gone unnoticed that the floor slab possesses some reinforcement. SRD's [11] original analysis had assumed that the floor slab possessed no significant bending or membrane stiffness and was modelled as an equivalent pressure loading.

### 5.7.3 Analysis

#### Liner Tear

A finite element analysis was undertaken to understand the mechanism which gave rise to the 22 in. (560 mm) vertical tear in the 1/16 in. (1.6 mm) thick liner, which led to the depressurization of the containment.

It was known from posttest examinations that the concrete area behind the liner was heavily cracked. A 45 degree section of the wall, incorporating this heavily cracked concrete region and the 3/16 in. (4.76 mm) insert plate was modelled - see Figure 5.7.2.

The containment wall section was modelled by sixteen 4-node shell elements with single point integration (ABAQUS type S4R) incorporating two layers to represent the liner and the concrete - Figure 5.7.3. The 4 layers of hoop rebar in the concrete at mid-cylinder height were numerically modelled. This model represented a section of a ring with the only vertical constraint provided at the lower edge.

The material properties used are shown in Figure 5.7.4. The version of the finite element program used (ABAQUS 4.6.161) is without the benefit of an implicit concrete model. Consequently, the concrete was treated as an elasto-plastic material with the same uniaxial material properties in both tension and compression (e.g., yield stress values). In the heavily cracked area of the wall section, the concrete was considered as having no strength in tension.[8]

Basemat Uplift

In SRD's original prediction of the containment performance [11], the finite element code ABAQUS version 4.5.171 was used. This version incorporates an implicit concrete model capable of representing yielding, cracking and crushing of the concrete.

The concrete model was represented in stress-space by two surfaces, the inner one representing yielding of the material and the outer one representing tensile cracking and compressive crushing. The inner surface is defined by the tensile and compressive yield stresses of the material while the outer surface is defined by uniaxial plastic strain values.

At the tensile failure surface, the concrete could be modelled with a tension stiffening effect to represent rebar debonding as the concrete cracks. In the original analysis, a uniaxial strain of 1.0% was used (see Figure 5.7.4b, curve 3) after which, the concrete was no longer capable of sustaining tensile loading.

The containment was modelled with axisymmetric shell elements, providing a crude but economical representation.

Three new analyses of the containment response were undertaken, but as mentioned previously, the current version of ABAQUS used by SRD does not possess a working concrete model, i.e. a model capable of representing yielding, cracking and crushing of the concrete. In the new analysis, the concrete of the containment was implemented by superimposing two element sets to represent the basemat. One element set possessed only compressive and the other only tensile properties. The tensile concrete was implemented in one of two ways, as an elastic perfectly-plastic (EPP) representation with a finite stress at 500 psi (3.5 MPa) - Figure 5.7.4b, curve 1 - and with a tension cut-off at 360 psi (2.5 MPa) - curve 2 - with strain softening to 72.5 psi (0.5 MPa). This plateau was introduced as the program could not cope with zero values of stress in the strain softening regime. The different ultimate tensile strengths of 500 psi and 360 psi (3.5 MPa and 2.5 MPa) arise as follows: the former

---

8. Ed. Note: Near the max test pressure, the concrete at cylinder midheight is completely cracked both in the free-field and near penetrations. By assuming only a localized section is cracked, an artificially strong stiffness discontinuity is created, which of course results in a severe strain concentration.

was an estimated value by Sandia ([11], pg. 17) and the latter comes from an ABAQUS default setting in the original concrete model of 6% of the maximum compressive stress. In the dome and cylinder region of the containment the concrete was represented simply as a no-tension material. Only the compressive element set allowed shear stresses. Using the same implementation as Weatherby ([11], pg. 49), the concrete shear modulus, G, was reduced by 4/5ths to account for the reduced shear stiffness after cracking.

Two finite element models were used for analyzing basemat uplift. The original model employed 46 3-node axisymmetric shell elements (ABAQUS type SAX2) - 11 representing the basemat, 20 the wall and 15 in the dome - with a single element through the containment thickness. Each element in turn was divided into two layers so as to represent the reinforced concrete and steel liner. The 12 in. (305 mm) reinforced concrete floor slab and 3 in. (76 mm) level and 3 in. (76 mm) protective course that rest on the basemat liner - see Figure 5.7.1 - were analyzed as an equivalent pressure loading, implying that they possess no significant membrane and bending stiffness.

For the three new analyses, the original element configuration in the dome and cylinder wall was retained but the eleven 3-node shell elements in the basemat were changed to eleven 2-node (SAX1) shell elements. An additional eight elements were added to represent the floor slab - Figure 5.7.5. As there is no mechanical connection between basemat and floor slab, a friction interface between the two layers of elements was introduced via gap elements which allow for a changing contact pattern by the gaps opening (but not contracting) and sliding - subject to a coefficient of friction, assumed to be 0.5.

Table 5.7.1 is a summary of the various analyses:

Table 5.7.1: Basemat and Concrete Implementation

| Analyses No. | Floor Slab Modelled | Coefficient of Friction interface | Concrete Representation- see Figure 5.7.4b |
|---|---|---|---|
| 1. | No | No | curve-1 (EPP) |
| 2. | Yes | = 0.5 | curve-2 |
| 3. | Yes | fully bonded | curve-2 |
| 4.* | No | No | curve-3 |

* Original Analysis

The three new analyses assumed the floor slab is unreinforced. Subsequently, it was realized that the floor slab had some light reinforcement ([12], pg. 25). This reinforcement essentially consists of two orthogonal mats at the top and bottom faces of the slab consisting of #3 rebar at 12 in. (305 mm) spacing. Consequently, Analysis No. 2 was repeated with reinforcement in the floor slab.

The addition of a floor slab may modify the uplift characteristics of the basemat by:

i) Increasing the bending stiffness by combining the floor slab and basemat.

ii) Modifying the pressure loading on the top of the basemat from a uniform gas pressure loading to a non-uniform contact pressure.

This would change the bending moment distribution on the basemat. At an extreme, the basemat uplift could be minimized, if the points of contact were confined to the edge of the basemat, by the basemat hogging and the floor slab remaining flat. This would result in a maximum restoring moment about the pole of the basemat.

The new analyses incorporated a multipoint constraint (MPC) at the basemat/wall junction (see Figure 5.7.5) so as to preserve the right angle connection during loading of the containment.

With the new analysis, soil structure interaction was modelled by the use of no-tension springs which allowed the basemat to deflect a maximum ≈0.004 in. (1/100 mm) under dead loading.

### 5.7.4 Results

Liner Tear

The section was loaded internally, by uniform pressure until a radial displacement ≈1.8 in. (46 mm) was reached. This displacement corresponded to the experimental measurement of 1.75 in. (44 mm) displacement of the containment wall at mid-cylinder height at 145 psig (1.0 MPa) [49].

At a radial displacement of 1.8 in. (46 mm), the internal pressure of the numerical model was 171 psig (1.18 MPa). This higher pressure was necessary to compensate for the lack of 'cantilever' bending which the containment undergoes but not the modelled wall section. At this pressure, the maximum tensile hoop stress in the uncracked concrete region was 415 psi (2.86 MPa).

A radial displacement plot (at 171 psig, 1.18 MPa) of the wall section is shown in Figure 5.7.6. This variation in radial displacement will give rise to hoop bending stresses.

A plot of the strain around the cylindrical section is shown in Figure 5.7.7. A 'spike' of 8.5% hoop strain is apparent at approximately 35 degrees, which corresponds to the position of the 22 in. (560 mm) tear in the liner. The single element integration rule chosen does not allow the strain peak location to be defined precisely but it is centered on a line some 4.5 in. (110 mm) from the edge of the insert plate.

The 8.5% hoop strain in an unrestrained ring is equivalent to $1.68 \times 8.5 = 14.3\%$ effective strain in a biaxial environment. (Assuming a biaxial strain ratio of 2:1, then the effective strain is 1.68 times the hoop strain [50]). A strain of 14.3% is approaching that at the ultimate tensile strength of the material - Figure 5.7.4.

## Basemat Uplift

The effect of various concrete and floor slab representations is shown in Figure 5.7.8.

The stiffest response is obtained when the floor slab is assumed to be rigidly bonded to the basemat (Analysis No. 3). The model with a friction interface (Analysis No. 2) and that without a floor slab but with a rigid elastic-plastic representation for the concrete (Analysis No. 1) show an equivalent response up to 72.5 psi (0.5 MPa). At this pressure the concrete in the former 'cracks' after the maximum tensile uniaxial stress is exceeded and thereafter loses strength, whereas in the latter, the strength of the concrete is retained at maximum stress by virtue of the finite tensile representation of the concrete.

An analysis using a zero coefficient of friction, has also been undertaken, but when plotted, the vertical displacements of Figure 5.7.8 are superimposed on the curve for a coefficient of friction = 0.5. Only in the horizontal plane do their displacements differ, with the floor slab ( the latter being stretched slightly - but a 2nd order of magnitude smaller than in the vertical direction. There is also no discernible difference in Figure 5.7.8, for the results of Analysis No. 2 with or without a reinforced floor slab.

The addition of right-angle multipoint constraint at the wall/basemat junction, has a minimal effect on uplift, verified from two equivalent analyses, run with and without MPC's.

During loading, all the results incorporating an interface between basemat and floor slab show them to be in contact sharing a common curvature. Figure 5.7.9 shows the contact force for Analysis No. 2 provided by the gap elements between the basemat and floor slab.

It has not proved possible, because of convergence problems in using superimposed elements to represent concrete and tensile properties, to exceed an applied pressure of ≈116 psig (0.8 MPa).

Nominally, the friction interface model shows a good comparison with the experimental results. SRD's original 3x understiff model with no explicit floor slab representation and a concrete model with a tension cut off is shown.

The effect on basemat uplift by the incorporation of either high or zero soil stiffness under the basemat had a minimal effect on basemat uplift.

### 5.7.5 Discussion

## Liner Tear

SRD's recent analysis has postulated a mechanism which would lead to high local strain concentrations in the liner that could result in liner tearing. The prediction is only valid if the concrete is assumed to be severely cracked in the region of the liner tear (and not cracked elsewhere) with consequently no strength in tension, at least in the hoop direction. This will result in localized hoop bending in the containment wall. The hoop bending will be accentuated by the increased stiffness of the insert plate which will tend to focus the deformation more dramatically in the tear region. In the actual containment, the strain concentration would probably be further

accentuated by the liner studs that attach the liner to the concrete. Around the areas of the insert plate the studs are at 2 in. (51 mm) centers. Hence the local liner deformation predicted numerically could be further concentrated over just a 2 in. (51 mm) distance.

From an axisymmetric analysis alone, there is no way of inferring the concrete in the experiment would be heavily cracked in the observed region and hence no way of predicting the local liner strain concentration arising from the cracking.

Basemat Uplift

From Figure 5.7.8, the predicted uplift from the three new analyses (1, 2 and 3) are all less than the previously predicted values. However, it is difficult to discern which, if any, are the most viable. Analysis No. 2 incorporating a friction interface and a concrete model embodying a tension stiffening effect would seem to overestimate the experimental displacement at maximum pressure (145 psig, 1 MPa) by possibly 0.08 in. (2 mm). However, interpretation of the experimental results is open to question, as at pressures below 72.5 psi (0.5 MPa), the displacements are negative. Ignoring this anomaly would suggest Analysis No. 1 with a finite concrete tensile uniaxial representation gave a good (extrapolated) comparison with the maximum experimental displacement. If Analysis No. 1 is valid, it would suggest that it is not necessary to model the stiffness of the floor slab.

Intuitively, Analysis No. 2, which incorporates a friction interface between the basemat & floor slab and a concrete model possessing a tension stiffening effect, would seem to be the most viable model. This model would give a fair, though understiff, representation of the maximum experimental displacements, if the latter were zeroed and the maximum displacement increased by ≈0.02 in. (0.5 mm).

Tension stiffening would seem to provide the most realistic representation of reinforced concrete, and is more defensible than a perfectly-plastic uniaxial response. The use of an elastic-perfectly plastic response may be justifiable for concrete under high confining pressures, where concrete is known to manifest ductile behavior before fracture.

As mentioned in Section 5.7.3.2, Analysis No. 2 incorporates, for numerical reasons, a small finite post-yield concrete tensile strength of 72.5 psi (0.5 MPa). This may have augmented the increased stiffness imparted by the floor slab to give the reduced basemat uplift, compared to SRD's original analysis.

The difference in response of modelling the floor slab with an interface or a rigid attachment can be ascribed to the integral bending stiffness of the former being less than the latter. Along the interface, both the floor slab and basemat share a common curvature. The bottom face of the floor slab will be in tension and hence prone to cracking, which will reduce its stiffness. Therefore it behaves as a beam with reduced stiffness lying atop of another beam, instead of one thick beam of basemat and floor slab combined with the floor slab thickness lying in the compressive (concave) curvature part of the beam.

With a rigid attachment, the floor slab is more prone to tensile membrane effects. Under internal pressurization, the walls are pushed out and hence apply membrane forces to the basemat which are then transmitted directly to the floor slab to cause

cracking. However, these tensile membrane stresses are small compared to those of bending.

It is not possible with these analyses to ascertain the effect of non-uniform contact pressure loading on the basemat uplift. Shell elements were used to represent both the basemat and floor slab and hence no vertical (contact) stresses are available. The contact forces in the gap elements in Figure 5.7.9 reveals little about the contact pressure. If F is the integrated contact force,

$$dF = 2\pi r \cdot P \cdot dr$$

and if P, the contact pressure were uniform, then $F \propto r^2$, which is similar to the form of the curves in Figure 5.7.9. Similar forms of curve can be obtained, if e.g. $P \propto r$, in which case $F \propto r^3$. The reason the contact force in Figure 5.7.9 declines slightly at the floor slab edge is unknown, but is thought to be a numerical artifact.

In practice, if the floor slab were to be substantially cracked along its bottom face, it could be expected that the nitrogen gas pressure would enter the fissures to provide an upthrust on the floor slab, which might wholly or partially negate the downward gas pressure on the top face. Consequently, there would be a net downward thrust on the basemat and the floor slab would not contribute a stiffness.

### 5.7.7 Conclusions

A simple numerical representation of a section of the Sandia reinforced concrete containment has been analyzed. The analysis has demonstrated, provided heavy localized concrete cracking has occurred, that the liner material attached to this area of concrete is capable of locally reaching high strains that are not much less that the strains at the ultimate tensile strength.

In SRD's original analysis, it has been shown that it was not a valid judgement to assume the floor slab had minimal effect on the performance of the basemat uplift. The floor slab should have incorporated a bending stiffness with a sliding interface between basemat and floor slab. However, as we are unable to make a direct comparison with our original analysis there is the possibility that other factors other than the incorporation of a floor slab provide a stiffening effect. Such an effect may be due to incorporating a finite, but low, post-yield concrete tensile strength.

### 5.7.8 Acknowledgements

SRD is grateful to Sandia for the extensive data supplied by them and for the opportunity to undertake this analysis. The author would also like to thank L. P. Harrop for his useful comments in the preparation of this text.
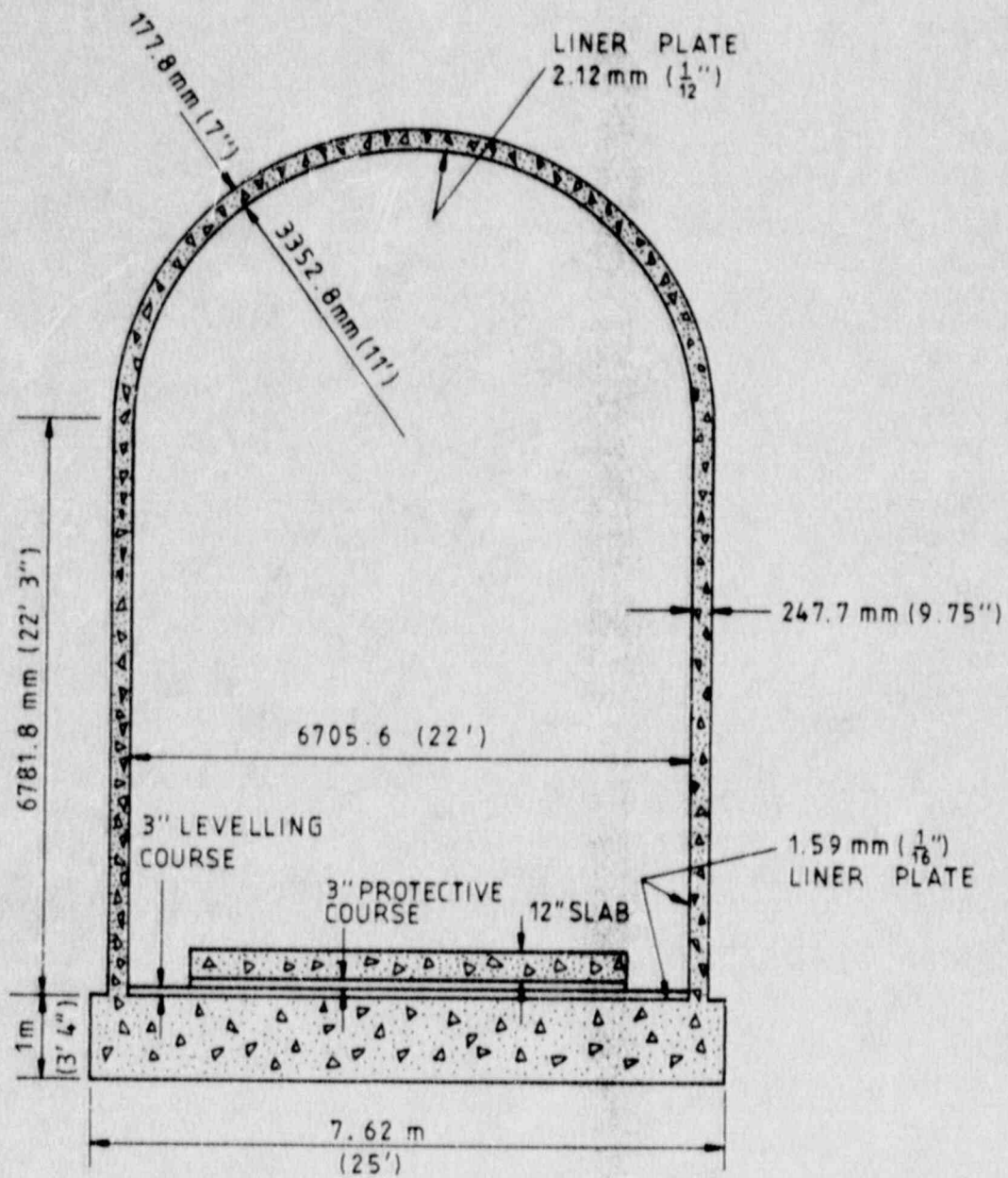
Figure 5.7.1 Schematic Diagram of the Sandia 1:6-Scale Model

CONCRETE CRACKED
IN THESE TWO REGIONS

11' RADIUS

INSERT PLATE

PRESSURE

REBAR

CONCRETE

$\frac{1}{16}''$ LINER ON
INNER SURFACE

2

1

REBAR DETAILS
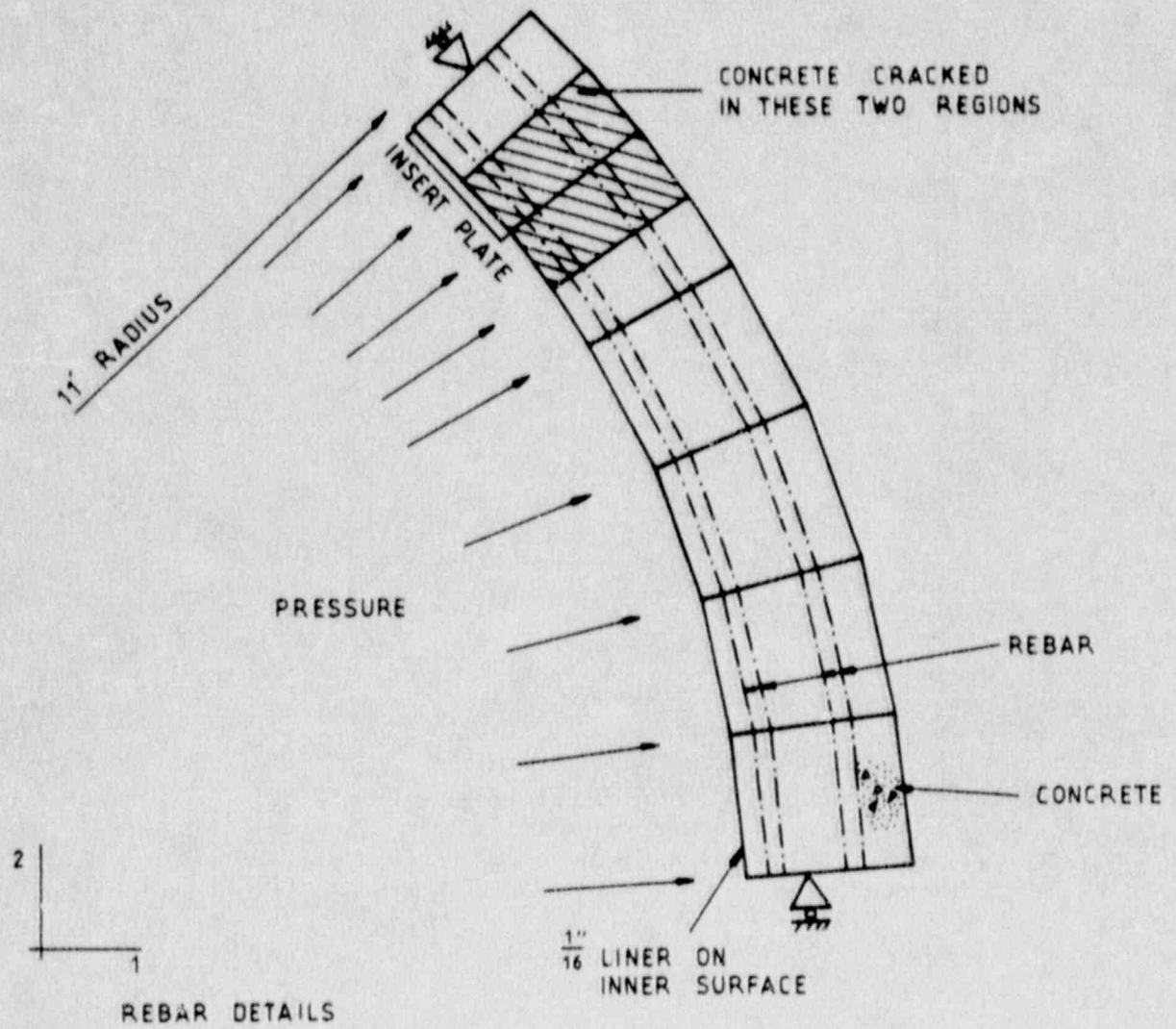
Figure 5.7.2  45° Section of the Containment Wall

FOLDED - OUT ELEVATION (ELEMENT & NODE NUMBERING)

APPLIED PRESSURE LOADING

PLAN
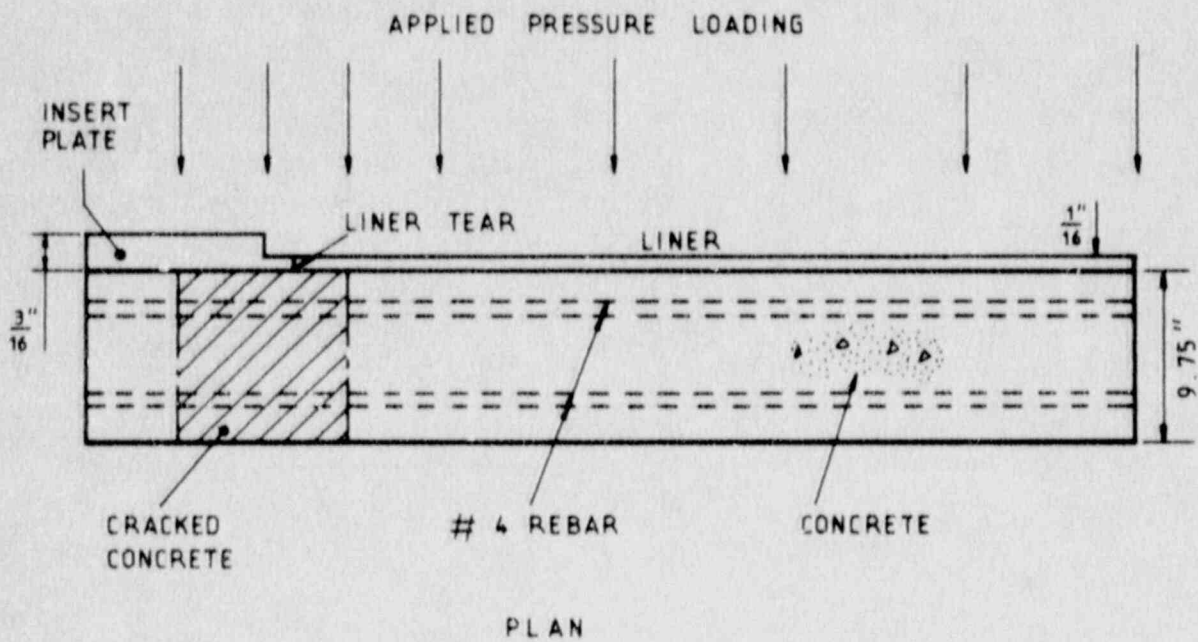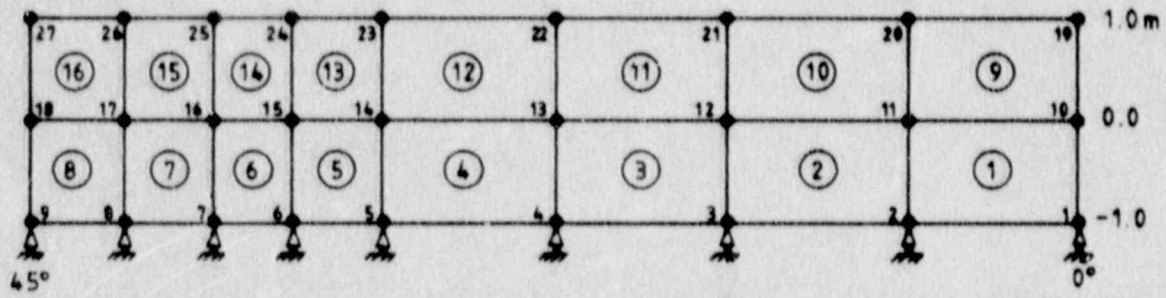
Figure 5.7.3 45° Modelled Section of the Containment Wall
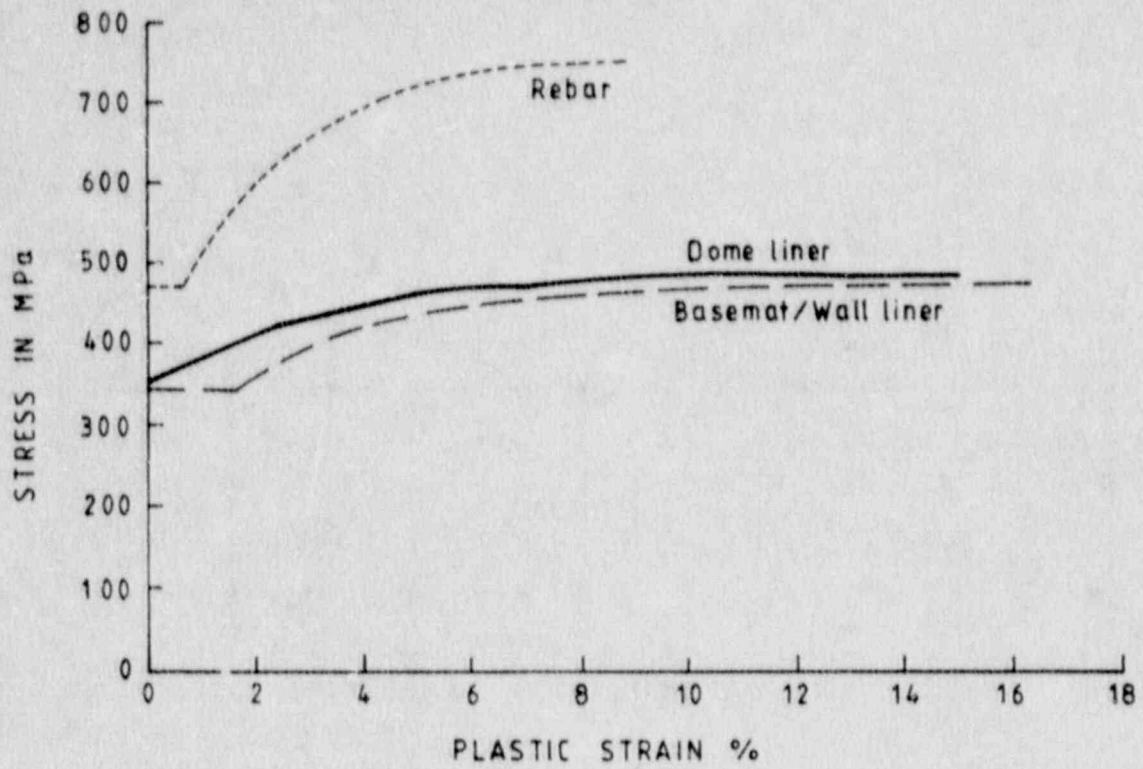
Figure 5.7.4a  Uniaxial Steel Stress-Strain Curves
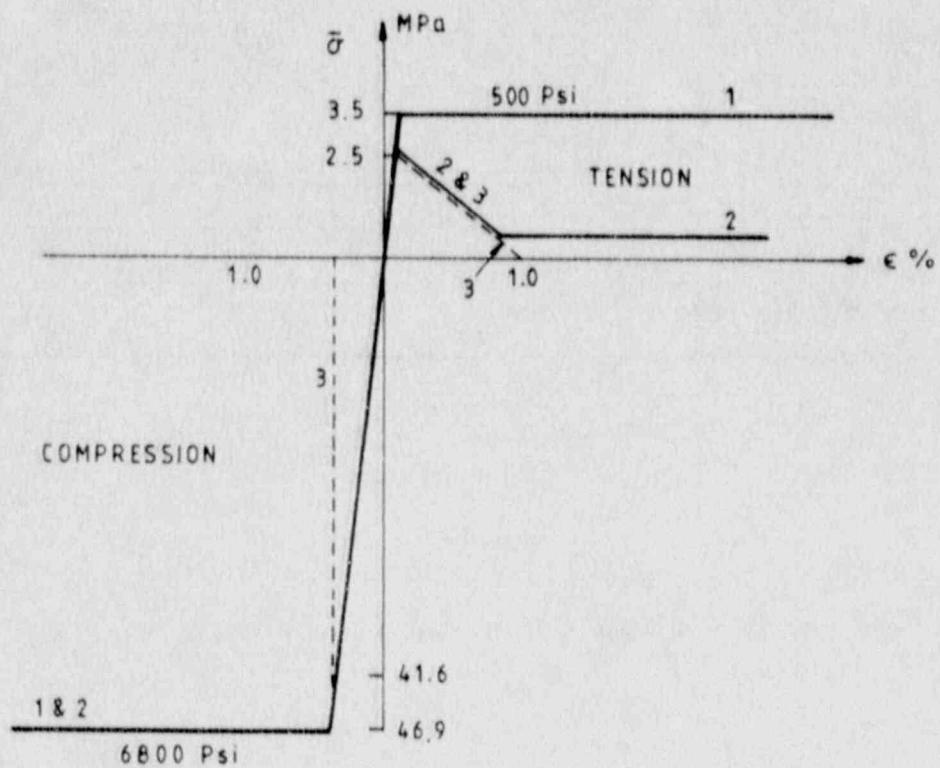


Figure 5.7.4b  Uniaxial Concrete Stress-Strain Curves
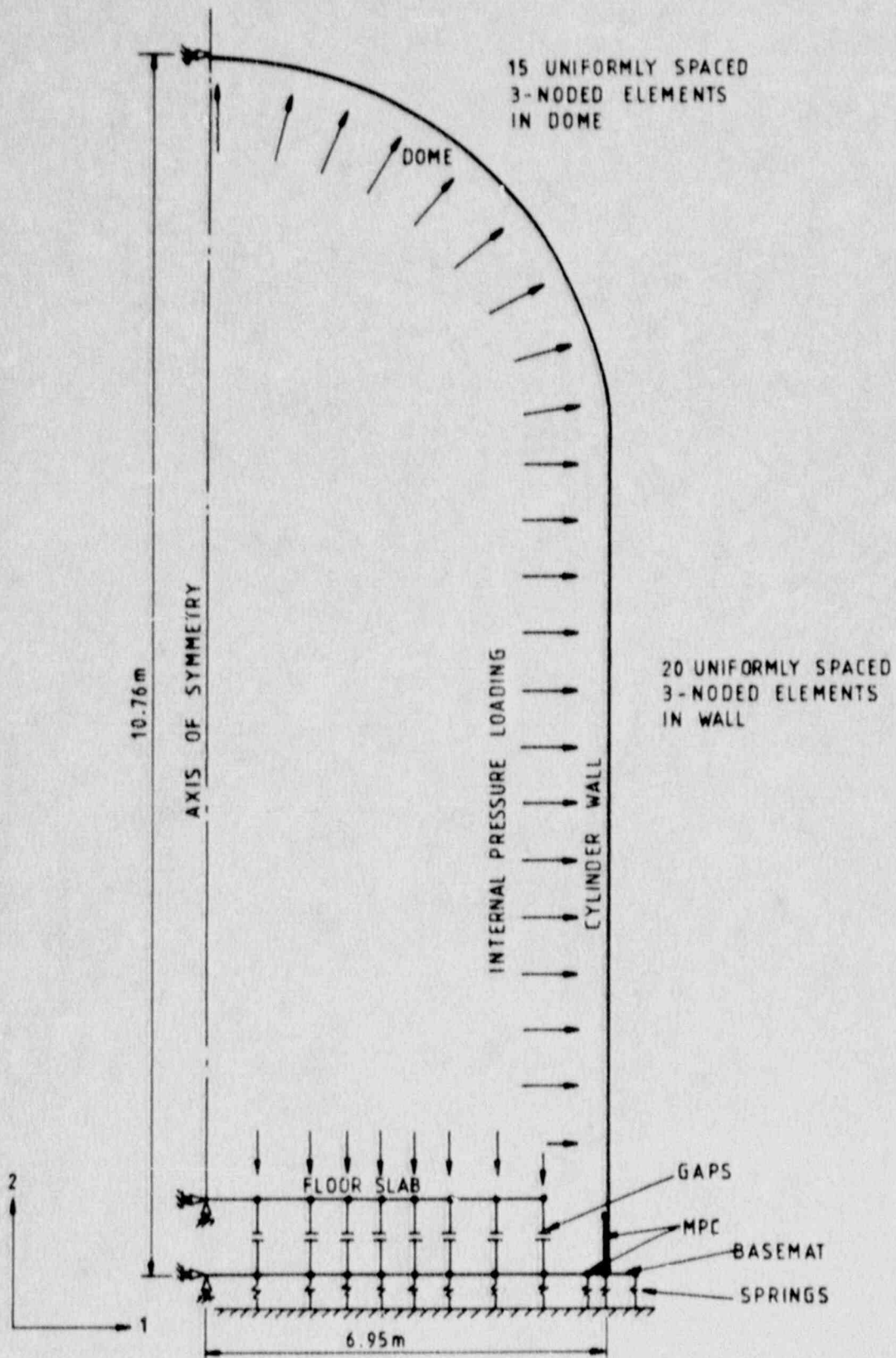
Figure 5.7.5 Axisymmetric Shell Model Showing the Floor Slab Representation
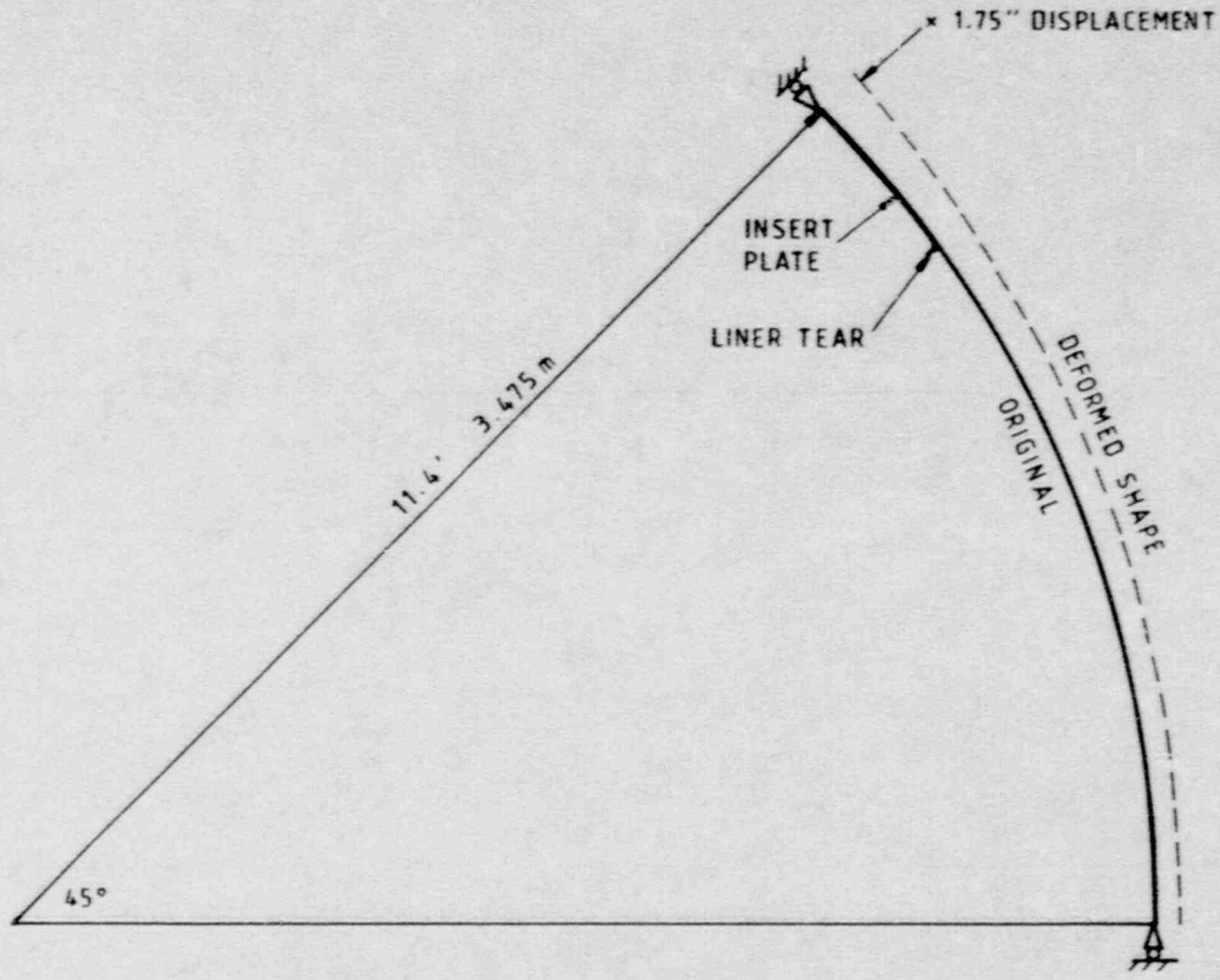
Figure 5.7.6  Displacement of 45° Section of the Containment Wall

LINER HOOP STRAIN (%)

10  9  8  7  6  5  4  3  2  1

45°

FOLD-OUT OF 45° SECTION

45°  c  0

CONTAINMENT WALL

0°

LINE TEAR

3/16 th INSERT PLATE (4.76 mm. THICK)

1/16 th LINER (1.73mm THICK)

CONCRETE (CRACKED (MODELLED AS A NO TENSION MATERIAL)
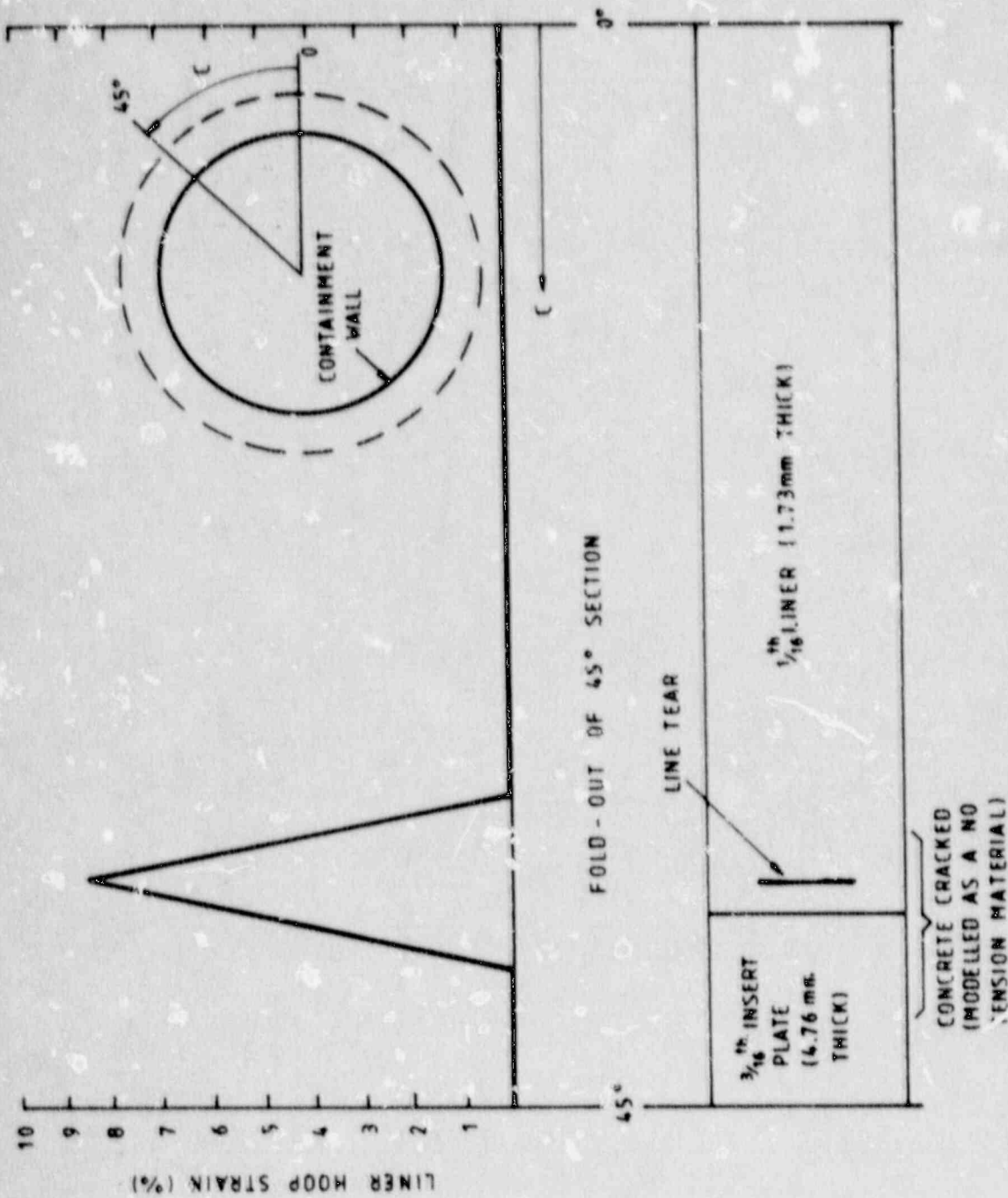
Figure 5.7.7 Liner Strain at Mid-Cylinder Height at Approximately 1.75 in. Maximum Radial Displacement
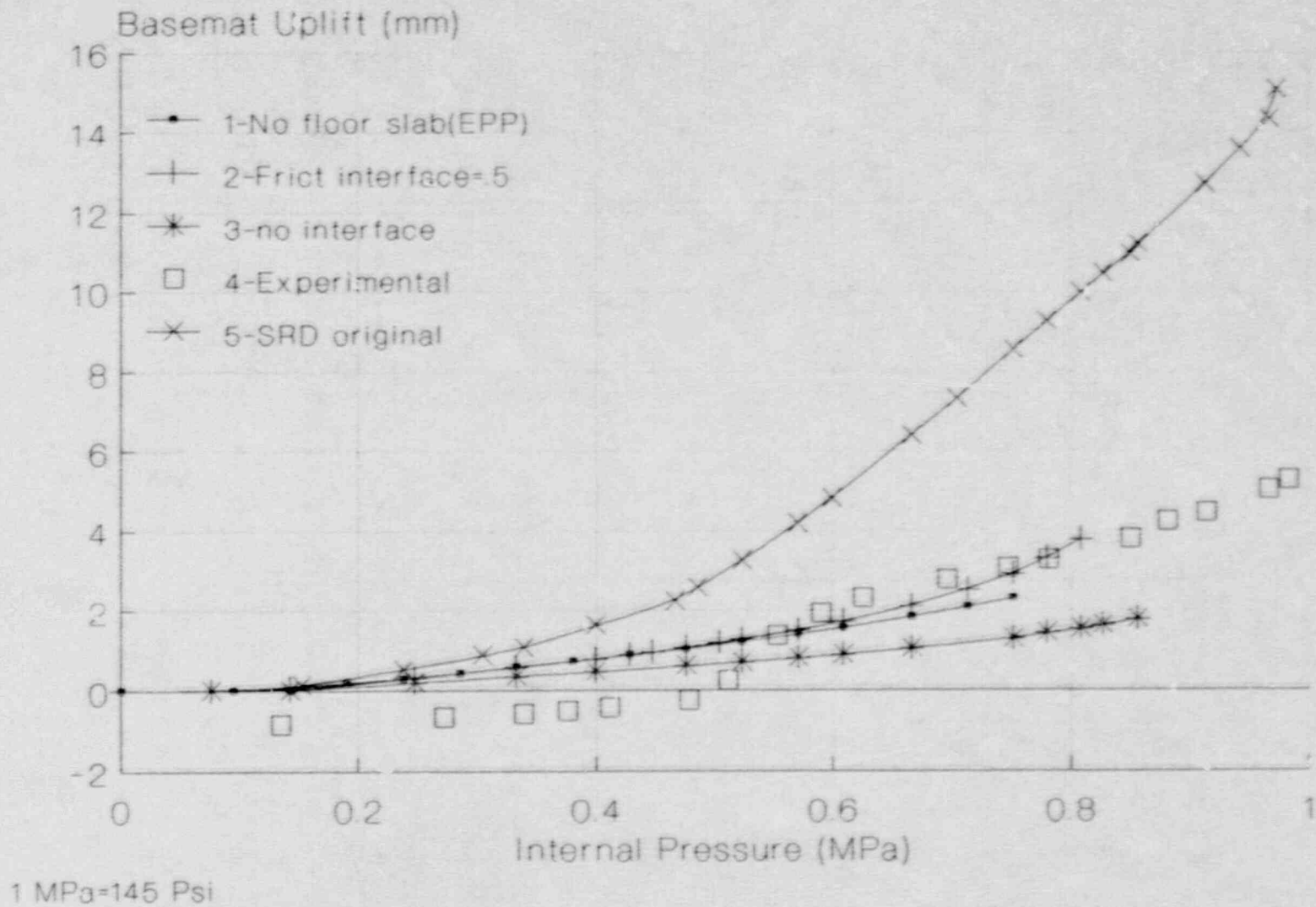
Figure 5.7.8  Basemat Uplift at Cylinder Wall Junction Relative to Basemat Center
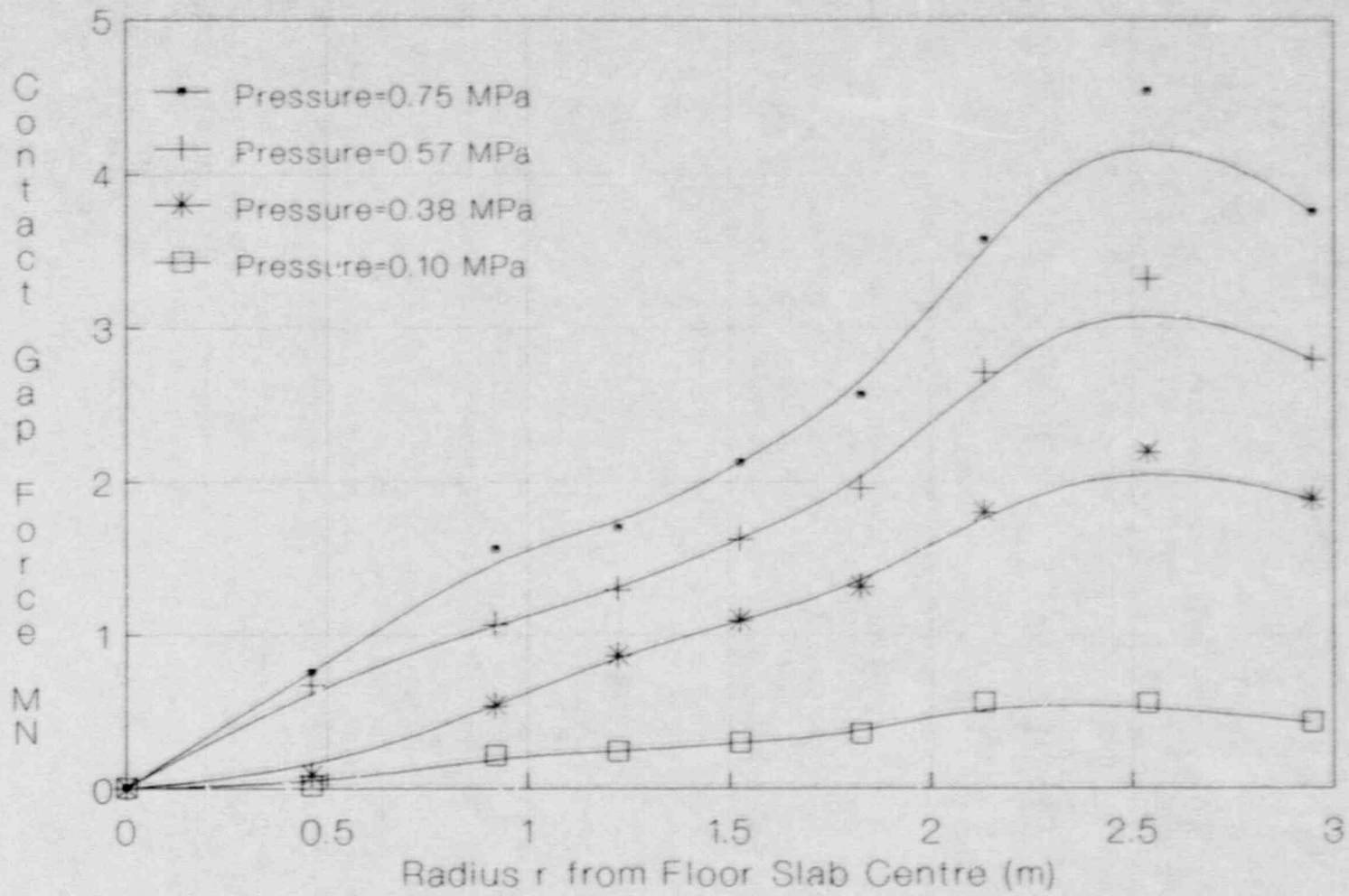
Figure 5.7.9 Contact Force Distribution at Interface of Basemat and Floor Slab

## 5.8 Gesellschaft für Reaktorsicherheit

This section was authored by P. Bachmann, P. Gruner, W. Kuntze and H. Schulz of Gesellschaft für Reaktorsicherheit, and J. Eibl and F.-H. Schlüter of the Institut für Massivbau und Baustofftechnologie, Universität Karlsruhe

### 5.8.1 Summary

Posttest investigations of a 1:6-scale lined and reinforced concrete containment model which was subjected to internal pressurization at the Sandia National Laboratories in July 1987 are reported. Measures employed to trace and to reduce deviations of pretest analysis results from the experiment are discussed.

A considerable amount of our investigations was devoted to gather the reasons which have led to the enhanced analytical response for basemat uplift.

To validate the analytically predicted strains of reinforcement an estimation of scattering of rebar strains due to cracks in concrete was performed.

The problem of accounting for strain concentrations in the liner at geometric irregularities was approached by employing section models for the respective structural area where the major tear in the liner was discovered after the test. The assessment of local liner tearing on grounds of computed strains was supported by experimental studies of the posttest phase performed at the University of Karlsruhe.

The numerical analyses and the supplementary tests were sponsored by the Bundesminister für Forschung und Technologie (BMFT) to whom the authors express their gratitude.

### 5.8.2 Introduction

Pretest analysis results of the structural behavior of the 1:6-scale lined and reinforced concrete containment model, which was subjected to internal pressurization at the Sandia National Laboratories in July 1987, were presented in a number of reports [11,51,52].

Although the predictions obtained with an axisymmetric finite element model of the containment met to a large extent the global performance of the structure in the test, further investigations were considered worthwhile to trace causes of deviations between test and analysis results at structural positions where agreement was less favorable. The largest discrepancies were found with respect to deformations of the basemat and of the dome. Here the measured displacements were overestimated by the pretest analysis by a factor of two to three, depending on the pressure level where data are compared. Hence, a considerable amount of effort was devoted to gather the reasons, which have led to the enhanced analytical response. To trace the causes of the discrepancies, anticipated effects were studied by employing simplified analytical tools. From these investigations it was found that the interaction between a one foot thick concrete mat on top of the basemat and the basemat is mainly responsible for the deviations. In the pretest model this interaction was not considered. Accounting for this effect in an analysis with the finite element model of the pretest computations yields with respect to test results significant improvements of calculated deformations of the basemat and of displacements of the dome apex as well.

A further topic to be dealt with in the posttest studies concerns the comparison of computed and measured strains of reinforcement that is embedded in cracked concrete. Strain measurements may be influenced to some extent by concrete cracks that cross the reinforcing steel in the vicinity of strain gages. To qualify the analytically predicted strains, it is important to know the range within which measured respective data might scatter. Estimations of possible bandwidths show that computed strains are located to a large extent within the scattering bands.

The high pressure test was terminated at a pressure of some 1 MPa (145 psig); pressurization could not be continued due to increased formation of leakage paths through the liner. After the test, a major tear in the liner was discovered near an edge of a thickened portion (insert plate containing penetrations) in the liner shell. Since geometric irregularities cannot properly be modelled with a highly symmetric idealization, the strain levels as computed with the axisymmetric model are too low to indicate liner failure within the pressure range which was scanned during the test. To account for strain concentrations at geometric irregularities, the problem was approached employing section models for the respective structural area. To distinguish strain contributions due to changes in liner thickness from strain concentrations at studs, which are restrained by embedment in concrete, plane stress finite element models were used. The boundary conditions and the deformations applied to the section models were chosen to reflect the as-in-the structure states. Strain enhancement factors as functions of deformation are derived, which can be related to internal pressure. The results are compared to failure strains as obtained from biaxial tests as well as to uniaxial ultimate strain data considering multiaxial stress conditions in the vicinity of a stud.

To predict with the plane stress model a-posteriori liner failure as it occurred during the test near 1 MPa (145 psig), it is necessary to estimate the dependence on internal pressure of liner deformations. This was attempted by use of a plane strain finite element model of a containment wall section that was composed of the liner and of supporting concrete as well as of the embedded reinforcement and which accounted for the coupling between the liner and the concrete via the action of a stud. Due to numerical difficulties the results of this investigation were however restricted to some 0.83 MPa (120 psig). Elimination of the causes responsible for the diverging results and resumption of the studies were beyond the budget scope.

Hence, a somewhat less sophisticated approach is presented to obtain an approximation to the pressure-deformation relationship. This analytical model allowed for the combined action of in-plane liner forces and forces in the hoop rebars as well as in the seismic reinforcement. Concrete was regarded as being a compression/no tension material. The liner/stud interaction was described parametrically.

The experimental studies of the posttest phase were performed at the University of Karlsruhe. They are intended to yield failure envelopes under biaxial strain conditions for the liner steel. The results of these tests serve as references for the assessment of liner tearing on grounds of computed strains. Further experimental investigations are related to the reduction of the load carrying capacity of rebars that are terminated within concrete when the bonds between steel and concrete deteriorate on account of lateral straining. The latter tests yield valuable information for the evaluation of the ultimate strength of reinforced structur'    .ons such as

the cylinder basemat transition region. The test results are presented in Section 5.8.8.3.

### 5.8.3 Investigations to Improve the Calculated Response of the Basemat

From the comparisons of analytical and experimental results for strains and displacements of the 1:6-scale containment model was deduced that one of the major deviations from measurements consists in the calculated displacement behavior of the basemat, as previously stated. The computed vertical displacement difference between a position near the cylinder-basemat junction and the center of the top surface of the fill slab overestimated the measured response. There are a variety of causes that might be responsible for this discrepancy, such as, too low stiffness of lower bending reinforcement; too soft soil reactions; and interactions between fill slab, protective course, leveling course and liner bottom as well as between basemat and mudmat. The effects of the fill slab and the mudmat were not accounted for in the pretest analysis model. The impact of these model features on the structural behavior will be dealt with in the next paragraphs.

### 5.8.3.1 Effects Contributing to the Bending Stiffness of the Basemat

To evaluate the influence of some of the effects mentioned above on the bending behavior of the basemat, the single contributions were estimated using approximations based upon simple elasticity concepts. As a criterion to check the relative importance of an effect, the level of internal pressure at which cracking at the lower basemat starts, i.e., when tensile stresses reach the tensile strength of concrete, was used. The following assumptions were made:

- Below the elastic limit of concrete, strains in concrete and strains in the lower bending reinforcement are assumed to be equal.

- The states of deformation at the rebars have central symmetry.

- The bending moment and the shear force at the cylinder-basemat junction are assumed to be equal to those of a long clamped cylinder subject to internal pressure.

Balancing radial moments with respect to the center of the basemat yields a formula to determine the amount of critical internal pressure, $P_{cr}$, at which cracking at the lower surface of the basemat is initiated (see Section 5.8.8.1). Application of this method helps to quantify the influence of various modelling conditions on the critical pressure, as may be seen from the following summary:

(a) Neglecting contributions of the fill slab and of the levelling and protective courses yields a critical pressure of 0.349 MPa (50.6 psig).

(b) Assuming the conditions as in (a) but increasing the cross-section areas of rebars of the bending reinforcement by a factor of two leads to a critical pressure of 0.370 MPa (53.7 psig).

(c) Taking into consideration the stiffening of the basemat due to the interaction with the fill slab and the courses by use of an effective thickness for the basemat, the critical pressure amounts to 0.575 MPa (83.4 psig).

These considerations suggest that the influence of the bending reinforcement on the bending stiffness is rather small. Hence, errors in modelling the stiffness of the reinforcement, which might arise from transforming a rectangular mesh of rebars into an equivalent assembly of radial rebars and hoop rebars (as required in the case of an axisymmetric model), do not have a significant impact. On the other hand, contributions due to the fill slab affect the overall bending behavior of the basemat to a large extent. The approach used to determine the influence of the fill slab tends, however, to overestimate the effect. The magnitude of tangential forces transmitted through the interface between fill slab and liner bottom will be limited by the contact friction. If the friction force is exceeded sliding along the contact surface will occur. To estimate $P_{cr}$ due to friction the formula in the appendix had to be extended slightly.

Based upon the conditions of (a) the interaction between fill slab and basemat was modelled by tangential frictional forces which act at the top surface of the basemat (see Figure 5.8.1). The method considers in a simplified model the dependence of the frictional forces on the internal pressure, assuming that the contact pressure is nearly uniform and equal to the internal pressure. The coefficient of friction was estimated to be 0.38 according to values reported in [61] for friction of concrete against steel. The critical pressure $P_{cr}$ amounts to 0.507 MPa (73.5 psig) in this case.

A similar estimation of the influence of friction between basemat and mudmat showed that major changes of $P_{cr}$ do not occur, because the normal forces due to the weight of the structure are much smaller than the normal forces due to internal pressure at levels of some 0.5 MPa (72 psig) and higher.

From these results it was concluded that a major improvement in the calculations for the performance of the basemat could be expected if, in the finite element model that was used for the pretest analyses, the interaction between fill slab and basemat is represented by use of frictional effects.

Results of such a finite element analysis are discussed later.

### 5.8.3.2 Studies of Basemat Uplift

At the University of Karlsruhe, the mechanisms of basemat uplifting were studied by varying structural elements of a basemat model. The axisymmetric section model of the 1:6-scale containment consisting of the basemat with soil spring foundation beneath, the 1 foot (305 mm) thick fill slab above, and parts of the lower cylindrical wall is shown in Figure 5.8.2. The fill slab is connected to the basemat by an orthotropic interface that has reduced stiffness in horizontal direction. The model calculations considered mainly variations of steel reinforcement, soil springs, and relevant material properties of concrete. The results of the various numerical analyses are shown in Figure 5.8.3 and are discussed as follows.

The measured displacements of basemat uplift relative to its center with increasing internal pressure are denoted by "experiment" in Figure 5.8.3. As the experimental curve starts with small negative displacement values, which seems to be somewhat unrealistic, the experimental curve was shifted in parallel translation to a zero value of displacement for zero pressure. This shifted experimental curve was taken as a basis for comparisons with numerical results.

The uppermost curve (1) represents the result of the pretest analysis, GRS 87. Major deviations from the experiment are evident; these deviations increase rapidly after the beginning of heavy cracking in the basemat at about 0.4 MPa (57 psig). In the axisymmetric model of the 1:6-scale containment that was used in the pretest analyses by GRS the basemat was modelled with all relevant reinforcing steel - in particular the upper and lower bending reinforcement - without considering effects of steel concrete interaction as it was done in the containment shell. The fill slab and the mudmat were not considered in the model GRS 87. The basemat was founded on soil springs with a total spring constant of $K = 7.5 \times 10^2$ MN/m ($4.28 \times 10^6$ lb/in.).

The results of parametric studies at University of Karlsruhe concerning the uplift of basemat are exhibited in Figure 5.8.3 as curves no. 2 to 5 and 7 to 10. Table 5.8.1 denotes the legend to these curves describing in short terms the structural variations performed at the basemat model shown in Figure 5.8.2. In the first parametric calculation (curve 3), not considering resultant forces at the cylinder-basemat junction but using a basemat model with fill slab, the final uplift at 1.0 MPa (145 psig) was nearly cut in half in comparison to the pretest analysis curve 1 (GRS 87), which did not consider the fill slab. As compared to the experimental findings, however, this final value is still too large by a factor of almost 3.

The first calculation (curve 3) was done using a bilinear elastic-plastic material model for the steel reinforcement. Considering the tension stiffening effect by modelling the interaction of steel and concrete after cracking of concrete by a modified stress-strain behavior of reinforcing steel [44] led to curve 2, in which only a slight alteration of the steep slope after beginning of cracking was observed. The displacement values for curve 2 are virtually identical to those for curve 3 at pressure levels above 0.5 MPa (72 psig). The parametric variations show that the displacement values of uplift become smaller with increasing stiffness of soil springs, as indicated by curves 4, 5, 7. An enhancement of the shear stiffness of concrete has the same effect. As the basemat is stiffened by the parameter variations the initiation of first severe cracking in the middle region is postponed to higher internal pressures as can be seen in Figure 5.8.3. The height and the slope of the step differ only slightly when it is shifted.

Curves 8 and 9 were obtained by incorporating into the analysis the restraining moment and lateral force acting at the junction of cylinder and basemat. Curve 8 results from a rather rough estimation of the moment. Curve 9 represents a more precise consideration of the restraining moment and lateral forces that are produced by internal pressure and prescribed displacements as obtained from linear analysis acting on nodal points at the lower cylindrical wall. By all these efforts in modelling realistic basemat behavior a strong improvement in agreement of numerical and experimental results was achieved: the maximum uplift at a pressure of 1.0 MPa (145 psig) was reduced from some 28 mm (1.1 in.) in curve 1 to 9 mm (0.35 in.) in curve 9, which is reasonably close to the maximum value of about 6 mm (0.24 in.) measured in the experiment. In spite of this, there remain major deviations between numerical and experimental curves. This is especially true for the distinct flat slope of displacement step measured in the experiment when enhanced crack spreading occurred; this feature of the experimental curve could not be matched satisfactorily by any of the performed analyses.

Table 5.8.1
Basemat Uplift Relative to Center of Basemat
Parametric Studies by University of Karlsruhe
Legend to Figure 5.8.3

Curve     Description

3     basemat with steel reinforcement (linear elastic-plastic)
      soil springs $K_1 = 1.16 \times 10^4$ MN/m ($6.62 \times 10^7$ lb/in.)
      fill slab with reinforcement on an orthotropic interface, reinforcement of
      mudmat considered

2     same as 3
      "tension stiffening" of steel reinforcement considered

4     same as 2
      soil springs $K_2 = 7.5 \times 10^2$ MN/m ($4.28 \times 10^6$ lb/in.)
      shear stiffness parameter of concrete (shefac) increased from 0.2 to 0.5
      reinforcement of mudmat at lower nodal points of basemat

5     same as 4
      soil springs $K_1 = 1.16 \times 10^4$ MN/m ($6.62 \times 10^7$ lb/in.)

7     same as 4
      rigid foundation

10    same as 3
      lower bending reinforcement increased by a factor of 8.

8     same as 7
      consideration of restraining moment at cylinder basemat intersection

9     same as 7
      more precise consideration of restraining moment by internal pressure and
      prescribed displacements at lower cylindrical wall.

### 5.8.3.3 Modification of Basemat in Global Containment Model

Following the parametric studies of influences on basemat uplift, a modification of
the global axisymmetric model used by GRS for pretest analysis was performed.
Figure 5.8.1 illustrates the modifications of the basemat implemented into the pretest
model GRS 87, now called GRS 88 F.

In the model GRS 87, the stiffness of the orthogonal net of rebars of the lower
bending reinforcement was distributed nearly uniformly to the circumferential ring
trusses and longitudinal trusses in radial direction of the axisymmetric idealization.
Now the lower bending reinforcement of the basemat of posttest model GRS 88 F

consists mainly of ring trusses standing for hoop reinforcement, whereas the stiffness of radial rebars is negligible. Hence, the in-plane stiffness of the orthogonal net of lower bending reinforcement was nearly completely simulated by using ring trusses in the representation of the axisymmetric model GRS 88 F. The stronger ring trusses produce a stronger confinement of concrete near the center of the basemat resulting in a shift in the initiation of hoop cracking of concrete to higher pressures. The overall influence of the bending reinforcement upon basemat uplift was found to be rather moderate as was already discussed in section 5.8.3.1

In the pretest model GRS 87, the 1 foot thick fill slab resting on the basemat with intermediate concrete courses protecting the bottom liner was not modelled at all. In the posttest model GRS 88 F, the reactions between fill slab and the basemat were considered by frictional forces acting on the upper surface of the basemat as indicated in Figure 5.8.1. The friction forces are determined as a function of internal pressure acting upon the fill slab. A friction coefficient of 0.38 was chosen for friction of concrete against steel [61], i.e., between fill slab and liner bottom including protective and leveling courses.

In the basemat model the horizontal friction forces were assigned to nodal points of the basemat liner according to the respective portions of surface area. By this means a moment that tends to diminish the uplift of the basemat is generated.

The result of posttest analysis with the modified model GRS 88 F is shown in Figure 5.8.4. In comparison to pretest analysis GRS 87, an evident improvement in the approximation of the experiment can be recognized. The final value of uplift at a pressure of 1.0 MPa (145 psig) was reduced to less than a half but remains still about double the measured value. The characteristic slope of increasing displacement values is shifted towards the measured position but its height, though diminished in comparison to model GRS 87, is overestimating the slope measured in the experiment. The results from model GRS 88 F are outlined also in Figure 5.8.3 as curve No. 6 and can be compared with the other results of the parametric studies.

If a real structural model of the fill slab would be integrated into the global containment model combined with a stiffer soil model and consideration of the mudmat, a further reduction of uplifting displacements seems to be possible and realistic.

The global behavior of the containment shell was in general not influenced significantly by the modifications in the modelling of the basemat, as shown in Figures 5.8.5 through 5.8.10[9]. Yet, a distinct improvement of the calculated vertical displacements of liner at dome apex, which are related to the upper center of basemat, is observed in Figure 5.8.11. This is a direct consequence of the more realistic displacement behavior of the basemat.

### 5.8.4 Estimations of Scatter of Rebar Strains Due to Cracks in Concrete

Cracking of reinforced concrete is observed to happen preferentially at positions where rebars cross tensile stresses. E.g., hoop cracks begin to form very often at meridional rebars of a concrete cylinder, whereas meridional cracks likewise start at

---

9. The shaded areas are referred to in section 5.8.4.

hoop rebars. Due to the regular arrangement of the reinforcement the spacing between major cracks may be quite constant.

In the space between adjacent cracks the strains in a rebar vary. They reach highest values at positions where cracked surfaces cross the rebar. Thus, measured strain levels may depend on the position of the strain gauge.

In order to judge whether computed strains fit reasonably well measured data, the possible bandwidth of strain scatter should be known. For this reason, the variations of strains along rebars were estimated using experimental experience combined with simple equilibrium concepts. The strains in rebars between cracks may be assumed with good approximation to vary according to a second order parabola like that shown in Figure 5.8.12. Considering a stress state for which the crack pattern is completely formed and requiring balancing of forces (carried by steel only) at the position of a crack with forces in the center between two cracks (carried by concrete and by steel) yields the following upper and lower strain limits:

$$\epsilon_u = \epsilon_m + \Delta\epsilon^+$$

$$\epsilon_l = \epsilon_m - \Delta\epsilon^-,$$

where

$$\Delta\epsilon^+ = (2/3) \cdot (l/s) \cdot \alpha \cdot f_t / (\mu_s \cdot E_s)$$

$$\Delta\epsilon^- = [1-(2/3) \cdot (l/s)] \cdot \alpha \cdot f_t / (\mu_s \cdot E_s)$$

As shown in Figure 5.8.12, $\epsilon_m$ denotes the average strain as measured across the total length s between adjacent cracks, $l$ measures the length over which concrete and steel are bound. The ratio $l/s$ amounts in general to some 0.8. The stresses carried by concrete in the center between cracks are estimated to be some 0.65 (= $\alpha$) of the tensile strength of concrete, $f_t$, well below yield point. Significant reduction of the scattering bandwidth is to be expected above the yield point of the steel reinforcement due to progressing bond deterioration. Young's modulus of steel is $E_s$ and $\mu_s$ denotes the steel content.

As an example upper and lower strain bounds for the hoop reinforcement of the cylindrical section of the 1:6-scale containment model are depicted in Figure 5.8.13. The scatter bandwidth amounts to some $0.9 \times 10^{-3}$ strain.

As may be seen from Figures 5.8.5 through 5.8.10, where computed and measured strains are plotted for various areas of the structure together with the strain bounds, theoretical and experimental data generally agree very well over a wide range of pressure within the limits of uncertainty.

It may therefore be concluded that further modifications of the global model that aim at an even better correspondence between measured and computed strains should not be taken into consideration.

### 5.8.5 Analyses of Strains in the Liner Near an Insert Plate

The axisymmetric idealization of the containment structure applied in pretest analyses was suited to describe the global deformation behavior, but it was not

tailored to investigations of local effects of shell loading with sufficient precision. Thus, the local major tear in the liner that occurred in the high pressure test near a thickened insert plate of the liner could not be predicted with the global axisymmetric model. The strain concentrations in the liner due to geometric irregularities of the structure, which are assumed to have caused the major liner tear, shall therefore be investigated in this posttest phase of analyses by means of appropriate section models of the relevant local liner region.

The insert plate of interest is located at cylinder midheight between Equipment Hatch A and Personnel Airlock A and has a wall width three times larger than the surrounding free-field liner sections. The major liner tear formed along the vertical edge of the insert plate (on the side nearest to Equipment Hatch A) reaching a total length of about 50 cm (20 in.). Enhanced straining is expected due to the change in wall thickness of adjacent liner sections. Further straining may be anticipated due to neighboring studs and concrete hoop cracks as well. Figure 5.8.14 depicts the local assembly of structural parts in the relevant liner region. In the drawing, it is assumed that a hoop crack was initiated at the position of a meridional rebar.

Because of these features, an enhancement of strains with respect to free-field liner straining can be expected in the thin liner sheet between the edge of the insert plate and the adjacent liner stud.

In the following three paragraphs the potential for liner tearing due to the mentioned structural inhomogeneities is evaluated employing two-dimensional finite element analyses of the respective liner section.

## 5.8.5.1 Investigation of Strain Enhancement Due to Local Stud Effect

The effect of strain enhancement in the vicinity of studs is analyzed with a plane stress model of the relevant liner region including the influence of the insert plate. The finite element mesh of approximately one-half of a relevant stud field with spacing 50 x 50 mm (2 x 2 in.) is shown in Figure 5.8.15. Two similar models were investigated; they are distinguished with respect to boundary conditions, which simulate either the presence or the absence of a localized stud in the corner of the modeled rectangular liner sheet where the mesh is refined. Thus, strain values with and without stud effects can be obtained for comparison. The different wall thicknesses of the thin liner where the stud is located and the thick insert plate with a chamfered edge are shown in Figure 5.8.15. The axes of the model coordinate system coincide with the circumferential (y-axis) and meridional (z-axis) directions of the global containment structure. The long side of the models with a length of 50 mm (1.97 in.) reflects the spacing between two stud locations in the structure, whereas the length of the short side is one-half of this distance. The boundary conditions of the models are as follows:

- The short side with or without stud represents a rigid boundary. This means that in the model with stud, the circular footing of the stud is also rigid.

- The long edges are clamped allowing displacements only in y-direction of the global coordinate system (see Figure 5.8.15)

For the thin liner sheet of 1.59 mm (1/16 in.) between stud and insert plate the material curve shown in Figure 5.8.16 is used as obtained from material tests by

Sandia. The stress-strain relationship is characterized by a distinct yield plateau between strain values from about 0.18% to 1.8%. This stress-strain curve is described in the analysis by the multilinear elastic-plastic material model available in ADINA [53]. For the thick insert plate itself a linear elastic material model is used. The modeled liner section is loaded in circumferential y-direction by prescribed displacements acting upon the short side of the insert plate opposite to the stud location. In the meridional z-direction total strains are assumed to be zero. This assumption seems to be justified by an evaluation of liner strains in the global containment structure resulting in a ratio of circumferential to meridional strains of about 8:1. The loading function of displacements applied to the modeled liner section is shown in Figure 5.8.17 as a function of internal pressure. It was obtained from the strain results of the global axisymmetric containment analysis at liner midheight. At the pressure of 1.0 MPa (145 psig), where liner failure occurred in the high pressure test, the displacement prescribed to the liner section model amounts to a value of about 0.6 mm (0.024 inch).

When the liner model without stud is loaded in this manner with a certain displacement value it strains uniformly. The deformations of the modeled liner sections without stud are demonstrated in Figure 5.8.18 when loaded with a displacement of 0.6 mm (0.024 inch).

Strains in y-direction are plotted in Figure 5.8.19 over the y-coordinate values of the liner section model. The corresponding loading pressure is marked as legend to the curves. If no stud is present, mainly two different strain levels can be distinguished over the whole modeled liner section. In the region of the insert plate the steel material remains elastic and the strain level is very low. Higher straining is recognized in the thin liner sheet where the yield point of the 1.59 mm (1/16 in.) liner material is already exceeded at a pressure loading of 0.8 MPa (116 psig). There is no variation in strain level over the whole lateral area of thin liner as stated before, that is, in this case of uniform structure and loading the strain value is only a function of wall thickness. The presented results for the elementary model of a liner section without stud serves as a basis for comparisons with the findings from the analogous model containing a local stud, which will be discussed in the following paragraph.

The deformations of the liner section with stud are shown in Figure 5.8.20. The model is again loaded with the prescribed displacement value at failure pressure of 0.6 mm (0.024 in.) as it was done with the liner model without stud according to Figure 5.8.17. At first sight there is little difference to be seen between the deformations of the two corresponding models with and without stud. However, in the vicinity of the local stud some deviations in deformations can be distinguished.

Strain development in the vicinity of the stud with increasing displacement loading is shown in Figure 5.8.21. The plot shows 12 curves representing strain values at the integration points of the 4 elements near the stud in the circular mesh pattern (see Figure 5.8.20) following the direction of the y-axis at the long side of the liner section. In the linear range at strain values not over 0.18% the straining of all studied elements is nearly identical. At 0.2 mm (0.008 in.) prescribed displacement, where the end of yielding is reached, the strain values come close together for a value of 1.7% approximately after a first strong enhancement of strains in the element nearest to the stud. Thus, an almost smooth distribution of strains is achieved in the stud vicinity after yielding. The strain hardening region begins with a steep slope of the stress-strain curves causing more divergence with increasing straining. The upper

curve of strains nearest to the stud footing reaches a value of about 11% when the loading displacement amounts to the value of 0.6 mm (0.024 in.).

The distribution of strains around the circular footing of the stud according to the nearest element integration points is shown for certain separate moments of loading in Figure 5.8.22. Highest strains in y-direction are reached obviously at the corner of the quarter stud fixed to the clamped long side of the section model. They diminish continuously to the stud corner fixed to the rigid short side of the model.

The strain field in the liner section model with stud for the displacement loading of 0.6 mm (0.024 in.) is shown in Figure 5.8.23. The arrows of principal strains are nearly completely aligned to the y-direction; orthogonal strains in x-direction cannot be identified because of the clamped edges of the section model. The drawing of strain arrows illustrates the strain concentration in the vicinity of the stud footing. The plot of the stress arrows in Figure 5.8.24 demonstrates in contrast to this that two principal stress directions are developed clearly in the liner section mostly coinciding with the y- and z-directions of the model. In the vicinity of the stud where largest stresses occur a small rotation of principal stress directions can be observed similar to the strain directions, see Figures 5.8.23 and 5.8.24.

The strains along the long side of the section model that is coupled to the stud are presented in Figure 5.8.25, which may be compared to the analogous Figure 5.8.19 of the model without stud. The strain level over the whole area of thin liner sheet is lifted by the local stud effect. The strain enhancement is concentrated at the stud footing where the strain curves raise into a sharp peak (see Figure 5.8.25). At the relevant pressure loading of 1.0 MPa (145 psig) the peak value of strains amounts to about 11% in the thin liner sheet nearest to the stud. When this value is compared to the strain value at the same liner location without stud action, which can be taken from Figure 5.8.19 as a value of about 4.3%, a strain enhancement factor of about 2.5 can be derived. Another comparison can be made to the global strain value of 1.2% in circumferential direction which was calculated by the axisymmetric containment model at midheight of the cylindrical liner. This global strain value is enlarged by a factor of nearly 10 caused by the local stud effect and the interaction of the insert plate with the thin liner sheet.

In general ultimate uniaxial strains will be reduced under multiaxial loading conditions. This well known fact can simply be expressed by use of a factor FAKT:

$$\epsilon_{um} = FAKT \cdot \epsilon_{uu}$$

where $\epsilon_{um}$ is the multiaxial ultimate strain, $\epsilon_{uu}$ is the uniaxial ultimate strain, and

$$FAKT = 2^{1-TF}$$

where TF is the triaxiality factor [54]. For a biaxial loading case, which is relevant to the containment liner, the triaxiality factor TF is determined as a function of the two principal stresses:

$$TF = \frac{\sigma_1 + \sigma_2}{(\sigma_1^2 + \sigma_2^2 - \sigma_1\sigma_2)^{1/2}}$$

where $\sigma_1$, $\sigma_2$ are the principal stresses, which can be calculated from the stress components in y- and z-direction of a structure according to the following relation:

$$\sigma_{1,2} = 0.5 \cdot (\sigma_y + \sigma_x) \pm 0.5[(\sigma_y - \sigma_x)^2 + 4\tau_{yx}]^{1/2}$$

In this way the reducing factor FAKT can be derived from the stress analysis of the liner section model with stud, which can be transformed subsequently into a multiaxial failure criterion.

The evaluation of the triaxiality factor for the element with highest strains next to the stud according to Figures 5.8.20 and 5.8.25 is shown in Figure 5.8.26 as a function of displacement loading of the liner section. For displacement values above 0.5 mm (0.02 in.) the triaxiality factor remains nearly constant at a value of approximately 1.72, which is roughly equal to the ideal value ($\sqrt{3}$) for cylindrical vessels under internal pressure. The resulting factor FAKT is plotted in Figure 5.8.27, leading to a value of about 0.61 for higher displacement loadings. When a uniaxial ultimate strain value of approximately 24% is taken into consideration according to the test values of Sandia for the 1.59 mm (1/16 in.) liner sheets, a multiaxial ultimate strain of about 14% can be determined by this method. This strain value can now be taken as a failure criterion for the biaxially loaded liner sheet in the vicinity of a stud. Going back to Figure 5.8.25, it can be recognized that this strain level is reached in the stud vicinity at a pressure loading of about 1.01 MPa (146.5 psig). According to the loading function of Figure 5.8.17 a prescribed displacement value of 0.65 mm (0.026 in.) corresponds approximately with this pressure. In comparison with the relevant displacement loading of 0.6 mm (0.024 in.) considered so far as corresponding to the critical failure pressure, this would mean an increase of about 8% in global containment loading until initiation of liner failure. An enhancement of circumferential strains at cylinder midheight as obtained from the global axisymmetric containment model would follow from this assumption. This influence could be caused by deviations from the circular deformation shape of a horizontal section of the containment cylinder resulting from the interaction with equipment hatches and airlocks as observed in the high pressure test. In addition the equivalent loading displacement that is consistent with the pressure at which the major tear in the liner actually formed (1 MPa, 145 psig) depends also on the local assembly of the structure in the respective area as will be shown in sections 5.8.5.2 and 5.8.5.3. Also from the considerations presented there, a somewhat larger equivalent displacement of about 0.65 mm (0.026 in.) seems to be more adequate than the value of 0.6 mm (0.024 in.) extrapolated from the global analysis.

The failure strain criterion of 14% determined analytically from the stress state in the liner sheet around the stud can also be compared with experimental results of biaxial liner tests conducted at the University of Karlsruhe (see Section 5.8.8.3). It shall be anticipated here that the correspondence between these two strain values was found to be satisfactory.

The analysis indicates that due to strain concentration in the vicinity of studs and due to enhancement of strains there, which result from geometric inhomogeneities, the strain level in the liner reaches ultimate values at about 1.0 MPa (145 psig). Considering the scatter of ultimate strain data, particularly if they are obtained under multiaxial conditions, and the unavoidable simplifications in analysis models, the calculations proved to be successful in confirming the test result.

### 5.8.5.2 Determination of Liner Deformations with a Section Model of the Containment Wall (FE-Analysis)

Deformations of liner in the vicinity of the major liner tear were further investigated by a supplemental section model that represents a horizontal cross-section of the relevant region of the cylindrical containment wall. The finite element section model is shown in Figure 5.8.28. It is set up in a plane strain formulation with a uniform thickness of all elements of 1 mm (0.039 in.). In this version of a section model the interesting liner stud in the direct vicinity of the major liner tear can be modeled explicitly so that the interaction of all relevant structural parts can be studied. The steel reinforcement is incorporated in the concrete containment wall; the position of the 2 layers of hoop reinforcement and the seismic reinforcement is analogous to Figure 5.8.31.

The material behavior of the liner is the same as described in the section 5.8.5.1 (see Figure 5.8.16). The material data for the modeled stud was determined according to Table 5.8.2 in such a way that the stud behavior is similar to the findings of experimental stud investigations performed by Sandia [55]. The material properties of the steel reinforcement are outlined in Table 5.8.3.

Table 5.8.2  Material Properties of Modeled Liner Stud
Bilinear Elastic-Plastic Material Model with Isotropic Hardening

$E^*$ = 10,280 N/mm² (1490 ksi)  Young's Modulus
$\sigma_y^*$ = 26.5 N/mm² (3.84 ksi)  Yield Stress
$\sigma_m$ = 29.9 N/mm² (4.34 ksi)  Maximum Stress
$\varepsilon_m$ = 0.2  Maximum Strain

The concrete material model of ADINA [53] is used to describe the nonlinear behavior of concrete including cracking and crushing. To define compression failure envelopes as needed for the ADINA concrete model the failure surface as proposed by Ottoson [56] was used. The preparation of input data for the concrete model is specified in [52]. The stud elements are coupled to the concrete elements via a soft transmission layer of elements with the exception of the stud head, which is embedded in concrete. By this means the adapted stud behavior [55] is assured.

The section model is loaded by internal pressure acting on the inner side of the liner so that the liner deformations in the vicinity of the major liner tear can be studied as a function of internal pressure.

Figure 5.8.29 exhibits the deformations in the interesting region of the section model at an internal pressure of 0.83 MPa (120 psig). The bending loading of stud and liner can be recognized, which, in combination with tension loading, leads to an enhancement of strains in the thin liner section between stud and insert plate. The calculation had to be stopped at this pressure level because of numerical problems in the equilibrium iterations so that no results for higher pressures are available with the plane strain model.

The relation between liner displacement and internal pressure up to the pressure level reached of 0.83 MPa (120 psig) is shown in Figure 5.8.30. The liner

displacements were integrated over all liner elements following a central line from the model edge at the insert plate where the next (fixed) stud is located to the middle of the footing of the modeled stud. In this way the displacements plotted in Figure 5.8.30 are the relative displacement values of the liner between two studs with interaction of the insert plate.

This partial result is compared with the result of a simplified analytical investigation of the same problem shown in Figure 5.8.33. The curve of Figure 5.8.30 corresponds with curve DS 24 in Figure 5.8.33. At a pressure level of 0.83 MPa (120 psig) the values of both curves agree well. Slope changes in the curve of the FE-Analysis are not visible since plastification proceeds gradually through several liner elements whereas in the simplified analysis the whole section becomes plastic after yielding is reached instantaneously at any point of the section. As the agreement of both results is satisfactory especially for higher pressure levels over 0.8 MPa (116 psig) the results of the simplified analysis between 0.83 and 1.0 MPa (120 and 145 psig) are taken for further discussion.

### 5.8.5.3 Determination of Liner Deformations with a Section Model of the Containment Wall (Simplified Analysis)

As previously mentioned, the determination of strain levels as obtained from plane stress analysis (see Section 5.8.5.1) is based on prescribed displacements, which are applied to the plane stress model of a liner section. To relate these displacements to the internal pressure history the approach described in Section 5.8.5.2 was used. However, the latter analysis could not be completed for reasons which have been mentioned already. Therefore, the problem was attacked using a method to be presented next.

The model with thickness of 1 mm (0.039 in.) along the viewing direction (Figure 5.8.31) is similar to that of Section 5.8.5.2. However, the stud is replaced by an elastic spring acting at position 2; the other end of the spring is assumed to move radially during pressurization. The space between liner, 2 hoops and seismic reinforcement (radial positions $r_i$, $r_1$, $r_2$ and $r_3$, respectively) is thought of transmitting only compressive forces.

Three sections along the liner are to be distinguished. In section 1, between nodal points 1 and 2, and section 2, between nodal points 2 and 3, the nonlinear stress-strain behavior of the 1.59 mm (1/16 in.) liner sheet is used. Section 3 between nodal points 3 and 4, representing a portion of the insert plate is attributed linear elastic material behavior. The modified elasto-plastic material behavior as described in [11,51,52] characterizes the stress-strain relations for hoop and the seismic reinforcement, respectively. Numerical data of material properties and of geometry are contained in Table 5.8.3.

Based on a kinematic relation and on equilibrium considerations for in-plane stresses of the various sections, strains and stresses in the liner may be extracted. A further relation defines global equilibrium between the applied internal pressure and the balancing forces resulting from stretching of the liner and the reinforcement. The method is outlined in Section 5.8.8.2.

The spring constant was adapted in such a manner that the relative displacements between nodal points 2 and 4 fit the corresponding results that were obtained with the plane strain model (see Section 5.8.5.2) between 0 and 0.83 MPa (0 and 120 psig).

A numerical value of some 1000 N/mm (5700 lb/in.) per unit length was found. This value is comparable with experimental data obtained by Sandia [55].

Table 5.8.3  Data for Simplified Analysis

Geometry:

$r_i$ = 3350 mm

$r_1$ = 3396 mm  $\ell_1$ = 63.5 mm  $d_1$ = 1.59 mm
$r_2$ = 3517 mm  $\ell_2$ = 17.46 mm  $d_2$ = 1.59 mm
$r_3$ = 3565 mm  $\ell_3$ = 33.34 mm  $d_3$ = 4.77 mm
                $\ell$ = 114.3 mm

$A$ = 129 mm$^2$
$\bar{A}$ = 93 mm$^2$

Material Properties:

|  | Liner (Uniaxial) | | Reinforcement (with steel/concrete interaction) | | | |
|---|---|---|---|---|---|---|
|  | | | Hoop Bars | | Equivalent Seismic | |
| $\epsilon$ (%) | $\sigma$ (N/mm$^2$) | | $\epsilon$ (%) | $\sigma$ (N/mm$^2$) | $\epsilon$ (%) | $\sigma$ (N/mm$^2$) |
| 0.0 | 0 | | 0.0 | 0.0 | 0.0 | 0.0 |
| 0.182 | 376 | | 0.0105 | 22.37 | 0.0105 | 22.37 |
| 1.74 | 376 | | 0.013 | 41.47 | 0.015 | 237.6 |
| 3.25 | 443 | | 0.0186 | 91.60 | 0.0925 | 295.0 |
| 7.13 | 495 | | 0.244 | 443.1 | 0.15 | 405.0 |
| 9.54 | 510 | | 1.16 | 501.2 | 0.25 | 440.0 |
| 16.37 | 524 | | 3.0 | 623.8 | 0.5 | 444.0 |
| 20.0 | 525 | | 5.0 | 694.3 | 10.0 | 446.0 |
|  |  | | 7.0 | 724.0 | 15.0 | 448.0 |
|  |  | | 10.0 | 739.0 | 20.0 | 450.0 |
|  |  | | 15.0 | 740.0 |  |  |
|  |  | | 20.0 | 740.0 |  |  |

Young's Modulus of Section 3:  $E = 214000$ N/mm$^2$
Stiffness of spring per unit length:  $k = 1000$ N/mm/mm

Results of this analysis are presented in Figures 5.8.32, 5.8.33 and 5.8.34, showing as functions of the internal pressure the radial displacement, the relative displacements between nodal points 2 and 3 (DS23) and between nodal points 2 and 4 (DS24), and finally the strains in sections 1 through 3 (EPS1, EPS2, EPS3) as well as the average strain (EPSQ).

The radial displacements (Figure 5.8.32) agree very well with the corresponding results of the pretest calculation with an axisymmetric finite element model [11,51,52]. The major slope changes of the strain curves in Figure 5.8.34 may be attributed to

- weakening of the seismic stress-strain behavior above a strain of some $0.15 \times 10^{-8}$ at 0.22 MPa (32 psig),

- beginning of liner yielding in section 2 at 0.65 MPa (94 psig),

- beginning of liner yielding in section 1 at 0.73 MPa (106 psig), and

- beginning of hoop yielding at about 0.88 MPa (128 psig).

The major result of this analytical investigation is presented in Figure 5.8.33. From this figure the relative displacement between nodal points 2 and 4 (DS24) amounts to some 0.65 mm (0.026 in.) at 1.0 MPa (145 psig), where according to the test major liner leakage developed.

This value is used in section 5.8.5.1 to obtain from a plane stress consideration the corresponding strain concentration in the vicinity of a liner anchor.

### 5.8.6 Synopsis of Posttest Results

In general the predictions obtained in pretest analyses using an axisymmetric finite element model of the containment met to a large extent the global performance of the structure in the test. However, larger discrepancies were found with respect to calculated deformations of the basemat, which were overestimated. To improve the performance of the basemat the action of the fill slab was included into the global containment model of the pretest stage by use of frictional forces. Thus, the bending behavior of the basemat was described more realistically. These modifications of the calculation model resulted in a satisfactory approximation to the experimental values.

Major investigations were performed to study strain concentrations at liner regions with local irregularities such as studs. By evaluating the results of several section models of the interesting area near a thickened insert plate at cylinder midheight where the major liner tear occurred in the experiment, a strain level of about 14% was determined at failure pressure of 1.0 MPa (145 psig). This result is comparable to multiaxial limit strain values obtained from uniaxial strain data of the liner steel. The failure strains are also supported by biaxial liner tests performed at the University of Karlsruhe. Thus, the occurrence of the major liner tear could be understood on grounds of analyses of the posttest phase.

### 5.8.7 General Conclusions Drawn from the Test and Pretest and Posttest Analyses

Finite element analyses were performed before and after the test of a lined and reinforced concrete containment model. Results of the pretest investigations were reported in NUREG/CR-4913 [11]. In this paper improvements of the calculation model to describe global behavior of the structure and additional analyses of local effects were presented. From these studies the following general aspects can be derived.

In the test the liner turned out to be the weakest link of the pressure retaining boundary. In view of small tears at various locations that were observed after the test, the tightness of the liner seems to have been nearly exhausted at many locations where geometric inhomogeneities caused strain concentrations. The formation of a major tear at a position where several effects superpose, such as load redistributions at a thickened insert plate, strain concentrations at liner anchor bolts and deviations

from homogeneous stress conditions due to a nearby hatch can therefore not be seen as an accidental event. Certainly initiation of leakage that might have been caused by improper manufacturing can, in this case, be excluded when assessing this evidence.

One is therefore lead to the conclusion that a repetition of the test with a similar model structure would essentially yield an equivalent answer.

The question however arises whether the behavior would be different if pressurization were applied to a 1:1 scale real containment structure. In the 1:6-scale model the thickness of the liner is very small (some 1.6 mm). Hence, strain concentrations due to welded anchor bolts will most probably penetrate through the whole depth of the liner sheet. This can be different in case of a 10 mm (0.39 in.) thick sheet of steel where strain enhancement might not pass through the whole depth, instead leaving a more or less unaffected part of the cross-section. In this case damaging due to anchor interaction might be confined to fibers of the liner near the surface on the side of the stud leading possible to tearing of the stud rather than to formation of a tear in the liner at this stage of pressurization. Under these conditions there is a chance that the liner of a real containment might fail at even higher pressure levels than those withstood by the 1:6 model containment. This being the case, other failure modes may become controlling, for instance, leakage at penetrations or even failure of parts of the concrete structure.

Up to now there have been no in-depth investigations of the degree of damage of various sections of the pressurized reinforced concrete shell. Several pretest analyses have predicted for instance that hoop failure could occur around some 1.2 MPa (174 psig). Shear failure of the concrete structure at the cylinder basemat junction was assumed at somewhat lower pressure values (between 1.15 and 1.2 MPa). Although not verified by the test there seems to be only a small margin between the failure mechanisms and a decision for real containments on grounds of the 1:6-scale test results is not a straight-forward one without further detailed analyses.

Taking furthermore into account that in a severe accident aside from pressurization also other loads may contribute to a threat for the integrity of the containment, e.g. jet impact, temperature etc., it is obvious that each loading scenario has to be dealt with separately and in detail.

For analysts, the most valuable outcome of the test was - and this was one of its major intentions - to verify computational models, analysis procedures and numerical material models. Up to the pressure level attained in the test this aim was reached. The excellent and very successful conduct of the test provided an extended database for comparison with pretest analysis results and for model improvements during the posttest phase as well. The test offered thus the unique possibility to sharpen analytical tools and to obtain faith in their performance.

Especially the investigations of the posttest phase yielded a great deal of insight into modeling requirements that have to be observed in order to predict adequately the response of structures that are loaded beyond the design limits. The lessons to be learned were, firstly to include all details of the structure which might have any influence on the global behavior (e.g., interactions between fill slab and basemat).

Secondly, it is necessary to estimate uncertainties in experimental results (e.g., unavoidable variations of measured strains of rebars in the neighborhood of cracked

concrete) and computed results as well, in order to be able to assess the quality of the answers.

Thirdly, local effects can only be dealt with properly if there are either analytical means available to derive from results of global analyses the behavior of various structural irregularities or if adequate section models are employed. (The third possibility to incorporate in a three dimensional analysis model all major details is in general not tractable.)

Considering the answers of pretest and posttest investigations in the light of test results an optimistic point of view concerning the capabilities of analysis methods seems to be justified. The preceding statement is, however, conditional on the assumption that the computational models contain all relevant features that characterize the exchange of loads between deformation controlling structural parts. Numerical material models and numerical procedures employed in the state-of-the-art finite element codes seem to work sufficiently accurate in this type of application. This holds for material descriptors of steel properties under uniaxial and multiaxial conditions for loading ranges up to failure. It must be noted that in some cases it is very difficult to obtain limit values within a sufficiently narrow scatter band. Particularly cumbersome are experiments to obtain ultimate strain data under multiaxial conditions. There is still some discussion as to the proper formulations to model concrete behavior in the high loading regime under complex stress patterns, such as combined compression, bending and shear. From the high-pressure test results obtained as of now it is not possible to draw any conclusions concerning the adequacy of employed numerical concrete models under these conditions, aside from the fact that gross failure was predicted by analyses at higher pressure levels than the level that could be reached in the test.

With respect to the application of computational tools to real containments the important question is, do these methods permit a sufficiently accurate determination of the loading level at which containment integrity is still preserved? In this context a completely realistic numerical description of reinforced concrete under the above mentioned conditions near the level of its ultimate load carrying capacity does not seem to be of utmost relevance. As deformation states of structures of this type below the ultimate compressive capacity of concrete can be presented within a certain scatter band rather well, the available analysis procedures may be regarded as being suited to yield a reliable answer.

### 5.8.8 Appendices to Section 5.8

#### 5.8.8.1 Determination of Cracking Pressure for Basemat

The critical pressure $P_{cr}$ at which cracks at the lower surface of the circular basemat of a cylindrical concrete containment begin to form may be obtained from the following equation:

$$P_{cr}/f_t = (8/3) \cdot D^2 \cdot (1 + r)/DN,$$

where

$$DN = (3 + \nu_c) \cdot a^2 - 8 \cdot (1 + D \cdot k)/k^2,$$

$$r = 3 \cdot (E_s/E_c) \cdot ((1 - \nu_c)/(1 - \nu_s)) \cdot A/(D \cdot d),$$

$$k = (3 \cdot (1 - \nu_c^2)/(a^2 \cdot t^2))^{1/4},$$

with the parameters:

| | | |
|---|---|---|
| D | : | thickness of basemat |
| t | : | thickness of cylinder |
| a | : | radius of cylinder midsurface |
| $\ddot{a}$ | : | spacing of rebars of reinforcement near lower surface of basemat |
| A | : | rebar cross-section area |
| $E_s$ | : | Young's modulus of steel |
| $E_c$ | : | Young's modulus of concrete |
| $f_t$ | : | uniaxial tensile strength of concrete |
| $\nu_s$ | : | Poisson's ratio of steel |
| $\nu_c$ | : | Poisson's ratio of concrete |

The derivations of the above equations are based upon the assumptions listed in paragraph 5.8.3.1.

### 5.8.8.2 Derivation of the displacement/pressure-relationship for the wall section of Figure 5.8.31

The meaning of the used symbols is as follows:

| | | |
|---|---|---|
| $r_i$ | : | radial position of liner center surface |
| $r_1$ | : | radial position of first hoop reinforcement |
| $r_2$ | : | radial position of second hoop reinforcement |
| $r_3$ | : | radial position of the seismic reinforcement |
| $\ell_1$ | : | length of liner section 1 |
| $\ell_2$ | : | length of liner section 2 |
| $\ell_3$ | : | length of liner section 3 |
| $\ell$ | : | length of total segment $(\ell_1 + \ell_2 + \ell_3)$ |
| $d_1$ | : | thickness of liner section 1 |
| $d_2$ | : | thickness of liner section 2 $(= d_1)$ |
| $d_3$ | : | thickness of liner section 3 |
| $\epsilon_1, \sigma_1$ | : | strain, stress of liner section 1 |
| $\epsilon_2, \sigma_2$ | : | strain, stress of liner section 2 |
| $\epsilon_3, \sigma_3$ | : | strain, stress of liner section 3 |
| $\epsilon$ | : | average strain of the three sections |
| S2 | : | circumferential displacement of liner at node 2 |
| S3 | : | circumferential displacement of liner at node 3 |
| DS23 | : | relative circumferential displacement of liner between nodes 2 and 3 |
| DS24 | : | relative circumferential displacement of liner between nodes 2 and 4 |
| k | : | stiffness of stud replacement |
| p | : | internal pressure |
| A | : | cross section area of one hoop rebar |
| $\bar{A}$ | : | cross section area of equivalent seismic rebar |
| ds | : | distance between studs in meridional direction of the containment |
| $\sigma_H$ | : | stress in hoop reinforcement |
| $\sigma_S$ | : | stress in seismic reinforcement |
| u | : | radial displacement |

### Kinematic Relation for the Liner

$$\epsilon_1 \cdot \ell_1 + \epsilon_2 \cdot \ell_2 + \epsilon_3 \cdot \ell_3 = \iota \cdot \ell \tag{5.8.1}$$

$$\iota = u/r_i \tag{5.8.2}$$

It is assumed that the radial displacement does not vary with the position of a particular point inside the containment wall.

The strain of section 1 can be expressed as:

$$\epsilon_1 = \iota + S2/\ell_1 \tag{5.8.3}$$

### Equilibrium Relations

Balancing of forces at node 2 yields

$$k \cdot S2 = \sigma_2 \cdot d_2 - \sigma_1 \cdot d_1 \tag{5.8.4}$$

and hence from equation 5.8.3

$$\iota = \epsilon_1 - (\sigma_2 \cdot d_2 - \sigma_1 \cdot d_1)/(\ell_1 \cdot k) \tag{5.8.5}$$

At node 3 force equilibrium results in the strain of section 3:

$$\epsilon_3 = \sigma_2 \cdot d_2/(E \cdot d_3) \tag{5.8.6}$$

The last formula holds on account of assumed linear elastic properties of section 3 with the Young's modulus E.

Employing equations 5.8.1, 5.8.3, 5.8.5 and 5.8.6 results in

$$\alpha \cdot \epsilon_1 + \beta \cdot \sigma_1\{\epsilon_1\} = F(\epsilon_2, k) \tag{5.8.7a}$$

with

$$\alpha = (1 - \ell_1/\ell) \cdot \ell_1 \tag{5.8.7b}$$

$$\beta = d_1/k$$

$$F = C \cdot \sigma_2\{\epsilon_2\} + \epsilon_2 \cdot \ell_2 \cdot \ell_1/\ell \tag{5.8.7c}$$

where

$$C = (1 + k \cdot \ell_1 \cdot \ell_3/(E \cdot d_3 \cdot \ell)) \cdot d_2/k \tag{5.8.7d}$$

### Solution of Equation 5.8.7a

For parametrically given values of the spring stiffness k and for predefined steps of the strain $\epsilon_2$ in the liner section 2, the function F can be evaluated. Equation (5.8.7a) then represents an implicit formulation for the strains $\epsilon_1$ in section 1, which is to be solved by iteration as the liner stress-strain behavior is nonlinear. The solutions $\epsilon_1$ depend on the current values of k and $\epsilon_2$. From eqs. (5.8.6) and (5.8.2) follow the

strain $\epsilon_3$ in section 3 and the radial displacement u. The relative displacements are obtained from

$$DS23 = \epsilon_2 \cdot \ell_2 \qquad (5.8.8a)$$

and

$$DS24 = \epsilon_2 \cdot \ell_2 + \epsilon_3 \cdot \ell_3 \qquad (5.8.8b)$$

Calculation of the Internal Pressure Related to Given Values of k and $\epsilon_2$

Requiring global force equilibrium between the internal pressure load and the loads carried by the liner and the reinforcement yields the approximate relation

$$p = (2 \cdot G1 \cdot A/ds + G2) \cdot r_i \qquad (5.8.9a)$$

with

$$G1 = \sigma_H \{\epsilon \cdot r_i/r_1\} + \sigma_H \{\epsilon \cdot r_i/r_2\} + 0.5 \cdot \bar{A} \cdot \sigma_S \{\epsilon \cdot r_i/r_3\}/A \qquad (5.8.9b)$$

and with

$$G2 = (\sigma_1 \cdot d_1 \cdot \ell_1 + \sigma_2 \cdot d_2 \cdot \ell_2 + \sigma_3 \cdot d_3 \cdot \ell_3)/\ell \qquad (5.8.9c)$$

Again, p is a function of predefined values for k and $\epsilon_2$.


### 5.8.8.3 Experimental Investigations

An experimental program with typical containment wall elements and liner elements has been carried out at the University of Karlsruhe to provide special data for the posttest analysis of the 1:6-scale model. In one test series, bond behavior of rebars in cracked concrete has been investigated. In another one, the ultimate strains in biaxially loaded liner sheets have been investigated. A summary of test procedures and test results is presented here. For further details refer to the reports [57] and [58].

Bond Behavior of Rebars in Cracked Concrete

In the containment model the seismic reinforcement as well as a part of the meridional rebars end in the dome region. If concrete cracks in these areas the cutoff bars gradually lose their ability to carry their part of the load due to debonding. Possibly a failure of the containment will be initiated due to these effects. As nothing could be found in the literature concerning decreasing bond resistance in cracked concrete some experiments have been performed to verify the analysis regarding this aspect.

The test specimen is shown principally in Figure 5.8.35. A concrete beam reinforced with 8 $\phi$ 12 mm BSt 420/500 in the longitudinal and 9 $\phi$ 12 mm in the transverse direction was used to simulate the hoop and meridional rebars, respectively, of the containment model. A controlled force, H (see Figure 5.8.35), was used to load the

specimen in tension until cracking occurred, after which one of the transverse rebars - meridional direction - was pulled out.

The specimen shown in Figure 5.8.36 had a length of 1500 mm (59 in.) a height of 460 mm (18 in.) and a thickness of 165 mm (6.5 in.). To ensure that a crack would pass along a vertical rebar the specimen was notched parallel to the rebar (see Figure 5.8.36). For the reinforcement a German rebar of 12 mm (0.47 in.) diameter was used, which is nearly equivalent to the U.S. #4 rebar. The concrete was similar to that used for the model test having a cylinder strength of $\beta_c$ = 43.5 MPa (6300 psi) and a Young's modulus of E = 29500 MPa (4.3x10$^6$ psi) at the age of 21 days, which also was the testing date for the specimen.

During the pull-out tests, the relative displacement between the rebar and concrete at both the top and bottom surface was measured as well as the pull-out force. Furthermore, some of the vertical rebars were equipped with interior strain gages, seven over the height, to record the strain distribution in the reinforcing bar.

In Figure 5.8.37 the pull-out force versus the relative displacement at the top surface is given for several crack widths: w = 0.1, 0.5, 1.2, 2.0 and 2.8 mm (0.004, 0.020, 0.047, 0.079, and 0.110 in.). The curves for w = 0.1 mm (0.004 in.) and w = 0.5 mm (0.020 in.) are nearly identical. Here tensile failure occurred in the rebars. One can recognize the yield plateau at V = 54 kN (12.1 kips), which is equivalent to a stress of $\sigma$ = 480 MPa (69.6 ksi). The peak value of the curve for w = 1.2 mm (0.047 in.) crack width nearly reaches the yield force, however the slope is much less than in the former curves. It represents a rebar failed due to debonding. The other two curves show a similar behavior with a reduced peak value.

A summary of all tests is shown in Figure 5.8.38 for the peak pull-out force versus the crack width. Each symbol represents a test result whereas the line is a trilinear approximation. There is no decrease of bond resistance up to a crack width of w = 0.8 mm (0.031 in.), after which it is gradually reduced until a value of w between 2.5-3.0 mm (0.098-0.118 in.) is reached. There is no resistance remaining beyond this limit. It should be noted that these peak values are reached naturally at different relative displacements.

Biaxial Liner Tests

Liner tearing was observed during the containment model test, and an appropriate failure criterion must be used to give a precise prediction of the phenomena. Sufficient knowledge of the ultimate strains under biaxial loading conditions is therefore of dominant interest for the posttest analysis.

The aim of these tests was to obtain a function $\epsilon_{2,u}$ = f($\epsilon_1$). In other words, the ultimate major principal strain is dependent on the current minor principal strain in a biaxially loaded liner sheet. Ultimate strain $\epsilon_u$ in this context is defined as the maximum strain value that occurs before necking (see Figure 5.8.39).

Original liner sheets from the Sandia model test were used in these experiments. Different specimens were tested to construct a failure envelope for several ratios of principal strains.

Proportional test bars were uniaxially loaded in a preliminary test series to obtain both the uniaxial stress-strain relationship and lateral contraction characteristic

(Poisson's ratio).  Results are given in Figures 5.8.40 and 5.8.41 and Table 5.8.4 (R0B1-R0B3).

Table 5.8.4 Ultimate Strain Combinations for Biaxial Loaded Liner Sheets

| Test No. | $\varepsilon_1$ (%) | $\varepsilon_2$ (%) | Remarks |
|---|---|---|---|
| R0B1 | -7.5 | 19.9 | Uniaxial Tension |
| R0B2 | -7.1 | 20.0 | Uniaxial Tension |
| R0B3 | -7.5 | 20.0 | Uniaxial Tension |
| R3B2 | -0.4 | 14.2 | Lateral Restrained |
| R3B3 | -0.3 | 14.8 | Lateral Restrained |
| R4B1 | 40.0 | 40.0 | Punch Stretching |
| R4B5 | 43.0 | 43.0 | Punch Stretching |
| R4B6 | 43.0 | 43.0 | Punch Stretching |
| R4B7 | 11.0 | 35.0 | Punch Stretching |
| R4B8 | 5.0 | 43.0 | Punch Stretching |
| R4B9 | 3.0 | 16.0 | Punch Stretching |

In a second series, cross-shaped specimens as shown in Figure 5.8.42 were stretched in the two principal directions.  The area of measuring was equipped with strain gages and LVDTs.  The first experiment showed a failure due to rupture of one wing of the cross.  Modifications of the specimen were made in form of slotting the wings (see Figure 5.8.42b) in order to concentrate the straining in the center of the sheet. Various numbers and types of slots were tested.  Biaxial strains up to 10% were measured, however it was not possible to obtain a failure in a region with dominant biaxial loading.  All specimens failed in regions of nearly uniaxial stressing.

It was the aim of a next series to concentrate the straining in a very small area of 20 x 20 mm (0.79 x 0.79 in.).  The test specimen was clamped between thick metal sheets to introduce the load.  Again these tests were not successful.  Failure occurred due to a combined tension/shear failure.

Another series was performed to obtain a characteristic point of the failure envelope, i.e., the point where $\varepsilon_1 = 0$.  A specimen as shown in Figure 5.8.43 was used.  Due to the geometry of the test specimen the lateral contraction could be excluded in a uniaxial tension test.  Results are given in Table 5.8.4 (R3B2-R3B3).

For metal forming processes it is necessary to know the ability of sheet material to withstand certain strain combinations without necking or fracture.  So called forming limit curves (FLC) are used to describe this ability.  They are experimentally constructed by punch or in-plane stretching.  A FLC is a possible failure criterion for a liner in a concrete containment, because the straining of the liner in a containment is similar to that of a forming process.

In a last test series the punch stretching technique, as described for example in [59], was used to determine biaxial ultimate strains in a liner sheet.  The test setup is shown in Figure 5.8.44.  A hemispherical punch stretches a blank which is firmly

clamped at the edges. Before the test a quadratic grid of 1 mm was drawn on the specimen, which was measured again after the test. From the change of the grid the maximum plastic strains in the sheet were obtained. Results of these tests are given in Table 5.8.4 (R4B1, R4B5 - R4B9). It should be noted however that Ghosh and Hecker [60] found that stretching limits in sheet metals from out-of-plane deformation are greater than those from in-plane deformation.

A first approximation of a biaxial failure envelope for the 1.59 mm (1/16 inch) thick liner sheet is given in Figure 58.45. It was obtained from results of all performed liner tests. As scattering is large and many parameters influence the behavior, more experimental work is necessary to affirm this curve and to obtain a proved failure criterion.

### 5.8.9 Acknowledgements

Friction Forces
due to Fill Slab
$T = \mu \cdot p$
$\mu = 0.38$ (Friction Coefficient)

98% of Stiffness of
Lower Bending Reinforcement
Modeled by Hoop Rebars
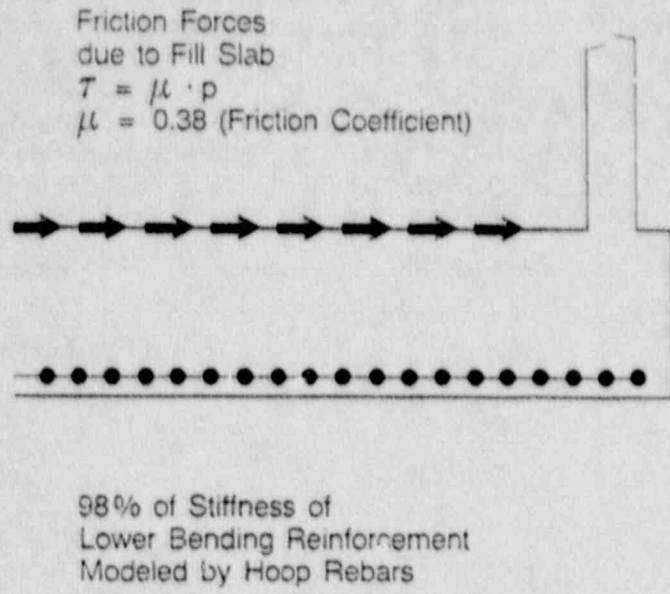
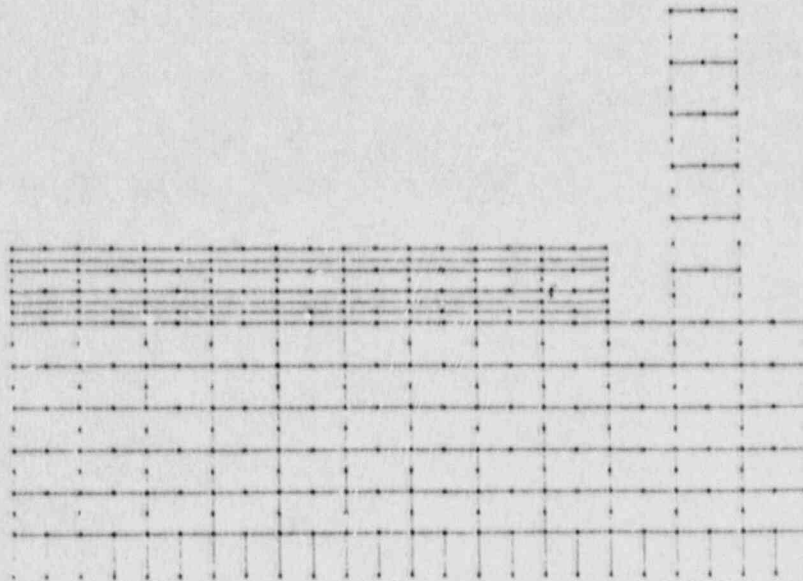Figure 5.8.1  Modifications of Model GRS 88 F

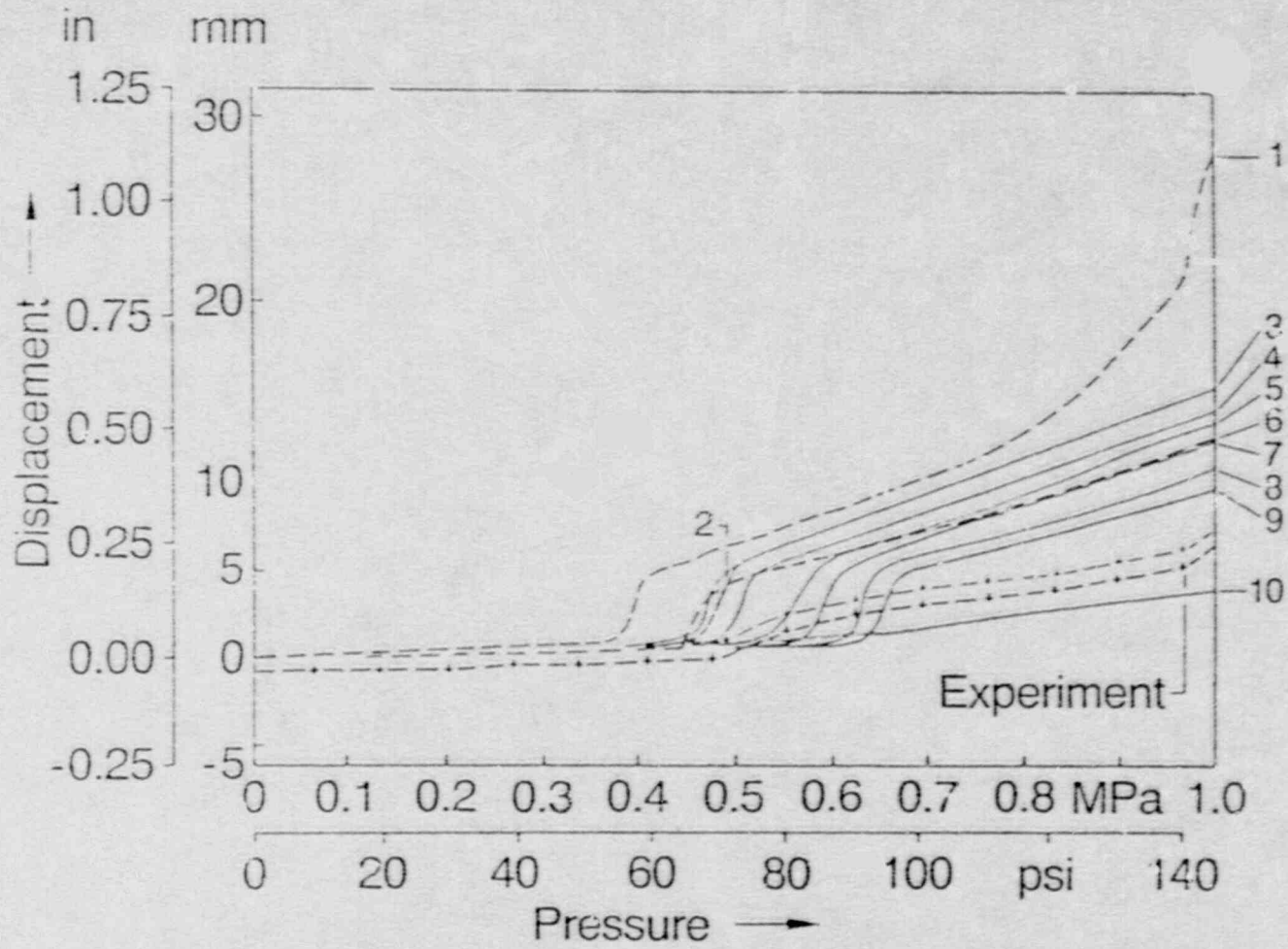Figure 5.8.2  Finite Element Model of Basemat

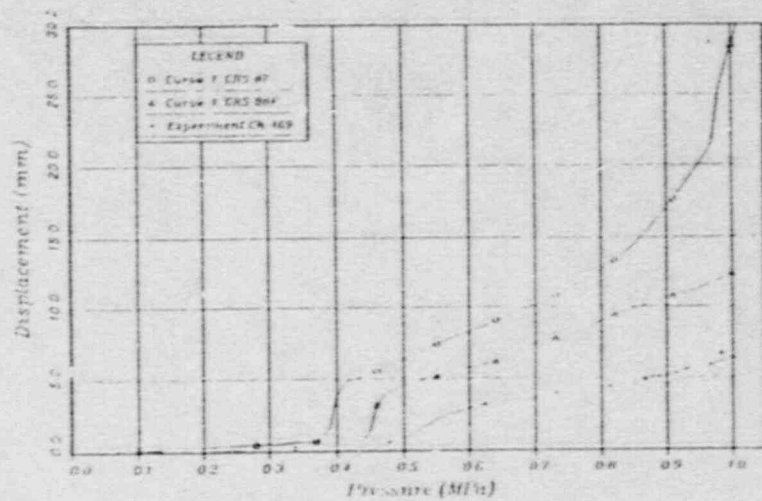Figure 5.8.3  Basemat Uplift Relative to Center of Basemat - Parametric Studies

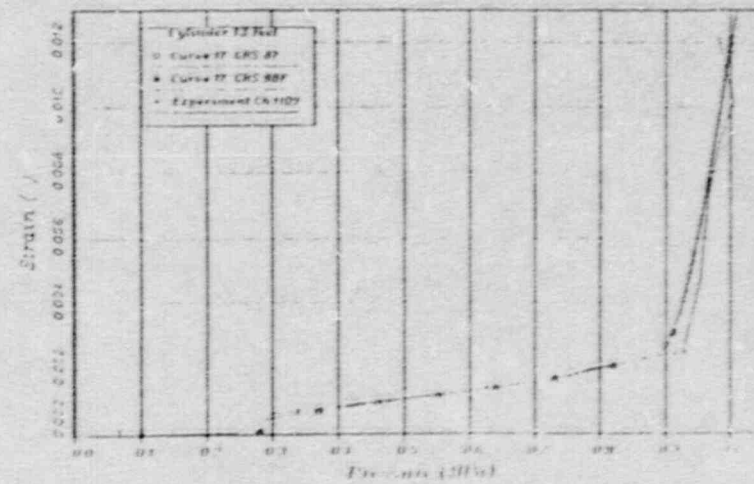Figure 5.8.4  Basemat Uplift
Relative to Center of Basemat



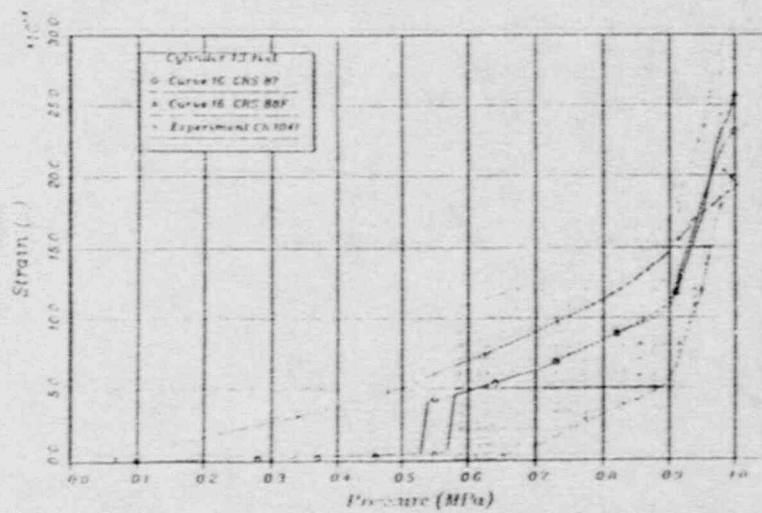Figure 5.8.5  Axial Strain
in Layer 6 Hoop Rebar at El 13 ft



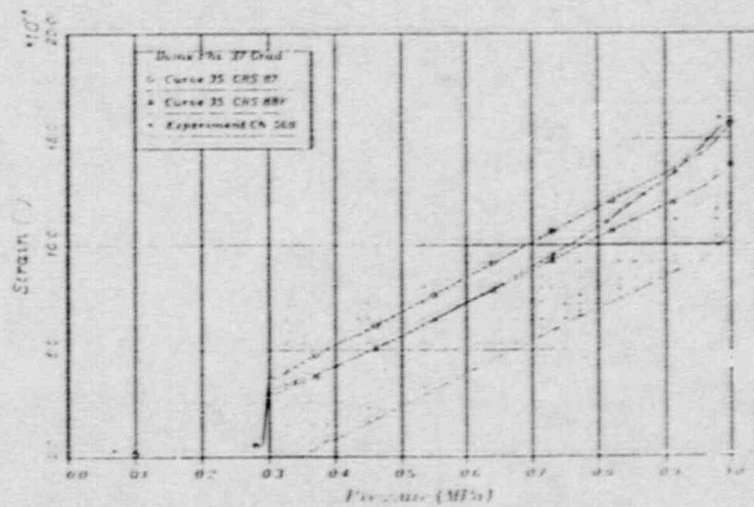Figure 5.8.6  Axial Strain in
Layer 5 Meridional Rebar at EL 13 ft



Figure 5.8.7  Axial Strain in
Layer 4 Hoop Rebar at $\phi = 37°$ (Dome)
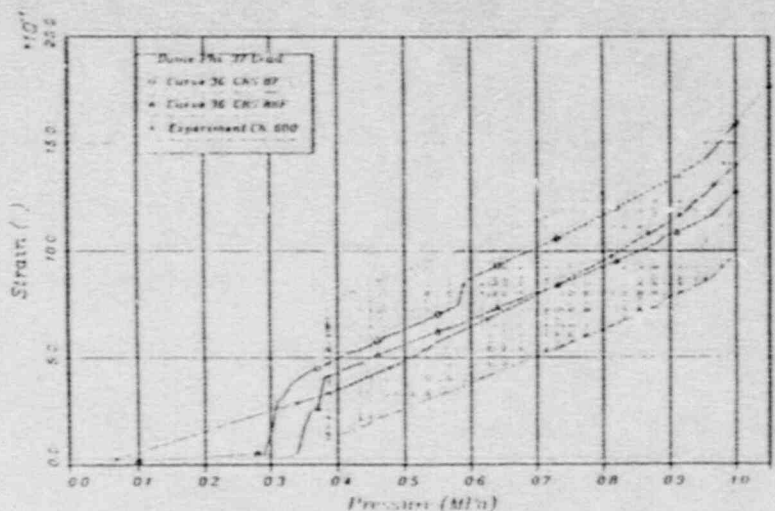
Figure 5.8.8  Axial Strain in
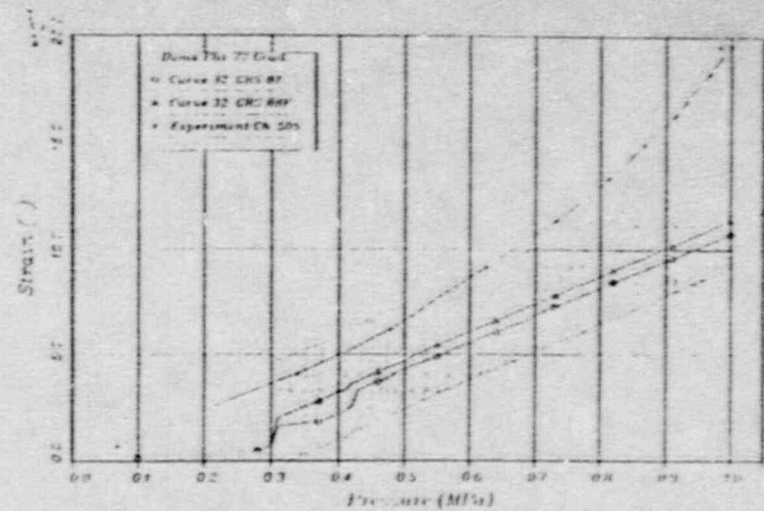Layer 5 Meridional Rebar at $\phi = 37°$ (Dome)



Figure 5.8.9  Axial Strain in
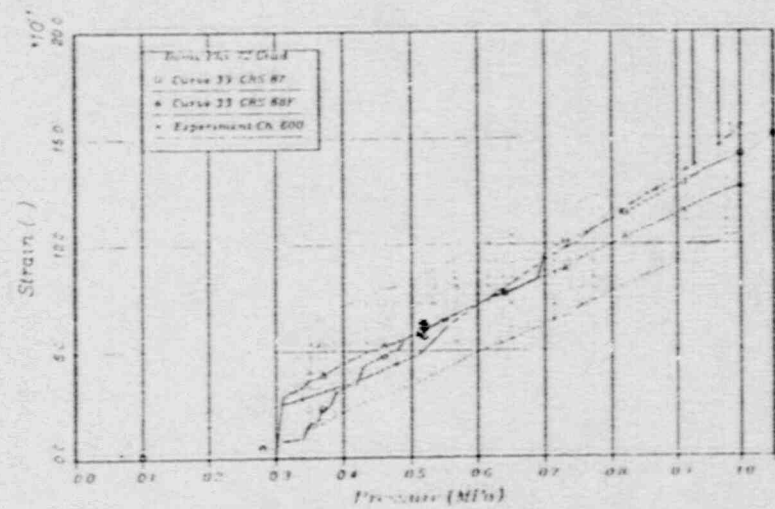Layer 2 Meridional Rebar at $\phi = 72°$ (Dome)



Figure 5.8.10  Axial Strain in
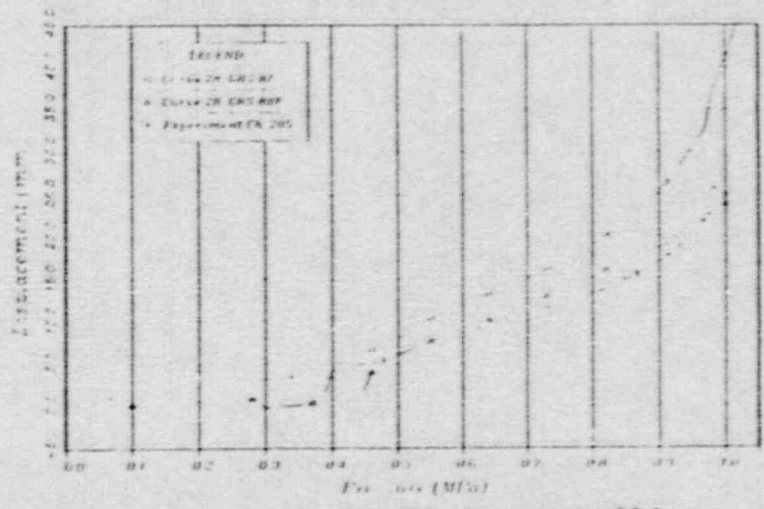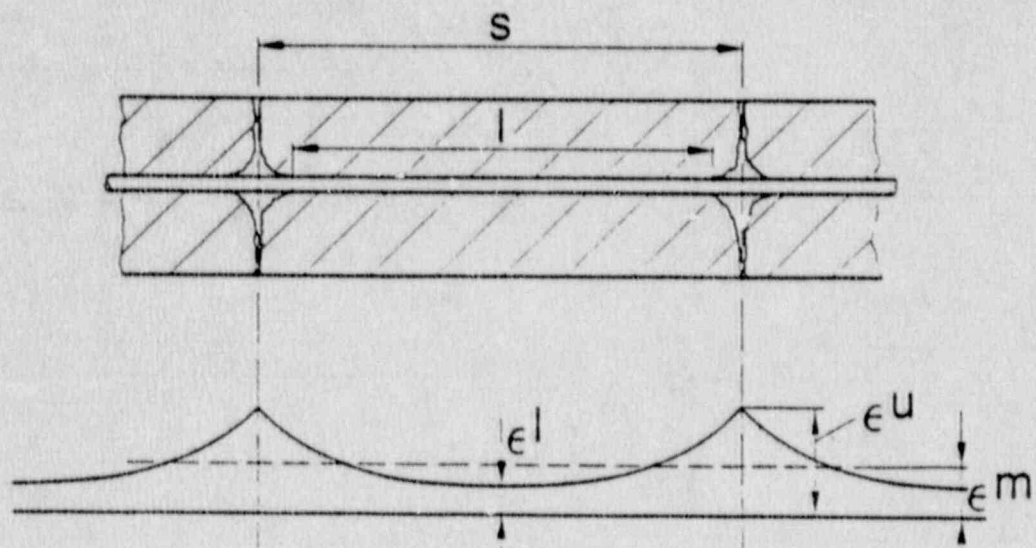Layer 5 Meridional Rebar at $\phi = 72°$ (Dome)



Figure 5.8.11  Vertical Displacement of Liner
at Dome Apex

$\epsilon^m$ average strain

$$\epsilon^u = \epsilon^m + \Delta\epsilon^+$$

$$\epsilon^l = \epsilon^m - \Delta\epsilon^-$$

$$\Delta\epsilon = F\left(l/s, \alpha, f_t, \mu_s, E_s\right)$$

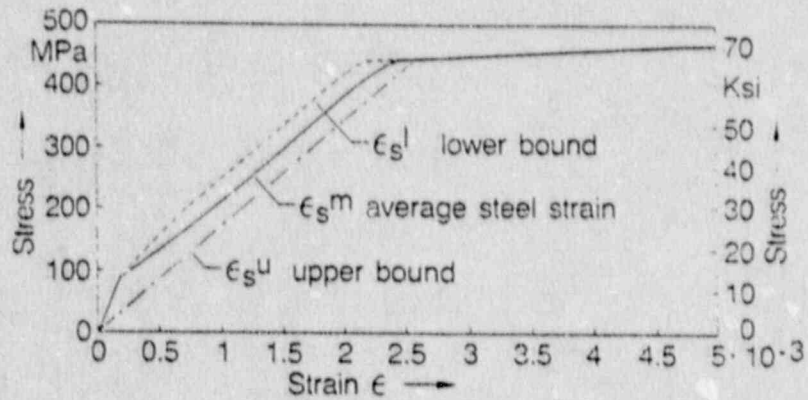Figure 5.8.12  Variation of Rebar Strains Due to Cracks in Concrete

Figure 5.8.13  Stress-Strain Curve for No. 4 Rebar -
Scattering of Strains in Rebar Embedded in Cracked Concrete



Figure 5.8.14  Local Model of Liner Tearing

4,76mm

y

z

1,59mm

Section Model with Stud

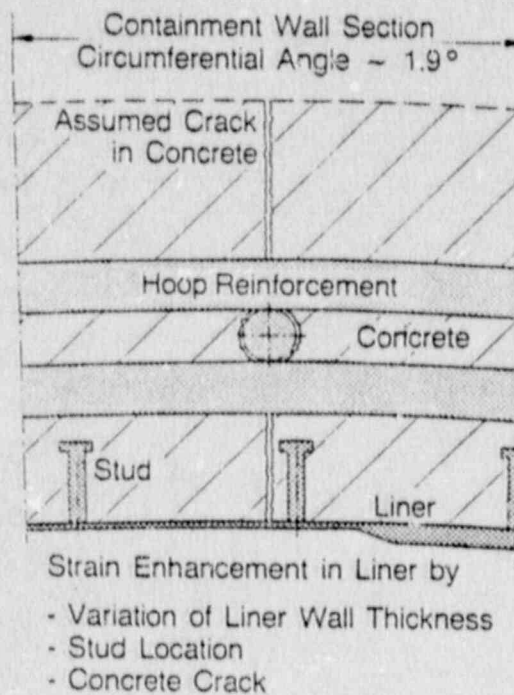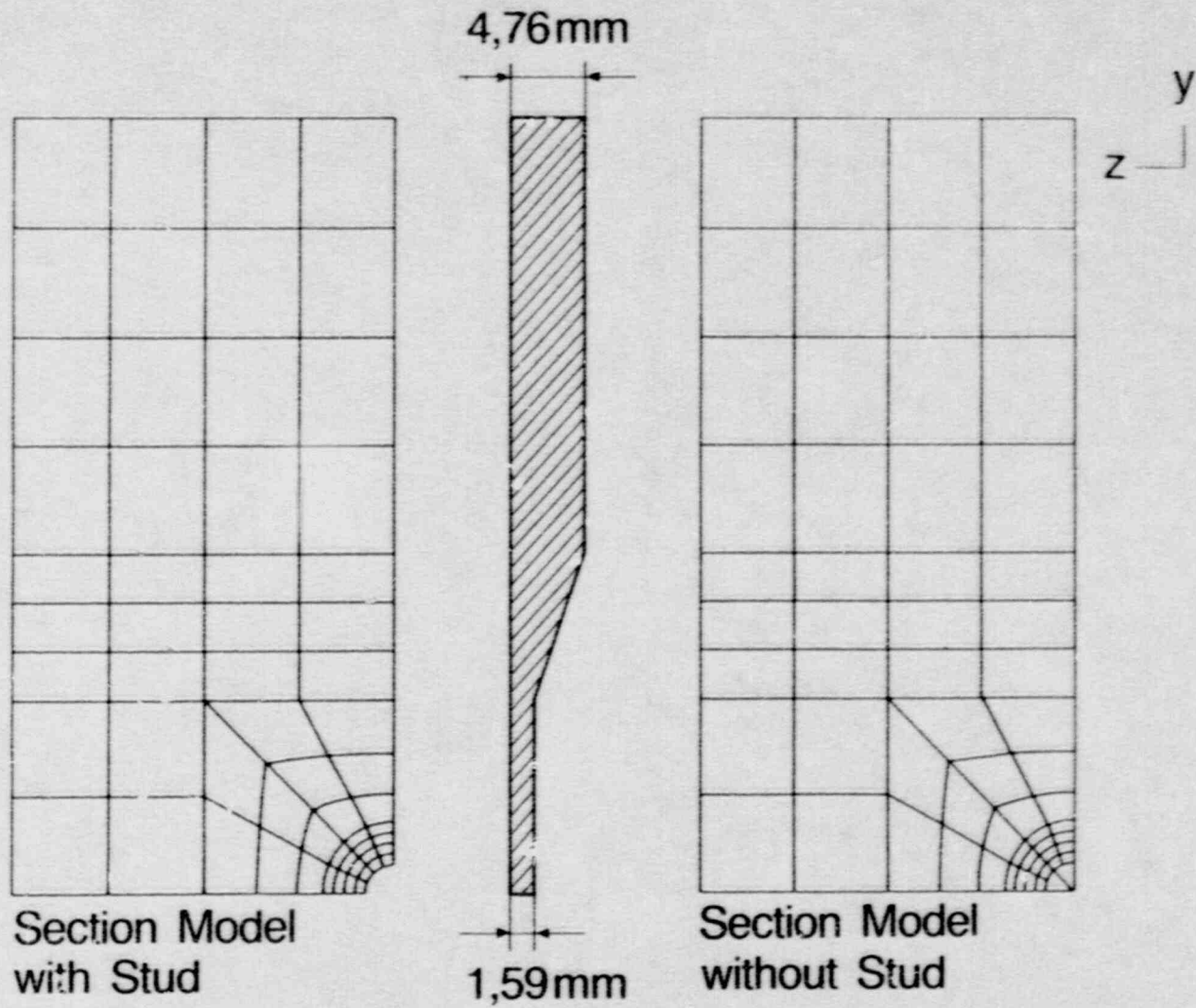Section Model without Stud

Figure 5.8.15  Finite Element Mesh for Plane Stress Models
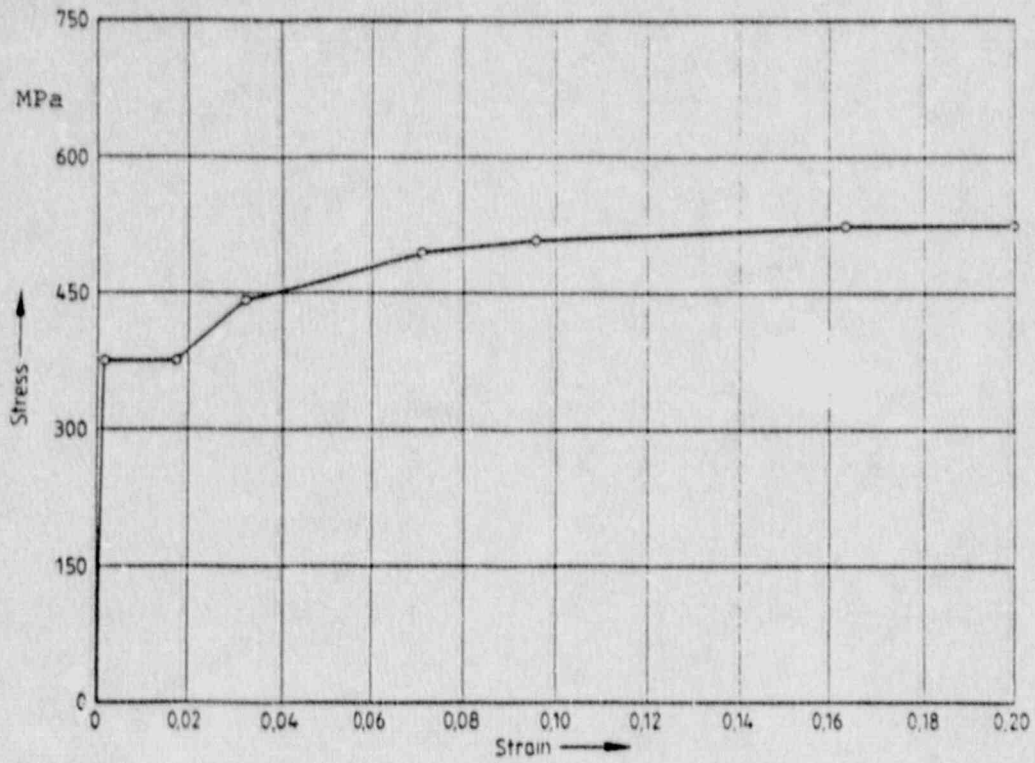
Figure 5.8.16  Stress-Strain Curve for 1/16 in. Liner Material
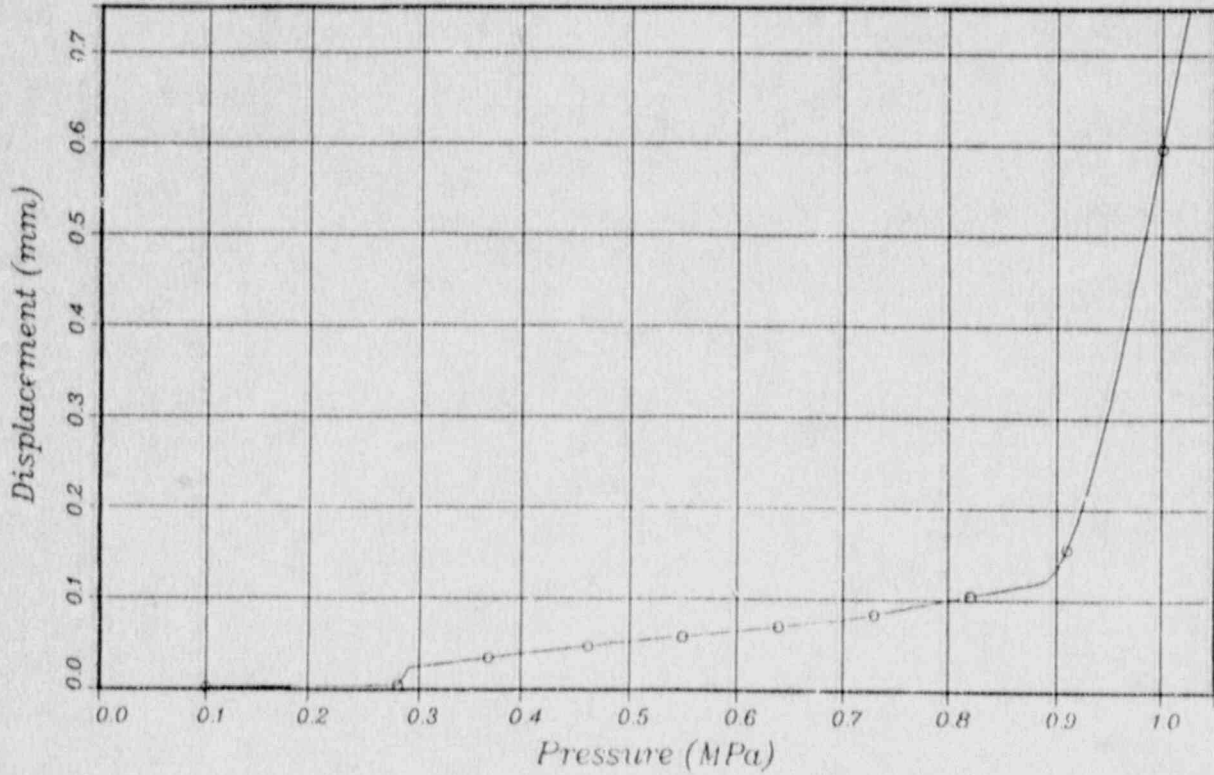


Figure 5.8.17 Loading Function for Plane Stress Models
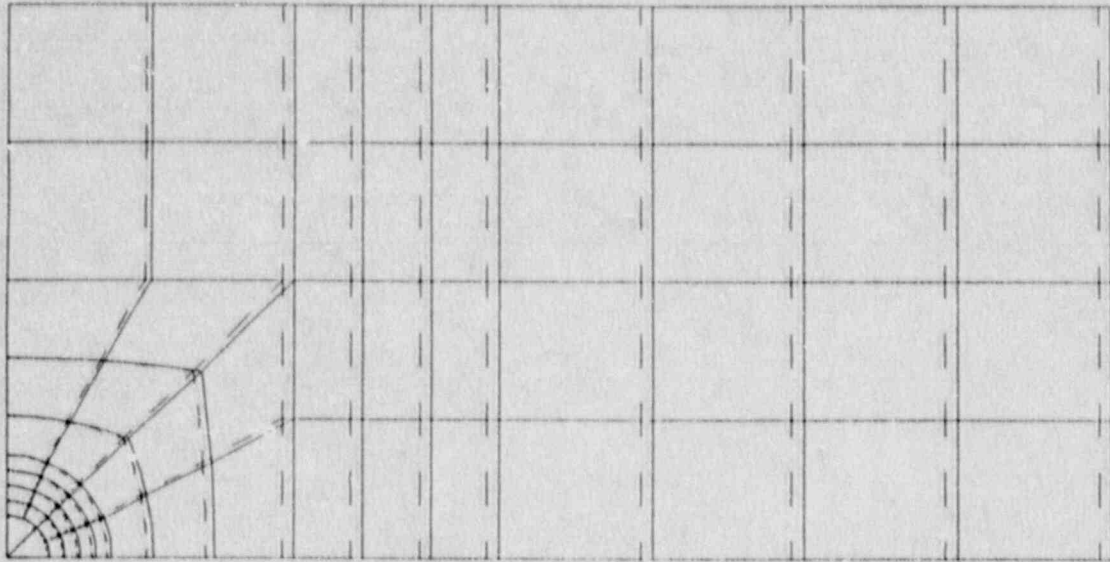
Figure 5.8.18 Deformed Shape of Plane Stress Model without Stud
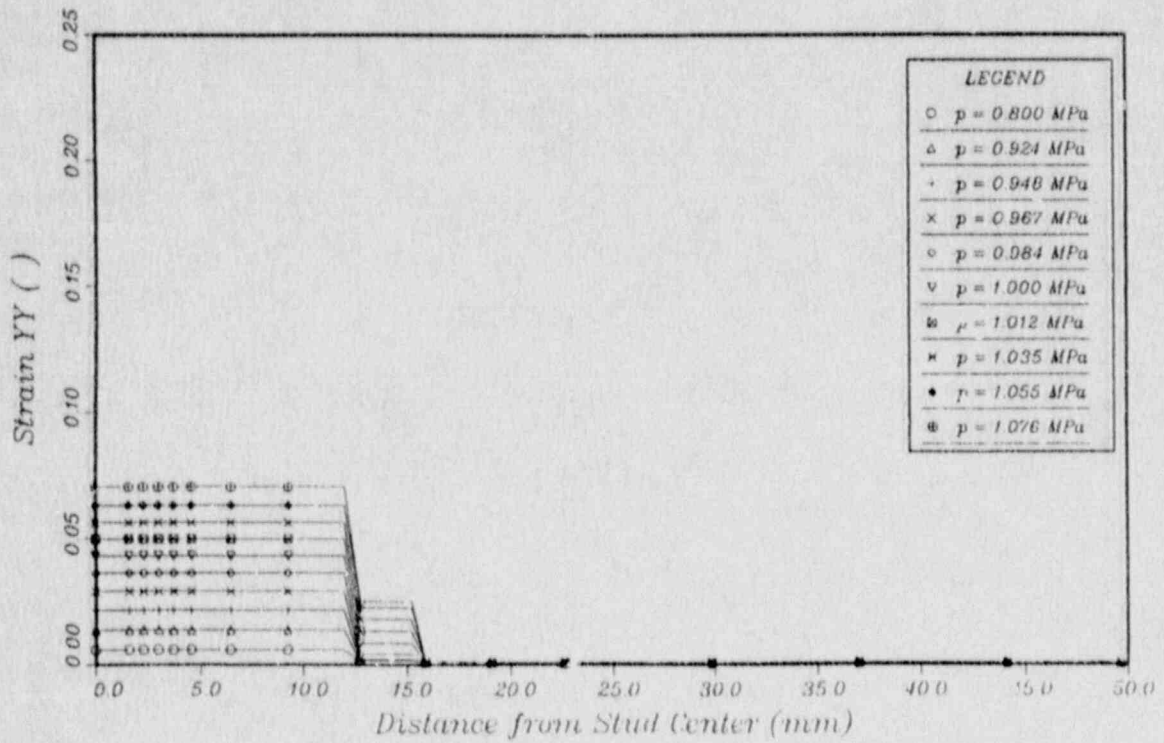


Figure 5.8.19 Strain Profile in Plane Stress Model without Stud
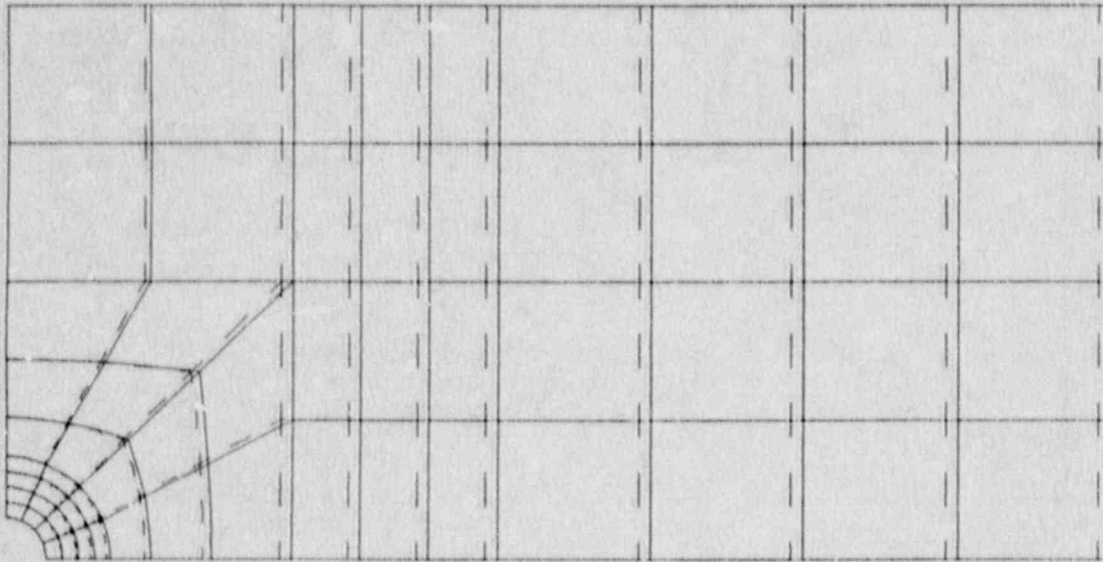
Figure 5.8.20  Deformed Shape of Plane Stress Model with Stud

ELEM 18. GP 1
ELEM 18. GP 4
ELEM 18. GP 7
ELEM 17. GP 1
ELEM 17. GP 4
ELEM 17. GP 7
ELEM 16. GP 1
ELEM 16. GP 4
ELEM 16. GP 7
ELEM 15. GP 1
ELEM 15. GP 4
ELEM 15. GP 7
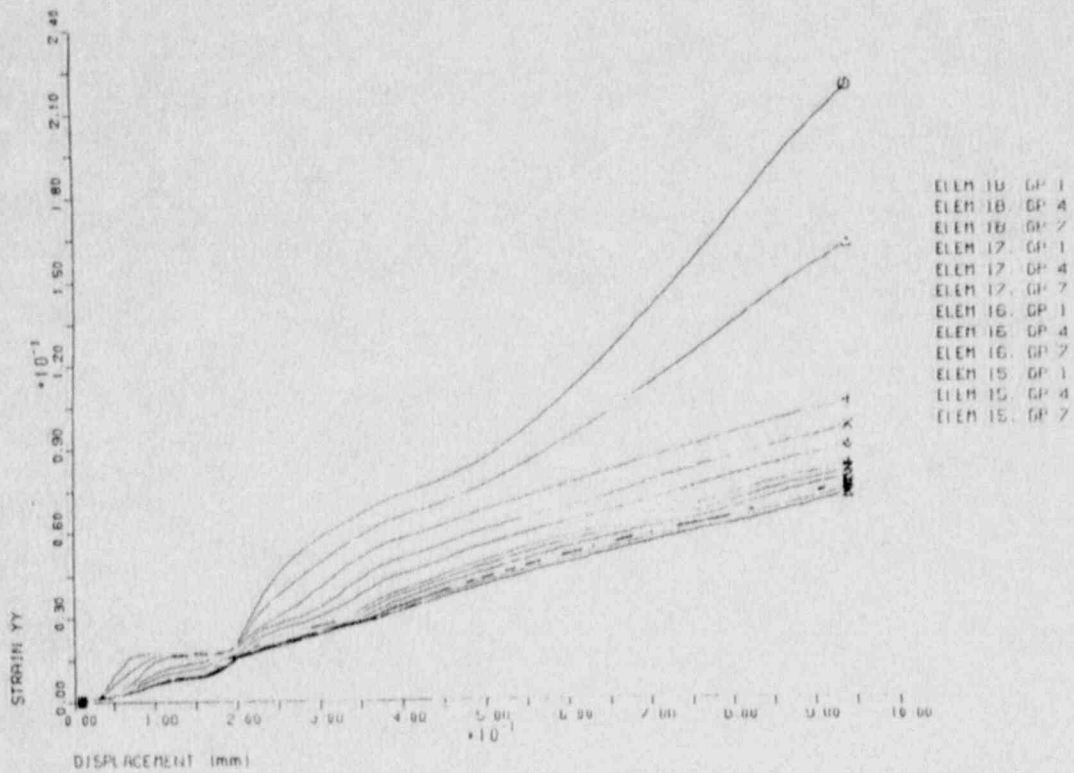
Figure 5.8.21  Strain vs. Displacement for Plane Stress Model with Stud
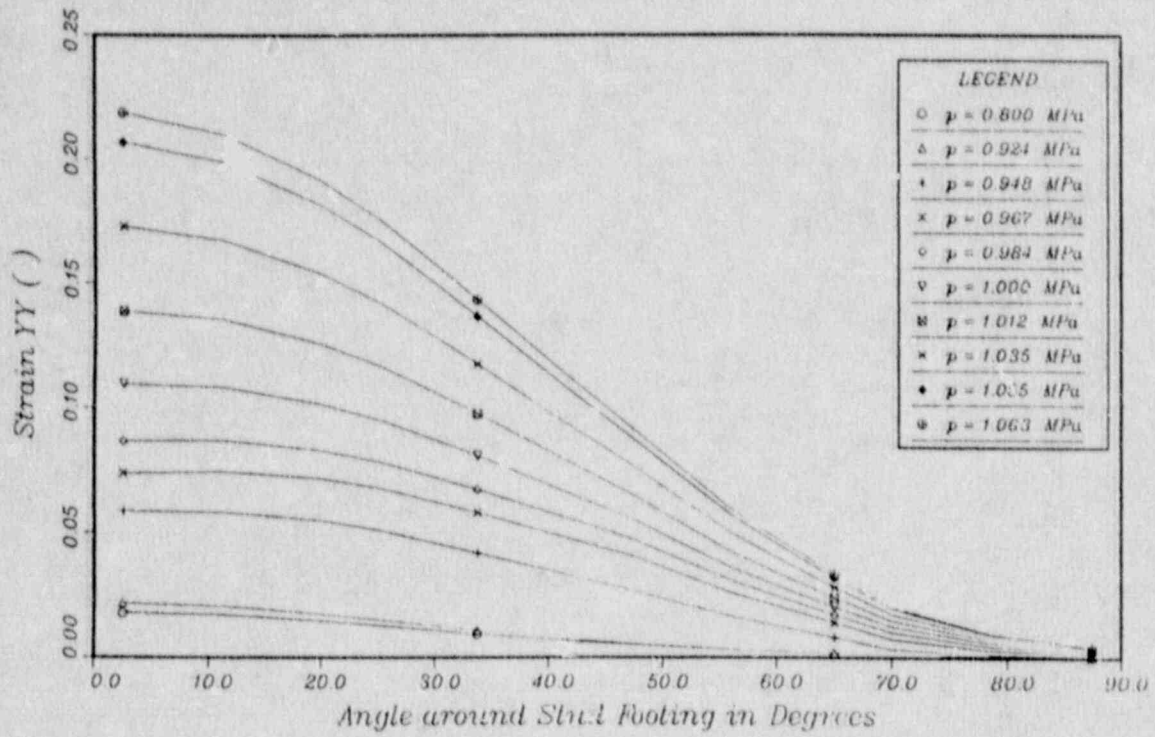
Figure 5.8.22  Strain Profile Around Stud Footing

ORIGINAL └───┘ 2.054

STRAIN TIME 0.600        2

══ : 0.0901          └── Y
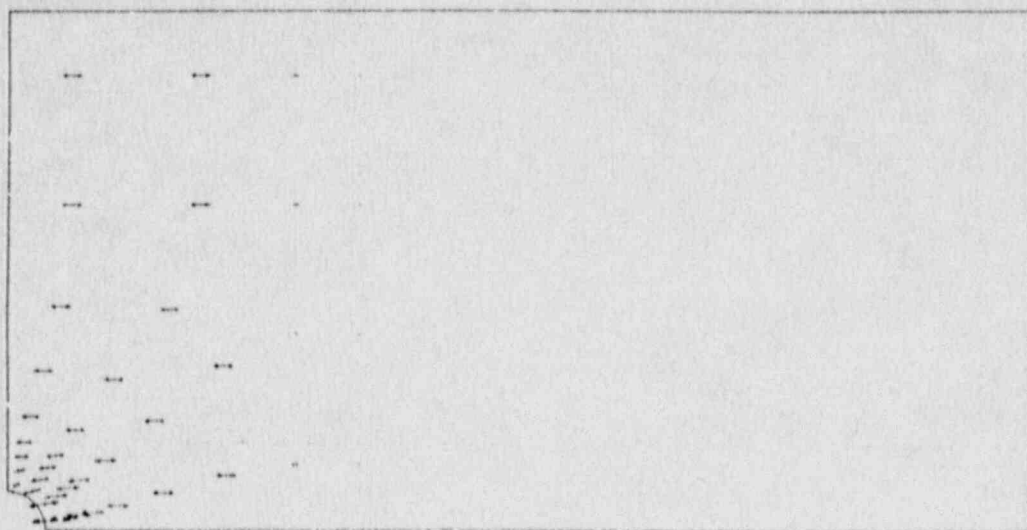


Figure 5.8.23  Strain Magnitudes for Displacement Loading of 0.6 mm (0.024 in.)
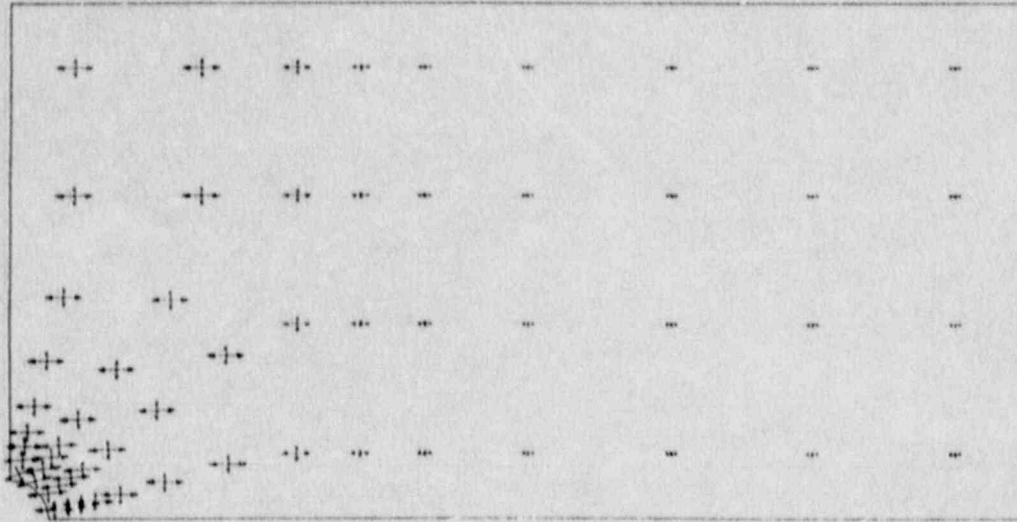
Figure 5.8.24  Stress Magnitudes for Displacement Loading of 0.6 mm (0.024 in.)
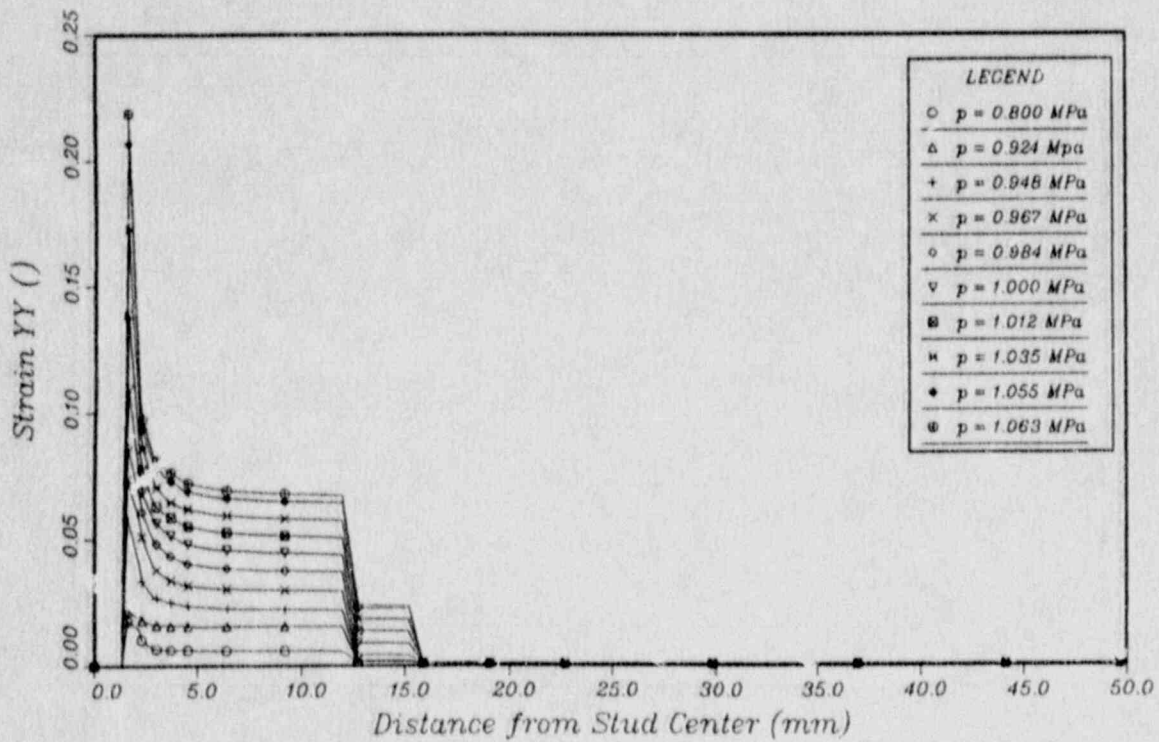


Figure 5.8.25  Strain Profile in Plane Stress Model with Stud
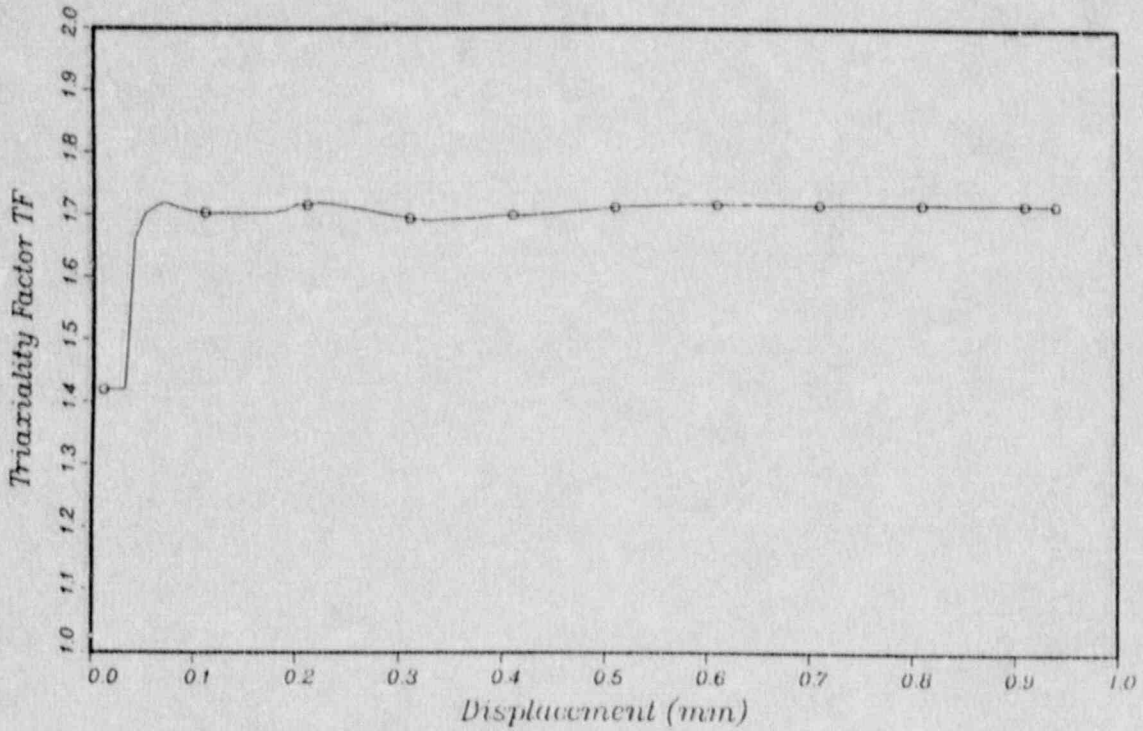
Figure 5.8.26  Triaxiality Factor vs. Displacement Loading
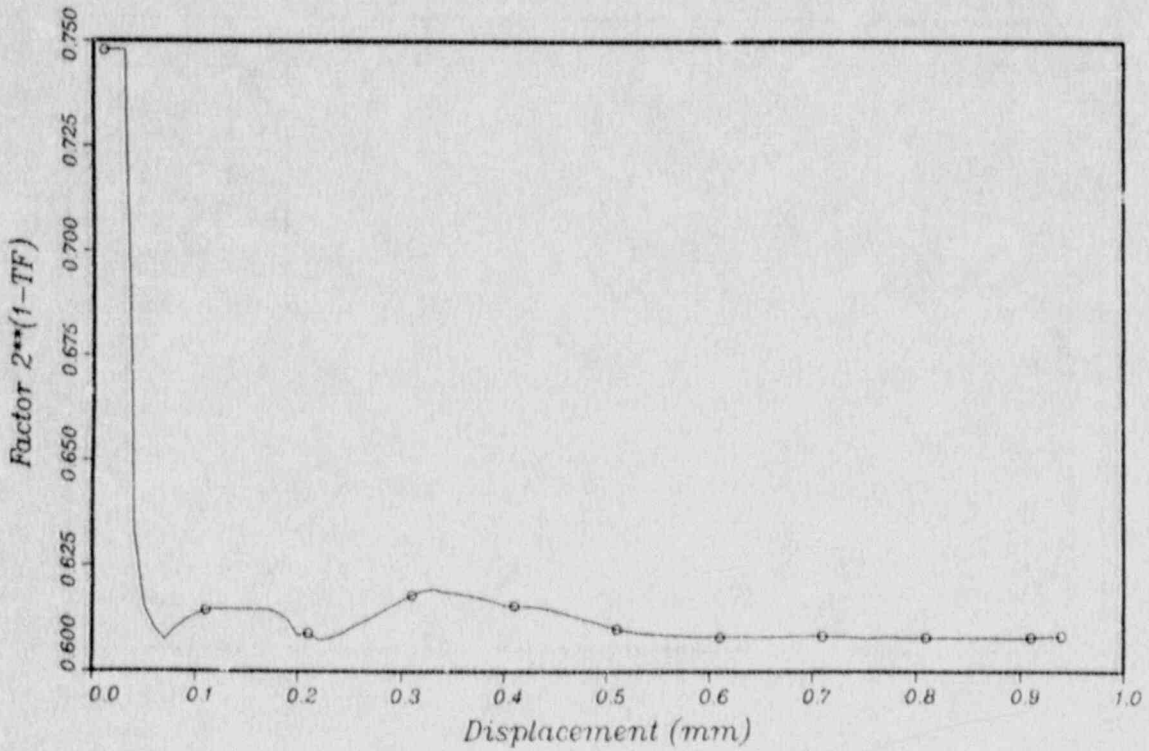


Figure 5.8.27  Ductility Reduction Factor vs. Displacement Loading

ORIGINAL ⊢——⊣ 10.00

Z
└─ Y
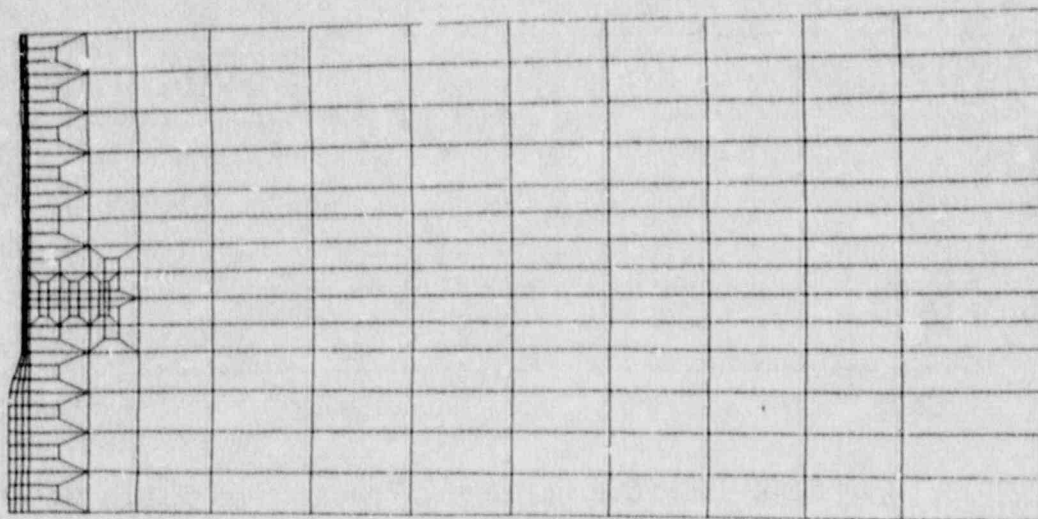
Figure 5.8.28  Section Model of Liner with Stud

Y
│
Z —— X
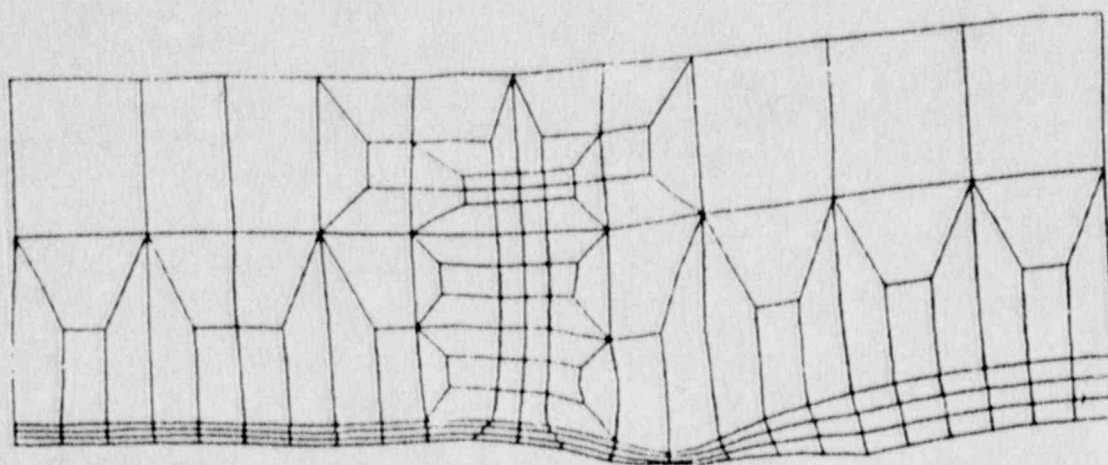
Figure 5.8.29  Deformed Shape of Section Model at 0.83 MPa (120 psig) x50
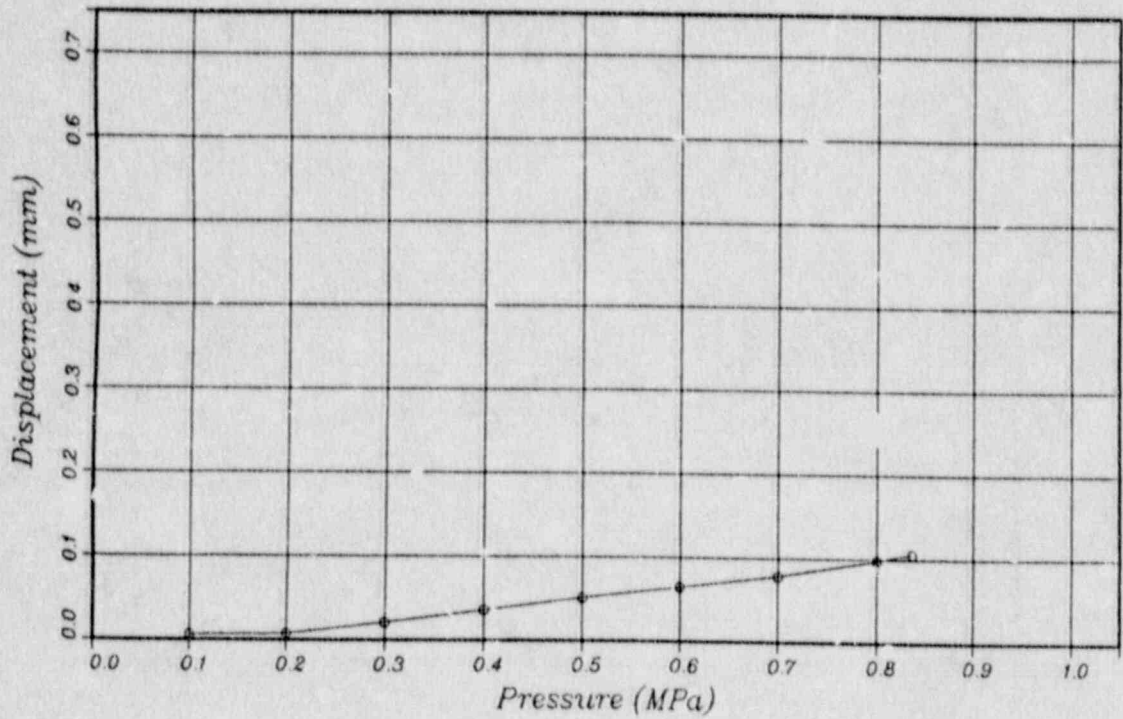
Figure 5.8.30 Liner Displacement vs. Pressure from Section Model
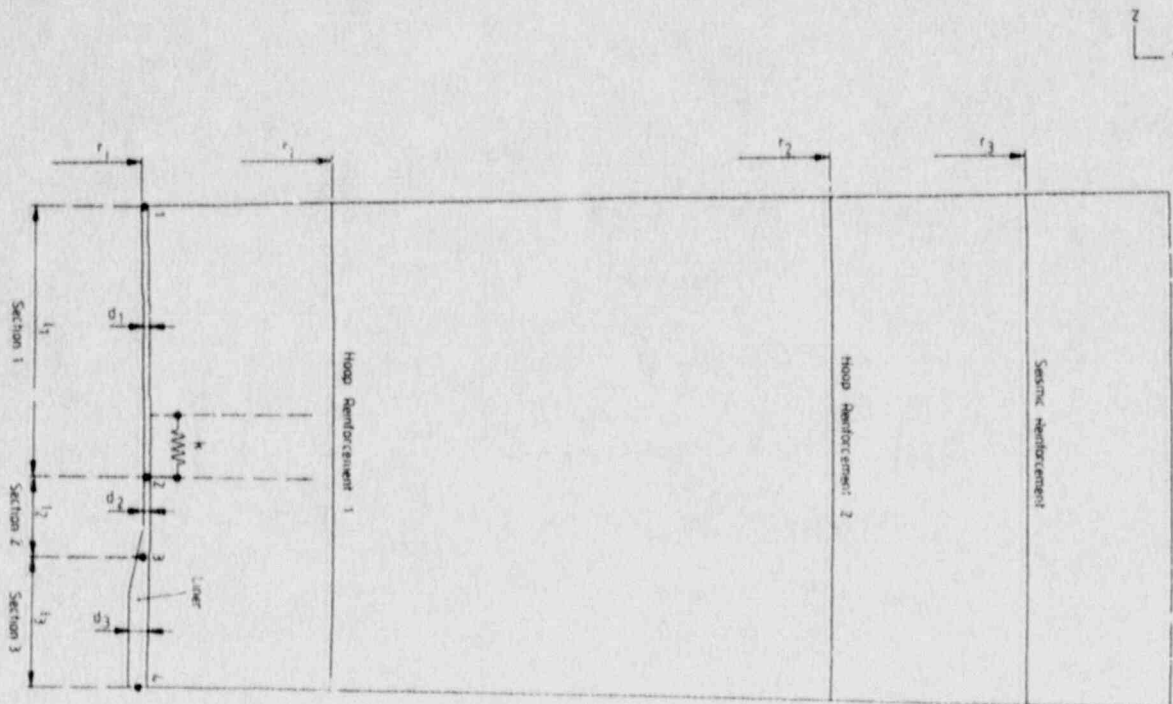


Figure 5.8.31 Simplified Analysis Model for Liner Tearing
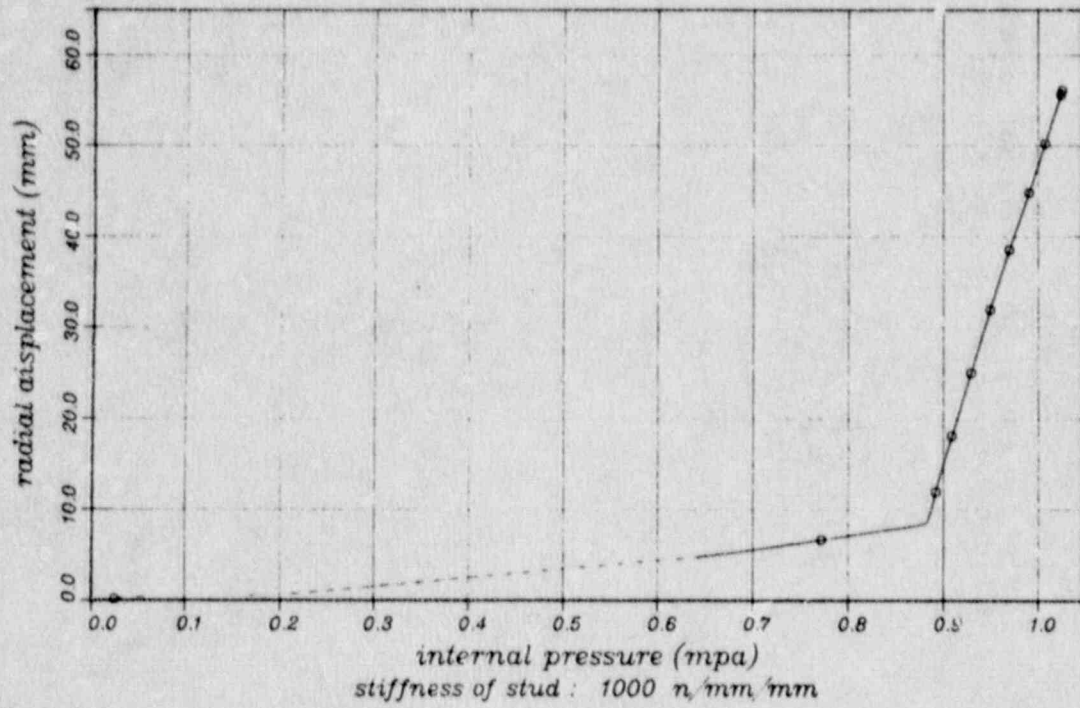
Figure 5.8.32  Radial Displacement of Liner (Simplified Analysis)
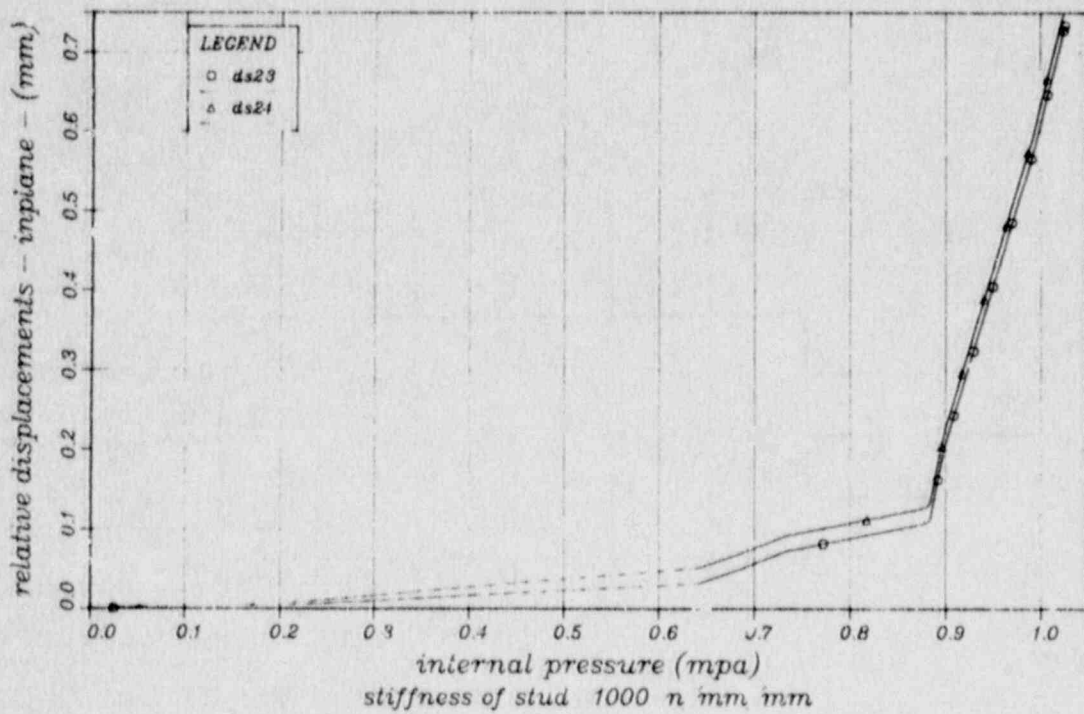


Figure 5.8.33  Relative In-Plane Displacement of Liner (Simplified Analysis)
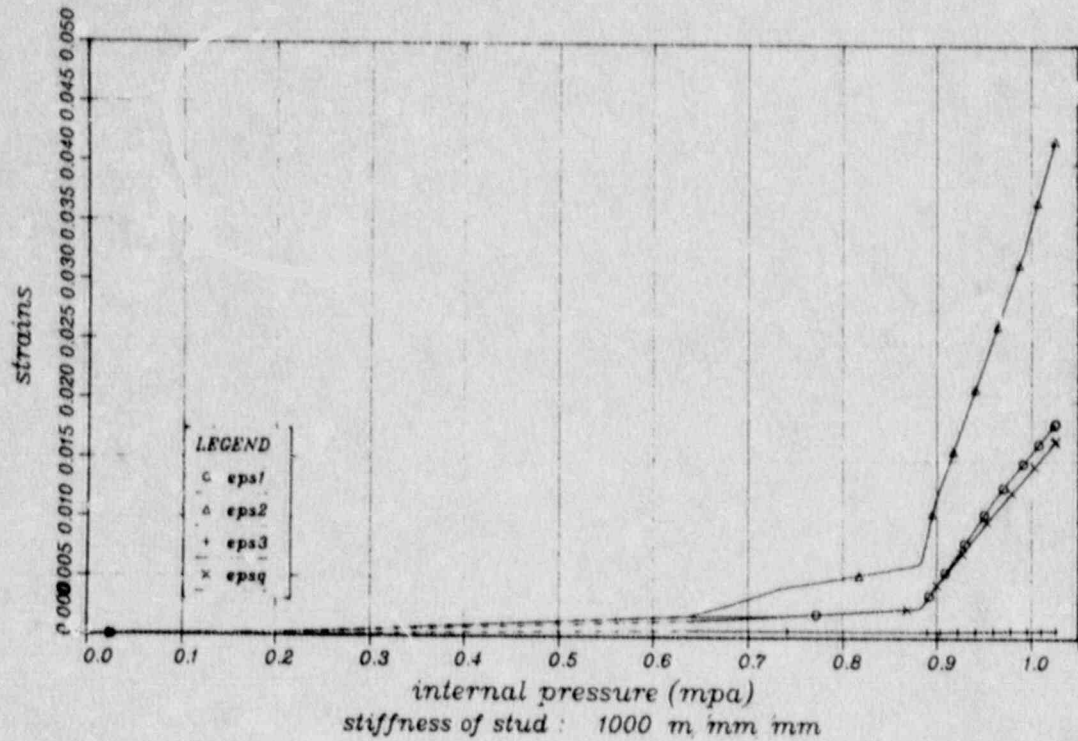
Figure 5.8.34  Liner Strain (Simplified Analysis)
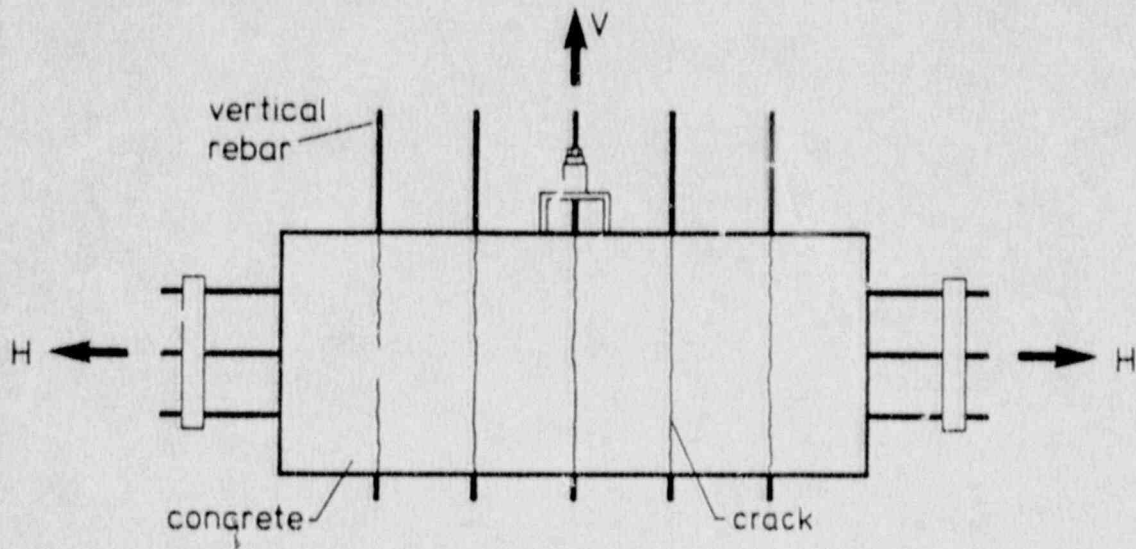


Figure 5.8.35  Test Set-up for Investigating Pull-Out Behavior of Rebars
in Cracked Concrete
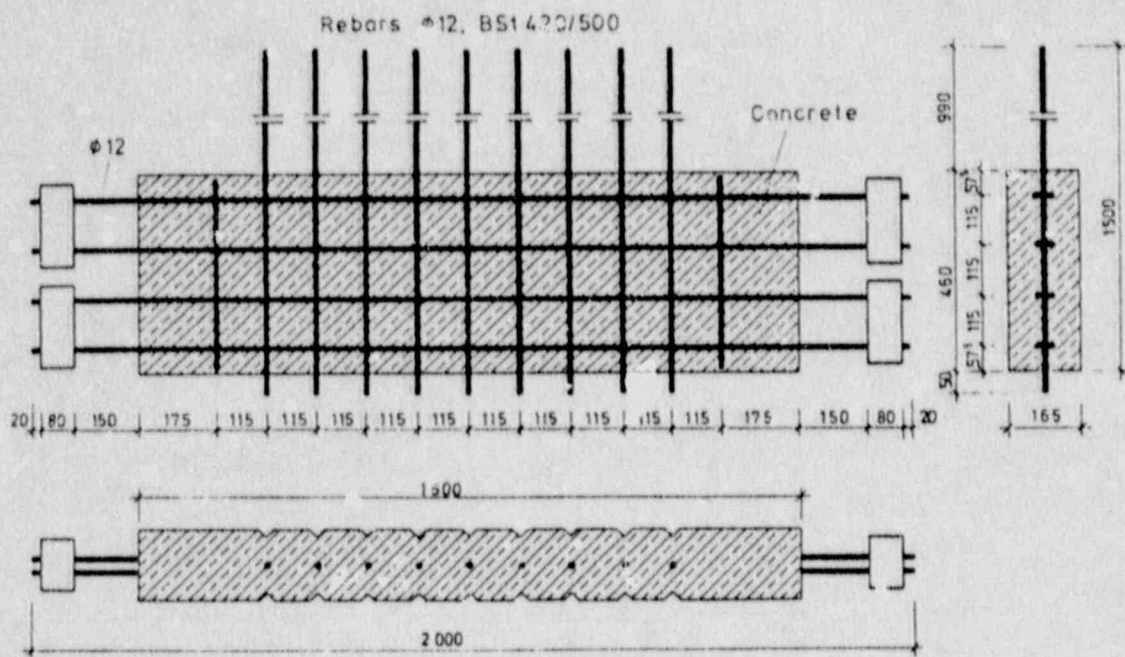
Figure 5.8.36 Details of the Pull-out Test Specimens
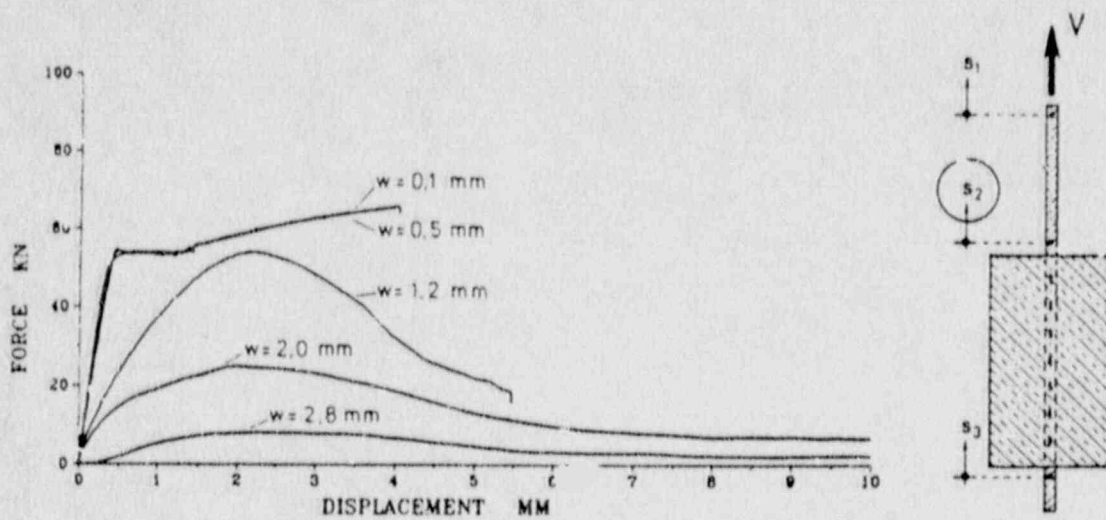


Figure 5.8.37 Pull-Out Force vs. Relative Displacement at the Top Surface
for Several Crack Widths, w
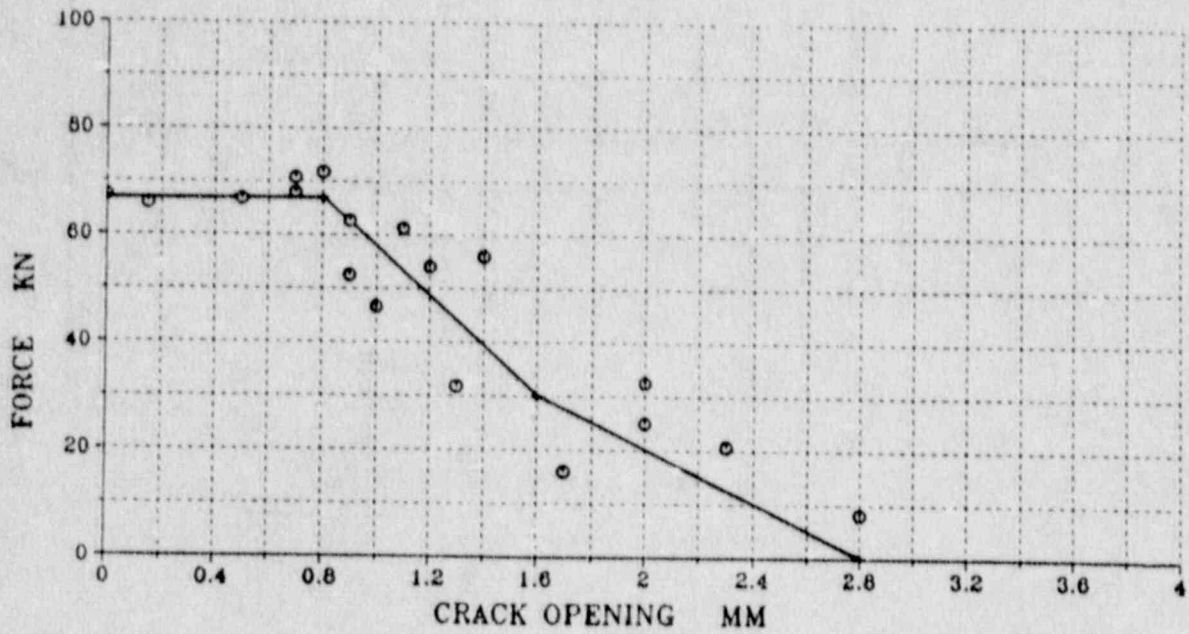
Figure 5.8.38  Maximum Pull-Out Resistance vs. Crack Width for all Tests
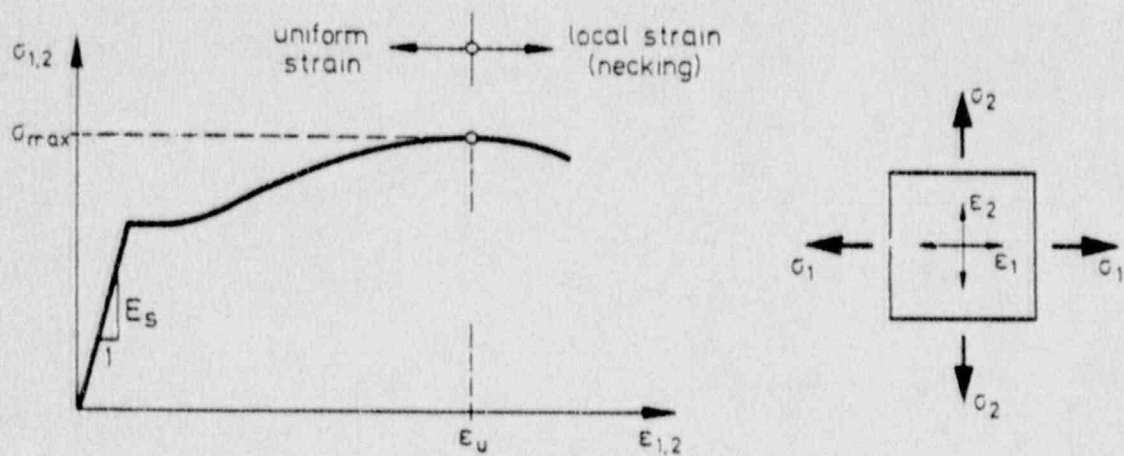


Figure 5.8.39  Ultimate Strains in a Liner Under Biaxial Loading
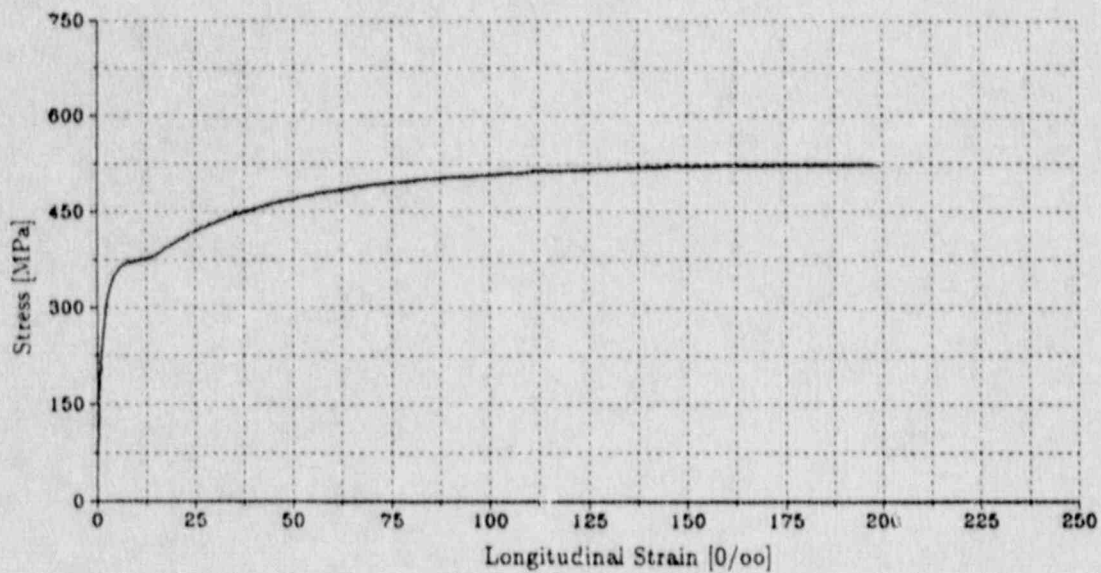
Figure 5.8.40  Uniaxial Stress-Strain Diagram
of a 1.59 mm (1/16 in.) Thick Liner Sheet
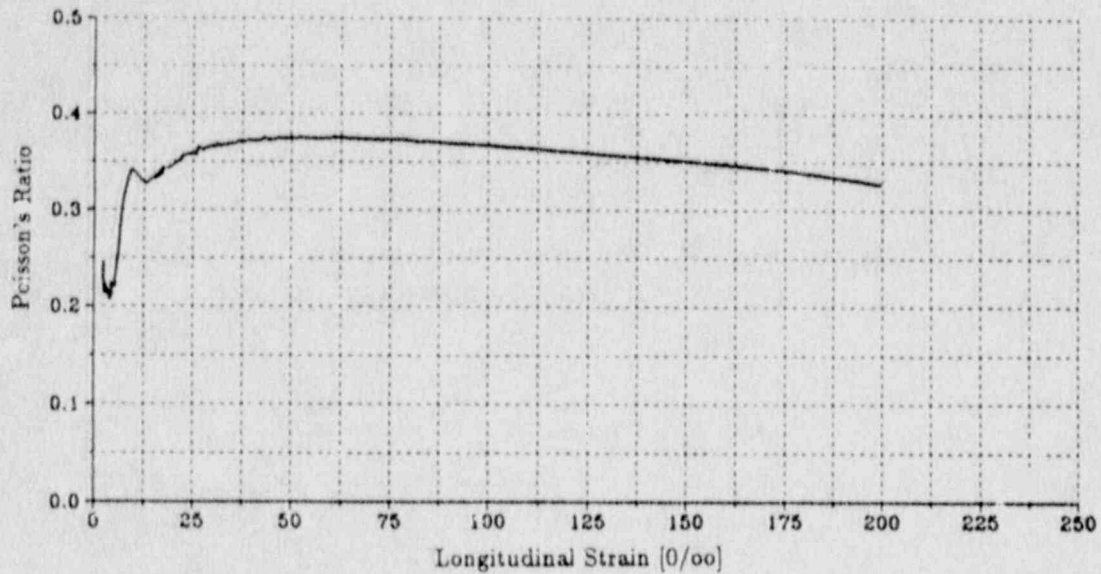


Figure 5.8.41  Poisson's Ratio During Uniaxial Tensile Test
(Refer to Figure 5.8.40)
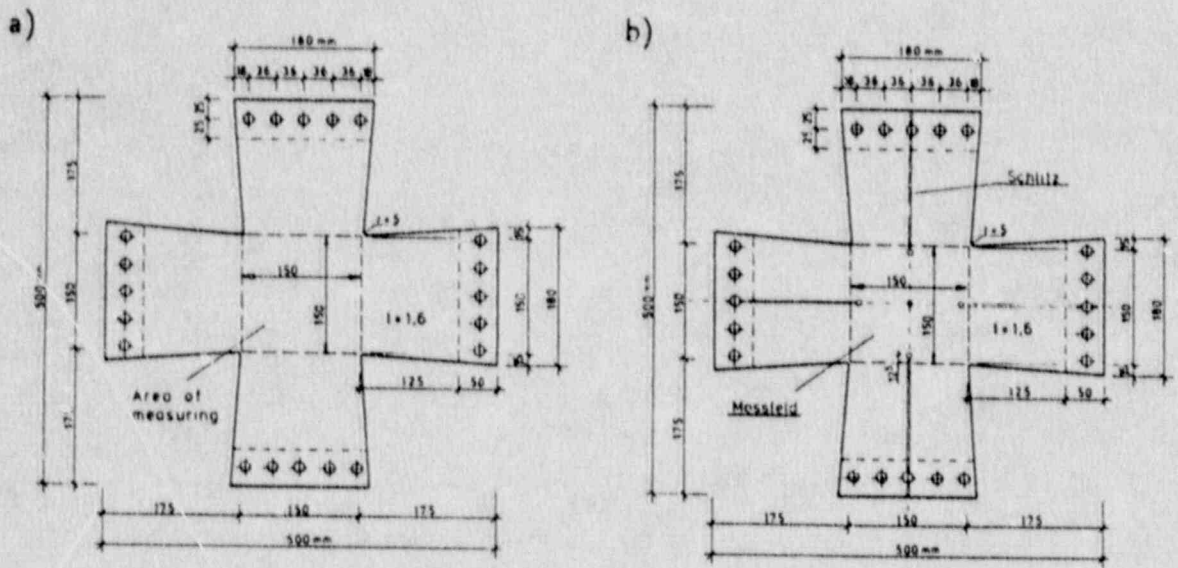
Figure 5.8.42 Liner Test Specimens a) without and b) with Slots
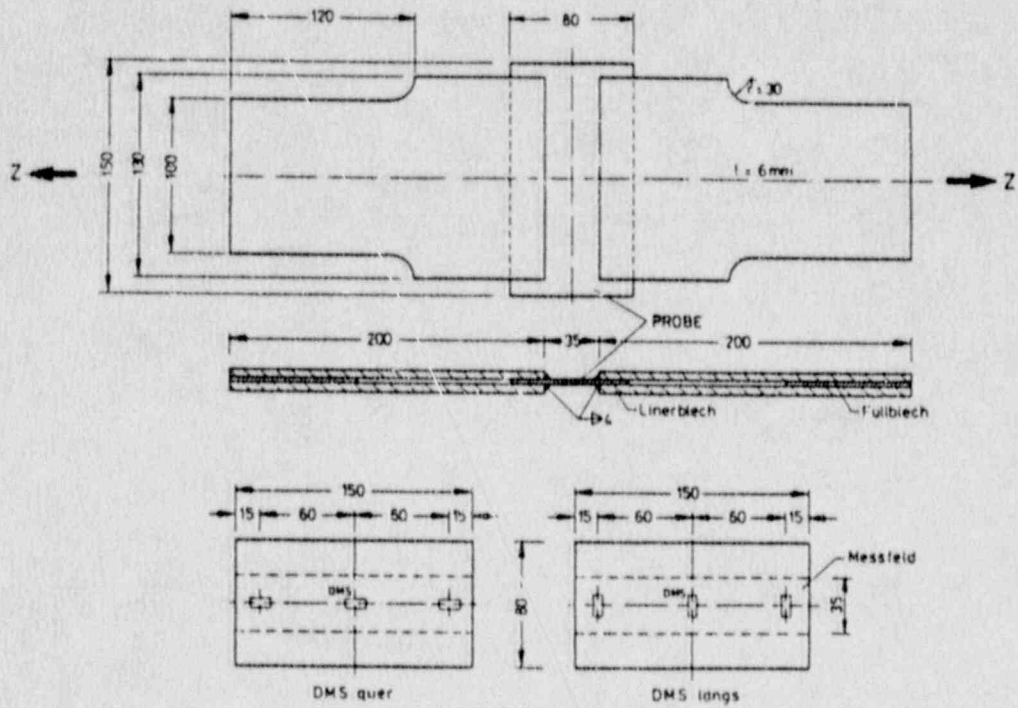


Figure 5.8.43 Specimens for Uniaxial Tension Tests with Lateral Strain Restrained
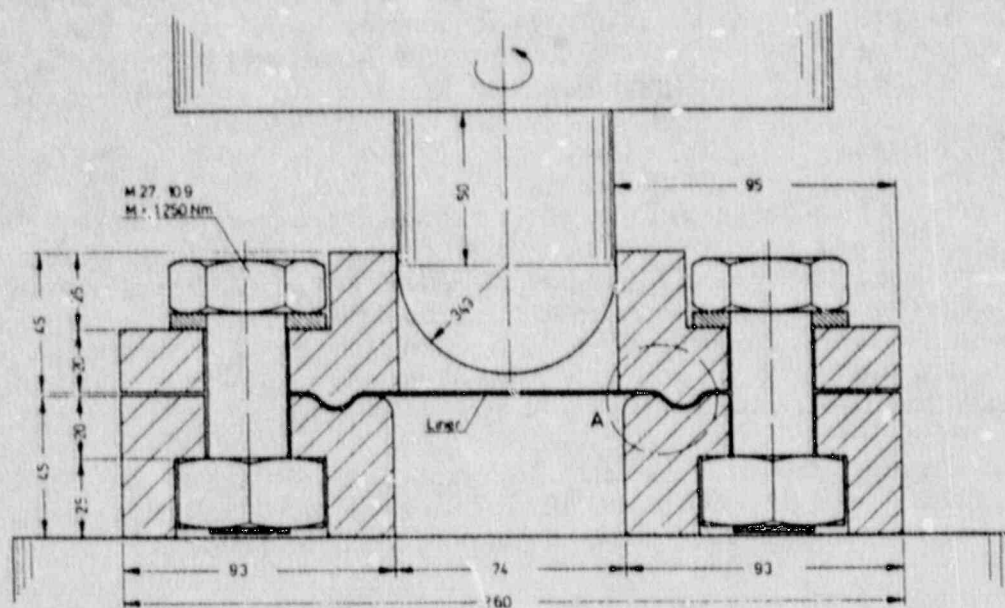
Figure 5.8.44  Test Set-up for Punch Stretching
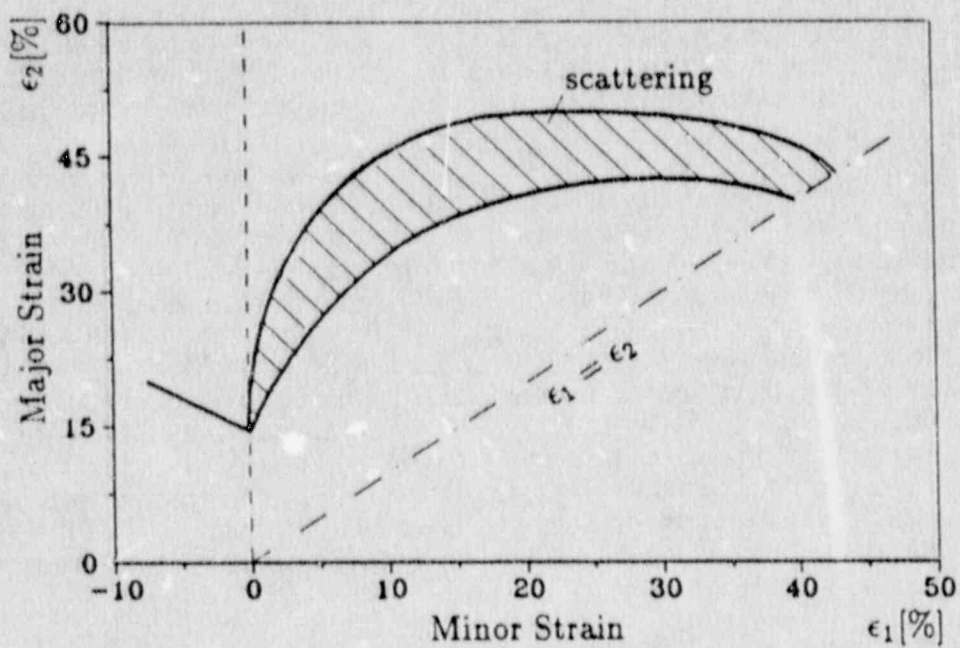


Figure 5.8.45  Approximation of Ultimate Strain Diagram
for Biaxial Loaded Liner Sheets

## 5.9 University of Illinois

This section describes a study of the internal forces at the slab-wall connection of the reinforced concrete containment model, which was performed by the Civil Engineering Department at the University of Illinois under contract to Sandia. The authors are H. P. Walther and M. A. Sozen.

### 5.9.1 Summary

The region near the base of the cylindrical wall of the containment structure is one of the critical locations from the viewpoint of structural resistance. Internal forces in that region cannot all be determined directly from the conditions of equilibrium. A study of the deformation data from the Structural Integrity Test and High Pressure Test confirmed the high quality of the measurements. The consistency of the data provided confidence for estimates of the shear and bending forces at the base of the containment wall.

Because strain data were converted to force assuming that the measurements started at a state of essentially no stress, all data from the two consecutive pressurizations of the containment were first aligned to produce a continuous record.

Based on the experimental data, the nominal shear stress (based on gross section) at the base of the wall was estimated to be 450 psi (3.1 MPa), which is approximately $5.7 \cdot \sqrt{f_c'}$, at the maximum test pressure of 145 psig (1.0 MPa). The shear stress occurred in combination with a (normal) tensile stress of 950 psi (6.5 MPa).

Applicability of predictive expressions for shear strength of reinforced concrete members is strictly limited to the range of parameters covered by the experimental data from which the expressions were derived. The combination of high normal tensile stress, longitudinal reinforcement distributed over the depth of the section, circumferential reinforcement stressed in tension, and presence of inclined shear reinforcement at the critical section place the conditions of the containment test beyond the range of confident projection of available methods and expressions for estimating shear strength.

The force conditions at the wall base can be rationalized in relation to a crude estimate of friction at the critical section. The compressive force on the concrete was 6.9 kip/in. (1.21 MN/m) and the shear force was 4.4 kip/in. (0.77 MN/m) at the maximum HPT pressure of 145 psig (1.0 MPa). But if the internal stress had reached the hypothesized maximum of 175 psig (1.2 MPa), projection of the wall shear force from the observed trend would put it at 5.9 kip/in. (1.03 MN/m). As discussed in Section 5.9.5, the compressive force on the section of maximum shear is not expected to exceed 6.9 kip/in. (1.21 MN/m) at an internal pressure of 175 psig (1.2 MPa). Accordingly, the ratio of shear to compressive force would increase from 0.6 at the maximum test pressure of 145 psig (1.0 MPa) to 0.9 at the hypothesized maximum of 175 psig (1.2 MPa). Interpreted simply in terms of friction, the likelihood of severe distortion at the base of the wall would have increased at internal pressures beyond 145 psig (1.0 MPa).

It is important to note that the shear at the wall base calculated from strain data appeared to be increasing at an increasing rate at the time of maximum test pressure.

## 5.9.2 Introduction

This section is a progress report on a study of the shear strength of the connection between the wall and the base slab of a 1:6-scale reinforced concrete containment structure tested at Sandia National Laboratories, Albuquerque, N.M. The study is being carried out at the Department of Civil Engineering of the University of Illinois, Urbana. Its overall object is to evaluate, using experimental and analytical information, the internal stress conditions at the wall-slab joint and to develop procedures for projecting the information obtained in the model containment test to containment structures with similar characteristics.

Procedures used for interpreting the deformation measurements and resulting estimates of internal forces at the wall-slab joint are described in the following sections. Detailed information about the dimensions, construction, and materials of the containment model (Figure 5.9.1) is provided in [12,63,64]. A series of analyses of the response of the containment structure to internal pressure are reported in [11].

## 5.9.3 Experimental Data

Data from the model reinforced concrete containment structure were obtained in two consecutive loadings: SIT (Structural Integrity Test, maximum pressure of 53 psig, 0.37 MPa) and HPT (High Pressure Test, maximum pressure of 145 psig, 1.0 MPa). In the data released, zero deformation readings in the two tests were independent of one another. At face value, the data from the SIT and HPT loadings would be plotted as illustrated in Figure 5.9.2, data from a particular gage for both tests being plotted in relation to an origin defined by zero pressure and zero deformation. It is evident from the relative positions of the data plotted in Figure 5.9.2 from the SIT and HPT loadings that the comparison is flawed. It is incongruous with behavior of reinforced concrete to develop a total displacement at 50 psig (0.34 MPa) that is lower in the second loading than in the first.

Figure 5.9.3 illustrates an experimentally determined relationship between applied moment and tensile reinforcement strain in a test that included three successive loading stages [62]. Because the test specimen was determinate, it was possible to plot moment against corresponding strain. It follows from the data shown that if it had been necessary to calculate moment from measured strain for loadings 2 and 3, it would have been essential to have information about the entire loading history. It would be erroneous, for example, to calculate moment from strains measured in loading 2 assuming that the curve for loading 2 starts at zero strain. The error in the moment computation could be compensated by recognizing that the initial slope of the moment-strain curve for loading 2 would be different from that for loading 1. But that would require information about the relative locations on the strain axis of the initial points of the moment-strain curves for loadings 1 and 2. In interpreting data from tests with multiple loadings that generate nonlinear response, it is customary and convenient to plot data "cumulatively" and make comparisons with results of theoretical models on that basis.

To interpret the data from the HPT, deformation data were aligned to obtain "continuous" pressure-deformation plots for SIT and HPT loadings. Because of the amount of data involved, the alignment was done using a formal algorithm that included three steps.

1.  The origin for data from the Structural Integrity Test was determined by fitting, using the least-squares method, a straight line to the data obtained at pressures from 5 to 16 psig (0.034 to 0.110 MPa). The location for "zero deformation" was assumed to be at the intersection of this line and the horizontal line at zero pressure.

2.  The residual deformation for the Structural Integrity Test was assumed to be at the intersection of a curve fitted to the data obtained during the unloading stage of the SIT and a horizontal line corresponding to zero pressure. The curve was fitted using the least-squares method with an exponent of four. If the calculated curvature at zero pressure of the fitted curve was found to be negative, the exponent was reduced in successive steps of one until the curvature at zero stress was positive.

3.  The data obtained during the HPT loading were aligned to start from the point on the deformation axis corresponding to the residual strain determined in step (2) above.

The aligned or "continuous" plots of the data from the SIT and HPT loadings for radial-displacement gage D87 are shown in Figure 5.9.4 for pressure up to 100 psig (0.69 MPa). Data from the HPT loading for the same gage are compared with aligned data in Figure 5.9.5. All interpretations in this paper are based on aligned data.

The impact of the alignment on data interpretation may be illustrated using the comparisons made by Dameron et al. [47] for calculated and measured radial displacement. Dameron et al. used data from radial gage D102 to compare results of calculation with those from the HPT loading (Figure 5.9.6a). Data from three additional radial displacement gages at the same elevation but at different azimuths are also compared in Figure 5.9.6 with the calculated curve by Dameron et al. It is noted that the comparison of calculated and measured data was excellent for gage D102 but not as good for the other three gages. The same comparisons are made in Figure 5.9.7 for aligned data. It appears that although the comparison for D102 is not as good as in Figure 5.9.6, the general agreement is better. Considering that Dameron et al. based their calculations on a model that ignored previous loading of the containment, the comparisons in Figure 5.9.7 represent the proper test for the calculated results. Comparisons of calculated and measured curves in Figure 5.9.7 demonstrate that the model by Dameron et al. [47] would be generally quite satisfactory for calculating pressure from measured displacement or displacement from pressure in the ranges of loading before as well as after yielding, a conclusion that would not be reached from Figure 5.9.6.

### 5.9.4 Deformation Response

To put the measurements made on the shear reinforcement in perspective, it is helpful to present and discuss representative strain measurements on longitudinal reinforcement and radial displacement measurements. With the help of Figures 5.9.10 through 5.9.17 and Table 5.9.1, the response of the containment wall is discussed and critical changes in pressure-deformation are identified and related to one another. This is followed by a discussion of the strains measured on the shear reinforcement and their relationships to strain measurements in the wall and in the base slab.

Types of wall reinforcement are identified in Figure 5.9.8. The vertical, hoop, and diagonal (seismic) bars were arranged in eight layers, with layer 1 near the inside surface of the wall. Designations of the strain gages on the vertical and diagonal bars and shear reinforcement (a #4 dowel connecting wall to slab and a stirrup) are also shown in Figure 5.9.8. Figure 5.9.9 shows the main reinforcement in the slab as well as the #4 dowel that has been shown in Figure 5.9.8.

Total reinforcement ratio was 3.4% (effective vertical reinforcement) and 2.8% (hoop reinforcement) in the wall and 0.6% (total radial) in the slab. Concrete cylinder strength at time of test was 6200 psi (42.7 MPa). The #4 bars had a yield stress of 64 ksi (441 MPa). Detailed descriptions of reinforcement, liner, and material properties are provided in [64].

The overall response of the containment structure may be described by the relationship between internal pressure and radial displacement indicated by displacement gage D87 located at approximately mid-height of the containment wall (Figures 5.9.1 and 5.9.5). Changes in the slope of the pressure-displacement curve are related to first cracking of the concrete at ~20 psig (0.14 MPa), local yielding at ~110 psig (0.76 MPa), and general yielding at ~130 psig (0.9 MPa). It is also evident from the slope of the curve near maximum pressure that if liner failure had not occurred, the structure would very likely have resisted larger internal pressures with increase in displacement. The estimate of approximately 175 psig (1.2 MPa) made in pretest analyses for structural strength (p. 7, [11]) is not unrealistic in view of the observed behavior of the containment structure during the high pressure test.

First cracking of the concrete was sensed by the gages on circumferential reinforcement (Figure 5.9.10a), on the inclined wall reinforcement or "seismic" reinforcement (Figure 5.9.10b), and on the vertical reinforcement near the wall-slab joint (Figure 5.9.10c) at about the same pressure.

As indicated in Table 5.9.1, the next significant event occurred as the pressure approached 110 psig (0.76 MPa). Yield strain was recorded in the vertical bar in layer 1 at the wall-slab connection (Figures 5.9.8 and 5.9.10c).

Yielding of the hoop reinforcement at cylinder midheight is indicated to have started as the pressure approached 130 psig (0.9 MPa), as shown in Figure 5.9.10a. This event led to the appearance of general yielding in the pressure-deformation data for circumferential, diagonal, and vertical reinforcement. However, it was after the inclined reinforcement reached its yield stress that the slope of the pressure-deformation curves started approaching a very low value. Strains were measured on the shear reinforcement at three locations around the circumference of the wall and near the slab-wall connection as shown in Figure 5.9.8. The pressure-strain data for a diagonal dowel bar and a stirrup (Figure 5.9.8) are shown in Figure 5.9.13. At a pressure of 80 psig (0.55 MPa), the slopes of both curves changed perceptibly. There was a decrease in the rate of strain increase with pressure. At 120 psig (0.83 MPa), the strain rate for the shear reinforcement started increasing. The reduction in the strain rate of the shear reinforcement that occurred at 80 psig (0.55 MPa) could not be related to any event in the measured response of the wall.

Figures 5.9.14 and 5.9.15 show the data from strain measurements on the top and bottom reinforcing bars in the base slab, respectively. A measure of the extension of the base slab along its radius is obtained by integrating the top and bottom reinforcement strains along the slab radius. The extensions of the slab calculated

from strain measurements are shown in Figure 5.9.16. The plots in Figure 5.9.17 compare the upward deflection at a radius of 11 ft (3.35 m) based on integration of measured slab strains and direct measurement of slab deflection. Because the slab strains were measured on two radially directed bars located within the top and bottom of the slab, with the lower bar aligned directly below the top bar, the difference in strain measured on a top and bottom gage, at the same radius, divided by the bar separation, defines the distribution of curvature. The uplift of the slab edge is calculated from the curvature distribution. The agreement, qualitative and quantitative, between the two curves in Figure 5.9.17 provides confidence for the use of the strains measured in the slab longitudinal reinforcement.

Figure 5.9.17 describes the history of the wall base. From the curve in Figure 5.9.17 it is seen that the wall base was essentially inert up to 70 psig (0.48 MPa). After that pressure was reached, cracking of the base slab near the wall introduced an added flexibility to the support. The reduction of the rate of increase of strain in the shear reinforcement is attributed to the change in support stiffness affected by base-slab cracking.

### 5.9.5 Moment at Base of Wall

The bending moment at the base of the wall was determined using the reinforcement strains indicated by strain gages Wr281, Br2, Wr225, Br23, Wr14, Br7, Br1481, and Br14 (Figure 5.9.8). The forces in the bars were calculated assuming a yield stress of 64 ksi (441 MPa). Yield stress for the liner was assumed to be 50 ksi (345 MPa). Steel modulus was taken as $29 \times 10^6$ psi (200 GPa) and increase in stress beyond yield was ignored. The compressive force on the section was determined from the difference between the net axial force applied to the section, due to dead load distributed along the circumference (dome and wall weight, W, equal to 0.3 kips/in. (0.05 MN/m)) and internal pressure (symbolized by pR/2), and the tension force determined from measured strains in the reinforcement and liner, $T_s$. The concrete compressive force, $C_c$, was calculated from the following equation: $pr/2 - W = T_s - C_c$. At each pressure step the neutral axis was determined from the distribution of vertical strain indicated by the measured strain on vertical reinforcing bars and by the vertical component of strain measured on inclined and diagonal bars, determined by assuming the hoop strain at that section was negligible. The compressive force was assumed to have a triangular stress distribution between the neutral axis and outer wall surface, which located the resultant compressive force one-third the distance from the outer wall surface to the neutral axis. The section moment was calculated about the plastic centroid, which was 6 in. (0.15 m) from the outside face of the wall. The plastic centroid is defined as the location of the resultant force when the entire section is uniformly compressed to a strain of 0.003.

The increase with pressure of moment at the wall base calculated from measured strain is shown in Figure 5.9.18. Moment calculations were initiated after cracking of the section because of lack of confidence in converting concrete tensile strains to force. It is seen that flexural yielding at base of wall occurred at approximately 120 psig (0.83 MPa). Recognizing that the curve should start at the origin, it may also be inferred from Figure 5.9.18 that the rate of increase of moment increased after initial cracking.

### 5.9.6 Shear Force at Base of Wall

Shear strength of reinforced concrete members is influenced by stress distributions in all three dimensions of the member. To consider the shear strength problem in terms of shear stresses on a single section of a member is a distortion of the actual phenomenon. Nevertheless, shear stresses at sections do provide index values to the likelihood of shear failure, especially because relevant knowledge has been traditionally organized in relation to nominal stresses at a critical section.

Figure 5.9.19 shows sets of idealized representations of internal forces acting at a section at the base of the containment wall and at a slab section colinear with the inside face of the wall (at radius = 11 ft (3.35 m), Figure 5.9.1). The total unit shear force, VT, on wall section AB (see Figure 5.9.19) cannot be determined directly from conditions of equilibrium. The internal pressure is symbolized in Figure 5.9.19 as $\sigma_g$ and the portion of the radial shear across the wall base carried by the basemat hoop rebars, located at a radius of 12.25 ft (3.73 m), is represented as $\sigma_h$.

Section AB is crossed by the diagonal dowel and a stirrup in which strains were measured (see Figure 5.9.8). The horizontal component of the forces in these two elements expressed as a unit force on a radius of 11 ft, referred to as VR, would make up part of the total force VT.

At the higher test pressures with the base slab cracked radially and circumferentially, the total unit shear force VT is balanced by the net normal unit tension force on section CD (see Figure 5.9.19) and the radial component of the hoop bars near the edge of the base slab. The force at section CD is produced by three elements: the liner, the reinforcing bars, and the intact concrete. The unit tensile force in the liner is relatively small and part of it may be transmitted directly to the liner on the wall, without creating a shear stress in section AB. The portion of the wall shear carried within the base by the outside hoop reinforcement is also small and may be estimated from the radial stretch at the top of the basemat, which was approximately 0.02 in. (0.5 mm) at the end of the high pressure test, as shown in Figure 5.9.16. Assuming that three #6 bars (two at 148 in. (3.76 m) radius and one at 137 in. (3.48 m) radius) carry a hoop strain of 0.00015 (calculated from the estimated radial displacement on a radius of 137 in. (3.48 m)), their contribution to the shear carrying capacity is less than 5 psi (0.034 MPa) across the gross wall section. At higher internal pressures, both the tensile and compressive forces on the concrete are negligible. Relating the total shear across section AB only to the tensile forces in the slab reinforcement is considered to be a good (and low) estimate of the actual shear force.

The variation of the unit shear VR, calculated from strains on shear reinforcement, with internal pressure is plotted in Figure 5.9.20. The first break in the curve at approximately 20 psig (0.14 MPa) is related to initial cracking of the concrete. As it was observed in the measured moment-pressure relationship (Figure 5.9.18), the rate of transfer of forces to the base slab increased apparently as a result of the fact that flexural cracks at slab base reduced the connection stiffness less than the vertical cracks in the containment wall reduced the circumferential stiffness of the wall.

The variation of the total unit shear VT on section AB is plotted in Figure 5.9.20 only for pressures above 110 psig (0.76 MPa) because, at lower pressures, contribution of concrete tensile strength makes the calculation of the total tensile force on section CD questionable.

The dashed line near the origin describes the relationship between internal pressure and nominal shear stress calculated from theory of elasticity using gross sections and a Poisson's ratio of zero. The curve is stopped at the stress corresponding to initial cracking but its slope suggests that the variation of the total shear stress was also affected by the changes in relative stiffness that influenced curve VR.

Figure 5.9.21 repeats the information in Figure 5.9.20 with the addition of calculated shear-pressure curves from [11]. Curve N1 was based on the solution contributed by HM Nuclear Installations Inspectorate (p. 234, [11]) and curves S3 and S4 refer to the solutions obtained at SANDIA for models 3 and 4 (p. 80, [11]).

It is interesting to note that the calculated shear-pressure relationships (N1, S3, and S4) are essentially linear up to near the maximum pressure. They appear to be insensitive to the stiffness changes in the slab. At maximum pressure, the shear stresses indicated by the measurements (VT) and by the three analytical solutions are comparable. However, the trends of the calculated results imply that the wall shear does not increase beyond that level while the trend of the curve VT indicates that the shear stress would continue to increase with increase in pressure.

At the maximum internal pressure of 145 psig (1.0 MPa), the unit shear force at wall base was 4.4 kips/in. (0.77 MN/m) corresponding to a nominal stress (based on gross section) of 450 psi (3.1 MPa) or $5.7 \cdot \sqrt{f_c'}$. The shear stress of 450 psi (3.1 MPa) existed in combination with a nominal tensile stress of 950 psi (6.5 MPa) on section AB. This combination of stresses places the phenomenon well out of the range of experience in reinforced concrete building structures. Three conclusions and a speculation result from the study of internal forces in the containment structure.

1. The variation of measured shear stress at the base of the wall was sensitive to changes in relative stiffness caused by initial cracking of the concrete in the wall, cracking of concrete in the base slab, and yielding of the hoop reinforcement.

2. For the particular geometry, material properties, and reinforcement arrangement of the test structure, a nominal shear stress of 450 psi (3.1 MPa) or $5.7 \cdot \sqrt{f_c'}$ was attained without evidence of shear distress. Hard information to help project this observation to other conditions is lacking. However, the apparent shear strength of the connection may be rationalized by noting that the unit compressive force on the section at maximum pressure (computed from measured reinforcement strains at wall base, measured internal pressure, and weight of containment structure above base) was approximately 6.9 kips/in. (1.21 MN/m). The unit shear force determined from measured strains in the slab reinforcement was 4.4 kips/in. (0.77 MN/m). The implied gross friction coefficient was less than two-thirds, a value that would be considered to be well within the safe domain for friction between rough concrete surfaces.

3. At the maximum internal pressure reached, the nominal shear stress in the base slab was approximately 240 psi (1.65 MPa) or $3 \cdot \sqrt{f_c'}$ in combination with a normal tensile stress of 110 psi (0.76 MPa). Strain measurements on the slab bars indicated the presence of cracks within the slab. The base slab was not an inert portion of the structure and affected the response at the wall-base connection.

At the time the test was stopped by tearing of the liner, the shear reinforcement at the wall-slab joint had essentially matured but the total shear was continuing to increase. From the rate of observed increase in shear at wall base, it is estimated that, at an internal pressure of 175 psig (1.2 MPa), wall shear could have reached approximately 5.9 kips/in. (1.03 MN/m) or 600 psi (4.14 MPa). The maximum compressive force on the section is estimated to be less than the 6.9 kips/in. (1.21 MN/m). Under those conditions, the likelihood of severe sliding distortion at the wall-slab joint is not negligible.
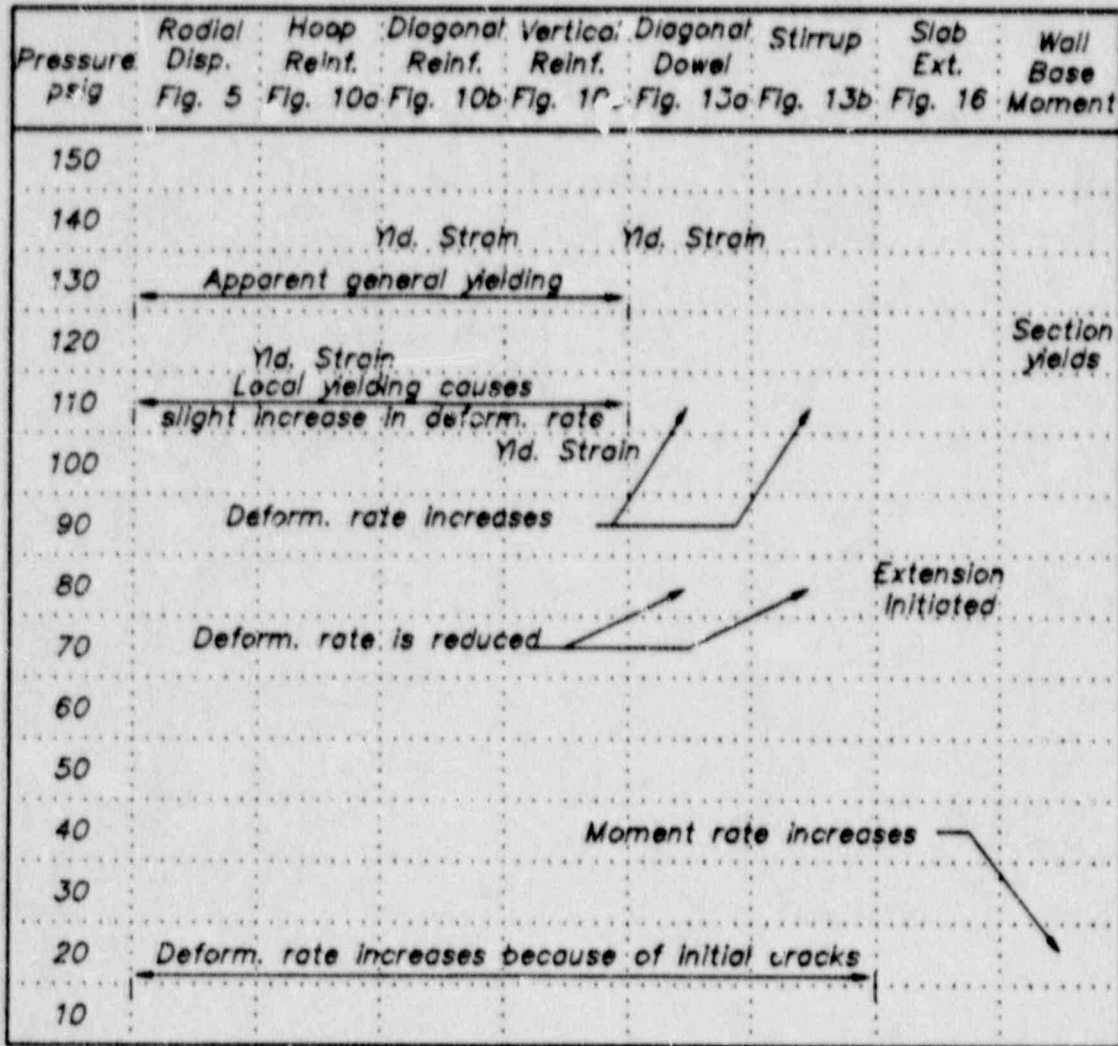
### 5.9.7 Acknowledgment

Table 5.9.1
Changes in Measured Pressure-Response Rates

| Pressure psig | Radial Disp. Fig. 5 | Hoop Reinf. Fig. 10a | Diagonal Reinf. Fig. 10b | Vertical Reinf. Fig. 10c | Diagonal Dowel Fig. 13a | Stirrup Fig. 13b | Slab Ext. Fig. 16 | Wall Base Moment |
|---|---|---|---|---|---|---|---|---|
| 150 | | | | | | | | |
| 140 | | | Yld. Strain | | Yld. Strain | | | |
| 130 | Apparent general yielding | | | | | | | |
| 120 | | Yld. Strain | | | | | | Section yields |
| 110 | Local yielding causes slight increase in deform. rate | | | | | | | |
| 100 | | | | Yld. Strain | | | | |
| 90 | Deform. rate increases | | | | | | | |
| 80 | | | | | | | Extension Initiated | |
| 70 | Deform. rate is reduced | | | | | | | |
| 60 | | | | | | | | |
| 50 | | | | | | | | |
| 40 | | | | | Moment rate increases | | | |
| 30 | | | | | | | | |
| 20 | Deform. rate increases because of initial cracks | | | | | | | |
| 10 | | | | | | | | |

5-338

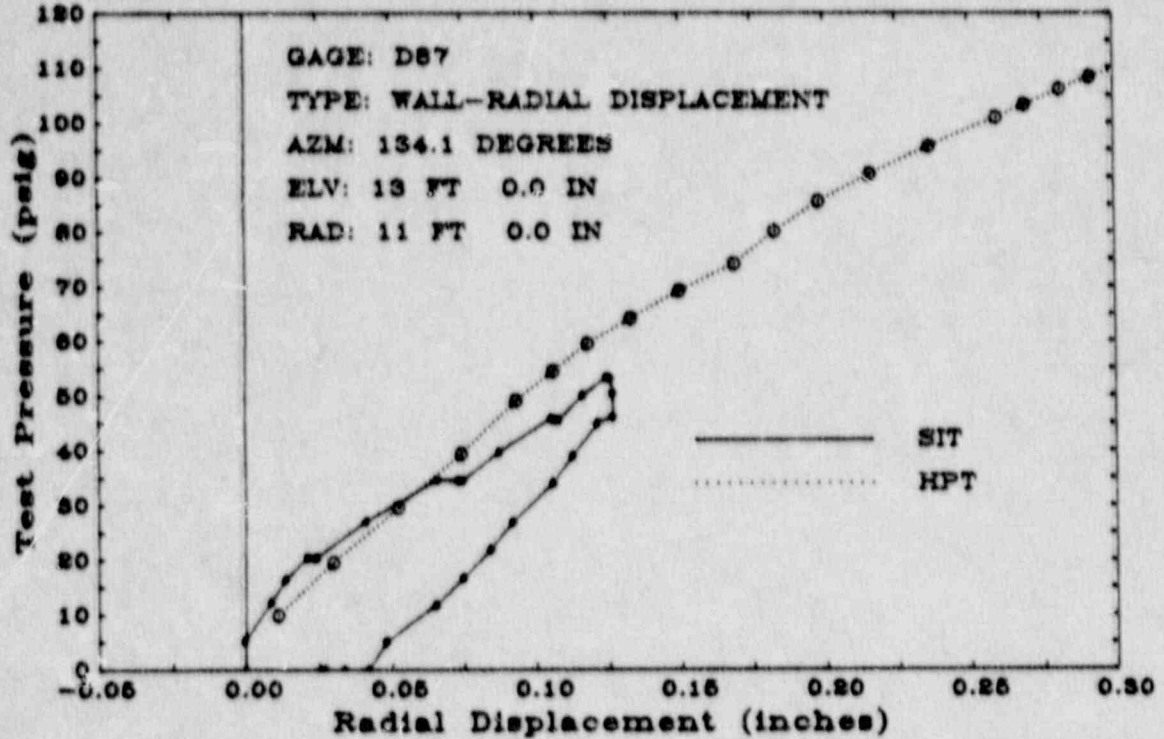Figure 5.9.1 Section of Reinforced Concrete Test Structure
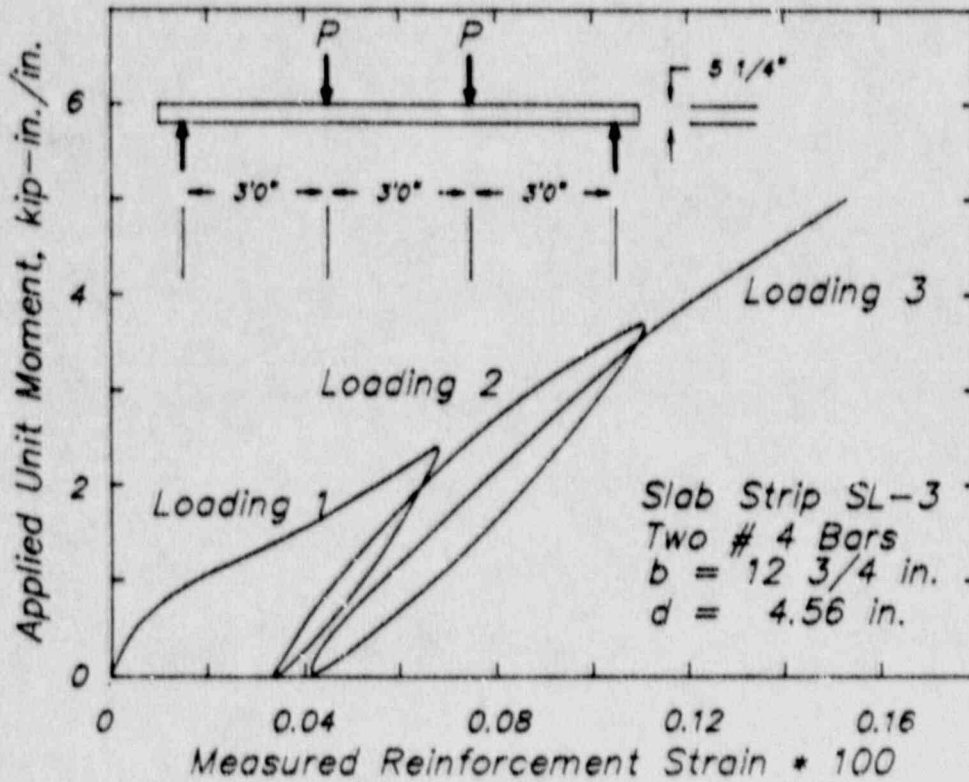
Figure 5.9.2 Sample of Plot from Reported Data



Figure 5.9.3 Measured Moment-Strain Relationship [62]

GAGE D87, CHAN #206, CONTINUOUS DATA, SIT & HPT

GAGE: D87
TYPE: WALL-RADIAL DISPLACEMENT
AZM: 136.1 DEGREES
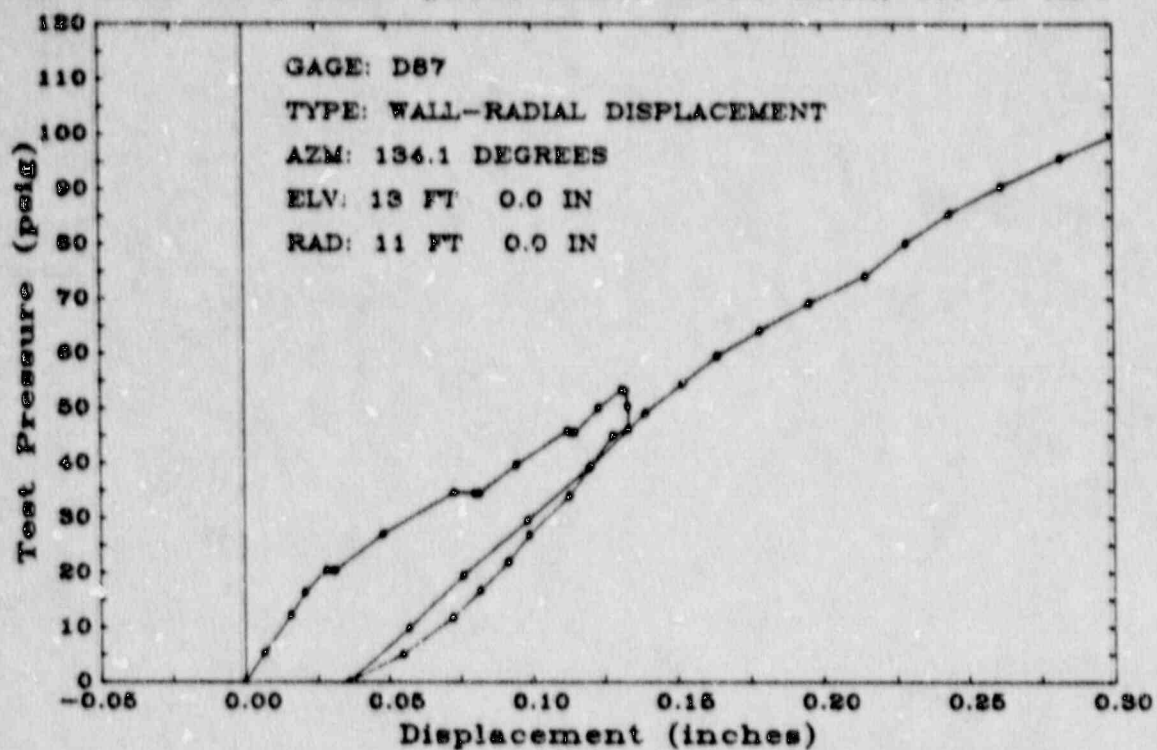ELV: 13 FT    0.0 IN
RAD: 11 FT    0.0 IN

Figure 5.9.4  Aligned Data for Radial Displacement Plotted Continuously
for SIT and HPT Loadings

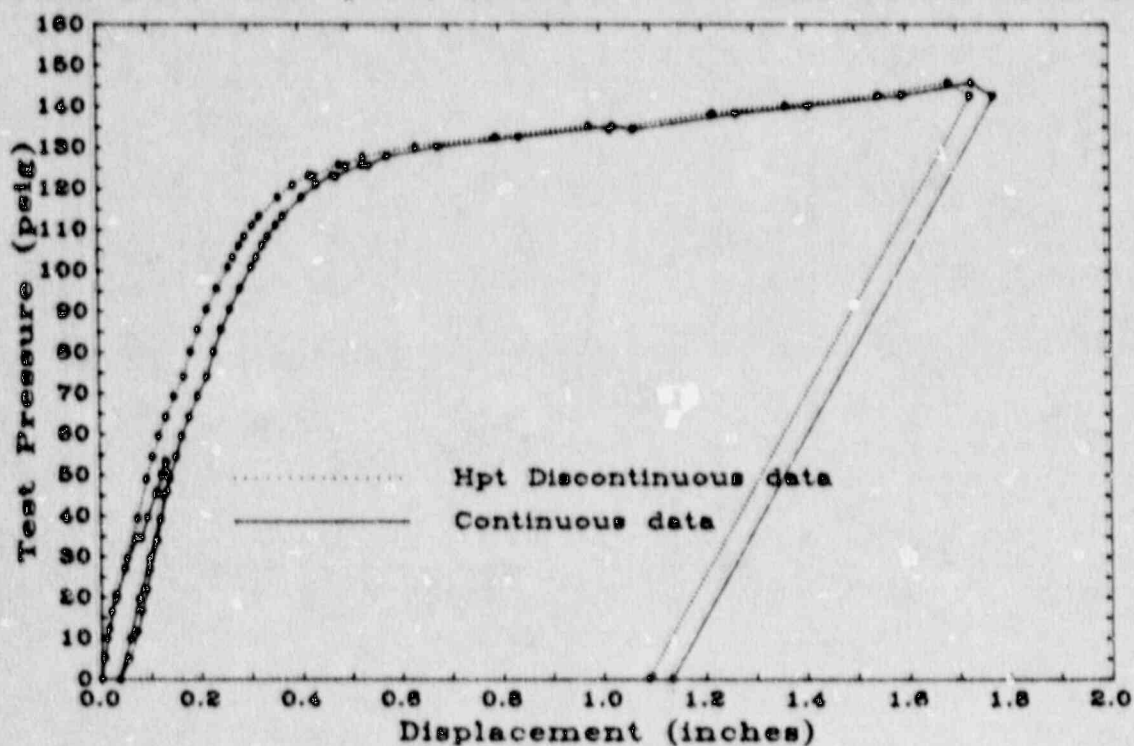GAGE D87, CHAN #206, DISCONTINUOUS and CONTINUOUS DATA

Hpt Discontinuous data
Continuous data

Figure 5.9.5  Comparison of Aligned (Continuous Plot) with Non-Aligned Data
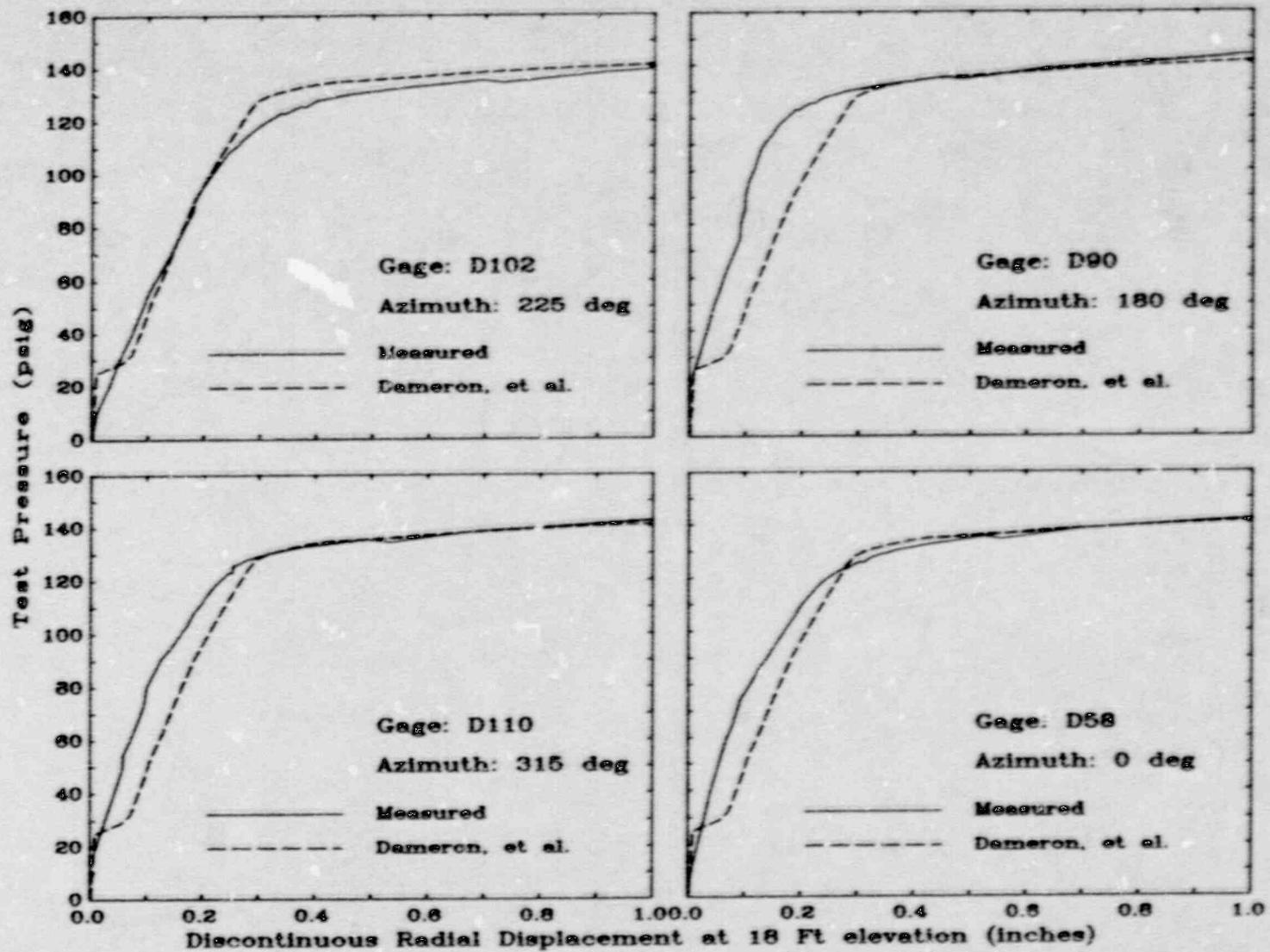
Figure 5.9.6 Comparison of Radial Displacement Calculated by Dameron et al. [47] with Measurements from HPT Loading
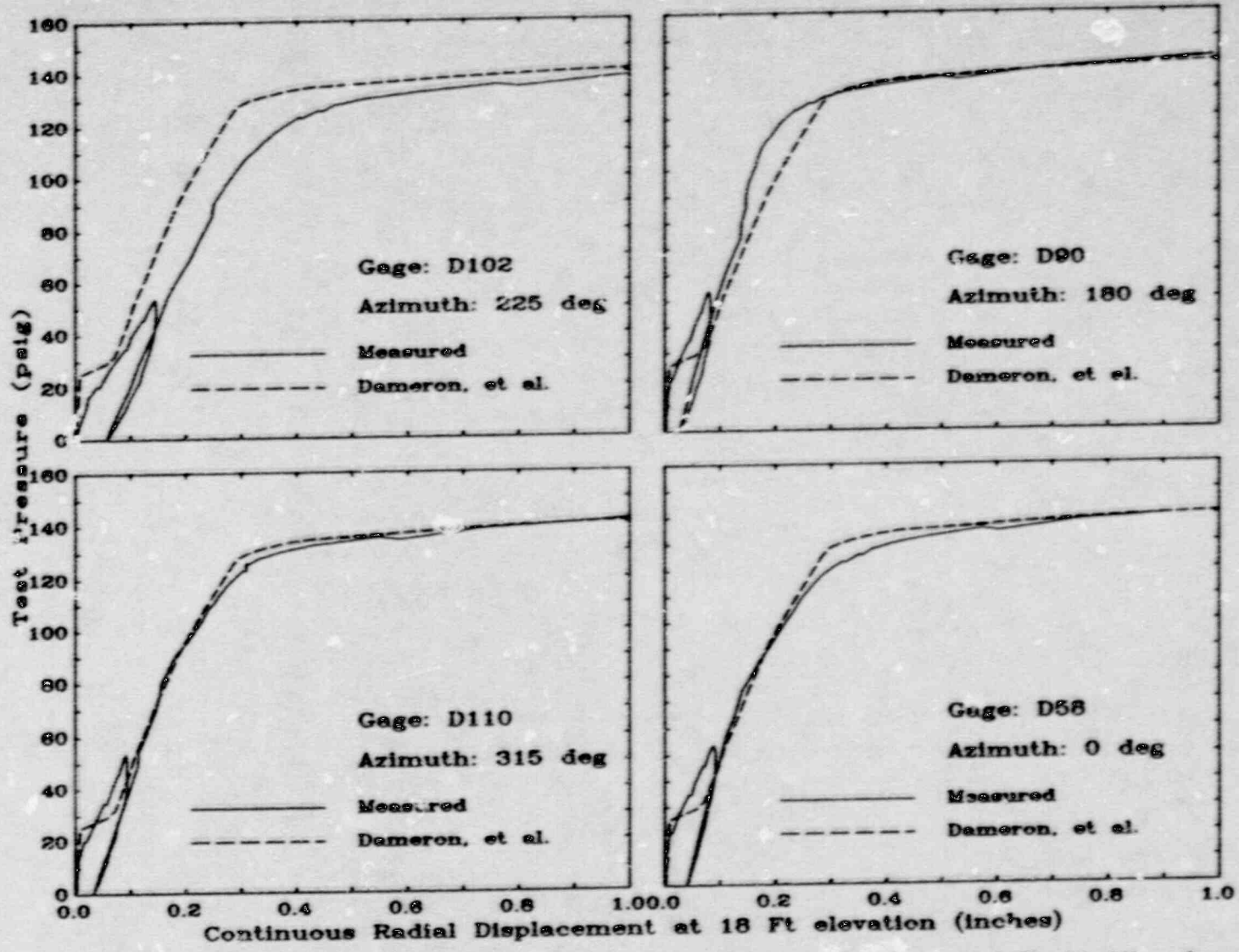
Figure 5.9.7 Comparison of Radial Displacement Calculated by Dameron et al. [47] with Aligned Displacement Data (Plotted Continuously for SIT and SFT)
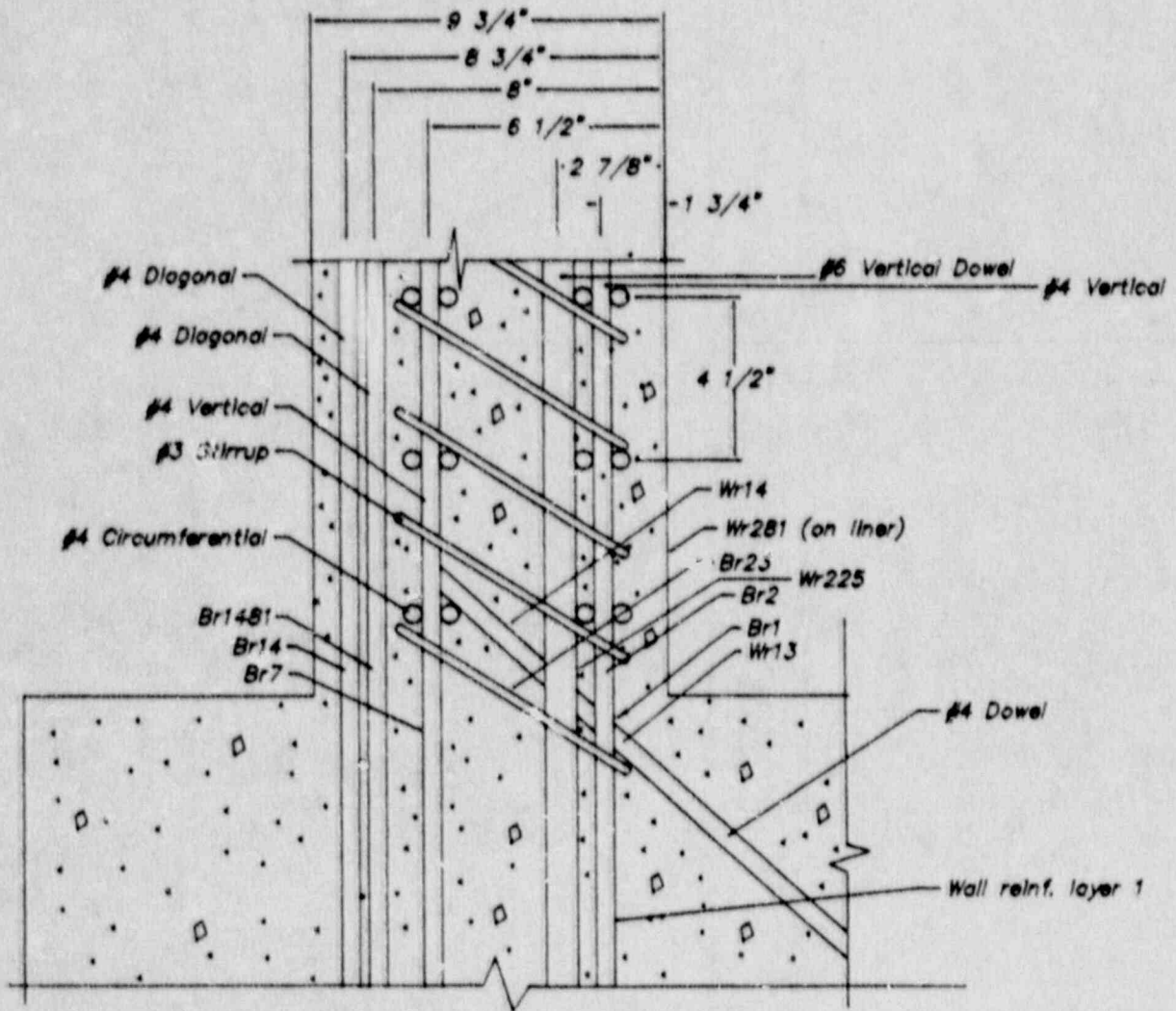
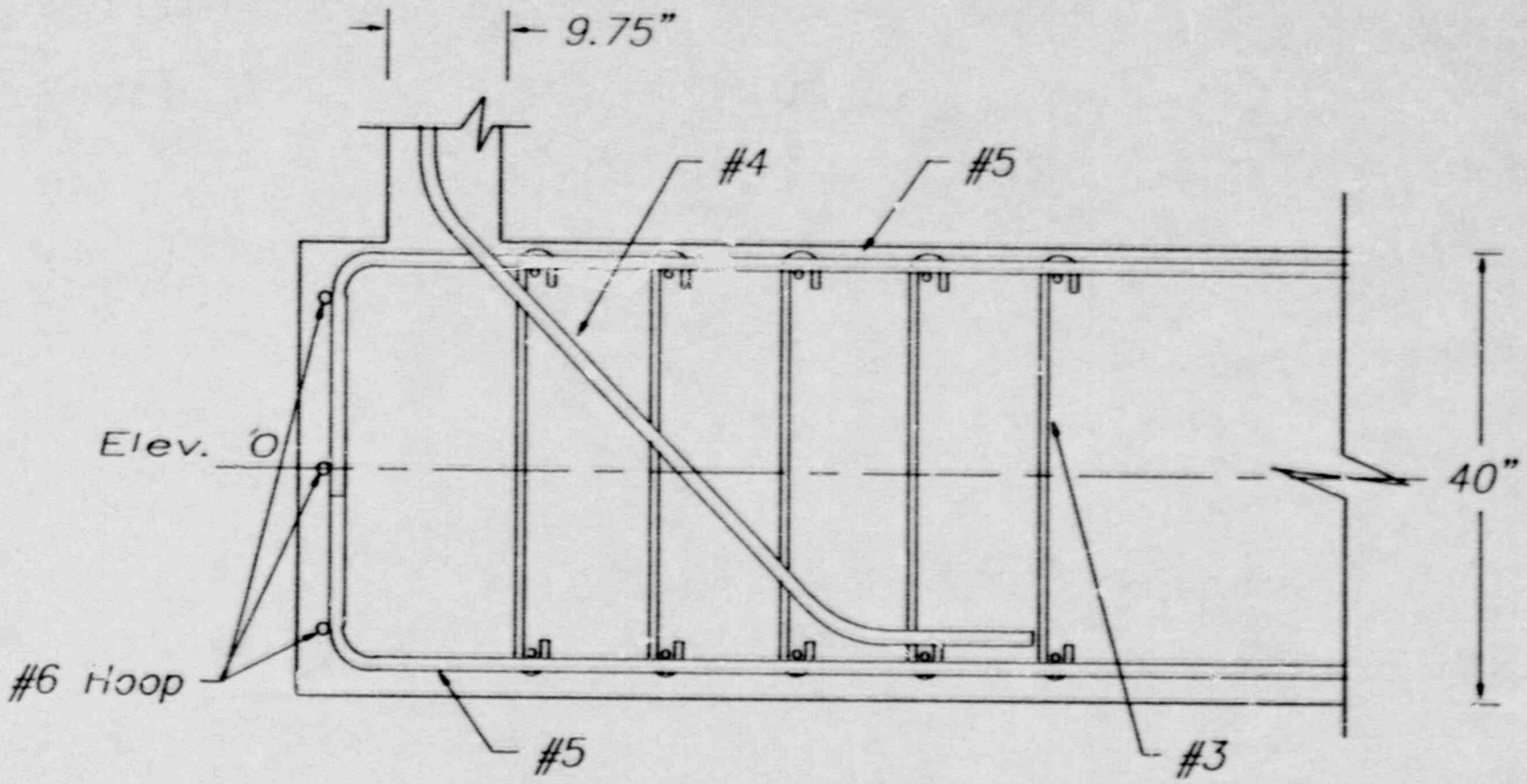Figure 5.9.8  Wall Reinforcement at Wall-Slab Connection

Figure 5.9.9 Slab (Basemat) Reinforcement
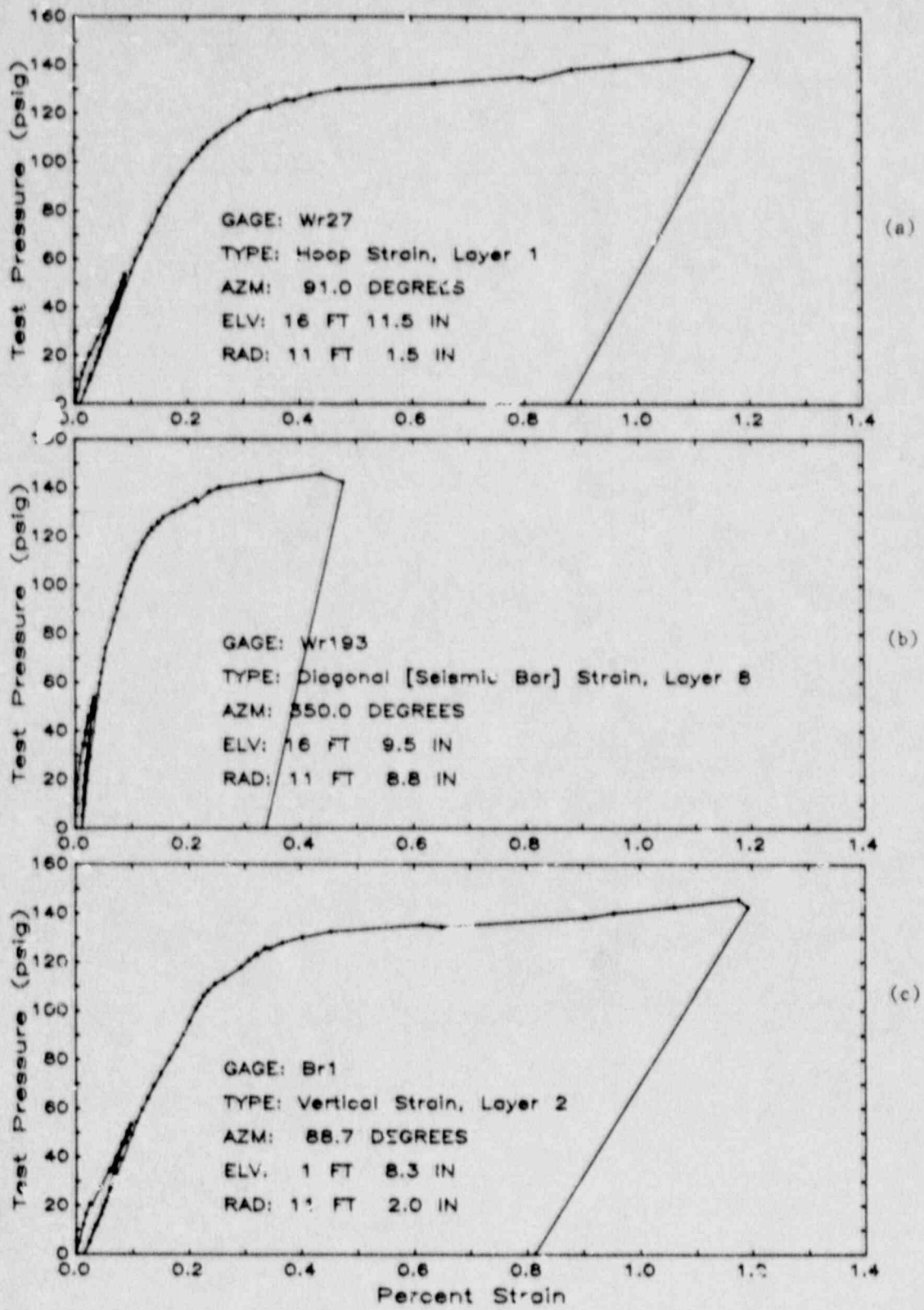
Figure 5.9.10 Samples of Strain Measured in Wall Reinforcement
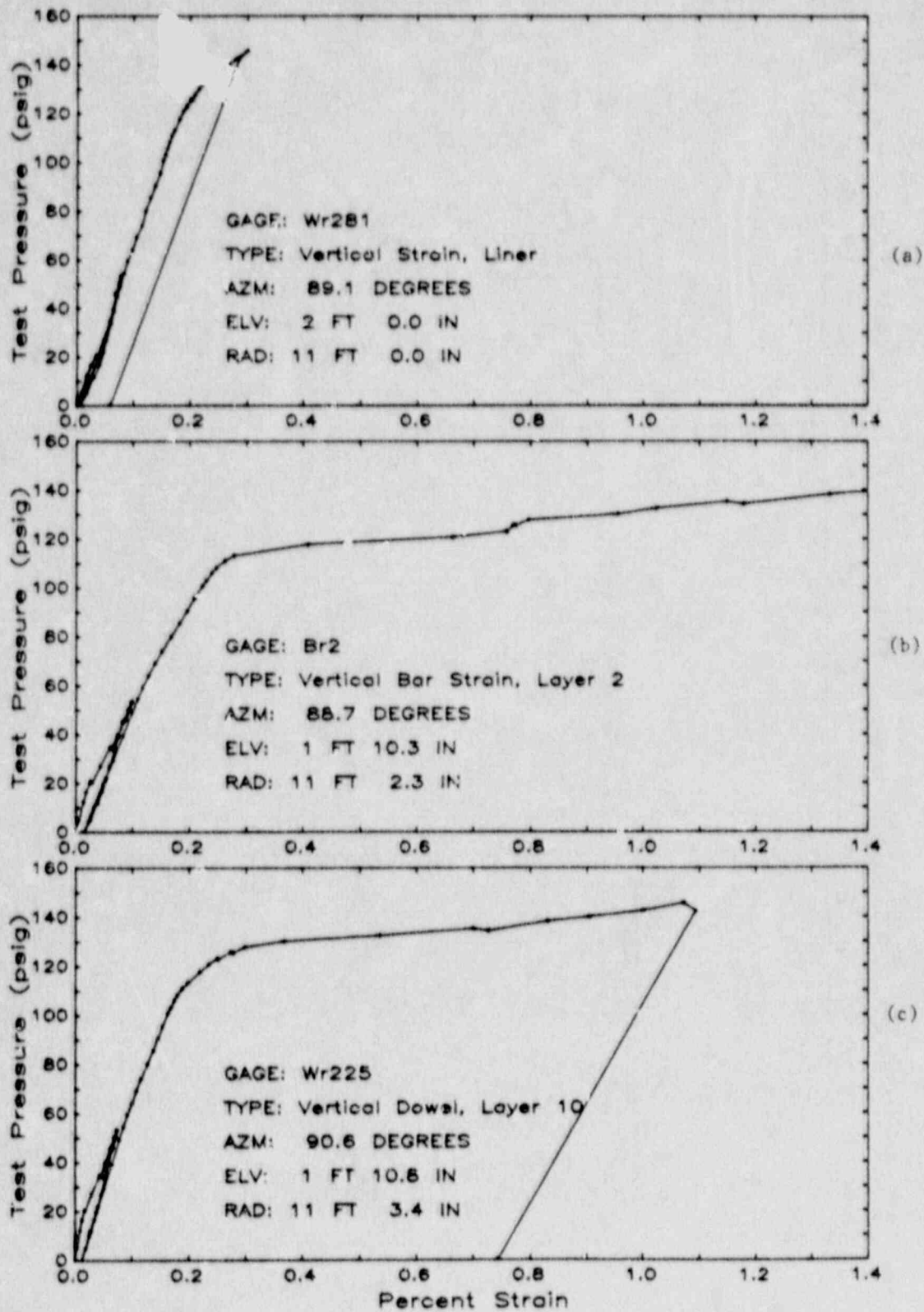
Figure 5.9.11 Measured Strain in Vertical Reinforcement at Wall-Slab Connection
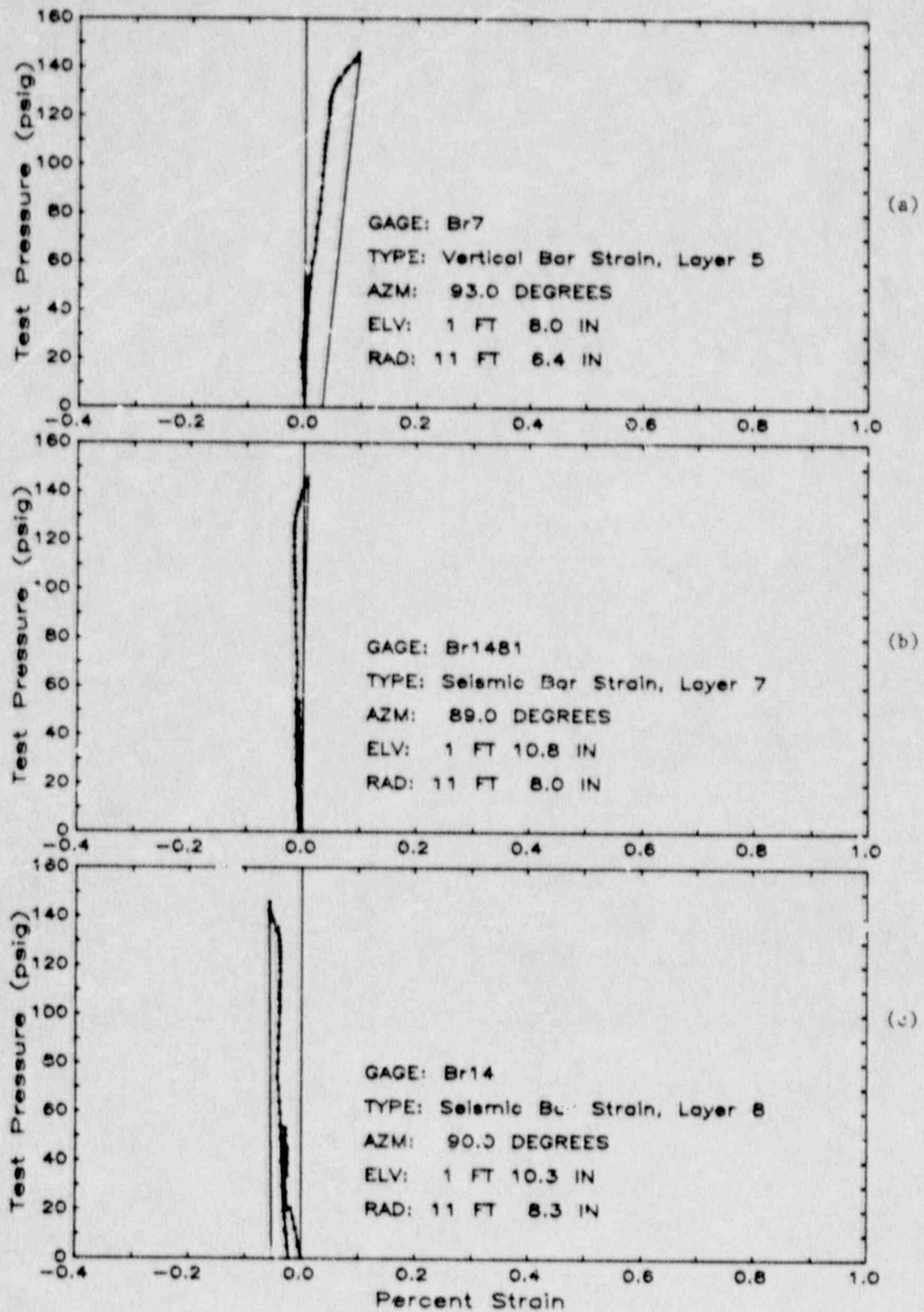
Figure 5.9.12 Measured Strain in Vertical and Diagonal Reinforcement at Wall-Slab Connection

5-348

(a)

GAGE: Wr14
TYPE: Diagonal Dowel, Layer 11
AZM:  91.9 DEGREES
ELV:  1 FT 10.5 IN
RAD:  11 FT  4.3 IN

(b)

GAGE: Br23
TYPE: Diagonal Shear Stirrup
AZM:  88.3 DEGREES
ELV:  1 FT  9.0 IN
RAD:  11 FT  5.0 IN
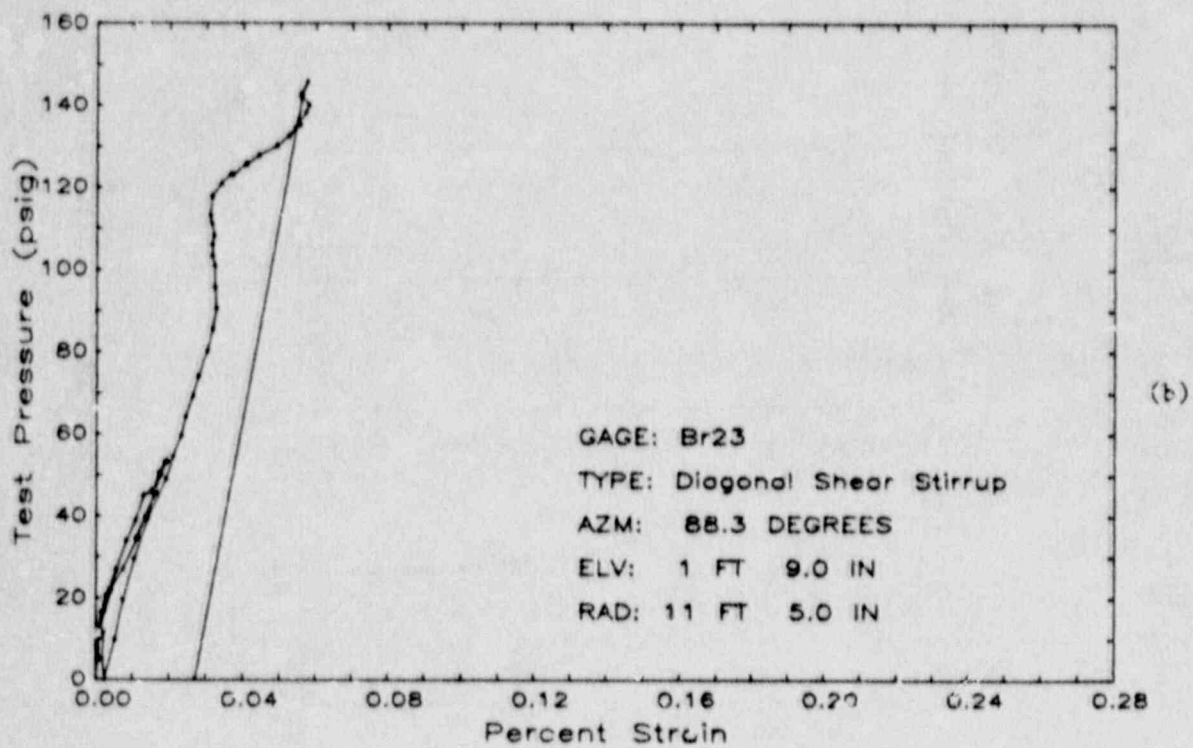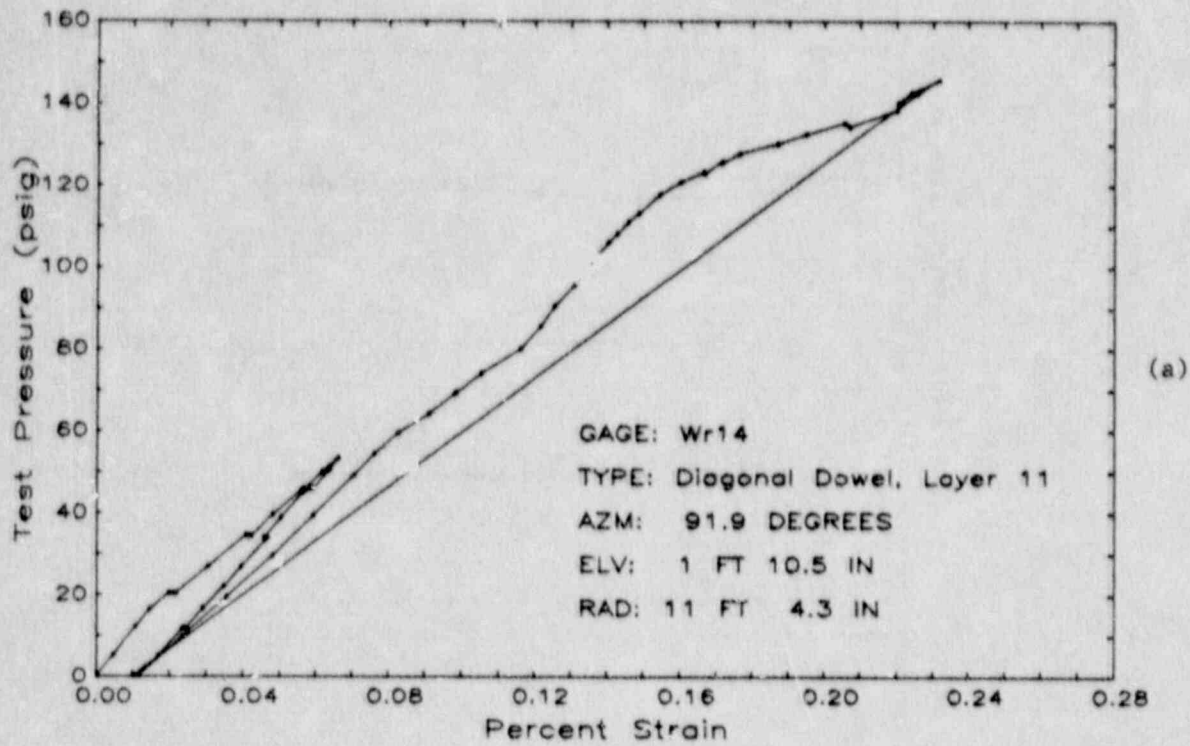
Figure 5.9.13  Measured Strain in Shear Reinforcement at Wall-Slab Connection

# RADIAL BAR STRAIN AT TOP OF BASEMAT
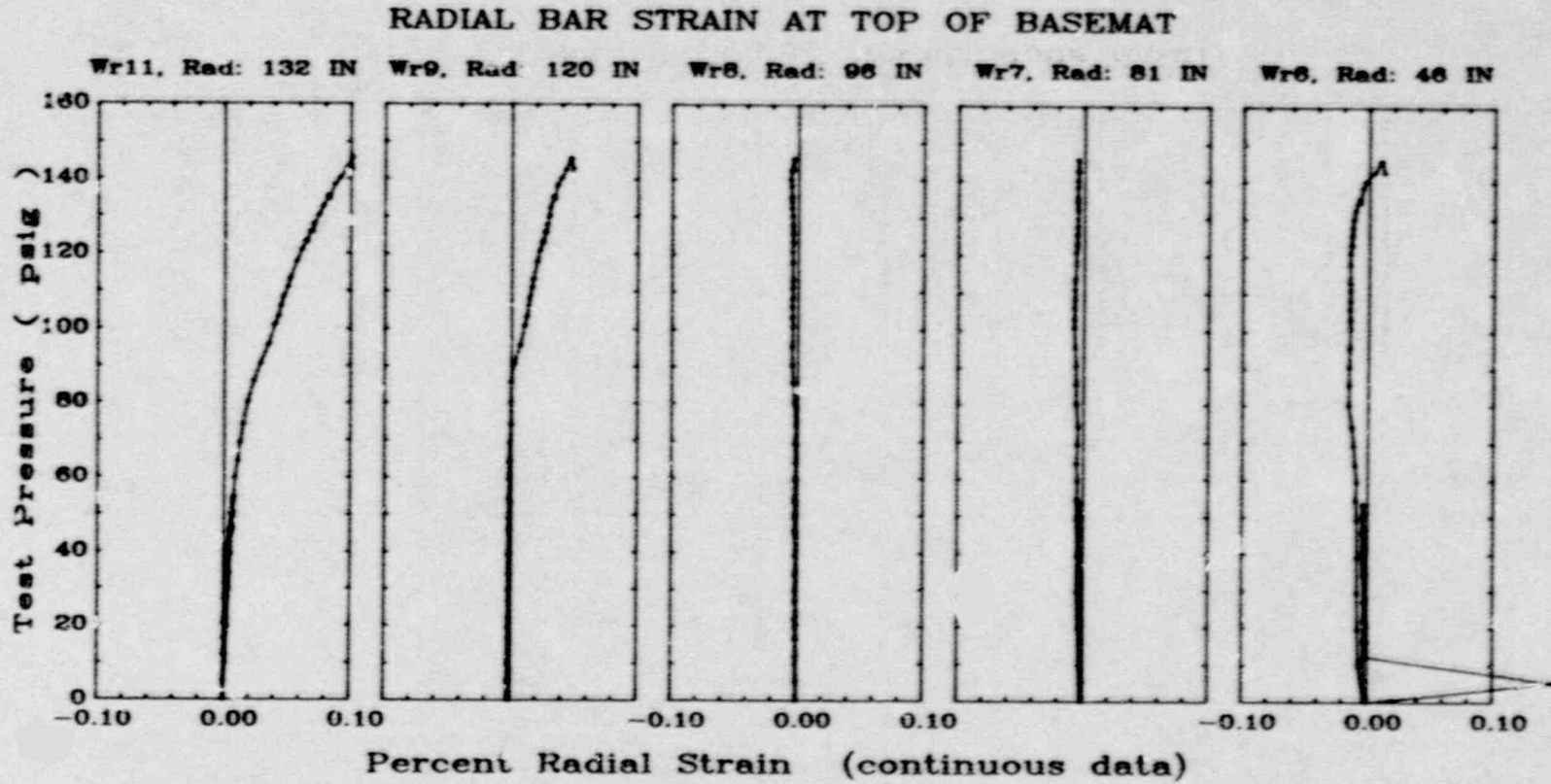


Figure 5.9.14  Measured Radial Strain in Top Reinforcement of Base Slab

# RADIAL BAR STRAIN AT BOTTOM OF BASEMAT
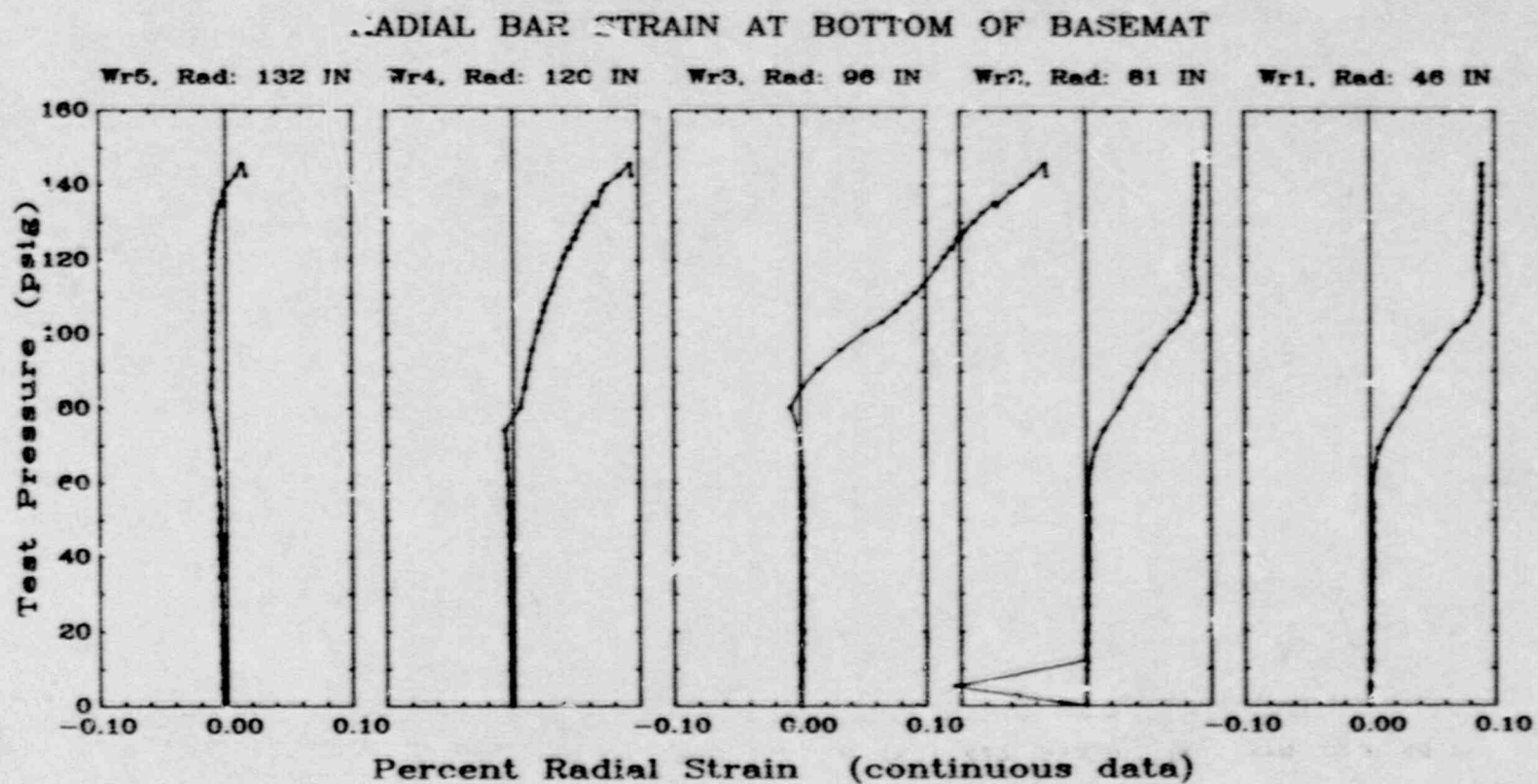


Figure 5.9.15  Measured Radial Strain in Bottom Reinforcement of Base Slab

5-351
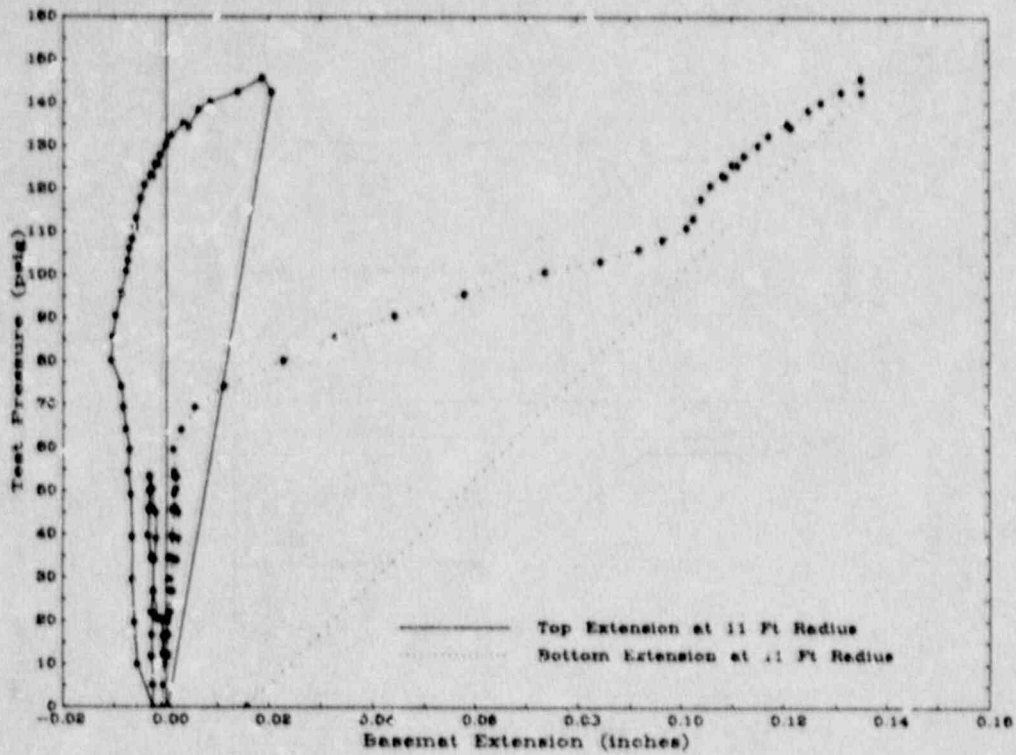
Figure 5.9.16 Extensions of Base Slab Based on Measured Radial Strain
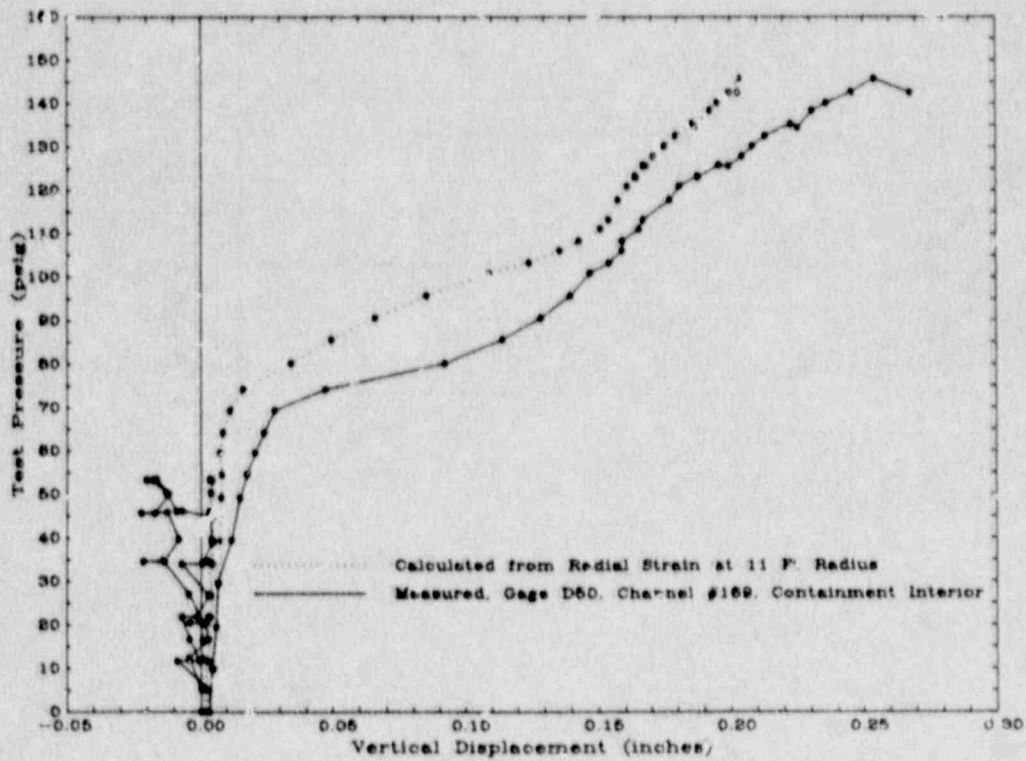


Figure 5.9.17 Uplift of Base Slab at Radius of 11 ft
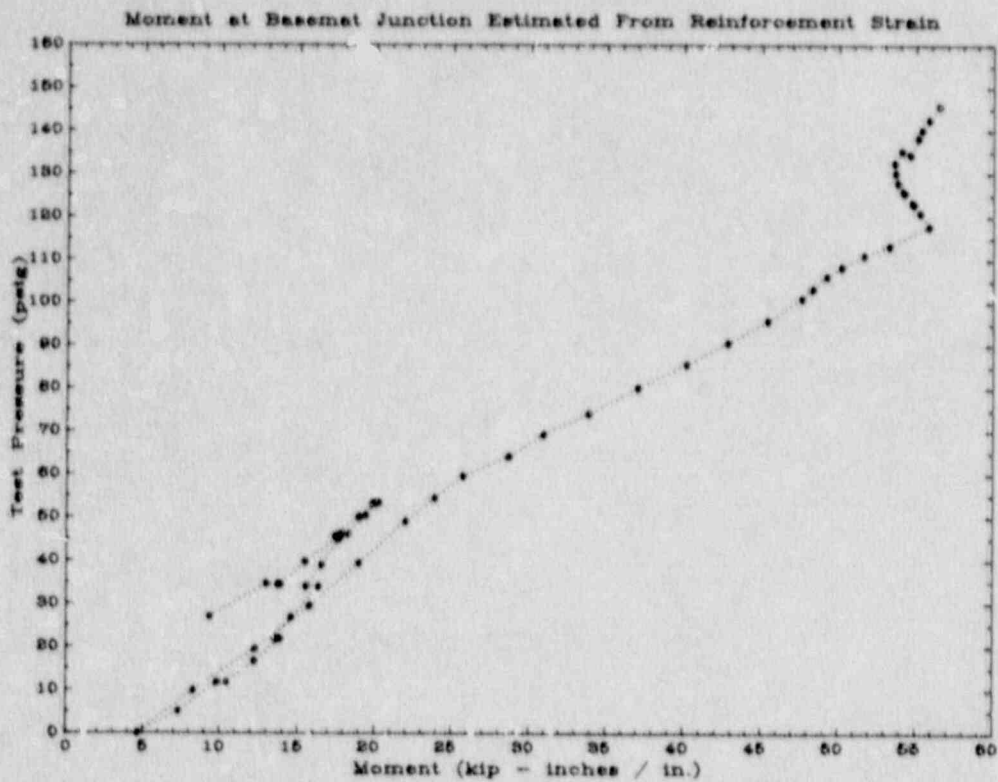
Figure 5.9.18 Variation of Moment at Wall Base with Pressure
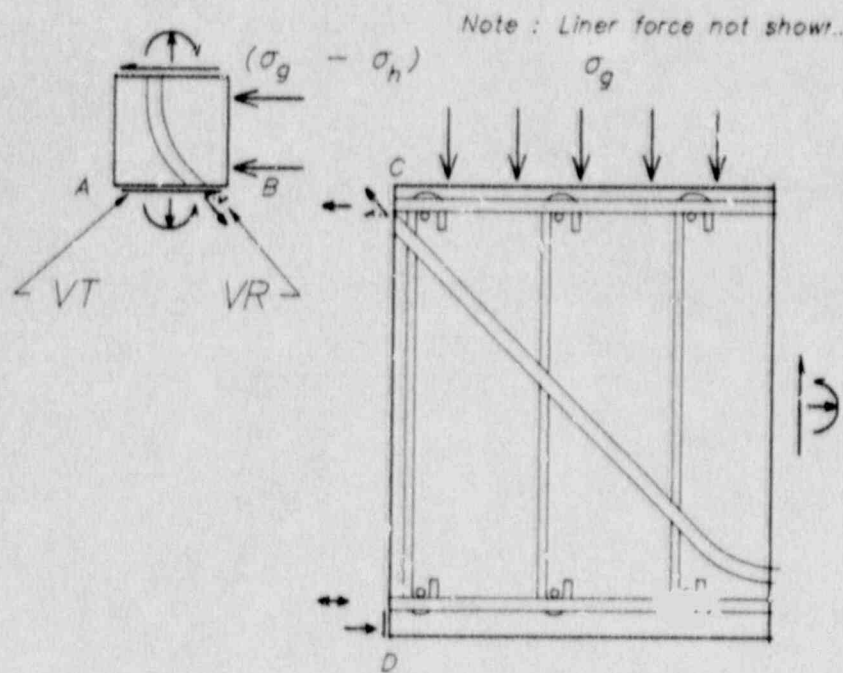


Figure 5.9.19 Idealized Internal Forces at Wall-Slab Connection
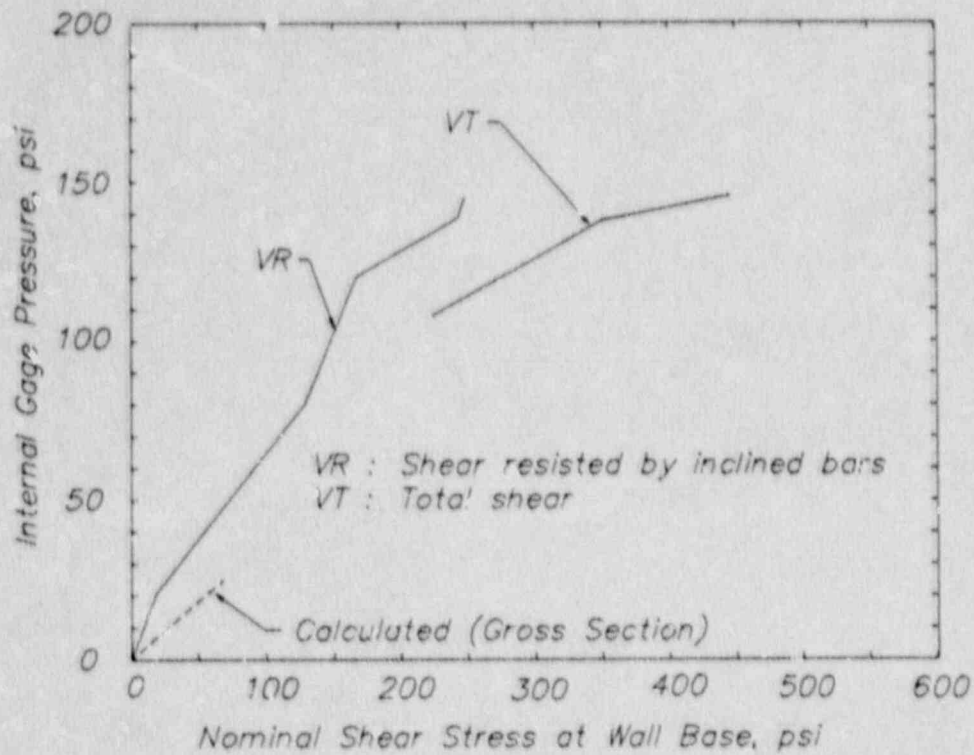
Figure 5.9.20 Radial Shear Stress at Base of Wall
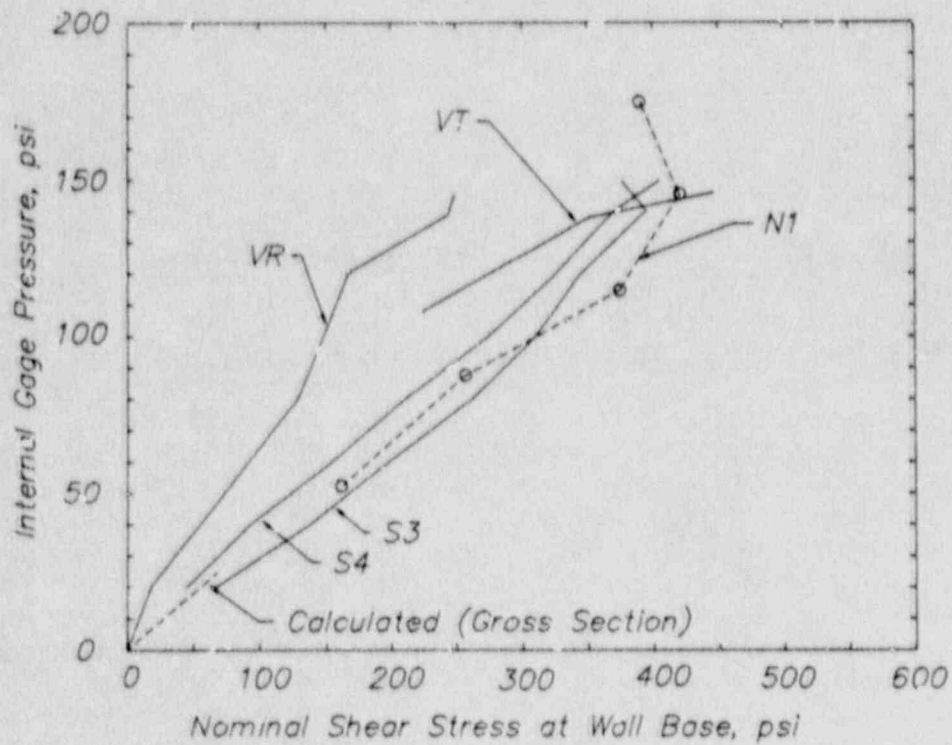


Figure 5.9.21 Comparison of Shear Stress at Wall Base
Based on Measurements and Calculations

## 6.0 CLOSURE

The 1:6-scale model high pressure test in July 1987 yielded a wealth of information on the behavior of reinforced concrete containments subject to overpressurization. This information has led to substantial improvements in analytical methods for evaluating reinforced concrete containment performance. In particular, models for predicting liner tearing have been advanced. There is a growing consensus with respect to the identification of the important mechanisms and features that cause liner strain concentrations and evaluation criterion for determining the liner ductility under multiaxial loading. These are important and significant developments derived from the analysis and testing of the 1:6-scale model.

However, there are still a number of issues that need to be resolved. Although there has been progress in developing analytical models for evaluating liner tearing, there are still a number of questions:

- Under what conditions will stud shear failure occur rather than liner tearing? How is the failure mode of the liner-anchorage system affected by scaling; by the ratio of liner thickness to stud diameter; and by membrane loading of the liner (before the development of high stud shear forces)?

- To what extent is the magnitude of liner strain concentrations affected by friction and bond between the concrete and liner; by dislocation motion at a crack; and by stud spacing?

- How is the magnitude of liner strain concentrations affected by the size and shape of insert plates? Does the shape of the insert plates affect crack propagation in the liner?

Sandia is developing a plan for 'separate-effects' tests with the objective of addressing these questions for reinforced concrete containments as well as prestressed concrete containments, which typically use line anchors to attach the liner to the concrete.

Furthermore, investigation and validation of methods for evaluating other potential failure modes is still needed. Shear failure is particularly difficult to evaluate; there is no generally recognized, reliable method of determining shear capacity of a reinforced concrete section under simultaneous application of tensile load and bending moment. Repressurization of the 1:6-scale model (after repairs are made to the liner) is one means for obtaining much needed data on the shear behavior of the cylinder-basemat intersection. Failure of large rebars where they are bent around penetrations has occurred in test specimens at relatively low plastic strains (compared to the bars ultimate strain) in an EPRI program. The effects of cold working on the available ductility of these bars should be studied further.

The fact that liner tearing was obtained in the 1:6-scale model does not by itself preclude different failure modes in actual reinforced concrete containments. For instance, the failure mode and capacity can be extremely sensitive to specific design details. If the stud spacing had been different, CEA's analysis suggest that liner tearing would have have been delayed, thereby increasing the likelihood of a different failure mode. The rate of pressurization and effects of temperature must also be considered. At high rates of pressurization, there is a possibility that sequential failure modes could occur, i.e., for very high rates of pressurization, liner

tearing may not arrest the pressure build-up within the containment and another failure mode could occur at slightly higher pressure. This is the basic reason for the emphasis on the development and validation of analysis methods. A reliable evaluation of containment performance must be based on careful, detailed analysis of the specific containment geometry and loading of interest. Analysis and testing of the 1:6-scale model have verified many (but not all) of the computational tools and analysis procedures needed to accomplish such an evaluation for reinforced concrete containments.

# 7.0 REFERENCES

[1] W. A. von Riesemann, et al., "U.S. NRC Containment Integrity Programs," Proc. 8th Intl. Conf. on Structural Mechanics in Reactor Technology, Brussels, Belgium, August 19-23, 1985, Paper J1/2.

[2] D. S. Horschel and T. E. Blejwas, "An Analytical Investigation of the Response of Steel Containment Models to Internal Pressurization," Proc. of the 7th Intl. Conf. on Structural Mechanics in Reactor Technology, Vol. J, August 22-26, 1983, Chicago, IL, pp. 297-304.

[3] R. T. Reese and D. S. Horschel, "Design and Fabrication of a 1:8- Scale Steel Containment Model," NUREG/CR-3647, SAND84-0048, Sandia National Laboratories, Albuquerque, NM, February 1985.

[4] L. N. Koenig, "Experimental Results for a 1:8-Scale Steel Model Nuclear Power Plant Containment Pressurized to Failure," NUREG/CR-4216, SAND85-0790, Sandia National Laboratories, Albuquerque, NM, December 1986.

[5] D. B. Clauss, "Comparison of Analytical Predictions and Experimental Results for a 1:8-Scale Steel Containment Model Pressurized to Failure," NUREG/CR-4209, SAND85-0679, Sandia National Laboratories, Albuquerque, NM, July 1985.

[6] D. B. Clauss, "Severe Accident Testing of Electrical Penetration Assemblies," NUREG/CR-5334, SAND89-0327, Sandia National Laboratories, Albuquerque, NM, October 1989.

[7] D. A. Brinson and G. A. Graves, "Evaluation of Seals for Mechanical Penetrations of Containment Buildings," NUREG/CR-5096, SAND88-7016, Sandia National Laboratories, Albuquerque, NM, August 1988.

[8] T. L. Bridges, "Containment Penetrations Elastomer Seal Leak Rate Tests," NUREG/CR-4944, SAND87-7118, Sandia National Laboratories, Albuquerque, NM, July 1987.

[9] J. T. Julien and S. W. Peters, "Leak and Structural Test of a Personnel Airlock for LWR Containments Subjected to Pressure and Temperature Beyond Design Limits," NUREG/CR-5118, SAND88-7155, Sandia National Laboratories, Albuquerque, NM, May 1989.

[10] D. B. Clauss, W. A. von Riesemann, and M. B. Parks, "Containment Penetrations," Proc. of the NRC/MITI Technical Information Exchange Workshop, May 16-18, 1988, Tokyo, Japan.

[11] D. B. Clauss, "Round-Robin Pretest Analyses of a 1:6-Scale Reinforced Concrete Containment Model Subject to Static Internal Pressurization," NUREG/CR-4913, SAND87-0891, Sandia National Laboratories, Albuquerque, NM, May 1987.

[12] D. S. Horschel, "Design, Construction, and Instrumentation of a 1/6-Scale Reinforced Concrete Containment Building," NUREG/CR-5083, SAND88-0030, Sandia National Laboratories, Albuquerque, NM, August 1988.

[13] D. S. Horschel, "Experimental Results from Pressure Testing a 1:6-Scale Nuclear Power Plant Containment," NUREG/CR-5121, SAND88-0906, Sandia National Laboratories, Albuquerque, NM, (Draft Copy available from U.S. Nuclear Regulatory Commission Public Document Room).

[14] D. B. Clauss, et al., "Progress Report on the Containment Integrity Programs," Proc. of the U.S. Nuclear Regulatory Commission - Sixteenth Water Reactor Safety Information Meeting, NUREG/CP-0097, Vol. 3, March 1989, pp. 311-338.

[15] A. H. Marchertas and R. F. Kulak, "Numerical Modeling of Concrete Under Thermal Loads," Nuclear Engineering and Design, Vol. 68, No. 2, 1981, pp. 225-236.

[16] A. H. Marchertas and R. F. Kulak, "A Coupled Heat Conduction and Thermal Stress Formulation Using Explicit Integration," ANL-82-47, Argonne National Laboratory, Argonne, IL, June 1982.

[17] A. H. Marchertas and R. F. Kulak, "Response Simulation of Concrete Structures to High Temperatures," Proc. of the Workshop on Containment Integrity, Vol. 1, NUREG/CP-0033, SAND82-1659, Sandia National Laboratories, Albuquerque, NM, October 1982, pp. 193-212.

[18] Y. Takahashi, "Elastic-Plastic Constitutive Modeling of Concrete," ANL-83-23, Argonne National Laboratory, Argonne, IL, March 1983.

[19] A. H. Marchertas, "Thermo-Mechanical Analysis of Concrete in LMFBR Programs," Nuclear Engineering and Design, Vol. 82, No. 1, 1984, pp. 47-62.

[20] R. F. Kulak, "A Finite Element Formulation for Fluid-Structure Inter-action in Three-Dimensional Space," J. of Pressure Vessel Technology, Vol. 103, No. 2, 1981, pp. 183-190.

[21] R. F. Kulak, "A Finite Element Quasi-Eulerian Method for Three-Dimensional Fluid-Structure Interactions," Computers and Structures, Vol. 18, No. 2, 1984, pp. 319-332.

[22] R. F. Kulak, "Three-Dimensional Fluid-Structure Coupling in Transient Analysis," Computers and Structures, Vol. 21, No. 3, 1985, pp. 529-542.

[23] P. A. Pfeiffer, et al., "Pretest Analysis - Argonne National Laboratory," in "Round-Robin Pretest Analyses of a 1:6-Scale Reinforced Concrete Containment Model Subject to Static Internal Pressurization," edited by D. B. Clauss, NUREG/CR-4913, SAND87-0891, Sandia National Laboratories, Albuquerque, NM, May 1987, pp. 82-129.

[24] R. A. Dameron, R. S. Dunham, Y. R. Rashid and M. F. Sullaway, "Methods for Ultimate Load Analysis of Concrete Containments, Phase 3: Pre-Test and Posttest Analysis of the Sandia 1:6 Scale Reinforced Concrete Containment," ANATECH Report to EPRI, EPRI NP-6261, January 1989.

[25] R. A. Dameron, R. S. Dunham, Y. R. Rashid and M. F. Sullaway, "Methods for Ultimate Load Analysis of Concrete Containments, Phase 3: Developing Criteria and Guidelines for Predicting Concrete Containment Leakage," ANATECH Report to EPRI, EPRI NP-6260SD, February 1989.

[26] R. S. Dunham, Y. R. Rashid, K. A. Yuan and Y. M. Lu, "Methods for Ultimate Load Analysis of Concrete Containments," ANATECH Report to EPRI, NP-4046, June 1985.

[27] J. Julien, T. Weinmann and D. Schultz, "Concrete Containment Structural Element Tests, Phase 1, Volumes 1, 2 and 3," Construction Technology Laboratories Report to EPRI, NP-3774, November 1984.

[28] R. A. Dameron, R. S. Dunham and Y. R. Rashid, "Methods for Ultimate Load Analysis of Concrete Containments: Second Phase," ANATECH Report to EPRI, NP-4869M, March 1987.

[29] N. Hanson, et al., "Concrete Containment Structural Element Tests, Phase 2," Construction Technology Labs. Final Report to EPRI, NP-4867M, August 1987.

[30] J. M. Raphael, "Tensile Strength of Concrete," ACI Journal Title No. 81-17, April 1984.

[31] Wang and Salmon, Reinforced Concrete Design, 3rd Edition, Harper & Row, 1979.

[32] Timoshenko and Woikowsky-Krieger, Theory of Plates and Shells, McGraw-Hill, 1959.

[33] R. A. Dameron, et al., "Methods for Ultimate Load Analysis of Concrete Containments: Third Phase; Second Tier Report - Procedure Manual and Guidelines for Using Concrete Containment Analysis Software," ANATECH report to EPRI, EPRI NP-6263-SD, January 1989.

[34] D. S. Horschel, "Synopsis of Results of a Test of a Reinforced Concrete Containment," Proc. of the Fourth Workshop on Containment Integrity, NUREG/CP-0095, SAND88-1836, Sandia National Laboratories, Albuquerque, NM, November 1988, pp. 324-340.

[35] D. F. Meinheit, et al., "Support Tests for Sandia National Laboratories Design of LWR Reinforced Concrete Containment Model," July 30, 1985.

[36] A. Millard, Ph. Jamet, G. Nahas and B. Barbé, "Analysis of the Sandia 1/6th scale concrete containment model using the CASTEM finite element system," Proc. of the 9th Intl. Conf. on Structural Mechanics in Reactor Technology, Vol. J, August 17-21, 1987, Lausanne, pp. 227-236.

[37] J. Riviere, B. Barbé, A. Millard and V. Koundy, "Comparison Between Theoretical and Experimental Results of 1:6 Scale Concrete Model Under Internal Pressure," Proc. of the Fourth Workshop on Containment Integrity, NUREG/CP-0095, SAND88-1836, Sandia National Laboratories, Albuquerque, NM, November 1988, pp. 357-376.

[38] PAFEC Ltd (1984); "Data Preparation User Manual Level 6.1," Pafec Limited, Nottingham.

[39] Ove Arup & Partners, "Sandia Scale Model Containment Pretest Analysis," Final Report, IE87-100, May 1987.

[40] J. Hallquist, "NIKE2D Users Manual," Lawrence Livermore National Library, UCID-1967, Rev 1., December 1986.

[41] R. Dameron et al., "Criteria and Guidelines for Predicting Concrete Containment Leakage," Proc. of the Fourth Workshop on Containment Integrity, NUREG/CP-0095, SAND88-1836, Sandia National Laboratories, Albuquerque, NM, November 1988, pp. 507-522.

[42] G. Orsini and G. Pino,"Analysis Predictions vs. Test Results of the 1:6-Scale Reinforced Concrete Containment Tested at Sandia National Laboratories," Proc. of the Fourth Workshop on Containment Integrity, NUREG/CP-0095, SAND88-1836, Sandia National Laboratories, Albuquerque, NM, November 1988, pp. 425-440.

[43] Comite' Euro-International du Beton, Bulletin d'information n°158-E, "Manual on Cracking and Deformations," 1985.

[44] J. Eibl, V. Neuroth and F.-H. Schlüter, Test Report, "Reinforced Concrete Elements Subjected to Uniaxial and Biaxial Direct Tension," Institut für Massivbau und Baustofftechnologie, Universität Karlsruhe, November 1986.

[45] E. Giuriani, "On the Effective Axial Stiffness of a Bar in Cracked Concrete," Proc. of the Intl. Conf. on Bond in Concrete, Paisley, Scotland, June 14, 1982.

[46] M. J. Manjoine, "Creep-Rupture Behavior of Weldments," Welding Journal, February 1982, p. 50.

[47] R. A. Dameron, R. S. Dunham, Y. R. Rashid and H. T. Tang, "Analytical Correlation and Posttest Analysis of the Sandia 1:6-Scale Reinforced Concrete Containment Test," Proc. of the Fourth Workshop on Containment Integrity, NUREG/CP-0095, SAND88-1836, Sandia National Laboratories, Albuquerque, NM, November 1988, pp. 441-458.

[48] P. Bachmann, P. Gruner, P. Eisert and W. Kuntze, "Progress in Posttest Analyses of a 1:6-Scale Lined and Reinforced Concrete Containment Model," Proc. of the Fourth Workshop on Containment Integrity, NUREG/CP-0095, SAND88-1836, Sandia National Laboratories, Albuquerque, NM, November 1988, pp. 377-394.

[49] Experimental Plots attached to a letter from D. B. Clauss, Sandia National Laboratories, to D. Phillips, U.K. Atomic Energy Authority, (and other round-robin participants), August 5, 1987.

[50] L. P. Harrop, "Simple Calculations to Predict the Behavior of the Sandia 1/6 Scale Model Reinforced Concrete Containment Building," Report no: SRD R 475, June 1988.

[51] W. M. Kuntze, P. Gruner, P. Eisert, and F.-H. Schlüter, "Failure Analysis of a 1:6-Scale Reinforced Concrete Containment Under Increasing Internal Pressure," Proc. of the Second Intl. Seminar on Containment of Nuclear Reactors, August 24-25, 1987, Ecole Polytechnique Federal De Lausanne, Switzerland, pp. 423-426.

[52] P. Bachmann, P. Eisert, P. Gruner, W. Kuntze, and H. Schulz, Gesellschaft für Reaktorsicherheit (GRS) mbH, J. Eibl and F.-H. Schlüter, Institut für Massivbau und Baustofftechnologie, Universität Karlsruhe, "Analyse zur Bestimmung des Versagensdruckes und des Ver sagensverhaltens eines Stahlbetoncontainments im Masstab 1:6 (Vorausberechnungen)," GRS-A-1415 (Maerz 1988), Gesellschaft für Reaktorsicherheit (GRS) mbH, Köln.

[53] K. J. Bathe, ADINA (Rev. 1984), Report AE 84-1, ADINA-Engineering Inc., Watertown, Mass. December 1984.

[54] M. J. Manjoine, "Elevated Temperature Mechanics of Metals," Preprints of the 4th international Seminar on: Inelastic Analysis and Life Prediction in High Temperature Environment, 7th SMiRT, August 1983.

[55] J. R. Weatherby, "Post-Test Analysis of a Piping Penetration in a 1:6-Scale Model of a Reinforced Concrete Containment Building," Proc. of the Fourth Workshop on Containment Integrity, NUREG/CP-0095, SAND88-1836, Sandia National Laboratories, Albuquerque, NM, November 1988, pp. 357-376.

[56] N. S. Ottosen, "A Failure Criterion for Concrete," Journ. Eng. Mec. Div., ASCE, Vol. 103, EM 4, August 1977.

[57] J. Eibl, F.-H. Schlüter and G. Terbeck, "Ultimate Strains of Liner Sheets Under Biaxial Tension," Test Report, Institut für Massivbau und Baustofftechnologie der Universität Karlsruhe, 1988.

[58] J. Eibl, F.-H. Schlüter and G. Terbeck, "Bond Behavior of Reinforcing Bars Located in Concrete Sections with Transverse Tension," Test Report, Institut für Massivbau und Baustofftechnologie, Universität Karlsruhe, 1988.

[59] R. Salzbrenner and P. Bortniak, "Formability Facility," SAND82-0690, Sandia National Laboratories, Albuquerque, NM, 1982.

[60] A. K. Ghosh and S. S. Hecker, "Stretching Limits in Sheet Metals: In-Plane Versus Out-of-Plane Deformation," Metallurgical Transactions, Vol. 5, October 1974.

[61] Stahl im Hochbau, Handbuch für die Anwendung von Stahl im Hoch- und Tiefbau, 14. Auflage, Band I/Teil 2, Herausgeber: Verien Deutscher Eisenhüttenleute, Düsseldorf, Verlag Stahleisen mbH, Düsseldorf, 1986.

[62] S. A. Guralnick and R. W. La Fraugh, "Laboratory Study of a 45-Foot Square Flat Plate Structure," Journal of the American Concrete Institute, Proceedings, V. 60, No. 9, September 1963, pp. 1107-1185.

[63] D. S. Horschel, "Construction of A 1:6 Scale Concrete Containment Model," Nuclear Engineering and Design, 104, Elsevier Publishers, Amsterdam, 1987, pp. 341-347.

[64] G. A. Knorovsky, P. W. Hatch, and M. R. Gutierrez, "Evaluation of Materials of Construction for the Reinforced Concrete Reactor Containment Model," NUREG/CR-5099, SAND88-0052, Sandia National Laboratories, Albuquerque, NM, September 1988.

[65] J. R. Weatherby, "Axisymmetric Analysis of a 1:6 Scale Reinforced Concrete Containment Building Using a Distributed Cracking Model for the Concrete," NUREG/CR-4969, SAND87-1670, Sandia National Laboratories, Albuquerque, NM, September 1987.

[66] "Soil Report," Project Sandia LWR Reinforced Concrete Containment Model, Project NO. 3245 J 066, Western Technologies, Inc., Albuquerque, NM, October 1985.

[67] J. R. Weatherby, "SNL Pretest Analyses," in "Round-Robin Pretest Analyses of a 1:6-Scale Reinforced Concrete Containment Model Subject to Static Internal Overpressurization," edited by D. B. Clauss, NUREG/CR-4913, SAND87-0891, Sandia National Laboratories, Albuquerque, NM, May 1987, pp. 40-81.

[68] B. Dodd and Y. Bai, "Ductile Fracture and Ductility," Academic Press, 1987, pp. 202-206.

# APPENDIX

This Appendix is a reproduction of the description of the design features and material properties in the 1:6-scale reinforced concrete containment model used in the pretest round-robin analysis report [A.1].

This section describes the geometry and material properties of the 1:6-scale model. It is not intended that all of the details of the model be described here, rather, the intent is to give the flavor of the features that are significant to a structural analysis.

## A.1 Geometry

A schematic of the 1:6-scale model, which was fabricated by United Engineers and Constructors, Inc. to a design pressure of 46 psig (0.317 MPa), is shown in elevation view in Figure A.1. The model consists of a basemat that is 300 in. (7620 mm) in diameter and 40 in. (1016 mm) thick and a cylinder and dome, both with an inside diameter of 264 in. (6706 mm) and having thicknesses of 9-3/4 and 7 in. (248 and 178 mm), respectively. A number of penetrations are found in the cylinder, including equipment hatches, personnel airlock representations, and piping clusters. A steel liner is used to provide a leak-tight pressure boundary; the liner thickness is 1/16 in. (1.59 mm) along the basemat and cylinder and 1/12 in. (2.11 mm) along the dome. Before the basemat liner was installed, a 3 in. (76 mm) thick concrete leveling course was placed on top of the basemat from the center out to the cylinder wall. (Effectively, the basemat is 43 in. (1092 mm) thick, except for that portion outside of the cylinder wall, which is 40 in. (1016 mm) thick). The model sits atop a "mudmat", which is used to provide a moisture barrier between the soil and the model basemat, that is 492 in. (12497 mm) in diameter and has a minimum thickness of 6 in. (152 mm). The soil is described as silty clay with sand. Based on bearing plate tests, an average soil modulus of 390 ksf/ft (61.26 MPa/m) was recommended by Western Technologies. It should be noted that this recommended value includes typical soil factors of safety that may not be appropriate for analytical models used to predict failure; for details of the soil tests the reader is referred to Reference A.2.

The reinforcing steel in the basemat consists of the following: (1) on the lower face, a rectangular grid of #6 rebar on 4 in. (102 mm) centers, (2) on the upper face, a rectangular grid of #5 rebar on 6 in. (152 mm) centers, #5 rebars in the radial direction, and #6 rebars in the circumferential direction, and (3) shear ties through the thickness of the basemat of #3 rebar. A typical cross section is shown in Figure A.2. At the basemat cylinder junction, additional layers of reinforcement are used, including shear ties, diagonal bars (layer 11), and an additional layer of meridional bars (layer 10), to carry the high shear forces and bending moments. Figure A.3 is a photograph of the model taken during construction that shows some of the reinforcement in the basemat and at the cylinder basemat junction.

A typical cross section of the cylinder wall in the free-field (away from penetrations) is depicted in Figure A.4. There are eight layers of reinforcement steel, including four layers of #4 rebar spaced at 4.5 in. (114 mm) in the hoop direction, two layers of #4 rebar spaced at 4.5 in. (114 mm) in the meridional direction, and two layers of orthogonal #4 rebar spaced at 6.25 in. (159 mm) and inclined at 45 degrees.
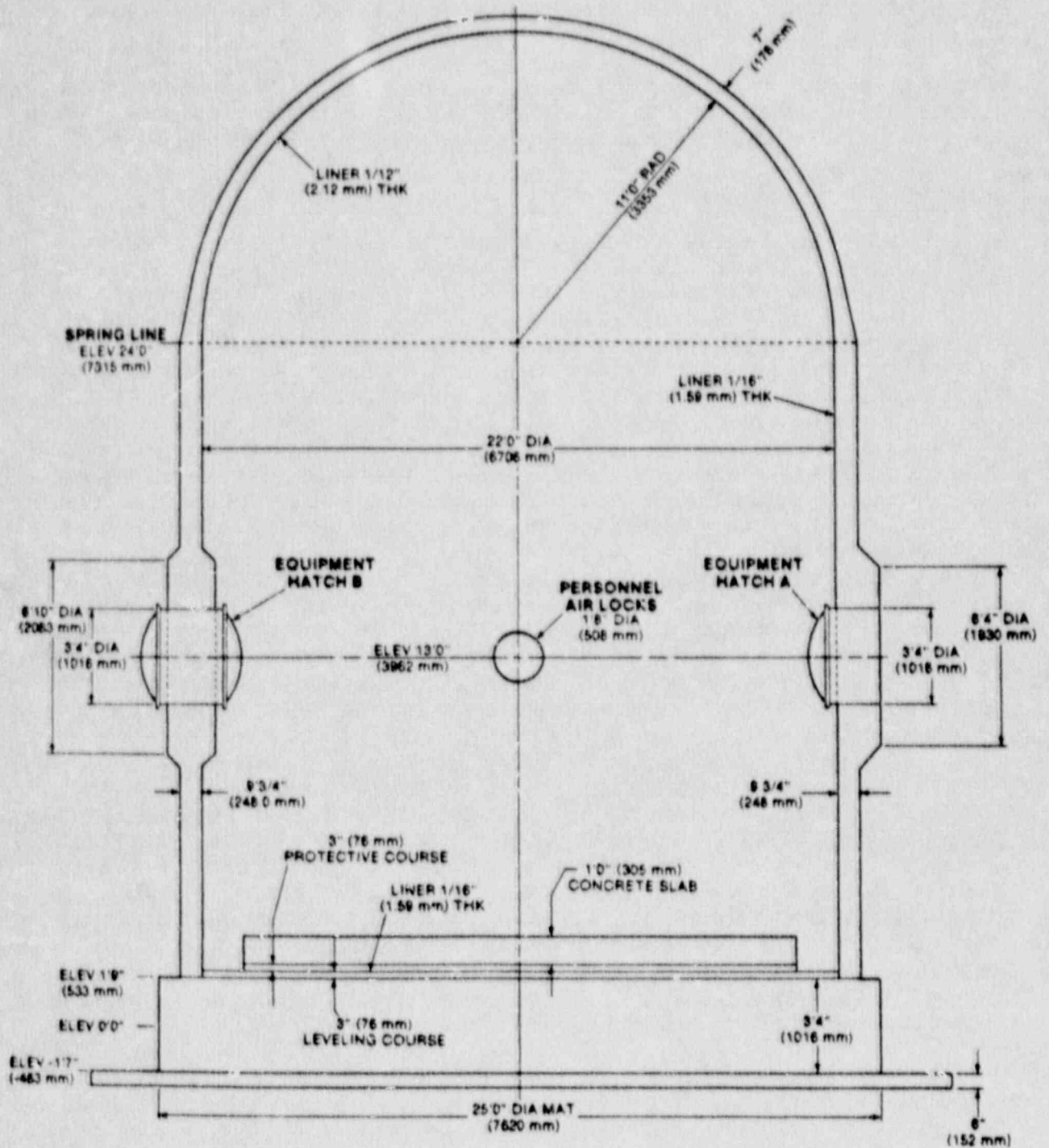
Figure A.1 Schematic of 1:6-Scale Reinforced Concrete Containment Model
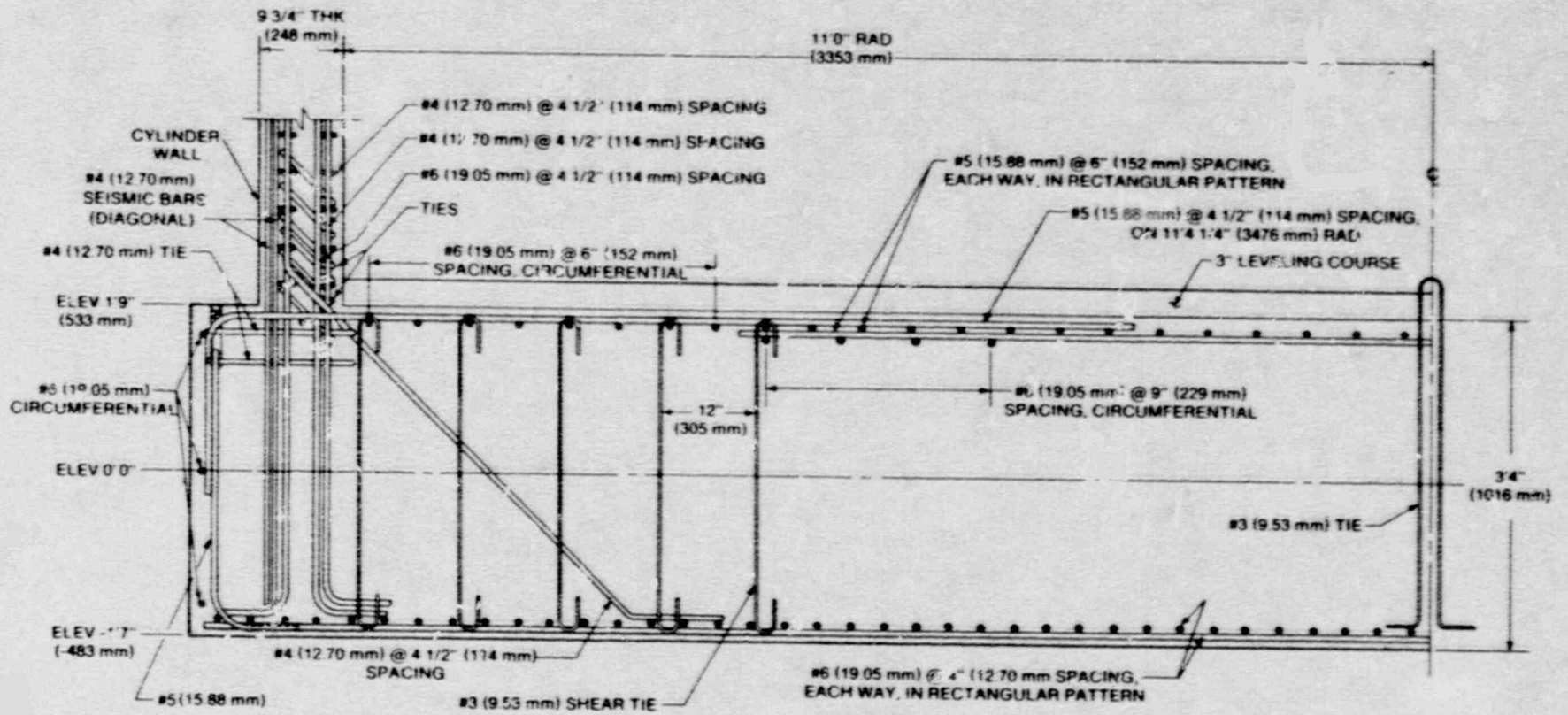- Elevation View

9 3/4" THK
(248 mm)

11'0" RAD
(3353 mm)

#4 (12.70 mm) @ 4 1/2" (114 mm) SPACING

#4 (12.70 mm) @ 4 1/2" (114 mm) SPACING

#6 (19.05 mm) @ 4 1/2" (114 mm) SPACING

#5 (15.88 mm) @ 6" (152 mm) SPACING,
EACH WAY, IN RECTANGULAR PATTERN

CYLINDER
WALL

#4 (12.70 mm)
SEISMIC BARS
(DIAGONAL)

#4 (12.70 mm) TIE

TIES

#5 (15.88 mm) @ 4 1/2" (114 mm) SPACING,
ON 11'4 1/4" (3476 mm) RAD

#6 (19.05 mm) @ 6" (152 mm)
SPACING, CIRCUMFERENTIAL

3" LEVELING COURSE

ELEV 1'9"
(533 mm)

#5 (19.05 mm)
CIRCUMFERENTIAL

12"
(305 mm)

#6 (19.05 mm) @ 9" (229 mm)
SPACING, CIRCUMFERENTIAL

ELEV 0'0"

3'4"
(1016 mm)

#3 (9.53 mm) TIE

ELEV -1'7"
(-483 mm)

#4 (12.70 mm) @ 4 1/2" (114 mm)
SPACING

#5 (15.88 mm)

#3 (9.53 mm) SHEAR TIE

#6 (19.05 mm) @ 4" (12.70 mm SPACING,
EACH WAY, IN RECTANGULAR PATTERN

Figure A.2  Reinforcement in the Basemat and Cylinder Basemat Junction
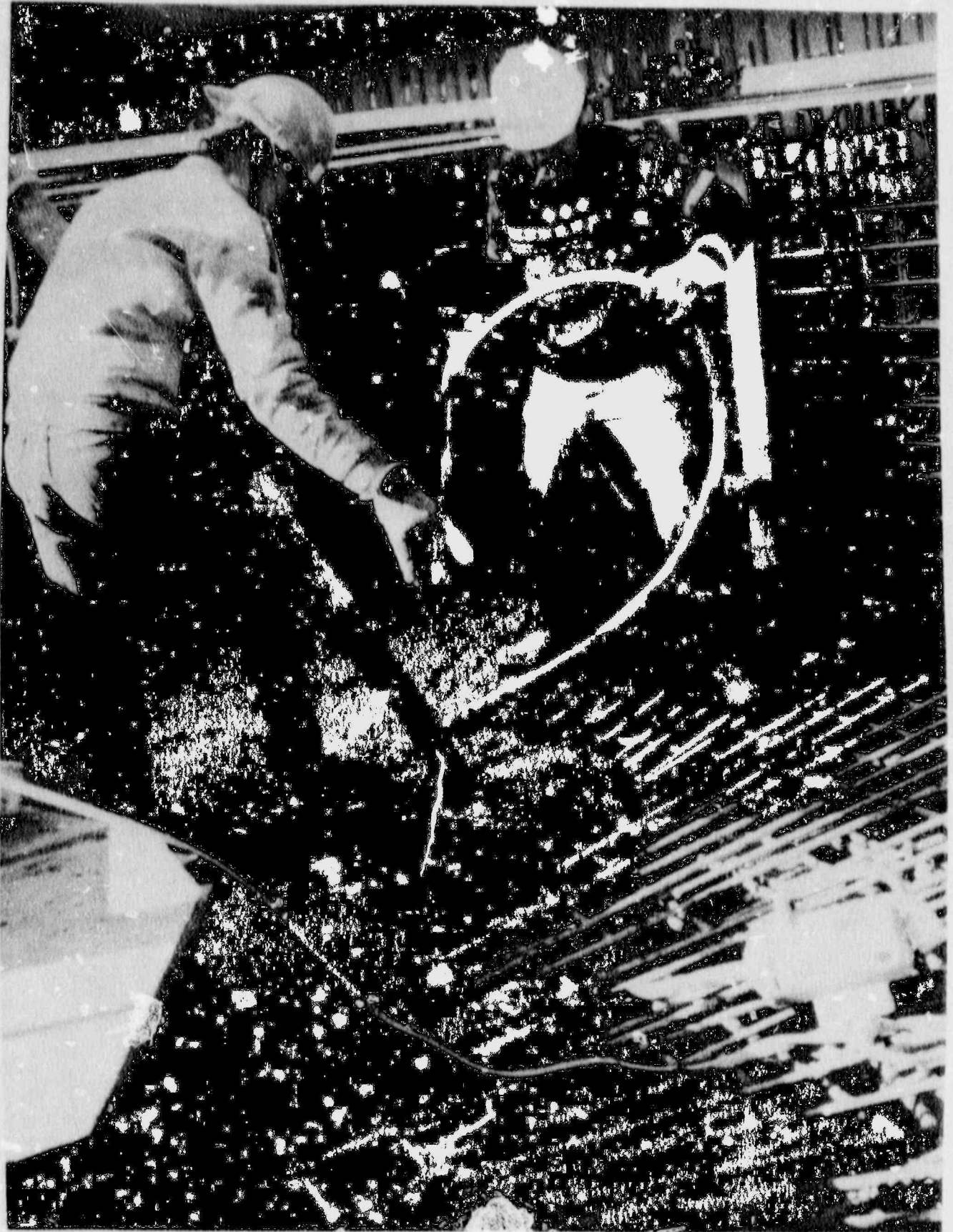
Figure A.3  Photograph During Construction of Basemat Cylinder Junction

REINFORCING BAR DETAILS

| LAYER | TYPE | SIZE |
|-------|------|------|
| 1 | HOOP | #4 |
| 2 | MERIDIONAL | #4 |
| 3 | HOOP | #4 |
| 4 | HOOP | #4 |
| 5 | MERIDIONAL | #4 |
| 6 | HOOP | #4 |
| 7 | SEISMIC (45° DIAG) | #4 |
| 8 | SEISMIC (45° DIAG) | #4 |
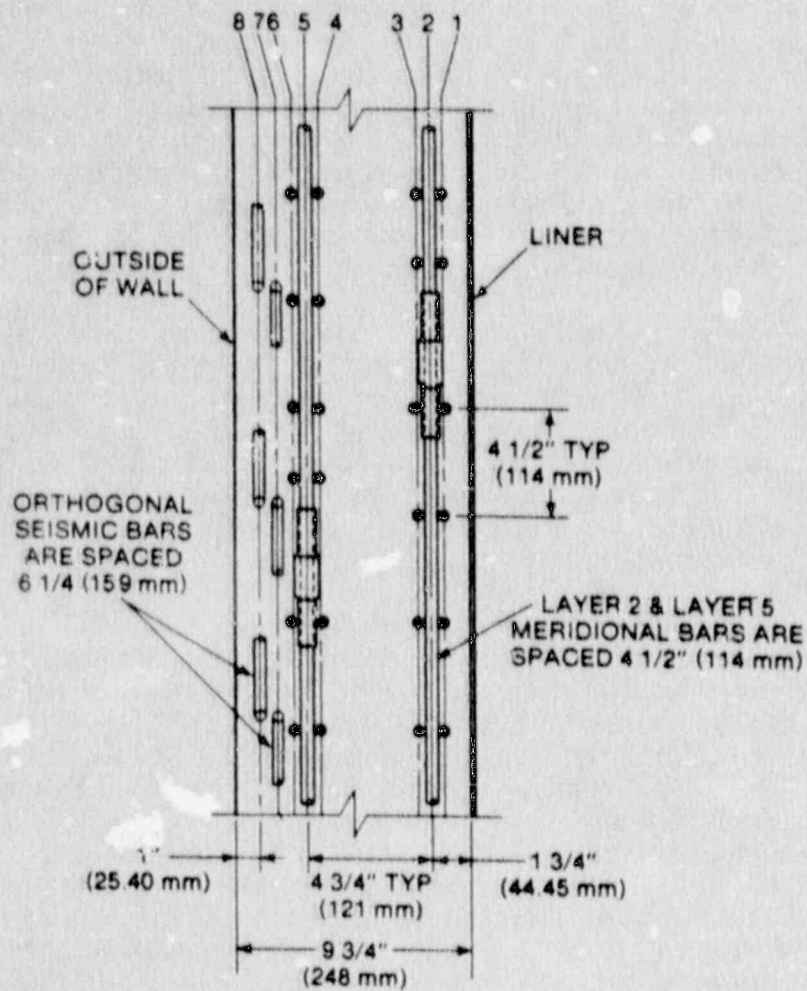


Figure A.4  Reinforcement in the Cylinder (free-field)

The wall thickness taper. from 9-3/4 to 7 in. (248 to 174 mm) beginning from the springline over an arc length of roughly 26 in. (660 mm). The diagonal (seismic) bars are terminated in the dome at an elevation of 30.83 ft. Half of the meridional bars are terminated at elevation 34.83 ft as shown in Figure A.5. The dome apex plates can also be seen in Figure A.5. Half of the meridional rebars above elevation 34.83 ft are tied into the dome apex plates.

The reinforcement patterns around the major penetrations are very complex and can be fully described only by reference to the construction drawings. Figures A.6 and A.7 are photographs of the reinforcement around equipment hatches A and B, which are typical of most penetrations. Reinforcement layers 1 through 8 are 'bent' around the major penetrations, as shown in Figures A.8 through A.13. Additional layers of reinforcement around penetrations, such as 'sun ray' (projecting radially outward from penetration) bars, circular bars around the penetration, and shear ties, can be seen in Figures A.6, A.7, and A.14.

The reinforcement in the mudmat consists of a rectangular pattern of #5 bars on 12 in. (305 mm) centers located approximately 2.5 in. (64 mm) below the top of the mudmat. A parafin based curing compound was sprayed on the mudmat, which was finished with a steel trowel, before the concrete for the basemat was placed. As a result, the bond between the concrete in the mudmat and basemat is expected to be negligible. Within a radius of 54 in. (1.37 m) of the center of the mudmat, a number of keyways were formed with matching keys in the basemat. This was intended to prevent the basemat from sliding relative to the mudmat. Although some analysts included the mudmat in their finite element models, SNL considers the structural coupling between the basemat and the mudmat to be insignificant.

The basemat liner is covered by a circular slab of concrete consisting of a 3 in. (76 mm) protective layer and a 12 in. (305 mm) pad for the model internal structure that is roughly 230 in. (58`` mm) in diameter. The basemat liner is not anchored to the concrete in the basemat or to the protective course above it. The basemat liner is welded to a quarter pipe section, referred to hereafter as the knuckle. The details of the attachment of the liner to the knuckle are shown in Figure A.15. Note that the diameter of the top protective course and pad of concrete is less than that of the cylinder, and thus the inside surface of the knuckle is not supported by concrete.

A stretch out of the cylinder liner is shown in Figure A.16, which also shows the layout of the penetrations in the model. The cylinder liner is anchored to the concrete by means of headed studs; the type and spacing of these studs varies. The first row of studs is approximately 0.8 in. (20.3 mm) above the top of the knuckle, and for elevations up to 6.5 ft, 1/2 in. (12.7 mm) long headed studs are used with a spacing of 2 x 2 in. (51 x 51 mm) up to elevation 5.17 ft and 4 x 4 in. (102 x 102 mm) between elevation 5.17 ft and 6.5 ft. Above elevation 6.5 ft, 3/4 in. (19 mm) long headed studs were used with 2 x 2 in. (51 x 51 mm) spacing near penetrations and 6 x 6 in. (152 x 152 mm) spacing elsewhere. Figures A.17 and A.18 are photographs of the liner with studs attached near the base of the cylinder (including the transition regions at elevations 5.17 ft and 6.5 ft) and near personnel airlock A, respectively. Around penetrations, thickened sections of the liner (3/16 in., 4.76 mm) were used (see Figure A.16). In the dome, the studs were uniformly spaced at 8 x 8 in. (203 x 203 mm). It should be noted that the cylinder liner was elastically formed whereas the dome section of the liner was dished by a pressing operation.
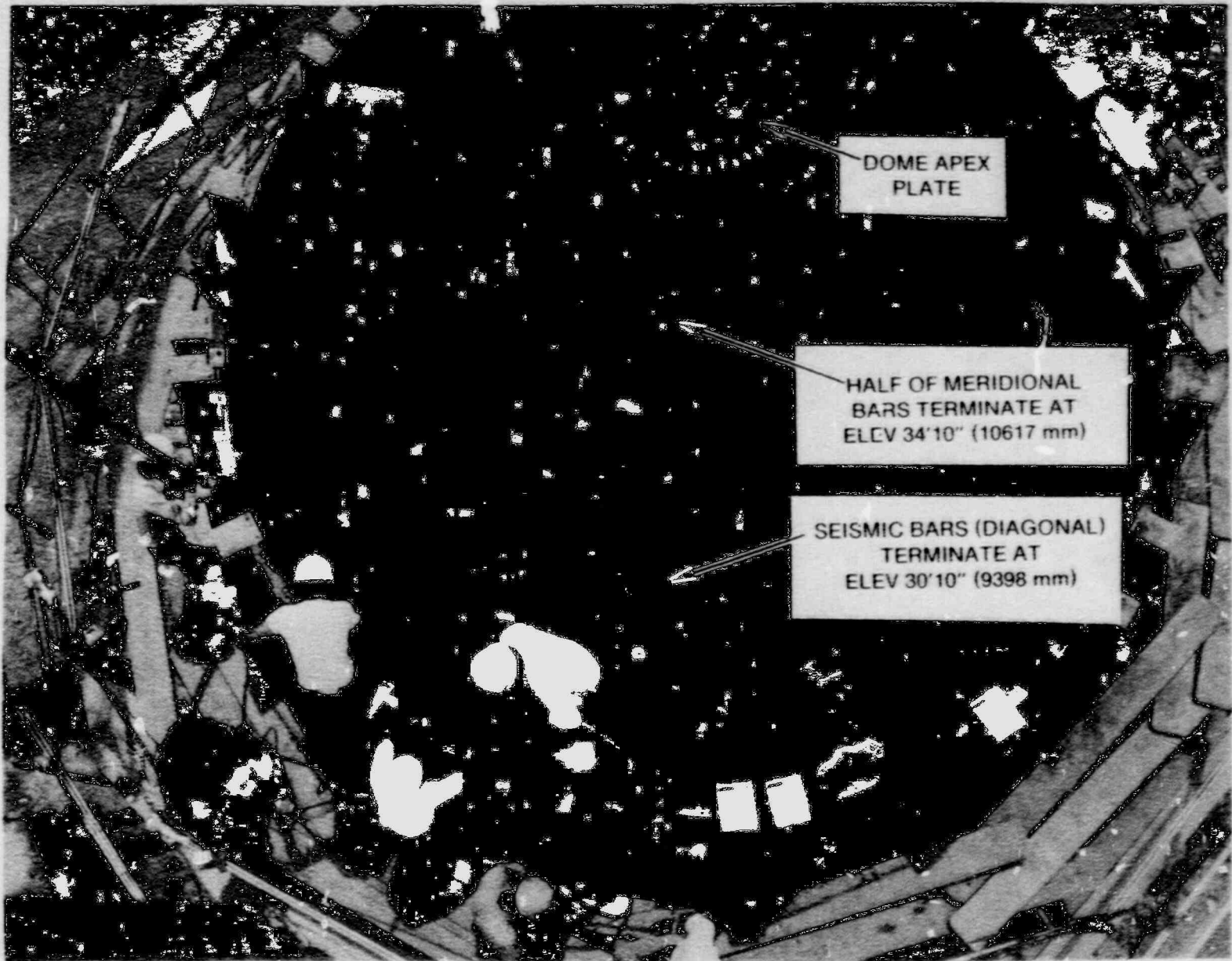
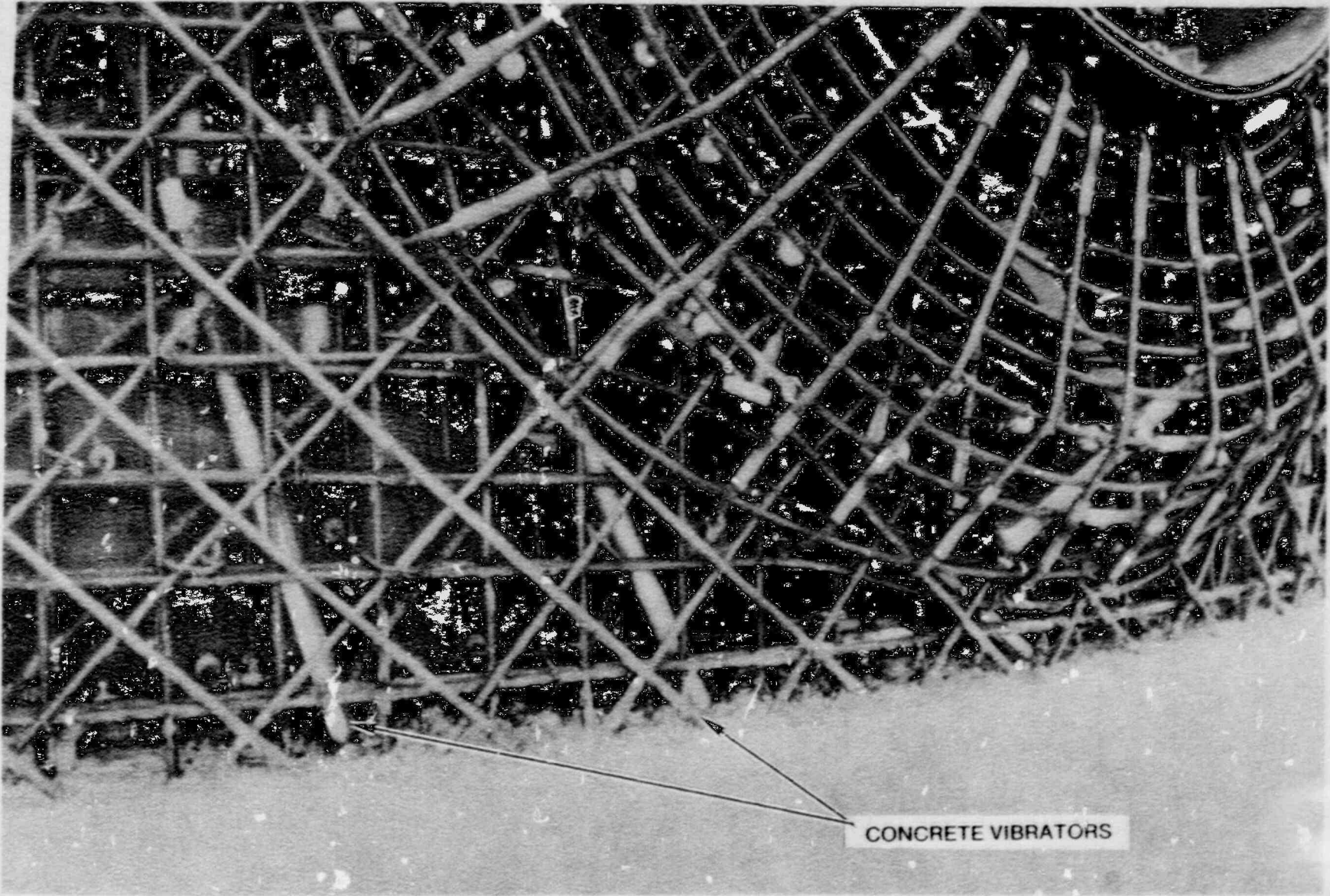Figure A.5  Photograph During Construction of Reinforcement in the Dome

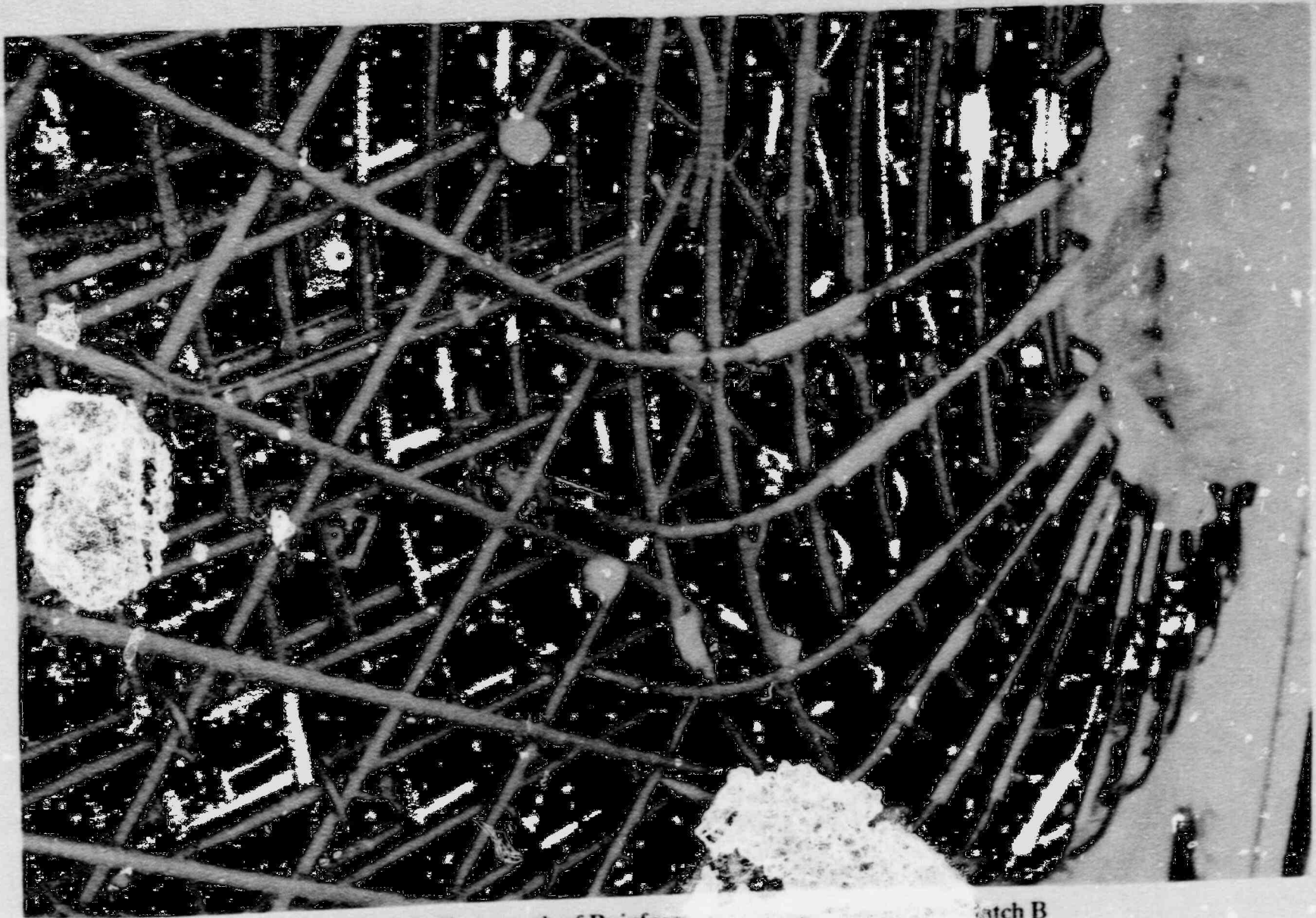CONCRETE VIBRATORS

Figure A.6  Photograph of Reinforcement Around Equipment Hatch A

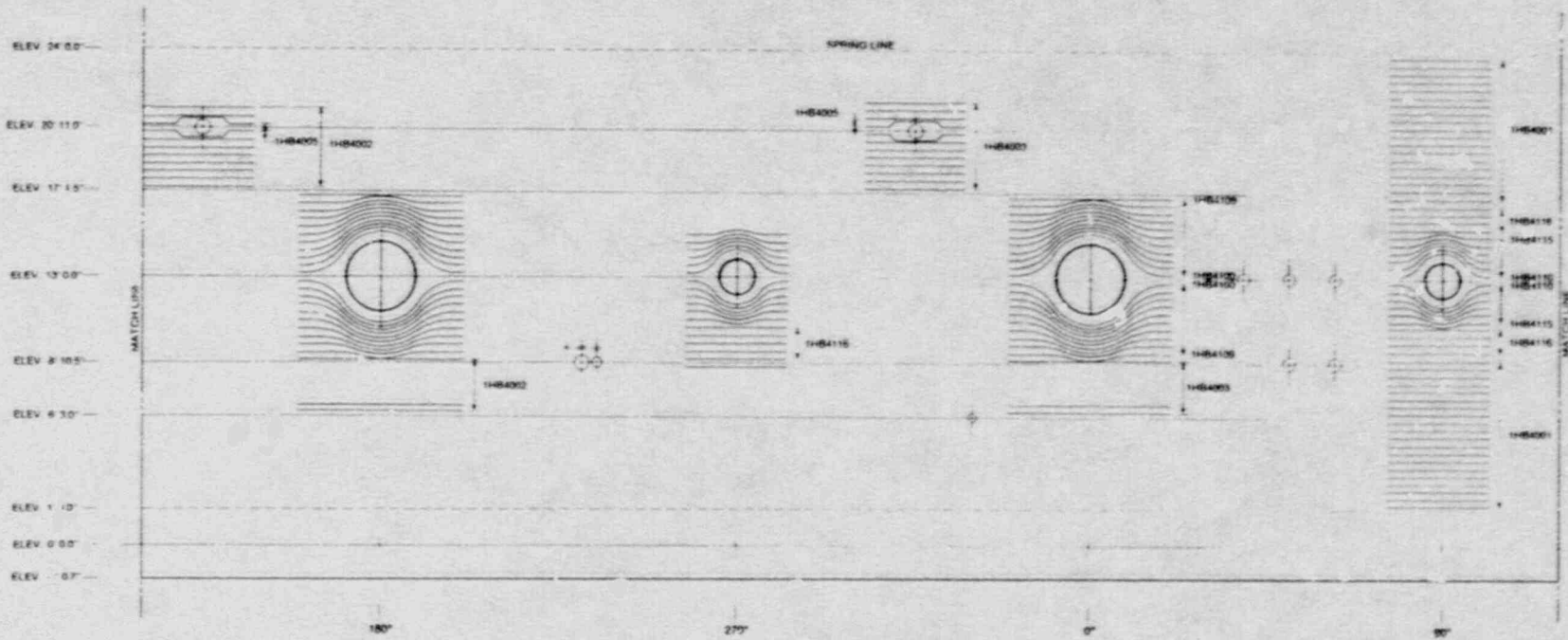Figure A.7  Photograph of Reinforce... ...atch B

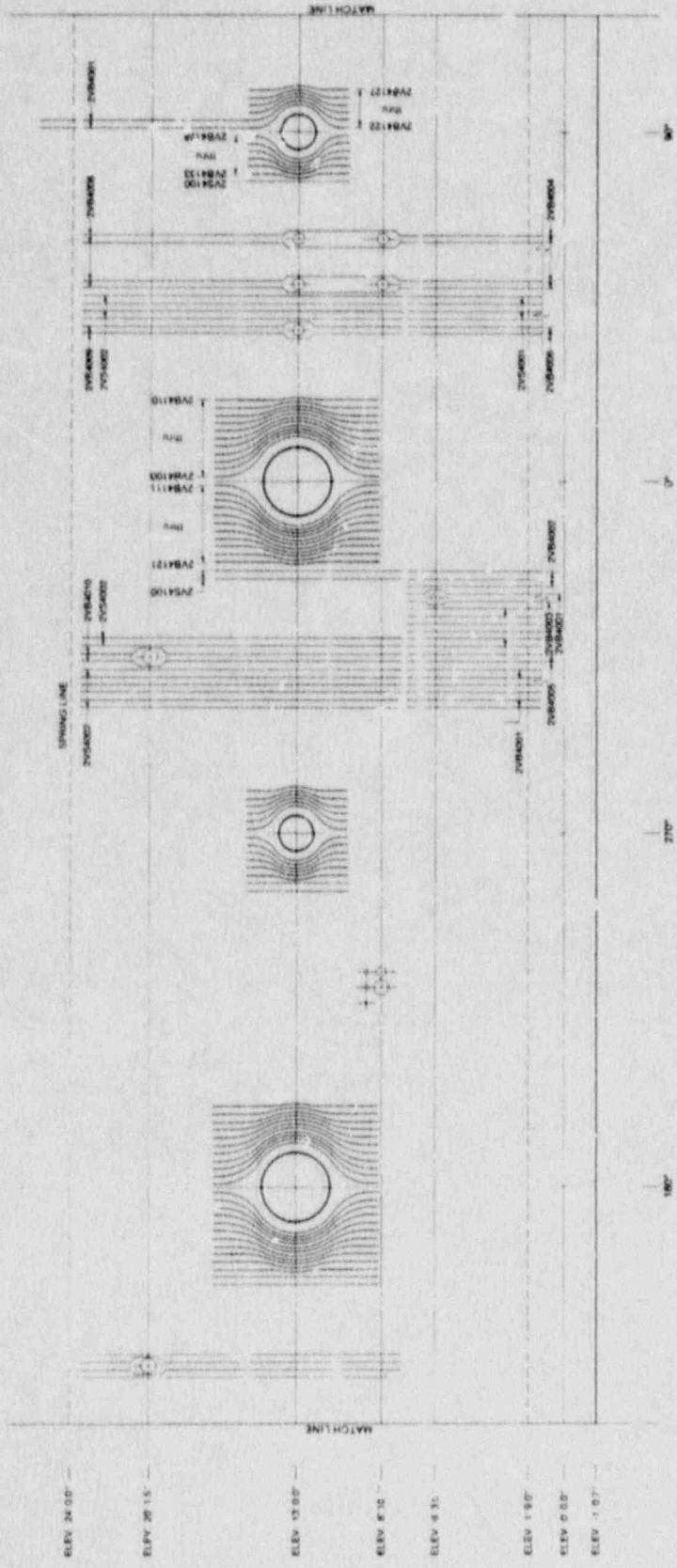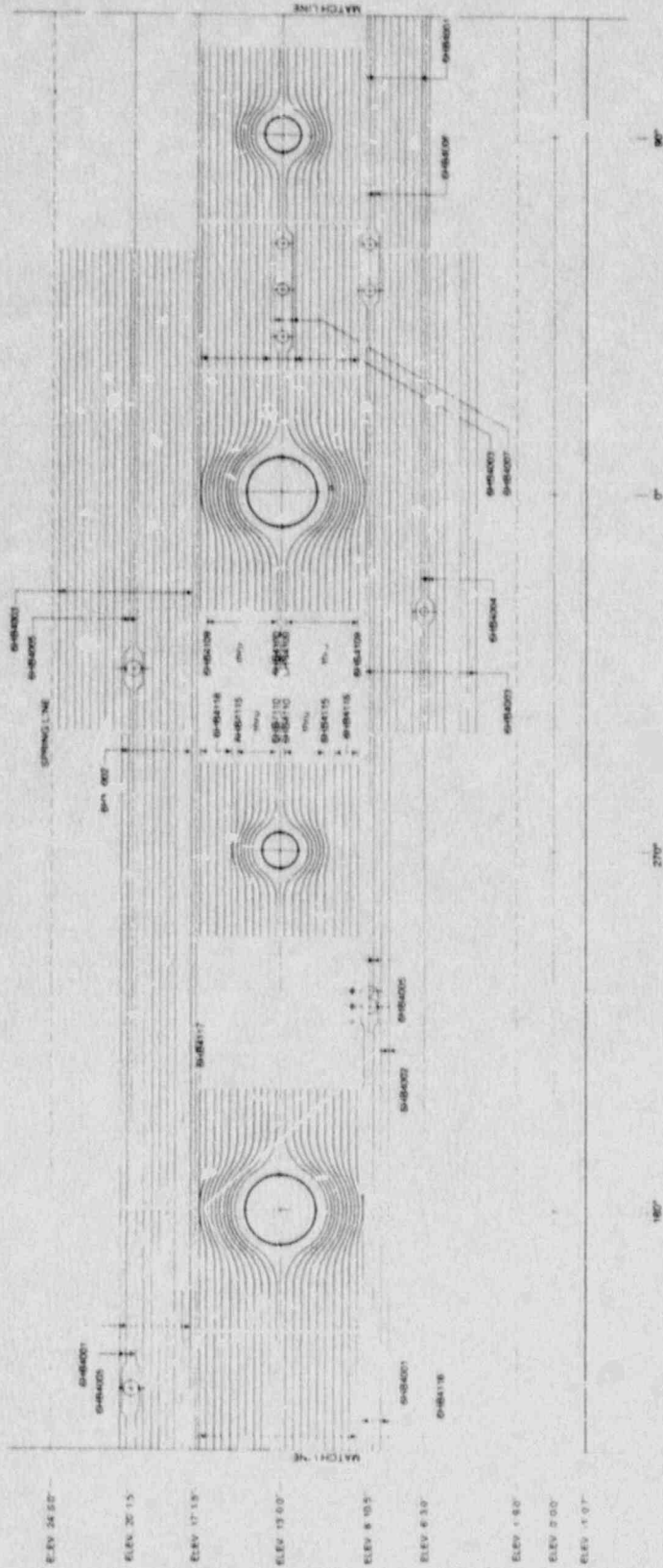Figure A.8 Cylinder Stretchout - Reinforcement Layers 1 and 3

Figure A.9 Cylinder Stretchout - Reinforcement Layer 2

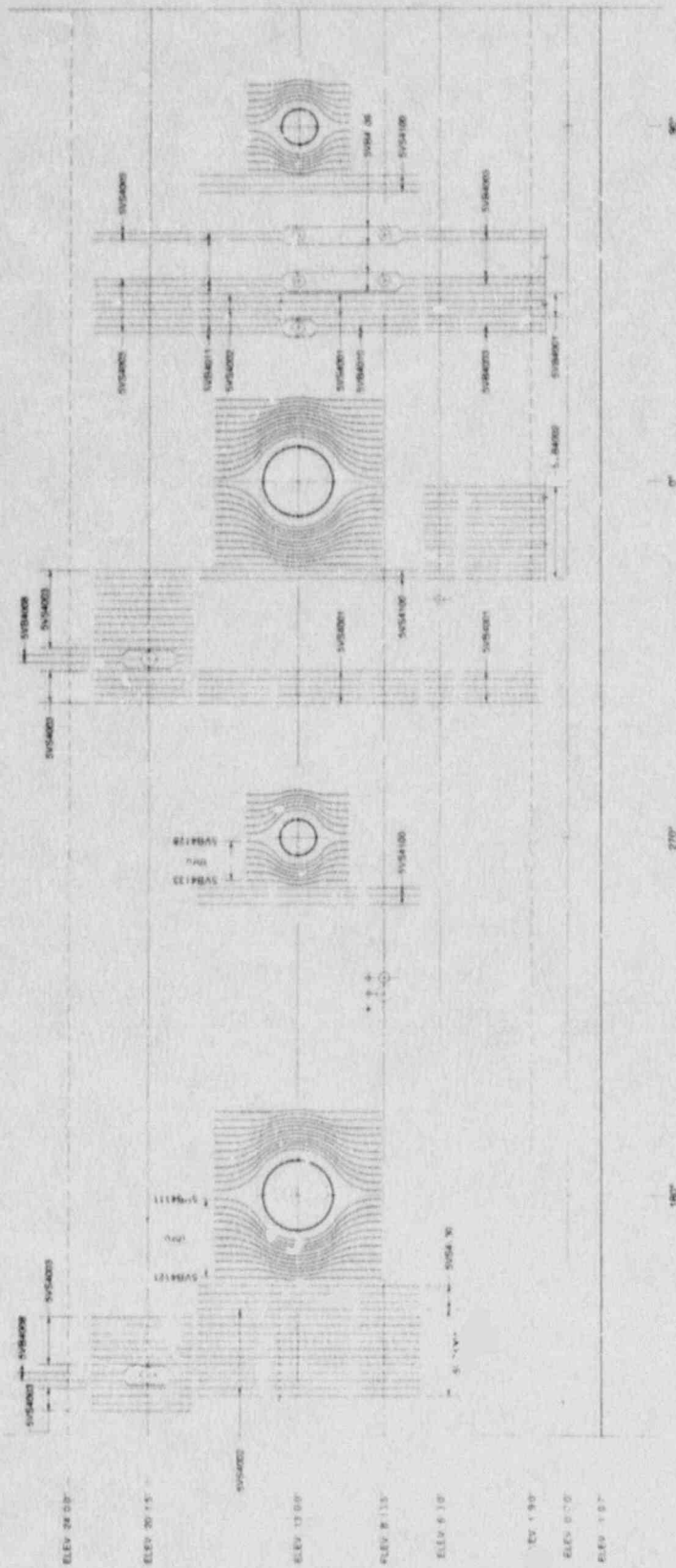Figure A.10 Cylinder Stretchout - Reinforcement Layers 4 and 6
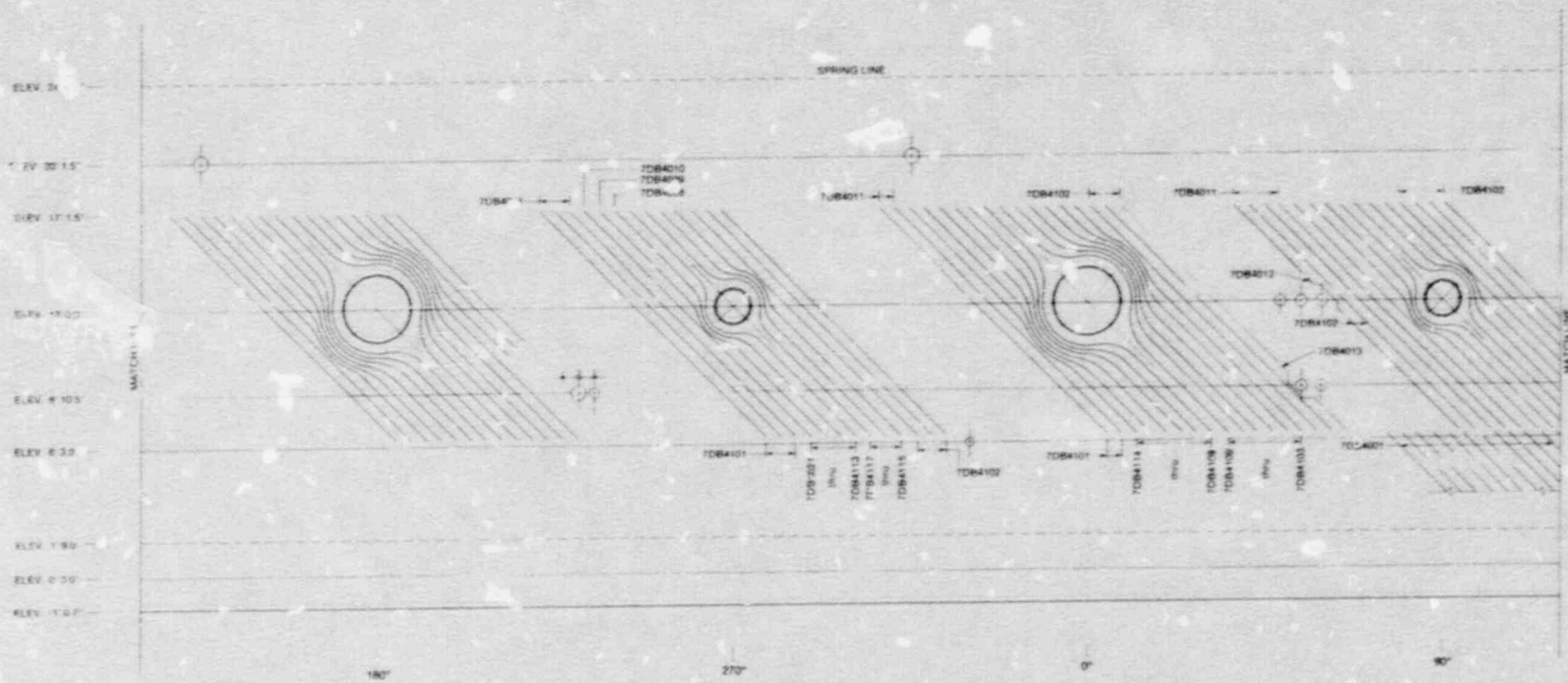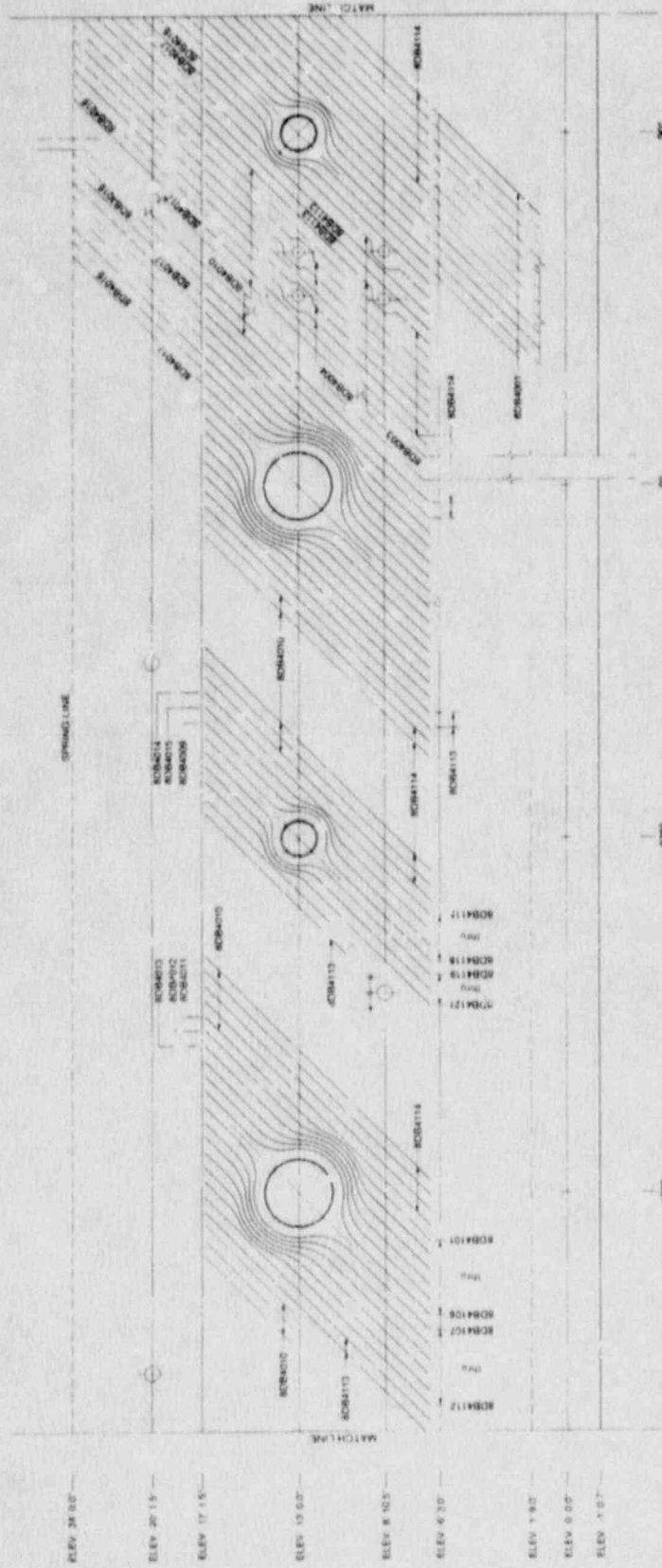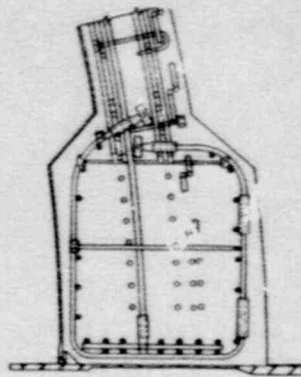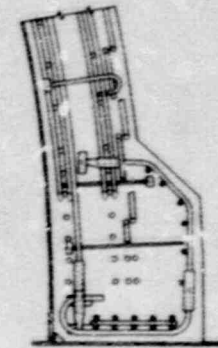
Figure A.11 Cylinder Stretchout - Reinforcement Layer 5

Figure A.12  Cylinder Stretchout - Reinforcement Layer 7

A-14

Figure A.13  Cylinder Stretchout - Reinforcement Layer 8
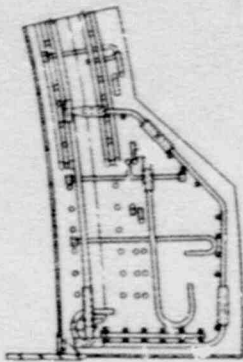
SECTION AT HORIZONTAL ₵ (3 O'CLOCK)    SECTION AT HORIZONTAL ₵ (3 O CLOCK)    SECTION AT HORIZONTAL ₵ (3 O'CLOCK)
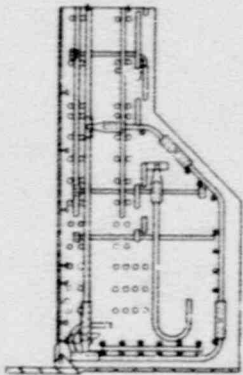
SECTION AT VERTICAL ₵ (12 O'CLOCK)    SECTION AT VERTICAL ₵ (12 O'CLOCK)
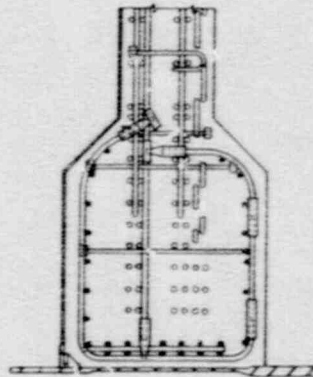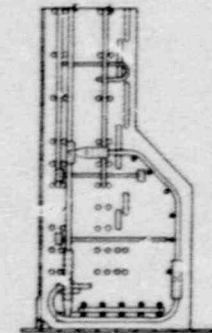
SECTION AT VERTICAL ₵ (12 O'CLOCK)

**BOSS @ Az 0°**    **BOSS @ Az 180°**    **PL-A @ Az 90° & 270°**

Figure A.14  Additional Reinforcement in Bosses of Selected Penetrations
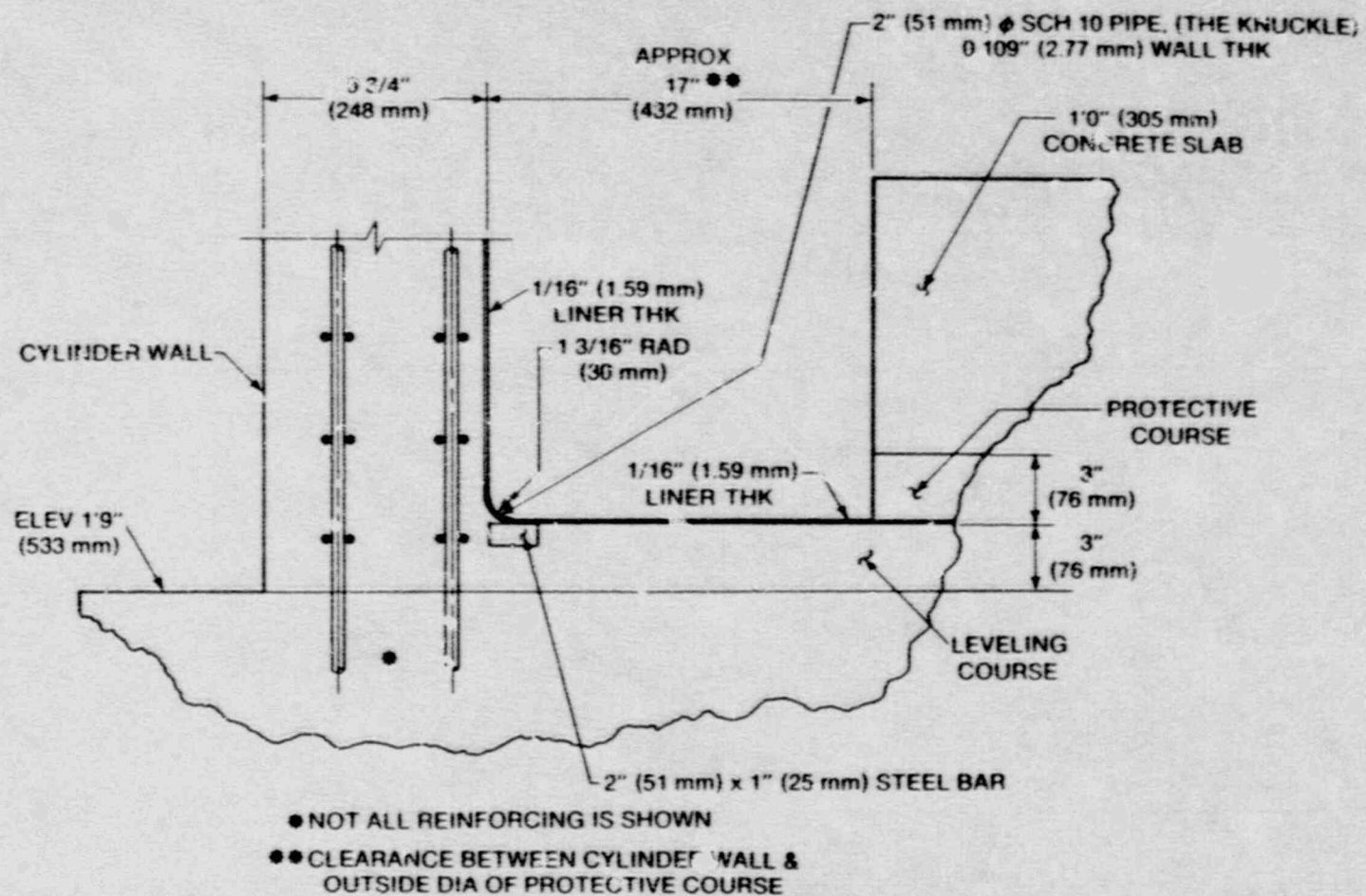
Figure A.15  Details of Liner Knuckle
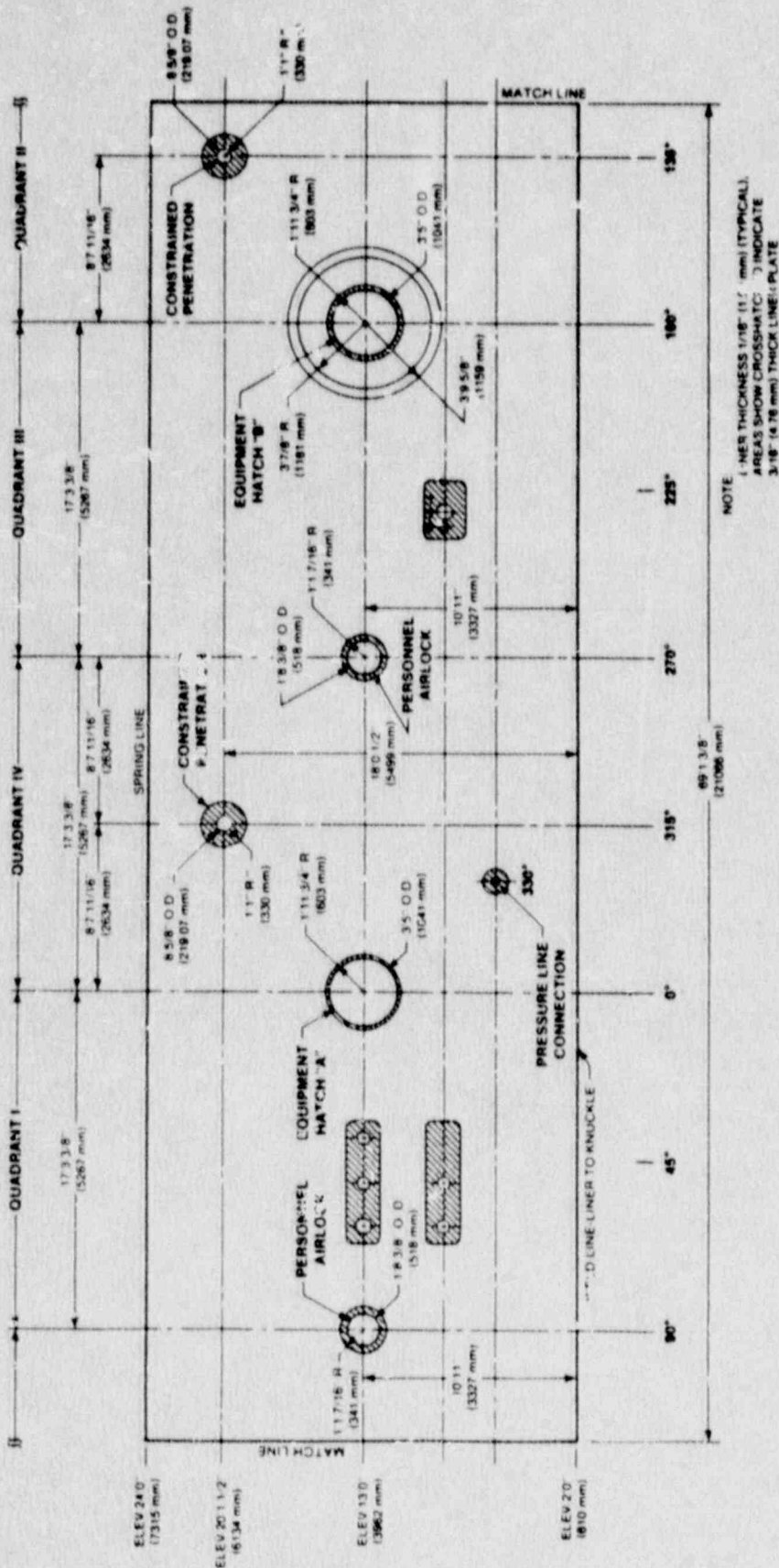
Figure A.16 Cylinder Stretchout - Liner Details
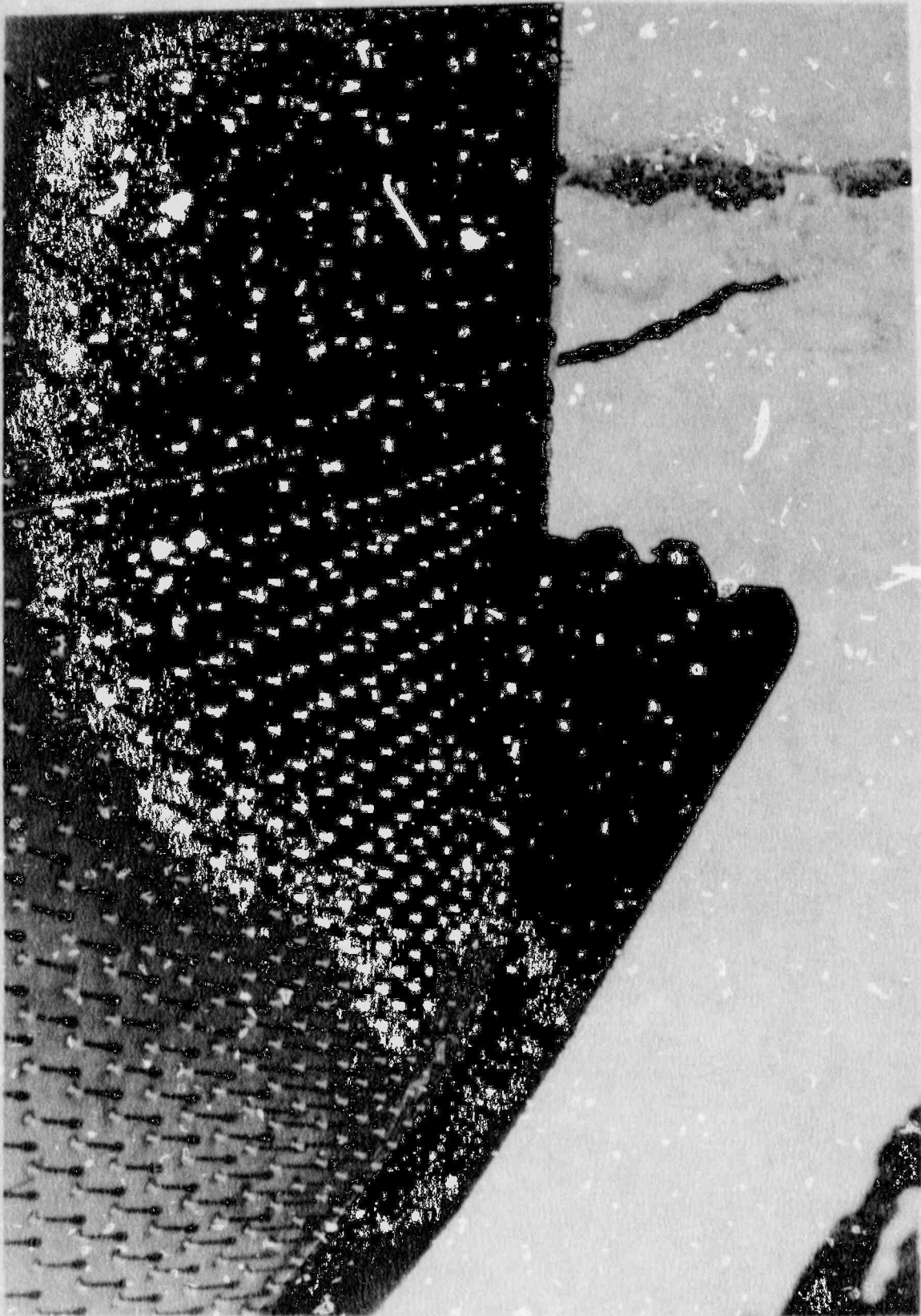
Figure A.17  Stud Pattern in Lower Cylinder
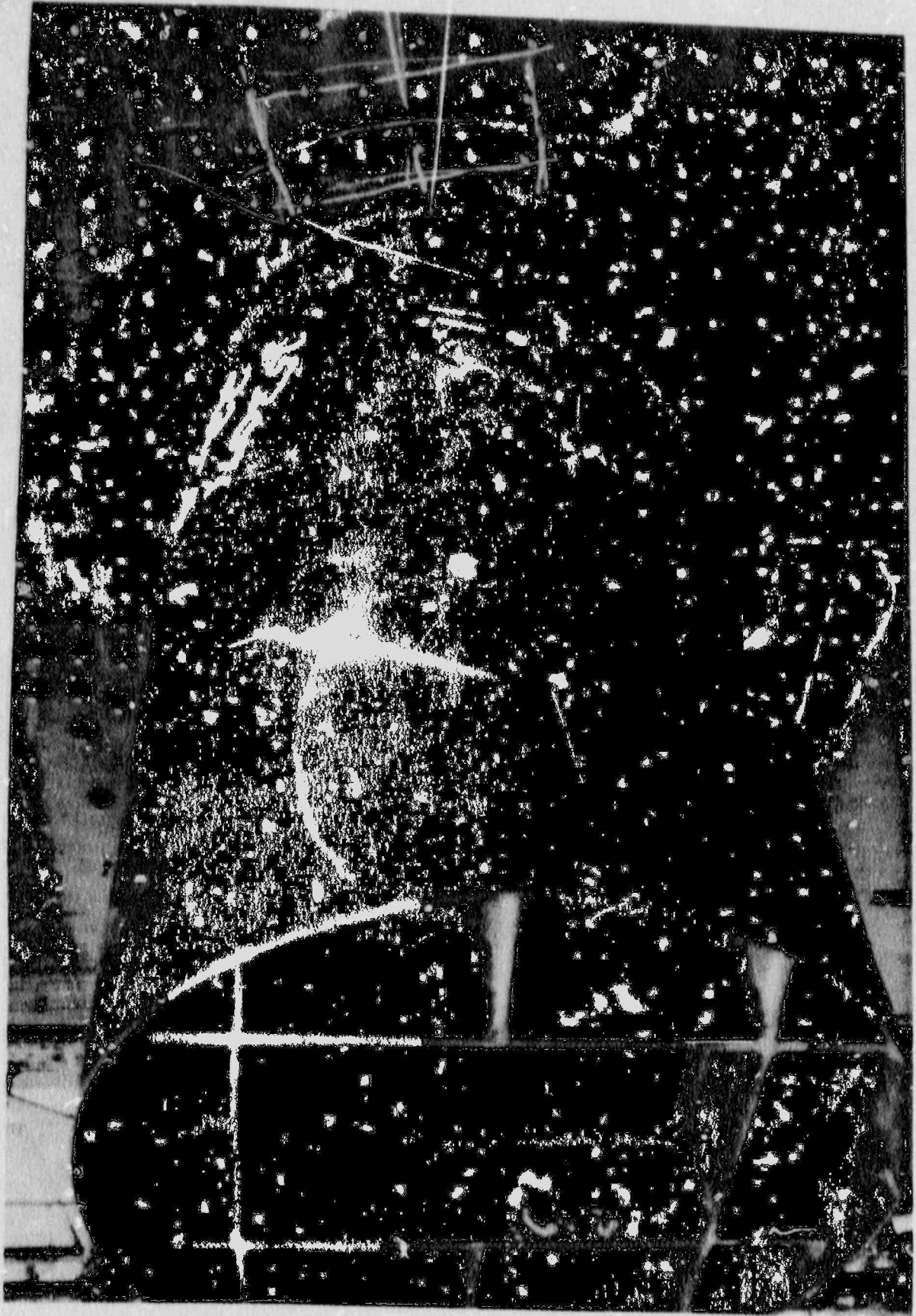
Figure A.18 Stud Pattern Around Personnel Airlock A

## A.2 As Measured Material Properties

All materials used in constructing the model have mechanical properties that are the same, or as nearly the same as possible as those used in actual reinforced concrete containment buildings. Reference stress-strain curves were derived based on actual measurements of the properties of the most widely used materials in the model, including the 1/16 and 1/12 in. (1.59 and 2.11 mm) thick liner material, the #4 rebar, and various lifts of the concrete.

The concrete used in the scale model was composed of well-rounded coarse aggregate with a nominal maximum size of 3/8 in. (9.5 mm). High-range water reducers (superplasticizers) were used with a water/cement ratio of 0.53. The concrete was centrally batched and hauled into the test site, which resulted in a consistent, high quality mix. In order to test the properties, 15 concrete cylinders were poured from each lift of the model (there were a total of 11 lifts; 1 for the basemat, 6 for the cylinder, and 4 for the dome). Direct tension, split cylinder, and compression tests have been run on specimens from each lift aged for 28 days, 4 months, or 6 months. Material properties of the concrete will also be measured at the time of high pressure testing. Standard cylinders were used in the split cylinder and compression tests; the direct tension tests were conducted with a dog-bone specimen developed by United Engineers. Based on the tests, it was felt that the variation in the properties between the different lifts was negligible (the data were within normal statistical limits fro a single lift of concrete). Thus, SNL has recommended a single stress-strain curve, as given in Table A.1, to represent the concrete for the entire model. The recommended curve is based on extrapolation of strength values out to the expected time of high pressure testing. The compressive strength is estimated at 6.8 ksi (46.9 MPa). The tensile response is assumed to be linear up to the ultimate tensile strength, which was estimated at 0.5 ksi (3.45 MPa).

---

### Table A.1 - Concrete Material Properties

Elastic Constants
  Young's modulus - 4800 ksi (33100 MPa)
  Poisson's ratio - 0.2
  Ultimate Tensile Strength - 500 psi (3.45 MPa)

Unconfined Compressive Stress-strain Curve

| Engineering Stress | | Engineering |
| --- | --- | --- |
| (ksi) | (MPa) | Strain |
| 1.0 | 6.9 | 0.00021 |
| 2.0 | 13.8 | 0.00045 |
| 3.0 | 20.7 | 0.00072 |
| 3.9 | 26.9 | 0.00100 |
| 5.0 | 34.5 | 0.00140 |
| 6.8 | 46.9 | 0.00200 |
| 6.8 | 46.9 | 0.00230 |
| 0.0 | 0.0 | 0.00600 |

---

Uniaxial tensile tests were conducted on the liner materials and the #4 rebar. Average results of these tests (the recommended values) are presented in Tables A.2 through A.4. For a given material, the measured properties were very consistent for the number of tensile coupons tested. The stress-strain curve for the #4 rebar is based on the nominal cross-sectional area, which is 0.2 in. (129 mm). For the liner materials, the stress-strain curve is based on the actual cross-sectional area of the tensile coupons; thus, the actual thickness of the liner should be used in an analytical model. However, the difference between the nominal thicknesses and the average actual thicknesses of the liner materials is small, as indicated by Table A.5. Therefore, the analytical results should not be particularly sensitive to this factor, especially since the liner represents less than 20% of the total strength of the containment model wall. Because the #4 rebar is predominant in the model, it was the only size rebar for which a complete stress-strain curve was made available. It was recommended that this stress-strain curve (see Table A.4) be used for all the reinforcing steel in the model; however, mill properties for each size of rebar used in the model were also made available to the analysts. The mill properties and nominal cross-sectional areas for the rebars used in the model are presented in Table A.6. Note that the properties in Table A.4 reflect a reduction in the ultimate strength caused by splices.

Table A.2 - Cylinder and Basemat Liner Properties

Elastic Constants:
    Modulus - 30000 ksi (207000 MPa)
    Poisson's ratio - 0.3
    Yield stress - 50.2 ksi (346 MPa)

Engineering Stress-strain curve

| Engineering Stress (ksi) | (MPa) | Plastic Strain |
|---|---|---|
| 50.2 | 346 | 0. |
| 50.2 | 346 | 0.0157 |
| 59.0 | 407 | 0.0308 |
| 66.0 | 455 | 0.0696 |
| 68.0 | 469 | 0.0937 |
| 70.0 | 482 | 0.1620 |

## Table A.3 - Dome Liner Properties

Elastic Constants:
Modulus - 30000 ksi  (207000 MPa)
Poisson's ratio - 0.3
Yield stress - 51.4 ksi (354 MPa)

Engineering Stress-strain curve

| Engineering Stress | | Plastic |
|---|---|---|
| (ksi) | (MPa) | Strain |
| 51.4 | 354 | 0. |
| 61.1 | 421 | 0.0230 |
| 66.9 | 461 | 0.0478 |
| 70.5 | 486 | 0.0977 |
| 71.0 | 489 | 0.1476 |

## Table A.4 - Rebar Material Properties

Elastic Constants:
Modulus - 31000 ksi  (214000 MPa)
Poisson's ratio - 0.3
Yield stress - 66.6 ksi (459 MPa)

Engineering Stress-strain curve

| Engineering Stress | | Plastic |
|---|---|---|
| (ksi) | (MPa) | Strain |
| 66.6 | 459 | 0. |
| 73.3 | 505 | 0.0094 |
| 85.6 | 590 | 0.0200 |
| 99.0 | 682 | 0.0430 |

## Table A.5 - Liner Thicknesses

Cylinder and Basemat Liner:
Nominal Thickness - 1/16 in. (1.59 mm)
Actual Thickness - 0.068 in. (1.73 mm)

Dome Liner:
Nominal Thickness - 1/12 in. (2.12 mm)
Actual Thickness - 0.090 in. (2.29 mm)

## Table A.6 - Mill Properties for Reinforcing Bar

| Bar Size | Nominal Area (in²) | (mm²) | Yield Strength (ksi) | (MPa) | Ultimate Strength (ksi) | (MPa) | Elongation (in/in) |
|----------|-------------------|-------|---------------------|-------|------------------------|-------|--------------------|
| 6 mm | 0.04 | 28 | 72.2 | 497 | 100.9 | 695 | 0.27 |
| 6 mm | 0.04 | 28 | 69.9 | 482 | 99.0 | 682 | 0.23 |
| #3 | 0.11 | 71 | 68.0 | 469 | 103.0 | 710 | 0.15 |
| #4 | 0.20 | 129 | 68.0 | 469 | 105.0 | 723 | 0.14 |
| #5 | 0.31 | 198 | 66.5 | 458 | 94.0 | 648 | 0.15 |
| #6 | 0.44 | 285 | 64.8 | 447 | 103.0 | 710 | 0.14 |

Appendix References

[A.1]   D. B. Clauss, "Round-Robin Pretest Analyses of a 1:6-Scale Reinforced Concrete Containment Model Subject to Static Internal Pressurization," NUREG/CR-4913, SAND87-0891, Sandia National Laboratories, Albuquerque, NM. May 1987.

[A.2]   "Soil Report," Project Sandia LWR Reinforced Concrete Containment Model, Project NO. 3243 J 066, Western Technologies, Inc., Albuquerque, NM, October 1985.

Distribution:

J. F. Costello (20 Copies)
USNRC/RES
Mail Stop NL/S-217A
5650 Nicholson Lane
Rockville, MD 20852

H. L. Graves, III
USNRC/RES
Mail Stop NL/S-217A
5650 Nicholson Lane
Rockville, MD 20852

US Department of Energy
Office of Nuclear Energy
Attn: A. Millunzi, Bernard J. Rock
D. Giessing (3 copies)
Mail Stop B-107
NE-540
Washington, DC 20545

CBI NaCon, Inc.
Attn: Thomas J. Ahl
800 Jorie Boulevard
Oak Brook, IL 60521

Wilfred Baker Engineering
Attn: Wilfred E. Baker
218 E. Edgewood Pl.
P. O. Box 6477
San Antonio, TX 78209

Battelle Columbus Laboratories
Attn: Richard Denning
505 King Avenue
Columbus, Ohio 43201

Bechtel Power Corporation
Attn: Asadour H. Hadjian
12400 E. Imperial Highway
Norwalk, CA 90650

Bechtel Power Corp.
Attn: T. E. Johnson, Subir Sen,
K. Y. Lee (3 copies)
15740 Shady Grove Rd.
Gaithersburg, MD 20877

Babcock & Wilcox Co.
Attn: James R. Farr
20 S. van Buren Ave.
Barberton, OH 44203

City College of New York
Dept. of Civil Engineering
Attn: C. Costantino (5 copies)
140 Street and Convent Ave.
New York, NY 10031

1245 Newmark CE Lab
University of Illinois
Attn: Prof. Mete A. Sozen (5 copies)
208 N. Romine
MC-250
Urbana, IL 61801

Stevenson & Associates
Attn: John D. Stevenson
9217 Midwest Ave.
Cleveland, Ohio 44125

United Engineers & Constructors, Inc.
Attn: Joseph J. Ucciferro
30 S. 17th St.
Philadelphia, PA 19101

Electrical Power Research Institute
Attn: H. T. Tang, Y. K. Tang,
Raf Sehgal, J. J. Taylor,
W. Loewenstein (5 copies)
3412 Hillview Avenue
PO Box 10412
Palo Alto, CA 94304

School of Civil & Environ. Engr.
Attn: Professor Richard N. White
Hollister Hall
Cornell University
Ithaca, NY 14853

NUTECH Engineers, Inc.
Attn: John Clauss
1111 Pasquinelli Drive, Suite 100
Westmont, Illinois 60559

Iowa State University
Department of Civil Engineering
Attn: L. Greimann
420 Town Engineering Bldg.
Ames, IA 50011

TVA
Attn: D. Denton, W9A18
400 Commerce Ave.
Knoxville, TN 37902

Los Alamos National Laboratories
Attn: C. Anderson
PO Box 1663
Mail Stop N576
Los Alamos, NM 87545

EQE Inc.
Attn: M. K. Ravindra
3300 Irvine Aveune
Suite 345
Newport Beach, CA 92660

University of Illinois
Attn: C. Siess
Dept. of Civil Engineering
Urbana, IL 61801

EBASCO Services, Inc.
Attn: Robert C. Iotti
Two World Trade Center
New York, NY 10048

EG&G Idaho
Attn: B. Barnes, T. L. Bridges
      (2 copies)
Willow Creek Bldg. W-3
PO Box 1625
Idaho Falls, ID 83415

Sargent & Lundy Engineers
Attn: A. Walser, P. K. Agrawal
      (2 copies)
55 E Monroe St.
Chicago, IL 60603

General Electric Company
Attn: E. O. Swain, D. K. Henrie,
      R. Gou (3 copies)
175 Curtner Ave.
San Jose, CA 95125

Westinghouse Electric Corp.
Attn: Vijay K. Sazawal
Waltz Mill Site
Box 158
Madison, PA 15663

Quadrex Corporation
Attn: Quazi A. Hossain
1700 Dell Ave.
Campbell, CA 95008

ANATECH International Corp.
Attn: Y. R. Rashid (5 copies)
3344 N. Torrey Pines Court
Suite 320
LaJolla, CA 92037

Oak Ridge National Laboratory
Attn: Steve Hodge
PO Box Y
Oak Ridge, TN 37830

Brookhaven National Laboratory
Attn: C. Hofmayer,T. Pratt,
      M. Reich (3 copies)
Building 130
Upton, NY 11973

Argonne National Laboratory
Attn: J. M. Kennedy (5 copies),
      R. F. Kulak, R. W.
      Seidensticker (7 copies)
9700 South Cass Avenue
Argonne, IL 60439

Tennessee Valley Authority
Attn: Nathaniel Foster
400 Summit Hill Rd.
W9D24C-K
Knoxville, Tennessee 37902

University of Wisconsin
Nuclear Engineering Dept.
Attn: Prof. Michael Corradini
Madison, WI 53706

Brookhaven National Laboratory
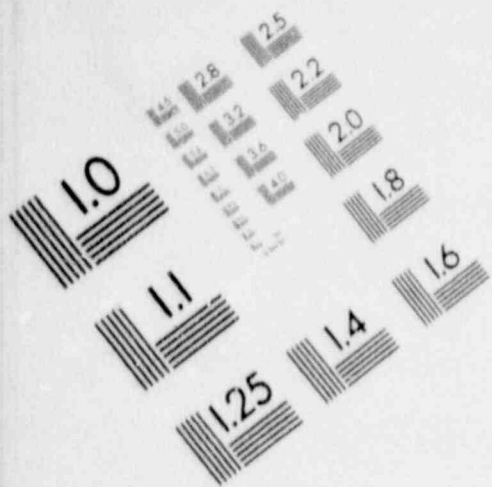Attn: Ted Ginsberg
Building 820M
Upon, NY 11973

Dept. of Chemical & Nuclear Engineering
University of California Santa Barbara
Attn: T. G. Theofanous
Santa Barbara, CA 93106

Northern Illinois University
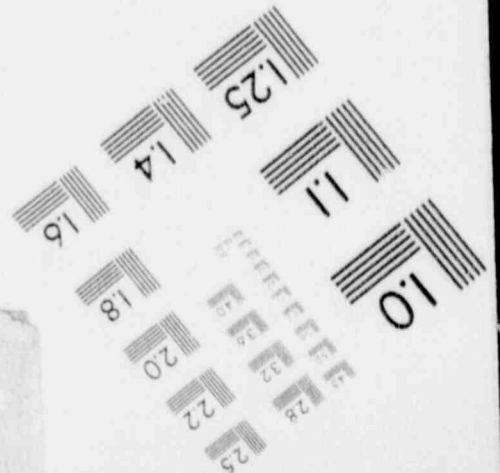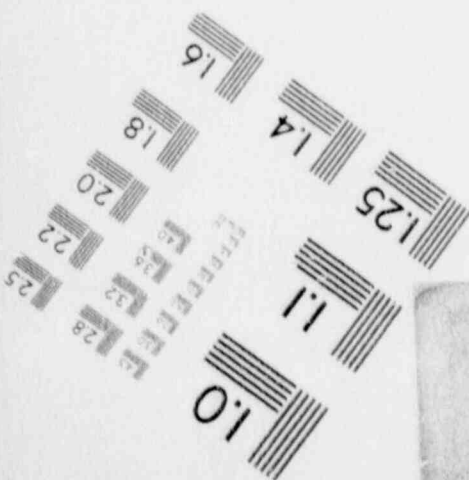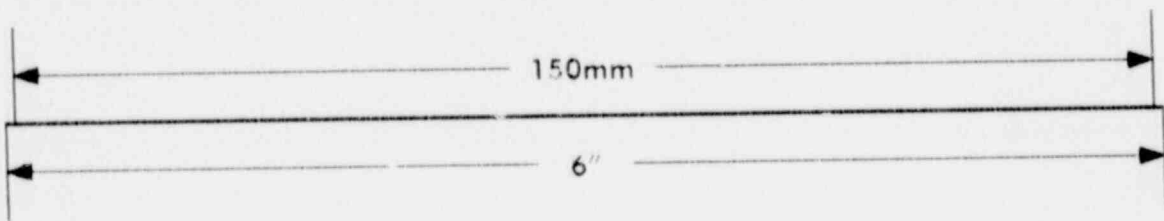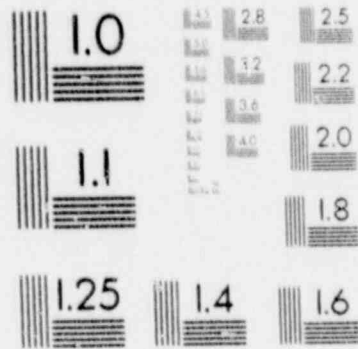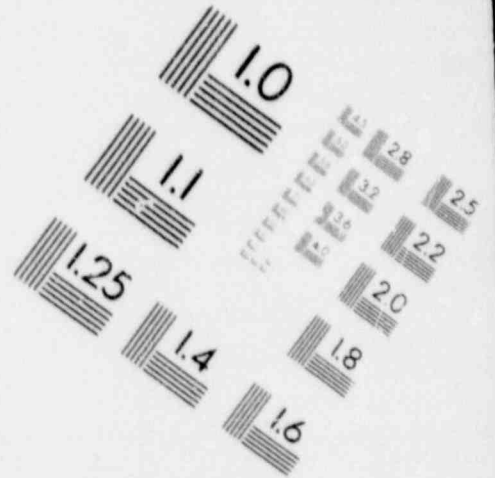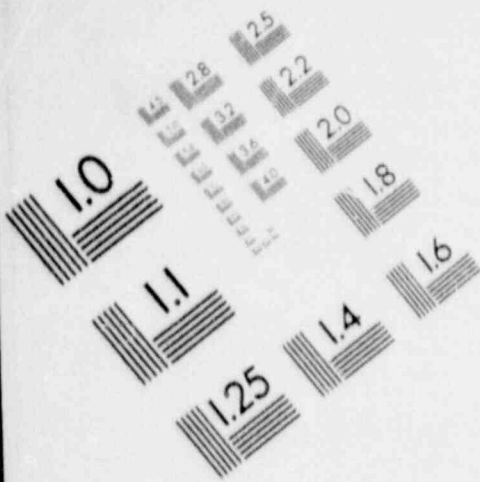Mechanical Engineering Dept.
Attn: A. Marchertas
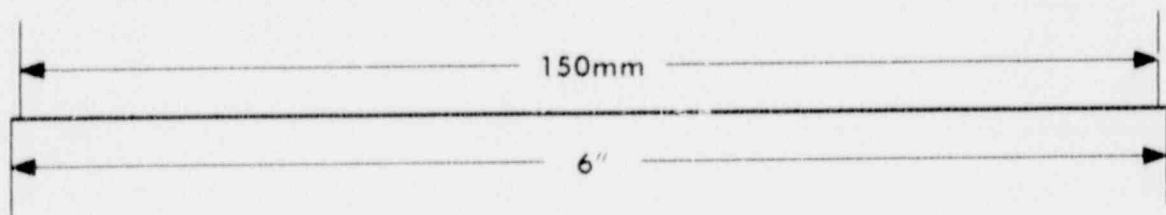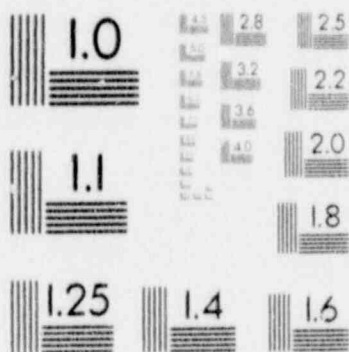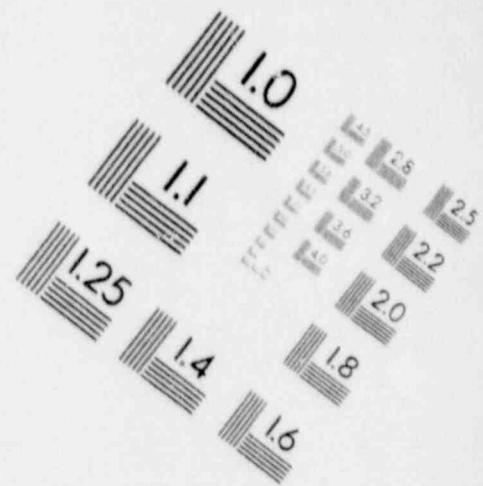DeKalb, IL 60115

# 1

## IMAGE EVALUATION
## TEST TARGET (MT-3)
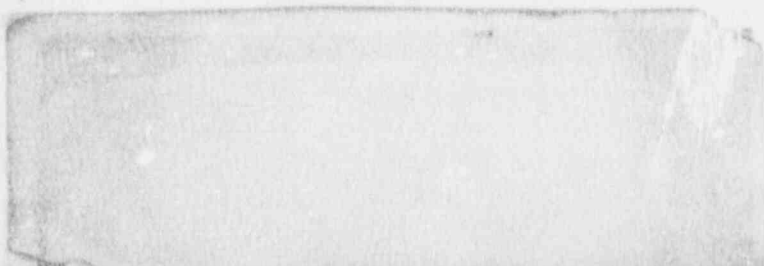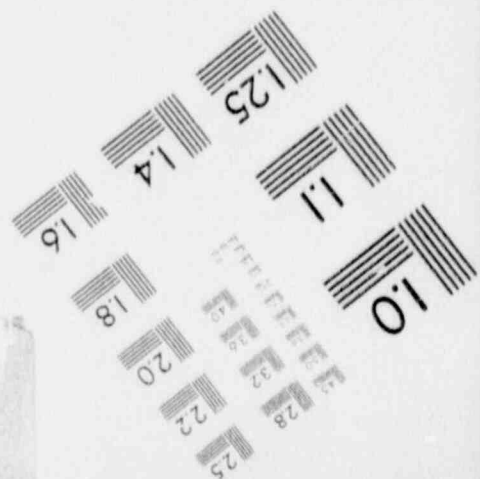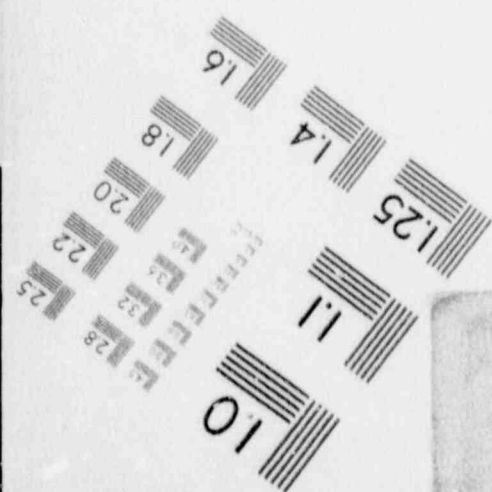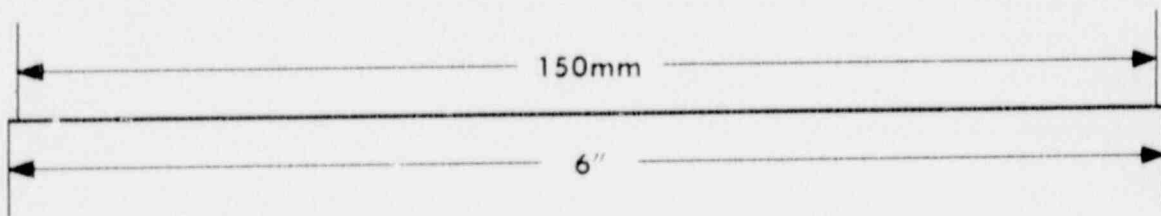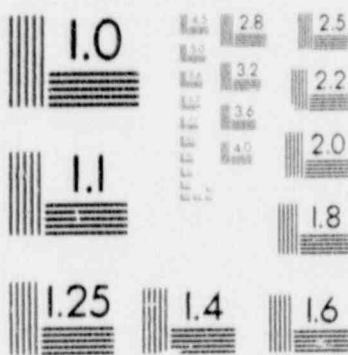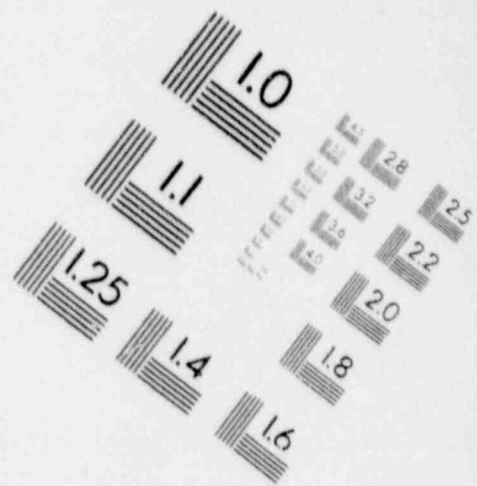
150mm

6"

# 1

## IMAGE EVALUATION
## TEST TARGET (MT-3)

150mm

6"

# 1

## IMAGE EVALUATION
## TEST TARGET (MT-3)

1.0

1.1

1.25

1.0    1.1    1.25
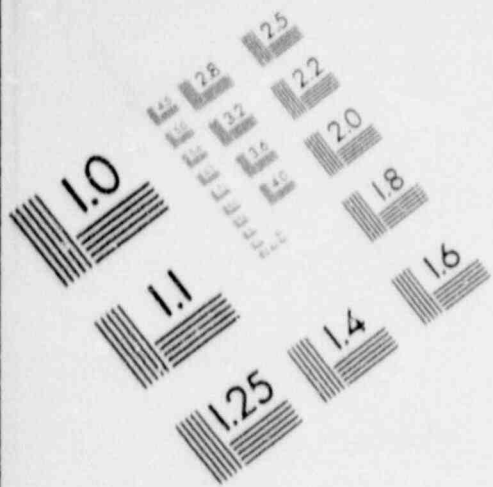
1.25    1.4    1.6

|← —————————— 150mm —————————— →|

|← —————————— 6" —————————— →|

# 1

## IMAGE EVALUATION
## TEST TARGET (MT-3)

150mm

6"
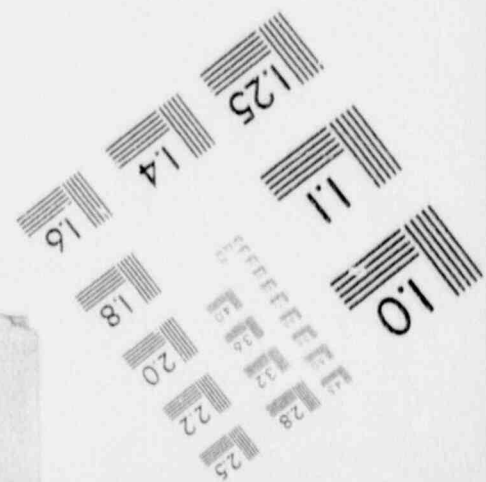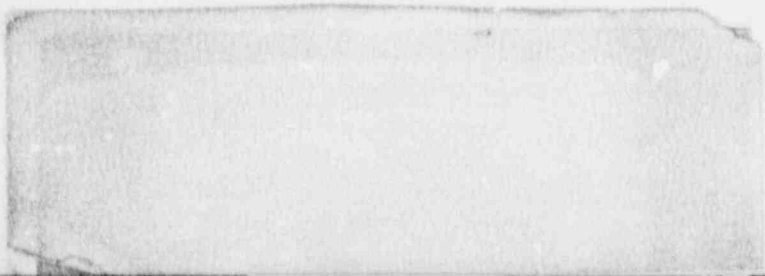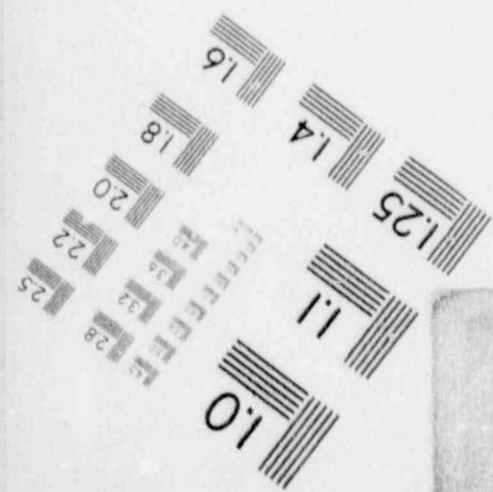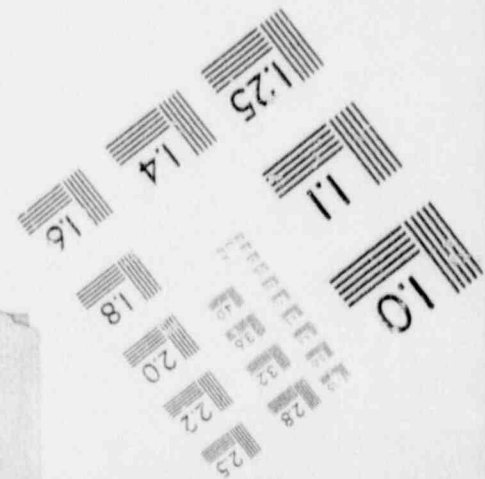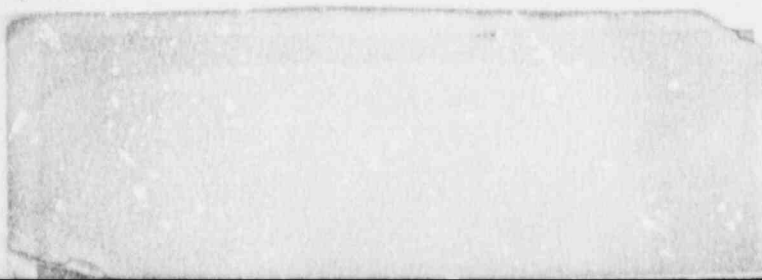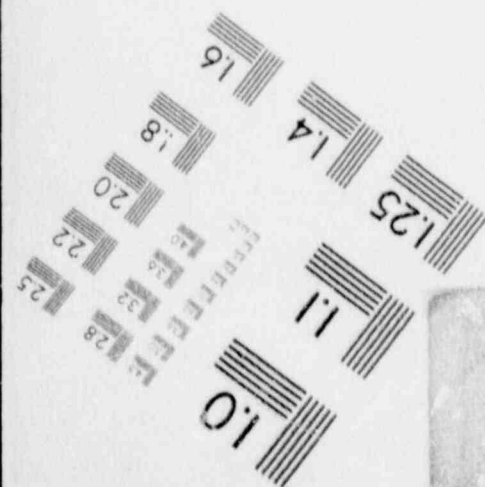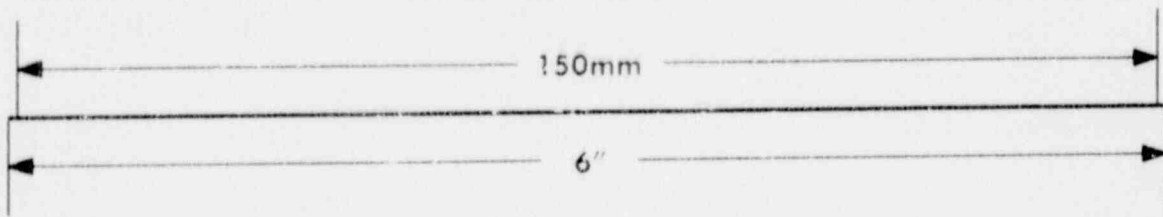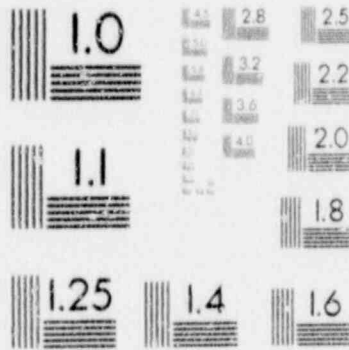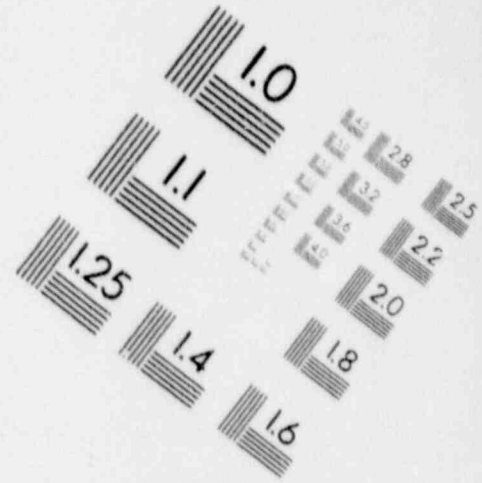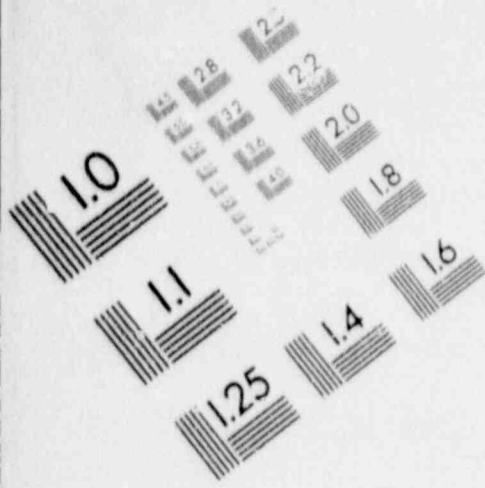
Institut fur Mechanik
Universitaet Innsbruck
Attn: Prof. G. I. Schueller
Technikerstr. 13
A-6020 Innsbruck
AUSTRIA

Nuclear Studies & Safety Dept.
Ontario Hydro
Attn: W. J. Penn
700 University Avenue
Toronto, Ontario
M5G 1X6
CANADA

University of Alberta
Dept. of Civil Engineering
Attn: Prof. D. W. Murray
Edmonton, Alberta
CANADA T6G 2G7

Commissariat a L'Energie Atomique
Centre d'Etudes Nucleaires de Saclay
Attn: M. Livolant, P. Jamet (2 copies)
F-91191 Gif-Sur-Yyette Cedex
FRANCE

Institut de Protection
        et de Surete Nucleaire
Commissariat a l'Energie Atomique
Attn: M. Barbe (5 copies)
F-92660 Fontenay-aux-Roses
FRANCE

OECD Nuclear Energy Agency
Attn: K. Stadie
Deputy Director, Safety & Regulation
38, Boulevard Suchet
F-75016 Paris
FRANCE

Kernforschungszentrum Karlsruhe GmbH
Attn: R. Krieg, P. Gast (2 copies)
Postfach 3640
D-7500 Karlsruhe
FEDERAL REPUBLIC OF GERMANY

Lehrstuhl fuer Reakordynamik
        und Reaktorsicherheit
Technische Universitaet Muenchen
Attn: Prof. H. Karwat
D-8046 Garching
FEDERAL REPUBLIC OF GERMANY

Staatliche Materialpruefungsanstalt (MPA)
University of Stuttgart
Attn: Prof. K. F. Kussmaul
Pfaffenwaldring 32
D-7000 Stuttgart 80 (Vaihingen)
FEDERAL REPUBLIC OF GERMANY

Gesellschaft fuer Reaktorsicherheit
Attn: H. Schulz, (5 copies), A.
        Hoefler, F. Schleifer (7 copies)
Schwertnergasse 1
D-5000 Koeln 1
FEDERAL REPUBLIC OF GERMANY

Kraftwerk Union AG
Attn: M. Hintergraber
Hammerbacherstr. 12-14
D-8520 Erlangen
FEDERAL REPUBLIC OF GERMANY

Ente Nazionale per l'Energia Elettrica
Attn: Francesco L. Scotto
v. le Regina Margherita, 137
Rome, ITALY

ISMES
Attn: A. Peano
Viale Giulio Cesare 29
I-24100 Bergamo
ITALY

ENEA-DISP
ACO-CIVME
Attn: Giuseppe Pino (5 copies)
Via Vitaliano Brancati, 48
I-00144 Roma
ITALY

Nuclear Power Construction Dept.
Tokyo Electric Power Company
Attn: Hideaki Saito
No. 1-3, Uchisaiwa-cho, 1-Chome
Chiyoda-ku
Tokyo, 100
JAPAN

Nuclear Equipment Design Dept.
Hitachi Works, Hitachi, Ltd.
Attn: O. Oyamada
3-1-1 Saiwai-Cho
Hitachi-Shi, Ibaraki-ken
JAPAN

Division of Technical Information
Japan Atomic Energy Research Institute
Attn: Jun-ichi Shimokawa
2-2, Uchisaiwai-cho 2-chome
Chiyoda, Tokyo 100
JAPAN

University of Tokyo
Institute of Industrial Science
Attn: Prof. H. Shibata
22-1, Roppongi 7
Minatu-ku, Tokyo
JAPAN

Civil Engineering Laboratory
Central Research Institute
　　　　of Electric Power Industry
Attn: Yukio Aoyagi
1646 Abiko Abiko-Shi Chiba
JAPAN

Kajima Corporation
Attn: K. Umeda
No. 1-1, 2-Chome Nishishinjuku
Shinjuku-ku
Tokyo 160
JAPAN

Nuclear Structures Dept.
Kajima Corporation
Attn: Kohji Ujiie
No. 5-30, Akasaka 6-Chome
Minato-ku
Tokyo 107
JAPAN

Muto Institute of Structural Mechanics
Attn: Tadashi Sugano
Room 3005 Shinjuku Mitsui Building
Shinjuku-ku
Tokyo, 163
JAPAN

Nuclear Power Engineering Test Center
Attn: Yoshio Tokumaru
6-2, 3-Chome, Toranomor
Minato-ku
Tokyo 105
JAPAN

Japan Atomic Energy Research Inst.
Attn: Kunihisa Soda, Toshikuni Isozaki
　　　　(2 copies)
Tokai-Mura, Ibaraki-Ken 319-11
JAPAN

Shimizu Construction Co., Ltd.
Attn: Toshihiko Ota
No. 4-17, Etchujima 3-Chome
Koto-Ku
Tokyo 135
JAPAN

Shimizu Construction Co., Ltd.
Attn: Toshiaki Fujimori
No. 18-1, Kyobashi 1-Chome
Chuo-ku
Tokyo 104
JAPAN

Nuclear Power Division
Shimizu Corp.
Attn: Yoichiro Takeuchi
Mita 43, Mori Bldg. 13F
No. 13-16, Mita 3-Chome
Minato-ku
Tokyo, 108
JAPAN

Technical Research Laboratory
Takenaka Corp.
Attn: Takahiro Kei
No. 5-14, 2-Chome, Minamisuna
Koto-ku, Tokyo
JAPAN

Universidad Politecnica
Escuela Tecnica Superior
de Ingenieros Industriales
Attn: Agustin Alonso
Madrid
SPAIN

Unidad Electrica S.A.
Attn: Jose Puga
UNESA
ES-28020 Madrid
SPAIN

Principia Espana, SA
Attn: Joaquin Marti
Orense, 36-2
28020 Madrid
SPAIN

Servicio Licenciamiento
Central Nuclear de Asco
Attn: D. Joaquin Sanchez Baptista
Tres Torres, 7
ES-08017 Barcelona
SPAIN

Central Nuclear de Almaraz
Attn: D. Jose Maria Zamarron
Subdirector Tecnico
Claudio Coello, 123
ES-28006 Madrid
SPAIN

Nuclenor, S.A.
Attn: D. Federico del Pozo Obeso
Director General
Hernan Cortes, 26
ES-39003 Santander
SPAIN

UNESA
Attn: D. Jose Puga Fernandez
Francisco Gervas, 3
ES-28020 Madrid
SPAIN

Studsvik Energiteknik AB
Attn: Kjell O. Johansson
S-611 82 Nykoping
SWEDEN

Swedish State Power Board
Nuclear Reactor Safety
Attn: Hans Cederberg, Per-Eric Ahlstrom,
    Ralf Espefaelt (3 copies)
S-162 87 Vallingby
SWEDEN

Swiss Federal Institute of Technology
Institute of Structural Engineering
Attn: W. Ammann
ETH-Hoenggerberg, HIL
CH-8093 Zurich
SWITZERLAND

Motor-Columbus Consulting Engineers, Inc.
Attn: K. Gahler, A. Huber, A. Schopfer
    (3 copies)
Parkstrasse 27
CH-5401 Baden
SWITZERLAND

EIR (Swiss Federal Institute for
    Reactor Research)
Attn: O. Mercier, P. Housemann (2 copies)
CH-5303 Wuerlingen
SWITZERLAND

Swiss Federal Nuclear Safety Inspectorate
Federal Office of Energy
Attn: S. Chakraborty
CH-5303 Wuerenlingen
SWITZERLAND

Swiss Federal Institute of Technology
Attn: Prof. F. H. Wittmann
Chemin de Bellerive 32
CH-1007 Lausanne
SWITZERLAND

Elektrowatt Ingenieurunternehmung AG
Attn: John P. Wolf
Bellerivestr. 36
CH-8022 Zurich
SWITZERLAND

Atomic Energy Establishment
Attn: Peter Barr
Winfrith
Dorchester Dorset
DT2 8DH
UNITED KINGDOM

Atomic Energy Authority
Safety and Reliability Directorate
Attn: D. W. Phillips (5 copies)
Wigshaw Lane, Culcheth
Warrington WA3 4NE
UNITED KINGDOM

HM Nuclear Installation Inspectorate
Attn: R. J. Stubbs
St. Peter's House, Stanley Precinct
Bootle L20 3LZ
UNITED KINGDOM

Taylor Woodrow Construction Limited
Attn: Carl Fleischer, Richard Crowder
(2 copies)
345 Ruislip Road
Southall, Middlesex
UB1 2QX
UNITED KINGDOM

Central Electricity Generating Board
Attn: J. Irving
Barnett Way
Barnwood, Gloucester
GL4 7RS
UNITED KINGDOM

Central Electricity Generating Board
Attn: Carl Lomas (5 copies)
Booths Hall
Chelford Road
Knutsford, Cheshire
WA16 8QG
UNITED KINGDOM

HM Nuclear Installations Inspectorate BrC
Attn: Peter Watson (5 copies)
St. Peter's House
Bootle, Mereyside L20 3LZ
UNITED KINGDOM

| | |
|---|---|
| 1521 | R. D. Krieg |
| 1521 | J. R. Weatherby |
| 3141 | S. A. Landenberger (5) |
| 3151 | W. I. Klein |
| 3153 | R. Gardner |
| 6500 | A. W. Snyder |
| 6510 | J. V. Walker |
| 6520 | D. L. Berry |
| 6521 | D. D. Carlson |
| 6522 | L. O. Cropp |
| 6523 | W. A. von Riesemann (26) |
| 6523 | D. B. Clauss |
| 6523 | R. N. Eyers |
| 6523 | D. S. Horschel |
| 6523 | L. D. Lambert |
| 6523 | J. S. Ludwigsen |
| 6523 | M. B. Parks |
| 6523 | J. J. Westmoreland |
| 6524 | W. R. Dawes, Jr. |
| 6525 | D. L. Berry, actg. |
| 8524 | J. A. Wackerly |

2. TITLE AND SUBTITLE

Round-Robin Analysis of the Behavior of a 1:6-Scale Reinforced Concrete Containment Model Pressurized to Failure: Posttest Evaluations

3. DATE REPORT PUBLISHED

| MONTH | YEAR |
|---|---|
| October | 1989 |

4. FIN OR GRANT NUMBER

FIN A1401

5. AUTHOR(S)

D. B. Clauss

6. TYPE OF REPORT

Topical

7. PERIOD COVERED *(Inclusive Dates)*

8. PERFORMING ORGANIZATION – NAME AND ADDRESS *(If NRC, provide Division, Office or Region, U.S. Nuclear Regulatory Commission, and mailing address; if contractor, provide name and mailing address.)*

Sandia National Laboratories
Albuquerque, NM 87185

9. SPONSORING ORGANIZATION – NAME AND ADDRESS *(If NRC, type "Same as above"; if contractor, provide NRC Division, Office or Region, U.S. Nuclear Regulatory Commission, and mailing address.)*

Division of Engineering
Office of Nuclear Regulatory Research
U.S. Nuclear Regulatory Commission
Washington, DC 20555

10. SUPPLEMENTARY NOTES

11. ABSTRACT *(200 words or less)*

In July 1987, a 1:6-scale model of a reinforced concrete containment building was pressurized incrementally to failure at a remote site at Sandia National Laboratories. The response of the model was recorded with more than 1000 channels of data (primarily strain and displacement measurements) at 37 discrete pressure levels. The primary objective of this test was to generate data that could be used to validate methods for predicting the performance of containment buildings subject to loads beyond their design basis.

Extensive analyses were conducted before the test to predict the behavior of the model. Ten organizations in Europe and the U.S. conducted independent analyses of the model and contributed to a report on the pretest predictions (NUREG/CR-4913). Predictions included structural response at certain predetermined locations in the model as well as capacity and failure mode.

This report discusses comparisons between the pretest predictions and the experimental results. Posttest evaluations that were conducted to provide additional insight into the model behavior are also described. The significance of the analysis and testing of the 1:6-scale model to performance evaluations of actual containments subject to beyond design basis loads is also discussed.

12. KEY WORDS/DESCRIPTORS *(List words or phrases that will assist researchers in locating the report.)*

concrete containment
containment model 1:6
containment integrity program

13. AVAILABILITY STATEMENT

Unlimited

14. SECURITY CLASSIFICATION

*(This Page)*

Unclassified

*(This Report)*

Unclassified

15. NUMBER OF PAGES

16. PRICE